Science of the Total Environment 864 (2023) 160879

Contents lists available at ScienceDirect

Science of the Total Environment

journal homepage: www.elsevier.com/locate/scitotenv

# Prediction of airborne pollen and sub-pollen particles for thunderstorm asthma outbreaks assessment

Slobodan Nickovic [a,b,*], Slavko Petković [b], Luka Ilić [a,1], Goran Pejanović [b], Zoran Mijić [a], Alfredo Huete [c], Guy Marks [d]

[a] Institute of Physics Belgrade, University of Belgrade, Pregrevica 118, 11080 Belgrade, Serbia
[b] Republic Hydrometeorological Service of Serbia, 11000 Belgrade, Serbia
[c] School of Life Sciences, University of Technology Sydney, Sydney, NSW, Australia
[d] University of New South Wales, Sydney, Australia

## HIGHLIGHTS

- A numerical model was used to predict extreme grass pollen events in Melbourne.
- Thunderstorm atmospheric conditions produce allergenic sub-pollen particles.
- Successful real-time numerical simulations of sub-pollen particles is demonstrated.
- Predicting sub-pollen particles could reduce thunderstorm asthma risks.
- The proposed model can be implemented for different regions and pollen types.

## GRAPHICAL ABSTRACT

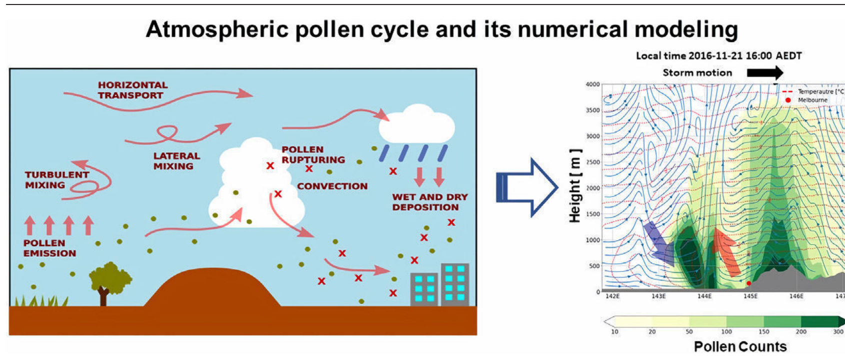


## ARTICLE INFO

Editor: Anastasia Paschalidou

*Keywords:*
Pollen numerical model
Particle rupturing
Extreme pollen episodes
Asthma epidemics

## ABSTRACT

When exposed to convective thunderstorm conditions, pollen grains can rupture and release large numbers of allergenic sub-pollen particles (SPPs). These sub-pollen particles easily enter deep into human lungs, causing an asthmatic response named thunderstorm asthma (TA). Up to now, efforts to numerically predict the airborne SPP process and to forecast the occurrence of TAs are unsatisfactory. To overcome this problem, we have developed a physically-based pollen model (DREAM-POLL) with parameterized formation of airborne SPPs caused by convective atmospheric conditions. We ran the model over the Southern Australian grass fields for 2010 and 2016 pollen seasons when four largest decadal TA epidemics happened in Melbourne. One of these TA events (in November 2016) was the worldwide most extreme one which resulted to nine deaths and hundreds of hospital patient presentations. By executing the model on a day-by-day basis in a hindcast real-time mode we predicted SPP peaks exclusively only when the four major TA outbreaks happened, thus achieving a high forecasting success rate. The proposed modelling system can be easily implemented for other geographical domains and for different pollen types.

## 1. Introduction

During the 1999–2016 grass pollen seasons (October–December), there were 17 severe thunderstorms associated with high number of asthma hospital presentations in Melbourne and regional Victoria, Australia (Bannister et al., 2021). These episodes were linked with heavy grass pollen loads originating from the neighbouring widespread grass pastures.

* Corresponding author at: Institute of Physics Belgrade, University of Belgrade, Pregrevica 118, 11080 Belgrade, Serbia.
*E-mail address:* nickovic@gmail.com (S. Nickovic).
[1] Now at Barcelona Supercomputing Center, Plaça Eusebi Güell, 1-3, 08034 Barcelona, Spain.

http://dx.doi.org/10.1016/j.scitotenv.2022.160879
Received 13 September 2022; Received in revised form 16 November 2022; Accepted 8 December 2022
Available online 12 December 2022

The epidemic of acute asthma attacks triggered by environmental conditions that can generate a high concentration of pollen ruptured fragments remaining in the air for several hours after a storm has passed are known as thunderstorm asthma (TA) events (D'Amato et al., 2016; Hughes et al., 2020).

During the globally most extreme Melbourne TA episode on 21 November 2016, large number of patients with breathing difficulties within a short time required medical help, thus causing extreme pressure on the city health system. This largest epidemic TA episode on record in Melbourne resulted in around 9900 patients' presentations at hospital emergency departments (AlQuran et al., 2021). Nine asthma-related deaths and almost 500 hospital admissions were recorded during the episode. The number of hospital visits increased by 992 % within 30 h (Thien et al., 2018). Three other Melbourne TA episodes during 2010–2016 occurred on 7, 12 and 25 November 2010, resulting to still considerable number of emergency admissions (Howden et al., 2011; Lindstrom et al., 2017; Report, 2017; Silver et al., 2018).

There is a close temporal link between the thunderstorm circulation, the increased pollen concentrations and the onset of the epidemic (Marks et al., 2001). The conceptual TA model of Taylor and Jonsson (2004) proposes that intact pollen grains entrained by updrafts into a thunderstorm are ruptured, thus releasing sub-pollen particles (SPPs) with up to a thousand allergenic particles released from a single intact grain. Released sub-pollen allergen-bearing cytoplasmic starch granules are small enough to deposit in the lower human airways, where they would have the potential to cause asthmatic responses in susceptible people. In Victoria (Australia), ryegrass (*Lolium perenne*) pollen is predominant (Thien et al., 2018) and its two most prevalent allergens are Lol p 1 and Lol p 5 (Hew et al., 2020; Suphioglu et al., 1992).

It is hypothesized that rupturing is caused by three combined effects within convective clouds: high humidity, lightning, and extreme upwind streams (Grundstein et al., 2017; Suphioglu et al., 1992; Taylor and Jonsson, 2004; Vaidyanathan et al., 2006; Visez et al., 2015). Thunderstorm downdrafts and outflows are assumed to bring these SPPs respirable allergens to ground level, thus increasing risks for TA epidemics (Taylor and Jonsson, 2004). Overall, TA epidemics can be generated if the following conditions exist: the presence of biological allergens such as grass pollen; the presence of small breathable particles formed from ruptured pollen in the convective atmosphere and brought to ground; and exposure of people predisposed to asthma symptoms caused by allergens (Marks and Bush, 2007).

Noting the lack of technological expertise capable to predict the catastrophic Melbourne November 2016 TA episode, the State of Victoria, Australia recommended development of a pollen forecasting model based on physical principles (Ebert et al., 2017; Management, 2017). In response to this request, the Victorian Department of Health and Human Services, in collaboration with the Bureau of Meteorology and research partners, proposed a TA forecasting system with the objective to issue early warnings for any future TA events (Bannister et al., 2021). The system uses a categorical risk-based approach and statistical forecasts of high ambient grass pollen concentrations which together generate the risk of epidemic thunderstorm asthma. After testing the proposed method in the hindcast mode and by correlating pollen data and data with hospital admissions, 13 out of 18 assessments of elevated TA risk were not related with high asthma hospital presentations. Thus, even when the synoptic situations indicate a probability for a TA, it often may not occur, resulting so to frequent false alarms.

An alternative to statistical models is the use of physically-based models in which the intact pollen concentration process is driven by numerical weather prediction parameters (Helbig et al., 2004; Luvall et al., 2013; Mahura et al., 2009; Pauling et al., 2019; Siljamo et al., 2013; Sofiev et al., 2013). If such models do not include formation and dispersion of allergenic SPPs, they cannot predict environmental conditions favourable for possible TA occurrences. Predictions of such models can therefore be used only as a proxy for possible asthma epidemic occurrence. The first pollen model with allergenic SPP formation parameterization has been developed (Wozniak et al., 2018) but used for pollen process studying, not for operational pollen prediction.

Numerical prediction of the whole grain pollen concentration is necessary but not sufficient condition for assessing the TAs occurrences. Current prognostic pollen models, statistical or physically based, either miss to indicate an incoming TA event or produce frequent false alarms. Recently developed physically based pollen model (Emmerson et al., 2021) has parameterized the SPPs production by mechanical wind force, high RH and lightning. This was for the first time to introduce SPPs concentration as a forecasting model parameter. Their tests however showed that humidity-induced rupturing did not produce expected peaks in pollen rupturing during the Melbourne 2016 TA episode and as stated by the authors, would likely lead to repeated false alarms if used in a predictive mode. Obviously, there is still missing successful forecasting tool to assess TAs occurrences based on modelled production of SPPs caused under favourable atmospheric conditions.

The objective of our study is to propose a novel numerical pollen model (furthermore referred as DREAM-POLL) capable to achieve a high success rate for assessing TA outbreaks using the predicted SPPs. In our model, the SPPs formation is made dependent on the convective conditions predicted by the atmospheric model which online drives the pollen process. The convection process involves extreme winds, lightning and elevated humidity, which are key mechanisms hypothesized to cause pollen rupturing (Taylor and Jonsson, 2004). Our choice to link convection conditions and production of allergenic SPPs is motivated by the fact that there is a high correlation between observed convergence lines (a precursor for convective storms) and the number of hospital asthma cases in Australia (Bannister et al., 2020): namely, 80 of 81 analysed hospital cases were exposed to convergence lines during the Victorian grass pollen season from 2009 to 2017. Convergence lines in case of thunderstorms (also known as gust fronts) are boundary lines between the cooler down drafted air from a thunderstorm and the warmer air near the ground.

In this paper, the proposed numerical model predicts not only the airborne intact pollen process but also production and dispersion of allergenic SPPs released from ruptured pollen grains under thunderstorm atmospheric conditions. The model has been tested for 2010 and 2016 pollen seasons when four largest decadal TA epidemics happened in Melbourne, Australia.

## 2. Methodology

### 2.1. Model description

DREAM-POLL represents a version of the DREAM aerosol atmospheric model (Nickovic et al., 2001; Pejanovic et al., 2012; Vukovic et al., 2014) modified here to predict pollen concentration dispersion. DREAM-POLL mathematically describes all major phases of the airborne pollen cycle, including emission of intact pollen from surface sources, vertical and horizontal transport, turbulent mixing, wet and dry deposition, as well as the SPPs formation/dispersion.

DREAM-POLL is an Euler-type model in which the prognostic pollen concentration continuity equation is on-line embedded into the high-resolution non-hydrostatic weather prediction NCEP WRF-NMM model (Janjic et al., 2001). This online approach allows synchronous numerical processing of both atmospheric and pollen processes. Here, pollen concentration is considered as one of the WRF-NMM prognostic variable.

WRF-NMM uses the terrain-following hybrid pressure-sigma coordinate in the vertical. The large-scale transport is based on the horizontal advection numerical scheme which, preserves energy and enstrophy (Janjić, 1984). The WRF-NMM physical parameterization package contains: the Mellor-Yamada-Janjic turbulence parameterization scheme for turbulence in the planetary boundary layer and in the free atmosphere (Janjić, 1994); the Monin-Obukhov surface layer scheme combined with the viscous sublayer (Janjić, 1994); the LISS soil scheme (Vukovic et al., 2010); a grid-scale cloud and microphysics parameterization; the Betts-Miller-Janjic (BMJ) convective adjustment scheme (Janjić, 1994); the GFDL longwave and shortwave radiation package; the mass conservative positive-definite horizontal advection scheme for scalars (applied to pollen concentration as well) which suppresses formation of false concentration maxima and reduces to a minimum numerical dispersion (Janjic et al., 2009).

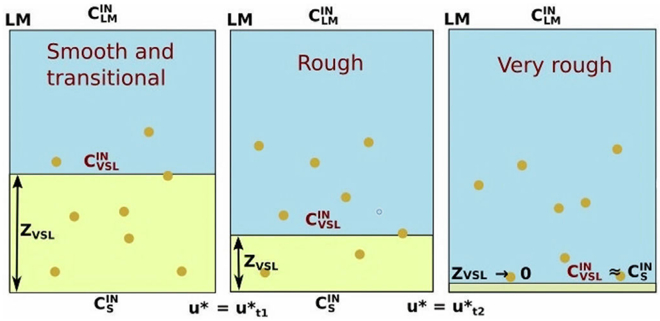


**Fig. 1.** Schematic description of the viscous sub-layer model (VSL). Emission under smooth and transitional regime happens for small $u_*$ when VSL is the thickest. In the rough mixing regime, the near-surface turbulence increases, and the VSL depth decreases. Under fully developed turbulent conditions (very rough regime), emission reaches its maximum, and VSL depth vanishes (Cvetkovic et al., 2022).

DREAM-POLL numerically simulates all major phases of intact, ruptured (empty shells) and SPPs pollen particles: the emission, horizontal and vertical turbulent mixing, long-range transport, and pollen wet and dry deposition. It includes gravitational settling, Brownian and turbulent deposition at the air-surface interface, and interception and impaction at surface roughness elements. The scheme accounts for properties of the depositing particles (size, density), the features of the depositing surfaces (roughness, land cover, land texture) and turbulent conditions in the lower atmosphere. The proposed pollen model is applicable to a pollen type for which the geographic distribution of pollinating plant fractions is available.

The pollen model numerically solves the following set of three pollen mass continuity equations:

$$\frac{\partial C_j}{\partial t} + DYN_j + \left(\frac{\partial C_j}{\partial t}\right)_{SOURCE} = 0 \quad j = 1, 2, 3 \tag{1}$$

Here, $C_1 = C^{IN}$, $C_2 = C^{RU}$ and $C_3 = C^{SP}$ are mass concentrations of intact, ruptured and SPPs pollen particles, respectively. The operator

$$\{DYN_j = u\frac{\partial C_j}{\partial x} + v\frac{\partial C_j}{\partial y} + \nabla_h(K_H\nabla_h C_j) + \frac{\partial}{\partial z}\left(K_V\frac{\partial C_j}{\partial z}\right) + (w - v_g)\frac{\partial C_j}{\partial z} + \left(\frac{\partial C_j}{\partial t}\right)_{SINK} = 0 \tag{2}$$

is the dynamic component of the continuity equation which is applied to the three particle types. Here: $u$, $v$ and $w$ are horizontal and vertical velocity components; $v_g$ is the Stokes gravitation settling velocity of pollen particles dependent on their sizes, shapes, and density; $\nabla_h$ is the horizontal gradient operator; $K_H$ and $K_V$ are the lateral and vertical mixing coefficients; subscripts *SOURCE* and *SINK* indicate sources and sinks of pollen particles.

The mass of a single pollen particle type $j$ (intact, ruptured or SPPs) for a given density $\rho_j$ and effective diameter $D_j$ is

$$m_j = \rho_j \times \left(\frac{1}{6}\pi D_j^3\right) \tag{3}$$

It is assumed that particles have a spherical shape. Using the aerodynamic parameters of pollen particles (see Supplemental Material) we convert in the further analysis their mass concentrations into grains per m$^3$.

The source term $\left(\frac{\partial C^{IN}}{\partial t}\right)_{SOURCE}$ in (1) calculates the emission of intact pollen grains from ground sources. The grains emission and its intensity depend on near-surface turbulent conditions involved in our emission scheme based on the viscous sublayer concept. A viscous sub-layer (VSL) with depth $z_{VSL}$ is inserted between the surface and the lowest model level to regulate the emission intensity, where $z_{VSL}$ varies with turbulence intensity (Janjic et al., 2001). VSL operates over three different regimes: smooth and transitional, rough, and very rough, as determined by

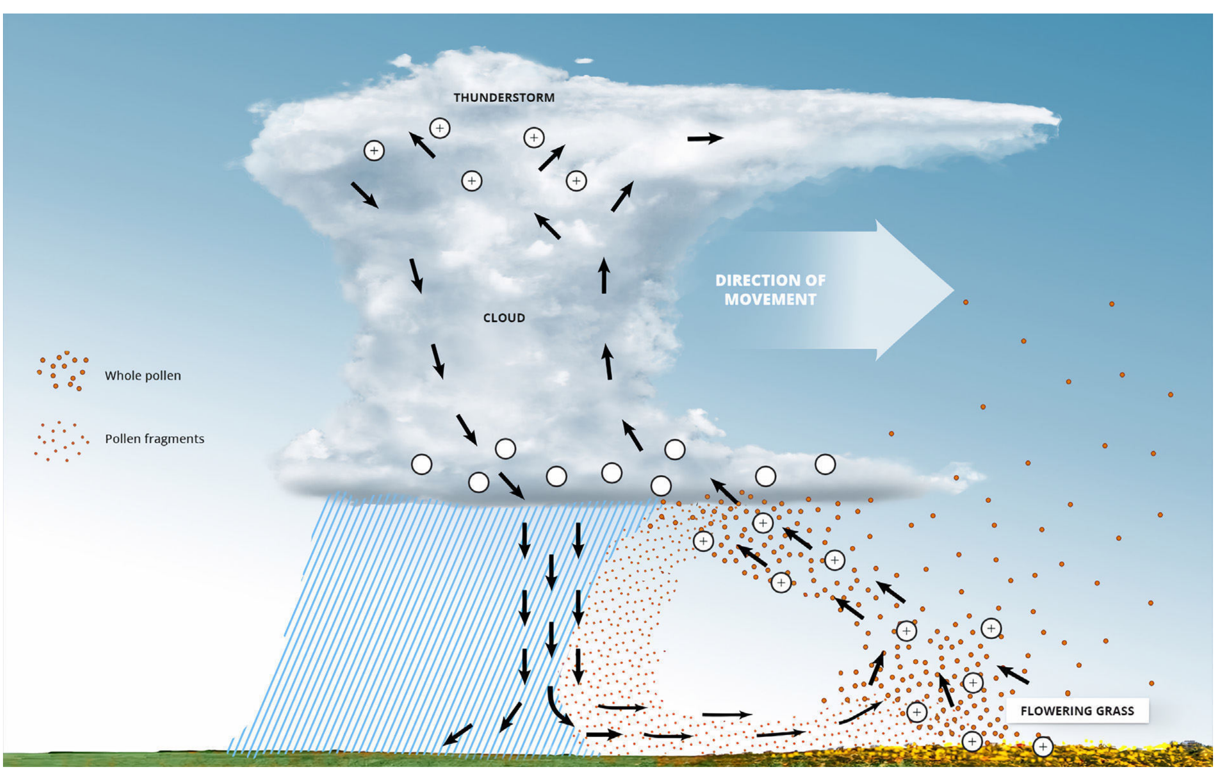


**Fig. 2.** Schematic representation of pollen rupturing under convective circulation. According to the Taylor-Jonsson hypothesis, intact pollen grains are lifted by convective updrafts and ruptured due to high humidity, wind force and electric charge effects in a thunderstorm cloud. Downdrafts then bring respirable allergenic pollen fragments to surface, according to (Cockcroft et al., 2018).

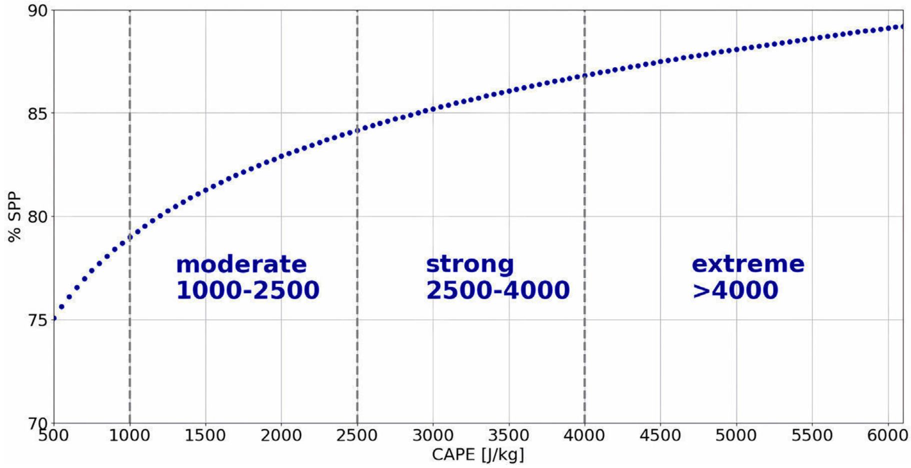


**Fig. 3.** Parameterization of SPPs production in the model. The percentage of intact pollen mass converted by convection to SPPs is proportional to CAPE.

corresponding friction velocity thresholds. When the very rough regime is achieved, VSL is completely ceased, and the emission is fully driven by turbulence of the free atmosphere (Fig. 1). The concentration emission flux is expressed in terms of the viscous sub-layer parameters by

$$F_S = \nu \frac{C_{VSL}^{IN} - C_S^{IN}}{z_{VSL}} \tag{4}$$

Here, $\nu$ is the air laminar viscosity, $C_S^{IN}$ and $C_{VSL}^{IN}$ are concentrations at the surface and at the top of VSL, respectively. The lower concentration boundary condition in the model is:

$$C_{VSL}^{IN} = \frac{C_S^{IN} + \omega C_{LM}^{IN}}{1 + \omega} \tag{5}$$

which is a weighted mean of $C_S^{IN}$ and the concentration at the lowest model level $C_{LM}^{IN}$. The weighting factor $\omega$ depends on turbulent and laminar mixing

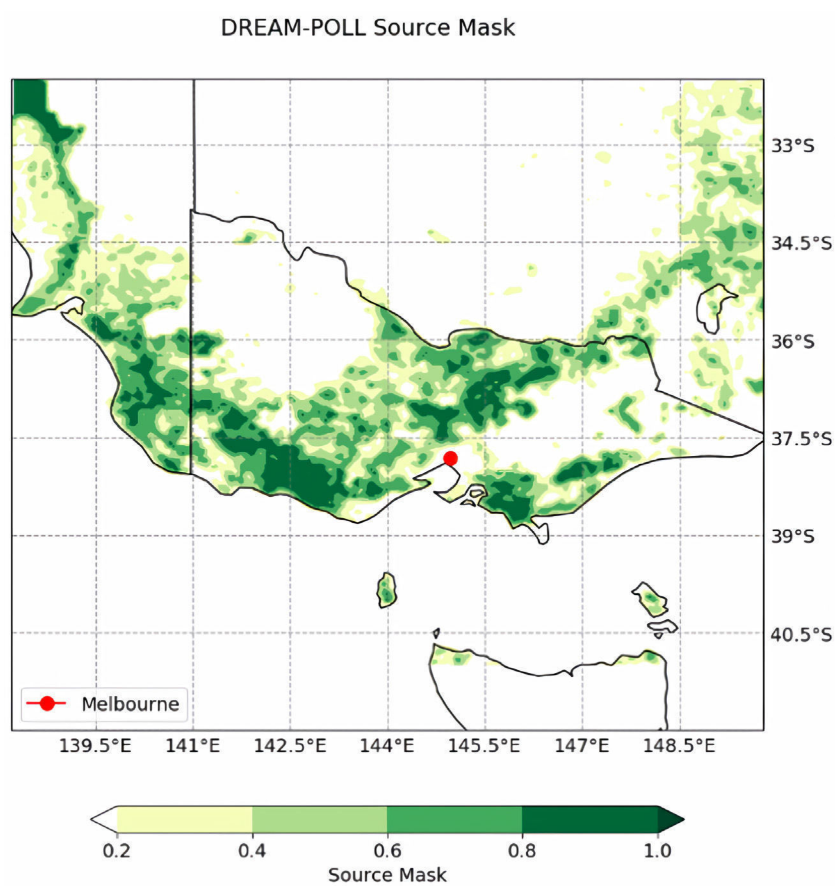


**Fig. 4.** Grass pollen fields designated as sources in our modelling experiments. Pasture grass fraction coverage over the State of Victoria in southeast Australia used as a pollen source map in the model. The 50-m resolution Australian Land Use and Management (ALUM) classification data (ABARES, 2017) was used to specify the grass fraction used in the model as potential pollen sources. The ALUM classes “Grazing modified pastures”, “Native/exotic pasture mosaic” and “Grazing irrigated modified pastures” were considered as grass fields (Emmerson et al., 2019).

**Table 1**
Pollen intrusions during Novembers of 2010 and 2016 which caused increased hospital admissions in Melbourne and Victoria hospitals. Shaded rows indicate occurrence of the major TA episodes. Intact pollen concentrations observed in Melbourne are shown as well.

| Date | Asthma-related Melbourne hospital admissions (per 24h)[1,2,3,] | Asthma-related hospital admissions for all Victorian, Bolded numbers: > 110 hospital admissions. Source: (Fig. 59 in Report, 2017)[2] | Observed intact pollen daily-averaged concentrations in Melbourne[2] $[m^{-3}]$ | Character of the episode |
|---|---|---|---|---|
| 7 Nov 2010 | n/a | **115** | 39 | Pollen intrusion; reported as a major TA episode |
| 13 Nov 2010 | 71[3] | **130** | 24 | Pollen intrusion; reported as a major TA episode |
| 17 Nov 2010 | n/a | 72 | 87 | Pollen intrusion; not reported as TA episode |
| 22 Nov 2010 | n/a | 77 | 117 | Pollen intrusion; not reported as TA episode |
| 24-25 Nov 2010 | 144 [2,3] | **210** | 56 | Pollen intrusion; reported as a major TA episode |
| 04 Nov 2016 | n/a | 90 | 129 | Pollen intrusion; not reported as TA episode |
| 07 Nov 2016 | n/a | 105 | 154 | Pollen intrusion; not reported as TA episode |
| 12-13 Nov 2016 | n/a | 75 | 129 | Pollen intrusion; not reported as TA episode |
| 17-18 Nov 2016 | n/a | 62 | 68 | Pollen intrusion; not reported as TA episode |
| 21 Nov 2016 | 380 [1,2*] | **500** | 102 | Pollen intrusion; reported as a major TA episode |

(*)The value is extrapolated from the 30 h hospital admission number.
(1)(Lindstrom et al., 2017).
(2)(Report, 2017).
(3)(Silver et al., 2018).

features. $C_S^{IN}$ is a power function of the friction velocity $u_*$ and of its threshold value $u_{*t}$ above which emission begins (Nickovic et al., 2001):

$$C_S^{IN} \sim u^2 \left[1 - \left(\frac{u_{*t}}{u_*}\right)^2\right] \ for \ u_* > u_{*t} \tag{6}$$

### 2.2. SPPs parametrization

We propose here a numerical parameterization scheme for SPPs formation from whole grains following the Taylor-Jonsson conceptual TA model (Taylor and Jonsson, 2004). This concept assumes that pollen rupturing is caused by the combined effects of convective thunderstorm conditions characterized with high humidity, extreme velocities, and electric forces (Fig. 2).

We calculate the amount of SPPs produced from intact pollen grains which are ruptured by the influence of the convective available potential energy (CAPE). CAPE is a parameter predicted by the atmospheric model driver. The recently proposed TA risk warning system for Victoria (Bannister et al., 2021), uses a version of CAPE to diagnose if a thunderstorm environment is favourable for pollen rupturing.

CAPE [$Jkg^{-1}$] describes the overall convective features of thunderstorms and it is defined as the vertically integrated air buoyancy:

$$CAPE = \int_{LCL}^{EL} g \frac{T - T'}{T} dz \tag{7}$$

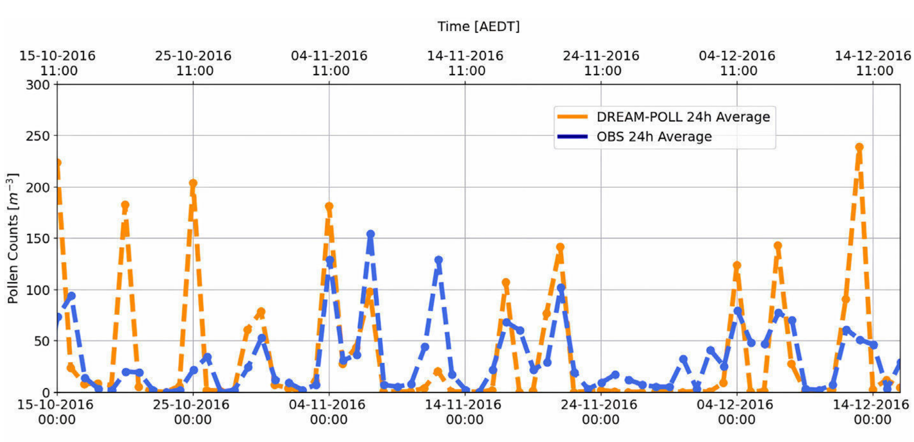


**Fig. 5.** Observed and modelled intact pollen concentrations for the period 15 October to 15 December 2016. Observations are collected at Melbourne University pollen count site (Parkville).

Here, $g$ is the gravity acceleration; $T$ and $T'$ are temperature of the air parcel and temperature of the surrounding air, respectively; LCL is the lifting condensation level (the bottom of the convection cloud) at which an unsaturated air parcel reaches its relative humidity 100 %; EL is the level at which the air parcel becomes as cool as the environment (Bloch et al., 2019; Moncrieff and Miller, 1976). CAPE describes the convective environment characterized with high humidity, extreme velocities and lightning which are the key potential triggers for pollen rupturing according to the Taylor-Jonsson hypothesis. CAPE is also closely linked to the moisture-dependent deep convection parameterization scheme in DREAM-POLL (Janjić, 1994). According to the US National Weather Service convection classification (https://www.weather.gov/lmk/indices#), weak, moderate, very unstable and extremely unstable convective conditions are respectively characterized with CAPE < 1000, 1000 < CAPE < 2500, 2500 < CAPE < 3500 and 3500 < CAPE < 4000 $Jkg^{-1}$. The maximum vertical velocity in convective clouds is calculated as $w_{\max} \approx \sqrt{2CAPE}$ (Cecil et al., 2014) where, for example, for CAPE = 1500 $Jkg^{-1}$, the vertical velocity could reach 55 $ms^{-1}$. The lightning intensity in convective clouds is also associate with CAPE (Cecil et al., 2014).

We parameterize the amount of convectively generated *SPPs* as a function of CAPE (Fig. 3):

$$\%SPPs = 0 \text{ for } CAPE \leq 500\,Jkg^{-1}$$

$$\%SPPs = \alpha + [\beta \times \log_{10}(CAPE)] \text{ for } CAPE > 500\,Jkg^{-1} \quad (8)$$

Here: %*SPPs* is the percentage the intact pollen mass converted by convection to *SPPs*; $\alpha = 40$ and $\beta = 13$ proposed here are tuneable parameters.

The model starts emitting pollen from a pre-specified surface sources when the near-ground turbulence exceeds a threshold. The emitted pollen is further transported by turbulence mixing and large-scale dynamics of the atmospheric model driver. At the end of their atmospheric cycle, pollen particles are settled to the ground by precipitation and near-surface dynamics as predicted by the atmospheric driver.

In our pollen rupturing parameterization, we calculate at every model time step the fragmented mass of sub-pollen particles released from ruptured pollen grains whenever CAPE predicted by the driver atmospheric model exceeds a pre-specified threshold (Eq. (8)). The intact, the ruptured, and the fragmented particles are driven by the model atmospheric dynamics, where the intact pollen particles are emitted from the ground, and the other two particle categories originate from a ruptured grain.

According to (Suphioglu et al., 1992) about 700 SPPs are realised from a single intact pollen in the model, and 70 % of pollen grains exposed to convection are ruptured (Wozniak et al., 2018), see Supplemental Material.

The overall mass of the emitted pollen is conserved during the model integration. Mass, diameter, and density of the three pollen particle types determine their aerodynamical behaviour. Specification of aerodynamic parameters of particle categories used in the model are given in the Supplemental Material.

Release of respirable-sized pollen allergens into the air has been also recorded for other pollens (e.g., birch and *Artemisia vulgaris*) and in other parts of the world (Burkart et al., 2021; Hoidn et al., 2005; Robichaud, 2021; Taylor et al., 2004; Taylor et al., 2002). For instance, the SPPs production from birch pollen involves a rupturing mechanism similar to that found in grasses (Grote et al., 2000; Taylor et al., 2004). Therefore, the proposed methodology can be applicable to other pollen types as well but including corresponding aerodynamical features (such as particle size, density, etc.).

### 2.3. Model setup

The major pollen-related input to the model is the geographical distribution of potential sources. A significant source of released allergenic pollen over the Southern Australia covered by the model domain is the non-native ryegrass (*Lolium perennial*), causing high rates of asthma in the population every pollen season (Suphioglu et al., 1992; Taylor and Jonsson, 2004). Geographical distribution of grass pollen sources is specified using the Australian Land Use and Management (ALUM) 50 m gridded data (ABARES, 2017). ALUM includes 193 land cover categories, of which "Grazing modified pastures", "Native/exotic pasture mosaic" and "Grazing irrigated modified pastures" are used to represent all grass pollen sources (Emmerson et al., 2021). Fractional coverage of these three classes together is shown in Fig. 4. Other grass types existing in the region (e.g., wheat and barley) are not considered as pollen sources since they are self-pollinating cultures which have minor contribution to the airborne pollen (Emmerson et al., 2021). The pollen fraction in the model grid box is calculated as a mean value of ALUM fractions belonging to this grid box. Intensity of the pollen emission in the model is made depended on near surface turbulent conditions.

The pollen advection and lateral diffusion are computed every 35 s, the emission and vertical diffusion are updated every 70 s, and the convection and large-scale precipitation are calculated every 140 s.

The model was run over the periods of 15 October–15 December 2010 and 2016. The initial and boundary conditions for the atmospheric model component were specified using weather prediction parameters of the European Centre for Medium-range Weather Forecast (ECMWF) global model. Since there are no satisfactory three-dimensional pollen concentration observations to be assimilated, the initial state of pollen concentration in the model was defined by the 24-h forecast from the previous day model run. Only for the "cold start" of the model at 15 October 2010 and 2016, the initial pollen concentrations were set to zero.

The model domain covers southeast Australia. Its spatial resolution is set to 28 model levels in the vertical spanning from the surface to 50 hPa. The horizontal grid distance is set to 1/20°, which is equivalent to a resolution of approximately 5 km. At this resolution, the model can spin-up severe convective systems (Janjic et al., 2005) and thus describe effects of thunderstorm conditions to the pollen airborne process (Grundstein et al., 2017). DREAM-POLL atmospheric initial and boundary conditions are specified using archived 10 km gridded global forecasts of ECMWF. The periods 15 October–15 December of 2010 and 2016 of our model experiment are characterized with the highest probability for high pollen concentrations, as shown (Fig. S2 in (Emmerson et al., 2019)). During these periods, four major Melbourne TAs were recorded (TA07NOV10, TA13NOV10, TA24NOV10 and TA21NOV16) (Cockcroft et al., 2018; Kevat, 2020; Lindstrom et al., 2017; Report, 2017; Silver et al., 2018). The model was run in a day-by-day hindcast mode, to emulate a real-time forecasting operation. Using the aerodynamic parameters of pollen particles (see Supplemental Material) we convert in the further analysis their mass concentrations into grains per $m^3$.

## 3. Results and discussion

Although rarely occurring, Melbourne TA epidemics have significant impact to public health. Between 1984 and 2016, the city experienced at least six thunderstorm asthma events (Silver et al., 2018), all of them occurred in November. During 2010–2016, four of these TAs resulting in

**Fig. 6.** Environmental conditions during thunderstorm asthma events. Table columns correspond to TA07NOV10, TA13NOV10, TA24NOV10, and TA21NOV16, respectively. A1–A4: Synoptic mean-sea level maps. B1–B4: radar images asthma events show convective activity at approximate times of TAs. C1–C4: SPPs ($1E^{-3}$ × grains $m^{-3}$) surface concentration (yellow-to-green palette); Red squares are approximate areas of radar images. D1–D4: Horizontal wind convergence (red palette) and predicted intact pollen concentration (grains $m^{-3}$) (yellow-to-green palette); NW-SE red dashed lines are fitted to points of maximum horizontal convergence to indicate the position of the front; Red squares are approximate areas of radar images; Orange dashed lines are perpendicular to the front crosses Melbourne and lies in the approximate direction of the front movement. E1–E4: Vertical cross sections along the normal to the front with pollen concentration in grains $m^{-3}$ (yellow-to-green palette), and velocity streamlines (blue lines) and temperature (red dashed lines); Melbourne location is a red dot in each panel; blue and red arrows indicate prevailing down- and up-draft circulations.

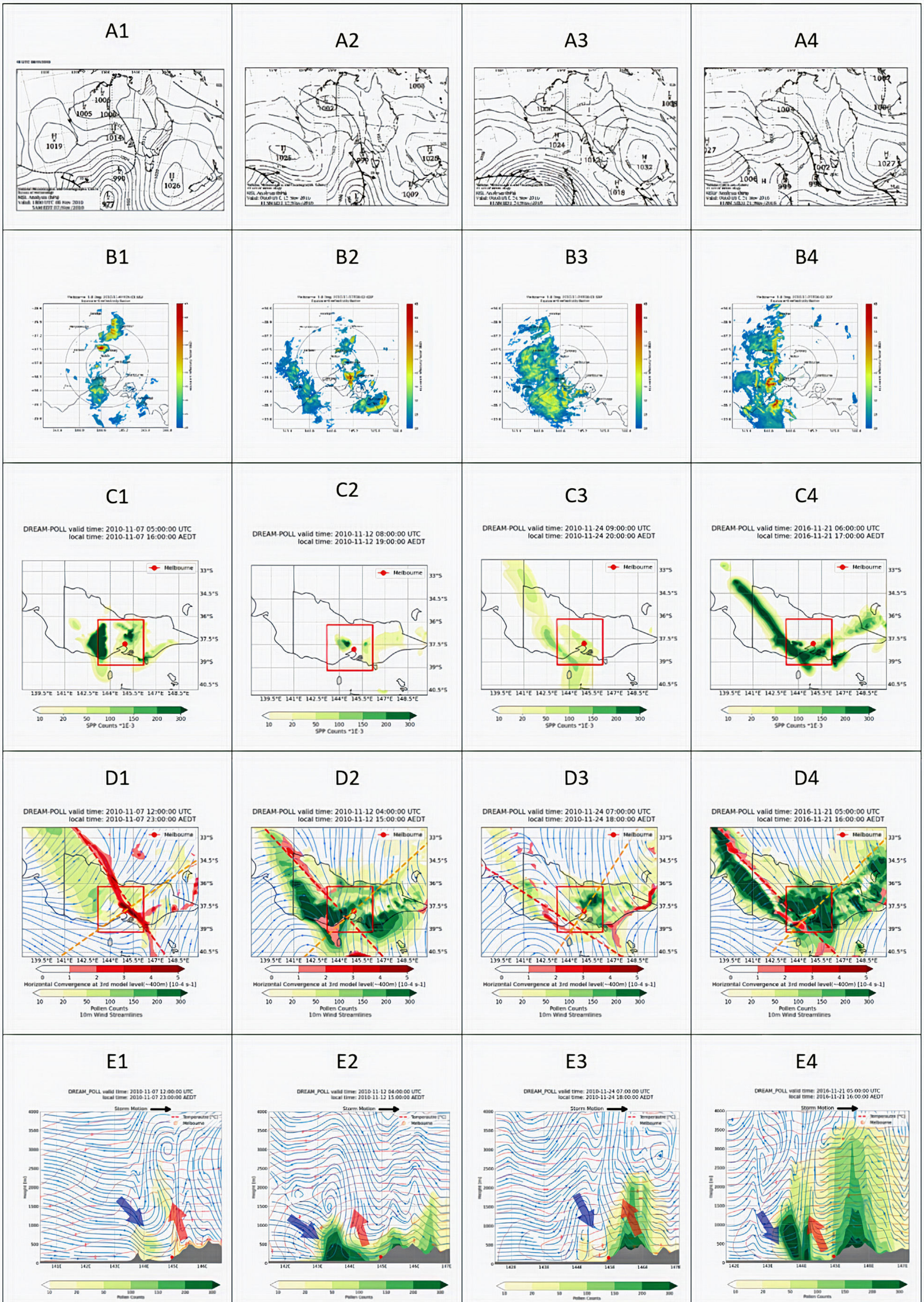

A1
A2
A3
A4
B1
B2
B3
B4
C1
DREAM-POLL valid time: 2010-11-07 05:00:00 UTC
local time: 2010-11-07 16:00:00 AEDT
C2
DREAM-POLL valid time: 2010-11-12 08:00:00 UTC
local time: 2010-11-12 19:00:00 AEDT
C3
DREAM-POLL valid time: 2010-11-24 09:00:00 UTC
local time: 2010-11-24 20:00:00 AEDT
C4
DREAM-POLL valid time: 2016-11-21 06:00:00 UTC
local time: 2016-11-21 17:00:00 AEDT
Melbourne
SPP Counts *1E-3
D1
DREAM-POLL valid time: 2010-11-07 12:00:00 UTC
local time: 2010-11-07 23:00:00 AEDT
D2
DREAM-POLL valid time: 2010-11-12 04:00:00 UTC
local time: 2010-11-12 15:00:00 AEDT
D3
DREAM-POLL valid time: 2010-11-24 07:00:00 UTC
local time: 2010-11-24 18:00:00 AEDT
D4
DREAM-POLL valid time: 2016-11-21 05:00:00 UTC
local time: 2016-11-21 16:00:00 AEDT
Horizontal Convergence at 3rd model level(~400m) [10-4 s-1]
Pollen Counts
10m Wind Streamlines
E1
E2
E3
E4
Storm Motion

high hospital presentations are recorded by medical authorities, happening on: 7 November 2010, 12–13 November 2010, 24 November 2010 and 21–22 November 2016 (Table 1) (Cockcroft et al., 2018; Howden et al., 2011; Kevat, 2020; Report, 2017; Silver et al., 2018). These episodes are onwards referenced as TA07NOV10, TA13NOV10, TA24NOV10 and TA21NOV16. TA21NOV16 was the worldwide most extreme event ever occurred, causing nine fatalities (Lindstrom et al., 2017). During these TA events, there were 115, 130, 210 and 500 asthma-related hospital admissions within 24 h, respectively, according to the evidence for all Victorian hospitals - Fig. 59 in (Report, 2017) (Table 1). Each TA event was accompanied with grass pollen intrusions and thunderstorms, coinciding with severe asthma epidemics (Report, 2017). However, many other high pollen intrusions occurred during the pollen season which did not trigger TAs. For example, there were two major pollen intrusions in 2010 and four in 2016 seasons (Table 1) causing no TAs. Obviously, the elevated intact pollen concentration is a necessary but not sufficient condition for TA outbreaks. For example, DREAM-POLL has predicted most of the observed intact pollen peaks in Melbourne during 15 October–15 December 2016 (Fig. 5), but only once, on 21 November, TA occurred. Therefore, a TA warning system based only on predicting intact pollen concentration can lead to frequent false alarms.

DREAM-POLL numerical experiment is used here to explore its capability to predict environmental conditions responsible for provoking Melbourne thunderstorm asthma episodes.

There are several similarities characterizing all four TA episodes. First, during each episode there were large-scale anticyclones on both sides of the Australian lateral coasts, accompanied with low-pressure troughs in between passing over Melbourne (Fig. 6.A1–A4). Radar observations diagnosed convective instability in the wider Melbourne region during afternoon/evening hours of each considered TA event (Fig. 6.B1–B4). For TA13NOV10, there were two lines on 12 Nov 2010 during the late afternoon. The first thunderstorm outflow reached the eastern suburbs of Melbourne, and then about an hour later, a more synoptically-driven convergence line moved over the whole Melbourne city area (Bannister, personal communication). For TA24NOV10, a convergence line moved eastwards across Melbourne in early evening (Bannister, idem); the storm front reached Melbourne around 20:00 AEDT (AEDT - Australian Eastern Daylight Time is the local time, equal to UTC + 11:00). On 21 November 2016 a multi-cell thunderstorm squall-line was passing the city area between 17:00 and 18:30 AEDT.

The simulated surface patterns of SPPs at the times of their arrivals to the city are shown in Fig. 6.C1–C4. Fig. 6.D1–D4, presenting the modelled intact pollen and the surface horizontal wind convergence (indicated by lines separating the warmer and colder air). The squall lines observed by radars correlate with the TA occurrences (Bannister et al., 2021). Another commonalty for the considered TAs is that pollen patterns are always transported to Melbourne from western or south-western directions.

There are also notable similarities in the vertical pollen dynamics as well. The emitted intact pollen is first lifted by warm updrafts to zones of the convection (Fig. 6.E1–E4), then ruptured there, after what SPPs are transported to the surface by cold downdrafts behind the squall line. Such atmospheric circulation patterns typical for convective storms (Laing, 2003) are reproduced by the model as well. Time evaluation of meteorological and pollen parameters during 1–21 November 2016 is shown in the animated gif (Supplement Video).

The 24-hour evolution of the predicted intact pollen concentration and SPPs for days of TAs occurrence in Melbourne is shown in Fig. 7. Having smaller size, SPPs have longer atmospheric lifetimes than intact pollen and stay airborne for longer a time before reaching the surface (Hughes et al., 2020). This can explain why SPP spikes here always develop with a

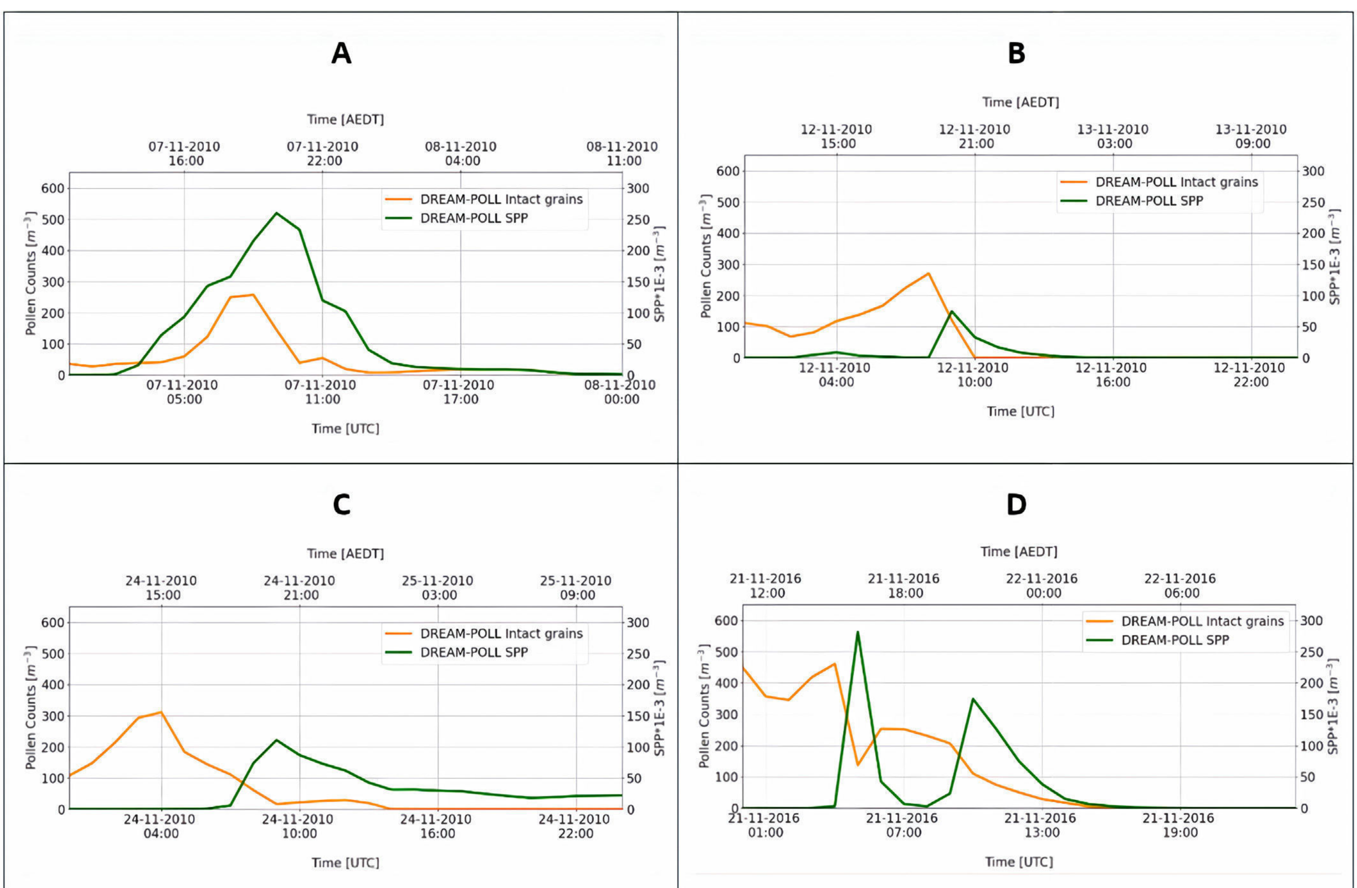


**Fig. 7.** A–C: Predicted hourly SPPs ($1E^{-3} \times$ grains $m^{-3}$) and intact (grains $m^{-3}$) pollen concentrations in Melbourne, for TA07NOV10, TA13NOV10, TA24NOV10 and TA21NOV16 TAs.

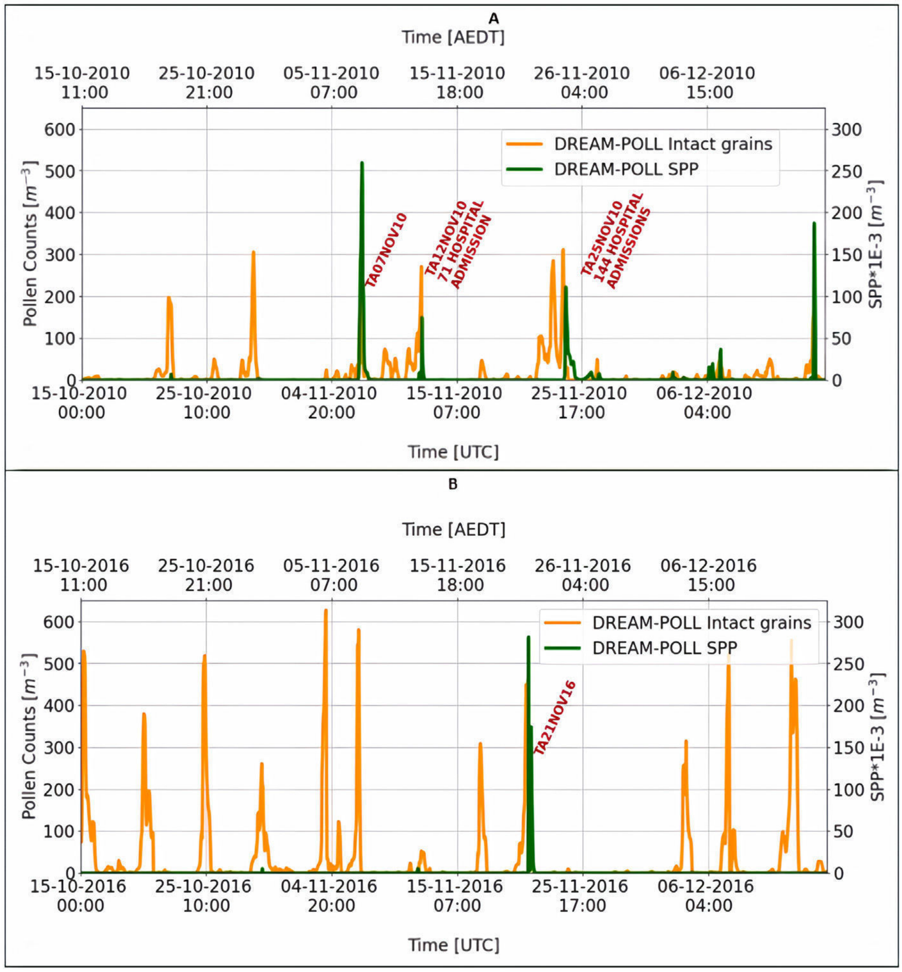


**Fig. 8.** Temporal variation of predicted hourly intact (grains $m^{-3}$) and SPPs ($1E^{-3}$ × grains $m^{-3}$) pollen concentrations for Melbourne. A: Period 15 October–15 December 2010; B: Period 15 October–15 December 2016.

delay of a few hours after the achieved intact pollen maxima. As a result, intact/SPP concentrations decrease/increase before/after the storm passages during the considered TAs (Fig. 7).

Verification of predicted SPPs is difficult since there are no routine daily measurements of SPPs and will unlikely be soon possible (Bannister et al., 2021). We therefore indirectly validate predicted SPPs against hospital data during the Melbourne TA events. During TA13NOV10, the SPPs maximum is predicted at 16:00. The hospital asthma presentation data show that the main 24-hour spike was from noon 12 November to noon 13 November, although two Melbourne hospitals were still spiked on 13–14 November (Bannister, personal communication). For TA25NOV10, the storm reached Melbourne around 20:00 AEDT 24 November 2010; during this event, most of the hospital admissions were recorded the following day (Silver et al., 2018). For TA21NOV16, two SPPs maxima predicted at 16:00 and 21:00 AEDT could contribute to prolonged exposure of the population to allergenic particles, thus casing extreme hospital acceptances. The predicted SPP spike concentrations for TA07NOV10, TA13NOV10, TA25NOV10 and TA21NOV16 are 259.650, 74.677, 110.979, and 281.334 grains $m^{-3}$, respectively. These values are within the lower end of observed ranges (Hughes et al., 2020; Suphioglu et al., 1992).

In our study we have performed a hard testing of DREAM-POLL, running it over 2010 and 2016 Australian grass pollen seasons during which the four largest Melbourne asthma episodes occurred (Fig. 8). As shown, many modelled intact pollen intrusions did not coincide with TA events. At the same time, SPP spikes are always predicted for each of the four major Melbourne TAs. Over the total of 60 successive days of the model run, there is only one SPP maximum on 14 December 2010 which might be considered as a false alarm. For this particular event we did not find medical evidence if there was an increased number of hospital visits.

The presented results show that the model has very high probability of detecting TAs (high hit rate) using the numerical parameterization of SPPs as a predictor.

## 4. Conclusions

Despite many efforts, there is not yet an available system in the community to accurately predict rarely-occurring but dangerous thunderstorm asthma events during pollen seasons. The main deficiency of pollen prognostic models is that they either frequently produce false alarms or do not predict TA events at all. To overcome these predictive limitations, we proposed here a physically based numerical pollen model which includes SPPs as a prognostic parameter. SPPs formation is parameterized as a function of atmospheric convection, following the Taylor-Jonsson TA conceptual model (Taylor and Jonsson, 2004). We ran DREAM-POLL in a day-by-day hindcast manner over two grass pollen seasons 15 October–15 December 2010 and 2016 in SE Australia. During these periods, the four largest decadal thunderstorm asthma episodes seriously affected Melbourne. During 60 recurring daily model runs, SPPs spikes coincided with all four major Melbourne TAs. Otherwise, for remaining 55 days SPPs concentrations were negligible except for a SPP peak on 14 December 2010 for which we did not have access to TA medical evidence. We could therefore consider this case as a possible but not confirmed false alarm.

We consider that the following components of DREAM-POLL are essential for its successful performance:

- *high horizontal and vertical model grid spacing used*; with this, convective and non-hydrostatic processes responsible for thunderstorm developments and SPPs formation are reasonable well resolved (Janjic et al., 2005);
- *SPPs and intact pollen concentrations are embedded as prognostic parameters into the atmospheric model driver*; this provides updates of pollen parameters by atmospheric fields at every model time step;
- *SPPs formation is parameterized as a function of convective instability*; with this approach, pollen rupturing is implicitly affected by thunderstorm high moisture, and by strong electric and wind forces, according to the Taylor-Jonsson TA hypotheses (Taylor and Jonsson, 2004).

Our results contrast with the results presented in (Emmerson et al., 2021) which are failing to predict the Melbourne 21 November TA. We believe that the following factors may have contributed to the successful outcome of our model: pollen concentrations are online driven in our system by predicted atmospheric parameters; our parameterization of the SPPs formation is strongly connected with the modelled convection conditions.

The high success rate of our model, to our knowledge, demonstrates for the first time in the community that TA occurrences can be predicted when appropriate numerical SPP representation is included in pollen modelling systems.

More field and laboratory measurements of SPPs, including their allergen contents (Grote et al., 2000; Mampage et al., 2022) should improve understanding of their airborne dynamics, and thus supporting better parameterization and prediction of rupturing process in pollen models. In addition, although the model reasonably predicted the temporal dynamics of intact pollens, a future study should include data from larger number of measurement sites and for more pollen seasons in order to further validate and improve the model.

Supplementary data to this article can be found online at https://doi.org/10.1016/j.scitotenv.2022.160879.

## CRediT authorship contribution statement

SN: development of the intact pollen model component, draft writing; SP: development of the of SPPs parameterization, setting up aerosol aerodynamic features, performing model experiments; LI: model validation; presentation of model results, results interpretation; GP: setting the atmospheric model, interpretation of results; ZM: results interpretation, validation, contribution to manuscript writing; AH: manuscript writing and conclusions, providing local observations; GM: contribution to specification of Thunderstorm Asthma conceptual model.

## Data availability

All model data generated in this study are available on request in a binary numerical format. The gridded pasture grass fraction coverage data used in the study is also available on request.

## Declaration of competing interest

The authors declare no competing interests.

## Acknowledgements

The authors acknowledge Prof. Ed Newbigin (the University of Melbourne, Australia) for supplying the pollen observation data. Tony Bannister (Australian Bureau of Meteorology, Victoria, Australia) helped for retrieving radar images and synoptic maps. The European Centre for Medium-Range Forecasting (ECMWF) forecasts are used for atmospheric initial and boundary conditions in DREAM-POLL. LI and ZM acknowledge funding provided by the Institute of Physics Belgrade, through a grant by the Ministry of Education, Science and Technological Development of the Republic of Serbia. Partial support has also been provided by the Republic Hydrometeorological Service of Serbia. The model experiments were performed using the computer facilities of the ECMWF and of the Institute of Physics Belgrade, Serbia. The authors acknowledge Bojan Spasojevic (VoodooFox, http://flatvoxel.com) for drawing Fig. 2.

## References

ABARES, 2017. Catchment Scale Land Use of Australia - Update September 2017 Australian Bureau of Agriculture and Resource Economics and Sciences. https://data.gov.au/data/dataset/c128490d-fb8f-49eb-9757-3ca1350b87c8.

AlQuran, A., Batra, M., Harry Susanto, N., Holland, A.E., Davies, J.M., Erbas, B., Lampugnani, E.R., 2021. Community response to the impact of thunderstorm asthma using smart technology. Allergy Rhinol. (Providence) 12. https://doi.org/10.1177/21526567211010728 21526567211010728.

Bannister, T., Csutoros, D., Arnold, A.-L., Black, J., Feren, G., Russell, R., Watson, A., Williams, S., Silver, J.D., Hughes, N., 2020. Are convergence lines associated with high asthma presentation days? A case-control study in Melbourne, Australia. Sci. Total Environ. 737, 140263. https://doi.org/10.1016/j.scitotenv.2020.140263.

Bannister, T., Ebert, E.E., Williams, T., Douglas, P., Wain, A., Carroll, M., Silver, J., Newbigin, E., Lampugnani, E.R., Hughes, N., Looker, C., Mulvenna, V., Csutoros, D., Jones, P.J., Davies, J.M., Suphioglu, C., Beggs, P.J., Emmerson, K.M., Huete, A., Nguyen, H., 2021. A pilot forecasting system for epidemic thunderstorm asthma in southeastern Australia. Bull. Am. Meteorol. Soc. 102 (2), E399–E420. https://doi.org/10.1175/bams-d-19-0140.1.

Bloch, C., Knuteson, R.O., Gambacorta, A., Nalli, N.R., Gartzke, J., Zhou, L., 2019. Near-real-time surface-based CAPE from merged hyperspectral IR satellite sounder and surface Meteorological Station data. J. Appl. Meteorol. Climatol. 58 (8), 1613–1632. https://doi.org/10.1175/JAMC-D-18-0155.1.

Burkart, J., Gratzl, J., Seifried, T.M., Bieber, P., Grothe, H., 2021. Isolation of subpollen particles (SPPs) of birch: SPPs are potential carriers of ice nucleating macromolecules. Biogeosciences 18 (20), 5751–5765. https://doi.org/10.5194/bg-18-5751-2021.

Cecil, D.J., Buechler, D.E., Blakeslee, R.J., 2014. Gridded lightning climatology from TRMM-LIS and OTD: dataset description. Atmos. Res. 135–136, 404–414. https://doi.org/10.1016/j.atmosres.2012.06.028.

Cockcroft, D.W., Davis, B.E., Blais, C.M., 2018. Thunderstorm asthma: an allergen-induced early asthmatic response. Ann. Allergy Asthma Immunol. 120 (2), 120–123. https://doi.org/10.1016/j.anai.2017.12.002.

Cvetkovic, B., Dagsson-Waldhauserová, P., Petkovic, S., Arnalds, Ó., Madonna, F., Proestakis, E., Gkikas, A., Vimic, A.V., Pejanovic, G., Rosoldi, M., Ceburnis, D., Amiridis, V., Lisá, L., Nickovic, S., Nikolic, J., 2022. Fully dynamic high-–resolution model for dispersion of icelandic airborne mineral dust. Atmosphere 13 (9), 1345. https://www.mdpi.com/2073-4433/13/9/1345.

D'Amato, G., Vitale, C., D'Amato, M., Cecchi, L., Liccardi, G., Molino, A., Vatrella, A., Sanduzzi, A., Maesano, C., Annesi-Maesano, I., 2016. Thunderstorm-related asthma: what happens and why. Clin. Exp. Allergy 46 (3), 390–396. https://doi.org/10.1111/cea.12709.

Ebert, E.E., Bannister, T., Silver, J., Csutoros, D., Carroll, M., Dampf, R., Davies, J., Emmerson, K., Grant, I., Huete, A., Looker, C., Mitchell, T., Nguyen, H., Sims, H., Wain, A., Williams, T., 2017. Thunderstorm asthma – challenges in predicting a rare event. CAWCR 11th Annual Workshop, Adding Value: Applications of Weather and Climate Services, Melbourne, Victoria.

Emmerson, K.M., Silver, J.D., Newbigin, E., Lampugnani, E.R., Suphioglu, C., Wain, A., Ebert, E., 2019. Development and evaluation of pollen source methodologies for the Victorian Grass Pollen Emissions Module VGPEM1.0. Geosci. Model Dev. 12 (6), 2195–2214. https://doi.org/10.5194/gmd-12-2195-2019.

Emmerson, K.M., Silver, J.D., Thatcher, M., Wain, A., Jones, P.J., Dowdy, A., Newbigin, E.J., Picking, B.W., Choi, J., Ebert, E., Bannister, T., 2021. Atmospheric modelling of grass pollen rupturing mechanisms for thunderstorm asthma prediction. PLoS One 16 (4), e0249488. https://doi.org/10.1371/journal.pone.0249488.

Grote, M., Vrtala, S., Niederberger, V., Valenta, R., Reichelt, R., 2000. Expulsion of allergen-containing materials from hydrated rye grass (Lolium perenne) pollen revealed by using immunogold field emission scanning and transmission electron microscopy. J. Allergy Clin. Immunol. 105 (6 Pt 1), 1140–1145. https://doi.org/10.1067/mai.2000.107044.

Grundstein, A., Shepherd, M., Miller, P., Sarnat, S.E., 2017. The role of mesoscale-convective processes in explaining the 21 November 2016 epidemic thunderstorm asthma event in Melbourne, Australia. J. Appl. Meteorol. Climatol. 56 (5), 1337–1343. https://www.jstor.org/stable/26179935.

Helbig, N., Vogel, B., Vogel, H., Fiedler, F., 2004. Numerical modelling of pollen dispersion on the regional scale. Aerobiologia 20 (1), 3–19. https://doi.org/10.1023/B:AERO.0000022984.51588.30.

Hew, M., Lee, J., Varese, N., Aui, P.M., McKenzie, C.I., Wines, B.D., Aumann, H., Rolland, J.M., Mark Hogarth, P., van Zelm, M.C., O'Hehir, R.E., 2020. Epidemic thunderstorm asthma susceptibility from sensitization to ryegrass (Lolium perenne) pollen and major allergen Lol p 5. Allergy 75 (9), 2369–2372. https://doi.org/10.1111/all.14319.

Hoidn, C., Puchner, E., Pertl, H., Holztrattner, E., Obermeyer, G., 2005. Nondiffusional release of allergens from pollen grains of Artemisia vulgaris and Lilium longiflorum depends mainly on the type of the allergen. Int. Arch. Allergy Immunol. 137 (1), 27–36. https://doi.org/10.1159/000084610.

Howden, M.L., McDonald, C.F., Sutherland, M.F., 2011. Thunderstorm asthma–a timely reminder. Med. J. Aust. 195 (9), 512–513. https://doi.org/10.5694/mja11.11044.

Hughes, D.D., Mampage, C.B.A., Jones, L.M., Liu, Z., Stone, E.A., 2020. Characterization of atmospheric pollen fragments during springtime thunderstorms. Environ. Sci. Technol. Lett. 7 (6), 409–414. https://doi.org/10.1021/acs.estlett.0c00213.

Janjic, Z., Black, T., Pyle, M., Rogers, E., Chuang, H.Y., DiMego, G., 2005. High resolution applications of the WRF NMM. 21st Conference on Weather Analysis and Forecasting, Washington DC.

Janjic, Z., Huang, H., Lu, S., 2009. A unified atmospheric model suitable for studying transport of mineral aerosols from meso to global scales. IOP Conf. Ser.: Earth Environ. Sci. 7, 012011. https://doi.org/10.1088/1755-1307/7/1/012011.

Janjić, Z.I., 1984. Nonlinear advection schemes and energy cascade on semi-staggered grids. Mon. Weather Rev. 112 (6), 1234–1245.

Janjić, Z.I., 1994. The step-mountain eta coordinate model: further developments of the convection, viscous sublayer, and turbulence closure schemes. Mon. Weather Rev. 122 (5), 927–945.

Janjic, Z.I., Gerrity, J.P., Nickovic, S., 2001. An alternative approach to nonhydrostatic modeling. Mon. Weather Rev. 129 (5), 1164–1178.

Kevat, A., 2020. Thunderstorm asthma: looking back and looking forward. J. Asthma Allergy 13, 293–299. https://doi.org/10.2147/JAA.S265697.

Laing, A.G., 2003. Mesoscale meteorology|Mesoscale convective systems. In: Holton, J.R. (Ed.), Encyclopedia of Atmospheric Sciences. Academic Press, pp. 1251–1261 https://doi.org/10.1016/B0-12-227090-8/00216-5.

Lindstrom, S.J., Silver, J.D., Sutherland, M.F., Treloar, A.B., Newbigin, E., McDonald, C.F., Douglass, J.A., 2017. Thunderstorm asthma outbreak of November 2016: a natural disaster requiring planning. Med. J. Aust. 207 (6), 235–237. https://doi.org/10.5694/mja17.00285.

Luvall, J.C., Sprigg, W.A., Levetin, E., Huete, A., Nickovic, S., Prasad, A., Pejanovic, G., Vukovic, A., de Water, P.Van, Budge, A.M., Hudspeth, W., Krapfl, H., Toth, B., Zelicoff, A., Myers, O., Bunderson, L., Ponce-Campos, G., Crimmins, T.M., Menache, M., Vujadinovic, M., 2013. Use of MODIS Satellite Data to Evaluate Juniperus spp. Pollen Phenology to Support a Pollen Dispersal Model, DREAM-POLL, to Support Public Health Allergy Alerts Earth Observation Systems and Applications for Public Health Models and Decisions 93rd American Meteorological Society Annual Meeting, Austin, TX.

Mahura, A., Baklanov, A., Korsholm, U., 2009. Parameterization of the birch pollen diurnal cycle. Aerobiologia 25 (4), 203–208. https://doi.org/10.1007/s10453-009-9125-7.

Mampage, C.B.A., Hughes, D.D., Jones, L.M., Metwali, N., Thorne, P.S., Stone, E.A., 2022. Characterization of sub-pollen particles in size-resolved atmospheric aerosol using chemical tracers. Atmos. Environ. X 15. https://doi.org/10.1016/j.aeaoa.2022.100177.

Management, I.-G.F.E., 2017. Review of response to the thunderstorm asthma event of 21–22 November 2016. V. S. Government. https://content.health.vic.gov.au/sites/default/files/migrated/files/collections/research-and-reports/t/thunderstorm-asthma-igem-review-final-report-april-2017.pdf.

Marks, G.B., Bush, R.K., 2007. It's blowing in the wind: new insights into thunderstorm-related asthma. J. Allergy Clin. Immunol. 120 (3), 530–532. https://doi.org/10.1016/j.jaci.2007.07.012.

Marks, G.B., Colquhoun, J.R., Girgis, S.T., Koski, M.H., Treloar, A.B., Hansen, P., Downs, S.H., Car, N.G., 2001. Thunderstorm outflows preceding epidemics of asthma during spring and summer. Thorax 56 (6), 468–471. https://doi.org/10.1136/thorax.56.6.468.

Moncrieff, M.W., Miller, M.J., 1976. The dynamics and simulation of tropical cumulonimbus and squall-lines. Q. J. R. Meteorol. Soc. 102, 373–394. https://doi.org/10.1002/qj.49710243208.

Nickovic, S., Kallos, G., Papadopoulos, A., Kakaliagou, O., 2001. A model for prediction of desert dust cycle in the atmosphere. J. Geophys. Res. Atmos. 106 (D16), 18113–18129. https://doi.org/10.1029/2000jd900794.

Pauling, A., Clot, B., Menzel, A., Jung, S., 2019. Pollen forecasts in complex topography: two case studies from the Alps using the numerical pollen forecast model COSMO-ART. Aerobiologia 36 (1), 25–30. https://doi.org/10.1007/s10453-019-09590-2.

Pejanovic, G.N.S., Petkovic, S., Vukovic, A., Djurdjevic, V., Vujadinovic, M., Dacic, M., 2012. Dust Operational Forecast System With Assimilation of Dust Analysed Data Regional Conference on Dust and Dust Storms, Kuwait.

Report, T.C.H.O.S., 2017. The November 2016 Victorian epidemic thunderstorm asthma event_ an assessment of the health impacts. t. V. Government. https://content.health.vic.gov.au/sites/default/files/migrated/files/collections/research-and-reports/t/thunderstorm-asthma-health-impact-2017-pdf.pdf.

Robichaud, A., 2021. A case study of birch pollen and the synergy with environmental factors: relation to asthma in Montreal, Canada. Atmosphere 12 (6).

Siljamo, P., Sofiev, M., Filatova, E., Grewling, L., Jager, S., Khoreva, E., Linkosalo, T., Ortega Jimenez, S., Ranta, H., Rantio-Lehtimaki, A., Svetlov, A., Veriankaite, L., Yakovleva, E., Kukkonen, J., 2013. A numerical model of birch pollen emission and dispersion in the atmosphere. Model evaluation and sensitivity analysis. Int. J. Biometeorol. 57 (1), 125–136. https://doi.org/10.1007/s00484-012-0539-5.

Silver, J.D., Sutherland, M.F., Johnston, F.H., Lampugnani, E.R., McCarthy, M.A., Jacobs, S.J., Pezza, A.B., Newbigin, E.J., 2018. Seasonal asthma in Melbourne, Australia, and some observations on the occurrence of thunderstorm asthma and its predictability. PLoS One 13 (4), e0194929. https://doi.org/10.1371/journal.pone.0194929.

Sofiev, M., Siljamo, P., Ranta, H., Linkosalo, T., Jaeger, S., Rasmussen, A., Rantio-Lehtimaki, A., Severova, E., Kukkonen, J., 2013. A numerical model of birch pollen emission and dispersion in the atmosphere. Description of the emission module. Int. J. Biometeorol. 57 (1), 45–58. https://doi.org/10.1007/s00484-012-0532-z.

Suphioglu, C., Singh, M.B., Taylor, P., Knox, R.B., Bellomo, R., Holmes, P., Puy, R., 1992. Mechanism of grass-pollen-induced asthma. Lancet 339 (8793), 569–572. https://doi.org/10.1016/0140-6736(92)90864-Y.

Taylor, P.E., Flagan, R.C., Miguel, A.G., Valenta, R., Glovsky, M.M., 2004. Birch pollen rupture and the release of aerosols of respirable allergens. Clin. Exp. Allergy 34 (10), 1591–1596. https://doi.org/10.1111/j.1365-2222.2004.02078.x.

Taylor, P.E., Flagan, R.C., Valenta, R., Glovsky, M.M., 2002. Release of allergens as respirable aerosols: a link between grass pollen and asthma. J. Allergy Clin. Immunol. 109 (1), 51–56. https://doi.org/10.1067/mai.2002.120759.

Taylor, P.E., Jonsson, H., 2004. Thunderstorm asthma. Curr. Allergy Asthma Rep. 4 (5), 409–413. https://doi.org/10.1007/s11882-004-0092-3.

Thien, F., Beggs, P.J., Csutoros, D., Darvall, J., Hew, M., Davies, J.M., Bardin, P.G., Bannister, T., Barnes, S., Bellomo, R., Byrne, T., Casamento, A., Conron, M., Cross, A., Crosswell, A., Douglass, J.A., Durie, M., Dyett, J., Ebert, E., Guest, C., 2018. The Melbourne epidemic thunderstorm asthma event 2016: an investigation of environmental triggers, effect on health services, and patient risk factors. Lancet Planet. Health 2 (6), e255–e263. https://doi.org/10.1016/s2542-5196(18)30120-7.

Vaidyanathan, V., Miguel, A.G., Taylor, P.E., Flagan, R.C., Glovsky, M.M., 2006. Effects of electric fields on pollen rupture. J. Allergy Clin. Immunol. 117 (2). https://doi.org/10.1016/j.jaci.2005.12.625.

Visez, N., Chassard, G., Azarkan, N., Naas, O., Sénéchal, H., Sutra, J.-P., Poncet, P., Choël, M., 2015. Wind-induced mechanical rupture of birch pollen: potential implications for allergen dispersal. J. Aerosol Sci. 89, 77–84. https://doi.org/10.1016/j.jaerosci.2015.07.005.

Vukovic, A., Rajkovic, B., Janjic, Z., 2010. Land Ice Sea Surface Model: Short Description and Verification. International Congress on Environmental Modelling and Software Modelling for Environment's Sake, Ottawa.

Vukovic, A., Vujadinovic, M., Pejanovic, G., Andric, J., Kumjian, M.R., Djurdjevic, V., Dacic, M., Prasad, A.K., El-Askary, H.M., Paris, B.C., Petkovic, S., Nickovic, S., Sprigg, W.A., 2014. Numerical simulation of "an American haboob". Atmos. Chem. Phys. 14 (7), 3211–3230. https://doi.org/10.5194/acp-14-3211-2014.

Wozniak, M.C., Solmon, F., Steiner, A.L., 2018. Pollen rupture and its impact on precipitation in clean continental conditions. Geophys. Res. Lett. 45 (14), 7156–7164. https://doi.org/10.1029/2018gl077692.

## Supplementary Material

## Prediction of airborne pollen and sub-pollen particles for thunderstorm asthma outbreaks assessment

Slobodan Nickovic[1, 2], Slavko Petković[2], Luka Ilić[1, 3], Goran Pejanović[2], Zoran Mijić[1], Alfredo Huete[4] and Guy Marks[5]

[1]Institute of Physics Belgrade, University of Belgrade, Pregrevica 118, 11080 Belgrade, Serbia

[2]Republic Hydrometeorological Service of Serbia, 11000 Belgrade, Serbia

[3]now at Barcelona Supercomputing Center, Plaça Eusebi Güell, 1-3, 08034 Barcelona, Spain

[4]School of Life Sciences, University of Technology Sydney, Sydney, NSW, Australia

[5]University of New South Wales, Sidney, Australia

*Corresponding author: nickovic@gmail.com

**Particle aerodynamic parameters**

Values of the aerodynamic parameters are either predefined or evaluated.

1) The diameter of intact grains is set to $D^{IN} = 34.0\mu m$ which is within the observed range (Emmerson et al., 2019; Hughes et al., 2020; Suphioglu et al., 1992) (Jung et al., 2018; Rathnayake et al., 2017; Taylor et al., 2004)
2) The mass of an intact grain is set to $m^{IN} = 18.5ng$ which is within the observed range (Emmerson et al., 2019; Rathnayake et al., 2017; Taylor et al., 2004)
3) The density of an intact grain $\rho^{IN} = 899kgm^{-3}$ is calculated from Eq. (3) and is within the observed range (Emmerson et al., 2019)
4) The calculated number of intact grains per $\mu g$ is $N^{IN}$ $=54\mu g^{-1}$
5) 700 SPPs (sub-pollen particles) are released from each single ruptured grain (Suphioglu et al., 1992)
6) 70% of intact pollen mass is transferred to masses of pollen shell and SPPs: $m^{RU} + m^{SP} = A \times m^{IN}$ ; $A = 0.7$
7) The volume of a pollen shell is 90% of the intact grain volume
8) The diameter of a pollen shell $D^{RU} = 32.8\mu m$ is calculated from Eq. (3)
9) The density of a pollen shell $\rho^{RU} = 210kgm^{-3}$ is calculated from Eq. (3)
10) The mass of a ruptured particle is $m^{RU} = B \times \left(A \times m^{IN}\right) = B \times \left(m^{RU} + m^{SP}\right) = 3.89ng$ ; $B = 0.3$
11) The calculated number of pollen shell per $\mu g$ is $N^{RU}$ $=257\mu g^{-1}$
12) The density SPPs is set to $\rho^{SP} = \rho^{IN}$
13) The diameter of a single SPP $D^{SP} = 2.82\mu m$ which is within the observed range (Jung et al., 2018; Suphioglu et al., 1992; Taylor et al., 2004; Taylor & Jonsson, 2004)
14) The calculated mass of a single SPP is $m^{SP} = \left(1.0 - B\right) \times \left(A \times m^{IN}\right) = 0.013ng$, which is within the observed range (Jung et al., 2018; Schäppi et al., 1999)
15) The calculated number of released SPPs per $\mu g$ is $\boldsymbol{N^{SP} = 94371\ \mu g^{-1}}$

Values of the predefined and calculated particle aerodynamic parameters considered above are summarized in Table S1.

**Table S1.** Aerodynamic parameters of particles specified as predefined ($^{p}$) or evaluated ($^{e}$)

| Particle type | Aerodynamic diameter of a particle | Particle density | Mass per pollen grain | Number of pollen grains per $\mu g$ |
|---|---|---|---|---|
| Intact pollen | $D^{IN} = 34.0 \mu m$ $^{p}$ | $\rho^{IN} = 899 kgm^{-3}$ $^{e}$ | $m^{IN} = 18.5 ng$ $^{p}$ | $N^{IN} = 54 \mu g^{-1}$ $^{e}$ |
| Pollen shell | $D^{RU} = 32.8 \mu m$ $^{e}$ | $\rho^{RU} = 209.8 kgm^{-3}$ $^{e}$ | $m^{RU} = 3.89 ng$ $^{p}$ | $N^{RU} = 257 \mu g^{-1}$ $^{e}$ |
| SPPs | $D^{SP} = 2.82 \mu m$ $^{e}$ | $\rho^{SP} = 899 kgm^{-3}$ $^{p}$ | $m^{SP} = 0.01 ng$ $^{e}$ | $N^{SP} = 94371 \mu g^{-1}$ $^{e}$ |

IN - intact grain; RU - ruptured grain; SP - sub-pollen

## References


Emmerson, K. M., Silver, J. D., Newbigin, E., Lampugnani, E. R., Suphioglu, C., Wain, A., & Ebert, E. (2019). Development and evaluation of pollen source methodologies for the Victorian Grass Pollen Emissions Module VGPEM1.0. *Geoscientific Model Development*, *12*(6), 2195-2214. https://doi.org/10.5194/gmd-12-2195-2019

Hughes, D. D., Mampage, C. B. A., Jones, L. M., Liu, Z., & Stone, E. A. (2020). Characterization of Atmospheric Pollen Fragments during Springtime Thunderstorms. *Environmental Science & Technology Letters*, *7*(6), 409-414. https://doi.org/10.1021/acs.estlett.0c00213

Jung, S., Estrella, N., Pfaffl, M. W., Hartmann, S., Handelshauser, E., & Menzel, A. (2018). Grass pollen production and group V allergen content of agriculturally relevant species and cultivars. *PLoS One*, *13*(3), e0193958. https://doi.org/10.1371/journal.pone.0193958

Rathnayake, C. M., Metwali, N., Jayarathne, T., Kettler, J., Huang, Y., Thorne, P. S., O'Shaughnessy, P. T., & Stone, E. A. (2017). Influence of rain on the abundance of bioaerosols in fine and coarse particles. *Atmospheric Chemistry and Physics*, *17*(3), 2459-2475. https://doi.org/10.5194/acp-17-2459-2017

Schäppi, G. F., Taylor, P. E., Pain, M. C., Cameron, P. A., Dent, A. W., Staff, I. A., & Suphioglu, C. (1999). Concentrations of major grass group 5 allergens in pollen grains and atmospheric particles: implications for hay fever and allergic asthma sufferers sensitized to grass pollen allergens. *Clin Exp Allergy*, *29*(5), 633-641. https://doi.org/10.1046/j.1365-2222.1999.00567.x

Suphioglu, C., Singh, M. B., Taylor, P., Knox, R. B., Bellomo, R., Holmes, P., & Puy, R. (1992). Mechanism of grass-pollen-induced asthma. *The Lancet*, *339*(8793), 569-572. https://doi.org/10.1016/0140-6736(92)90864-Y

Taylor, P. E., Flagan, R. C., Miguel, A. G., Valenta, R., & Glovsky, M. M. (2004). Birch pollen rupture and the release of aerosols of respirable allergens. *Clin Exp Allergy*, *34*(10), 1591-1596. https://doi.org/10.1111/j.1365-2222.2004.02078.x

Taylor, P. E., & Jonsson, H. (2004). Thunderstorm asthma. *Current Allergy and Asthma Reports*, *4*(5), 409-413. https://doi.org/10.1007/s11882-004-0092-3

*remote sensing*

*Article*

# Impacts of Extreme Space Weather Events on September 6th, 2017 on Ionosphere and Primary Cosmic Rays

**Aleksandra Kolarski, Nikola Veselinović, Vladimir A. Srećković, Zoran Mijić *, Mihailo Savić and Aleksandar Dragić**

Institute of Physics Belgrade, University of Belgrade, Pregrevica 118, 11080 Belgrade, Serbia
* Correspondence: zoran.mijic@ipb.ac.rs; Tel.:+381-11-3713134

**Abstract:** The strongest X-class solar flare (SF) event in 24th solar cycle, X9.3, occurred on 6 September 2017, accompanied by earthward-directed coronal mass ejections (CMEs). Such space weather episodes are known to cause various threats to human activities ranging from radio communication and navigation disturbances including wave blackout to producing geomagnetic storms of different intensities. In this study, SFs' ionospheric impacts and effects of accompanied heliospheric disturbances on primary cosmic rays (CR) are investigated. This work offers the first detailed investigation of characteristics of these extreme events since they were inspected both from the perspective of their electromagnetic nature, through very low frequency (VLF) radio waves, and their corpuscular nature of CR by multi-instrumental approach. Aside data recorded by Belgrade VLF and CR stations, data from GOES and SOHO space probes were used for modeling and analysis. Conducted numerical simulations revealed a significant change of ionospheric parameters (sharpness and effective reflection height) and few orders of magnitude increase of electron density. We compared our findings with those existing in the literature regarding the ionospheric response and corresponding parameters. In addition, Forbush decrease (FD) magnitude, corrected for magnetospheric effect, derived from measurements, and one predicted from power exponents used to parametrize the shape of energetic proton fluence spectra at L1 were compared and found to be in good agreement. Presented findings could be useful for investigation of atmospheric plasma properties, particles' modeling, and prediction of extreme weather impacts on human activities.

**Keywords:** solar flares; coronal mass ejections; atmospheric ionization; sudden ionospheric disturbances; ionospheric parameters; solar energetic particles; secondary cosmic ray flux; Forbush decreases

check for updates

**Citation:** Kolarski, A.; Veselinović, N.; Srećković, V.A.; Mijić, Z.; Savić, M.; Dragić, A. Impacts of Extreme Space Weather Events on September 6th, 2017 on Ionosphere and Primary Cosmic Rays. *Remote Sens.* **2023**, *15*, 1403. https://doi.org/10.3390/rs15051403

Academic Editors: Dario Sabbagh and Saioa A. Campuzano

Received: 17 January 2023
Revised: 23 February 2023
Accepted: 28 February 2023
Published: 2 March 2023



## 1. Introduction

As an important aspect of space weather applications, ionospheric responses to intense solar flares (SFs) and coronal mass ejections (CMEs) have been investigated for several decades [1–3]. Short in duration but huge explosive events on the Sun release high-energy particles and intense broad range radiation influencing the state of the Earth's upper atmosphere. While enhanced EUV radiation disturbs E and F regions of the ionosphere, during solar flares, X-ray radiation can increase by several orders of magnitude and cause an extra ionization within the ionospheric D-layer [4,5]. The increase in the rate of change of atmospheric ionization depends on both the flare class and the rate of change in flare radiations [6]. For the investigation of D-region behavior, radio wave measurements at very low and low frequencies (VLF-LF) are widely used [7–9]. SFs have a direct radio wave interference effect on Global Navigation Satellite System (GNSS) transmission and other radio systems [10–12]. High-frequency (HF) radio wave blackout and magnetic field variation have also been documented and studied [11,13].

Solar activity can produce extreme phenomena which are more likely around the maximum of the 11-year cycle. One such type of events are SFs that are, in most cases, followed by CMEs [14]. CME releases a large-scale flux of charged particles from solar corona with an accompanying embedded magnetic field. This additional flux of charged particles emerging in interplanetary space is defined as interplanetary coronal mass ejection (ICME). When propagating with speed greater than magnetosonic wave speed (in solar wind reference frame), ICME can form a shock due to interaction with ambient solar wind. In situ measurements of the environment performed by space probes at different locations in the heliosphere can provide information about various solar weather parameters. They also include direct measurements of fast-moving energetic particles that can be in temporal correlation with CMEs and SFs [15]. These particles can originate from the Sun, in which case they are called solar energetic particles (SEPs) or can be accelerated locally by an ICME related shock when they are referred to as energetic storm particles (ESPs). Several space probes placed at Lagrange point 1 (L1) between the Sun and the Earth constantly monitor this flux, in addition to a number of probes at Earth's vicinity and elsewhere throughout the heliosphere [16]. Enhancement of interplanetary magnetic field (IMF) creates additional modulation of cosmic ray (CR) and can lead to one of the transient phenomena, Forbush decrease (FD). FD is a rapid depression of measured CR flux (typically occurring within a day), followed by a gradual recovery that can last for several days [17]. Correlation between FD parameters (magnitude of decrease, duration, time evolution) and various parameters of solar wind plasma have been studied in the past [18–20].

Extreme space weather events can have severe impacts on wide areas of human activities. Historically, such events are not very frequent, but the probability of their occurrence over the next decade is not negligible (i.e., for geomagnetic storms, it has been estimated to be about 12% [21]). Extreme events can cause significant damage to sensitive satellite components and increase absorbed radiation dose in space, which can pose a serious health hazard to astronauts. Energetic particle flux during extreme solar activity events is studied and different models of the space environment are proposed for forecasting schemes. Even though many studies have been carried out, still, only limited information is available on an approximate assessment of the direct impact such events can have on technological infrastructure and what the indirect associated expenses would be [22].

Study of ionospheric reaction to SFs is currently very relevant research, given the prospect of improving the capacity and reliability of anticipating space weather disturbances, which might affect the performance of a wide range of space-borne and ground-based technological systems and pose a danger to human health and safety [23,24].

The 24th solar cycle began in December 2008 and although approaching the solar minimum and the low solar activity, several strong SFs occurred in September 2017, including the X9.3 class flare, the strongest one in that cycle [25,26]. A lot of studies have been published analyzing different aspects of these extreme weather events. The SF effect on the chemical structure of the upper and middle atmosphere is reported in [27]. In the study presented in [28], the analysis of total electron content (TEC) and rate of change of TEC index to probe the storm-time ionospheric TEC irregularities in the Indian longitude sector during the space weather events of 6–10 September 2017 was presented. During the flares, the total radio fade-out in the range of 30 to 90 min at the Hermanus and Sao Luis ionosondes is reported [29]. It is also observed that SFs' effects on the ionosphere last longer than the effects on the Earth's magnetic field [30]. The effects of the strong X9.3 flare of 6 September 2017, following its impact on the ionosphere and the resulting difficulties for existing (e.g., precise positioning and GNSS navigation support services) and future technologies (e.g., autonomous car navigation) have been analyzed [10].

In this paper, X-class SFs of 6 September 2017 ionospheric impacts and the effects of accompanied heliospheric disturbances on primary cosmic rays are investigated. The atmospheric D-region parameters and electron density are obtained and analyzed along with various heliospheric parameters (associated with the accompanying ICME) measured in-situ at L1, as well as flux of secondary cosmic ray muons measured on the ground and shallow-underground levels. Since all empirical models are based upon data obtained through numerous studies, such as International Reference Ionosphere model [31], each case study of extreme weather events is of great significance, not only for the atmospheric plasma properties investigations, but also for the particles' modeling procedures. With that goal, modulation of ionosphere and CR flux by intense X-class SF events was investigated through a multi-instrumental approach, by employing space- and ground-based observations on one hand, and by conducting proposed numerical simulations on the other hand, using both original VLF and CR measurements (from the same location in Belgrade) as well as data and results from other observing stations worldwide. Through extensive comparison, noticed agreements and disagreements between results are highlighted as well.

## 2. Materials and Methods

Galactic cosmic rays interact with interplanetary magnetic fields as they traverse our solar system. IMF is a solar magnetic field carried by the solar wind, a stream of charged particles propagating outward from the Sun. Interaction of CRs with IMF modulates CR flux as is also evident from measurements of CR flux intensity with Earth-based CR detectors [32]. Galactic cosmic rays, upon reaching Earth, interact with atmospheric atoms and molecule nuclei, generating a shower of secondary particles. Secondary CRs vertical flux, at the bottom of the atmosphere (at atmospheric depth 1000 $gcm^{-2}$), for particles' energies larger than 1GeV, is composed mainly of muons ($\approx$90 $m^{-2}s^{-1}sr^{-1}$), protons and neutrons ($\approx$2 $m^{-2}s^{-1}sr^{-1}$), electrons and positrons ($\approx$0.2 $m^{-2}s^{-1}sr^{-1}$), and charged pions ($\approx$0.04 $m^{-2}s^{-1}sr^{-1}$) as well as neutrinos [33]. Observation of these secondary CRs can be conducted in the atmosphere, on the ground or even underground, detecting one or several different types of produced particles. A worldwide network of neutron monitors (NM) and ground detectors that detect hadronic components of secondary CRs have been in use for decades. NMs are sensitive to primary CRs with energies of about 0.5–20 GeV. Another type of widely used Earth-based CR detectors are muon monitors, focused on detecting the muon component of secondary CRs. Muon monitors are sensitive to higher energies of primary CRs, thus complementing NMs measurements [34].

Belgrade CRs station is a part of the Low-background Laboratory for Nuclear Physics (LBLNP) at the Institute of Physics Belgrade (IPB), Serbia. It has two identical detector set-ups placed on two different levels, one on ground level (GLL) and the other in shallow-underground (UL). Underground level is situated below 12 m of loess overburden (25-m water equivalent). This setup allows for monitoring of secondary CR's muons flux that originates from two different energy ranges under the same environmental conditions (such as geomagnetic location, atmospheric parameters, experimental setup). Altitude of the station is 78 m above sea level, with a geomagnetic latitude of 39°32′N. Relation between the measured count rate of these energy-integrating detectors with flux of primary CRs at the top of the atmosphere was found using a calculated detector yield function. Additionally, due to the sensitivity of secondary muons to varying properties of the atmosphere, which acts as a moderator, correction of measured flux for atmospheric pressure and variation of temperature throughout the whole atmospheric column from the top of the atmosphere to the ground is needed. Details of the detector systems and response function of Belgrade CR station acquired using Monte Carlo simulation of CR transport, along with the description and results of atmospheric and efficiency corrections are presented in [35,36].

For inspection of the Earth's lower ionospheric response to intense solar activity during events of energetic solar outbursts (such as SFs and CMEs) during the descending branch of the 24th solar cycle, as in September 2017, VLF radio signal registrations from Belgrade's (BEL; 44.85°N, 20.38°E) Absolute Phase and Amplitude Logger (AbsPAL) station database were used. This system is a part of the Laboratory for Astrophysics and Physics of Ionosphere at the IPB, Serbia. Numerical simulations conducted in this paper rely on application of the well known and widely exploited technique of Long Wavelength Propagation Capability (LWPC) software [37] utilization on one hand, based on hop wave theory and the ionospheric exponential model [38,39], and on the FlarED′ Method and Approximate Analytic Expression application [5,40] on the other hand: the novel approach based on retrieving ionospheric parameters directly from solar X-ray radiation spectral components of soft range. Here, novel approach is applied on two cases of SF events within the strongest X-class (the weaker X2.2 and stronger X9.3), making the validation of the proposed approximate method firmly applicable and reliable across the entire X-class range, in addition to some previous recent research all regarding cases of weaker X-class SFs from the lower section of X-class range [5,8,40]. The methodology used relies on simultaneous monitoring of several VLF signals during regular and irregular ionospheric conditions, both for amplitude and phase, and obtaining properties of perturbations directly from observed recorded VLF data, by signal values' comparison between unperturbed and perturbed states. The details are presented in Section 3.2 and Supplementary Material.

## 3. Results

### *3.1. Solar Energetic Particles and Secondary Cosmic Ray Flux during and after Intense SF Events*

The strongest flare of solar cycle 24 (classified as X9.3) happened in early September 2017 during the declining phase of this solar cycle. Active region AR12673 [41] was the cause of unusual and intensive solar activity. This region produced several more SFs around that time with the most intense one occurring on 6 September 2017. The flare was closely followed by a severe geomagnetic storm that began on 7 September. In total, four different possibly related CMEs erupted within several days. The first of these was a halo CME that happened on 4 September which, together with the second one, affected CR flux and produced an intense Forbush decrease on 7 September. Magnitude of FD for 10 GV rigidity primary CR corrected for magnetospheric effect ($M_M$) [18] was $-7.7\%$ (quoted from IZMIRAN database of FD parameters [42]).

Solar activity and the accompanying heliospheric disturbance during early September 2017 have been studied in detail in a number of published articles that indicate that successive CMEs between 4–6 September produced complex transients. Complex interactions caused by the passage of ICME are not so simple to model, one consequence being that it is not so straightforward to predict time of arrival of the disturbance on Earth [43]. However, in-situ measurements by space probes at L1 can help in this regard. Based on data from Solar and Heliospheric Observatory (SOHO)/Large Angle and Spectrometric Corona-graph (LASCO)/C2 [44] and analysis given in [45], the first CME from AR12673 with a moderate speed of approximately 710 kms$^{-1}$ appeared on 4 September followed by a much faster (approx. 1350 kms$^{-1}$) second CME. These two CMEs merged in lower solar corona into a single structure producing single shock followed by a prolonged sheath region which was detected at L1 on 6 September. The second shock arrived at L1 on 7 September as a result of CME that occurred on 6 September. This CME had a high velocity of 1480 kms$^{-1}$ and its eruption coincides with the X9.3 SF. This shock was followed by a turbulent sheath region and a magnetic cloud. One repository where such measurements can be found compiled in the form of low- and high-resolution OMNI data can be found at GSFC/Space Physics Data Facility [46]. Low-resolution OMNI data (used in this study) contains hourly values for various heliospheric and geomagnetic indices. One of the probes that monitors variation of energetic proton flux at L1 is the ERNE instrument onboard SOHO probe [47]. It consists of two separate particle detectors with complementing detector energy ranges (for lower and higher particle energies) and provides energetic particle flux measurements in 20 energy bins (ranging from 1.3 up to 130 MeV per nucleon) with a time resolution of one hour (data are available at [48]). Apart from providing insight into SF/CME/ICME induced disturbance in the heliosphere, measurements done by this instrument could be useful for predicting the effects that these phenomena have on cosmic rays, as some studies have shown [49]. Proton flux recorded during early September 2017 is showed in Figure 1 and Figures S1 and S2 in Supplementary Material. As it is often difficult to determine the acceleration mechanism related to violent events on the Sun (especially when accelerated particles are detected near Earth), for the sake of simplicity, going forward, we will refer to both solar energetic particles (accelerated near the Sun) and energetic storm particles (accelerated in interplanetary space) as SEP.

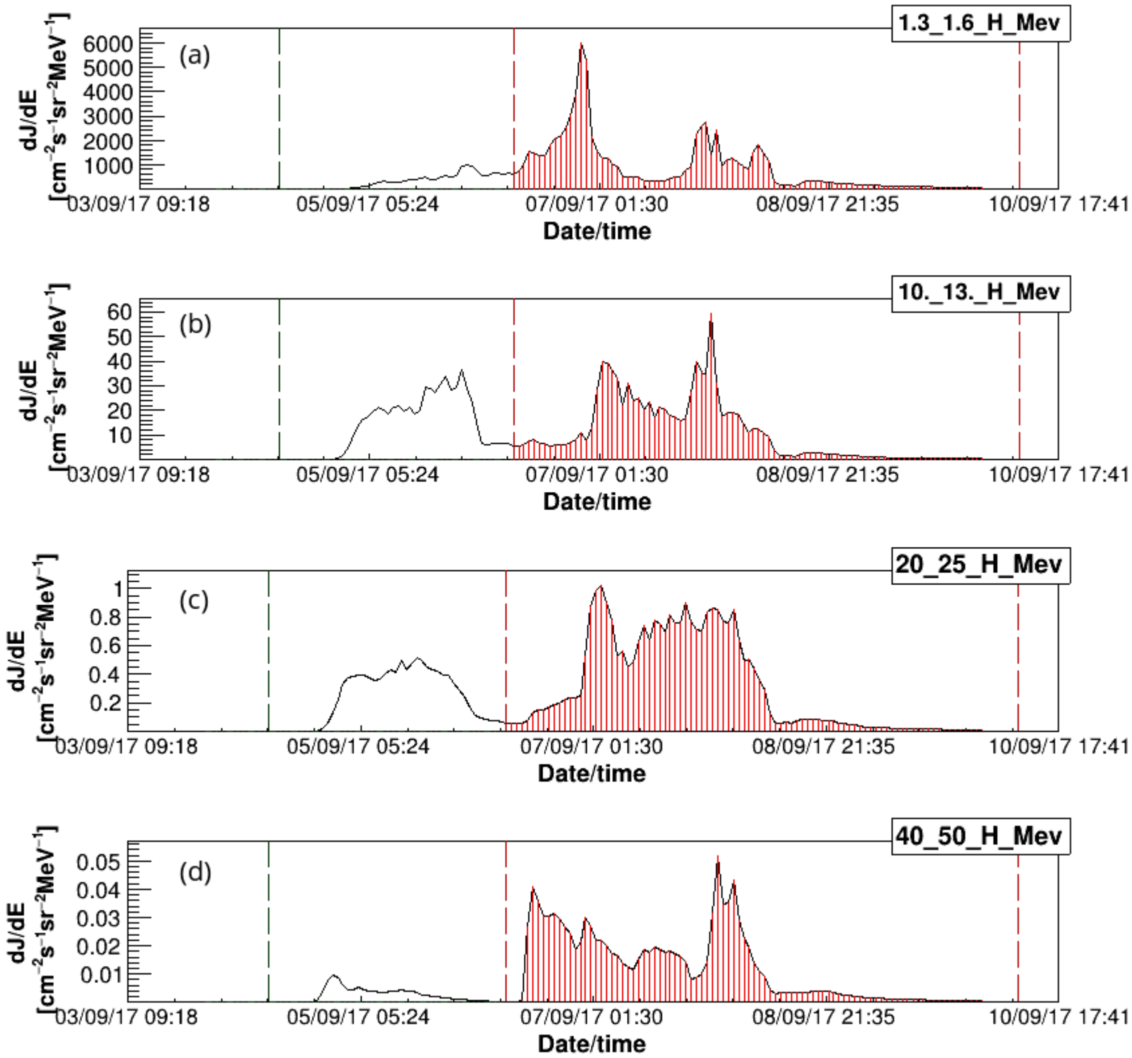


**Figure 1.** Hourly time series (UT) for several different proton channels from SOHO/ERNE ((**a**) 1.3–1.6 MeV, (**b**) 10–13 MeV, (**c**) 20–25 MeV, (**d**) 40–50 MeV channels' energy bands) for September 2017. Integration interval for spectral fluence is indicated with red vertical dashed lines.

In order to determine SEP fluence related to heliospheric disturbances and FD events during early September 2017, integration of SOHO/ERNE proton flux time series in separate energy channels is needed over the time period associated with a given FD event. Determination of this time period during complex solar activity in September 2017 is not simple or straightforward. Using procedures described in [36] that rely on the IZMIRAN database, as well as neutron monitor data and data measured at Belgrade muon station, we can determine optimal integration intervals more reliably.

Generally, SEP fluence spectrum exhibits a change of slope (sometimes referred to as a "knee"). Several different models are proposed to describe this characteristic shape [50–52]. We chose to use the double power law proposed in [53] given by Equation (1):

$$f(E) = \begin{cases} E^{-a} exp\left(-\frac{E}{E_k}\right), \; E < (b-a)E_k \\ E^{-b}[(b-a)E_k]^{b-a} exp(a-b), \; E > (b-a)E_k \end{cases} \quad (1)$$

where $E$ is the particle energy, $E_k$ is the "knee" energy (at which the break in the spectrum occurs), $a$ and $b$ are power exponents related to energy ranges below and above $E_k$, respectively. Exponents $a$ and $b$ are determined by fitting the proton fluence spectrum using Equation 1 and are used to parameterize its shape. $E_k$ is set as a fixed parameter and is determined from the known dependence of "knee" energy on integral fluence. More detailed description of the procedure can be found in [49]. The shape of fluence spectrum and fitted double power law for the September event are shown in Figure 2. Obtained values were −1.16 for exponent $a$ and −2.5 for exponent $b$ (taking 6.8 MeV as value for "knee" energy).

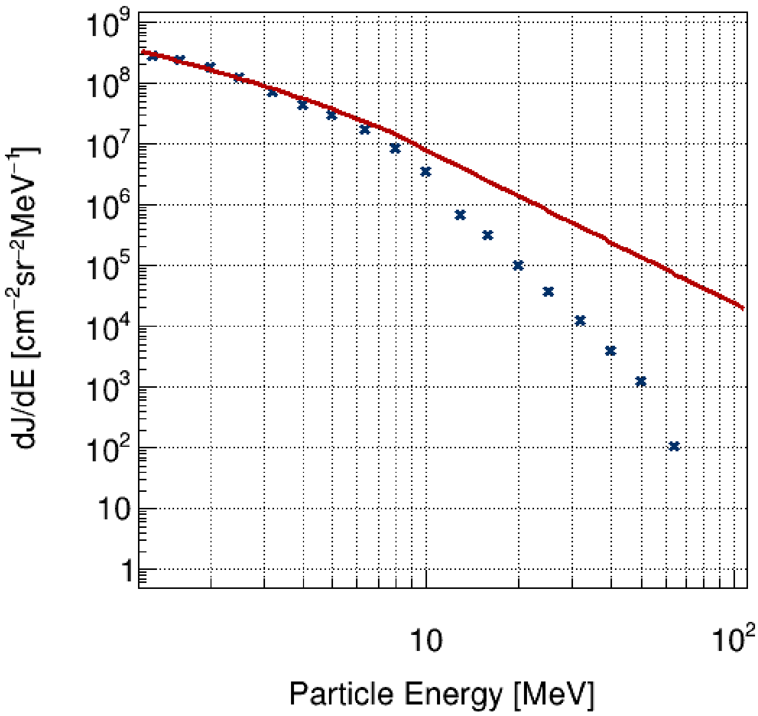


**Figure 2.** Fluence spectrum for energetic protons measured by SOHO/ERNE at L1 during FD in September 2017. Data points represent fluence integrated in different energy channels over time of duration of the event, while red line represents the fitted double power law.

Observed underestimate of fluence in higher energy channels can be explained by the assumption that there are contributions of low energy CR in these energy ranges that are suppressed with additional heliospheric disturbance and can be more pronounced for more extreme solar activity events. Additionally, this discrepancy between model and measured fluence can be due to saturation of high energy channels during events with greater SEP flux [54].

Contribution of these higher energy channels to integral flux is rather small and it does not significantly affect total flux, however, it does add to higher uncertainty of $b$, which is why this exponent is seldom used in analysis. Based on the established correlation between $a$ exponent and FD magnitude corrected for magnetospheric effect [49], an estimated value of 8.3% was obtained for $M_M$, which is in reasonably good agreement with the value found in the IZMIRAN database. Large disturbances in the heliosphere in early September 2017 that cause large FD are part of a complex event that can lead to disturbance in the magnetosphere and primary CR flux variability, but also influence dynamic processes in the ionosphere.

### *3.2. Monitoring Low Altitude Mid-Latitude Ionosphere during intense SF events*

Monitoring of the mid-latitude ionospheric D-region (50–90 km) from BEL station during September 2017 were simultaneously conducted for all VLF signals recorded by the AbsPAL system. Geographical position of BEL VLF system and the VLF transmitters (GQD/22.10 kHz, Anthorn UK and TBB/26.70 kHz, Bafa Turkey) are given in Figure S3. Both shown signals are of short great circle paths (GCPs) propagating mostly over land. In general, the GQD signal arrives to Belgrade from the north, in NW-SE direction, with

GCPGQD = 1982 km covering almost two time zones, while TBB signal arrives from the south, in SE-NW direction, with GCPTBB = 1020 km covering one time zone (Table 1). Corresponding incident solar X-ray flux data were obtained from the Geostationary Operational Environmental Satellite (GOES) database [55].

**Table 1.** VLF transmitting sites.

| | Freq. (kHz) | Country | Latitude (°) | Longitude (°) | GCP (km) | Prop. Path Direction |
|---|---|---|---|---|---|---|
| Transmitter: | | | | | | |
| GQD | 22.10 | UK | 54.73 N | 2.88 W | 1982 | NW to SE |
| TBB | 26.70 | Turkey | 37.43 N | 27.55 E | 1020 | SE to NW |

We studied data from 6 September 2017 belonging to the descending branch of the 24th solar cycle, with the strongest SF event X9.3 reported during the last solar cycle and the earth-directed CME which produced FD. September 2017 was the most active month during 2017, with a total of 99 SFs reported, of which there were 68 C, 27 M, and four X class events. During 6 September 2017, there were seven SFs reported in total, of which there were two C, three M, and two X-class SFs. Such intense solar activity significantly affected Earth's lower ionosphere, which can be clearly observed both as amplitude and phase perturbations on sub-ionospheric propagating VLF signals and was documented on BEL AbsPAL recordings. The two strongest SFs reported on 6 September 2017, i.e., X2.2 and X9.3—overall the strongest SF from the last solar cycle, as observed on GQD and TBB signal traces, practically occurred during the established stable daytime ionospheric conditions, when both traces were entirely sunlit. BEL GQD data during the entire day of 6 September 2017, with the accompanying incident solar X-ray flux from soft spectral range (0.1–0.8 nm) are given in Figure S4. As the best representative quiet day, 3 September 2017 was chosen. As observed on GQD signal, solar-induced sudden ionospheric disturbances (SIDs) are denoted by black arrows accompanied with the time of each SF event's occurrence in UT. Both amplitude and phase perturbation follow the SF events' evolution, with time delays corresponding to the sluggishness of the ionosphere [56]. Oscillatory character of the perturbations characteristic for GQD signal registered by BEL station, can still be recognized on the signal's phase, especially in the case of the weaker SF, while in the case of the amplitude, this feature is no longer observable mostly due to inducing SF's intensity [5,7,57–59]. Although these two SF occurred back-to-back, it is possible to determine individual contributions of each SF on signal recordings. It can be stated that, although these SFs strongly impacted the Earth-ionosphere waveguide for several hours, as observed from BEL station, the mid-latitude lower ionosphere fully recovered and went back to its regular conditions. Preflare ionospheric state can be treated as quiet.

Comparison between GQD and TBB signal recordings, arriving from opposite directions to the BEL station, but both of short GCPs, is given in Figure 3, as an enlarged section related to time evolution of X2.2 and X9.3 SFs.

Amplitude change in both signals is of similar behavior, simply following the incident solar X-ray radiation, with similar relative change in the amplitude amount compared to unperturbed conditions $\Delta A \approx 7$ dB. However, in the case of the TBB signal, there is a more rapid decreasing trend after the peak value corresponding to the maximal amplitude change in both SF cases. In the case of the GQD signal, relative change in the phase amount compared to unperturbed conditions $\Delta Ph$ (°) is several tens of degrees, with still recognizable oscillatory behavior characteristic for BELGQD. Unfortunately, in the case of the TBB signal, phase data were unusable so that further analysis, neither qualitative nor quantitative and neither any of the numerical simulations, were not possible to conduct. The TBB signal recordings given are purely interesting from the point of view of amplitude comparison with the GQD signal, with total opposite GCPs as recorded in Belgrade.

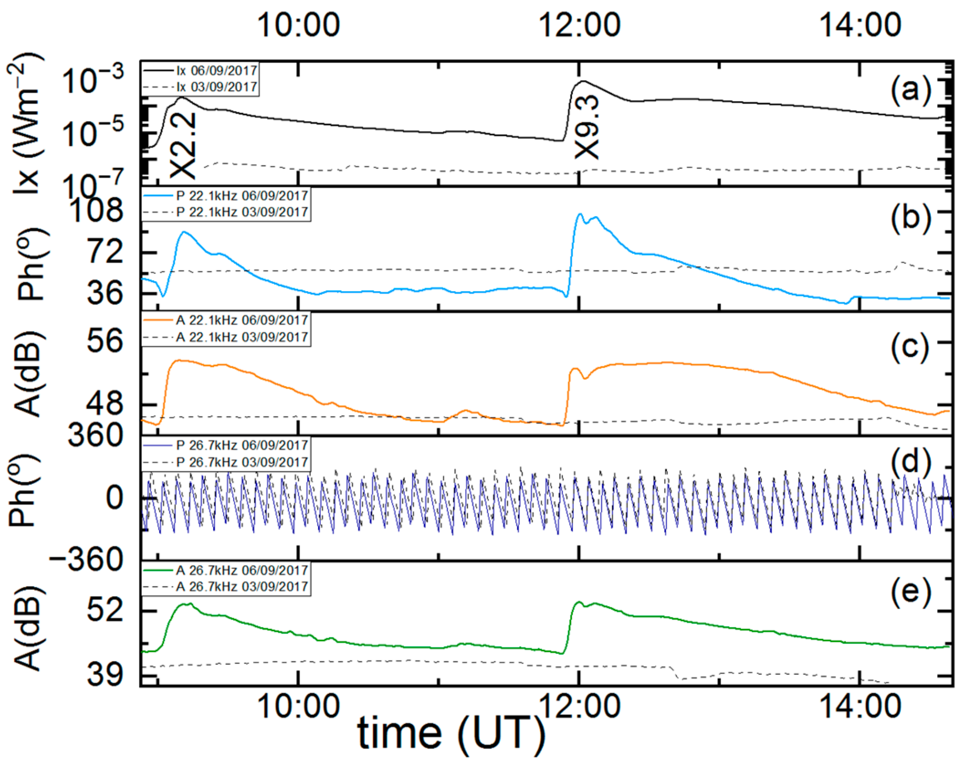


**Figure 3.** Simultaneous variations of X-ray flux (**a**) with phase delay, (**b**) amplitude delay, (**c**) variations of GQD/22.10 kHz and phase delay, (**d**) amplitude delay, (**e**) variations of TBB/26.70 kHz signals versus universal time UT during occurrence of X2.2 and X9.3 class SFs of 6 September 2017. Observed amplitude and phase perturbations with the quiet signal of 3 September 2017 (dashed black) are measured at Belgrade station. Time variation of soft X-ray irradiance is measured by GOES-15 satellite.

### *3.3. Analysis of Signal Propagation Parameters during Intense SF Events*

SFs' occurrence time and evolution were both favorable regarding applied modeling procedures, due to stable daytime GQD waveguide conditions. This was particularly significant for application of the first of previously mentioned numerical procedures in the Methods section, i.e., application of Wait's theory through LWPC software utilization, based upon the two-component exponential model. VLF sub-ionospheric propagation simulations, depending on pair of so-called Wait's parameters β (km$^{-1}$) and $H'$ (km) (representing time-dependent parameter of lower ionospheric boundary sharpness and VLF signal's reflection height), are conducted using Equation (2) valid for daytime ionosphere [39]:

$$N_e(h, H', \beta) = 1.43 \cdot 10^{13} \cdot e^{(-0.15 \cdot H')} \cdot e^{[(\beta - 0.15) \cdot (h - H')]}, \ (\mathrm{m}^{-3}) \quad (2)$$

Parameters β and $H'$ for unperturbed daytime ionospheric conditions are within software predefined as 0.3 km$^{-1}$ and 74 km, respectively, while for each case of perturbed conditions, they must be individually modeled as input parameter pairs along GCP, depending on determined measured amplitude and phase perturbations. Modeling procedure is based on trial-and-error technique, with the goal of achieving the best fit between measured and simulated values of amplitude and phase perturbations obtained through modeling. Results from this numerical procedure in the case of X2.2 and X9.3 SFs of 6 September 2017, for their entire time evolution, are given in Figure 4. Both sharpness (Figure 4b) and effective reflection height (Figure 4a) are in correlation with incident soft X-ray flux (Figure 4c).

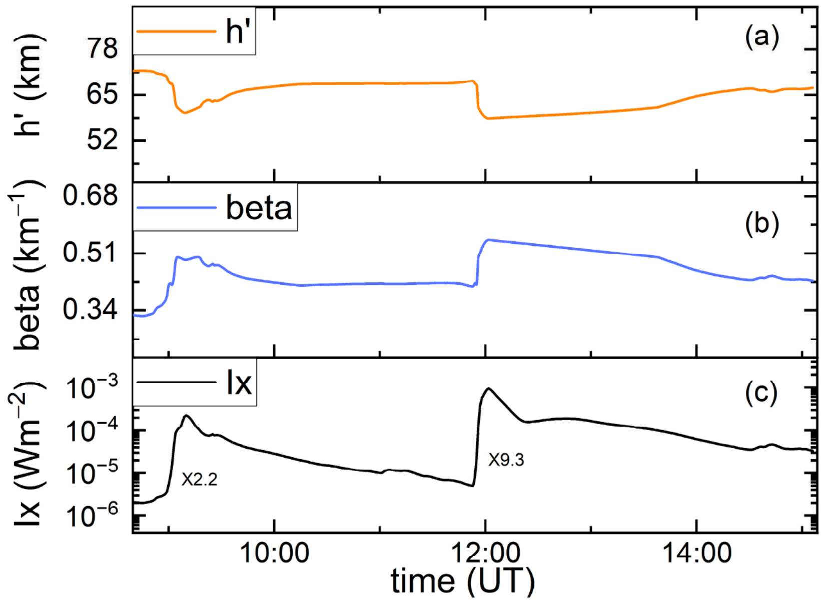


**Figure 4.** Simultaneous variations of the effective reflection height $h'$, (**a**) sharpness β, (**b**) and X-ray flux (**c**) during the occurrence of two successive X-ray flares of 6 September 2017.

Obtained modeled values of sharpness and reflection heights corresponding to X-ray flux peaks revealed: in the case of X2.2 SF at 09:10 UT with $Ix_{max}$ = 2.2658·10$^{-4}$ Wm$^{-2}$, sharpness increased for amount of 0.13 km$^{-1}$ and reflection height was lowered for 14 km, while in the case of X9.3 SF at 12:02 UT with $Ix_{max}$ = 9.3293·10$^{-4}$ Wm$^{-2}$, sharpness increased for the amount of 0.25 km$^{-1}$ and reflection height was lowered for 15.6 km, compared with their predefined unperturbed values.

Electron density was calculated at the reflection height, when $h = H'$ throughout altitude range corresponding to lower ionosphere (50–90 km), but it must be noted that at the range boundaries, results obtained from calculations should be taken with caution due to possible model failure. Electron density profiles corresponding to the influence of two X-class SFs from 6 September 2017, as observed on the GQD signal at BEL station, are given in Figure 5, in black and red for X2.2 and X9.3 SFs respectively, while quiet ionospheric conditions are given in blue. Conducted calculations indicate that *Ne* for these two SFs differ within one order of magnitude throughout the entire altitude range. Looking separately, at a height of 74 km, compared to unperturbed ionospheric state, *Ne* increased by almost three and about 3.5 orders of magnitude during the cases of weaker and stronger SF events respectively.

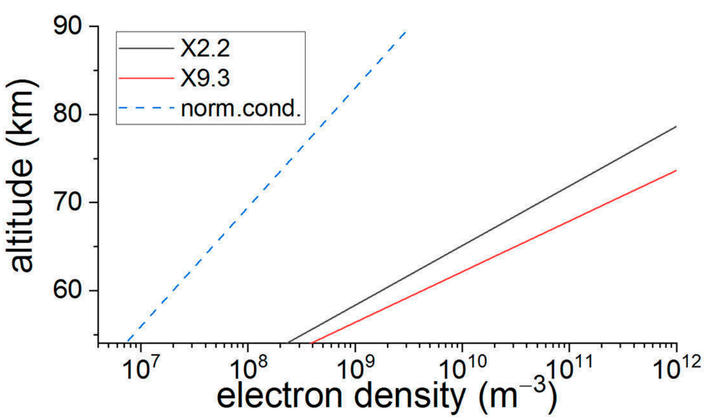


**Figure 5.** The height profile of electron density at peak time for two successive X-class SFs of 6 September 2017.

For time evolution of X2.2 and X9.3 SFs of 6 September 2017, during about 12 h, a novel approach for obtaining GQD signal propagation parameters, sharpness β and reflection height $H'$ from incident solar X-ray irradiance, was applied by employing the FlarED' Method and Approximate Analytic Expression application, where electron density is calculated with simple logarithmic second-degree polynomial Equation (3) specially designed to take ionospheric response time delay through height-dependent coefficients into calculations (for more details see [5,40]):

$$log\ Ne(h, Ix) = a_1(h) + a_2(h) \cdot log\ Ix + a_3(h) \cdot (log\ Ix)^2 \quad (3)$$

where $a_1(h)$, $a_2(h)$, and $a_3(h)$ are height-dependent coefficients, $Ix$ is solar X-ray flux (Wm$^{-2}$), and $h$ is height (km). Such calculated $Ne$ values are in good agreement with those obtained using other simulation methods related to the two-component exponential model and VLF sub-ionospheric propagation simulations conducted through the use of LWPC software [40]. Figure 6 presents a 12-h variation of solar X-ray flux within two spectral bands provided by GOES-15 and -13 satellites (Figure 6a) and the corresponding $Ne$ (m$^{-3}$) during these two X-class SFs (Figure 6b).

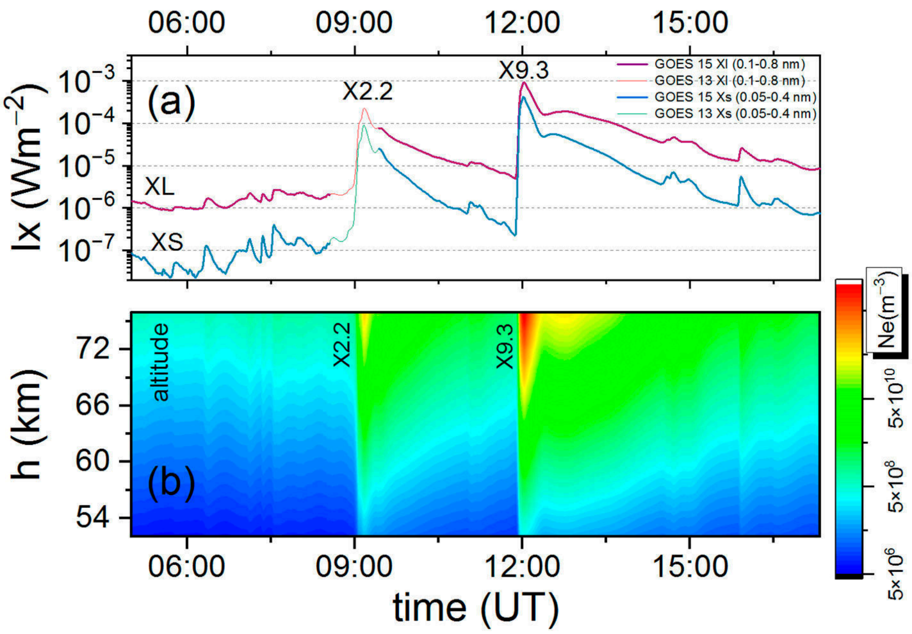


**Figure 6.** Variation of X-ray flux (**a**) as measured by GOES-15 and -13 satellites and the surface plot of corresponding electron density profile (**b**) versus universal time UT during two successive X-class SFs of 6 September 2017. The results are obtained using simple approximative Equation (3).

### *3.4. Analysis of Cosmic Ray Flux Registered by Belgrade Station during Early September 2017*

As a result of solar activity at the beginning of September 2017, a strong FD was detected, resulting in a decrease of CR flux of close to 15% (as observed on the South Pole [60]). The effect was also detected on lower latitudes, being intense enough to be detected by underground muon monitors that are generally sensitive to higher energies of galactic CRs. To get a better perspective of data recorded by Belgrade muon station during this period (both by GLL and UL), we compared it against selected neutron monitor measurements (provided by the Neutron Monitor Database [61]). For this purpose, we chose three NMs: one on the opposite hemisphere with low effective vertical geomagnetic cutoff rigidity $R_c$, one near the North Pole, and one relatively close to Belgrade muon station with a comparable $R_c$. All selected stations have different asymptotic directions, $R_c$, and altitude and are generally sensitive to primary CR with lower median rigidity then CR detected by Belgrade muon station. Median rigidity ($R_m$) is the rigidity of primary CR where half of all contributions to detector count rate originates from primary CR with rigidity lower than that specific value. Basic characteristics for NM stations are as follows: South Pole (SOPO, 90.00°S, altitude 2820 m, $R_c$ = 0.1 GV, median rigidity $R_m$ = 10 GV), Thule (THUL, 76.5°N, 68.7°W, 26 m, $R_c$ = 0.3 GV, $R_m$ = 12.6 GV), and Athens (ATHN, 37.97°N, 23.78°E, 260 m, $R_c$ = 8.53 GV, $R_m$ = 25.1 GV). Belgrade muon station, as mentioned before, measures muon flux on ground level (GLL, 44.85°N, 20.38°E, 75 m, $R_c$ = 5.3 GV, $R_m$ = 63 GV) and underground level (UL, 44.85°N, 20.38°E, 75 m, $R_c$ = 12 GV, $R_m$ = 122 GV). Median rigidity for NM stations is retrieved from [62]. For Belgrade muon station, $R_m$ values for GLL and UL were determined using the response function obtained by means of Monte Carlo simulation for CR transport. Time series of detected flux for all stations during early September 2017 are given in Figure 7. Flux is normalized using a ten-day average before the FD. This longer interval was chosen due to unusually high solar activity during the period of interest.

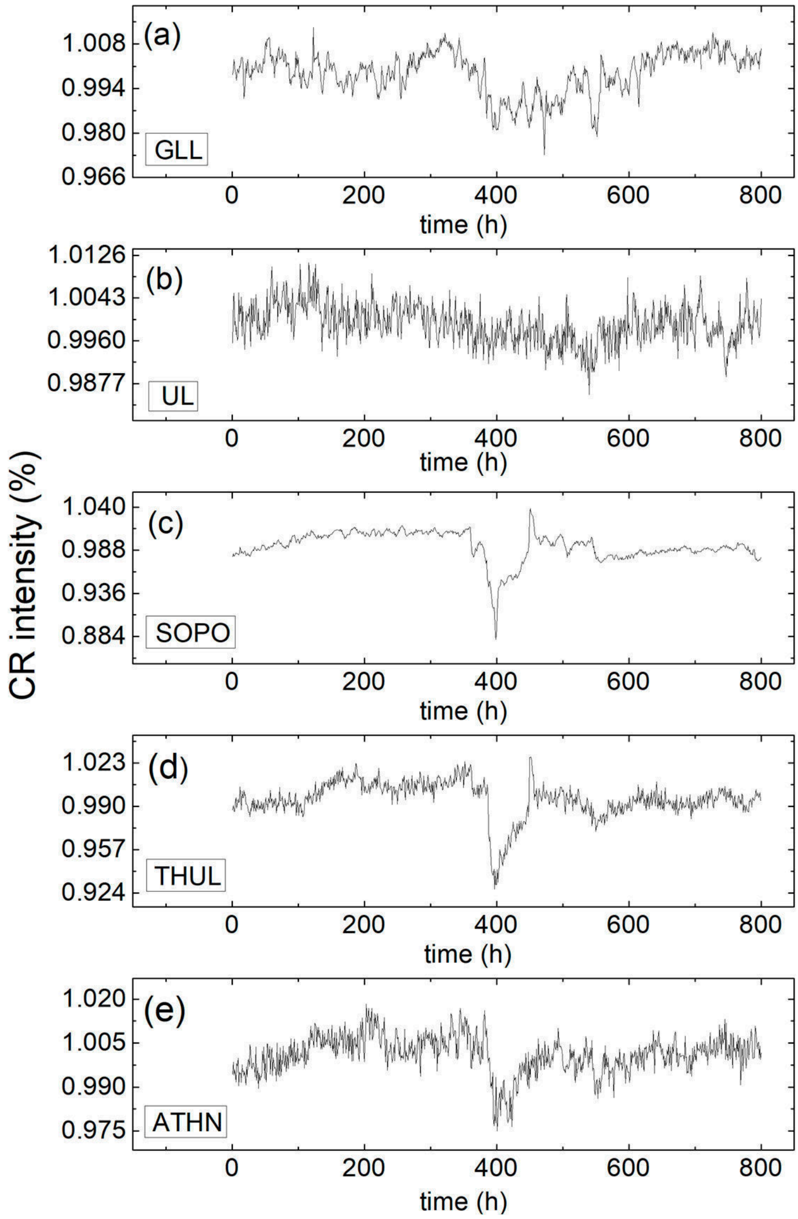


**Figure 7.** Normalized time series of secondary CR flux detected at several ground and one shallow-underground monitors: (**a**) ground (GLL) and (**b**) underground (UL) detector at Belgrade muon station, (**c**) South pole NM (SOPO), (**d**) Thule NM (THUL), and (**e**) Athens NM (ATHN).

Hourly time series show that all stations detected FD around the same time, however, time profiles are not the same. This is due to the specific sensitivity of selected CR stations to primary CR with different rigidities. Additionally, the measured magnitude of the FD is not the same for all detector stations. As expected, UL, GLL, and Athens, with higher cutoff and median rigidity, recovered from sharp depression sooner than stations at higher latitudes (with lower $R_c$). For a more quantitative description of the relationship between observations from selected monitors, cross-correlation analysis of hourly time series for different stations can be applied using Pearson coefficient with a 2-tail test for significance. Correlation coefficients between data recorded by these ground stations during September 2017 are given in Table 2.

**Table 2.** Statistical correlation between ground stations during September 2017.

| Pearson Corr. | ATHN | SOPO | GLL | UL | THUL |
|---|---|---|---|---|---|
| ATHN | 1 | 0.55084 | 0.43443 | 0.5056 | 0.61535 |
| SOPO | | 1 | 0.18941 | 0.45194 | 0.81747 |
| GLL | | | 1 | 0.69325 | 0.36496 |
| UL | | | | 1 | 0.51526 |
| THUL | | | | | 1 |

These ground (and one shallow-underground) stations have different locations, different cut-off rigidities, and different energy-dependent detection efficiency of the detectors. All these differences can lead to better understanding of these different correlation coefficients.

Further insight can be gathered by comparing variability of CR flux measured by different stations, as well as geomagnetic activity and selected space weather parameters for the early part of September, which are presented in Figure 8. One-hour time resolution was used for all data. The ICME list compiled by Richardson and Cane [63] and the CME list provided by SOHO/LASCO [64] were used to precisely time the near Earth passage of two ICMEs observed during this period (respective time intervals indicated in Figure 8 by dashed blue lines).

In the days following early September X-flares, two sudden storm commencements (SSCs), or two shocks, arrived during the last hours of 6–7 September (indicated by solid blue lines in Figure 8). They were followed by a sheath region and ICME ejecta. Interaction of shock and sheath region of ICME2 with ICME1 ejecta, visible in the sudden change of solar wind parameters, led to the observed intense geomagnetic activity and consequent FD. This CME-CME interaction with its complex structure was the main reason for the extensive geomagnetic storm [65] and a strong detected FD. With arrival of the first ICME, CR flux showed a small decrease detected as a low-magnitude FD by NM stations [66] (at 23:43:00 UT on 6 September, with magnitude of 1.8% according to IZMIRAN database).

When the second fast interplanetary shock arrived and interacted with ejecta from the previous ICME, a sharp decrease in CR flux and one of the largest FDs in solar cycle 24 was detected (at 23:00:00 UT on 7 September, with magnitude of 7.7% according to IZMIRAN database). Main FD was clearly visible even with muon detectors, which leads to the conclusion that inhomogeneities in the heliosphere created by interaction of these two ICMEs modulated CR extensively. The recovery phase of this FD was influenced by disturbed interplanetary condition, the effect being dependent on particle energy as was evident by comparing profiles of CR time series recorded by different stations. Before the end of the recovery phase, another flare (X8.2 of 10 September) led to a small ground level enhancement (GLE), the last one of solar cycle 24 (GLE #72). Recovery time of the main FD was approximately three days in total, which is a relatively short period for such a large CR modulation. Cross-correlation coefficients between CR time series measured by Belgrade muon station and selected space weather parameters for the period of six days (during 5–10 September) are given in Table 3.

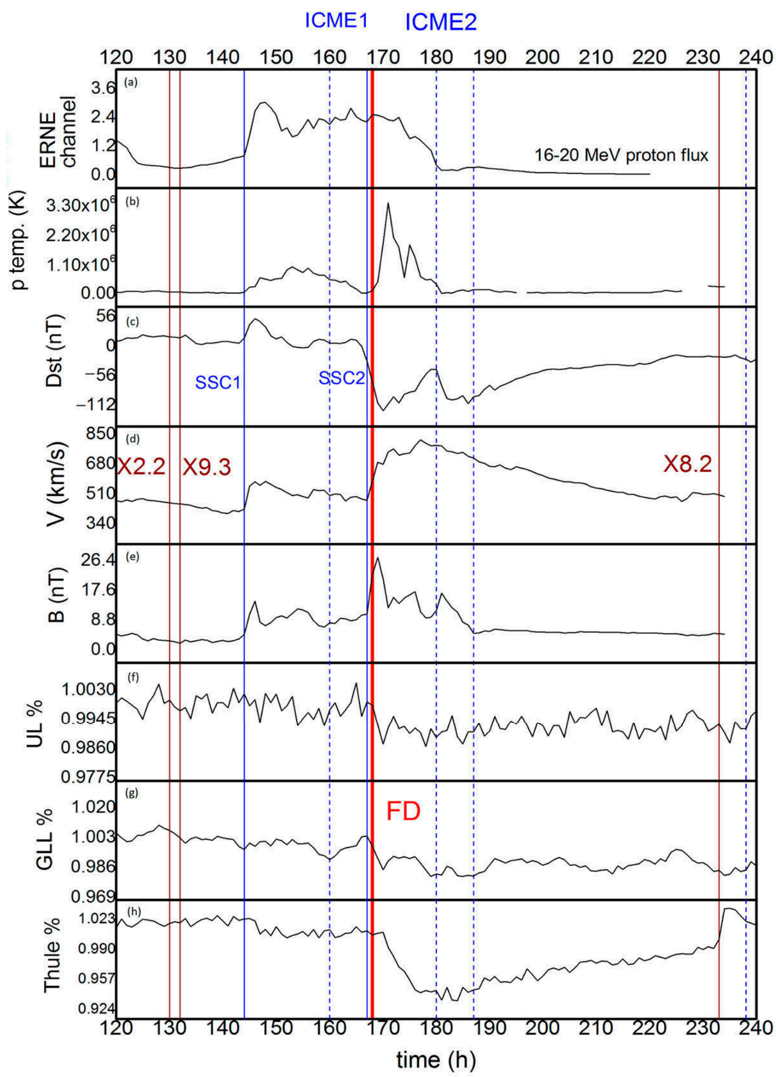


**Figure 8.** Hourly variation in CR intensity measured at ground station ((**f**) UL, (**g**) GLL, (**h**) Thule), (**e**) magnitude of interplanetary magnetic field B, (**d**) velocity of solar wind V, (**c**) Dst index, (**b**) proton temperature, and (**a**) one of the proton channels measured by ERNE/SOHO during early September 2017 (period 4th–10th).

**Table 3.** Statistical correlation (with significance) between time series of CR flux measured at ground stations and selected space weather parameters during 5–10 September 2017.

| Pearson Corr. | Thule | | GLL | | UL | |
|---|---|---|---|---|---|---|
| Thule | 1 | | | | | |
| GLL | 0.67213 | ($<10^{-6}$) | 1 | | | |
| UL | 0.62741 | ($<10^{-6}$) | 0.75552 | ($<10^{-6}$) | 1 | |
| Average B | −0.238 | (<0.008) | −0.242 | 0.007 | −0.243 | <0.007 |
| SW speed | −0.80562 | ($<10^{-6}$) | −0.62829 | ($<10^{-6}$) | −0.58503 | ($<10^{-6}$) |
| Dst Index | 0.77923 | ($<10^{-6}$) | 0.6979 | ($<10^{-6}$) | 0.65494 | ($<10^{-6}$) |
| Proton Channel 16–20 MeV | 0.43083 | $<10^{-5}$ | 0.38276 | $<10^{-4}$ | 0.31715 | $<10^{-3}$ |

During this period, apparent correlation can be established between selected parameters. This correlation is larger for Thule NM than in the case of Belgrade Muon monitor. Due to the short period, correlation between proton flux at L1 and detected CR flux on all stations is exaggerated.

## 4. Discussion

The cascade of strong solar activity from AR12673 that occurred in early September 2017 was among others characterized by a number of SFs. Several concurrent interconnecting CMEs/ICMEs emerged in a relatively short period, inducing a disturbance in the heliosphere. The complex structure of interacting CMEs/ICMEs produced an extensive geomagnetic storm and ionospheric disturbance and affected the flux of primary CR (visible as a FD). Additionally, the mentioned phenomena were responsible for the increased flux of energetic particles in interplanetary space. The origin and acceleration mechanism for energetic protons measured at L1 is not so straightforward to determine due to complicated interactions of all effects potentially involved. In case these particles originate from the Sun, correlation between SF properties and SEP fluence is supposed to be rather poor, although it is suggested that primary acceleration of SEP to higher energies occur in close proximity to the flare site [67,68]. If, on the other hand, these particles are accelerated in interplanetary space due to the passage of ICME shock, some correlation can be established (i.e., between measured proton fluence and CME/ICME velocity). However, regardless of their origin, the shape of energetic proton fluence spectrum can hold useful information about heliospheric disturbance and can even provide insight into the effect that this disturbance has on the flux of primary CR in interplanetary space (especially when more intense events are concerned). That was also demonstrated in this case, where the magnitude of the corresponding FD corrected for magnetospheric effect estimated from proton fluence spectra was in good agreement with the value for $M_M$ calculated based on NM measurements.

Impacts of the soft range X-ray solar electromagnetic radiation released from two powerful SF events from 6 September 2017 onto the European mid-latitude ionospheric D-region were monitored and inspected based on recordings from BEL narrowband VLF receiving station, belonging to a global ground-based VLF network system. Lower ionospheric disturbances induced by incident soft range X-ray radiation were indirectly examined regarding simultaneous perturbations of VLF radio signals' propagation parameters within the Earth-ionosphere waveguide, with analysis conducted for signals with short GCPs (Table 1; Figure S3).

Aside from quiet ionospheric preflare conditions, SFs' occurrence times were also favorable in terms of applied modeling procedure using the LWPC software package, since analyzed signals on their GCPs towards BEL station were transmitted through waveguides under already established stable daytime ionospheric conditions. Since this procedure relies on trial-and-error technique in acquiring the best fitting pair of Wait's parameters for depicting real measured data with the modeled data, and from that, by obtaining information regarding lower ionospheric conditions based on modeled ones, both of these prerequisites significantly eased an already highly challenging task of modeling X-class SFs and especially those most energetic among them. In such disturbed conditions, both ionospheric plasma properties and related corresponding VLF signal propagation parameters are drastically changed compared with the regular state. Accordingly, electron density height profiles are also changed in regard to both time and space distributions. As expected, the evolution of observed VLF signals' perturbations was with similar characteristics, following a lower ionospheric response to incident solar X-ray flux with delay times corresponding to the sluggishness of the ionosphere and were of amounts expected for cases of such powerful events (Figure 3). Their back-to-back occurrence did not allow for individual duration specification of each SF's impact on analyzed VLF signals, however, their individual contribution was possible to determine. According to registered VLF BEL data, after a several-hour lasting disturbance, the lower ionosphere fully recovered (Figure S4).

For the state of maximal perturbation that corresponds to SFs' X-ray flux peaks, perturbed GQD signal's amplitudes are 118% and 117% of unperturbed, while phases are 165% and 192% of unperturbed. Wait's parameters are in correlation with incident soft X-ray flux and modeling results based upon exponential conductivity increase with height within the ionosphere suggesting that perturbed sharpnesses are 143.3% and 183.3% of unperturbed, while perturbed reflection heights are 81% and 78.9% of unperturbed, respectively to SFs (Figure 4). As expected, in the case of the stronger SF event, propagation was more affected by the induced disturbance, causing the reflecting edge boundary to become significantly sharper, while reflecting edge height descended for 1.6 km$^{-1}$ more than in case of the weaker one. Numerically, simulated ionospheric conditions fit well with observed ones, as indirectly obtained through GQD signal's amplitude and phase measurements. Due to its short GCP and stable daytime ionospheric conditions, averaged conditions that were held within the waveguide during the modeling procedure can be considered reliable. Electron densities calculated using Equation (2) for the D-region altitude range show about one order of magnitude difference between analyzed SFs at their peak, giving a reflection height of 74 km an increase in electron density of 82.1% compared between stronger and weaker events (Figure 5).

The effects on the ionosphere of the largest SF event of the last decade, X9.3 together with X2.2, occurred on 6 September 2017, observed through GQD VLF signal response in relation to the SF class, were compared with some other cases of strong SF events, including several major SFs (2003–2011 of class X28+–X6.9) and other SFs (from 2006–2017 of class X1–X9.3 and from period 1994-1998 in range X1–X5). Figure S5 provides a comparison of the results obtained in this study (black stars) and those available in the literature [5,7,8,69–77]. Presented ionospheric parameters (β and *H'*) and corresponding electron densities are related to results from two hundred cases of SF events recorded in Belgrade on GQD trace in the period of 2003–2017 in other mid-latitudinal ionospheric sectors and the low-latitudinal ionospheric sector. In order to ensure better insight into the tendency of parameters with the SF events' strength, smaller diagrams containing the entire C–X-class range are embedded in Figure S5. It can be seen that values of signal parameters for some X-class events are quite scattered.

Our results fit well with the general trend (linear fit), considering that most of the available cases taken into consideration are from the mid-latitudinal sector. A significant discrepancy notable in the enlarged X-class section, related to results from [69] and [70], is probably caused by latitudinal factor (due to low-latitudinal observations likewise as suggested in [71] and similarly due to observations obtained more towards higher-latitude compared with Belgrade receiver site, respectively). A novel proposed approximate method that employs approximative Equation (3) for obtaining ionospheric parameters was validated both for cases of weaker and stronger SFs and expanded further towards the upper boundary of X-class range, as compared to recent previous studies employing this technique. Applied novel approach provides mapping of the entire ionospheric altitude range (Figure 6) in a simpler and easier to conduct manner. Results obtained in this study using this novel approach applied to X-class SFs could be useful for validation of the available ionospheric models and as input data for other climate models.

Furthermore, increased solar activity at the beginning of September 2017 had a significant effect on cosmic rays observed as a decrease in measured flux by all relevant CR stations. Intensity of the event was such that the energy range of affected primary CR was wide enough for the effect to be detected both by neutron monitors and muon detectors. The decrease was even observable in shallow-underground muon measurements, although to a much lesser extent. Temporal agreement between measurements taken by different detectors was good, while the shape of detected FD varied, as would be expected due to difference in location, instrument design, and sensitivity. Cross-correlation analysis of hourly time series for different stations (presented in Table 2) shows expected positive correlation, where obtained coefficients are consistent with values expected based on differences in detector location, particular setups, station specific environmental conditions, and most importantly, the energy (rigidity) range of primary CR they are sensitive to. GLL and UL have the same position, however, correlation is not so high (≈0.7) due to different $R_c$ and $R_m$. Nevertheless, this correlation is higher than that between either of the detectors and any of the neutron monitor stations. NMs have more similar $R_c$ and $R_m$ values, so this correlation is greater despite their different location. As far as correlation between measured CR flux and selected space weather and geomagnetic parameters is concerned, a larger correlation observed for NM (Table 3) can almost certainly be attributed to the fact that muon detectors are sensitive to higher energy CR (which are less modulated by disturbances in the heliosphere). Correlation between selected proton channel (particles with energy between 16 and 20 MeV) and CR flux is exaggerated as it is a consequence of a relatively short time interval taken for analysis. This value is greatly reduced if a longer interval is taken into consideration, even appearing as a small anticorrelation. This is expected as proton flux with its turbulent magnetic field scatters CR and thus can produce a decrease in detected CR flux. Inverse correlation of magnetic field and solar wind speed with CR flux is anticipated due to the same reason.

Forbush decrease in early September 2017 was caused by compound solar wind disturbance formed due to the interaction of several ICMEs. This time interval is particularly interesting because it happens in a descending-to-minimum phase of a solar cycle. The apparent multitude of solar activity is more characteristic to other phases. For example, similar series of successive CMEs led to FD in March 2012 [78] during the ascending phase of the solar cycle, but this heightened activity of the Sun, isolated between relatively quiet periods, allows for better study of the phenomena. Forecasting these multiple CME interaction events and predicting time of arrival is very difficult [45] but needed, so this series of events can be a good case study.

Although no apparent correlation between SF intensity and solar wind and FD parameters is clearly demonstrable, the majority of more intense FDs are caused by a CME/ICME following a significant SF, thus indicating a likely connection. For one such complex event, accompanying disturbances induced in the heliosphere, magnetosphere, and ionosphere are generally directly attributed to different sources and establishing clear relationships between various parameters used to describe them is far from straightforward. Yet, based on some general features, it is possible to make rudimentary event classification, where within certain classes, some of these relationships may be more pronounced. Strong flares do not necessarily produce a significant FD (although can have an associated GLE, as is the case for X14.4 flare that occurred on 15 April 2001), can produce both strong FDs and GLEs (e.g., GLE #69 on 20 January 2005, GLE #66 on 28 October and GLE #67 on 2 November 2003), or can produce strong FD but without associated GLE (e.g., 7 March 2012, related to X5.4 flare and September 2017 event studied here). It has been shown [49,79] that events that fall in this last category exhibit stronger correlations between FD magnitude and some space weather parameters, specifically average CME speed. More recently, a correlation between FD magnitude (especially in the case of more intense FDs) and shape of energetic proton spectra measured at L1 has been reported for this class of events. As the number of such events is relatively low, it is of significance that results presented in this work are consistent with the indicated relationship. For reference, dependence of FD magnitude on selected SF, CME, and geomagnetic parameters for some of the mentioned events is given in Figure S6.

## 5. Conclusions

The influence of severely disturbed space weather conditions of 6 September 2017 on parameters of the Earth's atmosphere was studied, in relation to the relatively close and far surroundings of the Earth. The influence of strong X-class SFs on the ionosphere and primary cosmic rays, based on space- and ground-based observations on one hand and simulations on the other hand, are presented. It contributes to better understanding of solar-terrestrial coupling processes and how primary cosmic rays and the ionosphere respond under conditions during the X-class SF events. Based on the results presented, the following conclusions can be drawn:

- SEP fluence during strongly disturbed conditions of the heliosphere in early September 2017 was calculated from SOHO/ERNE data and modeled using double power law. Relationships between power exponents used to parameterize the shape of fluence spectrum and FD magnitude corrected for magnetospheric effect are consistent with ones expected for this type of event. Hourly time series of secondary CR flux, detected by several ground-based monitors and one shallow-underground monitor, show that all stations detected FD at the same time. Cross-correlation between these time series, and between CR time series and some geomagnetic activity indices, as well as selected IMF and solar wind parameters, are presented. Sensitivity of different stations to primary CR with different rigidity results in different time profiles, maximal decreases, and duration of recovery phase of FD;

- We observed that a correlation between heliospheric and geomagnetic parameters decreases with increase of median energy of the CR detected by different stations and that shows an extension of CR modulation of complex CME-CME interaction structure initiated with strong SFs;
- Impact of intense solar activity onto the Earth's lower ionosphere, through analyzed X-class SFs, was clearly observed (perturbed amplitudes are 118% and 117% of unperturbed, while perturbed phases are 165% and 192% of unperturbed, for X2.2 and X9.3, respectively). BEL AbsPAL recordings of registered VLF signals during SF events are in correlation with X-ray flux (with time delays corresponding to the sluggishness of the ionosphere). Although X2.2 and X9.3 occurred back-to-back, it was possible to determine individual contributions of each SF based upon registered VLF signals;
- Numerical simulations were conducted through the application of the LWPC software package and the FlarED' Method and Approximate Analytic Expression application's novel approach. The ionospheric parameters (sharpness and effective reflection height) and electron density are in correlation with incident X-ray flux of soft range. *Ne* for these two SFs revealed the difference within one order of magnitude throughout the entire altitude range considered. Compared to quiet ionospheric conditions, *Ne* at the reference height increased by several orders of magnitude during both SF events. As monitored by BEL VLF station in the mid-latitudinal sector, both presented X-class SFs are common in properties and behavior, as could be expected for intense SF events, according to their strength. However, there is a significant difference in estimations of ionospheric parameters related to some other cases of reported X-class SFs from different sectors.

Although there are numerous papers related to the influence of SF events on Earth's ionosphere, the vast majority of present case studies of selected SF events, more or less are extensively related to numbers of examined cases. X-class SF events have never been systematically studied in terms of lower ionospheric response. Coupling processes between such extreme space weather events and the lower ionosphere are not well understood. In addition, many intense SF events are related to other energetic solar events like CMEs and SEPs. Comprehensive research is needed especially in terms of retrieving a global (worldwide) lower ionospheric response to such strong events from propagation parameters of radio signals as a remote sensing technique. Case studies, although restricted to some selected events and with great contribution of "local" components contained within obtained and presented results, would provide substantial contributions.

This study emphasized the relevance of the ionospheric response, which was analyzed using a multi-instrument method, and gave a comprehensive examination of the events from the Sun to the Earth. It gave an insight into the sudden increase in ionization during the storm and strong SFs from the beginning of September 2017 and the potential effects on radio communication. Since conditions in the D-region of the ionosphere have a dramatic effect on high frequency communications and low frequency navigation systems, the ionospheric responses (and its parameters like β, *H'* and *Ne*) to severe SFs are a key topic of study in ionospheric physics and are considered to be an important factor for space weather predictions, improvement of empirical models, and applications of machine learning techniques in atmospheric sciences.

**Supplementary Materials:** The following supporting information can be downloaded at: https://www.mdpi.com/article/10.3390/rs15051403/s1, Figure S1: Differential SEP fluxes during extreme solar event in September 2017, measured by SOHO/ERNE energetic particle sensors LET (Low Energy Detector) proton channels. Red vertical dashed lines indicate the time for the start and the end of interval used to calculate the integral flux.; Figure S2: Differential SEP fluxes during extreme solar event in September 2017, measured by SOHO/ERNE energetic particle sensors HET (High Energy Detector) proton channels. Red vertical dashed lines indicate the time for the start and the end of interval used to calculate the integral flux.; Figure S3: The geographic position of Belgrade (BEL) VLF receiver and the GQD transmitter (54.73°N, 2.88°W), Anthorn UK and TBB transmitter (37.43°N, 27.55°E) Bafa Turkey with GCP of sub-ionospheric propagating VLF signals.; Figure S4: Simultaneous variations of X-ray flux (red), phase (blue), and amplitude (orange) of GQD/22.10 kHz signal versus universal time UT during occurrence of X2.2 and X9.3 class solar flares of 6 September 2017 (from upper to lower panel). Observed amplitude and phase perturbations on GQD radio signal, as well as quiet signal (dashed black), are measured at Belgrade station. Time variation of soft X-ray irradiance is measured by GOES-15 satellite.; Figure S5: Lower ionospheric response to SF events of different strength across X-class (shaded gray area), obtained indirect modeling of VLF signals' propagation parameters: (a) sharpness $\beta$ ($km^{-1}$), and (b) effective reflection height $H'$, (km) and (c) estimated corresponding electron densities $Ne$ ($m^{-3}$), in function of X-ray flux; results from our research are presented by black stars.; Figure S6: Magnitude of the FD versus the average CME velocity between the Sun and the Earth, calculated using the time of the beginning of the associated CME observations (a) Minimal Dst-index in the event, (b) maximal X-ray flare power (c) with associated flare indicated in red.

**Author Contributions:** Conceptualization, V.A.S.; writing—original draft preparation, V.A.S., A.K. and N.V.; writing—review and editing A.K., N.V., V.A.S., Z.M., M.S. and A.D. The authors had full access to the data and took responsibility for their integrity. All authors have read and agreed to the published version of the manuscript.

**Funding:** This work was funded by the Institute of Physics Belgrade, University of Belgrade, through a grant by the Ministry of Science, Technological Development and Innovations of the Republic of Serbia.

**Data Availability Statement:** VLF data were recorded at the Institute of Physics Belgrade, University of Belgrade and can be obtained upon request. Please contact V.A.S.

**Acknowledgments:** The article is based upon work from COST Action CA18212—Molecular Dynamics in the GAS phase (MD-GAS), supported by COST (European Cooperation in Science and Technology). Authors thank D. Šulić for instrumental set-up and useful discussions. OMNI data was made available by NASA/GSFC's Space Physics Data Facility's OMNIWeb service. This CME catalog is generated and maintained at the CDAW Data Center by NASA and The Catholic University of America in cooperation with the Naval Research Laboratory. SOHO is a project of international cooperation between ESA and NASA. We acknowledge the NMDB database, founded under the European Union's FP7 program (contract no.213007) for providing data. We also gratefully acknowledge using data from the catalogue of Forbush effects and interplanetary disturbances provided by Cosmic Ray Group at the IZMIRAN Space Weather Prediction Center at Pushkov Institute of Terrestrial Magnetism, Ionosphere, and Radio Wave Propagation of the Russian Academy of Sciences.

**Conflicts of Interest:** The authors declare no conflict of interest. The funders had no role in the design of the study; in the collection, analyses, or interpretation of data; in the writing of the manuscript, or in the decision to publish the results.

## References

1. Manju, G.; Pant, T.K.; Devasia, C.V.; Ravindran, S.; Sridharan, R. Electrodynamical response of the Indian low-mid latitude ionosphere to the very large solar flare of 28 October 2003—A case study. *Ann. Geophys.* **2009**, *27*, 3853–3860. [CrossRef]
2. Fu, H.; Zheng, Y.; Ye, Y.; Feng, X.; Liu, C.; Ma, H. Joint Geoeffectiveness and Arrival Time Prediction of CMEs by a Unified Deep Learning Framework. *Remote Sens.* **2021**, *13*, 1738. [CrossRef]
3. Sahai, Y.; Becker-Guedes, F.; Fagundes, P.R.; Lima, W.L.C.; de Abreu, A.J.; Guarnieri, F.L.; Candido, C.M.N.; Pillat, V.G. Unusual ionospheric effects observed during the intense 28 October 2003 solar flare in the Brazilian sector. *Ann. Geophys.* **2007**, *25*, 2497–2502. [CrossRef]
4. Le, H.; Liu, L.; Chen, Y.; Wan, W. Statistical analysis of ionospheric responses to solar flares in the solar cycle 23. *J. Geophys. Res. Space Phys.* **2013**, *118*, 576–582. [CrossRef]
5. Srećković, V.A.; Šulić, D.M.; Ignjatović, L.; Vujčić, V. Low Ionosphere under Influence of Strong Solar Radiation: Diagnostics and Modeling. *Appl. Sci.* **2021**, *11*, 7194. [CrossRef]
6. Kelley, M.C. *The Earth's Ionosphere: Plasma Physics and Electrodynamics*; Academic Press: Cambridge, MA, USA, 2009.

7. Barta, V.; Natras, R.; Srećković, V.; Koronczay, D.; Schmidt, M.; Šulic, D. Multi-instrumental investigation of the solar flares impact on the ionosphere on 05–06 December 2006. *Front. Environ. Sci.* **2022**, *10*, 904335. [CrossRef]
8. Kolarski, A.; Srećković, V.A.; Mijić, Z.R. Response of the Earths Lower Ionosphere to Solar Flares and Lightning-Induced Electron Precipitation Events by Analysis of VLF Signals: Similarities and Differences. *Appl. Sci.* **2022**, *12*, 582. [CrossRef]
9. Nina, A. Modelling of the Electron Density and Total Electron Content in the Quiet and Solar X-ray Flare Perturbed Ionospheric D-Region Based on Remote Sensing by VLF/LF Signals. *Remote Sens.* **2022**, *14*, 54. [CrossRef]
10. Berdermann, J.; Kriegel, M.; Banyś, D.; Heymann, F.; Hoque, M.M.; Wilken, V.; Borries, C.; Heßelbarth, A.; Jakowski, N. Ionospheric Response to the X9.3 Flare on 6 September 2017 and Its Implication for Navigation Services Over Europe. *Space Weather* **2018**, *16*, 1604–1615. [CrossRef]
11. Yasyukevich, Y.; Astafyeva, E.; Padokhin, A.; Ivanova, V.; Syrovatskii, S.; Podlesnyi, A. The 6 September 2017 X-Class Solar Flares and Their Impacts on the Ionosphere, GNSS, and HF Radio Wave Propagation. *Space Weather* **2018**, *16*, 1013–1027. [CrossRef]
12. De Paula, V.; Segarra, A.; Altadill, D.; Curto, J.J.; Blanch, E. Detection of Solar Flares from the Analysis of Signal-to-Noise Ratio Recorded by Digisonde at Mid-Latitudes. *Remote Sens.* **2022**, *14*, 1898. [CrossRef]
13. Demyanov, V.V.; Yasyukevich, Y.V.; Ishin, A.B.; Astafyeva, E.I. Ionospheric super-bubble effects on the GPS positioning relative to the orientation of signal path and geomagnetic field direction. *GPS Solut.* **2012**, *16*, 181–189. [CrossRef]
14. Yashiro, S.; Gopalswamy, N. Statistical relationship between solar flares and coronal mass ejections. *Proc. Int. Astron. Union* **2008**, *4*, 233–243. [CrossRef]
15. Desai, M.; Giacalone, J. Large gradual solar energetic particle events. *Living Rev. Sol. Phys.* **2016**, *13*, 3. [CrossRef]
16. Freiherr von Forstner, J.L.; Guo, J.; Wimmer-Schweingruber, R.F.; Dumbović, M.; Janvier, M.; Démoulin, P.; Veronig, A.; Temmer, M.; Papaioannou, A.; Dasso, S.; et al. Comparing the Properties of ICME-Induced Forbush Decreases at Earth and Mars. *J. Geophys. Res. Space Phys.* **2020**, *125*, e2019JA027662. [CrossRef]
17. Cane, H.V. Coronal Mass Ejections and Forbush Decreases. *Space Sci. Rev.* **2000**, *93*, 55–77. [CrossRef]
18. Belov, A.V.; Eroshenko, E.A.; Oleneva, V.A.; Struminsky, A.B.; Yanke, V.G. What determines the magnitude of forbush decreases? *Adv. Space Res.* **2001**, *27*, 625–630. [CrossRef]
19. Papaioannou, A.; Belov, A.; Abunina, M.; Eroshenko, E.; Abunin, A.; Anastasiadis, A.; Patsourakos, S.; Mavromichalaki, H. Interplanetary Coronal Mass Ejections as the Driver of Non-recurrent Forbush Decreases. *Astrophys. J.* **2020**, *890*, 101. [CrossRef]
20. Belov, A.; Shlyk, N.; Abunina, M.; Belova, E.; Abunin, A.; Papaioannou, A. Solar Energetic Particle Events and Forbush Decreases Driven by the Same Solar Sources. *Universe* **2022**, *8*, 403. [CrossRef]
21. Riley, P.; Love, J.J. Extreme geomagnetic storms: Probabilistic forecasts and their uncertainties. *Space Weather* **2017**, *15*, 53–64. [CrossRef]
22. Eastwood, J.P.; Biffis, E.; Hapgood, M.A.; Green, L.; Bisi, M.M.; Bentley, R.D.; Wicks, R.; McKinnell, L.A.; Gibbs, M.; Burnett, C. The Economic Impact of Space Weather: Where Do We Stand? *Risk Anal.* **2017**, *37*, 206–218. [CrossRef] [PubMed]
23. Kumar, A.; Kashyap, Y.; Kosmopoulos, P. Enhancing Solar Energy Forecast Using Multi-Column Convolutional Neural Network and Multipoint Time Series Approach. *Remote Sens.* **2023**, *15*, 107. [CrossRef]
24. Alabdulgader, A.; McCraty, R.; Atkinson, M.; Dobyns, Y.; Vainoras, A.; Ragulskis, M.; Stolc, V. Long-Term Study of Heart Rate Variability Responses to Changes in the Solar and Geomagnetic Environment. *Sci. Rep.* **2018**, *8*, 2663. [CrossRef] [PubMed]
25. Bruno, A.; Christian, E.R.; de Nolfo, G.A.; Richardson, I.G.; Ryan, J.M. Spectral Analysis of the September 2017 Solar Energetic Particle Events. *Space Weather* **2019**, *17*, 419–437. [CrossRef]
26. Chamberlin, P.C.; Woods, T.N.; Didkovsky, L.; Eparvier, F.G.; Jones, A.R.; Machol, J.L.; Mason, J.P.; Snow, M.; Thiemann, E.M.B.; Viereck, R.A.; et al. Solar Ultraviolet Irradiance Observations of the Solar Flares During the Intense September 2017 Storm Period. *Space Weather* **2018**, *16*, 1470–1487. [CrossRef]
27. Pikulina, P.; Mironova, I.; Rozanov, E.; Karagodin, A. September 2017 Solar Flares Effect on the Middle Atmosphere. *Remote Sens.* **2022**, *14*, 2560. [CrossRef]
28. Vankadara, R.K.; Panda, S.K.; Amory-Mazaudier, C.; Fleury, R.; Devanaboyina, V.R.; Pant, T.K.; Jamjareegulgarn, P.; Haq, M.A.; Okoh, D.; Seemala, G.K. Signatures of Equatorial Plasma Bubbles and Ionospheric Scintillations from Magnetometer and GNSS Observations in the Indian Longitudes during the Space Weather Events of Early September 2017. *Remote Sens.* **2022**, *14*, 652. [CrossRef]
29. Amaechi, P.O.; Akala, A.O.; Oyedokun, J.O.; Simi, K.G.; Aghogho, O.; Oyeyemi, E.O. Multi-Instrument Investigation of the Impact of the Space Weather Events of 6–10 September 2017. *Space Weather* **2021**, *19*, e2021SW002806. [CrossRef]
30. Curto, J.J.; Marsal, S.; Blanch, E.; Altadill, D. Analysis of the Solar Flare Effects of 6 September 2017 in the Ionosphere and in the Earth's Magnetic Field Using Spherical Elementary Current Systems. *Space Weather* **2018**, *16*, 1709–1720. [CrossRef]
31. Bilitza, D. IRI the International Standard for the Ionosphere. *Adv. Radio Sci.* **2018**, *16*, 1–11. [CrossRef]
32. Moraal, H. Cosmic-Ray Modulation Equations. *Space Sci. Rev.* **2013**, *176*, 299–319. [CrossRef]
33. Dorman, L.I. *Cosmic Rays in the Earth's Atmosphere and Underground*; Springer: Dordrecht, The Netherlands, 2004; Volume 303, p. 862.
34. Zhang, J.L.; Tan, Y.H.; Wang, H.; Lu, H.; Meng, X.C.; Muraki, Y. The Yangbajing Muon–Neutron Telescope. In *Nuclear Instruments and Methods in Physics Research Section A: Accelerators, Spectrometers, Detectors and Associated Equipment*; Elsevier: Amsterdam, The Netherlands, 2010; Volume 623, pp. 1030–1034. [CrossRef]

35. Veselinović, N.; Dragić, A.; Savić, M.; Maletić, D.; Joković, D.; Banjanac, R.; Udovičić, V. An underground laboratory as a facility for studies of cosmic-ray solar modulation. In *Nuclear Instruments and Methods in Physics Research Section A: Accelerators, Spectrometers, Detectors and Associated Equipment*; Elsevier: Amsterdam, The Netherlands, 2017; Volume 875, pp. 10–15.
36. Savić, M.; Maletić, D.; Dragić, A.; Veselinović, N.; Joković, D.; Banjanac, R.; Udovičić, V.; Knežević, D. Modeling Meteorological Effects on Cosmic Ray Muons Utilizing Multivariate Analysis. *Space Weather* **2021**, *19*, e2020SW002712. [CrossRef]
37. Ferguson, J. *Computer Programs for Assessment of Long-Wavelength Radio Communications, Version 2.0: User's Guide and Source Files*; Space and Naval Warfare Systems Center: San Diego, CA, USA, 1998.
38. Mitra, A.P. *Lonospheric Effects of Solar Flares*; Springer: Berlin/Heidelberg, The Netherlands, 1974; Volume 46.
39. Wait, J.R.; Spies, K.P. *Characteristics of the Earth-Ionosphere Waveguide for VLF Radio Waves*; US Department of Commerce, National Bureau of Standards: Gaithersburg, MD, USA, 1964; Volume 13.
40. Srećković, V.A.; Šulić, D.M.; Vujčić, V.; Mijić, Z.R.; Ignjatović, L.M. Novel Modelling Approach for Obtaining the Parameters of Low Ionosphere under Extreme Radiation in X-Spectral Range. *Appl. Sci.* **2021**, *11*, 11574. [CrossRef]
41. AR12673 History. Available online: http://helio.mssl.ucl.ac.uk/helio-vo/solar_activity/arstats/arstats_page4.php?region=12673 (accessed on 14 December 2022).
42. Space Weather Prediction Center (IZMIRAN). Available online: http://spaceweather.izmiran.ru/eng/dbs.html (accessed on 22 January 2022).
43. Wold, A.M.; Mays, M.L.; Taktakishvili, A.; Jian, L.K.; Odstrcil, D.; MacNeice, P. Verification of real-time WSA−ENLIL+Cone simulations of CME arrival-time at the CCMC from 2010 to 2016. *J. Space Weather Space Clim.* **2018**, *8*, A17. [CrossRef]
44. Gopalswamy, N.; Yashiro, S.; Michalek, G.; Stenborg, G.; Vourlidas, A.; Freeland, S.; Howard, R. The SOHO/LASCO CME Catalog. *Earth Moon Planets* **2009**, *104*, 295–313. [CrossRef]
45. Werner, A.L.E.; Yordanova, E.; Dimmock, A.P.; Temmer, M. Modeling the Multiple CME Interaction Event on 6–9 September 2017 with WSA-ENLIL+Cone. *Space Weather* **2019**, *17*, 357–369. [CrossRef]
46. SPDF - OMNIWeb Service. Available online: https://spdf.gsfc.nasa.gov/pub/data/omni/low_res_omni/ (accessed on 10 November 2022).
47. Torsti, J.; Valtonen, E.; Lumme, M.; Peltonen, P.; Eronen, T.; Louhola, M.; Riihonen, E.; Schultz, G.; Teittinen, M.; Ahola, K.; et al. Energetic particle experiment ERNE. *Sol. Phys.* **1995**, *162*, 505–531. [CrossRef]
48. Multi-Source Spectral Plots (MSSP) of Energetic Particle. Available online: https://omniweb.gsfc.nasa.gov/ftpbrowser/flux_spectr_m.html (accessed on 25 October 2022).
49. Savić, M.; Veselinović, N.; Dragić, A.; Maletić, D.; Joković, D.; Udovičić, V.; Banjanac, R.; Knežević, D. New insights from cross-correlation studies between solar activity indices and cosmic-ray flux during Forbush decrease events. *Adv. Space Res.* **2022**, *71*, 2006–2016. [CrossRef]
50. Band, D.; Matteson, J.; Ford, L.; Schaefer, B.; Palmer, D.; Teegarden, B.; Cline, T.; Briggs, M.; Paciesas, W.; Pendleton, G.; et al. BATSE Observations of Gamma-Ray Burst Spectra. I. Spectral Diversity. *Astrophys. J.* **1993**, *413*, 281. [CrossRef]
51. Ellison, D.C.; Ramaty, R. Shock acceleration of electrons and ions in solar flares. *Astrophys. J.* **1985**, *298*, 400–408. [CrossRef]
52. Mottl, D.A.; Nymmik, R.A.; Sladkova, A.I. Energy spectra of high-energy SEP event protons derived from statistical analysis of experimental data on a large set of events. *AIP Conf. Proc.* **2001**, *552*, 1191–1196. [CrossRef]
53. Zhao, L.; Zhang, M.; Rassoul, H.K. Double power laws in the event-integrated solar energetic particle spectrum. *Astrophys. J.* **2016**, *821*, 62. [CrossRef]
54. Miteva, R.; Samwel, S.W.; Zabunov, S.; Dechev, M. On the flux saturation of SOHO/ERNE proton events. *Bulg. Astron. J.* **2020**, *33*, 99.
55. NOAA National Centers for Environmental Information. Available online: https://satdat.ngdc.noaa.gov/sem/goes/data/avg/ (accessed on 10 October 2022).
56. Žigman, V.; Grubor, D.; Šulić, D. D-region electron density evaluated from VLF amplitude time delay during X-ray solar flares. *J. Atmos. Sol.-Terr. Phys.* **2007**, *69*, 775–792. [CrossRef]
57. Kolarski, A.; Grubor, D. Sensing the Earth's low ionosphere during solar flares using VLF signals and goes solar X-ray data. *Adv. Space Res.* **2014**, *53*, 1595–1602. [CrossRef]
58. Kolarski, A.; Srećković, V.A.; Mijić, Z.R. Monitoring solar activity during 23/24 solar cycle minimum through VLF radio signals. *Contrib. Astron. Obs. Skaln. Pleso* **2022**, *52*, 105. [CrossRef]
59. Šulić, D.; Srećković, V.A.; Mihajlov, A.A. A study of VLF signals variations associated with the changes of ionization level in the D-region in consequence of solar conditions. *Adv. Space Res.* **2016**, *57*, 1029–1043. [CrossRef]
60. Dorman, L.; Tassev, Y.; Velinov, P.I.Y.; Mishev, A.; Tomova, D.; Mateev, L. Investigation of exceptional solar activity in September 2017: GLE 72 and unusual Forbush decrease in GCR. *J. Phys. Conf. Ser.* **2019**, *1181*, 012070. [CrossRef]
61. Neutron Monitor Database. Available online: https://www.nmdb.eu/ (accessed on 20 October 2022).
62. Kojima, H.; Shibata, S.; Oshima, A.; Hayashi, Y.; Antia, H.; Dugad, S.; Fujii, T.; Gupta, S.K.; Kawakami, S.; Minamino, M.; et al. Rigidity Dependence of Forbush Decreases. In Proceedings of the 33rd International Cosmic Ray Conference, Rio de Janeiro, Brazil, 2–9 July 2013.
63. Near-Earth Interplanetary Coronal Mass Ejections Since January 1996. Available online: https://izw1.caltech.edu/ACE/ASC/DATA/level3/icmetable2.htm (accessed on 15 October 2022).

64. Soho Lasco Cme Catalog Cdaw Data Center. Available online: https://cdaw.gsfc.nasa.gov/CME_list/ (accessed on 10 November 2022).
65. Scolini, C.; Chané, E.; Temmer, M.; Kilpua, E.K.J.; Dissauer, K.; Veronig, A.M.; Palmerio, E.; Pomoell, J.; Dumbović, M.; Guo, J.; et al. CME–CME Interactions as Sources of CME Geoeffectiveness: The Formation of the Complex Ejecta and Intense Geomagnetic Storm in 2017 Early September. *Astrophys. J. Suppl. Ser.* **2020**, *247*, 21. [CrossRef]
66. Badruddin, B.; Aslam, O.P.M.; Derouich, M.; Asiri, H.; Kudela, K. Forbush Decreases and Geomagnetic Storms During a Highly Disturbed Solar and Interplanetary Period, 4–10 September 2017. *Space Weather* **2019**, *17*, 487–496. [CrossRef]
67. Miteva, R.; Klein, K.L.; Malandraki, O.; Dorrian, G. Solar Energetic Particle Events in the 23rd Solar Cycle: Interplanetary Magnetic Field Configuration and Statistical Relationship with Flares and CMEs. *Sol. Phys.* **2013**, *282*, 579–613. [CrossRef]
68. Ravishankar, A.; Michałek, G. Non-interacting coronal mass ejections and solar energetic particles near the quadrature configuration of Solar TErrestrial RElations Observatory. *Astron. Astrophys.* **2020**, *638*, A42. [CrossRef]
69. Pandey, U.; Singh, B.; Singh, O.P.; Saraswat, V.K. Solar flare induced ionospheric D-region perturbation as observed at a low latitude station Agra, India. *Astrophys. Space Sci.* **2015**, *357*, 35. [CrossRef]
70. Gavrilov, B.G.; Ermak, V.M.; Lyakhov, A.N.; Poklad, Y.V.; Rybakov, V.A.; Ryakhovsky, I.A. Reconstruction of the Parameters of the Lower Midlatitude Ionosphere in M- and X-Class Solar Flares. *Geomagn. Aeron.* **2020**, *60*, 747–753. [CrossRef]
71. Venkatesham, K.; Singh, R. Extreme space-weather effect on D-region ionosphere in Indian low latitude region. *Curr. Sci.* **2018**, *114*, 1923–1926. [CrossRef]
72. Thomson, N.R.; Rodger, C.J.; Clilverd, M.A. Large solar flares and their ionospheric D region enhancements. *J. Geophys. Res. Space Phys.* **2005**, *110*. [CrossRef]
73. Grubor, D.; Šulić, D.; Žigman, V. The response of the Earth-ionosphere VLF waveguide to the January 15-22 2005 solar events. In Proceedings of the IUGG XXIV General Assembly, Perugia, Italy, 2–13 July 2007.
74. Kolarski, A.; Grubor, D. Monitoring VLF signal perturbations induced by solar activity during January 2005. In Proceedings of the The XIX Serbian Astronomical Conference, Belgrade, Serbia, 13–17 October 2020; pp. 387–390.
75. Kumar, S.; Kumar, A.; Menk, F.; Maurya, A.K.; Singh, R.; Veenadhari, B. Response of the low-latitude D region ionosphere to extreme space weather event of 14–16 December 2006. *J. Geophys. Res. Space Phys.* **2015**, *120*, 788–799. [CrossRef]
76. Tan, L.M.; Thu, N.N.; Ha, T.Q.; Marbouti, M. Study of solar flare induced D-region ionosphere changes using VLF amplitude observations at a low latitude site. *Indian J. Radio Space Phys.* **2014**, *43*, 197–246.
77. McRae, W.M.; Thomson, N.R. Solar flare induced ionospheric D-region enhancements from VLF phase and amplitude observations. *J. Atmos. Sol.-Terr. Phys.* **2004**, *66*, 77–87. [CrossRef]
78. Zhao, L.L.; Zhang, H. Transient galactic cosmic-ray modulation during solar cycle 24: A comparative study of two prominent forbush decrease events. *Astrophys. J.* **2016**, *827*, 13. [CrossRef]
79. Lingri, D.; Mavromichalaki, H.; Belov, A.; Eroshenko, E.; Yanke, V.; Abunin, A.; Abunina, M. Solar Activity Parameters and Associated Forbush Decreases During the Minimum between Cycles 23 and 24 and the Ascending Phase of Cycle 24. *Sol. Phys.* **2016**, *291*, 1025–1041. [CrossRef]

# Supplementary Material

## Impacts of extreme space weather events on September 6th, 2017 on ionosphere and primary cosmic rays

Aleksandra Kolarski, Nikola Veselinović, Vladimir A. Srećković, Zoran Mijić*, Mihailo Savić and Aleksandar Dragić

Institute of Physics Belgrade, University of Belgrade, Pregrevica 118, 11080 Belgrade, Serbia
*Correspondence: zoran.mijic@ipb.ac.rs; Tel.:+381 11 3713134

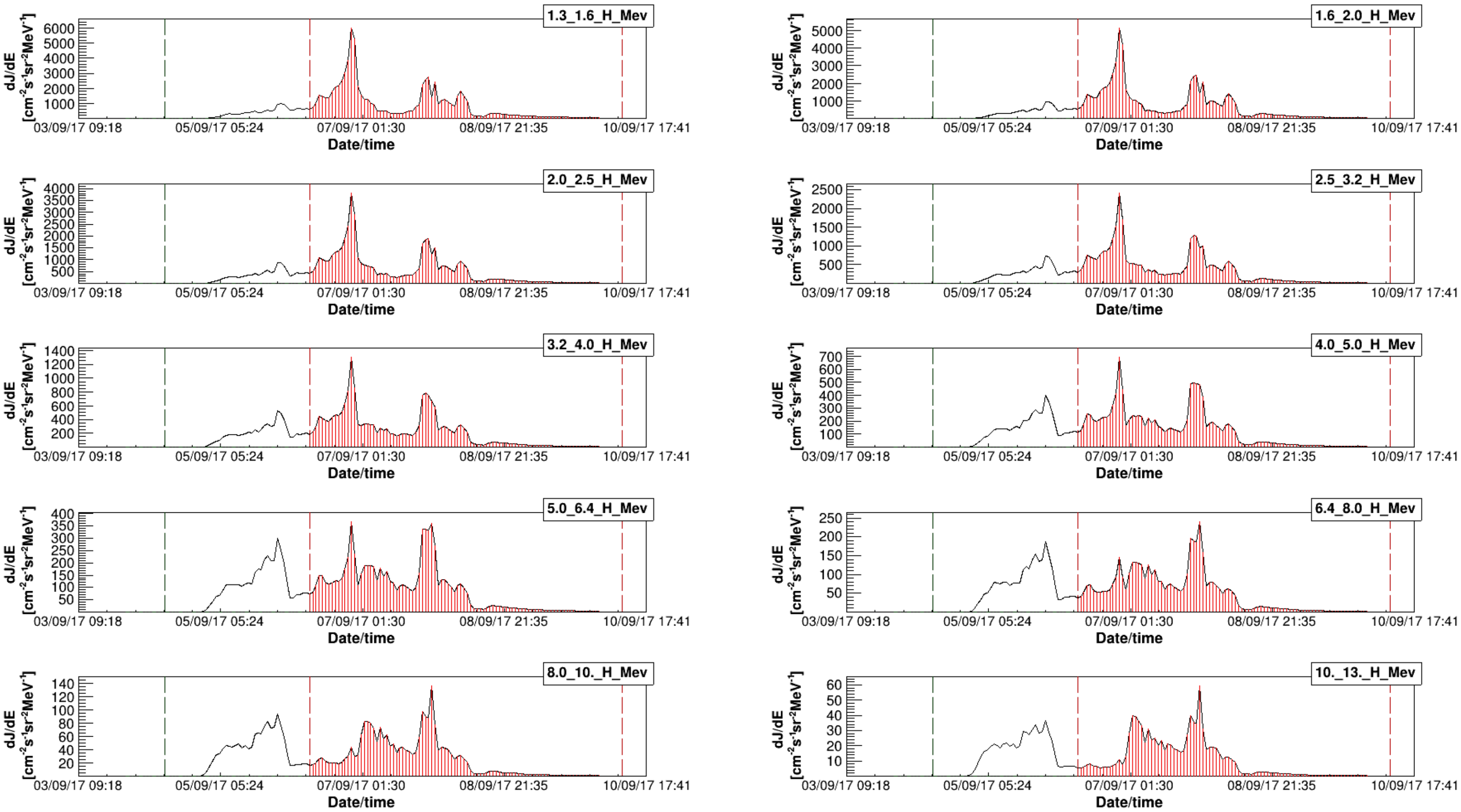


**Figure S1**. Differential SEP fluxes during extreme solar event in September 2017, measured by SOHO/ERNE energetic particle sensors LET (Low Energy Detector) proton channels. Red vertical dashed lines indicate the time for the start and the end of interval used to calculate the integral flux.

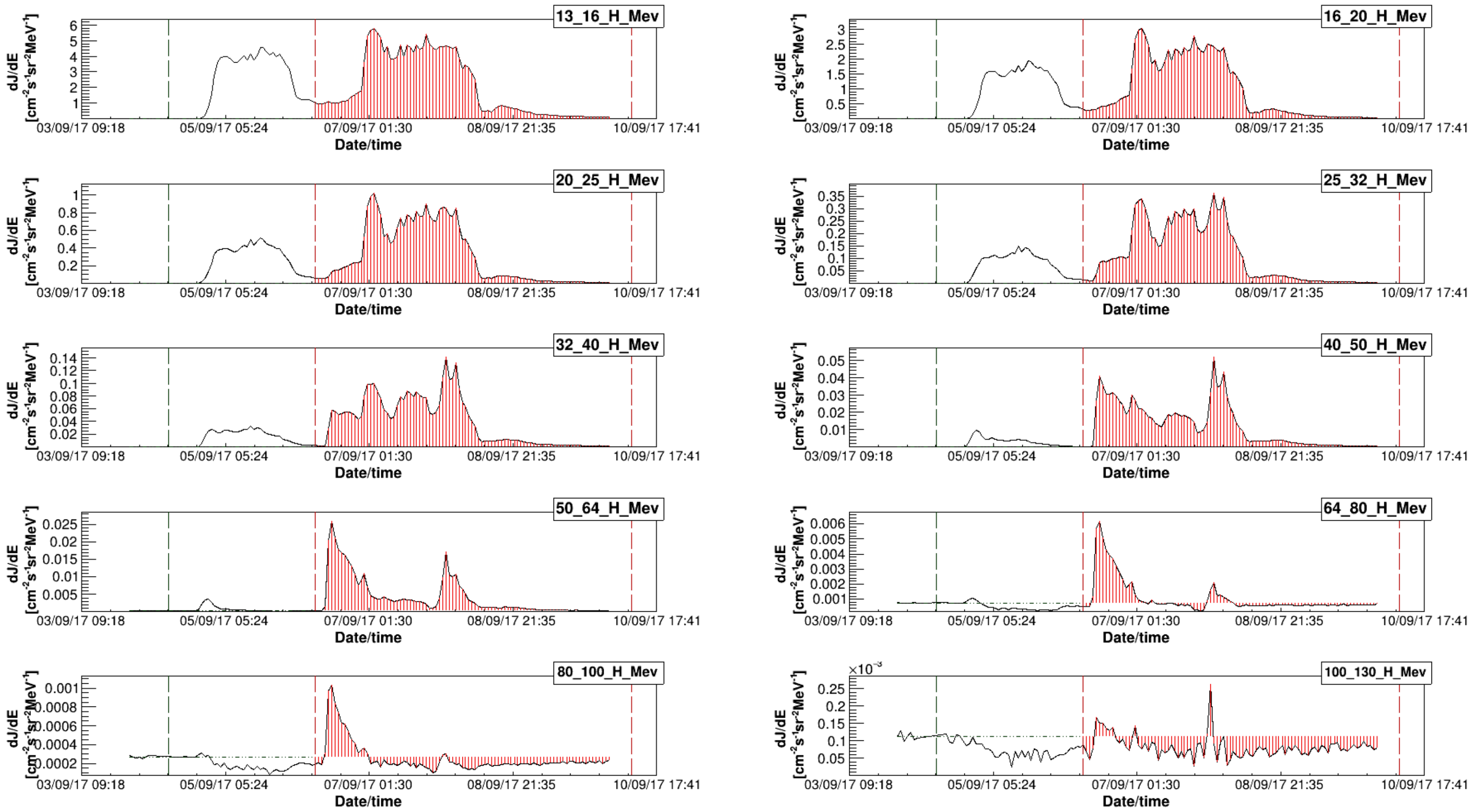


**Figure S2.** Differential SEP fluxes during extreme solar event in September 2017, measured by SOHO/ERNE energetic particle sensors HET (High Energy Detector) proton channels. Red vertical dashed lines indicate the time for the start and the end of interval used to calculate the integral flux.

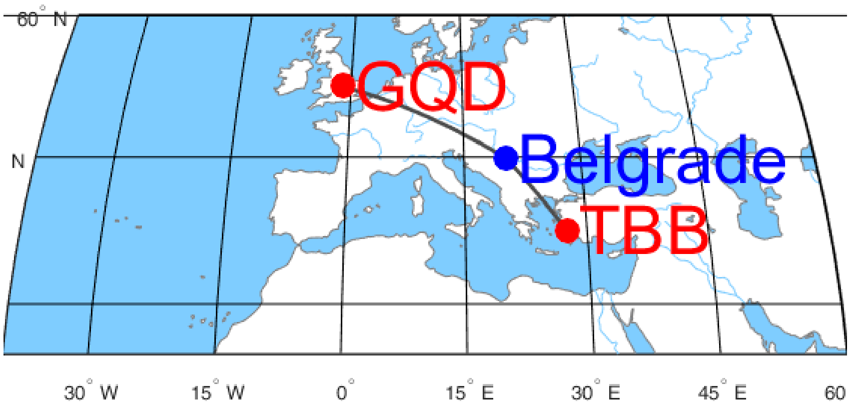


**Figure S3.** The geographic position of Belgrade (BEL) VLF receiver and the GQD transmitter (54.73° N, 2.88° W) Anthorn UK and TBB transmitter (37.43° N, 27.55° E) Bafa Turkey with GCP of sub-ionospheric propagating VLF signals.

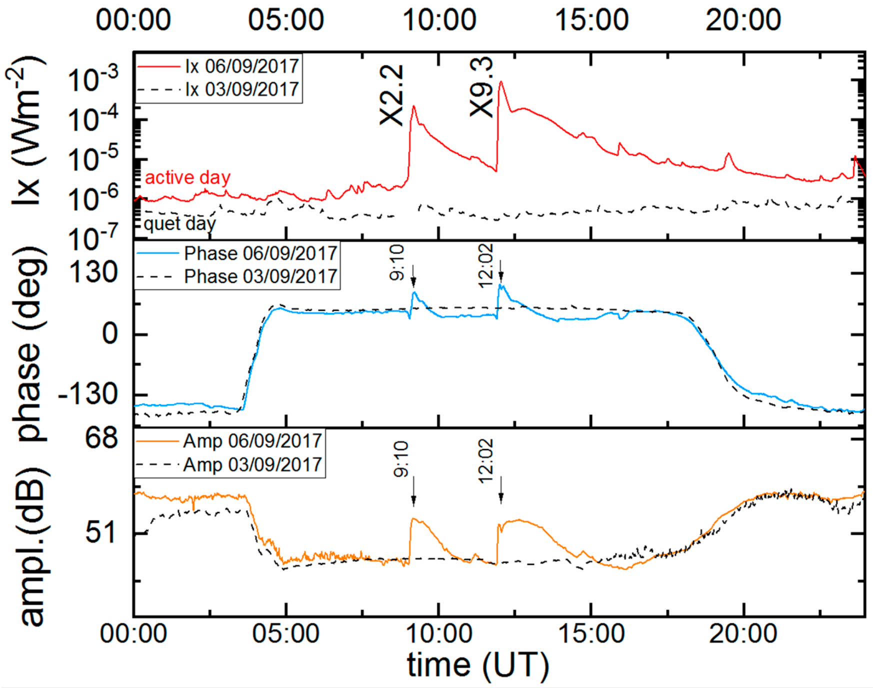


**Figure S4.** Simultaneous variations of X-ray flux (red), phase (blue) and amplitude (orange) of GQD/22.10 kHz signal versus universal time UT during occurrence of X2.2 and X9.3 class SFs of September 6th, 2017 (from upper to lower panel). Observed amplitude and phase perturbations on GQD radio signal, as well as quiet signal (dashed black), are measured at Belgrade station. Time variation of soft X-ray irradiance is measured by GOES-15 satellite.

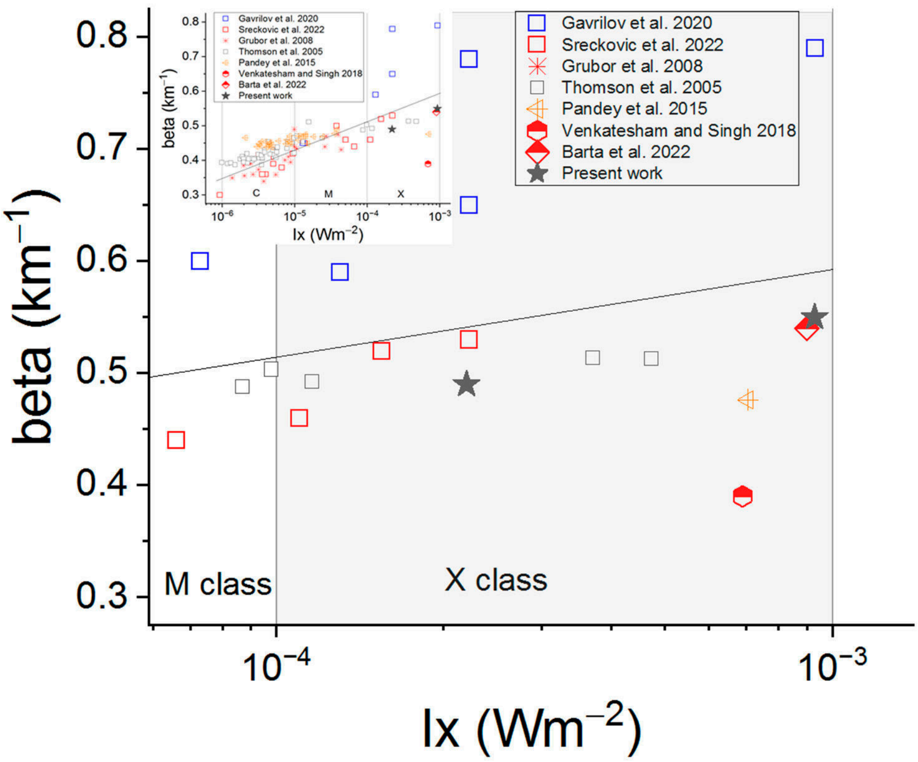

beta (km$^{-1}$)
Ix (Wm$^{-2}$)
M class
X class
Gavrilov et al. 2020
Sreckovic et al. 2022
Grubor et al. 2008
Thomson et al. 2005
Pandey et al. 2015
Venkatesham and Singh 2018
Barta et al. 2022
Present work


(a)

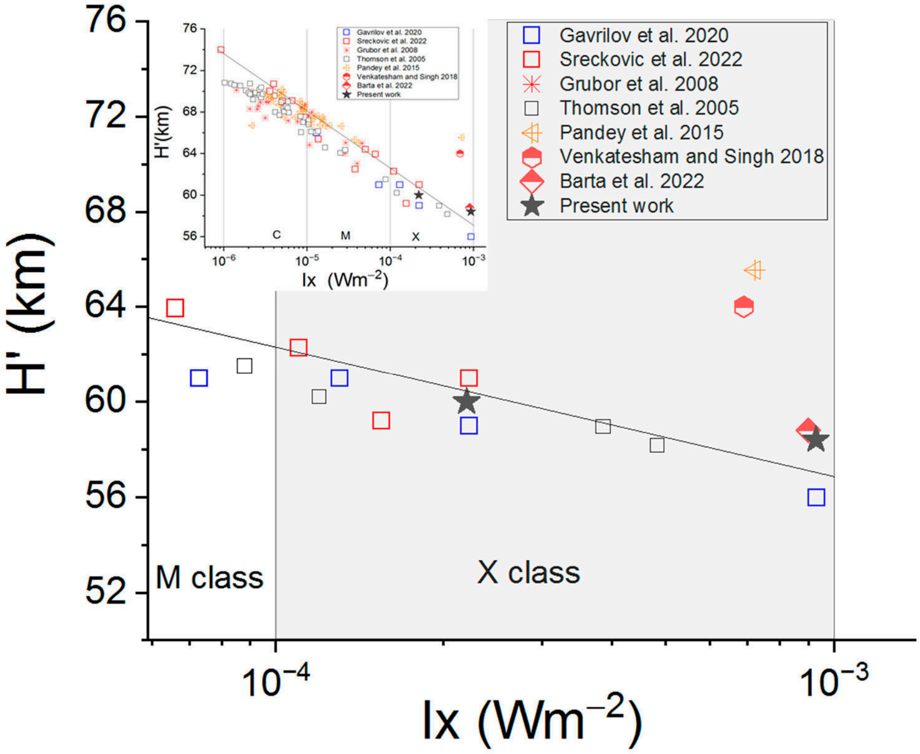

H' (km)
Ix (Wm$^{-2}$)
M class
X class
Gavrilov et al. 2020
Sreckovic et al. 2022
Grubor et al. 2008
Thomson et al. 2005
Pandey et al. 2015
Venkatesham and Singh 2018
Barta et al. 2022
Present work


(b)

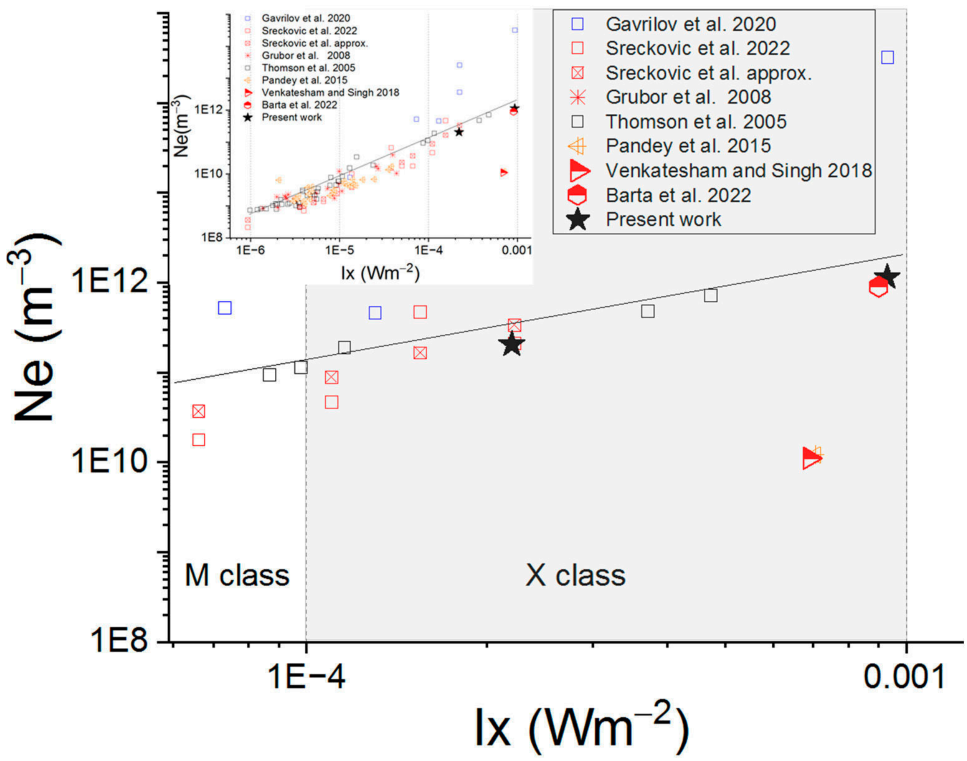


(c)

**Figure S5.** Lower ionospheric response to SF events of different strength across X-class (shaded gray area), obtained indirect through modeling of VLF signals' propagation parameters: (a) sharpness β (km$^{-1}$) and (b) effective reflection height *H'* (km) and (c) estimated corresponding electron densities *Ne* (m$^{-3}$), in function of X-ray flux; results from our research are presented by black stars.

Our results (black stars) are compared to other studies including several major cases of strong SF events from period 2003-2011 with SF cases of class X28+–X6.9 (a-d) and with some other cases from period 2006-2017 covering range X1-X9.3 (e-i) and from period 1994-1998 in range X1-X5 (j):

a) X6.9 of August 9th, 2011 at 08:05UT - strongest SF of 24th solar cycle, associated with CME and SPE events; at low-latitude site [71,69]
b) X9 of December 5th, 2006 at 10:35UT – strongest SF in 2006 and eighth of 23rd solar cycle; at mid-latitude site (Belgrade VLF database) [7]
c) X28+ of November 4th, 2003 at 19:53UT – one of strongest solar flares ever recorded and strongest of 23rd solar cycle associated with CME and SPE events, from very active period October 20th-November 5th, 2003 including X10.1 of October 29th, 2003 at 20:49UT and X8.3 of November 2nd, 2003 at 17:25UT third and fourth in 2003 and sixth and ninth of 23rd solar cycle, both associated with CME; at mid-latitude site [72]
d) X7.1 of January 20th, 2005 at 07:01UT – second strongest SF in 2005 and tenth of 23rd solar cycle associated with CME and SPE events, from active period January 15th–22nd, 2005; at mid-latitude site (Belgrade VLF database) [73,74]

e) X1.1-X2.2 of June 10th and 11th, 2014 (CME?) & X17.2 of October 28th, 2003 (associated with CME and SPE events); at mid-latitude site (Belgrade VLF database) [5]
f) X1.3 of September 7th, 2017; at mid-latitude site (Belgrade VLF database) [8]
g) X1.3-X9.3 of June 10th, 2014 & September 6th–10th, 2017, with strongest two of them (both above X5) associated with CME; at mid-latitude site, but a bit northward from Belgrade [70]
h) X1.5 of December 14th, 2006 at 22:15UT; at low-latitude site [75]
i) X1-X3.2 in period May–December 2013, all associated with CME and one of the weaker ones associated with SPE; at low-latitude site [76]
j) X3-X5 in period 1994-1998, some associated with CME and SEP events; at mid latitude site [77]

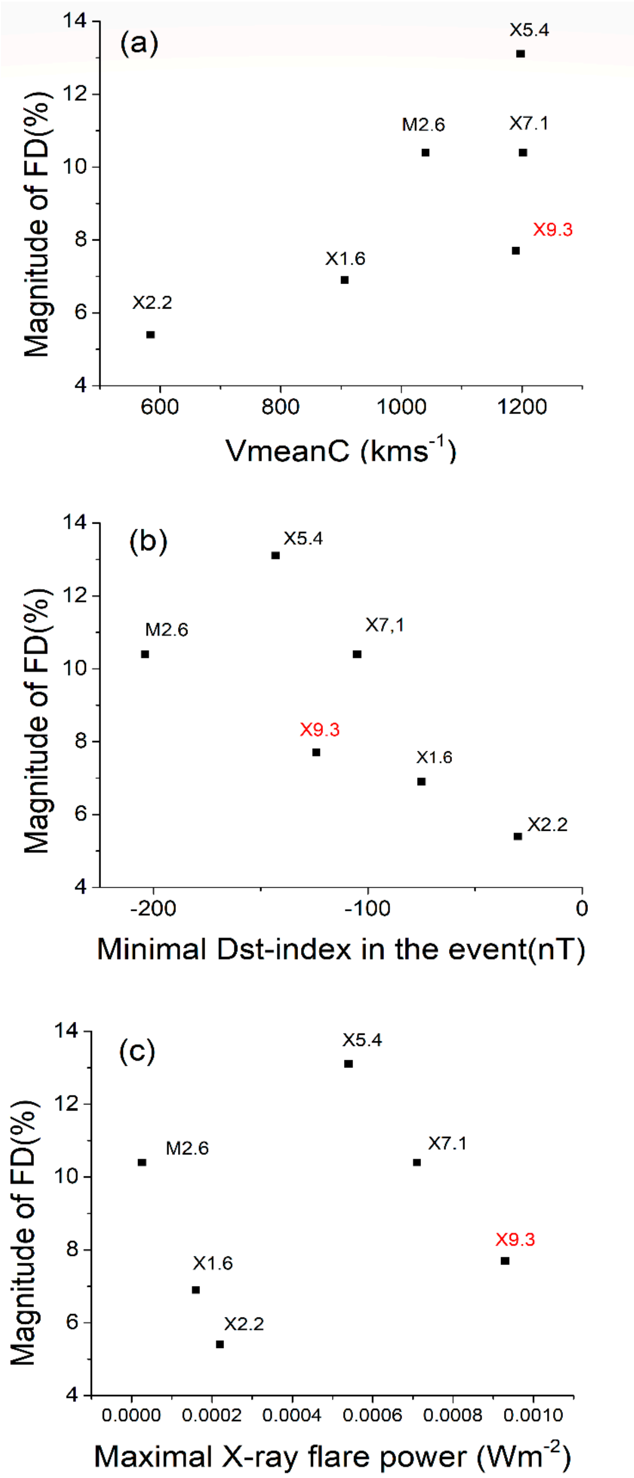


**Figure S6.** Magnitude of the FD versus the average CME velocity between the Sun and the Earth, calculated using the time of the beginning of the associated CME observations (a), Minimal Dst-index in the event (b), maximal X-ray flare power (c), with associated flare indicated in red.

Atmos. Chem. Phys., 20, 10775–10789, 2020
https://doi.org/10.5194/acp-20-10775-2020


Atmospheric Chemistry and Physics
Open Access
EGU

# An EARLINET early warning system for atmospheric aerosol aviation hazards

**Nikolaos Papagiannopoulos[1,2], Giuseppe D'Amico[1], Anna Gialitaki[3,4], Nicolae Ajtai[5], Lucas Alados-Arboledas[6], Aldo Amodeo[1], Vassilis Amiridis[3], Holger Baars[7], Dimitris Balis[4], Ioannis Binietoglou[8], Adolfo Comerón[2], Davide Dionisi[9], Alfredo Falconieri[1], Patrick Fréville[10], Anna Kampouri[3,4], Ina Mattis[11], Zoran Mijić[12], Francisco Molero[13], Alex Papayannis[14], Gelsomina Pappalardo[1], Alejandro Rodríguez-Gómez[2], Stavros Solomos[3], and Lucia Mona[1]**

[1]Consiglio Nazionale delle Ricerche – Istituto di Metodologie per l'Analisi Ambientale (CNR-IMAA), C. da S. Loja, Tito Scalo (PZ), Italy
[2]CommSensLab, Dept. of Signal Theory and Communications, Universitat Politècnica de Catalunya, Barcelona, Spain
[3]IAASARS, National Observatory of Athens, Athens, Greece
[4]Laboratory of Atmospheric Physics, Physics Department, Aristotle University of Thessaloniki, Thessaloniki, Greece
[5]Faculty of Environmental Science and Engineering, Babes–Bolyai University of Cluj Napoca, Cluj, Romania
[6]Department of Applied Physics, University of Granada, Granada, Spain
[7]Leibniz Institute for Tropospheric Research (TROPOS), Leipzig, Germany
[8]National Institute of R&D for Optoelectronics (INOE), Magurele, Romania
[9]Consiglio Nazionale delle Ricerche – Istituto di Scienze Marine (CNR-ISMAR), Rome, Italy
[10]Observatoire de Physique du Globe (OPGC-LaMP), Clermont-Ferrand, France
[11]Deutscher Wetterdienst, Meteorologisches Observatorium Hohenpeißenberg, Hohenpeissenberg, Germany
[12]Institute of Physics Belgrade, University of Belgrade, Belgrade, Serbia
[13]Centro de Investigaciones Energéticas, Medioambientales y Tecnológicas, Department of Environment, Madrid, Spain
[14]Laser Remote Sensing Unit, Physics Department, National Technical University of Athens, Athens, Greece

**Correspondence:** Nikos Papagiannopoulos (nikolaos.papagiannopoulos@imaa.cnr.it)

Received: 24 February 2020 – Discussion started: 27 February 2020
Revised: 5 June 2020 – Accepted: 3 August 2020 – Published: 15 September 2020

**Abstract.** A stand-alone lidar-based method for detecting airborne hazards for aviation in near real time (NRT) is presented. A polarization lidar allows for the identification of irregular-shaped particles such as volcanic dust and desert dust. The Single Calculus Chain (SCC) of the European Aerosol Research Lidar Network (EARLINET) delivers high-resolution preprocessed data: the calibrated total attenuated backscatter and the calibrated volume linear depolarization ratio time series. From these calibrated lidar signals, the particle backscatter coefficient and the particle depolarization ratio can be derived in temporally high resolution and thus provide the basis of the NRT early warning system (EWS). In particular, an iterative method for the retrieval of the particle backscatter is implemented. This improved capability was designed as a pilot that will produce alerts for imminent threats for aviation. The method is applied to data during two diverse aerosol scenarios: first, a record breaking desert dust intrusion in March 2018 over Finokalia, Greece, and, second, an intrusion of volcanic particles originating from Mount Etna, Italy, in June 2019 over Antikythera, Greece. Additionally, a devoted observational period including several EARLINET lidar systems demonstrates the network's preparedness to offer insight into natural hazards that affect the aviation sector.

Published by Copernicus Publications on behalf of the European Geosciences Union.

## 1 Introduction

During the aviation crisis related to the volcanic eruption of Eyjafjallajökull, Iceland, in 2010, the European Aerosol Research Lidar Network (EARLINET; Pappalardo et al., 2014) provided range-resolved information to the World Meteorological Organization (WMO) on a daily basis (reports available at: https://www.earlinet.org, last access: 31 October 2019). The reports communicated the altitude, time, and location of the volcanic clouds over Europe. Furthermore, the time–height evolution of the lidar returns was freely available in near real time (NRT) on the EARLINET website. The nonautomated, non-harmonized, and non-homogenized process and the lack of tailored products for natural hazards made the EARLINET data disregarded in the decision-making process.

The lessons learned from the Eyjafjallajökull crisis emphasized the vulnerability of air transportation to natural hazards (Bolic and Sivcev, 2011). Volcanic ash plumes, as well as desert dust outbreaks, present an imminent threat to aviation as they lead, among others, to poor visibility with considerable consequences to flight operations (Bolic and Sivcev, 2011; Middleton, 2017). Aircraft that do fly in volcanic/desert dust conditions can have a variety of damage from scouring of surfaces to engine failure (Eliasson et al., 2016). The aftermath of an encounter can be immediate, reducing flight safety; furthermore, it can financially affect the airlines due to higher maintenance costs and the replacement of mechanical equipment.

Furthermore, the Eyjafjallajökull eruption highlighted the gap in the availability of real-time measurements and monitoring information for airborne hazards. Specifically, the lack of height-resolved information, a key aspect in flight planning and mitigation strategies, became evident. In the frame of the Horizon 2020 research project EUNADICS-AV (European Natural Disaster Coordination and Information System for Aviation; https://www.eunadics.eu, last access: 31 October 2019) funded by the European Commission, different organizations worked together in a consortium to provide relevant data during situations when aviation is affected by airborne hazards (e.g., volcanic ash, desert dust, biomass burning, radionuclide). Crucial for the overall success of the project and the early warning system (EWS) design were the review of the available observations and the collection of specific requirements from the different stakeholders that once more pointed out the importance of height-resolved information.

A polarization lidar is an important tool to characterize the different aerosols. This system permits the discrimination of light-depolarizing coarse-mode particles such as volcanic and desert dust and fine-mode particles such as smoke particles and anthropogenic pollution (e.g., Tesche et al., 2011; Mamouri and Ansmann, 2017). Further, the lidar setup allows for the retrieval of coarse-mode and fine-mode backscatter coefficients for wavelengths of 532 and 1064 nm (e.g., Tesche et al., 2009). When synergistically used with a photometer, it is possible to retrieve their mass concentration profile (e.g., Ansmann et al., 2012; Lopatin et al., 2013; Chaikovsky et al., 2016).

During the last years, EARLINET has strongly increased its observing capacity with the addition of new stations and a system upgrade, namely, the installation of depolarization channels. In addition, the further development of the Single Calculus Chain (SCC) (D'Amico et al., 2015, 2016; Mattis et al., 2016) under the ACTRIS (Aerosols, Clouds and Trace gases Research InfraStructure Network) umbrella eliminated the inconsistencies in the retrieval procedures and in the signal error calculation, automated the data evaluation, and now allows for NRT data processing and the generation of tailored products network-wide. EARLINET has already demonstrated the network's NRT capabilities, as well as assisted modeling studies in NRT evaluation and assimilation (Wang et al., 2014; Sicard et al., 2015). As a consequence, EARLINET is prepared to provide prompt, height-resolved information and tailored products that were greatly missed during the 2010 aviation crisis. Therefore, a methodology for an early warning system based solely on EARLINET data is developed.

In Sect. 2, we present the EARLINET remote sensing network and the data that we used in this study. In Sect. 3, we introduce the methodology of the EARLINET-based EWS. In Sect. 4, we present the results obtained by applying the methodology to real measurements and the lessons learned from a multi-station EARLINET observational period. Finally, in Sect. 5, we give our conclusions and indicate directions for future work.

## 2 EARLINET

The European Aerosol Research Lidar Network (EARLINET; Pappalardo et al., 2014) was established in 2000, provides aerosol profiling data on a continental scale, and is now part of the Aerosols, Clouds, and Trace gases Research InfraStructure (ACTRIS; https://www.actris.eu, last access: 31 October 2019). Nowadays, more than 30 stations are active and perform measurements according to the network's schedule (one daytime and two nighttime measurements per week). Figure 1 illustrates the network's geographic extent and the location of the active EARLINET stations (green squares) and the joining EARLINET stations (yellow squares), together with the non-active site of Finokalia (red square), for which lidar data are used in this study. Further measurements are devoted to special events, such as volcanic eruptions, forest fires, and desert dust outbreaks (e.g., Mona et al., 2012; Pappalardo et al., 2013; Ortiz-Amezcua et al., 2017; Granados-Muñoz et al., 2016). The majority of the EARLINET stations operate multi-wavelength Raman lidars that combine a set of elastic and nitrogen inelastic channels and are equipped with depolarization channels. This li-

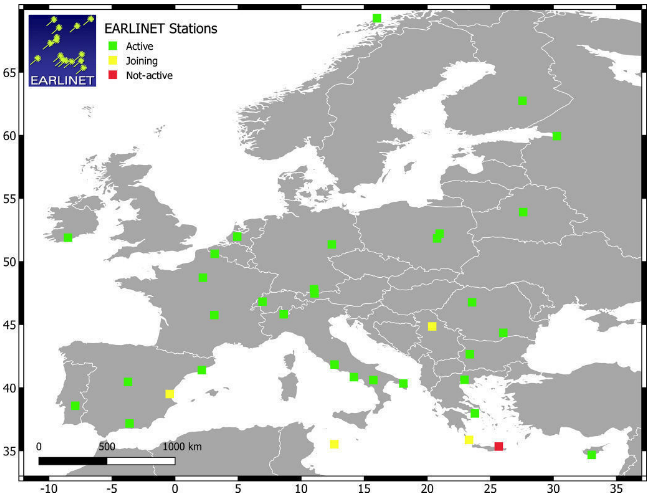


**Figure 1.** The EARLINET network in Europe. The green squares indicate the active stations, the yellow squares indicate the joining stations, and the red square indicates the non-active Finokalia, Greece, station.

dar configuration allows for the retrieval of intensive aerosol profiles, such as the particle lidar ratio, particle Ångström exponent, and particle depolarization ratio. These variables are shown to vary with the aerosol type and location, and, consequently, EARLINET stations are able to characterize the aerosol load (Müller et al., 2007). Accordingly, EARLINET has established tools for automatic aerosol characterization (Nicolae et al., 2018; Papagiannopoulos et al., 2018).

To ensure a homogeneous, traceable, and quality-controlled analysis of raw lidar data across the network, a centralized and fully automated analysis tool, called the Single Calculus Chain (SCC), has been developed within EARLINET (D'Amico et al., 2015, 2016; Mattis et al., 2016). Raw lidar data are first submitted to the central SCC server by each EARLINET station, and several lidar products are generated automatically. In particular, low-resolution (in both time and space) uncalibrated preprocessed products provided by the SCC EARLINET Lidar Pre-Processor (ELPP) module (D'Amico et al., 2016) and aerosol optical properties vertical profiles provided by the SCC EARLINET Lidar Data Analyzer (ELDA) module (Mattis et al., 2016) are made available. Recently a new version of the SCC has been released providing also standardized high-resolution preprocessed lidar products. These new products include the calibrated attenuated backscatter coefficient and volume linear depolarization ratio time series at instrumental time and space resolution. Particular attention has been paid to the calibration of the high-resolution products; an automatic and fully traceable calibration procedure using the low-resolution SCC-retrieved particle backscatter and extinction coefficients has been designed and implemented in the SCC framework.

The cloud screening module is responsible for cloud identification in uncalibrated lidar signals and especially with low clouds since such clouds do not permit the aerosol optical property retrieval by ELDA. Note that the cloud removal is also essential in our EWS methodology. The input of the algorithm is the high-resolution preprocessed signals produced by the SCC HiRELPP (High-Resolution EARLINET Pre-Processor) module. The current cloud screening detects clouds as bins with irregularly high values in signal and edge strength (Nixon and Aguado, 2019; Tramutoli, 1998). The algorithm works well with uncalibrated signals recorded by multiple lidar systems across EARLINET. However, the false detection of aerosol-laden bins as cloud can occur, especially in cases where there is high contrast between an aerosol layer and the rest of the atmosphere. For this reason, the development of a cloud screening module based on calibrated lidar signals and quantitative criteria is foreseen.

The calibrated high-resolution data along with the cloud screening output are essential for the proposed methodology and are used in the EWS. The methodology to derive the particle high-resolution data that are described in Sect. 3 is first cloud cleared and second based on 5 min and 30 m averaged profiles in order to increase the signal-to-noise ratio.

### 2.1 The sites of Finokalia and Antikythera, Greece

The EARLINET component of NOA (National Observatory of Athens) for the period of April 2017 until May 2018 was deployed through the NOA lidar system on the north coast of Crete. The Finokalia Atmospheric Observatory (35.34° N, 25.67° E) is a research infrastructure with activities covering in situ aerosol characterization, 3-D aerosol distribution, and gas precursors. Since June 2018, the system has been located on the island of Antikythera, where a suite of remote sensing sensors are installed in order to study the properties of natural aerosol particles (e.g., sea salt, dust, volcanic ash) in Mediterranean background conditions. The islands of Crete and Antikythera are very often affected by windblown dust originating from the Sahara due to their proximity to the African coastline, and this can be along the traveled path of volcanic dust and sulfate aerosols from the Italian active volcanoes (e.g., Hughes et al., 2016).

The NOA lidar system Polly$^{XT}$ (e.g., Engelmann et al., 2016) operates in the frame of EARLINET and under the umbrella of ACTRIS. The system is equipped with three elastic channels at 355, 532, and 1064 nm, two vibration-rotation Raman channels at 387 and 607 nm, two linear depolarization channels at 355 and 532 nm, and one water vapor channel at 407 nm. Depending on the atmospheric conditions, the combined use of its near-range and far-range telescopes provides reliable vertical profiles of aerosol optical properties from 0.2–0.4 km to almost 16 km in height.

### 2.2 Additional data

For the detection of the desert dust plume, satellite imagery from the Spinning Enhanced Visible Infrared Imager (SE-

VIRI) is used. SEVIRI is a line-by-line scanning radiometer on board the Meteosat Second Generation (MSG) geostationary satellite. It provides data in 12 spectral bands every 15 min for the full Earth disk area. The spatial resolution is around 3 km at the nadir, which is different from the high-resolution visible (HRV) band (1 km). In this study, we used a largely accepted multi-temporal scheme of satellite data analysis (Tramutoli, 2007) to detect the dust plume over the Mediterranean basin. In particular, we used the $\mathrm{eRST_{DUST}}$ (enhanced robust satellite technique for dust detection) algorithm (Marchese et al., 2017), which combines an index analyzing the visible radiance (at around 0.6 µm) to another one based on the brightness temperature difference (BTD) of the signal measured by the SEVIRI spectral channels centered at 10.8 and 12 µm wavelengths.

For the detection of the volcanic dust, we use the Lagrangian transport model FLEXPART (FLEXible PARTicle dispersion model; Brioude et al., 2013; Stohl et al., 2005) in a forward mode to simulate the dispersion of volcanic emissions from Mount Etna, Italy. Dispersion simulations are driven by hourly meteorological fields from the Weather Research and Forecasting model (WRF; Skamarock et al., 2008) at 36 km×36 km horizontal resolution. The initial and boundary conditions for the off-line coupled WRF–FLEXPART runs are taken from the National Center for Environmental Prediction (NCEP) final analysis (FNL) dataset at a 1° × 1° resolution at 6-hourly intervals. The sea surface temperature (SST) is taken from the NCEP 0.5° × 0.5° analysis. The simulated case study did not include an eruptive stage; therefore, the initial injection height is set from the crater level (3.3 km at sea level, a.s.l.) up to 4 km a.s.l. A total of 10 000 tracer particles are released for this simulation. Dry and wet deposition processes are also enabled in these runs. Saharan dust transport is also described in WRF with the Air Force Weather Agency (AFWA) scheme (Jones et al., 2012).

## 3 Methodology

### 3.1 Retrieval of the particle parameters in temporally high resolution

The delivery of an alert using EARLINET data is based on a two-step approach. In the first step, the high-resolution calibrated data are used to estimate the particle backscatter coefficient and the particle linear depolarization ratio. In order to retrieve the particle backscatter coefficient, an iterative methodology is adapted. The methodology, described in Di Girolamo et al. (1999), is able to retrieve a particle backscatter coefficient with an overall error of no more than 50 %. Prior to that, the cloud contaminated pixels are removed from the data using the cloud screening algorithm developed for the SCC (see Sect. 2).

The method is similar to that of Mattis et al. (2016) in which SCC is employed to derive optical products from elastic backscatter signals. For an ever-available NRT and automated aerosol retrieval, we use channels for elastic backscattering, including depolarization, since Raman observations during daytime have been hitherto challenging.

The calibrated attenuated backscatter coefficient provided by the SCC can be written as

$$\beta_{\mathrm{att}}(\lambda,r)=\left[\beta_{\mathrm{molec.}}(\lambda,r)+\beta_{\mathrm{par}}(\lambda,r)\right]T^2_{\mathrm{molec.}}(\lambda,r)T^2_{\mathrm{par}}(\lambda,r), \quad (1)$$

where $\beta_{\mathrm{par}}(\lambda,r)$ and $\beta_{\mathrm{molec.}}(\lambda,r)$ are, respectively, the backscatter coefficient for particles (par) and molecules (molec.); $T^2_{\mathrm{par}}(\lambda,r)$ and $T^2_{\mathrm{molec.}}(\lambda,r)$ represent the two-way attenuation to and from range $r$ due to, respectively, particles and molecules at wavelength $\lambda$. The latter can be expressed as

$$T^{-2}_{\mathrm{par/molec.}}(\lambda,r)=\exp\left[-2\int_0^R \alpha^{-1}_{\mathrm{par/molec.}}(\lambda,r)\mathrm{d}r\right], \quad (2)$$

where $\alpha_{\mathrm{par}}(\lambda,r)$ and $\alpha_{\mathrm{molec.}}(\lambda,r)$ are the particle and molecular extinction coefficients, respectively. The term $\lambda$ is omitted from the subsequent expressions as the analysis explicitly focuses on 532 nm. The terms $\alpha_{\mathrm{molec.}}(r)$ and $\beta_{\mathrm{molec.}}(r)$ can be estimated from temperature and pressure profiles.

In an initial step, the attenuation in the atmosphere is neglected, $\alpha^{(0)}_{\mathrm{par}}(r)=0\,\mathrm{m}^{-1} \Rightarrow T^{(0)^2}_{\mathrm{par}}(r)=1$, which reduces Eq. (1) to

$$\beta^{(1)}_{\mathrm{par}}(r)=\beta_{\mathrm{molec.}}(r)\left[\frac{\beta_{\mathrm{att}}(r)}{\beta_{\mathrm{molec.}}(r)T^2_{\mathrm{molec.}}(r)}-1\right]. \quad (3)$$

The particle extinction coefficient is estimated by multiplying $\beta^{(1)}_{\mathrm{par}}(r)$ with a constant lidar ratio, $S_{\mathrm{par}}$. Using the particle extinction coefficient in Eq. (1) we derive a new backscatter coefficient given by

$$\beta^{(2)}_{\mathrm{par}}(r)=\beta_{\mathrm{molec.}}(r)\left[\frac{\beta_{\mathrm{att}}(r)}{\beta_{\mathrm{molec.}}(r)T^2_{\mathrm{molec.}}(r)T^{(1)^2}_{\mathrm{par}}(r)}-1\right]. \quad (4)$$

Baars et al. (2017) developed a method to derive atmospheric parameters in temporally high resolution, and they refer to the product of Eq. (4) as the quasi-particle backscatter coefficient, which serves as the best estimate for the particle backscatter coefficient. However, here the particle backscatter,

$$\beta^{(i)}_{\mathrm{par}}(r)=\beta_{\mathrm{molec.}}(r)\left[\frac{\beta_{\mathrm{att}}(r)}{\beta_{\mathrm{molec.}}(r)T^2_{\mathrm{molec.}}(r)T^{(i-1)^2}_{\mathrm{par}}(r)}-1\right], \quad (5)$$

is calculated in the $i$th iteration step from the calibrated attenuated backscatter coefficient. The procedure is successfully terminated if the absolute difference between the backscatter coefficient of two subsequent profiles is smaller than a fixed threshold. The absolute difference, $\Delta_\beta$, is defined as

$$\Delta\beta^{(i)}=\left|\int\beta^{(i)}_{\mathrm{par}}\mathrm{d}r-\int\beta^{(i-1)}_{\mathrm{par}}\mathrm{d}r\right|. \quad (6)$$

We found that fewer than 10 steps are required for a difference of 1 % for the cases examined herein.

The particle depolarization ratio at 532 nm can be defined as (Baars et al., 2017)

$$\delta_{\text{par}} = [\delta_{\text{vol}}(r)+1] \times \left( \frac{\beta_{\text{molec.}}(r)\,[\delta_{\text{molec.}} - \delta_{\text{vol}}(r)]}{\beta_{\text{par}}(r)\,[1+\delta_{\text{molec.}}]} \right)^{-1} - 1, \quad (7)$$

where $\delta_{\text{molec.}}$ is the molecular depolarization ratio and is calculated theoretically (Behrendt and Nakamura, 2002). The term $\delta_{\text{vol}}(r)$ denotes the volume depolarization ratio, and it is the output of SCC.

The input lidar ratio value used in the retrieval could significantly affect the results. Papagiannopoulos et al. (2018) used $48 \pm 13$ sr for fresh volcanic particles and $55 \pm 7$ sr for desert dust particles observed over EARLINET sites in their aerosol classification, which illustrates the variability of this intensive parameter. The uncertainty induced due to the assumption of the lidar ratio can easily exceed 20 % (Sasano et al., 1985) and presents an important source that affects the retrieval. In this study, $S_{\text{par}} = 50$ sr is chosen for the backscatter coefficient retrieval as it is a good compromise for many EARLINET sites and different aerosol conditions (Papayannis et al., 2008; Müller et al., 2007; Mona et al., 2014; Papagiannopoulos et al., 2016). Figure 2 shows a desert dust layer around 3 km over the Potenza EARLINET station on 4 April 2016, 18:47–22:15 UTC. The backscatter coefficient at 532 nm retrieved for 30, 50, and 70 sr along with the backscatter coefficient from the Raman method is shown (Fig. 2a). The three curves almost coincide in the upper part (relative difference is around 5 %) and deviate from one another by less than 35 % in the lower portion of the profile where local aerosol is mixed with dust particles.

The performance of the iterative method for $S_{\text{par}} = 50$ sr can be assessed in Fig. 2b. The overall agreement is very good with the relative difference being around 4 %; however, the iterative method underestimates almost everywhere the Raman method due to the assumption of $S_{\text{par}} = 50$ sr instead of the measured $43 \pm 7$ sr. Figure 2c highlights the effect when the directly measured lidar ratio is plotted against the fixed lidar ratio. Evidently, the curves agree fairly well for the aerosol layer (e.g., desert dust) in the free troposphere and deviate from the layer below (i.e., values over 50 sr). As discussed above, the inference of the lidar ratio is an important factor, yet a lidar ratio value valid for a common volcanic dust and desert dust layer will provide a robust solution for this approach.

### 3.2 Aviation alert delivery

In the second step, the location and the intensity of the volcanic dust and desert dust event are identified. Mona and Marenco (2016) reported that particle depolarization ratio values were around 35 % for freshly emitted particles from various volcanoes and that the values decrease with time. Similarly, pure Saharan dust particles are supposed

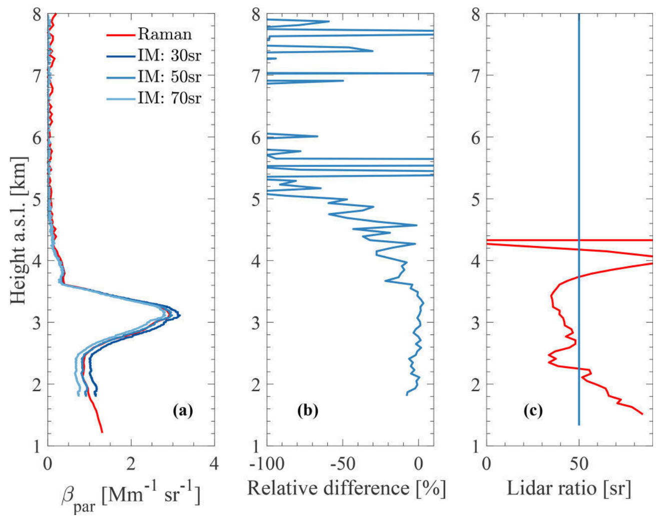


**Figure 2. (a)** The 532 nm backscatter coefficient retrieved with the iterative method (IM) for 30, 50, and 70 sr along with the backscatter coefficient determined with the Raman method (standard SCC product) measured at Potenza (760 m a.s.l.), Italy, on 4 April 2016, 18:47–22:15 UTC. The lidar system of Potenza has a full overlap at around 1.15 km a.s.l. for 532 nm (Madonna et al., 2018). **(b)** The relative difference between the iterative method (IM: 50 sr) and the Raman method backscatter coefficient. **(c)** The lidar ratio profile measured with the Raman method and the fixed lidar ratio used for the iterative method.

to have a slightly smaller particle depolarization ratio of 31 % (Freudenthaler et al., 2009). Since nonspherical particles such as volcanic and desert dust particles yield high particle depolarization ratio values, the one-step polarization-lidar photometer networking (POLIPHON) method is used (e.g., Ansmann et al., 2012).

The particle depolarization ratio is used to separate the nonspherical particles contribution to the particle backscatter coefficient. Mamouri and Ansmann (2014) describe in detail the retrieval process; however, here we treat volcanic dust and desert dust inextricably. The volcanic dust and desert dust backscatter coefficient can be expressed by

$$\beta_{\text{c}} = \beta_{\text{par}} \frac{\left(\delta_{\text{par}} - \delta_{\text{nc}}\right)(1+\delta_{\text{c}})}{(\delta_{\text{c}} - \delta_{\text{nc}})\left(1+\delta_{\text{par}}\right)}, \quad (8)$$

where the coarse (c) and non-coarse (nc) depolarization ratios are set to $\delta_{\text{c}} = 0.31$ and $\delta_{\text{nc}} = 0.05$, respectively. For values $\delta_{\text{par}} < \delta_{\text{nc}}$, we need to set $\beta_{\text{nc}} = \beta_{\text{par}}$. Similarly, when $\delta_{\text{par}} > \delta_{\text{c}}$, we set $\beta_{\text{c}} = \beta_{\text{par}}$.

Until the aviation crisis in 2010, planes were advised to avoid the volcanic plumes regardless of the aerosol concentration (Guffanti et al., 2010). Recently, the International Civil Aviation Organization (ICAO, 2014) established three ash concentration thresholds which play a key role in the decision-making process. Aircraft are allowed to fly below 0.2 mg m$^{-3}$, whereas they are forbidden to fly over 2 and 4 mg m$^{-3}$ (depending on the aircraft's resilience).

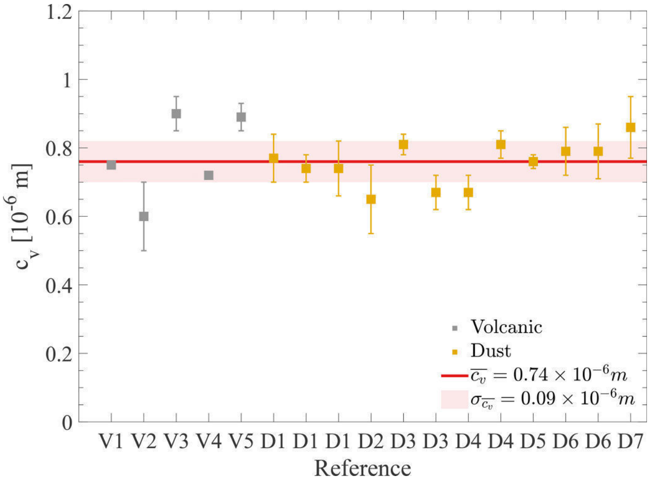


**Figure 3.** The scatter plot indicates the mean and the standard deviation of the conversion factor, $c_\mathrm{v}$, for the different literature references. The plot is color coded with respect to "Volcanic" (gray) and "Dust" (orange) observations. The red line highlights the overall mean conversion factor and the reddish-pink rectangle shows the standard deviation – i.e., $(0.76 \pm 0.06) \times 10^{-6}$ m.

**Table 1.** The code used in Fig. 3 and the respective reference.

| Code | Reference |
|---|---|
| V1 | Ansmann et al. (2010) |
| V2 | Ansmann et al. (2011) |
| V3 | Ansmann et al. (2012) |
| V4 | Devenish et al. (2012) |
| V5 | Sicard et al. (2012) |
| D1 | Ansmann et al. (2012) |
| D2 | Binietoglou (2014) |
| D3 | Córdoba-Jabonero et al. (2018) |
| D4 | Mamali et al. (2018) |
| D5 | Mamouri and Ansmann (2014) |
| D6 | Mamouri and Ansmann (2017) |
| D7 | Ansmann et al. (2019) |

The methodology proposed by Ansmann et al. (2012) for the estimation of aerosol mass concentration profiles employs data from a single-wavelength polarization lidar. The methodology retrieves mass concentration profiles with an uncertainty of 20 %–30 %, and it has proven to be robust and applicable to very different scenarios (e.g., Mamali et al., 2018; Córdoba-Jabonero et al., 2018) that need one wavelength and can be applied to cloudy skies. We chose to convert the three ash concentration thresholds into particle backscatter coefficient. The threshold values for the particle backscatter coefficient, $\beta_\mathrm{th}$, are estimated as

$$\beta_\mathrm{th} = M \frac{1}{\rho c_\mathrm{v} S}, \tag{9}$$

where $M$ is the mass concentration given by ICAO, $\rho$ the volcanic and desert dust bulk density, $c_\mathrm{v}$ the mass-to-extinction conversion factor, and $S$ the volcanic and desert dust lidar ratio. All the terms have to be assumed constant, and they are selected from the literature. The above concentration thresholds (e.g., 0.2, 2, 4 mg m$^{-3}$) are used for the term $M$. For the $\rho$, we used the value 2.6 g cm$^{-3}$ that corresponds to a commonly used value for volcanic and desert dust applications (e.g., Gasteiger et al., 2011; Ansmann et al., 2012; Binietoglou et al., 2015; Mamali et al., 2018). The term $S$ is chosen to be 50 sr as a good compromise for fresh volcanic particles (e.g., Ansmann et al., 2011) and Saharan dust (e.g., Wiegner et al., 2012).

The term $c_\mathrm{v}$ can be estimated using Aerosol Robotic Network (AERONET) observations as being the ratio of the coarse column volume concentration, $\upsilon_\mathrm{c}$, to the coarse mode aerosol optical thickness, $\tau_\mathrm{c}$. More information on the different retrievals and AERONET data processing can be found in Ansmann et al. (2012), Mamouri and Ansmann (2017), and Ansmann et al. (2019). However, for an EWS and day–night availability, we have to select a constant value for volcanic dust and desert dust. Figure 3 shows an overview of AERONET-based $c_\mathrm{v}$ values. To interpret the horizontal axis of the figure, one should also look at Table 1. The figure is separated into volcanic (gray points) and desert (orange points) dust and depicts the range of the observed values; furthermore, the plot shows the mean and standard deviation for the overall average of the conversion factors. It is evident from Fig. 3 that for both volcanic and desert dust the values accumulate between 0.6 and $0.9 \times 10^{-6}$ m with a mean of $(0.76 \pm 0.06) \times 10^{-6}$ m. It is worth noting that although most of the conversion factors were estimated using carefully selected AERONET observations, Mamouri and Ansmann (2017) and Ansmann et al. (2019) use a climatology to derive the conversion factor.

The conversion factor for the coarse particles (i.e., volcanic and desert dust) varies strongly with the distance from the source and, in the case of volcanic eruptions, with the eruption type. Ansmann et al. (2012) highlight that, when particles larger than 15 µm (i.e., the higher limit of the assumed particles radii for the AERONET data analysis scheme) are present, the mass concentration may be underestimated by more than 100 %. The conversion factor in the case of dense and coarser plumes should be much higher and, consequently, will have an adverse impact on our EWS approach. For instance, Pisani et al. (2012) used a conversion factor of $0.6 \times 10^{-5}$ m for a freshly erupted volcanic plume near Mount Etna in Italy. A similar increase, although less pronounced, in the conversion factor can be observed in Mamouri and Ansmann (2017) and Ansmann et al. (2019), in which the authors retrieve a dust coarse-mode conversion factor (i.e., the values reported in Fig. 3). It is believed that particles bigger than 10 µm usually fall quickly to the ground, whereas smaller particles can travel over long distances (Goudie and Middleton, 2006; Wilson et al., 2012). Conversely, van der Does et al. (2016) and Ryder et al. (2018)

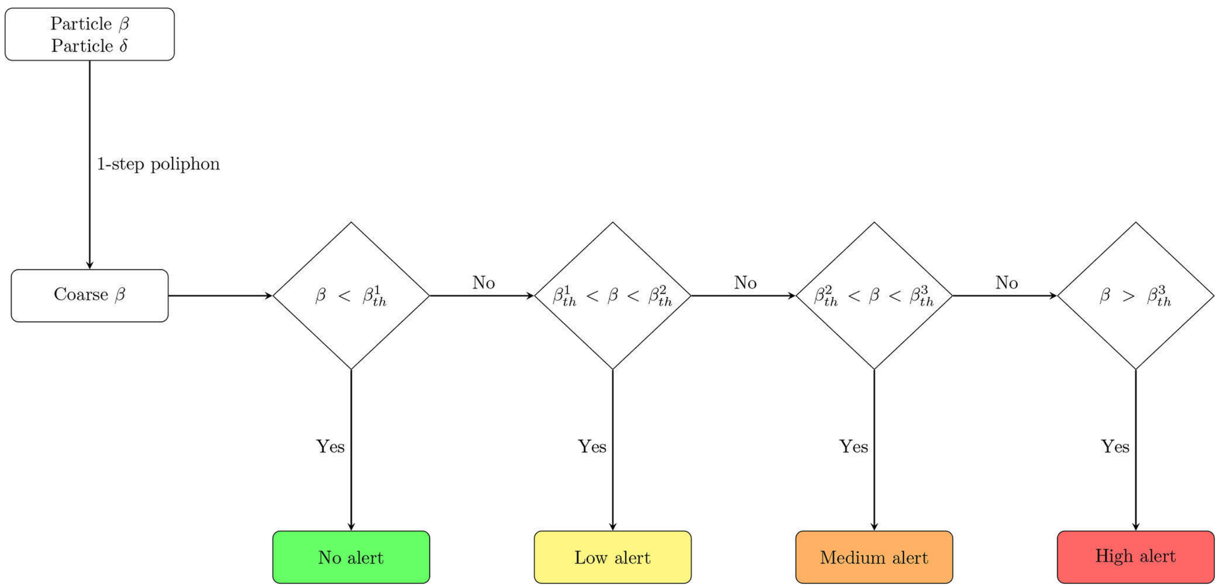


**Figure 4.** The EARLINET alert delivery scheme for aviation. The particle backscatter coefficient and depolarization ratio are used to estimate the coarse backscatter coefficient (one-step POLIPHON method). Three levels are considered that correspond to "Low alert" for particle concentrations higher than 0.2 $\mathrm{mg\,m^{-3}}$ and lower than 2 $\mathrm{mg\,m^{-3}}$, "Medium alert" for concentrations higher than 2 $\mathrm{mg\,m^{-3}}$ and lower than 4 $\mathrm{mg\,m^{-3}}$, and "High alert" for mass concentrations higher than 4 $\mathrm{mg\,m^{-3}}$. The three backscatter coefficient thresholds are $\beta_{\mathrm{th}}^{1} = 1.7 \times 10^{-6}\,\mathrm{m^{-1}\,sr^{-1}}$, $\beta_{\mathrm{th}}^{2} = 1.7 \times 10^{-5}\,\mathrm{m^{-1}\,sr^{-1}}$, and $\beta_{\mathrm{th}}^{3} = 3.4 \times 10^{-5}\,\mathrm{m^{-1}\,sr^{-1}}$.

have illustrated that the desert dust size far away from its source is much coarser than previously suggested, and this has been incorporated into climate models. In light of the above, we chose as the conversion factor in our approach the maximum retrieved value, which is $0.9 \times 10^{-6}$ m (Ansmann et al., 2012). Hence, the thresholds for the particle backscatter coefficient become $1.7 \times 10^{-6}$ (for 0.2 $\mathrm{mg\,m^{-3}}$), $1.7 \times 10^{-5}$ (for 2 $\mathrm{mg\,m^{-3}}$), and $3.4 \times 10^{-5}\,\mathrm{m^{-1}\,sr^{-1}}$ (for 4 $\mathrm{mg\,m^{-3}}$). Given also that the EARLINET stations are far from the active European volcanoes (i.e., Mount Etna and the Icelandic volcanoes), we consider that the selected AERONET-derived conversion factor holds for most of the situations.

Figure 4 illustrates the decision flowchart for the aviation alert delivery in which three alert levels are available: low alert ($0.2 < M_{\mathrm{c}} < 2\,\mathrm{mg\,m^{-3}}$), medium alert ($2 < M_{\mathrm{c}} < 4\,\mathrm{mg\,m^{-3}}$), and high alert ($M_{\mathrm{c}} > 4\,\mathrm{mg\,m^{-3}}$), indicating the increasing amount of dust particles that are likely dangerous for flight operations. The coarse backscatter coefficient due to the highly depolarizing particles is estimated first. Next, the coarse backscatter coefficient is checked, and the level of alert is decided. Furthermore, to avoid isolated false alarms in the EWS product, we incorporated a linear spatial smoothing filter. It is the average of the pixels contained in the neighborhood of each pixel, for which we defined a 3 pixel × 3 pixel grid. A similar methodology has been demonstrated within an international demonstration exercise for the purpose of the EUNADICS-AV project, in which an artificial Mount Etna eruption was simulated (Hirtl et al., 2020).

## 4 Results

In this section, we apply the described methodology to potential perilous events recently detected by the stations of Finokalia and Antikythera, Greece. The observations refer to the same lidar system that was initially deployed in Finokalia and later moved to the island of Antikythera. The aim is not to present a detailed analysis of investigated cases but instead to demonstrate the potential of this methodology to be integrated as a tailored EARLINET product for the fast alerting of airborne hazards relevant to flight operations.

### 4.1 Desert dust particle case

During March 2018, frequent intense dust storms affected Greece with the region of Libya being the originating source (Kaskaoutis et al., 2019). Strong surface and middle and upper troposphere Khamsin winds transported dust northwards for four distinct periods (i.e., 4–7, 17, 21–22, 25–26 March). Solomos et al. (2018) examined in detail the record-breaking episode of 21–22 March, when surface concentrations exceeded 6 $\mathrm{mg\,m^{-3}}$ on 22 March and resulted in the closure of the Heraklion airport.

Here we focus on 21 March when the dust cloud initially appeared over Crete. Figure 5 shows the dust map derived from SEVIRI data along with the cloud cover at 12:00 UTC. The dusty pixels are depicted in two different colors as a function of the confidence levels of the dust detection scheme (i.e., brown means high confidence and orange mid–low con-

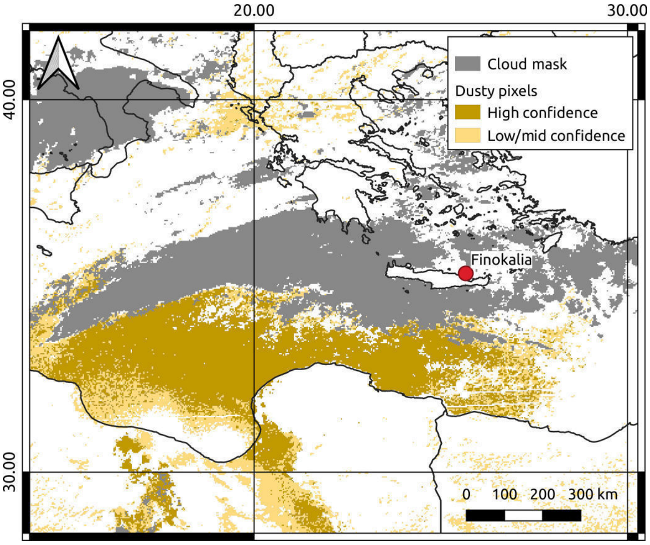


**Figure 5.** The dust SEVIRI product (Marchese et al., 2017) at 12:00 UTC on 21 March 2018 is represented in confidence levels (i.e., brown pixels refer to high confidence and orange pixels to mid–low confidence). The gray pixels indicate the cloud cover.

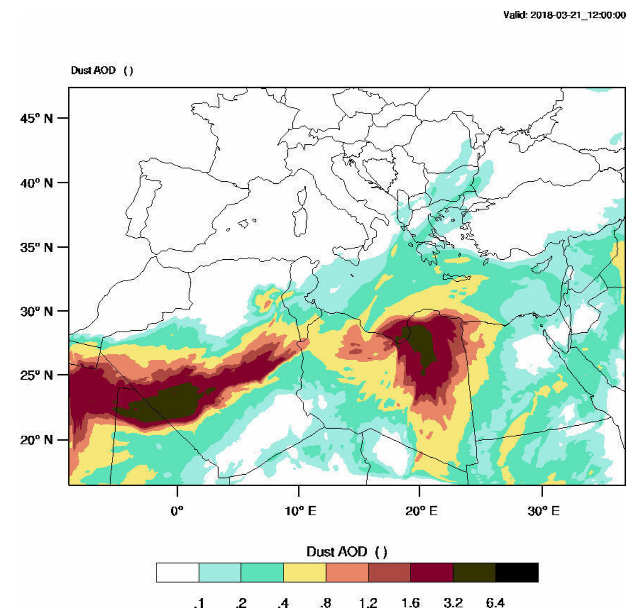


**Figure 6.** WRF-Chem dust aerosol optical depth (AOD) on 21 March 2018 12:00 UTC.

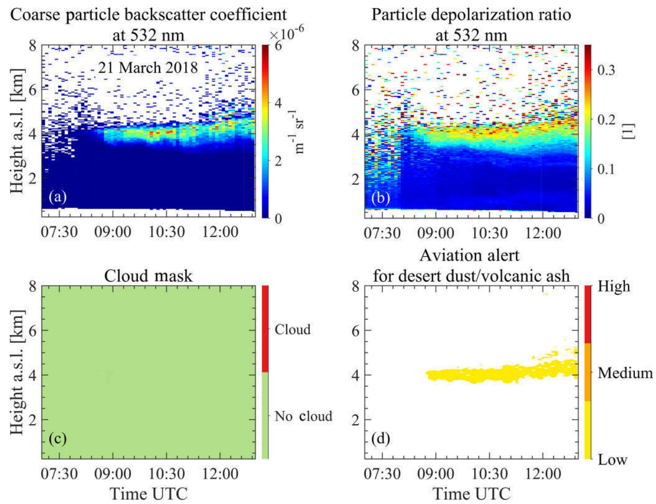


**Figure 7.** EARLINET observations at Finokalia on 21 March 2018: **(a)** the coarse particle backscatter coefficient at 532 nm, **(b)** the particle depolarization ratio at 532 nm, **(c)** the cloud screening output, and **(d)** the alert for aviation. Note that the cloud screening product is given at its full resolution – i.e., the vertical resolution is 7.5 m, and the temporal resolution is 30 s – and all the other products have a resolution of 30 m and 5 min instead.

fidence). In particular, the dust cloud moves from northern Africa towards the eastern Mediterranean, where the cloud cover impedes the dust detection over insular Greece, although the map demonstrates the intensity and the geographic extent of the dust event. The situation of the dust transport at 12:00 UTC on 21 March 2018 is also evident from the WRF-Chem (WRF model coupled with Chemistry) dust aerosol optical depth (AOD) in Fig. 6. The entire eastern Mediterranean is affected by this episode, and the simulated AOD exceeds 0.4 over certain parts of eastern Crete near the Finokalia station.

The coarse particle backscatter coefficient, the particle depolarization ratio at 532 nm (as described in Sect. 3.1), the cloud mask, and the tailored product for the period 07:00–13:00 UTC are shown in Fig. 7. The dust particles arrive over Finokalia around 08:00 UTC in a filament-like layer of about 4 km, wherein the dust particles exhibit high values of the particle depolarization ratio. Figure 7d shows the alert product for aviation, which demonstrates a low level alert indicating a considerable amount of dust particles in the troposphere that are likely dangerous for flight operations. In particular, the coarse particle backscatter coefficient at 532 nm exhibits values up to $6 \times 10^{-6}\,\mathrm{m^{-1}\,sr^{-1}}$, which exceeds the threshold value of $1.7 \times 10^{-6}\,\mathrm{m^{-1}\,sr^{-1}}$. In addition, this case illustrates the advantage of a ground-based lidar system to operate below high clouds that obstruct satellite observations (see Fig. 5) and, therefore, provides important insight.

As the event was aggravated in the following hours, the lidar signal is most likely attenuated which highlights the limitation of the methodology. However, the alert delivery could act as a pre-alerting tool for aviation by pinpointing the specific aerosol conditions. A similar approach for airport operations has been developed using automatic lidars and ceilometers for the prediction of fog formation (Haeffelin et al., 2016).

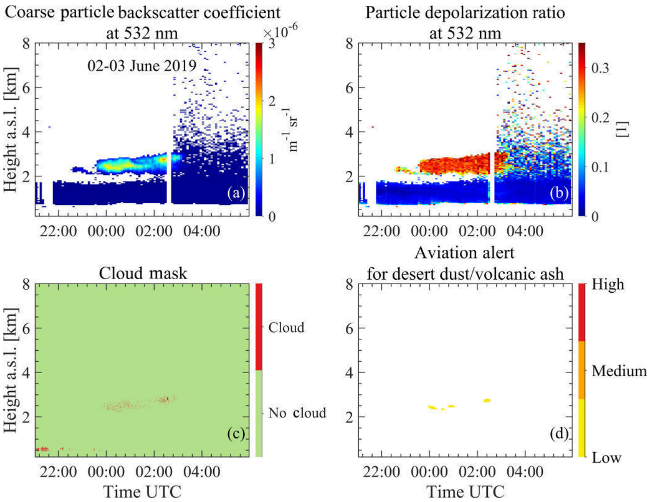


**Figure 8.** EARLINET observations at Antikythera on 2–3 June 2019: **(a)** the coarse particle backscatter coefficient at 532 nm, **(b)** the particle depolarization ratio at 532 nm, **(c)** the cloud screening output, and **(d)** the alert for aviation. Note that the cloud screening product is given at its full resolution – i.e., the vertical resolution is 7.5 m, and the temporal resolution is 30 s – and all the other products have a resolution of 30 m and 5 min instead.

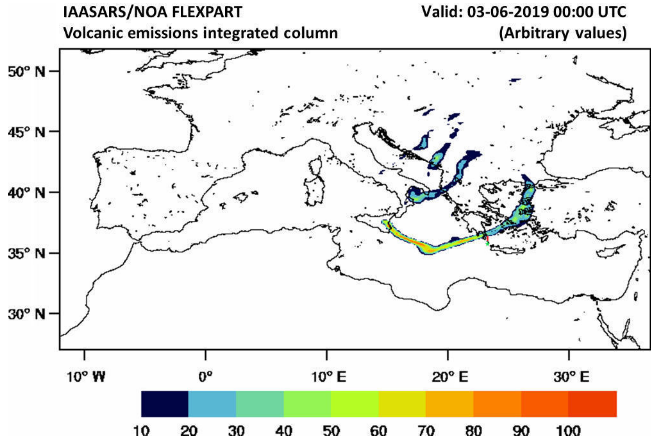


**Figure 9.** FLEXPART vertically integrated volcanic ash particles (arbitrary values) originating from Mount Etna on 3 June 2019 at 00:00 UTC. The green star indicates the location of Antikythera, and the red line is the misplacement of the simulated plume from the lidar station.

## 4.2 Volcanic and desert dust particle case

The eruption of the volcano Mount Etna which began in the early hours of 30 May 2019 injected ash into the atmosphere at an altitude of 3.5–4.0 km (Toulouse Volcanic Ash Advisory Center report at 11:21 UTC, 30 May). The volcanic activity ceased most likely on 3 June (https://ingvvulcani.wordpress.com, last access: 31 October 2019). This volcanic activity did not lead to any air traffic disruption, as was the case for the explosion on 20 July. The latter caused flight rerouting and delays (Amato, 2019).

Aerosol particles of possibly volcanic origin were monitored with the multi-wavelength lidar of NOA over Antikythera, Greece. The eastward advection of volcanic particles from Mount Etna presents a common pathway and has been previously investigated by means of active remote sensing (e.g., Hughes et al., 2016; Zerefos et al., 2006). The presence of these elevated layers above Greece could be a result of the continuous Mount Etna activity of the past few days. Figure 8 shows two distinct layers with different characteristics for the period from 21:00 UTC on 2 June to 06:00 UTC on 3 June. The first layer is initially observed between 1 and 2 km on 2 June and remains visible for the rest of the temporal window. The particle backscatter coefficient is around $1 \times 10^{-6}\,\mathrm{m^{-1}\,sr^{-1}}$, and the particle depolarization ratio is below 5 % and differentiates from the second layer above. The second layer is seen after 23:30 UTC on 2 June until 03:00 UTC on 3 June and resides in the range of 2–3 km. The layer particle depolarization ratio is well above 20 % and indicates non-spherical particles. Moreover, it exhibits a higher particle backscatter coefficient ($\sim 3 \times 10^{-6}\,\mathrm{m^{-1}\,sr^{-1}}$). As a result, the alert is triggered for the latter. It is noteworthy that, as seen in the cloud mask, few pixels within the same aerosol layer are wrongly classified as clouds and are used instead in the alert delivery. The improvement of the cloud masking module is currently ongoing and is expected to eliminate false cloud detection, but nonetheless the aerosol layer is very well captured by the method.

The identification of the source of the two aerosol layers is made through an analysis of FLEXPART and WRF-Chem simulations. Figure 9 indicates the eastward transport of a relatively thin ($\sim$ 60 km horizontal width) volcanic ash plume from Mount Etna towards Greece. As shown by the FLEXPART simulation, this plume propagated eastwards from Sicily towards the Ionian Sea, reaching parts of southern Greece. The simulated plume is misplaced by about 70 km towards the north from the EARLINET Antikythera station; however, its vertical structure is still evident in the cross section of Fig. 10. The eastward motion and the vertical profile of simulated aerosol volcanic plume corroborate the existence of volcanic particles in the upper layer of Fig. 8. The non-depolarizing structures below 2 km are sea-salt particles possibly mixed with dust particles. Limited concentrations ($> 0.04\,\mathrm{mg\,m^{-3}}$) of dust are simulated at these heights by the WRF-Chem model (Fig. 11) and are accompanied by increased relative humidity near the surface, thus implying hygroscopic growth and more spherical particles in this area. In synthesis, both observations and model simulations advocate for the identification of likely volcanic dust and aged desert dust particles in the same aerosol scene but in separate layers. Consequently, the alert delivered refers to volcanic dust.

**Table 2.** EARLINET stations that participated in the EUNADICS-AV exercise during 5–6 March 2019. The percentage of the measurements made for the 2 consecutive days and the specific temporal windows is reported. The "X" denotes the stations for which it was possible to derive the alert for aviation – i.e., the availability of a calibrated backscatter coefficient and depolarization ratio of 532 nm.

| EARLINET station | Measurements performed (%) | | EWS |
|---|---|---|---|
| | 5 March, 11:00–17:00 UTC | 6 March, 07:00–12:00 UTC | |
| Antikythera (GR) | 100 | 100 | X |
| Athens* (GR) | 100 | 100 | |
| Barcelona (ES) | 100 | 0 | X |
| Belgrade* (SRB) | 100 | 100 | |
| Clermont-Ferrand* (FR) | 33 | 40 | |
| Cluj* (RO) | 100 | 80 | |
| Granada (ES) | 17 | 20 | X |
| Hohenpeissenberg (DE) | 100 | 100 | X |
| Leipzig (DE) | 100 | 100 | X |
| Madrid (ES) | 33 | 0 | |
| Potenza (IT) | 100 | 100 | X |
| Rome – Tor Vergata (IT) | 100 | 100 | |
| Thessaloniki* (GR) | 83 | 100 | |

The * indicates the stations equipped with a depolarization channel, although this information was not available during the exercise.

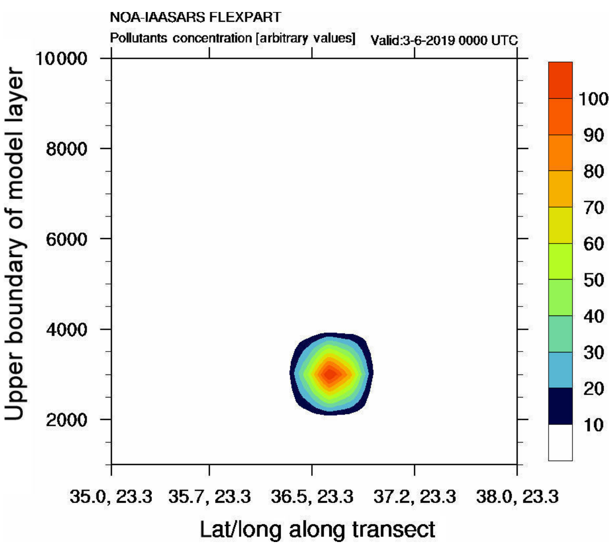


**Figure 10.** FLEXPART vertical cross section of the simulated volcanic particles (in arbitrary values) over the greater Antikythera region. The exact location of the cross section is indicated by the red line in Fig. 9.

## 4.3 Lessons learned from the EUNADICS-AV exercise

The application of the EWS and the timely delivery of the EARLINET data were tested in real time during the EUNADICS-AV exercise, in which EARLINET stations performed synchronous measurements. The EUNADICS-AV demonstration exercise in March 2019, based on a fictitious volcanic eruption, demonstrated that tailored observations, as well as model services, can profitably support aviation stakeholders (Hirtl et al., 2020).

In particular, 13 EARLINET stations contributed to the exercise according to a predefined measurement schedule – i.e., from 11:00 to 17:00 UTC on 5 March 2019 and from 07:00 to 11:00 UTC on 6 March 2019 – independent of the station's capabilities with respect to the EWS. This decision stems from the opportunity to assess the sequence of procedures for real-time data retrieval and data visualization. In addition, the measurements schedule, the stations submitted raw lidar data to the SCC server every hour, which were automatically available on the EARLINET Quicklook Interface (https://quicklooks.earlinet.org/, last access: 16 January 2019). For the majority of the stations and temporal windows, low clouds and cirrus clouds were observed. Table 2 summarizes the measurements gathered per hour segment and the station capabilities with respect to the EWS. In total, 73 % of the measurements were performed successfully, whereas rain and staffing the stations mostly inhibited the rest. Moreover, only for six of the stations was it possible to retrieve the tailored product mainly because of the lack of the depolarization information during the exercise. The tailored product did not produce any alert as the aerosol layers were neither volcanic dust nor desert dust, and they did not yield high backscatter coefficient values. Hence, results of the exercise are not shown here; nonetheless, the EARLINET observations are available through the EARLINET Quicklook Interface.

Overall, the raw lidar data were streamed and processed in less than 30 min from the measurement, enabling the timely delivery of the lidar data and the tailored product when pos-

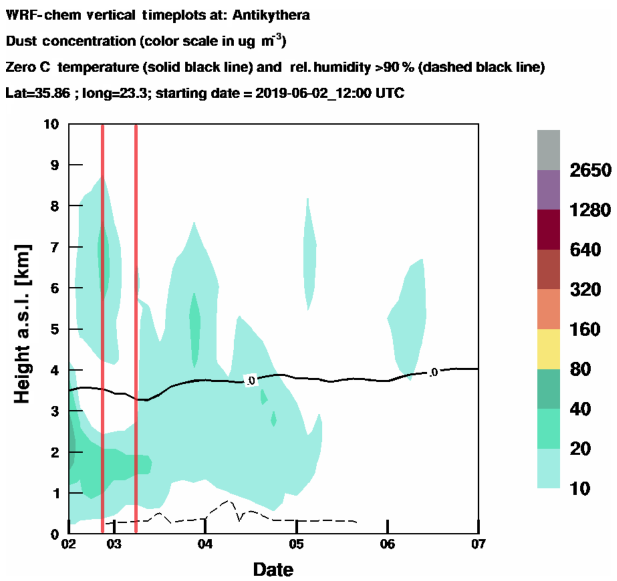


**Figure 11.** WRF-Chem time–height cross section of simulated dust concentration ($\mu g\,m^{-3}$) over Antikythera starting on 2 June at 12:00 UTC. The solid black line is the 0 °C isotherm, and the dashed black line indicates 90 % relative humidity. The red lines correspond to the time domain of the lidar observations – i.e., from 21:00 UTC on 2 June 2019 until 06:00 UTC on 3 June 2019.

sible. Furthermore, the demonstration exercise was the first occasion in which the proposed methodology was tested in NRT, and the obtained results suggest that the network could actively support stakeholders in decision-making during an aviation crisis.

## 5 Conclusions

A tailored product for aviation hazards by means of high-resolution lidar data has been proposed for the first time to our knowledge. In particular, the methodology employs single-wavelength EARLINET high-resolution data (i.e., 532 nm calibrated backscatter coefficient and 532 nm calibrated volume linear depolarization ratio) and yields NRT alerts based on established aerosol mass concentration thresholds. The methodology aims to provide an EARLINET EWS for the fast alerting of airborne hazards exploiting the SCC advancements and to mitigate the effects of a future aviation crisis. The application on EARLINET data from the eastern Mediterranean demonstrated the strength of the methodology in identifying possible dangers for aviation from volcanic ash and desert dust plumes.

One of the key challenges for a NRT automated alert delivery is the calibration of the backscatter and depolarization profiles as the elastic and depolarization channels are used. The EARLINET SCC ensures the absolute calibration of the lidar signals. As a source of high uncertainties in the retrieval of the particle backscatter coefficient, the inference of the lidar ratio was acknowledged. Accordingly, an iterative method has been developed to work with high-resolution lidar data, which compares well with particle backscatter coefficient profiles retrieved with the Raman method.

Additionally, and equally important in the alert delivery approach, there is the conversion factor with which the mass concentration thresholds are converted into a particle backscatter coefficient. The AERONET-derived conversion factors are known to be restricted by the AERONET data inversion scheme and to underestimate large to giant particles. Therefore, the selected conversion factor was chosen (i.e., $0.9 \times 10^{-6}$ m) as the maximum value of the literature review with reference to fresh volcanic and desert dust observations.

The NRT operation of EARLINET during the EUNADICS-AV exercise was successfully demonstrated. The successful application of the method in NRT has been achieved during the EUNADICS-AV exercise. The raw data, upon being uploaded to the SCC server, were automatically processed and became freely accessible through the EARLINET portal and available in order to initiate the alert delivery. The exercise demonstrated the strength of the network, which, if promptly triggered, can enable measurements in the case of natural hazards for aviation.

In addition, a similar approach can be extended to lidar systems operated by the European volcano observatories. Two examples of such observatories in Europe are the Istituto Nazionale di Geofisica e Vulcanologia – Osservatorio Etneo (INGV-OE) and the Icelandic Meteorological Office (IMO). INGV-OE is responsible for monitoring Mount Etna, while IMO is responsible for monitoring all volcanic activity in Iceland.

This method is highly versatile as it can adapt to other wavelengths, and the aerosol backscatter thresholds can be set to accommodate different volcanic and desert dust scenarios by adjusting the conversion factor, the lidar ratio, the bulk density, and the mass concentration levels. In addition, even if developed on the basis of EARLINET, it can be applied to such lidar systems as those that are part of Galion (AD-Net, LALINET, MPLNET), as well as to current (CALIPSO; Cloud-Aerosol Lidar and Infrared Pathfinder Satellite Observation) and future (EarthCARE; Earth Clouds, Aerosols and Radiation Explorer) lidar-based satellite missions.

*Code availability.* The code is available upon request (contact mail: nikolaos.papagiannopoulos@imaa.cnr.it).

*Data availability.* The EARLINET data are accessible through the EARLINET database web portal https://data.earlinet.org (login required, last access: 10 September 2020).

*Author contributions.* The conceptualization and design of this study were carried out by NP and LM. GD is the lead scientist and curator of the EARLINET SCC data. IM and IB created the calibration and cloud mask module for the EARLINET SCC, respectively. VA and AG are the principal investigator (PI) and data originator for the EARLINET stations of Finokalia and Antikythera, respectively. SS and AK performed FLEXPART model simulations for the Antikythera case study. AF retrieved the dust product from SEVIRI data for the Finokalia case study. AA, AC, AP, ARG, DD, DM, FM, HB, IM, LAA, NA, PF, VM, and ZM are either the PIs or the key personnel of the stations involved in the measurements exercise and ensured the high-quality operation of the respective lidars. The interpretation of results was determined from discussions involving all authors. The original draft of the paper was written by NP and reviewed and edited by all the coauthors.

*Competing interests.* The authors declare that they have no conflict of interest.

*Special issue statement.* This article is part of the special issue “EARLINET aerosol profiling: contributions to atmospheric and climate research”. It is not associated with a conference.

*Acknowledgements.* The authors acknowledge EARLINET for providing aerosol lidar profiles (https://www.earlinet.org, last access: 31 October 2019). We thank the ACTRIS-2 and ACTRIS preparatory phase projects that have received funding from the European Union’s Horizon 2020 Framework Program for Research and Innovation (grant agreement no. 654109) and from European Union’s Horizon 2020 Coordination and Support Action (grant agreement no. 739530), respectively. This work has been conducted within the framework of the EUNADICS-AV project, which has received funding from the European Union’s Horizon 2020 research program for Societal Challenges – Smart, Green and Integrated Transport under grant agreement no. 723986. Furthermore, the research leading to these results has received funding from the COST Action CA16202, supported by the COST Association (European Cooperation in Science and Technology). The project e-shape (EuroGEOSS Showcases: Applications Powered by Europe), funded under the European Union’s Horizon 2020 program (grant agreement no. 820852), is also acknowledged. Part of the work performed for this study was funded by the Ministry of Research and Innovation through Program I – Development of the National Research-Development System, subprogram 1.2 – Institutional Performance – Projects of Excellence Financing in RDI (grant no. 19PFE/17.10.2018) and by the Romanian National Core Program (grant no. 18N/2019). VA acknowledges support of this work by the European Research Council (ERC) under the European Community’s Horizon 2020 Framework Program for Research and Innovation grant agreement 725698 (D-10 TECT).

*Financial support.* This research has been supported by the ACTRIS-2 (grant no. 654109), the ACTRIS preparatory phase (grant no. 739530), the EUNADICS-AV (grant no. 723986), the E-shape (EuroGEOSS Showcases: Applications Powered by Europe) (grant no. 820852), the Ministry of Research and Innovation through Program I – Development of the National Research-Development System, Subprogram 1.2 – Institutional Performance – Projects of Excellence Financing in RDI (grant no. 19PFE/17.10.2018), the Romanian National Core Program (grant no. 18N/2019), and the European Commission, H2020 Research Infrastructures (D-TECT (grant no. 725698)).

*Review statement.* This paper was edited by Eduardo Landulfo and reviewed by three anonymous referees.

## References

Amato, G.: Cenere dall’Etna, disagi in mattinata all’aeroporto di Catania, La Repubblica, available at: https://palermo.repubblica.it/cronaca/2019/07/20/news/cenere_dall_etna_disagi_all_aeroporto_di_catania-231613901/?ref=search (last access: 10 September 2020), 2019 (in Italian).

Ansmann, A., Tesche, M., Groß, S., Freudenthaler, V., Seifert, P., Hiebsch, A., Schmidt, J., Wandinger, U., Mattis, I., Müller, D., and Wiegner, M.: The 16 April 2010 major volcanic ash plume over central Europe: EARLINET lidar and AERONET photometer observations at Leipzig and Munich, Germany, Geophys. Res. Lett., 37, L13810, https://doi.org/10.1029/2010GL043809, 2010.

Ansmann, A., Tesche, M., Seifert, P., Groß, S., Freudenthaler, V., Apituley, A., Wilson, K. M., Serikov, I., Linné, H., Heinold, B., Hiebsch, A., Schnell, F., Schmidt, J., Mattis, I., Wandinger, U., and Wiegner, M.: Ash and fine-mode particle mass profiles from EARLINET-AERONET observations over central Europe after the eruptions of the Eyjafjallajökull volcano in 2010, J. Geophys. Res.-Atmos., 116, D00U02, https://doi.org/10.1029/2010JD015567, 2011.

Ansmann, A., Seifert, P., Tesche, M., and Wandinger, U.: Profiling of fine and coarse particle mass: case studies of Saharan dust and Eyjafjallajökull/Grimsvötn volcanic plumes, Atmos. Chem. Phys., 12, 9399–9415, https://doi.org/10.5194/acp-12-9399-2012, 2012.

Ansmann, A., Mamouri, R.-E., Hofer, J., Baars, H., Althausen, D., and Abdullaev, S. F.: Dust mass, cloud condensation nuclei, and ice-nucleating particle profiling with polarization lidar: updated POLIPHON conversion factors from global AERONET analysis, Atmos. Meas. Tech., 12, 4849–4865, https://doi.org/10.5194/amt-12-4849-2019, 2019.

Baars, H., Seifert, P., Engelmann, R., and Wandinger, U.: Target categorization of aerosol and clouds by continuous multiwavelength-polarization lidar measurements, Atmos. Meas. Tech., 10, 3175–3201, https://doi.org/10.5194/amt-10-3175-2017, 2017.

Behrendt, A. and Nakamura, T.: Calculation of the calibration constant of polarization lidar and its dependency on atmospheric temperature, Opt. Express, 10, 805–817, https://doi.org/10.1364/OE.10.000805, 2002.

Binietoglou, I.: Synergies of ground-based remote sensing techniques for aerosol mass profiling, PhD thesis, University of Basilicata, 139 pp., 2014.

Binietoglou, I., Basart, S., Alados-Arboledas, L., Amiridis, V., Argyrouli, A., Baars, H., Baldasano, J. M., Balis, D., Belegante, L., Bravo-Aranda, J. A., Burlizzi, P., Carrasco, V., Chaikovsky, A., Comerón, A., D’Amico, G., Filioglou, M., Granados-

Muñoz, M. J., Guerrero-Rascado, J. L., Ilic, L., Kokkalis, P., Maurizzi, A., Mona, L., Monti, F., Muñoz Porcar, C., Nicolae, D., Papayannis, A., Pappalardo, G., Pejanovic, G., Perreira, S., Perrone, M., Pietruczuk, A., Posyniak, M., Rocadenbosch, F., Rodríguez-Gómez, A., Sicard, M., Siomos, N., Szkop, A., Taradellas, E., Tsekeri, A., Vukovic, A., Wandinger, U., and Wagner, J.: A methodology for investigating dust model performance using synergistic EARLINET/AERONET dust concentration retrievals, Atmos. Meas. Tech., 8, 3577–3600, https://doi.org/10.5194/amt-8-3577-2015, 2015.

Bolic, T. and Sivcev, Z.: Eruption of Eyjafjallajökull in Iceland: Experience of European Air Traffic Management, Trans. Res. Record, 2214, 136–143, https://doi.org/10.3141/2214-17, 2011.

Brioude, J., Arnold, D., Stohl, A., Cassiani, M., Morton, D., Seibert, P., Angevine, W., Evan, S., Dingwell, A., Fast, J. D., Easter, R. C., Pisso, I., Burkhart, J., and Wotawa, G.: The Lagrangian particle dispersion model FLEXPART-WRF version 3.1, Geosci. Model Dev., 6, 1889–1904, https://doi.org/10.5194/gmd-6-1889-2013, 2013.

Chaikovsky, A., Dubovik, O., Holben, B., Bril, A., Goloub, P., Tanré, D., Pappalardo, G., Wandinger, U., Chaikovskaya, L., Denisov, S., Grudo, J., Lopatin, A., Karol, Y., Lapyonok, T., Amiridis, V., Ansmann, A., Apituley, A., Alados-Arboledas, L., Binietoglou, I., Boselli, A., D'Amico, G., Freudenthaler, V., Giles, D., Granados-Muñoz, M. J., Kokkalis, P., Nicolae, D., Oshchepkov, S., Papayannis, A., Perrone, M. R., Pietruczuk, A., Rocadenbosch, F., Sicard, M., Slutsker, I., Talianu, C., De Tomasi, F., Tsekeri, A., Wagner, J., and Wang, X.: Lidar-Radiometer Inversion Code (LIRIC) for the retrieval of vertical aerosol properties from combined lidar-radiometer data: development and distribution in EARLINET, Atmos. Meas. Tech., 9, 1181–1205, https://doi.org/10.5194/amt-9-1181-2016, 2016.

Córdoba-Jabonero, C., Sicard, M., Ansmann, A., del Águila, A., and Baars, H.: Separation of the optical and mass features of particle components in different aerosol mixtures by using POLIPHON retrievals in synergy with continuous polarized Micro-Pulse Lidar (P-MPL) measurements, Atmos. Meas. Tech., 11, 4775–4795, https://doi.org/10.5194/amt-11-4775-2018, 2018.

D'Amico, G., Amodeo, A., Baars, H., Binietoglou, I., Freudenthaler, V., Mattis, I., Wandinger, U., and Pappalardo, G.: EARLINET Single Calculus Chain–overview on methodology and strategy, Atmos. Meas. Tech., 8, 4891–4916, https://doi.org/10.5194/amt-8-4891-2015, 2015.

D'Amico, G., Amodeo, A., Mattis, I., Freudenthaler, V., and Pappalardo, G.: EARLINET Single Calculus Chain – technical – Part 1: Pre-processing of raw lidar data, Atmos. Meas. Tech., 9, 491–507, https://doi.org/10.5194/amt-9-491-2016, 2016.

Devenish, B., Thomson, D., Marenco, F., Leadbetter, S., Ricketts, H., and Dacre, H.: A study of the arrival over the United Kingdom in April 2010 of the Eyjafjallajökull ash cloud using ground-based lidar and numerical simulations, Atmos. Environ., 48, 152–164, 2012.

Di Girolamo, P., Ambrico, P. F., Amodeo, A., Boselli, A., Pappalardo, G., and Spinelli, N.: Aerosol observations by lidar in the nocturnal boundary layer, Appl. Opt., 38, 4585–4595, https://doi.org/10.1364/AO.38.004585, 1999.

Eliasson, J., Watson, I. M., and Weber, K.: Volcanic Ash: Hazard Observation, In Situ Observations of Airborne Ash From Manned Aircraft, Elsevier, 89–98, 2016.

Engelmann, R., Kanitz, T., Baars, H., Heese, B., Althausen, D., Skupin, A., Wandinger, U., Komppula, M., Stachlewska, I. S., Amiridis, V., Marinou, E., Mattis, I., Linné, H., and Ansmann, A.: The automated multiwavelength Raman polarization and water-vapor lidar Polly$_{XT}$: the neXT generation, Atmos. Meas. Tech., 9, 1767–1784, https://doi.org/10.5194/amt-9-1767-2016, 2016.

Freudenthaler, V., Esselborn, M., Wiegner, M., Heese, B., Tesche, M., Ansmann, A., Müller, D., Althausen, D., Wirth, M., Fix, A., Ehret, G., Knippertz, P., Toledano, C., Gasteiger, J., Garhammer, M., and Seefeldner, M.: Depolarization ratio profiling at several wavelengths in pure Saharan dust during SAMUM 2006, Tellus B, 61, 165–179, https://doi.org/10.1111/j.1600-0889.2008.00396.x, 2009.

Gasteiger, J., Groß, S., Freudenthaler, V., and Wiegner, M.: Volcanic ash from Iceland over Munich: mass concentration retrieved from ground-based remote sensing measurements, Atmos. Chem. Phys., 11, 2209–2223, https://doi.org/10.5194/acp-11-2209-2011, 2011.

Goudie, A. and Middleton, N. J.: Desert Dust in the Global System, Springer-Verlag Berlin Heidelberg, 287 pp., https://doi.org/10.1007/3-540-32355-4, 2006.

Granados-Muñoz, M. J., Navas-Guzmán, F., Guerrero-Rascado, J. L., Bravo-Aranda, J. A., Binietoglou, I., Pereira, S. N., Basart, S., Baldasano, J. M., Belegante, L., Chaikovsky, A., Comerón, A., D'Amico, G., Dubovik, O., Ilic, L., Kokkalis, P., Muñoz Porcar, C., Nickovic, S., Nicolae, D., Olmo, F. J., Papayannis, A., Pappalardo, G., Rodríguez, A., Schepanski, K., Sicard, M., Vukovic, A., Wandinger, U., Dulac, F., and Alados-Arboledas, L.: Profiling of aerosol microphysical properties at several EARLINET/AERONET sites during the July 2012 ChArMEx/EMEP campaign, Atmos. Chem. Phys., 16, 7043–7066, https://doi.org/10.5194/acp-16-7043-2016, 2016.

Guffanti, M., Schneider, D. J., Wallace, K. L., Hall, T., Bensimon, D. R., and Salinas, L. J.: Aviation response to a widely dispersed volcanic ash and gas cloud from the August 2008 eruption of Kasatochi, Alaska, USA, J. Geophys. Res.-Atmos., 115, D00L19, https://doi.org/10.1029/2010JD013868, 2010.

Haeffelin, M., Laffineur, Q., Bravo-Aranda, J.-A., Drouin, M.-A., Casquero-Vera, J.-A., Dupont, J.-C., and De Backer, H.: Radiation fog formation alerts using attenuated backscatter power from automatic lidars and ceilometers, Atmos. Meas. Tech., 9, 5347–5365, https://doi.org/10.5194/amt-9-5347-2016, 2016.

Hirtl, M., Arnold, D., Baro, R., Brenot, H., Coltelli, M., Eschbacher, K., Hard-Stremayer, H., Lipok, F., Maurer, C., Meinhard, D., Mona, L., Mulder, M. D., Papagiannopoulos, N., Pernsteiner, M., Plu, M., Robertson, L., Rokitansky, C.-H., Scherllin-Pirscher, B., Sievers, K., Sofiev, M., Som de Cerff, W., Steinheimer, M., Stuefer, M., Theys, N., Uppstu, A., Wagenaar, S., Winkler, R., Wotawa, G., Zobl, F., and Zopp, R.: A volcanic-hazard demonstration exercise to assess and mitigate the impacts of volcanic ash clouds on civil and military aviation, Nat. Hazards Earth Syst. Sci., 20, 1719–1739, https://doi.org/10.5194/nhess-20-1719-2020, 2020.

Hughes, E. J., Yorks, J., Krotkov, N. A., da Silva, A. M., and McGill, M.: Using CATS near-real-time lidar observations to monitor and constrain volcanic sulfur dioxide (SO2) forecasts, Geophys. Res. Lett., 43, 11089–11097, https://doi.org/10.1002/2016GL070119, 2016.

Jones, S. L., Adams-Selin, R., Hunt, E. D., Creighton, G. A., and Cetola, J. D.: Update on modifications to WRF-CHEM GOCART for fine-scale dust forecasting at AFWA, in: AGU Fall Meeting Abstracts, A33D-0188, 2012.

Kaskaoutis, D., Rashki, A., Dumka, U., Mofidi, A., Kambezidis, H., Psiloglou, B., Karagiannis, D., Petrinoli, K., and Gavriil, A.: Atmospheric dynamics associated with exceptionally dusty conditions over the eastern Mediterranean and Greece in March 2018, Atmos. Res., 218, 269–284, https://doi.org/10.1016/j.atmosres.2018.12.009, 2019.

Lopatin, A., Dubovik, O., Chaikovsky, A., Goloub, P., Lapyonok, T., Tanré, D., and Litvinov, P.: Enhancement of aerosol characterization using synergy of lidar and sun-photometer coincident observations: the GARRLiC algorithm, Atmos. Meas. Tech., 6, 2065–2088, https://doi.org/10.5194/amt-6-2065-2013, 2013.

Madonna, F., Rosoldi, M., Lolli, S., Amato, F., Vande Hey, J., Dhillon, R., Zheng, Y., Brettle, M., and Pappalardo, G.: Intercomparison of aerosol measurements performed with multiwavelength Raman lidars, automatic lidars and ceilometers in the framework of INTERACT-II campaign, Atmos. Meas. Tech., 11, 2459–2475, https://doi.org/10.5194/amt-11-2459-2018, 2018.

Mamali, D., Marinou, E., Sciare, J., Pikridas, M., Kokkalis, P., Kottas, M., Binietoglou, I., Tsekeri, A., Keleshis, C., Engelmann, R., Baars, H., Ansmann, A., Amiridis, V., Russchenberg, H., and Biskos, G.: Vertical profiles of aerosol mass concentration derived by unmanned airborne in situ and remote sensing instruments during dust events, Atmos. Meas. Tech., 11, 2897–2910, https://doi.org/10.5194/amt-11-2897-2018, 2018.

Mamouri, R. E. and Ansmann, A.: Fine and coarse dust separation with polarization lidar, Atmos. Meas. Tech., 7, 3717–3735, https://doi.org/10.5194/amt-7-3717-2014, 2014.

Mamouri, R.-E. and Ansmann, A.: Potential of polarization/Raman lidar to separate fine dust, coarse dust, maritime, and anthropogenic aerosol profiles, Atmos. Meas. Tech., 10, 3403–3427, https://doi.org/10.5194/amt-10-3403-2017, 2017.

Marchese, F., Sannazzaro, F., Falconieri, A., Filizzola, C., Pergola, N., and Tramutoli, V.: An Enhanced Satellite–Based Algorithm for Detecting and Tracking Dust Outbreaks by Means of SEVIRI Data, Remote Sens., 9, 537, https://doi.org/10.3390/rs9060537, 2017.

Mattis, I., D'Amico, G., Baars, H., Amodeo, A., Madonna, F., and Iarlori, M.: EARLINET Single Calculus Chain – technical – Part 2: Calculation of optical products, Atmos. Meas. Tech., 9, 3009–3029, https://doi.org/10.5194/amt-9-3009-2016, 2016.

Middleton, N. J.: Desert dust hazards: A global review, Aeolian Res., 24, 53–63, https://doi.org/10.1016/j.aeolia.2016.12.001, 2017.

Mona, L. and Marenco, F.: Volcanic Ash: Hazard Observation, Lidar Observations of Volcanic Particles, Elsevier, 161–173, 2016.

Mona, L., Amodeo, A., D'Amico, G., Giunta, A., Madonna, F., and Pappalardo, G.: Multi-wavelength Raman lidar observations of the Eyjafjallajökull volcanic cloud over Potenza, southern Italy, Atmos. Chem. Phys., 12, 2229–2244, https://doi.org/10.5194/acp-12-2229-2012, 2012.

Mona, L., Papagiannopoulos, N., Basart, S., Baldasano, J., Binietoglou, I., Cornacchia, C., and Pappalardo, G.: EARLINET dust observations vs. BSC-DREAM8b modeled profiles: 12-year-long systematic comparison at Potenza, Italy, Atmos. Chem. Phys., 14, 8781–8793, https://doi.org/10.5194/acp-14-8781-2014, 2014.

Müller, D., Ansmann, A., Mattis, I., Tesche, M., Wandinger, U., Althausen, D., and Pisani, G.: Aerosol-type-dependent lidar ratios observed with Raman lidar, J. Geophys. Res., 112, D16202, https://doi.org/10.1029/2006JD008292, 2007.

Nicolae, D., Vasilescu, J., Talianu, C., Binietoglou, I., Nicolae, V., Andrei, S., and Antonescu, B.: A neural network aerosol-typing algorithm based on lidar data, Atmos. Chem. Phys., 18, 14511–14537, https://doi.org/10.5194/acp-18-14511-2018, 2018.

Nixon, M. and Aguado, A.: Feature Extraction and Image Processing for Computer Vision, Academic Press, 632 pp., 2019.

Ortiz-Amezcua, P., Guerrero-Rascado, J. L., Granados-Muñoz, M. J., Benavent-Oltra, J. A., Böckmann, C., Samaras, S., Stachlewska, I. S., Janicka, Ł., Baars, H., Bohlmann, S., and Alados-Arboledas, L.: Microphysical characterization of long-range transported biomass burning particles from North America at three EARLINET stations, Atmos. Chem. Phys., 17, 5931–5946, https://doi.org/10.5194/acp-17-5931-2017, 2017.

Papagiannopoulos, N., Mona, L., Alados-Arboledas, L., Amiridis, V., Baars, H., Binietoglou, I., Bortoli, D., D'Amico, G., Giunta, A., Guerrero-Rascado, J. L., Schwarz, A., Perreira, S., Spinelli, N., Wandinger, U., Wang, X., and Pappalardo, G.: CALIPSO climatological products: evaluation and suggestions from EARLINET, Atmos. Chem. Phys., 16, 2341–2357, https://doi.org/10.5194/acp-16-2341-2016, 2016.

Papagiannopoulos, N., Mona, L., Amodeo, A., D'Amico, G., Gumà Claramunt, P., Pappalardo, G., Alados-Arboledas, L., Guerrero-Rascado, J. L., Amiridis, V., Kokkalis, P., Apituley, A., Baars, H., Schwarz, A., Wandinger, U., Binietoglou, I., Nicolae, D., Bortoli, D., Comerón, A., Rodríguez-Gómez, A., Sicard, M., Papayannis, A., and Wiegner, M.: An automatic observation-based aerosol typing method for EARLINET, Atmos. Chem. Phys., 18, 15879–15901, https://doi.org/10.5194/acp-18-15879-2018, 2018.

Papayannis, A., Amiridis, V., Mona, L., Tsaknakis, G., Balis, D., Bösenberg, J., Chaikovski, A., De Tomasi, F., Grigorov, I., Mattis, I., Mitev, V., Müller, D., Nickovic, S., Pérez, C., Pietruczuk, A., Pisani, G., Ravetta, F., Rizi, V., Sicard, M., Trickl, T., Wiegner, M., Gerding, M., Mamouri, R. E., D'Amico, G., and Pappalardo, G.: Systematic lidar observations of Saharan dust over Europe in the frame of EARLINET (2000–2002), J. Geophys. Res., 113, D10204, https://doi.org/10.1029/2007JD009028, 2008.

Pappalardo, G., Mona, L., D'Amico, G., Wandinger, U., Adam, M., Amodeo, A., Ansmann, A., Apituley, A., Alados Arboledas, L., Balis, D., Boselli, A., Bravo-Aranda, J. A., Chaikovsky, A., Comerón, A., Cuesta, J., De Tomasi, F., Freudenthaler, V., Gausa, M., Giannakaki, E., Giehl, H., Giunta, A., Grigorov, I., Groß, S., Haeffelin, M., Hiebsch, A., Iarlori, M., Lange, D., Linné, H., Madonna, F., Mattis, I., Mamouri, R. E., McAuliffe, M. A. P., Mitev, V., Molero, F., Navas-Guzmán, F., Nicolae, D., Papayannis, A., Perrone, M. R., Pietras, C., Pietruczuk, A., Pisani, G., Preißler, J., Pujadas, M., Rizi, V., Ruth, A. A., Schmidt, J., Schnell, F., Seifert, P., Serikov, I., Sicard, M., Simeonov, V., Spinelli, N., Stebel, K., Tesche, M., Trickl, T., Wang, X., Wagner, F., Wiegner, M., and Wilson, K. M.: Four-dimensional distribution of the 2010 Eyjafjallajökull volcanic cloud over Europe observed by EARLINET, Atmos. Chem. Phys., 13, 4429–4450, https://doi.org/10.5194/acp-13-4429-2013, 2013.

Pappalardo, G., Amodeo, A., Apituley, A., Comerón, A., Freudenthaler, V., Linné, H., Ansmann, A., Bösenberg, J., D'Amico, G., Mattis, I., Mona, L., Wandinger, U., Amiridis, V., Alados-Arboledas, L., Nicolae, D., and Wiegner, M.: EARLINET: towards an advanced sustainable European aerosol lidar network, Atmos. Meas. Tech., 7, 2389–2409, https://doi.org/10.5194/amt-7-2389-2014, 2014.

Pisani, G., Boselli, A., Coltelli, M., Leto, G., Pica, G., Scollo, S., Spinelli, N., and Wang, X.: Lidar depolarization measurement of fresh volcanic ash from Mt. Etna, Italy, Atmos. Environ., 62, 34–40, https://doi.org/10.1016/j.atmosenv.2012.08.015, 2012.

Ryder, C. L., Marenco, F., Brooke, J. K., Estelles, V., Cotton, R., Formenti, P., McQuaid, J. B., Price, H. C., Liu, D., Ausset, P., Rosenberg, P. D., Taylor, J. W., Choularton, T., Bower, K., Coe, H., Gallagher, M., Crosier, J., Lloyd, G., Highwood, E. J., and Murray, B. J.: Coarse-mode mineral dust size distributions, composition and optical properties from AER-D aircraft measurements over the tropical eastern Atlantic, Atmos. Chem. Phys., 18, 17225–17257, https://doi.org/10.5194/acp-18-17225-2018, 2018.

Sasano, Y., Browell, E. V., and Ismail, S.: Error caused by using a constant extinction/backscattering ratio in the lidar solution, Appl. Opt., 24, 3929–3932, https://doi.org/10.1364/AO.24.003929, 1985.

Sicard, M., Guerrero-Rascado, J. L., Navas-Guzmán, F., Preißler, J., Molero, F., Tomás, S., Bravo-Aranda, J. A., Comerón, A., Rocadenbosch, F., Wagner, F., Pujadas, M., and Alados-Arboledas, L.: Monitoring of the Eyjafjallajökull volcanic aerosol plume over the Iberian Peninsula by means of four EARLINET lidar stations, Atmos. Chem. Phys., 12, 3115–3130, https://doi.org/10.5194/acp-12-3115-2012, 2012.

Sicard, M., D'Amico, G., Comerón, A., Mona, L., Alados-Arboledas, L., Amodeo, A., Baars, H., Baldasano, J. M., Belegante, L., Binietoglou, I., Bravo-Aranda, J. A., Fernández, A. J., Fréville, P., García-Vizcaíno, D., Giunta, A., Granados-Muñoz, M. J., Guerrero-Rascado, J. L., Hadjimitsis, D., Haefele, A., Hervo, M., Iarlori, M., Kokkalis, P., Lange, D., Mamouri, R. E., Mattis, I., Molero, F., Montoux, N., Muñoz, A., Muñoz Porcar, C., Navas-Guzmán, F., Nicolae, D., Nisantzi, A., Papagiannopoulos, N., Papayannis, A., Pereira, S., Preißler, J., Pujadas, M., Rizi, V., Rocadenbosch, F., Sellegri, K., Simeonov, V., Tsaknakis, G., Wagner, F., and Pappalardo, G.: EARLINET: potential operationality of a research network, Atmos. Meas. Tech., 8, 4587–4613, https://doi.org/10.5194/amt-8-4587-2015, 2015.

Skamarock, W. C., Klemp, J. B., Dudhia, J., Gill, D. O., Barker, D. M., Duda, M. G., Huang, X.-Y., Wang, W., and Powers, J. G.: A Description of the Advanced Research WRF Version 3, Ncar technical note 475, National Center for Atmospheric Research, Boulder, Colorado, USA, 125 pp., 2008.

Solomos, S., Kalivitis, N., Mihalopoulos, N., Amiridis, V., Kouvarakis, G., Gkikas, A., Binietoglou, I., Tsekeri, A., Kazadzis, S., Kottas, M., Pradhan, Y., Proestakis, E., Nastos, P. T., and Marenco, F.: From Tropospheric Folding to Khamsin and Foehn Winds: How Atmospheric Dynamics Advanced a Record-Breaking Dust Episode in Crete, Atmosphere, 9, 240, https://doi.org/10.3390/atmos9070240, 2018.

Stohl, A., Forster, C., Frank, A., Seibert, P., and Wotawa, G.: Technical note: The Lagrangian particle dispersion model FLEXPART version 6.2, Atmos. Chem. Phys., 5, 2461–2474, https://doi.org/10.5194/acp-5-2461-2005, 2005.

Tesche, M., Ansmann, A., Müller, D., Althausen, D., Engelmann, R., Freudenthaler, V., and Groß, S.: Vertically resolved separation of dust and smoke over Cape Verde using multiwavelength Raman and polarization lidars during Saharan Mineral Dust Experiment 2008, J. Geophys. Res.-Atmos., 114, D13202, https://doi.org/10.1029/2009JD011862, 2009.

Tesche, M., Müller, D., Groß, S., Ansmann, A., Althausen, D., Freudenthaler, V., Weinzierl, B., Veira, A., and Petzold, A.: Optical and microphysical properties of smoke over Cape Verde inferred from multiwavelength lidar measurements, Tellus B, 63, 677–694, https://doi.org/10.1111/j.1600-0889.2011.00549.x, 2011.

Tramutoli, V.: Robust AVHRR techniques (RAT) for environmental monitoring: theory and applications, in: Earth Surface Remote Sensing II, edited by: Cecchi, G. and Zilioli, E., Vol. 3496, International Society for Optics and Photonics, SPIE, 101–113, https://doi.org/10.1117/12.332714, 1998.

Tramutoli, V.: Robust Satellite Techniques (RST) for Natural and Environmental Hazards Monitoring and Mitigation: Theory and Applications, in: 2007 International Workshop on the Analysis of Multi-temporal Remote Sensing Images, IEEE, 1–6, https://doi.org/10.1109/MULTITEMP.2007.4293057, 2007.

van der Does, M., Korte, L. F., Munday, C. I., Brummer, G.-J. A., and Stuut, J.-B. W.: Particle size traces modern Saharan dust transport and deposition across the equatorial North Atlantic, Atmos. Chem. Phys., 16, 13697–13710, https://doi.org/10.5194/acp-16-13697-2016, 2016.

Wang, Y., Sartelet, K. N., Bocquet, M., Chazette, P., Sicard, M., D'Amico, G., Léon, J. F., Alados-Arboledas, L., Amodeo, A., Augustin, P., Bach, J., Belegante, L., Binietoglou, I., Bush, X., Comerón, A., Delbarre, H., García-Vízcaino, D., Guerrero-Rascado, J. L., Hervo, M., Iarlori, M., Kokkalis, P., Lange, D., Molero, F., Montoux, N., Muñoz, A., Muñoz, C., Nicolae, D., Papayannis, A., Pappalardo, G., Preissler, J., Rizi, V., Rocadenbosch, F., Sellegri, K., Wagner, F., and Dulac, F.: Assimilation of lidar signals: application to aerosol forecasting in the western Mediterranean basin, Atmos. Chem. Phys., 14, 12031–12053, https://doi.org/10.5194/acp-14-12031-2014, 2014.

Wiegner, M., Gasteiger, J., Groß, S., Schnell, F., Freudenthaler, V., and Forkel, R.: Characterization of the Eyjafjallajökull ashplume: Potential of lidar remote sensing, Phys. Chem. Earth Pt. A/B/C, 45/46, 79–86, https://doi.org/10.1016/j.pce.2011.01.006, 2012.

Wilson, T. M., Stewart, C., Sword-Daniels, V., Leonard, G. S., Johnston, D. M., Cole, J. W., Wardman, J., Wilson, G., and Barnard, S. T.: Volcanic ash impacts on critical infrastructure, Phys. Chem. Earth Pt. A/B/C, 45/46, 5–23, 2012.

Zerefos, C., Nastos, P., Balis, D., Papayannis, A., Kelepertsis, A., Kannelopoulou, E., Nikolakis, D., Eleftheratos, C., Thomas, W., and Varotsos, C.: A complex study of Etna's volcanic plume from ground-based, in situ and space-borne observations, International J. Remote Sens., 27, 1855–1864, https://doi.org/10.1080/01431160500462154, 2006.

*applied sciences*

*Article*

# Response of the Earth's Lower Ionosphere to Solar Flares and Lightning-Induced Electron Precipitation Events by Analysis of VLF Signals: Similarities and Differences

**Aleksandra Kolarski [1], Vladimir A. Srećković [2] and Zoran R. Mijić [2,*]**

[1] Technical Faculty Mihajlo Pupin, University of Novi Sad, Đure Đakovića bb, 23000 Zrenjanin, Serbia; aleksandra.kolarski@tfzr.rs
[2] Institute of Physics Belgrade, University of Belgrade, Pregrevica 118, 11080 Belgrade, Serbia; vlada@ipb.ac.rs
* Correspondence: zoran.mijic@ipb.ac.rs

**Abstract:** The lower ionosphere influences the propagation of electromagnetic (EM) waves, satellite and also terrestrial (anthropic) signals at the time of intense perturbations and disturbances. Therefore, data and modelling of the perturbed lower ionosphere are crucial in various technological areas. An analysis of the lower ionospheric response induced by sudden events during daytime-solar flares and during night-time-lightning-induced electron precipitation was carried out. A case study of the solar flare event recorded on 7 September 2017 and lightning-induced electron precipitation event recorded on 16 November 2004 were used in this work. Sudden events induced changes in the ionosphere and, consequently, the electron density height profile. All data are recorded by Belgrade (BEL) radio station system and the model computation is used to obtain the ionospheric parameters induced by these sudden events. According to perturbed conditions, variation of estimated parameters, sharpness and reflection height differ for analysed cases. Data and results are useful for Earth observation, telecommunication and other applications in modern society.

**Keywords:** atmosphere; radio signal; disturbances; data; modelling

**Citation:** Kolarski, A.; Srećković, V.A.; Mijić, Z.R. Response of the Earth's Lower Ionosphere to Solar Flares and Lightning-Induced Electron Precipitation Events by Analysis of VLF Signals: Similarities and Differences. *Appl. Sci.* **2022**, *12*, 582. https://doi.org/10.3390/app12020582

Academic Editor: Amalia Miliou

Received: 25 November 2021
Accepted: 5 January 2022
Published: 7 January 2022



## 1. Introduction

The ionosphere, as a huge layer of the atmosphere, has physical and chemical properties that depend on the incident radiation and local energetic processes [1,2]. In particular, the lower ionospheric region and the fluctuations of its parameters are very important for human life and many activities on Earth and require continuous measurements, observations and available information [3].

In-situ observations of the lower ionospheric layers are difficult and expensive and, consequently, remote sensing measurements are mainly used for investigating this region [4,5]. High-energy events, triggered from an external source or inside the atmosphere, can induce ionospheric disturbances and as a consequence affect all processes within [6].

For example, during solar flares (SFs) the increase in the ionospheric electron concentration at all altitudes is noticeable. Solar flares are giant explosions on the surface of the Sun when a huge amount of electromagnetic energy is released across the entire electromagnetic spectrum [7]. The enhanced extreme ultraviolet (EUV) radiation is absorbed at higher altitudes ionizing the E (90–150 km above Earth's surface during daytime conditions) and F (160–400 km, same) regions of the ionosphere (see e.g., [8]). During SFs, electromagnetic radiation within soft X-rays in a wavelength range of 0.1–0.8 nm, significantly oversteps the ionization of the Lyman-a spectral line 121.6 nm and cosmic rays, becoming a major source of ionization at a range of altitudes corresponding to the D region (50–90 km, same), causing enhanced ionization and absorption of the EM waves that propagate within the Earth-ionosphere waveguide [9,10]. As a result of radiation effects, the solar induced ionospheric disturbances and plasma irregularities cause perturbations in the amplitude and phase of radio signals.

Furthermore, some processes create localised areas of increased electron density in the low ionosphere and thus change its properties. Radio waves, generated by atmospheric discharge and propagating along geomagnetic field lines into the plasmasphere, get into transversal cyclotron resonance with energetic electron beams (30–300 keV) moving in the opposite direction. As a consequence of such interaction, electron precipitation into the atmosphere takes place. Electron precipitation produces localised areas of increased electron density in the low ionosphere (on heights corresponding to D–region heights of 50–90 km [11–13]), known as localised ionization enhancement (LIE) [14]. Perturbations in very low frequency (VLF) propagation, known as trimpi events, can be explained by formation of such areas. Classic trimpi events [15] are phase delay and/or amplitude perturbations of VLF signals propagating in the Earth-ionosphere waveguide. Whistlers occur about one second after a corresponding atmospheric discharge and propagate in the magnetosphere along geomagnetic field lines [16]. Electron precipitation, caused by ducted whistlers, is explained in [17]. Since disturbances of VLF signals are a consequence of electron precipitation caused by atmospheric discharges, they are named as lightning-induced electron precipitation events (LEP). In addition to the above-mentioned phenomena, which can be detected as disturbances in VLF propagation, there are a number of other phenomena which can be optically detected in areas above thunderclouds. The formation of ducts of enhanced electroconductivity between thunderclouds and the ionosphere is connected with such phenomena [18–20]. Trimpi perturbations can be simultaneously monitored on multiple adjacent traces of VLF signals. Based on adjacent VLF signals recordings comparison, LIE dimensions and spatial position can be estimated by numerical modelling, depending on the transmitter frequency, VLF signal great circle path (GCP) length and position of LIE in relation to the VLF signal path.

Disturbances in propagation of VLF radio signals at the Belgrade station BEL (located at the Institute of Physics Belgrade (44.85° N, 20.38° E), Serbia) were observed and the model computation is used to obtain the atmosphere parameters induced by these sudden events. According to perturbed conditions, variation of estimated parameters, sharpness and reflection height differ for the analysed cases.

## 2. Methods

For the examination of the ionospheric composition, altitudes, locations and other properties, experts usually make use of satellites equipped with suitable sensors, GPS, sonde, radars, various optical instruments, or balloons, rocket probes, etc. A widely used technique for remote sensing of the Earth's ionosphere exploits radio signals (e.g., [21–24]), and for altitude range that corresponds to the ionospheric lowest layer, i.e., the D region, VLF radio signal range is preferred (e.g., [25–30]). Remote sensing of the lower ionosphere by utilisation of radio signals in the VLF range is based on the hop wave theory (see, e.g., [31–34]). These techniques are successfully used for exploration of Earth's lower ionosphere's response to a number of processes, with their origin from extra-terrestrial to terrestrial environments (e.g., [35–41]).

The methodology used and results of mid-latitude lower ionosphere diagnostic obtained by this technique, based on VLF radio signals recorded at the Belgrade receiver site, in cases of regular and irregular solar-terrestrial conditions, can be found in, e.g., [23,37,39,42–50]. In our study, at the ionosphere altitudes 50–90 km (D region), measurements rely on radio wave propagation technique, i.e., monitoring of phase and amplitude of VLF radio signals. For this reason, the perturbation of VLF phase delay and amplitude was estimated as a difference between values of the perturbed signal induced by external disturbance and signal in the normal unperturbed conditions. The details are described in the next section.

*Used Numerical Model*

A standard technique for retrieving ionospheric parameters during sudden ionospheric disturbances (SIDs) is based on comparing the registered amplitude and phase changes with the equal values computed by Long Wavelength Propagation Capability (LWPC) software [51], as interpreted in [9,10]. To determine electron density from recorded amplitude and phase variations, a trial and error procedure can be utilized, with the density profile being changed until the LWPC predicted amplitude and phase matched the monitored data (see, e.g., [42]). As a result, the calculated beta and $H'$ values can be employed in subsequent computations and simulations (e.g., electron gain and electron loss processes coefficient, etc.).

## 3. Results

### *3.1. Lower Ionosphere during SF Event*

The monitoring and investigation of VLF data has been carried out simultaneously with the examination of the correlative incoming solar X-ray fluxes collected from the Geostationary Operational Environmental Satellite (GOES).

In the presence of SIDs, a standard numerical procedure for the estimation of plasma parameters is based on comparison of the recorded changes of amplitude and phase with the matching values acquired in simulations by the LWPC numerical software package as explained in [9,44,46,47].

We studied data for 7 September 2017, as an example of a day with strong X1.3 class SFs that caused SID and seriously affected the VLF signal. It should be noted that the development to the flux of X-ray lasted almost one hour.

The monitored and simulated changes of amplitude ($\Delta A$) and phase delay ($\Delta P$) compared to normal day-time levels for a signal emitted on frequency 24 kHz from Cutler (44.65° N, 67.30° W), ME, USA, with codename NAA measured at the BEL site is presented in Figure 1. Besides the good agreement between simulated and monitored data, X-ray flux peak and VLF signal perturbation happened synchronously i.e., energetic radiation perturbed the ionosphere which, in turn, caused the activation of disturbances in radio signal.

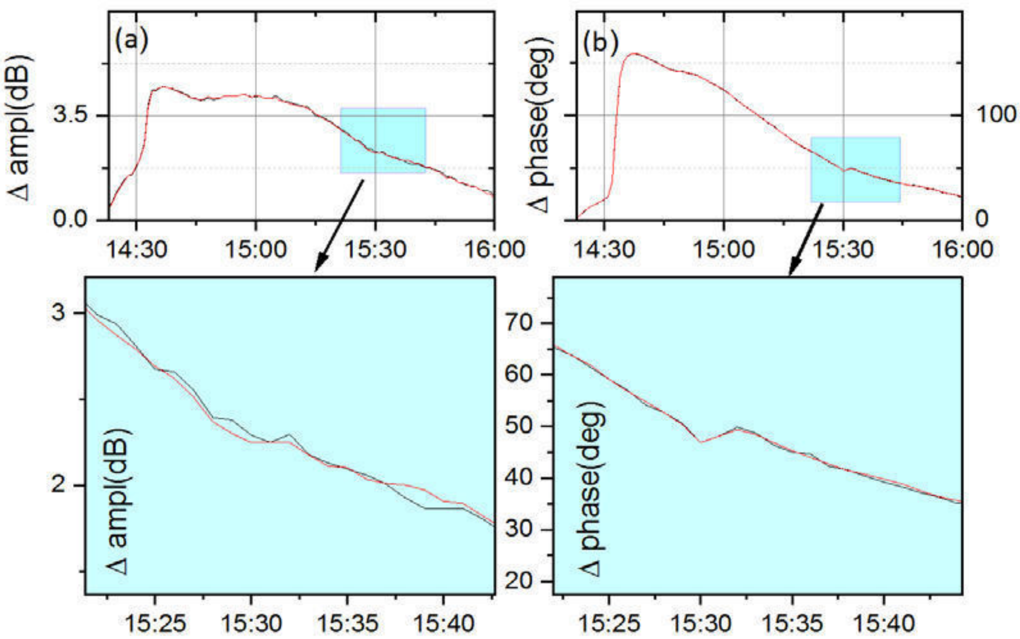


**Figure 1.** Measured and simulated amplitude (**a**), and phase delay (**b**) excesses of NAA radio signal during X1.3 class SF on 7 September 2017.

Figure 2 presents obtained values of effective reflection height $H'$ and the sharpness $\beta$ during almost two hours, i.e., during occurrences of SFs on 7 September 2017. During X1.3 class SFs, the shape of reflection height is in anticorrelation and the sharpness is in correlation with X-ray flux.

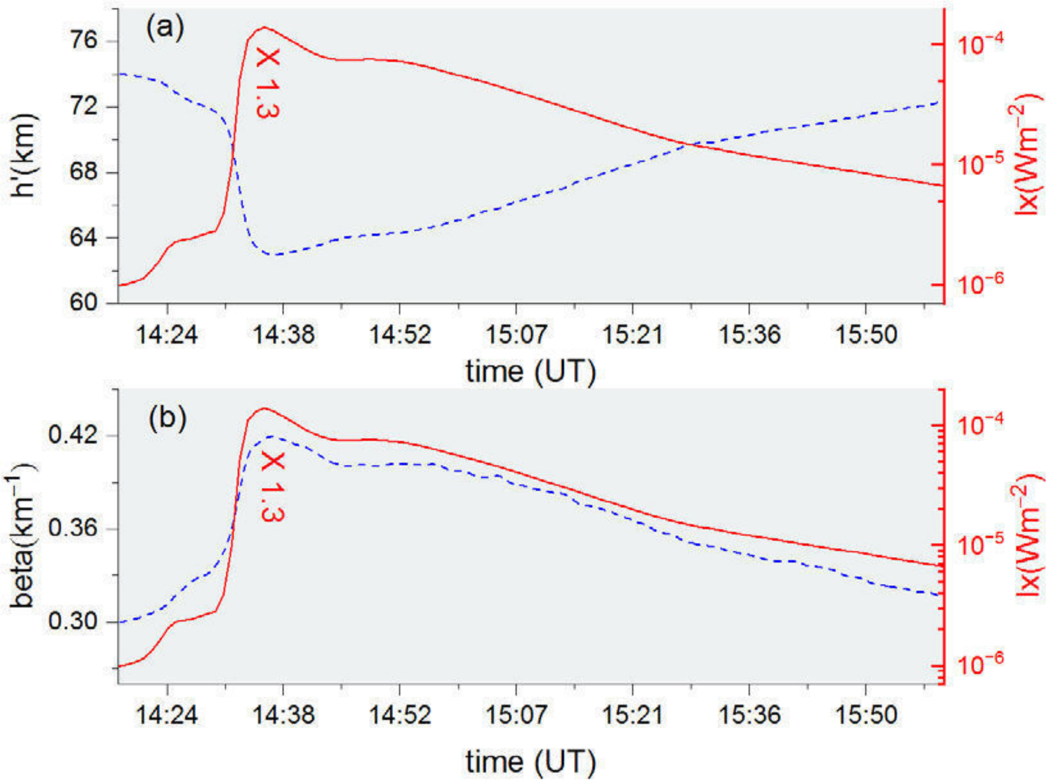


**Figure 2.** Parameters $H'$ (**a**), and $\beta$ (**b**) and X-ray flux (right axis) during occurrence of X1.3 class SF on 7 September 2017.

The change of the reflection height is a normal behaviour, i.e., after the beginning of SFs the reflection height decreases to a minimum and after peaks of X-ray flux it rises to the preflare value (see Figure 2a). The shape of sharpness is correlated with the shape of recorded X-ray flux increase. During the X1.3 SF, the sharpness increases to a maximum and after the SF peak (14:36 UT) it decreases to the pre-flare value (Figure 2b). At peak time (14:36 UT), the X-ray flux is $Ix = 1.3 \times 10^{-4}$ Wm$^{-2}$, and the $H'$ lowers by 13 km to a value $H'$ ~63 km. The sharpness values increase to 0.42 km$^{-1}$ at peak time 14:36 UT on 7 September 2017.

Electron density profile changes can demonstrate the variation in distribution of ionization at the D-layer due to SFs. Figure 3a presents the simultaneous change of X-ray flux, and the corresponding *Ne* (Figure 3b) obtained at reference height 74 km versus UT during occurrence of X1.3 class SF on 7 September 2017. It can be seen that the electron density is in correlation with X-ray flux and, *Ne* increased by almost two orders of magnitude during the X1.3 class SF.

The current study is important because most results concerning investigation in the D-region are scattered and vary in order of magnitude (see [9,23,52,53]), thus it is necessary to take into account all the data and correct the existing data. Sudden events induce changes in the ionosphere and, consequently, the electron density height profile. It is useful to obtain new results by analysing the similarities and differences, especially for case studies, i.e., when solar flares last significantly longer and perturb the ionosphere in a specific way. An additional aim is the simultaneous analysis of the lower ionospheric response and electron density height profile variations in the lower ionosphere induced by sudden events during daytime solar flares and during night-time lightning-induced electron precipitation.

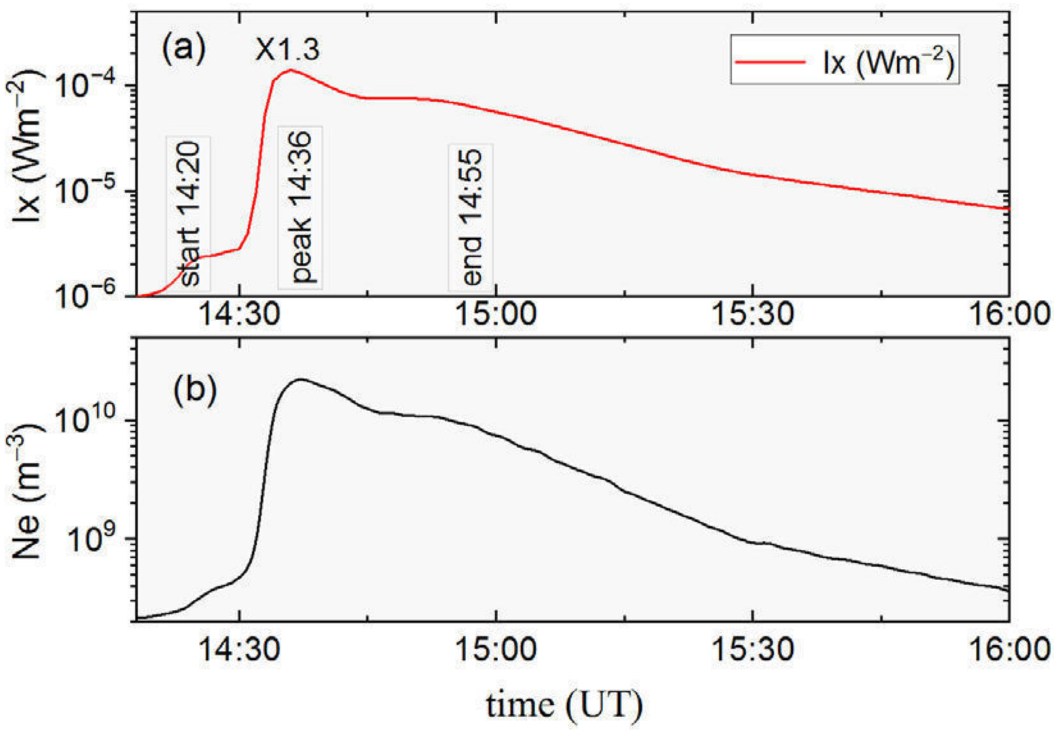


**Figure 3.** X-ray flux measured by the GOES satellite (**a**), and evaluated electron density profiles (**b**) during occurrence of X1.3 class SF on 7 September 2017.

### 3.2. Signal Propagation Parameters during LEP Event

Lightning-induced electron precipitation, i.e., LEP, is triggered by an extremely low frequency (VLF and ELF) portion of EM energy released by lightning discharges that manage to reach the Earth's magnetosphere and by propagating as whistler mode wave interactions with electrons from radiation belts forcing them to precipitate to lower altitudes of 60–120 km, causing an increase in electron density. Such localised and transient electron density enhancements in the D-region altitude range can produce significant amplitude and phase delay perturbations on narrowband VLF signals (with change in amplitude level up to 6 dB and in phase delay of about 20 degrees, typically with rise times up to 1 s and signal decay below 100 s) propagating through or near-by the disturbed region (e.g., [18,48,54] and references therein). An LEP event occurred on 16 November 2004 and its impact on VLF signal traces NAA/24.0 kHz and GQD/22.1 kHz (signal with codename GQD emitted from Anthorn (52.40° N, 1.20° W), GB) was selected for analysis. The presented LEP event is one of the typical LEPs recorded by the Belgrade VLF station, from those during the period 2008–2010 [48,55], similar in absolute perturbation amplitude change of up to 5 dB and phase delay of up to a few tens of degrees with maximal duration of up to two minutes. Amplitude (solid lines) and phase delay (dotted lines) registrations, with resolution 0.1 s on NAA and GQD signals, before, during and after the LEP event occurred on 16 November 2004 and are presented in Figure 4a,b, respectively. Moments at which amplitude and phase delay values for unperturbed (regular) and perturbed (irregular) ionospheric conditions in waveguide were read, are marked with red and blue arrows.

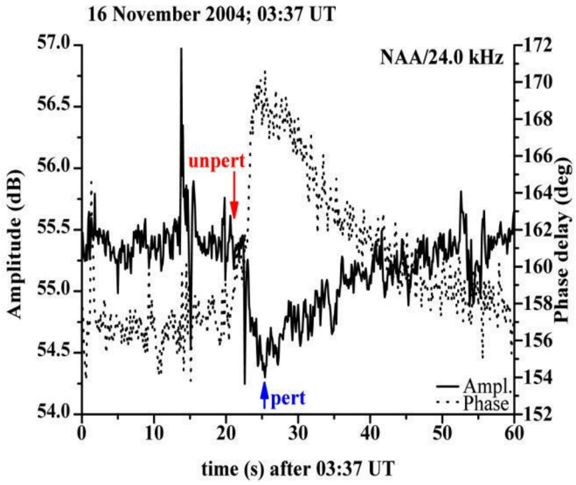


(**a**)

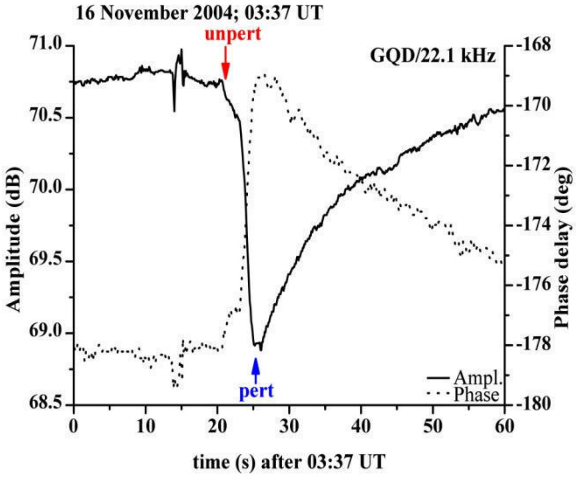


(**b**)

**Figure 4.** Amplitude (solid lines) and phase delay (dotted lines) time evolution before and during the LEP event occurred on 16 November 2004 on considered VLF signal traces: (**a**) NAA/24.0 kHz and (**b**) GQD/22.1 kHz.

### 3.3. Modelling and Simulation during LEP Event

NAA/24 kHz signal propagates along W–E direction and has a long (GCP distance D = 6540 km) and mostly oversea path, while GQD/22.1 kHz signal propagates along a short (GCP distance D = 1980 km) and mostly overland path (Figure 5). Disturbance occurred on both analysed signal traces, so it is reasonable to assume that ionospheric irregularity caused by an LEP event was located in the vicinity of the Belgrade receiver site. That is why, both for unperturbed and perturbed ionospheric conditions, the VLF propagation conditions were modelled only in that section of waveguide which is just a few hundred km away from the Belgrade receiver site (44.85° N, 20.38° E).

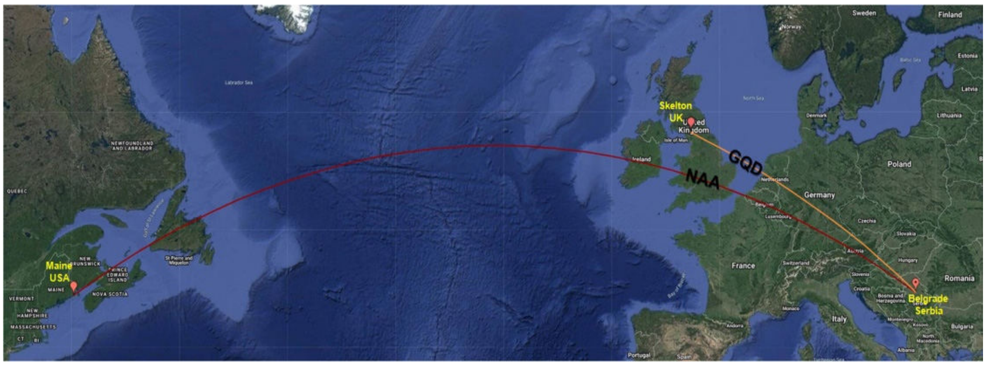


**Figure 5.** Possible paths for considered NAA/24.0 kHz (red) and GQD/22.1 kHz (yellow) VLF signals emitted towards Belgrade (Serbia) from Maine (USA) and Skelton (UK).

By means of Long Wavelength Propagation Capability computer program (LWPCv21) [51], the propagation paths of NAA/24.0 kHz and GQD/22.1 kHz signals were simulated and modelled. Best fitting pairs of parameters sharpness β ($km^{-1}$) and reflection height $H'$ (km) were estimated in order to obtain values as close as possible to real measured values of the signals' phase delay (deg) and amplitude (dB) at the place of the receiver in Belgrade, for both cases of regular and disturbed ionospheric conditions in observed sections of waveguides. The estimated amplitude and phase delay values obtained by the LWPCv21 program are in good agreement with real measured values at the Belgrade receiver site (Table 1: first and third rows indicate unperturbed VLF signal values, while the second and fourth rows indicate the perturbed ones).

**Table 1.** Measured and estimated amplitude and phase delay values of NAA and GQD signals during the LEP event that occurred on 16 November 2004.

| VLF Signal | Time UT 0337 UT + | Measured Values | | | | LWPC Simulation | | | |
|---|---|---|---|---|---|---|---|---|---|
| | | $A$ (dB) | $\Delta A$ (dB) | $P$ (°) | $\Delta P$ (°) | $A$ (dB) | $\Delta A$ (dB) | $P$ (°) | $\Delta P$ (°) |
| NAA/24.0 kHz unperturbed values | 20.16 s | 55.42 | 0 | 157.08 | 0 | 55.63 | 0 | 173.18 | 0 |
| NAA/24.0 kHz perturbed values | 25.54 s | 54.37 | −1.05 | 170.03 | 12.95 | 54.62 | −1.01 | 195.02 | 21.84 |
| GQD/22.1 kHz unperturbed values | 20.16 s | 70.70 | 0 | −178.05 | 0 | 70.40 | 0 | −214.88 | 0 |
| GQD/22.1 kHz perturbed values | 25.54 s | 68.96 | −1.74 | −169.05 | 9 | 68.65 | −1.75 | −209.22 | 5.66 |

The amplitude change $\Delta A$ (dB), was obtained as the difference between the maximum value of the amplitude during the perturbation and the value of the amplitude in undisturbed signal. The phase delay change $\Delta P$ (°) was obtained as the difference between the phase delay value that corresponds in time to the maximum value of the amplitude during the perturbation and phase delay value in the undisturbed signal interval that corresponds in time to the amplitude value chosen as unperturbed.

The model for the propagation of VLF signals within the Earth-ionosphere waveguide is defined by pairs of parameters ($\beta$, $H'$) and analytically described by equations for the calculation of the electron density height profile $N_e(z)$ ($m^{-3}$) during daytime ionospheric conditions is given in [56]. The procedure for the computation of the electron density height profile is based on the equation for determining the electron density $N_e(z)$ ($m^{-3}$) within the Earth-ionosphere waveguide during night-time conditions [14], where the electron density was calculated as a function of a certain pair of parameters $\beta$ and $H'$, at the height z (km), based on the equation adapted for the nocturnal ionosphere [14]. Electron density height profile $N_e(z)$ ($m^{-3}$), for given parameters $\beta$ and $H'$, was calculated using the expression for the night-time ionosphere given by [14]:

$$N_e(z, H', \beta) = 1.86 \times 10^{11} \cdot e^{-0.15 \cdot z} \cdot 78.57 \cdot e^{\beta(z - H')}, \quad (m^{-3}) \tag{1}$$

Parameter $\beta$, for night-time ionospheric conditions, is in the range 0.47–0.50 km$^{-1}$, while parameter $H'$ is in the range 50–87 km. Electron density was calculated at the reflection height, when $z = H'$, and in that case (1) takes the form:

$$N_e(z) = 146.1402 \times 10^{11} \cdot e^{-0.15 \cdot z}, \quad (m^{-3}) \tag{2}$$

For modelling of parameters $\beta$ and $H'$, the LWPC software was used. Detailed methodology, related to utilisation of LWPC software and VLF signal propagation modelling for different cases, can be found in [14,29,56,57]. Here, the procedure for modelling parameters $\beta$ and $H'$ is only outlined. The basic parameters of the propagation medium, the sharpness of the upper boundary of the Earth-ionosphere waveguide $\beta$ and the height of the signal's reflection $H'$ are related to the electron density $N_e(z)$ within the waveguide. Each change in the electron density in the waveguide changes the propagation parameters, amplitude and phase delay of the VLF signal. According to the LWPM model, for regular night-time conditions in the ionosphere, the program code takes the parameter $\beta$ as 0.40 km$^{-1}$ and the parameter $H'$ as 87 km. However, to model the values of the amplitude and phase delay of the VLF signal, in each individual case, it is necessary to independently determine the appropriate parameter pairs ($\beta$, $H'$) as input parameters, so that the simulated values of the amplitude and phase delay obtained as output by the computation, correspond to the measured values of the amplitude and phase delay as close as possible, as the best fitting pair.

The procedure itself consists of numerous trials, in which parameter pairs (β, $H'$) are manually defined as input parameters and the program gives calculated amplitude and phase delay as the output values. Program output is dependent on numerous factors (such as signal frequency, bearing angle, receiver and transmitter locations, observed date and time, solar zenith angle, geomagnetic dip and electro-conductivity of lower waveguide boundary) that are imbedded as background data in calculations.

During night-time ionospheric VLF transmission, signal's amplitude is more stable than phase delay. During modelling, we focused on providing (β, $H'$) parameter pairs to obtain a really good agreement for relative amplitude change $\Delta A$ (dB) for both analysed signals, while still obtaining a relatively good agreement for relative change in phase delay $\Delta P$ (°). Simulated amplitude and phase delay values for NAA/24.0 kHz and GQD/22.1 kHz along GCP path, for the unperturbed (red) and perturbed (blue) state in waveguides on 16 November 2004, are presented in Figures 6 and 7, respectively. Areas of amplitude and phase delay changing near the Belgrade receiver site are framed and as zoomed in panels presented on the right.

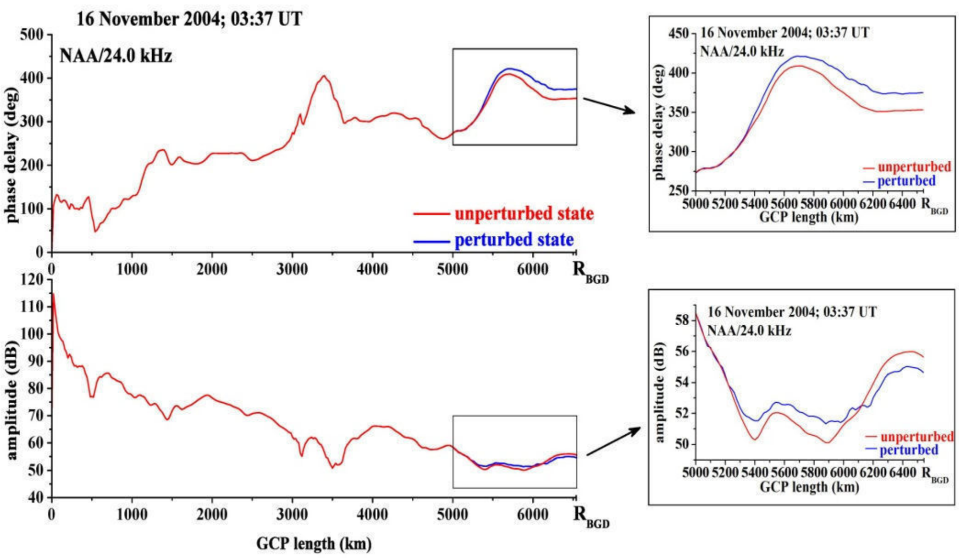


**Figure 6.** Simulated amplitude and phase delay along GCP path towards the Belgrade receiver, for unperturbed (red) and perturbed (blue) ionospheric states for NAA/24.0 kHz VLF signal waveguides, on 16 November 2004.

Parameters β and $H'$ changing along GCP path, for NAA/24.0 kHz (dashed lines) and GQD/22.1 kHz (dotted lines) VLF signal waveguides, for unperturbed (red) and perturbed (blue) ionospheric states, on 16 November 2004, are presented in Figure 8a,b, respectively (for waveguide sections of 1980 km along GCPs looking towards the Belgrade receiver; direction of view on x axis is presented by black arrows, pointing from left to right at the bottom scale when looking from transmitter T towards receiver R and pointing from left to right at the upper scale if looking from receiver R towards transmitter T). Using the expression (1), for given parameter pairs (β, $H'$), electron density height profile $N_e(z)$ within ionospheric irregularity, in perturbed section of waveguide, for both analysed VLF signals, was calculated. Irregularity modelling indicates that both VLF signal traces, in some part of the waveguide, encounter an area of enhanced electron density. Electron density changing along GCP path, for NAA/24.0 kHz (dashed line) and GQD/22.1 kHz (dotted line) VLF signal waveguides, for unperturbed (red) and perturbed (blue) ionospheric states on 16 November 2004, are presented on Figure 9 (in length of 1980 km, as looking from Belgrade towards both transmitters). Electron densities along GCPs for unperturbed state (Figure 9—red) were calculated based on modelled parameter pairs (β, $H'$) posted as unperturbed for all characteristic altitudes (Figure 8—red), where parameters β and $H'$ undergo changes due to signal propagation within the unperturbed waveguide. Electron densities along GCPs for perturbed state (Figure 9—blue) were calculated based on modelled parameter pairs (β, $H'$) for all characteristic altitudes (Figure 8—blue), where parameters undergo changes due to present irregularity and deviated from their posted unperturbed values.

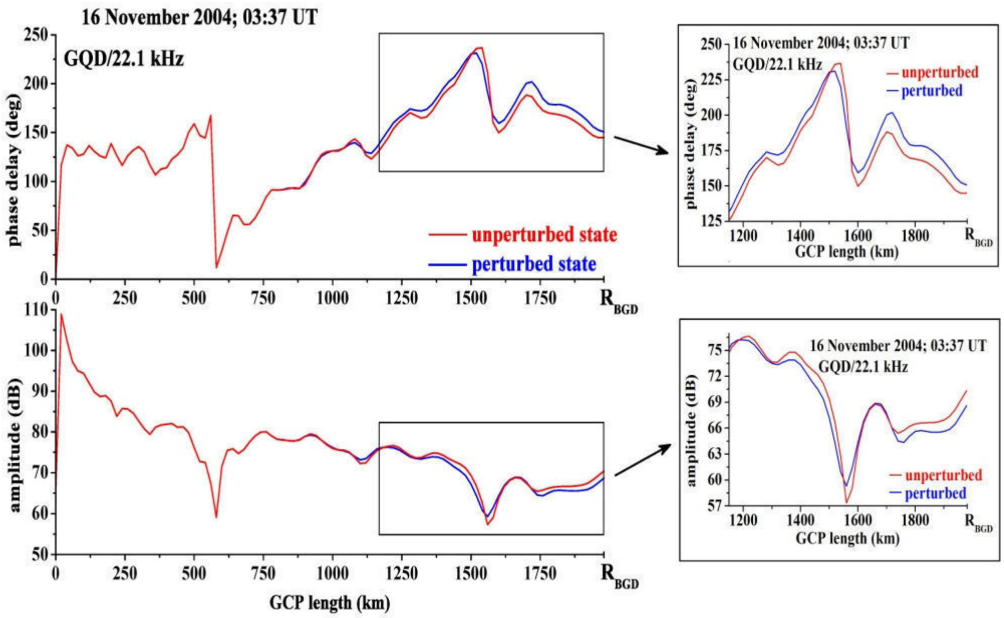


**Figure 7.** Simulated amplitude and phase delay along GCP path towards the Belgrade receiver, for unperturbed (red) and perturbed (blue) ionospheric states for GQD/22.1 kHz VLF signal waveguides, on 16 November 2004.

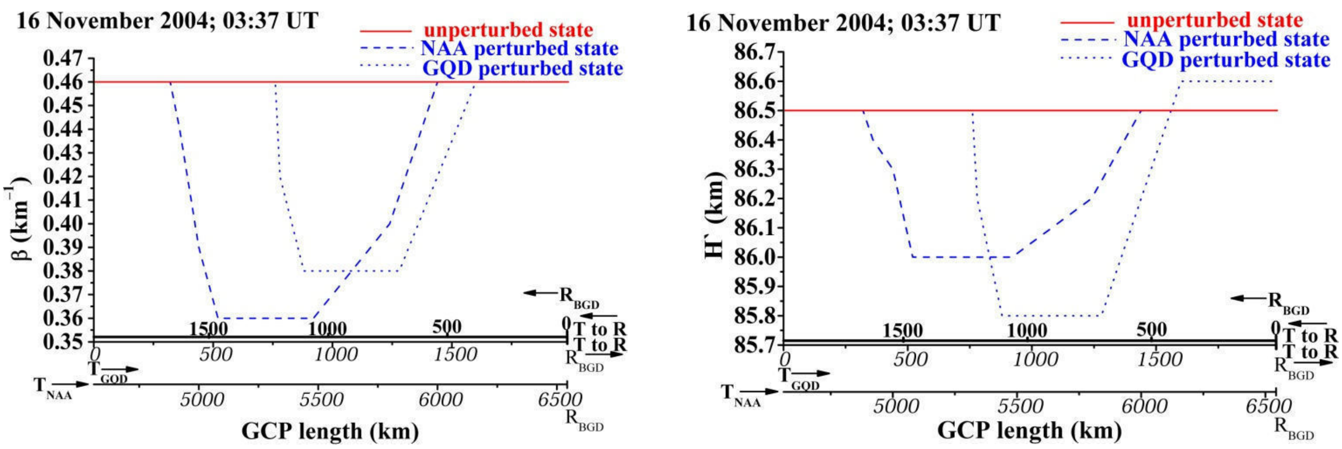


(**a**) (**b**)

**Figure 8.** Parameter β and $H'$ changing along GCP path towards the Belgrade receiver, for considered VLF signal waveguides (NAA in dashed lines and GQD in dotted lines), for unperturbed (red) and perturbed (blue) ionospheric states, on 16 November 2004 (R is for receiver, T is for transmitter, black arrows on x axis point the direction of view): (**a**) parameter β and (**b**) parameter $H'$.

Transmission in entirely nocturnal unperturbed ionospheric conditions, in the case of short GCPs is described by LWPC program usually with only one parameter pair (β, $H'$), while in the case of moderate GCPs usually with several parameter pairs (β, $H'$), along the entire path. It should be noted, that in this case, the unperturbed conditions were also modelled in order to provide the best possible match with real measured data. As already mentioned, since the perturbation was recorded on both monitored signals, in order to provide the best possible match with real measured data, in cases of perturbed conditions, sections of paths of several hundred km away from Belgrade towards transmitters, were modelled.

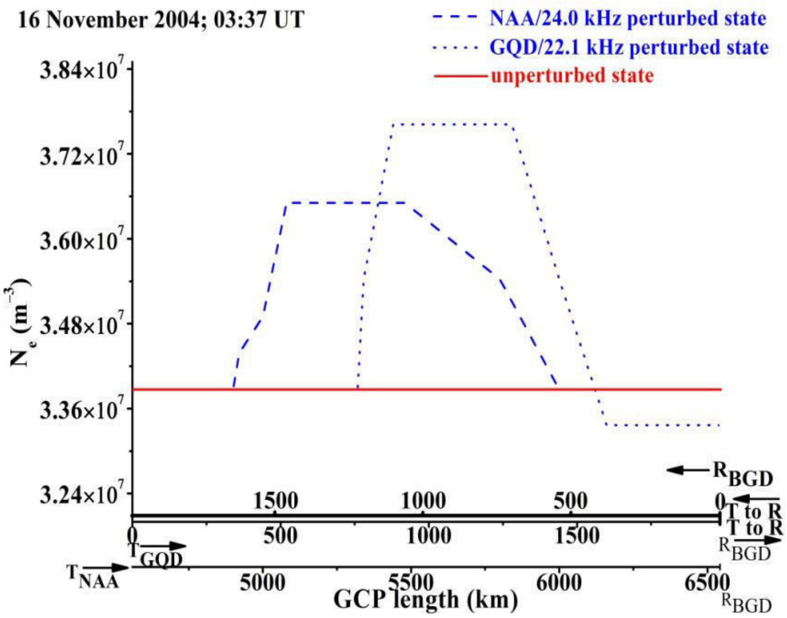


**Figure 9.** Electron density changing along GCP path towards the Belgrade receiver, for considered VLF signal waveguides (NAA/24.0 kHz in dashed line and GQD/22.1 kHz in dotted line), for unperturbed (red) and perturbed (blue) ionospheric states, on 16 November 2004 (R is for receiver, T is for transmitter, black arrows on x axis point the direction of view).

On the NAA signal trace section, where ionospheric irregularity occurs, the calculated maximum value of electron density is $3.65 \times 10^7$ m$^{-3}$, while in unperturbed ionospheric conditions, on the same NAA signal path section, it is $3.39 \times 10^7$ m$^{-3}$. On the GQD signal trace section, where ionospheric irregularity occurs, the calculated maximum value of electron density is $3.76 \times 10^7$ m$^{-3}$, while in unperturbed ionospheric conditions, on same GQD signal path section, it is $3.39 \times 10^7$ m$^{-3}$. In Figure 9, the electron density height profiles in the altitude range 60–90 km, for unperturbed and perturbed conditions due to the analysed LEP event were calculated at the reflection heights in the case of both monitored VLF signals (altitude 86 km for NAA and 85.8 km for GQD in Figure 8b), in the area of the most prominent electron density change along GCPs (e.g., at about 5300 km in the case of NAA and 1100 km in the case of the GQD signal looking from the transmitter towards the Belgrade receiver, i.e., at the approximate location of about 1100 km looking from Belgrade towards both transmitters) are given. Electron density $N_e(z)$ height profiles for GQD (at reflection height 85.8 km) and NAA (at reflection height 86 km) signals, calculated for the altitude range 60–90 km, for 16 November 2004, are given in Figure 10.

In order to create an easier and more convenient use of results presented in the analysis conducted in this paper, an expression for electron density $Ne(z)$ at reflection height is introduced in the form of a polynomial function as given in the equation below:

$$\log Ne(z, H',\ \beta) = \sum_{i=0}^{1} a_i \cdot z^i, \tag{3}$$

where $z$ is height in km, and dimensionless quantities take values of $a_0$ = −5.88339 and $a_1$ = 0.15635.

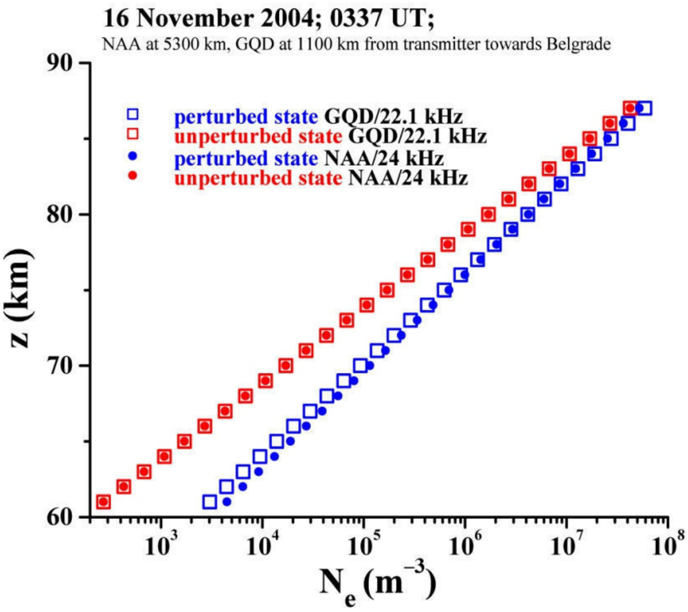


**Figure 10.** Electron density $N_e(z)$ height profiles for GQD (at reflection height 85.8 km) and NAA (at reflection height 86 km) signals, calculated for altitude range 60–90 km, for 16 November 2004, at 03:37 UT, in the area of the most prominent electron density change along GCPs at a location approximately 1100 km looking from Belgrade towards both transmitters. The unperturbed state for GQD signal is given in red hollow squares, the perturbed state for GQD signal is given in blue hollow squares, unperturbed state for NAA signal is given in red solid circles and perturbed state for NAA signal is given in blue solid circles.

### *3.4. Analysis of the LEP Event*

In perturbed ionospheric conditions at the Belgrade receiver site (44.85° N, 20.38° E), an increase in phase delay and decrease in amplitude for both analysed VLF signals, are registered (Figures 4 and 10). Such behaviour can be explained by lowering the VLF signal reflection height (delay in the phase is less) and, respectively, by reducing the sharpness of the ionized environment lower edge. In perturbed waveguides, modal minima are mitigated compared to the unperturbed ionospheric state. In the perturbed NAA waveguide, reflection height decreased from 86.5 km (characteristic value for normal unperturbed night-time ionospheric conditions) to 86 km, while reflection edge sharpness decreased from 0.46 $km^{-1}$ (characteristic value for normal unperturbed night-time ionospheric conditions) to 0.36 $km^{-1}$, which is a value characteristic for daytime ionospheric conditions. Changes in GQD propagation are similar: in perturbed waveguide, reflection height decreased from 86.5 km to 85.8 km, while reflection edge sharpness decreased from 0.46 $km^{-1}$ to 0.38 $km^{-1}$ (value characteristic for daytime ionospheric conditions). A less sharp lower edge of the ionized environment enables the VLF signal to penetrate into the ionized environment, and at the same time, VLF signal deviant energy absorption takes place. It is well known that β is a function of ω. After an LEP event, an NAA signal pair ($\beta/H'$) have values (0.46 $km^{-1}$/86.5 km) and GQD have values (0.46 $km^{-1}$/86.6 km), so it can be said that the ionosphere is fully recovered. Same ionospheric conditions (($\beta/H'$) have values of 0.46 $km^{-1}$/86.5 km) that apply for areas outside of the irregularity, too. Obtained values of ($\beta/H'$) pairs are in agreement with [48], who reported β in the range 0.48–0.5 $km^{-1}$ and $H'$ in the range 85.3–87 km for cases of short signals with a mid-latitudinal transmission, also with [57] who reported β in the range 0.46–0.5 $km^{-1}$ and $H'$ in the range 84–87 km for cases of short and moderate length signals in most cases with mid-latitudinal transmission, and [54], who reported β in the range 0.307–0.42 $km^{-1}$ and $H'$ in the range 80.3–87 km for cases of short length signals in most cases with mid-latitudinal transmission. An obtained relative change in reflection height during analysed perturbation of 0.5 km and

0.7 km in cases of NAA and GQD signals, respectively, are in agreement with the results reported by [54,55] who reported ranges of 7–10 km and 3.7–6.7 km, respectively. Measured and simulated relative change in amplitude and phase delay values (Table 1) are in line with [18] and reference therein, an amplitude difference ~6 dB and ~20 deg of phase shift and [48,54] who reported relative measured and modelled amplitude and phase change of 1.4 and 1.5 dB and 9 and 8 deg and up to 2.01 and 1.74 dB and 3.63 and 3.15 deg, respectively. Calculated maximum electron density values (for NAA signal $N_{e\ pert}$ (86.5 km) = $3.65 \times 10^7$ m$^{-3}$ and $N_{e\ unpert}$ (86 km) = $3.39 \times 10^7$ m$^{-3}$ and for GQD signal $N_{e\ pert}$ (86.5 km) = $3.76 \times 10^7$ m$^{-3}$ and $N_{e\ unpert}$ (85.8 km) = $3.39 \times 10^7$ m$^{-3}$) are in agreement with [48] who reported $N_{e\ unpert}$ (87 km) = $3.14 \times 10^7$ m$^{-3}$ and $N_{e\ pert}$ (85.3 km) = $3.67 \times 10^7$ m$^{-3}$, while [54] reported higher values and a steeper slope (variation of $N_{e\ pert}$ (84 km) from ambient $N_{e\ unpert}$ (84 km) reported $1.519 \times 10^8$ and $0.607 \times 10^8$ m$^{-3}$, respectively). The errors, introduced by the technique used, place the uncertainty of the results between 10% and 25% (see, e.g., [23]). More precisely we estimate that the total error, i.e., noise error and the calibration error is ~5% in amplitude and phase delay, which is in agreement with [58]. Moreover, the absolute amplitude variation between the recorded values and the signal amplitude and phase values acquired using LWPC is usually 10–20% which gives uncertainty of the results between 10% and 25%. Electron densities and ionospheric parameters obtained by different models and techniques [23,30,47,59] vary by about one order of magnitude (factor 10). Electron density ratios related to flare Ixmax given in [60] are within one order of magnitude and for unperturbed flare conditions given in [61] are smaller. Results obtained by VLF technique and LWPCV2.1 software are satisfactory for conducted qualitative analysis presented in this work.

By NAA signal trace modelling, it was found that ionospheric irregularity related to LIE outreach from 4920 km to 5800 km when looking along the GCP path from transmitter to receiver, thus, LIE extent is 880 km, with corresponding coordinates (0.7° E, 51.5° N) and (12° E, 48.3° N). By GQD signal trace modelling, ionospheric irregularity outreach was found from 780 km to 1440 km when looking along the GCP path from transmitter to receiver, thus, LIE extent is 660 km, with corresponding coordinates (7.4° E, 51.4° N) and (14.9° E, 48° N). Modelled LIE extent for both cases is in agreement with [54,57] who reported precipitation patches estimated as at least 1500 × 600 km and spatial extent of disturbance as 728 km, respectively. Assumed geographical position of modelled irregularity in NAA and GQD waveguides, i.e., electron density increases in D–region due to energetic electron precipitation (see Figure 9), is presented by a blue oval in Figure 11, indicating that energetic electron precipitation took place over central Europe.

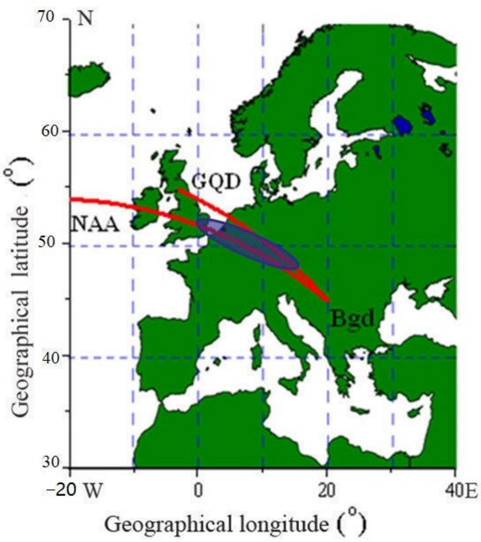


**Figure 11.** Geographical position of modelled LIE (blue oval) related to energetic electron precipitation on 16 November 2004.

## 4. Conclusions and Perspectives

Ionospheric conditions highly differ depending on the time of day when sudden disturbances occur, with a transition period between stable daytime and stable night-time ionospheric conditions, i.e., during dawn and sunset being especially challenging for modelling. Regular night-time ionospheric conditions are described with parameter pairs (β, $H'$) within a range of values, that is 0.47–0.50 km$^{-1}$ and 50–87 km, respectively, while in unperturbed daytime ionospheric conditions, this pair is defined only by one pair (0.3 km$^{-1}$, 74 km). In the case of perturbation presence, ionospheric conditions are changed affecting VLF transmission within the Earth-ionosphere waveguide, inducing signal's amplitude and phase delay to deviate from their regular values. In such disturbed environment, parameter pairs (β, $H'$) also deviate from their regular values, depicting the change in electron density that takes place, following the causative agent's behaviour. In the case of the examined LEP event example, parameter pairs (β, $H'$) changed according to perturbed nocturnal waveguides. Specifically, in the case of the NAA signal parameter, $H'$ went through a decrease from 86.5 km (characteristic value for normal unperturbed night-time ionospheric conditions in pre-LEP state) to 86 km at LEP's peak and returned to its regular value of 86.5 km in post-LEP conditions, while parameter reflection edge sharpness β decreased from 0.46 km$^{-1}$ (characteristic value for normal unperturbed night-time ionospheric conditions before LEP occurrence) to 0.36 km$^{-1}$ at LEP's peak, which is the value characteristic for daytime ionospheric conditions and returned to 0.46 km$^{-1}$, its regular value after the influence of the LEP event. Similar behaviour is also present in the case of GQD trace, where parameter $H'$ went through a decrease from 86.5 km to 85.8 km at LEP's peak and returned to 86.6 km, while reflection edge sharpness β decreased from 0.46 km$^{-1}$ to 0.38 km$^{-1}$ and returned to 0.46 km$^{-1}$. It can be concluded that after the influence of the analysed LEP event, the ionosphere is fully recovered in both waveguides, still remaining slightly higher, reflecting the edge height in the case of the GQD signal. Electron density change is one order of magnitude below regular values.

Regarding measured $\Delta A$ (dB) and $\Delta P$ (°), in the case of the LEP event, they are in a range of −1 to −2 dB and +9 to +13° (where the minus sign denotes decrease and plus sign increase in signal values compared to pre-LEP state). In the case of mid- and strong flare events, $\Delta A$ (dB) and $\Delta P$ (°) are usually of higher values [38,62,63], and especially in X-class flare events such as the one analysed here, where they took values of about +4 dB and +159°, respectively. At the maximum X-ray irradiance during X1.3 class flare event that occurred on 7 September 2017, as the response within lower ionosphere, the reflecting edge height decreased by 13 km to the height 63 km, and the reflection edge sharpness increased to the value 0.42 km$^{-1}$, while the induced electron density increase reached almost two orders of magnitude compared to the regular value. The analysed flare event lasted for almost two hours, while it took much longer for the lower ionosphere to fully recover.

Data related to the ionospheric research and the results obtained are of great use for various Earth observations and especially for telecommunications, while they also can be significant to other applications in modern society. Modelling ionospheric parameters is crucial for validation of proposed models. Results presented in this paper are related to modelling the plasma response of the ionospheric lowest region, to some high energy events, as recorded by radio signals. The presented results are important for the modelling of this region but also useful for future atmospheric aerosol–electricity interactions research in climate science. Monitoring and observing ionospheric characteristics related to the mid-latitude European ionosphere using VLF signals is particularly important, especially bearing in mind that beside the Hungarian system, this is the only available source of such data [64]. The computational results can differ by a factor of ten depending on which method is used, thus it is important to present new modelling results and make comparisons to the results obtained by the same or similar technique. The findings are significant in light of possible future collaboration on VLF studies in this part of Europe.

**Author Contributions:** Conceptualization, A.K.; writing—original draft preparation, A.K.; writing—review and editing A.K., V.A.S. and Z.R.M. The authors had full access to the data and take responsibility for their integrity. All authors have read and agreed to the published version of the manuscript.

**Funding:** This work was funded by the Institute of Physics Belgrade through a grant by the Ministry of Education, Science, and Technological Development of the Republic of Serbia. This article/publication is based upon work from COST Action CA17126—Towards understanding and modelling intense electronic excitation (TUMIEE), supported by COST (European Cooperation in Science and Technology).

**Institutional Review Board Statement:** Not applicable.

**Informed Consent Statement:** Not applicable.

**Data Availability Statement:** VLF data recorded at the Institute of Physics, University of Belgrade, Belgrade, Serbia can be obtained upon a request. Please contact V.A.S.

**Acknowledgments:** Authors thank D. Šulić for instrumental set-up and useful discussions.

**Conflicts of Interest:** The authors declare no conflict of interest. The funders had no role in the design of the study; in the collection, analyses, or interpretation of data; in the writing of the manuscript, or in the decision to publish the results.

## References

1. Kelley, M.C. *The Earth's Ionosphere: Plasma Physics and Electrodynamics*; Academic Press: Oxford, UK, 2009.
2. Rycroft, M.J. Electrical processes coupling the atmosphere and ionosphere: An overview. *J. Atmos. Sol. Terr. Phys.* **2006**, *68*, 445–456. [CrossRef]
3. Kourtidis, K.; André, K.S.; Karagioras, A.; Nita, I.-A.; Sátori, G.; Bór, J.; Kastelis, N. The influence of circulation weather types on the exposure of the biosphere to atmospheric electric fields. *Int. J. Biometeorol.* **2021**, *65*, 93–105. [CrossRef]
4. Cummer, S.A.; Inan, U.S. Ionospheric E region remote sensing with ELF radio atmospherics. *Radio Sci.* **2000**, *35*, 1437–1444. [CrossRef]
5. Mannucci, A.J.; Hajj, G.A.; Iijima, B.A.; Komjathy, A.; Meehan, T.K.; Pi, X.Q.; Srinivasan, J.; Tsurutani, B.T.; Wilson, B.; Zhang, L.D. GPS-based remote sensing of the geospace environment: Horizontal and vertical structure of the ionosphere and plasmasphere. In Proceedings of the Instruments, Science, and Methods for Geospace and Planetary Remote Sensing, Honolulu, HI, USA, 30 December 2004; pp. 1–13.
6. Goodman, J.M. *Space Weather & Telecommunications*; Springer: New York, NY, USA, 2005; Volume 382.
7. Tandberg-Hanssen, E.; Emslie, A.G. *The Physics of Solar Flares*; Cambridge University Press: Cambridge, UK, 1988; Volume 14.
8. Berényi, K.; Barta, V.; Kis, Á. Midlatitude ionospheric F2-layer response to eruptive solar events-caused geomagnetic disturbances over Hungary during the maximum of the solar cycle 24: A case study. *Adv. Space Res.* **2018**, *61*, 1230–1243. [CrossRef]
9. Šulić, D.; Srećković, V.; Mihajlov, A. A study of VLF signals variations associated with the changes of ionization level in the D-region in consequence of solar conditions. *Adv. Space Res.* **2016**, *57*, 1029–1043. [CrossRef]
10. Šulić, D.; Srećković, V. A comparative study of measured amplitude and phase perturbations of VLF and LF radio signals induced by solar flares. *Serb. Astron. J.* **2014**, *188*, 45–54. [CrossRef]
11. Reid, G.C. *Ion Chemistry in the D Region*; Academic Press: Cambridge, MA, USA, 1976; Volume 12, pp. 375–413.
12. Brasseur, G.P.; Solomon, S. *Aeronomy of the Middle Atmosphere: Chemistry and Physics of the Stratosphere and Mesosphere*; Springer Science & Business Media: Dordrecht, The Netherlands, 2006; Volume 32.
13. Nicolet, M.; Aikin, A. The formation of the D region of the ionosphere. *J. Geophys. Res.* **1960**, *65*, 1469–1483. [CrossRef]
14. Nunn, D. On the numerical modelling of the VLF Trimpi effect. *J. Atmos. Sol. Terr. Phys.* **1997**, *59*, 537–560. [CrossRef]
15. Helliwell, R.; Katsufrakis, J.; Trimpi, M. Whistler-Induced Amplitude Perturbations in VLF Propagation. *J. Geophys. Res.* **1973**, *78*, 4679–4688. [CrossRef]
16. Helliwell, R.A. *Whistlers and Related Ionospheric Phenomena*; Stanford University Press Stanford: Palo Alto, CA, USA, 1965; Volume 50.
17. Strangeways, H. *Lightning, Trimpis and Sprites*; Oxford University Press: Oxford, UK, 1996; Volume 1993, pp. 741–780.
18. Silber, I.; Price, C. On the use of VLF narrowband measurements to study the lower ionosphere and the mesosphere–lower thermosphere. *Surv. Geophys.* **2017**, *38*, 407–441. [CrossRef]
19. Trichtchenko, L.; Zhukov, A.; Van der Linden, R.; Stankov, S.; Jakowski, N.; Stanisławska, I.; Juchnikowski, G.; Wilkinson, P.; Patterson, G.; Thomson, A. November 2004 space weather events: Real-time observations and forecasts. *Space Weather* **2007**, *5*, 1–17. [CrossRef]
20. Rodger, C.J. Subionospheric VLF perturbations associated with lightning discharges. *J. Atmos. Sol. Terr. Phys.* **2003**, *65*, 591–606. [CrossRef]

21. Belenkiy, M.; Orlov, A.; Petrova, G.; Uvarov, A. Modeling of the electron density profile of the lower ionosphere (45–75 km) for sudden ionospheric disturbance conditions based on the data on sudden phase anomalies of VLF signals. *Int. J. Geomag. Aeron.* **2006**, *6*, GI3007. [CrossRef]
22. McKinnell, L.-A.; Friedrich, M. A neural network-based ionospheric model for the auroral zone. *J. Atmos. Sol. Terr. Phys.* **2007**, *69*, 1459–1470. [CrossRef]
23. Žigman, V.; Grubor, D.; Šulić, D. D-region electron density evaluated from VLF amplitude time delay during X-ray solar flares. *J. Atmos. Sol. Terr. Phys.* **2007**, *69*, 775–792. [CrossRef]
24. Chakrabarti, S.; Pal, S.; Sasmal, S.; Mondal, S.; Ray, S.; Basak, T.; Maji, S.; Khadka, B.; Bhowmick, D.; Chowdhury, A. VLF campaign during the total eclipse of July 22nd, 2009: Observational results and interpretations. *J. Atmos. Sol. Terr. Phys.* **2012**, *86*, 65–70. [CrossRef]
25. Thomson, N.R.; Rodger, C.J.; Clilverd, M.A. Daytime D region parameters from long-path VLF phase and amplitude. *J. Geophys. Res.* **2011**, *116*, 1–12.
26. McRae, W.M.; Thomson, N.R. VLF phase and amplitude: Daytime ionospheric parameters. *J. Atmos. Sol. Terr. Phys.* **2000**, *62*, 609–618. [CrossRef]
27. McRae, W.M.; Thomson, N.R. Solar flare induced ionospheric D-region enhancements from VLF phase and amplitude observations. *J. Atmos. Sol. Terr. Phys.* **2004**, *66*, 77–87. [CrossRef]
28. Thomson, N.R.; Rodger, C.J.; Clilverd, M.A. Large solar flares and their ionospheric D region enhancements. *J. Geophys. Res.* **2005**, *110*, 1–10.
29. Thomson, N.R.; Clilverd, M.A.; McRae, W.M. Nighttime ionospheric D region parameters from VLF phase and amplitude. *J. Geophys. Res.* **2007**, *112*, 1–14.
30. Basak, T.; Chakrabarti, S.K. Effective recombination coefficient and solar zenith angle effects on low-latitude D-region ionosphere evaluated from VLF signal amplitude and its time delay during X-ray solar flares. *Astrophys. Space. Sci.* **2013**, *348*, 315–326. [CrossRef]
31. Budden, K. *Radio Waves in the Ionosphere*; Cambridge Univ. Press: Cambridge, UK, 1961.
32. Budden, K.G. *The Wave-Guide Mode Theory of Wave Propagation*; Logos Press: London, UK, 1961.
33. Wait, J.R. *Electromagnetic Waves in Stratified Media*; Pergamon Press: Oxford, UK, 1970; Volume 3.
34. Mitra, A.P. *Ionospheric Effects of Solar Flares*; Springer: Berlin/Heidelberg, The Netherlands, 1974; Volume 46.
35. Balan, N.; Alleyne, H.; Walker, S.; Reme, H.; McCrea, I.; Aylward, A. Magnetosphere–ionosphere coupling during the CME events of 07–12 November 2004. *J. Atmos. Sol. Terr. Phys.* **2008**, *70*, 2101–2111. [CrossRef]
36. Inan, U.S.; Lehtinen, N.G.; Moore, R.; Hurley, K.; Boggs, S.; Smith, D.; Fishman, G. Massive disturbance of the daytime lower ionosphere by the giant γ-ray flare from magnetar SGR 1806–20. *Geophys. Res. Lett.* **2007**, *34*, 8103–8108. [CrossRef]
37. Žigman, V.; Kudela, K.; Grubor, D. Response of the Earth's lower ionosphere to the ground level enhancement event of December 13, 2006. *Adv. Space Res.* **2014**, *53*, 763–775. [CrossRef]
38. Srećković, V.A.; Šulić, D.M.; Ignjatović, L.; Vujčić, V. Low Ionosphere under Influence of Strong Solar Radiation: Diagnostics and Modeling. *Appl.Sci.* **2021**, *11*, 7194. [CrossRef]
39. Nina, A.; Srećković, V.; Radovanović, M. Multidisciplinarity in research of extreme solar energy influences on natural disasters. *Sustainability* **2019**, *11*, 974. [CrossRef]
40. Cannon, P.; Angling, M.; Barclay, L.; Curry, C.; Dyer, C.; Edwards, R.; Greene, G.; Hapgood, M.; Horne, R.B.; Jackson, D. *Extreme Space Weather: Impacts on Engineered Systems and Infrastructure*; Royal Academy of Engineering: Carlton House Terrace, London, 2013.
41. McMorrow, D. *Impacts of Severe Space Weather on the Electric Grid*; JASON: McLean, VA, USA, 2011; pp. 22102–27508.
42. Kolarski, A.; Grubor, D. Sensing the Earth's low ionosphere during solar flares using VLF signals and goes solar X-ray data. *Adv. Space Res.* **2014**, *53*, 1595–1602. [CrossRef]
43. Kolarski, A.; Grubor, D. Comparative analysis of VLF signal variation along trajectory induced by X-ray solar flares. *J. Astrophys. Astr.* **2015**, *36*, 565–579. [CrossRef]
44. Kolarski, A.; Grubor, D.; Šulić, D. Diagnostics Of The Solar X-Flare Impact On Lower Ionosphere Through The Vlf-Naa Signal Recordings. *Open Astron.* **2011**, *20*, 591–595. [CrossRef]
45. Nina, A.; Čadež, V.; Srećković, V.; Šulić, D. The influence of solar spectral lines on electron concentration in terrestrial ionosphere. *Open Astron.* **2011**, *20*, 609–612. [CrossRef]
46. Nina, A.; Čadež, V.; Srećković, V.; Šulić, D. Altitude distribution of electron concentration in ionospheric D-region in presence of time-varying solar radiation flux. *Nucl. Instrum. Meth. B* **2012**, *279*, 110–113. [CrossRef]
47. Nina, A.; Čadež, V.; Šulić, D.; Srećković, V.; Žigman, V. Effective electron recombination coefficient in ionospheric D-region during the relaxation regime after solar flare from 18 February 2011. *Nucl. Instrum. Meth. B* **2012**, *279*, 106–109. [CrossRef]
48. Šulić, D.; Nina, A.; Srećković, V. Numerical Simulations Of The Effect Of Localised Ionospheric Perturbations On Subionospheric VLF Propagation. *arXiv* **2014**, arXiv:1405.3783.
49. Nina, A.; Čadež, V.M.; Popović, L.Č.; Srećković, V.A. Diagnostics of plasma in the ionospheric D-region: Detection and study of different ionospheric disturbance types. *Eur. Phys. J. D* **2017**, *71*, 189. [CrossRef]
50. Nina, A.; Simić, S.; Srećković, V.A.; Popović, L.Č. Detection of short-term response of the low ionosphere on gamma ray bursts. *Geophys. Res. Lett.* **2015**, *42*, 8250–8261. [CrossRef]

51. Ferguson, J. *Computer Programs for Assessment of Long-Wavelength Radio Communications, Version 2.0: User's Guide and Source Files*; Space and Naval Warfare Systems Center: San Diego, CA, USA, 1998.
52. Gavrilov, B.; Ermak, V.; Lyakhov, A.; Poklad, Y.V.; Rybakov, V.; Ryakhovsky, I. Reconstruction of the Parameters of the Lower Midlatitude Ionosphere in M-and X-Class Solar Flares. *Geomagn. Aeron.* **2020**, *60*, 747–753. [CrossRef]
53. Kumar, A.; Kumar, S. Solar flare effects on D-region ionosphere using VLF measurements during low-and high-solar activity phases of solar cycle 24. *Earth Planets Space* **2018**, *70*, 29. [CrossRef]
54. Kerrache, F.; Nait Amor, S.; Kumar, S. Ionospheric D region disturbances due to FAC and LEP associated with three severe Geomagnetic Storms as observed by VLF Signals. *J. Geophys. Res.* **2021**, *126*, e2020JA027838. [CrossRef]
55. Šulić, D.; Žigman, V.; Nina, A. Study of the observed amplitude and phase perturbations on VLF signals from lighting induced electron precipitation and reconstruction of D-region electron density height profile. In Proceedings of the 4rd VERSIM Workshop 2010, Prague, Czech Republic, 13–17 September 2010.
56. Wait, J.R.; Spies, K.P. *Characteristics of the Earth-Ionosphere Waveguide for VLF Radio Waves*; US Department of Commerce, National Bureau of Standards: Boulder, CO, USA, 1964; Volume 13.
57. Clilverd, M.A.; Nunn, D.; Lev-Tov, S.J.; Inan, U.S.; Dowden, R.L.; Rodger, C.J.; Smith, A.J. Determining the size of lightning-induced electron precipitation patches. *J. Geophys. Res.* **2002**, *107*, SIA 10–SIA 11. [CrossRef]
58. Bainbridge, G.; Inan, U.S. Ionospheric D region electron density profiles derived from the measured interference pattern of VLF waveguide modes. *Radio Sci.* **2003**, *38*, 16-11–16-21. [CrossRef]
59. Palit, S.; Basak, T.; Mondal, S.; Pal, S.; Chakrabarti, S. Modeling of very low frequency (VLF) radio wave signal profile due to solar flares using the GEANT4 Monte Carlo simulation coupled with ionospheric chemistry. *Atmos. Chem. Phys.* **2013**, *13*, 9159–9168. [CrossRef]
60. Grubor, D.; Šulić, D.; Žigman, V. Classification of X-ray solar flares regarding their effects on the lower ionosphere electron density profile. *Ann. Geophys.* **2008**, *26*, 1731–1740. [CrossRef]
61. Nina, A.; Čadež, V.M. Electron production by solar Ly-α line radiation in the ionospheric D-region. *Adv. Space Res.* **2014**, *54*, 1276–1284. [CrossRef]
62. Bouderba, Y.; NaitAmor, S.; Tribeche, M. Study of the solar flares effect on VLF radio signal propagating along NRK-ALG path using LWPC code. *J. Geophys. Res.* **2016**, *121*, 6799–6807. [CrossRef]
63. Feng, J.; Han, B.; Gao, F.; Zhang, T.; Zhao, Z. Analysis of Global Ionospheric Response to Solar Flares Based on Total Electron Content and Very Low Frequency Signals. *IEEE Access* **2021**, *9*, 57618–57631. [CrossRef]
64. Barta, V.; Haldoupis, C.; Sátori, G.; Buresova, D.; Chum, J.; Pozoga, M.; Berényi, K.A.; Bór, J.; Popek, M.; Kis, Á. Searching for effects caused by thunderstorms in midlatitude sporadic E layers. *J. Atmos. Sol. Terr. Phys.* **2017**, *161*, 150–159. [CrossRef]

data

MDPI

*Data Descriptor*

# Data for Photodissociation of Some Small Molecular Ions Relevant for Astrochemistry and Laboratory Investigation

**Vladimir A. Srećković [1,*], Ljubinko M. Ignjatović [1], Aleksandra Kolarski [1], Zoran R. Mijić [1], Milan S. Dimitrijević [2,3] and Veljko Vujčić [2]**

[1] Institute of Physics Belgrade, University of Belgrade, 11080 Belgrade, Serbia
[2] Astronomical Observatory, 11060 Belgrade, Serbia
[3] Observatoire de Paris, Sorbonne Université, Université PSL, CNRS, LERMA, F-92190 Meudon, France
* Correspondence: vlada@ipb.ac.rs; Tel.: +381-(0)11-37-13-000

**Abstract:** The calculated photodissociation data of some small molecular ions have been reported. The cross-sections and spectral rate coefficients data have been studied using a quantum mechanical method. The plasma parameters, i.e., conditions, cover temperatures from 1000 to 20,000 K and wavelengths in the EUV and UV region. The influence of temperature and wavelength on the spectral coefficients data of all of the investigated species have been discussed. Data could also be useful for plasma diagnostics in laboratory, astrophysics, and industrial plasmas for their modelling.

**Dataset:** Supplementary File.

**Dataset License:** CC-BY 4.0

**Keywords:** atomic and molecular data; photodissociation; small molecules; radiative processes; spectroscopy; astrochemistry; planetary chemistry; planetary geochemistry; modelling



**Citation:** Srećković, V.A.; Ignjatović, L.M.; Kolarski, A.; Mijić, Z.R.; Dimitrijević, M.S.; Vujčić, V. Data for Photodissociation of Some Small Molecular Ions Relevant for Astrochemistry and Laboratory Investigation. *Data* **2022**, *7*, 129. https://doi.org/10.3390/data7090129

Academic Editor: Jamal Jokar Arsanjani

Received: 17 July 2022
Accepted: 9 September 2022
Published: 11 September 2022



## 1. Summary

Atomic and molecular databases and data have become crucial for data interpretation, diagnostics, and the creation of models and simulations of intricate physical processes [1–4]. The importance of studying optical properties in different fields, especially when modelling those systems, is of particular interest [5–7]. If the required data, i.e., information, are available, we can simulate the spectral properties [8–11].

One can note the current importance of the investigation of optical properties of various small molecules and corresponding atomic and molecular data [12–17]. Here, we investigate the photodissociation processes that occur in non-symmetric systems that contain hydrogen and helium, and alkali atoms, ions, and molecular-ions. As noted in [18], the helium hydride ionic molecule has been discovered to be one of the primary constituents in He/H plasma sources, including synchrotron devices, high voltage glow discharges, inductively coupled plasma generators, capacitively coupled RF discharges, and magnetically confined plasmas, and plays a very special role in the advancement of thermonuclear fusion nowadays. The majority of alkali hydride species, both ionic and neutral, are highly important for comprehending how the molecular universe was created and developed [19]. Although they have a role in a number of astrophysical and astrochemical processes such as radiative transfer, their spectroscopy is mostly unknown in both theory and observation, especially when it comes to molecule ions [20]. In addition, one can note the potential importance of the aluminum monohydride cation in solar and in laboratory investigations [21,22].

Our aim is to obtain spectroscopic information, i.e., data, about such systems. We determined the spectral absorption rate coefficients and average cross-sections for molecular ions $AlH^+$, $HeH^+$, and $HK^+$. The outcomes, i.e., the data gathered, could be used for various applications, such as plasma chemistry or experiments such as PLEIADES synchrotron [23–25], for modelling atmospheres of diverse environments such as the interstellar medium, planets, and dwarf stars, and also in the plasma fusion area [7,26–30].

## 2. Data Description

A dataset, i.e., new results for the average cross-section, as well as the spectral absorption rate coefficients for small molecular ions $AlH^+$, $HeH^+$, and $HK^+$ has been provided (see Tables S1–S9). In addition, the results are illustrated in this section by Figures 1 and 2 and also in Supplementary Materials.

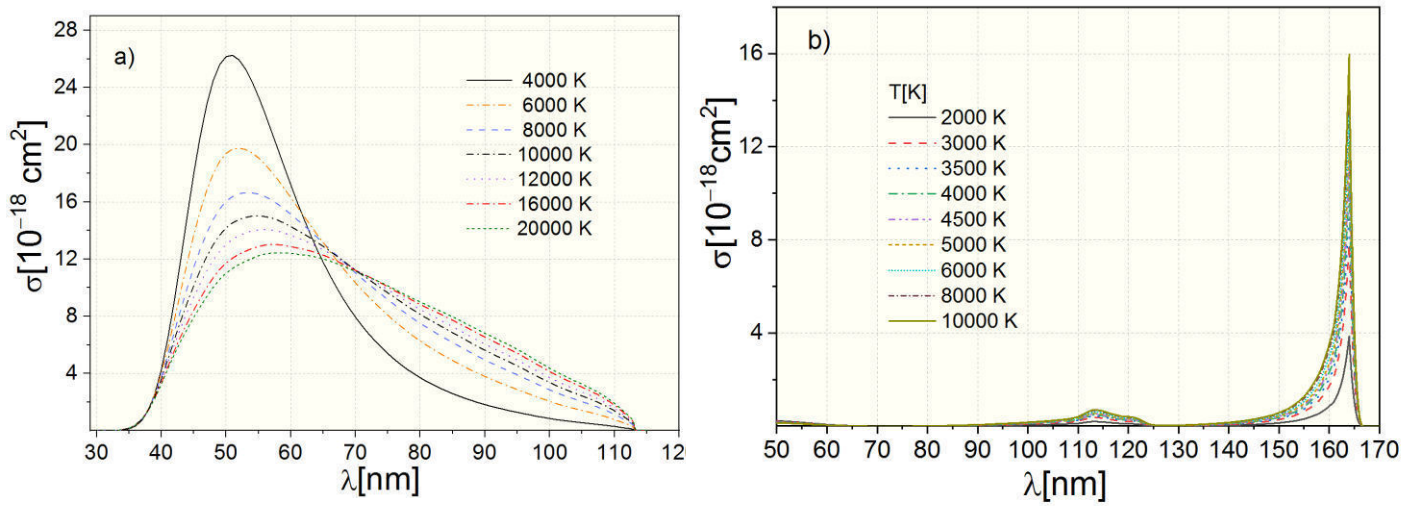


**Figure 1.** Examples of the averaged cross-section for photodissociation for some small molecular ions for the wide region of temperatures in EUV and VUV spectral region. (**a**) The averaged cross-section for photodissociation of the $HeH^+$ molecular-ion, as a function of wavelength and temperature. (**b**) The averaged cross-section for photodissociation of the AlH+ molecular-ion, as a function of wavelength and temperature.

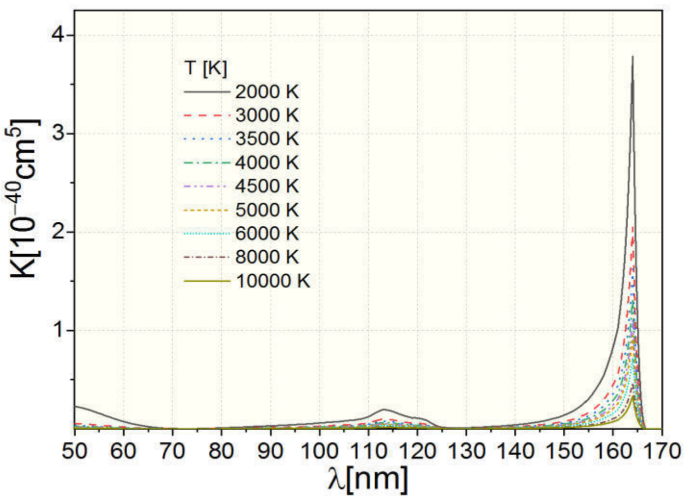


**Figure 2.** The photodissociation spectral rate coefficients K(λ, T) for the case of $AlH^+$ molecular ions as a function of wavelength and temperature.

The averaged cross-section for photodissociation for some small molecular ions for the wide region of temperatures in EUV and VUV spectral region are depicted in Figure 1a,b.

Figure 1a,b demonstrates that the temperature dependence of the mean thermal photoionization cross-section differs considerably for those species. In addition, the maxima of the cross section for those molecular ions are located at different wavelengths and with different behaviors (with slow and faster changes). Looking at Figure 1a,b and the data in the tables, it can be seen that cross-section maxima for $HeH^+$ are located around 50 nm. It is very wide (several tens of nm), i.e., cross-section slowly increases and also slowly decreases. The opposite behavior is shown by the $KH^+$ cross-section. The maxima are very sharp and at a wavelength of about 125 nm. In addition, $AlH^+$ has sharp maxima, but is located at higher wavelengths. All average cross-section data for photodissociation are presented in the Supplementary Material.

As an example, the behavior of the aluminum hydride cation photodissociation rate coefficient K(λ, T) data is graphically shown in Figure 2 as a function of wavelength and temperature. A similar behavior, i.e., shape can be observed as its average cross section. All of the data are organized into tables in the Supplementary Material for all of the analyzed species.

## 3. Methods

The spectral rate coefficients and average cross-sections were obtained using a quantum mechanical method in which the photodissociation process was studied as an outcome of radiative transitions among the ground state and the first excited adiabatic electronic state of the species, i.e., molecular-ion [5]. Here, in the dipole approximation, the transitions were caused by the electronic component of the ion-atom system interacting with the electromagnetic field. Within this theory, the mean thermal photodissociation cross-section can be given by:

$$\sigma(\lambda, T) = \frac{\sum\limits_{J,v} (2J+1) e^{\frac{-E_{J,v}}{kT}} \cdot \sigma_{J,v}(\lambda)}{\sum\limits_{J,v} (2J+1) e^{\frac{-E_{J,v}}{kT}}} \tag{1}$$

where $E_{J,v}$ denotes the energies of the states with the respect to the ground rovibrational states. In the above equation, $\sigma_{J,v}(\lambda)$ is the partial cross-sections for the rovibrational states with specified quantum numbers $J$ and $v$, given, e.g., in [5], with the dipole approximation. According to the processes' stated mechanism, the photon with energy $\epsilon_\lambda$ is absorbed close to the resonance point $R = R_\lambda$, where $R_\lambda$ is the root of the equation $U_{12}(R) \equiv U_1(R) - U_2(R) = \epsilon_\lambda$. Here, the ground electronic state is represented by $U_1(R)$, while the first excited electronic state is represented by $U_2(R)$.

The photodissociation spectral rate coefficient can be presented using Equation (1) by the expression

$$K(\lambda, T) = \sigma(\lambda, T) \cdot \left( \frac{g_1 g_2}{g_{12}} \left( \frac{\mu k T}{2\pi\hbar^2} \right)^{\frac{3}{2}} \cdot \frac{1}{\sum\limits_{J,v} (2J+1) e^{\frac{E_{dest} - E_{J,v}}{kT}}} \right)^{-1} \tag{2}$$

In Equation (2) $g_{12}$, $g_1$, and $g_2$ denote the electronic statistical weights of the considered species, i.e., molecular ions, atoms, and ions, and $E_{dest}$ is the molecular-ion dissociative energy. The theory, mechanism, and other needed quantities can be found in [5] in detail.

To prepare easier and more satisfying usage of calculated data in modelling as well as in an explanation of the experimental results in laboratories, we provide a simple fitting formula. We provide a simplified formula to prepare the calculated data for easier and more satisfactory employment in modelling and in the justification of experimental results in lab settings. Based on a least-square method, the photodissociation spectral rate coefficients for investigated small molecular ions can be presented as a logarithmic second-degree polynomial: $\log(K(\lambda, T)) = \sum\limits_{k=0}^{2} p_k(\lambda)(\log(T))^k$. In the Supplementary Tables coefficients,

$p_k(\lambda)$ for the selected fits and range of parameters for the aluminum hydride cation, helium hydride cation, and potassium hydride cation are given. We note that the simplified expression can be valid outside the range of defined plasma conditions, but their use should be taken with caution. In addition, we present Figure S1 in the Supplement Material, which simultaneously presents the photodissociation spectral rate coefficients data and simplified formula data on the example of $HeH^+$.

We note that both the cross-section and rate coefficient can be described by more sophisticated formulas. However, it is unclear how simple some of them are to use and whether they are appropriate when quick analysis and product delivery are crucial. The formula should be simple to use and allow for quick computations and practical analysis.

## 4. User Notes

A dataset with new results for photodissociation for corresponding molecular ion species is shown in Supplementary Material Tables S1–S9, which is appropriate for further use.

The presented data can be used in practice in different areas of science and in several possible ways:

- for laboratory research (spectroscopic investigation, synchrotron experiments, etc.)
- for industry and technology application
- for the advancement of chemistry and modelling of various layers of different atmospheres
- for potential astrophysical use (early universe chemistry and interstellar gas investigation)
- for various theoretical studies

Notably, the data and its analysis highlight interdisciplinary nature and usage, e.g., in physics, chemistry, astrophysics, astroinformatics, and astrobiology [24,31–35].

**Supplementary Materials:** The following supporting information are available online at https://www.mdpi.com/article/10.3390/data7090129/s1. Tables S1, S2, and S3 present data for average photodissociation cross-sections for molecular ions $AlH^+$, $HeH^+$, and $KH^+$. Tables S4, S5, and S6 the photodissociation spectral rate coefficients for investigated species. Tables S7, S8, and S9 present data for simplified formulas for photodissociation spectral rates. Figure S1 presents the simultaneous photodissociation spectral rate coefficients data and simplified formula data for the example of $HeH^+$.

**Author Contributions:** Conceptualization, V.A.S.; formal analysis, L.M.I., V.V. and V.A.S.; validation, V.A.S. and L.M.I.; visualization, V.A.S. and V.V.; writing—original draft, V.A.S.; writing—review and editing, V.A.S., Z.R.M., A.K. and M.S.D. All of the authors contributed equally to this work. All authors have read and agreed to the published version of the manuscript.

**Funding:** This work was funded by the Institute of Physics Belgrade through a grant by the Ministry of Education, Science, and Technological Development of the Republic of Serbia. This article/publication is based on work from COST Action CA18222–Attosecond Chemistry (AttoChem), supported by COST (European Cooperation in Science and Technology).

**Institutional Review Board Statement:** Not applicable.

**Informed Consent Statement:** Not applicable.

**Data Availability Statement:** All data are in the Supplement Material.

**Acknowledgments:** We would also like to express our gratitude to Magdalena Christova for her time and effort put into this work, as well as for a fruitful discussion.

**Conflicts of Interest:** The authors declare no conflict of interest. The funders had no role in the design of the study; in the collection, analyses, or interpretation of data; in the writing of the manuscript; or in the decision to publish the results.

## References


1. Albert, D.; Antony, B.K.; Ba, Y.A.; Babikov, Y.L.; Bollard, P.; Boudon, V.; Delahaye, F.; Del Zanna, G.; Dimitrijević, M.S.; Drouin, B.J.; et al. A Decade with VAMDC: Results and Ambitions. *Atoms* **2020**, *8*, 76. [CrossRef]
2. Majlinger, Z.; Dimitrijević, M.S.; Srećković, V.A. Stark Broadening of Co II Lines in Stellar Atmospheres. *Data* **2020**, *5*, 74. [CrossRef]
3. Ryabchikova, T.; Piskunov, N.; Kurucz, R.; Stempels, H.; Heiter, U.; Pakhomov, Y.; Barklem, P.S. A major upgrade of the VALD database. *Phys. Scr.* **2015**, *90*, 054005. [CrossRef]
4. Marinković, B.; Pejčev, V.; Filipović, D.; Šević, D.; Milosavljević, A.; Milisavljević, S.; Rabasović, M.; Pavlović, D.; Maljković, J. Cross section data for electron collisions in plasma physics. In *Journal of Physics: Conference Series*; IOP Publishing: Bristol, UK, 2007; p. 012006.
5. Srećković, V.A.; Ignjatović, L.M.; Jevremović, D.; Vujčić, V.; Dimitrijević, M.S. Radiative and collisional molecular data and virtual laboratory astrophysics. *Atoms* **2017**, *5*, 31. [CrossRef]
6. Aloui, R.; Elabidi, H.; Sahal-Bréchot, S. Sr V–VI line widths in hot white dwarf atmospheres. *Mon. Not. R. Astron. Soc.* **2022**, *512*, 1598–1607. [CrossRef]
7. Mihajlov, A.; Sakan, N.; Srećković, V.; Vitel, Y. Modeling of the continuous absorption of electromagnetic radiation in dense Hydrogen plasma. *Open Astron.* **2011**, *20*, 604–608. [CrossRef]
8. Dimitrijević, M.S.; Srećković, V.A.; Ignjatović, L.M.; Marinković, B.P. The role of some collisional processes in AGNs: Rate coefficients needed for modeling. *New Astron.* **2021**, *84*, 101529. [CrossRef]
9. Sahal-Bréchot, S.; Elabidi, H. Stark broadening for Br VI and Kr V-VII lines in hot star atmospheres. *Astron. Astrophys.* **2021**, *652*, A47. [CrossRef]
10. Hauschildt, P.H.; Baron, E. A 3D radiative transfer framework-VI. PHOENIX/3D example applications. *Astron. Astrophys.* **2010**, *509*, A36. [CrossRef]
11. Husser, T.O.; Wende-von Berg, S.; Dreizler, S.; Homeier, D.; Reiners, A.; Barman, T.; Hauschildt, P.H. A new extensive library of PHOENIX stellar atmospheres and synthetic spectra. *Astron. Astrophys.* **2013**, *553*, A6. [CrossRef]
12. Beuc, R.; Pichler, G. High-Temperature Optical Spectra of Diatomic Molecules: Influence of the Avoided Level Crossing. *Atoms* **2020**, *8*, 28. [CrossRef]
13. Beuc, R.; Movre, M.; Horvatić, B. Time-efficient numerical simulation of diatomic molecular spectra. *Eur. Phys. J. D* **2014**, *68*, 59. [CrossRef]
14. Pichler, G.; Beuc, R.; Kokaj, J.; Sarkisyan, D.; Jose, N.; Mathew, J. Photoionization of KCs Molecule: Origin of the Structured Continuum? *Atoms* **2020**, *8*, 24. [CrossRef]
15. Rebholz, M.; Ding, T.; Aufleger, L.; Hartmann, M.; Meyer, K.; Stooß, V.; Magunia, A.; Wachs, D.; Birk, P.; Mi, Y. XUV-Initiated Dissociation Dynamics of Molecular Oxygen ($O_2$). *J. Phys. Chem. A* **2021**, *125*, 10138–10143. [CrossRef] [PubMed]
16. Pop, N.; Iacob, F.; Niyonzima, S.; Abdoulanziz, A.; Laporta, V.; Reiter, D.; Schneider, I.; Mezei, J.Z. Reactive collisions between electrons and $BeT^+$: Complete set of thermal rate coefficients up to 5000 K. *At. Data Nucl. Data Tables* **2021**, *139*, 101414. [CrossRef]
17. Niyonzima, S.; Pop, N.; Iacob, F.; Larson, Å.; Orel, A.; Mezei, J.Z.; Chakrabarti, K.; Laporta, V.; Hassouni, K.; Benredjem, D. Low-energy collisions between electrons and $BeD^+$. *Plasma Sources Sci. Technol.* **2018**, *27*, 025015. [CrossRef]
18. Loreau, J.; Liévin, J.; Palmeri, P.; Quinet, P.; Vaeck, N. Ab initio calculation of the 66 low-lying electronic states of $HeH^+$: Adiabatic and diabatic representations. *J. Phys. B At. Mol. Opt. Phys.* **2010**, *43*, 065101. [CrossRef]
19. Magnier, S. Theoretical determination of the electronic structure of $KH^+$. *Chem. Phys.* **2006**, *326*, 375–380. [CrossRef]
20. Levine, J. *The Photochemistry of Atmospheres*; Elsevier: Amsterdam, The Netherlands, 2012.
21. Srećković, V.; Mihajlov, A.; Ignjatović, L.M.; Dimitrijević, M. Ion-atom radiative processes in the solar atmosphere: Quiet Sun and sunspots. *Adv. Space Res.* **2014**, *54*, 1264–1271. [CrossRef]
22. Kokish, M.; Dietrich, M.; Odom, B. Simple and compact nozzle design for laser vaporization sources. *J. Phys. B At. Mol. Opt. Phys.* **2016**, *49*, 035301. [CrossRef]
23. Giuliani, A.; Milosavljević, A.R.; Canon, F.; Nahon, L. Contribution of synchrotron radiation to photoactivation studies of biomolecular ions in the gas phase. *Mass Spectrom. Rev.* **2014**, *33*, 424–441. [CrossRef] [PubMed]
24. Milosavljević, A.R.; Nicolas, C.; Lemaire, J.; Dehon, C.; Thissen, R.; Bizau, J.M.; Réfrégiers, M.; Nahon, L.; Giuliani, A. Photoionization of a protein isolated in vacuo. *Phys. Chem. Chem. Phys.* **2011**, *13*, 15432–15436. [CrossRef] [PubMed]
25. Ranković, M.L.; Cerovski, V.; Canon, F.; Nahon, L.; Giuliani, A.; Milosavljević, A.R. Photodissociation of protonated Leucine-Enkephalin peptide in the VUV range. In *Journal of Physics, Conference Series*; IOP Publishing: Bristol, UK, 2015; p. 112030.
26. Carniato, S.; Bizau, J.M.; Cubaynes, D.; Kennedy, E.T.; Guilbaud, S.; Sokell, E.; McLaughlin, B.; Mosnier, J.P. Vibrationally and spin-orbit-resolved inner-shell X-ray absorption spectroscopy of the $NH^+$ molecular ion: Measurements and ab initio calculations. *Atoms* **2020**, *8*, 67. [CrossRef]
27. Stwalley, W.C.; Zemke, W.T. Spectroscopy and structure of the Lithium Hydride diatomic molecules and ions. *J. Phys. Chem. Ref. Data* **1993**, *22*, 87–112. [CrossRef]
28. Yan, L.; Qu, Y.; Liu, C.; Wang, J.; Buenker, R.J. Ab initio many-electron study for the low-lying states of the alkali hydride cations in the adiabatic representation. *J. Chem. Phys.* **2012**, *136*, 124304. [CrossRef]
29. Mihajlov, A.; Sakan, N.; Srećković, V.; Vitel, Y. Modeling of continuous absorption of electromagnetic radiation in dense partially ionized plasmas. *J. Phys. A Math. Theor.* **2011**, *44*, 095502. [CrossRef]

30. Al-Modlej, A.; Alraddadi, R.; Ben Nessib, N. Energy levels and oscillator strengths for carbon isoelectronic sequence from CI to Ne V. *Eur. Phys. J. Plus* **2018**, *133*, 379. [CrossRef]
31. Milosavljević, A.R.; Giuliani, A.; Nicolas, C. Gas-phase near-edge X-ray absorption fine structure (NEXAFS) spectroscopy of nanoparticles, biopolymers, and ionic species. In *X-ray and Neutron Techniques for Nanomaterials Characterization*; Springer: Berlin/Heidelberg, Germany, 2016; pp. 451–505.
32. Singh, S.V.; Vishakantaiah, J.; Meka, J.K.; Sivaprahasam, V.; Chandrasekaran, V.; Thombre, R.; Thiruvenkatam, V.; Mallya, A.; Rajasekhar, B.N.; Muruganantham, M. Shock processing of amino acids leading to complex structures—implications to the origin of life. *Molecules* **2020**, *25*, 5634. [CrossRef]
33. Adamovich, I.; Baalrud, S.; Bogaerts, A.; Bruggeman, P.; Cappelli, M.; Colombo, V.; Czarnetzki, U.; Ebert, U.; Eden, J.; Favia, P. The 2017 Plasma Roadmap: Low temperature plasma science and technology. *J. Phys. D Appl. Phys.* **2017**, *50*, 323001. [CrossRef]
34. Adamovich, I.; Agarwal, S.; Ahedo, E.; Alves, L.; Baalrud, S.; Babaeva, N.; Bogaerts, A.; Bourdon, A.; Bruggeman, P.; Canal, C. The 2022 Plasma Roadmap: Low temperature plasma science and technology. *J. Phys. D Appl. Phys.* **2022**, *55*, 373001. [CrossRef]
35. d'Ischia, M.; Manini, P.; Moracci, M.; Saladino, R.; Ball, V.; Thissen, H.; Evans, R.A.; Puzzarini, C.; Barone, V. Astrochemistry and Astrobiology: Materials Science in Wonderland? *Int. J. Mol. Sci.* **2019**, *20*, 4079. [CrossRef] [PubMed]

applied sciences

MDPI

*Article*

# Novel Modelling Approach for Obtaining the Parameters of Low Ionosphere under Extreme Radiation in X-Spectral Range

**Vladimir A. Srećković [1,*], Desanka M. Šulić [2], Veljko Vujčić [3], Zoran R. Mijić [1] and Ljubinko M. Ignjatović [1]**

[1] Institute of Physics Belgrade, University of Belgrade, Pregrevica 118, 11080 Belgrade, Serbia; zoran.mijic@ipb.ac.rs (Z.R.M.); ljuba@ipb.ac.rs (L.M.I.)
[2] Faculty of Ecology and Environmental Protection, University Union—Nikola Tesla, 11000 Belgrade, Serbia; dsulic@unionnikolatesla.edu.rs
[3] Astronomical Observatory, Volgina 7, 11060 Belgrade, Serbia; veljko@aob.rs
* Correspondence: vlada@ipb.ac.rs; Tel.: +381-(0)11-37-13-000

**Abstract:** Strong radiation from solar X-ray flares can produce increased ionization in the terrestrial D-region and change its structure. Moreover, extreme solar radiation in X-spectral range can create sudden ionospheric disturbances and can consequently affect devices on the terrain as well as signals from satellites and presumably cause numerous uncontrollable catastrophic events. One of the techniques for detection and analysis of solar flares is studying the variations in time of specific spectral lines. The aim of this work is to present our study of solar X-ray flare effects on D-region using very low-frequency radio signal measurements over a long path in parallel with the analysis of X-spectral radiation, and to obtain the atmospheric parameters (sharpness, reflection height, time delay). We introduce a novel modelling approach and give D-region coefficients needed for modelling this medium, as well as a simple expression for electron density of lower ionosphere plasmas. We provide the analysis and software on GitHub.

**Keywords:** solar radiation; sun activity; disturbances; radio spectra; X-spectral domain; Lyman-alpha



**Citation:** Srećković, V.A.; Šulić, D.M.; Vujčić, V.; Mijić, Z.R.; Ignjatović, L.M. Novel Modelling Approach for Obtaining the Parameters of Low Ionosphere under Extreme Radiation in X-Spectral Range. *Appl. Sci.* **2021**, *11*, 11574. https://doi.org/10.3390/app112311574

Academic Editor: Harry D. Kambezidis

Received: 20 October 2021
Accepted: 1 December 2021
Published: 6 December 2021



## 1. Introduction

Solar flares (SFs) are giant eruptions on the surface of the Sun [1,2] that release huge amounts of electromagnetic energy over the whole electromagnetic spectrum [3–7]. Levels of photoionization processes in the ionosphere depend on plasma composition along with radiation spectral ranges at specific altitudes [8]. Information on certain solar spectral lines could be of importance in research of solar flares [9,10]. The enhanced Extreme Ultraviolet (EUV) radiation is absorbed at higher terrestrial altitudes additionally ionizing E and F regions of the ionosphere [11]. In addition, Lyman-alpha and X-rays penetrate more deeply into the ionosphere, reaching the D-region and causing enhanced ionization and absorption of electromagnetic (EM) waves there [12–14]. Solar flares can be classified into different classes based on their peak emission in the X-ray 0.1–0.8 nm spectral range as B ($\geq 10^{-7}$ Wm$^{-2}$), C ($\geq 10^{-6}$ Wm$^{-2}$), M ($\geq 10^{-5}$ Wm$^{-2}$), and X ($\geq 10^{-4}$ Wm$^{-2}$) classes [15–17].

The abrupt increase in X-radiation and EUV emission following solar flares causes additional ionization and increased absorption of EM waves in the sunlit part of the Earth's ionosphere. At the time of SFs and consequently during sudden ionospheric disturbances (SIDs), the gain of the atmosphere electron density at all heights is noticeable [18,19]. As a consequence of radiation influence, SFs create SIDs and induce disturbance in the monitored amplitude and phase of Very Low-Frequency (VLF in narrow band 3–30 kHz) radio signals, primarily in the D layer, which is located between the Earth's lower atmosphere, which has dense air, and its strongly conducting ionosphere [20,21]. These events of X-ray SFs have been monitored by Geostationary Operational Environmental Satellite (GOES) [15].

In this paper we will focus on the VLF technique—on amplitude and phase signals of worldwide transmitters of signals monitored by BEL VLF system (Belgrade, Serbia) [22]. VLF signals from the emitters located all over the world are continuously recorded by the BEL system. Events of X-ray SFs monitored by GOES satellites are further identified using a radio station's system of receivers. For these events, VLF wave enhancements are measured and analysed for the daytime atmosphere. In continuation of our previous research, the aim of this contribution is to present our study of solar X-ray flare effects and to obtain the daytime atmospheric parameters and ionization rate induced by this extreme radiation, and to provide a simple equation for altitude-dependent electron density of D-region plasma which depends on X-ray spectral intensity and sluggishness of the medium. Finally, we discuss how the approximately obtained altitude-dependent electron density relies on the shape of X-ray flux. The python scripts for calculating ionosphere parameters can be found on GitHub: https://github.com/sambolino/flarED (accessed on 17 October 2021).

The text is organized as follows: Section 2 briefly presents methods for observing the D-region and introduces a methodology. Section 3 provides the details of numerical results, analyses, and introduces a simple expression of electron density of the D-region. In Section 4 the results are discussed together with further directions of research.

## 2. SFs Impact

We have studied the VLF amplitude ($A$) and phase ($P$), acquired by recording VLF radio signals broadcast by NAA transmitter at Maine, USA (44.63° N, 67.28° W) during solar-induced SIDs. The data were recorded by Belgrade VLF system (44.85° N, 20.38° E). The BEL stations can synchronously record several radio signals broadcast by different transmitters. The technicalities and description of the BEL VLF system are presented in [22]. The NAA-BEL path is sufficiently long (6540 km) and correctly oriented west–east.

Here, we present the study of SIDs induced by the large SFs of solar cycles 24 and 25. The acquisition and research of VLF signals has been carried out together with the investigation of the corresponding X-ray fluxes obtained from GOES. In this research, the registered data of incoming solar radiation X-ray flux in the XRS spectral range of 0.1–0.8 nm are of primary interest.

### *2.1. Monitoring SF*

We have studied the amplitude and phase data, obtained by monitoring VLF radio signals emitted by NAA/24.00 kHz transmitter during solar-induced SIDs. During SIDs, a regular method for signal examination and the determination of ionospheric parameters rely on the comparison between the registered variation of amplitude and phase and the matching values acquired with simulations by the Long-Wave Propagation Capability (LWPC) numerical software package [23,24], as explained in [20,25,26].

As an instructive example of a monitored active day, we present 7 September 2017 (see Figure 1). Three M-class solar flares erupted from sunspot AR2673 of magnitudes M2.4, M1.5, and M7.3, followed by a huge X1.3-class SF. Energy and particulates hurled at the Earth while the proton flux velocity was two times greater than normal. The aurora borealis was also seen.

In Figure 1 we present measured amplitude (lower panel) and phase (upper panel) for NAA/24.00 kHz signal on high solar activity during M1.5 ($I_x$ = 1.5 × $10^{-5}$, $\mathrm{Wm}^{-2}$ at peak time, 09:54 UT), M7.3 (10:15 UT), C3 (12:14 UT) and X1.3 (14:36 UT) events on 7 September 2017 as a function of time. There were visible changes in the VLF daily signal during the C, M and X flares (see signal peaks on panels). From Figure 1, one can see that these VLF and GOES peaks during the daytime happened almost simultaneously (with a time delay of the order of minutes).

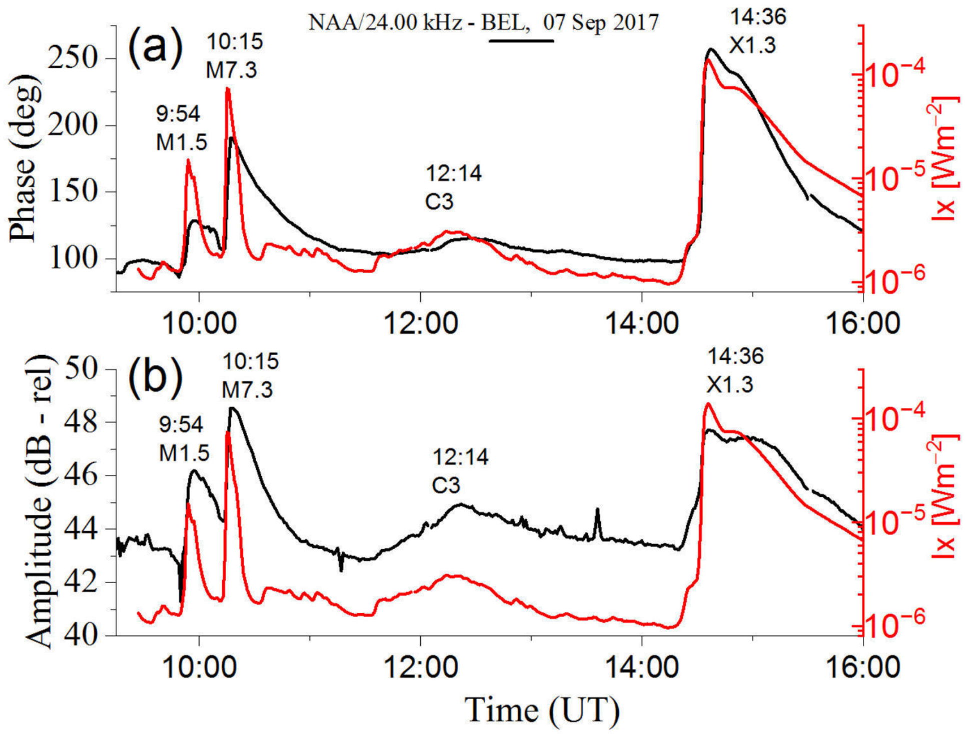


**Figure 1.** Time variation of X-ray irradiance on the right axes, NAA/24.00 kHz signal phase (**a**) and amplitude (**b**) during M1.5 (09:54 UT), M7.3 (10:15 UT), C3 (12:14 UT) and X1.3 (14:36 UT) events on 7 September 2017.

In this work we have calculated the amplitude increase $\Delta A_{rec}$, defined as the difference between the maximum amplitude $A_{\max}$ registered during the flare and the regular amplitude during quiet condition $A_{quiet}$ as:

$$\Delta A_{rec} = A_{\max} - A_{quiet} \tag{1}$$

In the same way, phase delay increase $\Delta P_{rec}$ has been calculated as:

$$\Delta P_{rec} = P_{\max} - P_{quiet} \tag{2}$$

The time delay $\Delta t$ can be defined as: $\Delta t = t_{\text{Amax}} - t_{\text{Imax}}$ where $t_{\text{Amax}}$ is the time of maximum of VLF amplitude $A_{\max}$ and $t_{\text{Imax}}$ is time of maximum of X-ray irradiance $I_{\max}$ [20]. The time delay is nearly similar to the D-region sluggishness [13] and is an important quantity that can be used to study the ionospheric response to the flares [27]. The quantity $\Delta t$ depends on flare intensity and other factors, and usually takes values of about a few minutes [16,27].

For the representative quiet days, i.e., conditions, we have chosen the days under low solar activity. The conditions were that the daylight maximum of X-ray flux had to be lower than $10^{-6}$ Wm$^{-2}$ in the 0.1–0.8 nm XL band.

### 2.2. Used Numerical Methods

#### 2.2.1. Two-Component Exponential Model and Simulations

The daytime two-parameter exponential profile of electron density can be used for VLF modelling [28] and is given by:

$$N_e(h, H', \beta) = 1.43 \cdot 10^{13} \exp(-0.15 \cdot H') \exp[(\beta - 0.15) \cdot (h - H')] \ [\text{m}^{-3}]. \tag{3}$$

Here, $\beta$ in km$^{-1}$ is a time-dependent parameter of sharpness, $H'$ is a reflection height in km, and $h$ is the height in kilometres above surface.

During SIDs, a regular method for the obtaining of ionospheric parameters is based on comparison of the registered variation of amplitude and phase (Equations (1) and (2)) with the equal values obtained in computation by the LWPC software [23] as interpreted in [20,25,26]. $N_e$ can be obtained from the measured amplitude and phase changes by a trial-and-error method where density profile is modified until the LWPC computed amplitude and phase match with monitored data (see, e.g., [22]). Thus, the obtained parameters $\beta$ and $H'$ can be applied for further calculation and simulations (Equation (3), etc.).

2.2.2. FlarED' Method

In [29], i.e., GitHub: https://github.com/sambolino/flarED (accessed on 17 October 2021), the database is created with SID VLF data ($\Delta A_{rec}$, $\Delta P_{rec}$ ) parameters, sharpness $\beta$ and reflection height $H'$ for different values of $I_x$, i.e., different classes of solar flares (during the period of ascending phase and maximum of the solar cycle 24 and 25). Solar flares are monitored and analysed by VLF technique and $\Delta A_{rec}$, $\Delta P_{rec}$ while parameters $\beta$ and $H'$ in database are obtained by the method described in [20]. The python scripts for calculating ionosphere parameters can be found https://github.com/sambolino/flarED (accessed on 19 September 2021). For the input values of solar X-ray flux, parameters $\beta$ and $H'$ can be evaluated and altitude values of electron density for the low terrestrial ionosphere can be calculated. Users can easily calculate time series and hight profile of electron density. The results, i.e., data, can be plotted and exported in csv.

2.2.3. Approximate Analytic Expression

In order to create an easier and more adequate use of results and data, we give an electron density specially modified simple logarithmic second-degree polynomial expression, with height-dependent coefficients taking into account the delay time of the ionosphere response. The python scripts for calculating electron density by this specially modified expression can be found at https://github.com/sambolino/flarED (accessed on 10 October 2021). Additionally, for details see Section 3.2.

## 3. Results and Discussion

### *3.1. Analyses of SF Events*

An example of flare-induced phase and amplitude perturbations, measured for the NAA/24.00 kHz signal on an active day of 10 May 2013, is given in Figure 2 (red lines on both panels). The unperturbed daytime values of phase and amplitude were measured on 9 May 2013 (black lines on both panels in Figure 2). There were visible changes in the VLF daily signal during the duration of M1.3 SF (peak time, 12:56 UT) and C2.5 SF (peak time, 14:37 UT).

One can see visible variations in amplitude and phase. SID VLF changes at the time of the maximum of SF of M1.3 and C2.5 SF classes are $\Delta A$ = 4.2 dB, $\Delta P$ = 68.19 deg and $\Delta A$ = 1.06 dB, $\Delta P$ = 19.20 deg, respectively (see Table 1 and Figure 3c,d). It can be seen that during SF class C, amplitude and phase disturbances are not well defined, but are still noticeable.

Figure 3 shows simultaneous variations of the sharpness $\beta$, effective reflection height $H'$, amplitude and phase (recorded and simulated), electron density at reference height (74 km) and X-ray flux, during the occurrence of two successive flares on 10 May 2013 from Figure 3a–e, respectively.

For the period around SFs on 10 May 2013, we have calculated the time-dependent $H'$ and $\beta$ parameters as shown in Figure 3a,b. During M1.3- and C2.5-class SFs on 10 May 2013, the change of $H'$ with time has normal behaviour. After the start of the SFs it falls to a minimum, and after X-ray peak it keeps growing to a preflare value. Sharpness behaviour is connected with form of registered increase of VLF amplitude, i.e., $\beta$ rises sharply to a maximum, and after the peak of X-ray flux it drops to a preflare value. At 12:56 UT, i.e., at peak time of the M1.3-class SF, with $I_x$ = 1.36·10$^{-5}$ Wm$^{-2}$, $H'$ decreases to a value of 67 km and the $\beta$ rises to 0.41 km$^{-1}$. At C2.5-class SF peak time (14:37 UT) with $I_x$ = 2.59·10$^{-6}$ Wm$^{-2}$ the $H'$ decreases to 72 km and the $\beta$ increase to 0.32 km$^{-1}$. It can be noted that the reflection height and the sharpness are in correlation with X-ray flux shape.

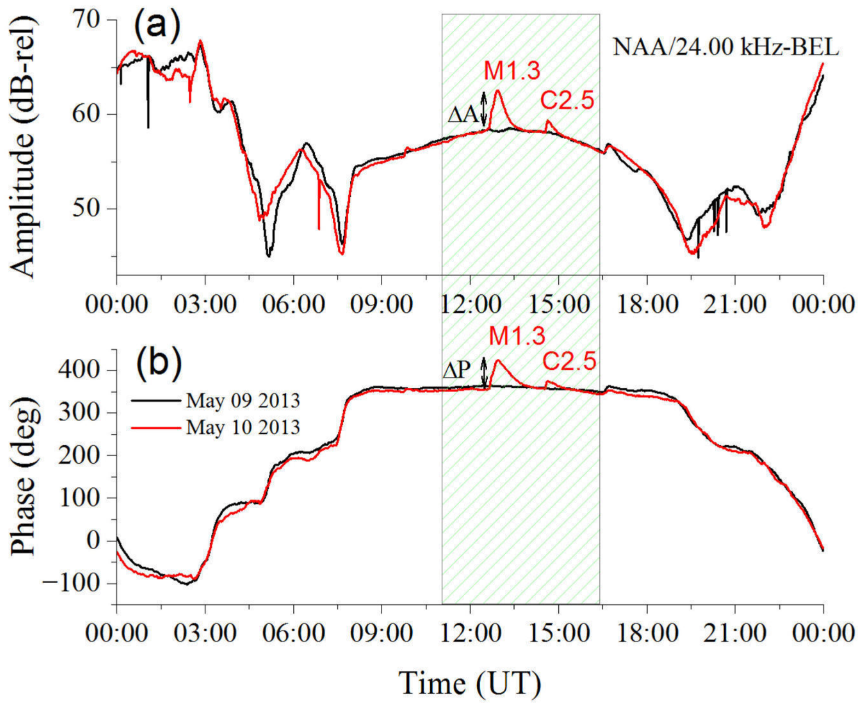


**Figure 2.** Measured variation of amplitude (**a**) and phase (**b**) on NAA signals for 9 May 2013 (quiet day) and 10 May 2013 with noticeable SF events.

**Table 1.** The data on SFs, amplitude and phase perturbations of VLF signals caused by different events analysed in this study.

| | SF Tim | | | SID VLF Signatures | | | SF Data | |
|---|---|---|---|---|---|---|---|---|
| **SF (Class, Date)** | **Start [UT]** | **Peak [UT]** | **End [UT]** | **Δ*A* [dB]** | **Δ*P* [deg]** | **Δ*t* [min]** | **$I_x$ max XL [Wm$^{-2}$]** | **Active Region** |
| M1.3 10.05.2013 | 12:37 | 12:56 | 13:04 | 4.20 | 68.19 | 0 | $1.36 \times 10^{-5}$ | 1745 |
| C2.5 10.05.2013 | 14:30 | 14:37 | 14:42 | 1.06 | 19.20 | 1 | $2.59 \times 10^{-6}$ | 1745 |
| M1.8 12.06.2014 | 09:23 | 09:37 | 09:42 | 4.50 | 51.47 | 4 | $1.81 \times 10^{-5}$ | 2085 |
| M2.7 12.06.2014 | 10:14 | 10:21 | 10:27 | 5.72 | 83.01 | 2 | $2.74 \times 10^{-5}$ | 2087 |
| X1.0 11.06.2014 | 08:59 | 09:06 | 09:10 | 5.54 | 90.45 | 3 | $1.00 \times 10^{-4}$ | 2087 |
| X1.3 07.09.2017 | 14:20 | 14:36 | 14:55 | 4.50 | 159 | 1 | $1.39 \times 10^{-4}$ | 2673 |

Figure 4 shows the height profile, i.e., vertical electron-density profile before, after and during the M1.3- and C2.5-class solar flares that occurred on 10 May 2013. Electron-density altitude profile changes describe the variation of ionization at the D layer due to SF events and are relevant for mapping the low ionosphere [30,31] and moreover are important for checking the validity of the method and results [32] as shown in many examples. For unperturbed (preflare) ionospheric conditions (blue line) and post flare, there is a moderate increment in $N_e$ (from 2.8·10$^{7}$ m$^{-3}$ at $h$ = 60 km height, to 6.7·10$^{8}$ m$^{-3}$ at the upper part of this region, i.e., at $h$ = 80 km). These lines have almost the same behaviour. Completely different slope and behaviour have black and dashed dotted–dotted pink lines at peak times of M- and C-class SFs with increment from ~$7{\cdot}10^7$ m$^{-3}$ at 60 km height to $1.6{\cdot}10^{10}$ m$^{-3}$ and $4{\cdot}10^9$ m$^{-3}$, respectively. It can be noted that the electron density profiles moved to higher electron densities with different slopes when compared to the density profile of the preflare ionospheric condition. These changes in altitude profile of electron density are important for the nature of VLF propagation.

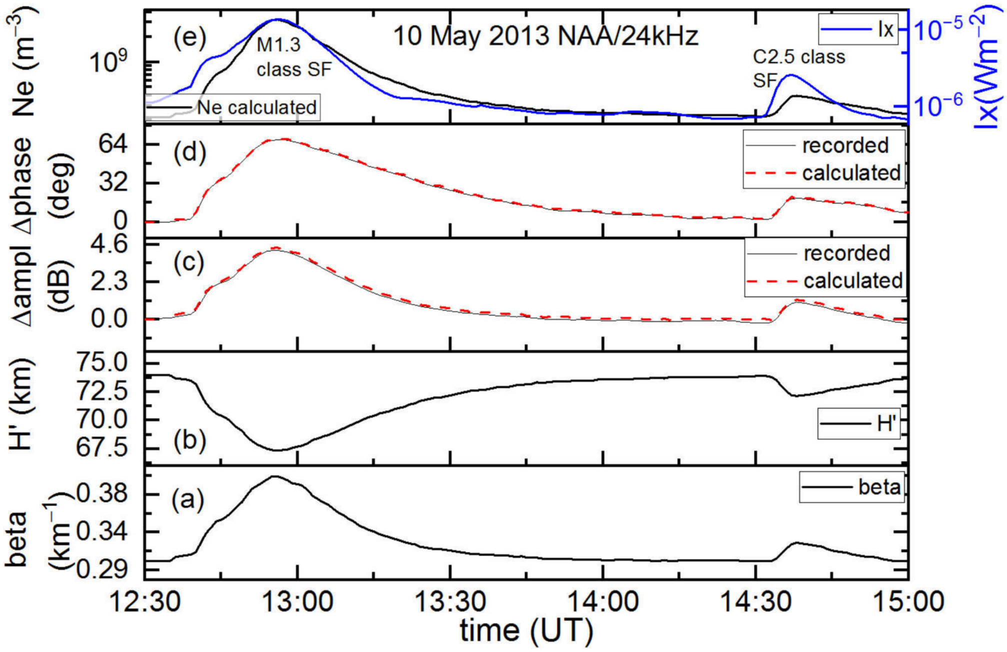


**Figure 3.** Simultaneous variations of the sharpness $\beta$ (**a**), effective reflection height $H'$ (**b**), VLF amplitude (**c**) and phase (**d**) excess recorded and simulated, electron density at reference height (**e**) and X-ray flux (on the right axis (**e**)) during the occurrence of two successive SFs on 10 May 2013.

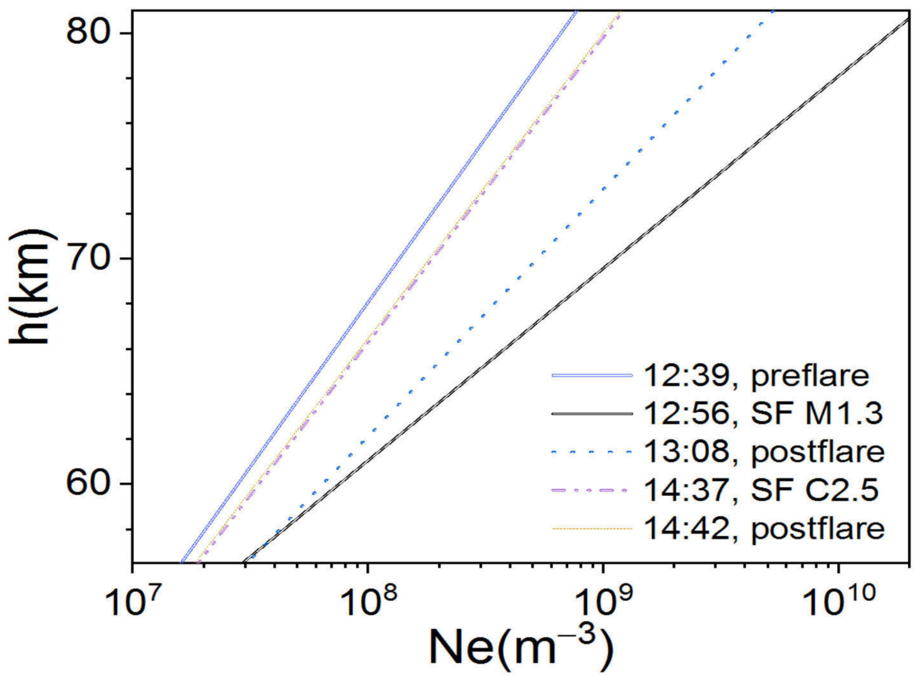


**Figure 4.** The altitude profile of electron density during two successive SFs on 10 May 2013.

X-ray flux, amplitude, and phase of NAA/24.00 kHz radio signal as a function of UT during strong M-class successive SF on 12 June 2014 is presented in Figure 5. The lower panel shows perturbation of amplitude and X-ray flux, and in the upper panel perturbation of phase and X-ray flux is presented. We analysed two successive M-class solar flares (M1.8 with peak time 09:37 UT and M2.7 with peak time 10:21 UT). There were visible changes in the VLF daily signal during the duration of M1.8 SF and M2.7 SF. SID amplitude and phase changes at the peak time of SF of M1.8 and M2.7 SF classes are $\Delta A$ = 4.5 dB, $\Delta P$ = 51.47 deg and $\Delta A$ = 5.72 dB, $\Delta P$ = 83.01 deg, respectively (see Table 1 and Figure 6c,d).

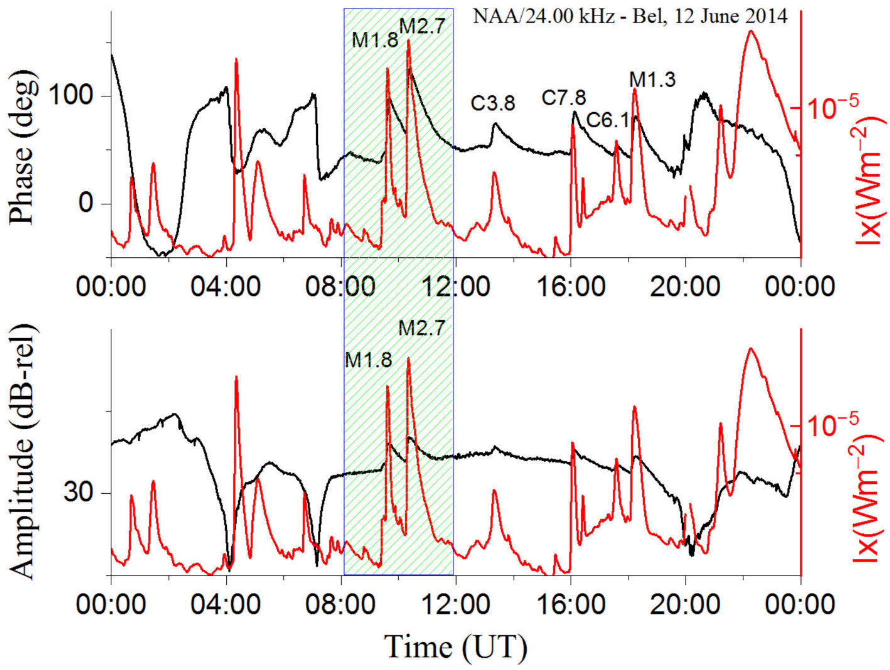


**Figure 5.** X-ray flux, amplitude, and phase of NAA signal during strong successive flares on 12 June 2014. (Lower panel) Amplitude and X-ray flux variation; (Upper panel) phase and X-ray flux variation.

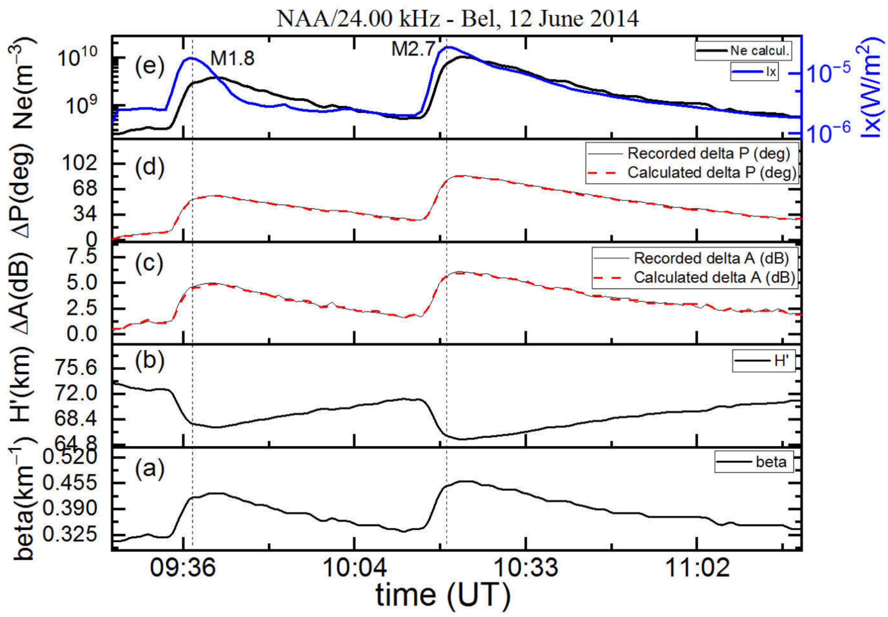


**Figure 6.** Variations of the sharpness $\beta$ (**a**), effective reflection height $H'$ (**b**), VLF amplitude (**c**) and phase (**d**) recorded and simulated, reference height electron density (**e**) and X-ray flux (on the right axis (**e**)), during the occurrence of two successive M-class SFs on 12 June 2014.

Sharpness $\beta$, effective reflection height $H'$, amplitude and phase of VLF signals (recorded and simulated), electron density at reference height, and X-ray flux during the presence of two M flares on 12 June 2014 are presented in Figure 6 on the upper to lower panels, respectively.

For the period around SF on 12 June 2014, we have calculated the time-dependent effective reflection height and sharpness as shown in Figure 6b,a. Generally, as in previous example, the shape of $H'$ and $\beta$ are in correlation with solar X-ray flux. During occurrences of M1.8- and M2.7-class SFs on 12 June 2014, the changes of $H'$ during time have a normal nature. $H'$ lowers in intensity to a minimum after SFs beginning and it rises to a preflare value after X-ray flux peaks. The structure of $\beta$ is correlated with the amplitude shape. At the time of this SF, it rose quickly to a maximum after the SF peak time and then collapsed to preflare size. At peak time of the M1.8-class SF, ($I_x = 1.81 \cdot 10^{-5}$ Wm$^{-2}$), $H'$ lowers to a value of 67 km and $\beta$ rises to 0.42 km$^{-1}$. At peak time 10:21 UT during M2.7-class SF with flux $I_x = 2.7 \cdot 10^{-5}$ Wm$^{-2}$, the $H'$ decreases to 65 km and the sharpness increases to 0.46 km$^{-1}$.

The $N_e$ at reference height is also in correlation with the intensity and shape of X-ray flux during the analysed time period (see Figure 6e).

Figure 7 presents the values of simulated amplitude and phase of the NAA signal along the GCP distance, obtained for quiet and disturbed ionospheric state during SFs on 12 June 2014. The simulations of propagation were performed using LWPC code. Amplitude and phase values of NAA signal proportionally increase with increasing X-ray intensity along the whole path. During the initial and main phase of the SID event, the signal variations are more frequent. SID events in the D-region are most noticeable as changes in the phase of VLF radio signals.

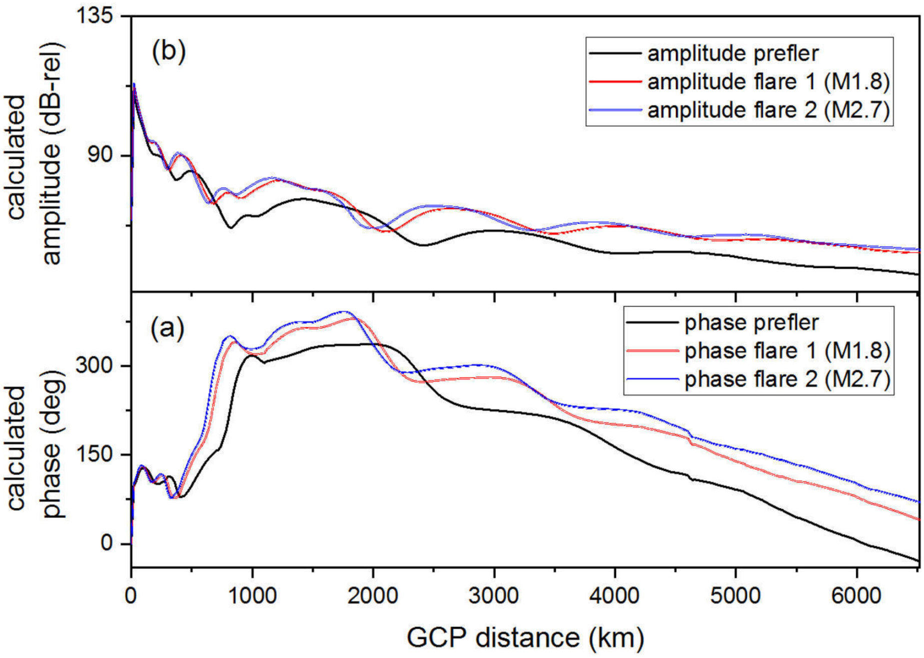


**Figure 7.** The phase (**a**) and amplitude (**b**) of the NAA/24.0 kHz signal along the GCP distance from Maine, USA, to BEL VLF station, Belgrade, obtained for quiet and disturbed ionospheric state during SFs on 12 June 2014.

The height profile, i.e., vertical $N_e$ density profile before, after and during the M1.8- and M2.7-class solar flares on 12 June 2014 are shown in Figure 8. For unperturbed (preflare) conditions (black dashed line), one can see a slow increment of $N_e$ (from $3.2 \cdot 10^7$ m$^{-3}$ at 60 km height, to about $9.7 \cdot 10^8$ m$^{-3}$ at 80 km height). Different slopes have a pink line and dashed red lines (at peak times of M-class SFs), with an increment from ~$6 \cdot 10^7$ m$^{-3}$ and ~$1.2 \cdot 10^8$ m$^{-3}$ at 60 km height to $1.45 \cdot 10^{10}$ m$^{-3}$ and $5 \cdot 10^{10}$ m$^{-3}$ at 80 km height, respectively.

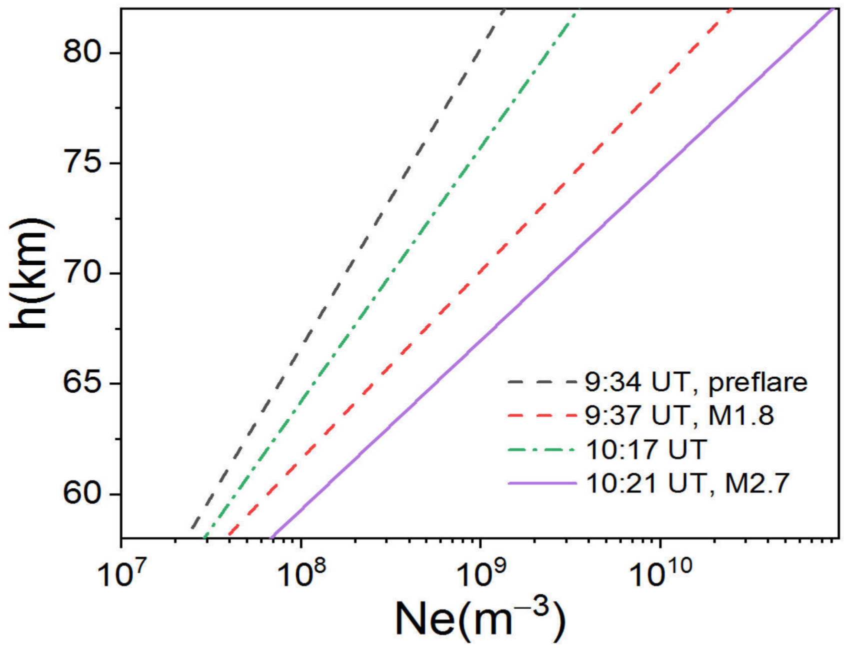


**Figure 8.** The altitude profile of electron density during two successive M-class SFs on 12 June 2014.

Strong SF: In order to cover the whole $I_x$ spectral range needed for further analysis, we studied X-class solar flares with flux $\geq 10^{-4}$ $Wm^{-2}$. Figure 9 presents the values of the monitored and simulated excess of amplitude and phase of the NAA signal simultaneously with X-ray flux during SF on 11 June 2014. Measured and simulated signal values are in good agreement, i.e., almost identical. Barely visible differences are at the right corner of the figure, i.e., during relaxation time and the end of SF.

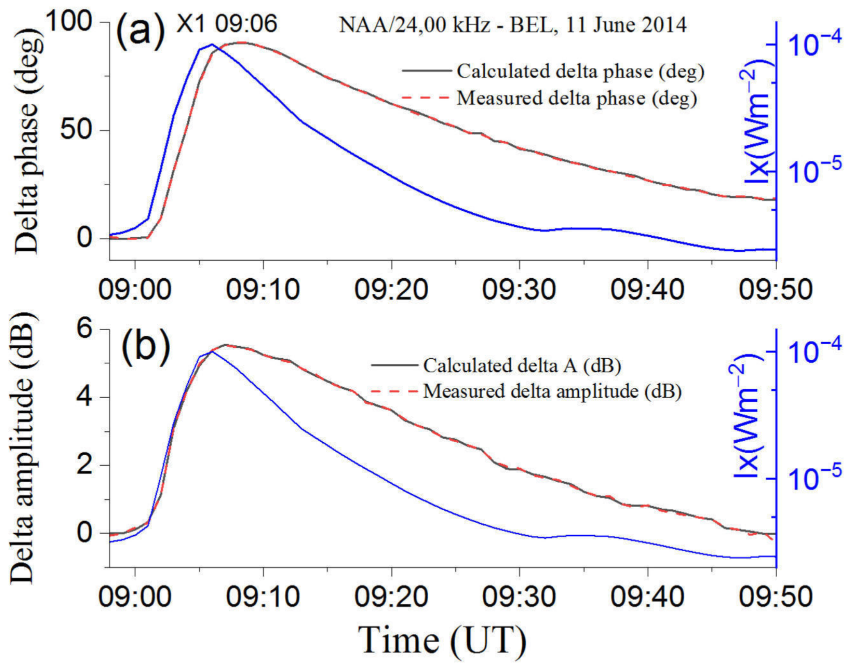


**Figure 9.** Time variation of X-ray irradiance (on the right axes), NAA/24.00 kHz signal phase (**a**) and amplitude (**b**) enhancement during M1.0 (09:06 UT) events on 11 June 2014.

Additionally, amplitude and phase values of NAA signal proportionally increase with increasing X-ray intensity, and during relaxation time (right wings of signal) amplitude values decrease more slowly than the flux due to ionosphere sluggishness. For the period around SF on 11 June 2014, we have calculated the quantities needed for modelling such as the effective reflection height $H'$ and the sharpness $\beta$, as shown in lower panels of Figure 10. One can see that the time profile, i.e., shape of reflection height and the sharpness are in correlation with X-ray flux. More precisely, $\beta$ has almost the same form as $I_x$ but shifted by $\Delta t$, while $H'$ has a reverse shape.

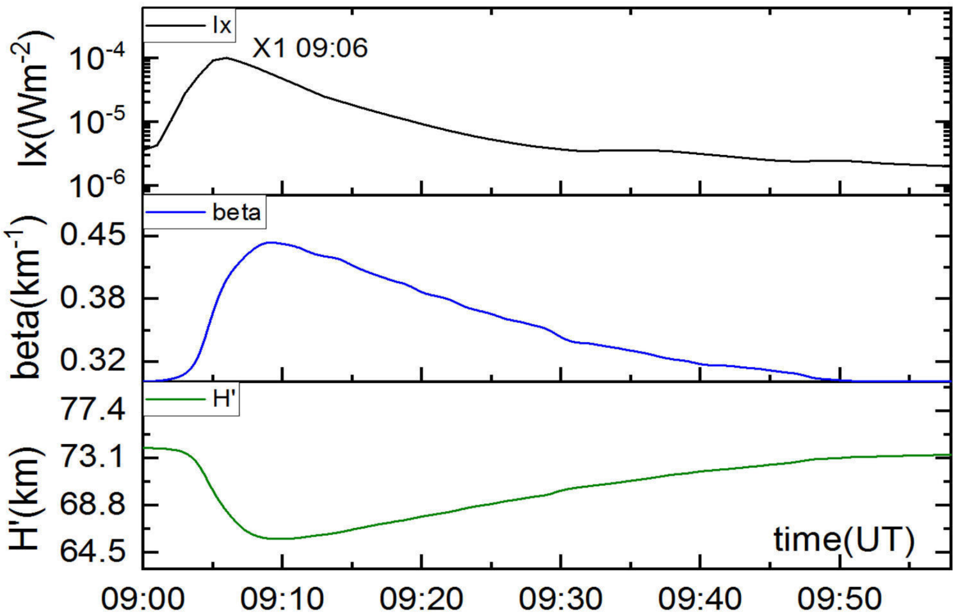


**Figure 10.** Variations in the effective reflection height $H'$, sharpness $\beta$ and X-ray irradiance during the occurrence of SF on 11 June 2014 are shown in panels from lower to upper, respectively.

*3.2. Approximative Expressions and Simulations*

Nowadays, more complicated methods and formulas exist and can be used in this field of science [27,33,34]. They are mostly related to calm conditions in the ionosphere, but still they are also used for perturbed conditions. However, the question arises of how easy some of them are for use and whether they are applicable when speed of analysis and obtaining products are important. The idea is to make the formula easy to use as well as to enable rapid calculations and analysis, such as for example the IRI model—the international standard empirical model for the terrestrial ionosphere [35,36].

In order to create an easier and more adequate use of the results and data, here we introduce the electron-density expression:

$$\log Ne(h, Ix(t), t+\Delta t) = \begin{cases} \sum_{i=0}^{2} a_i(h)\cdot(\log(I_x^{\max}))^i, & t \le t_{Ix^{\max}} \quad \text{a)} \\ y0 + (2 * A/pi) * (w/(4*(t-xc)^2 + w^2)), & t > t_{Ix^{\max}} \quad \text{b)} \end{cases} \tag{4}$$

where, $t_{\mathrm{Imax}}$ is time of maximum of X-ray flux ($\mathrm{Wm}^{-2}$) and $h$ is height (km), $\Delta t$ is time delay defined earlier in the text and $a_i(h)$ represents height-dependent dimensionless coefficients. Here, $y0 + (2 * A/pi) * (w/(4*(t-xc)^2 + w^2))$ is Lorentzian function. Equation (4) gives more than satisfactory results when simplified (which was our intention to make it easy to use), i.e., when (4a) is valid for the whole time interval. Consequently, instead of whole Equation (4) we can use a simple logarithmic second-degree polynomial expression for theentire time interval, with height-dependent coefficients:

$$\log Ne(h, Ix(t), t+\Delta t) = \sum_{i=0}^{2} a_i(h)\cdot(\log(I_x^{\max}))^i \tag{5}$$

Height-dependent coefficients $a_i(h)$ can be found in the Github project. Compared to paper [37], here for the first time we introduce $\Delta t$ and improve the expression by taking into account the delay time of the ionosphere response, making it more physical.

Time delay $\Delta t$ in min can be presented (we use it further in the investigation) by linear dependence on the logarithm of X-ray flux (see, e.g., Figure 11)

$$\Delta t = \sum_{i=0}^{1} c_i \cdot (\log(I_x^{\max}))^i \text{ [min]} \tag{6}$$

where dimensionless quantities take values $c_0$ = 0.45385 and $c_1$ = −0.44863 and $I_x{}^{\max}$ is X-ray flux at peak time in [Wm$^{-2}$]. Further in the investigation we will use expression (6), which can be additionally corrected by inserting various influences. Of course, a more sophisticated formula might have been developed, but such precision was unnecessary since the values of the D-region parameters are known to fluctuate by an order of magnitude. The goal was to make the formula simple to use while also allowing for quick calculations and analysis.

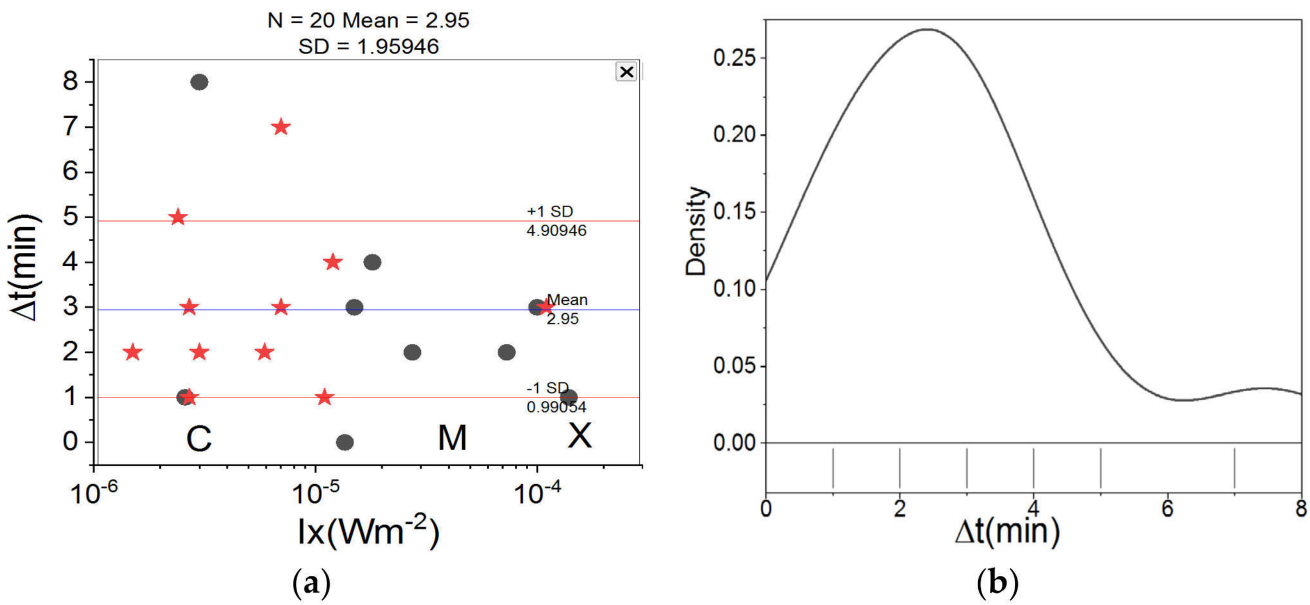


**Figure 11.** (**a**) The time delay $\Delta t$ between the VLF amplitude max and the peak of SF X-ray flux as a function of peak flux (black circles are data from present investigation, red stars data from [27]; (**b**) Distribution of $\Delta t$ data points (a rug plot).

In Figure 11a, we present values of obtained time delay $\Delta t$ between the X-ray flux and the VLF amplitude as a function of peak flux. Black circles are data from present work and red stars are data from [27], obtained under the same conditions, i.e., with the same equipment and for the same transmitter–receiver path. Additionally, in Figure 11b we provide the distribution of $\Delta t$ data points—a rug plot. The time delay between the X-ray flux and the VLF amplitude maximum $\Delta t$ has a mean value of about 3 min. For C-class SFs, $\Delta t$ is more scattered and has the highest variation, and for the larger values of flux $I_x$ (M- and X-class SFs), the increase is the smallest.

From Figure 6 of the paper by Hayes et al. [38], one can see that presented data are scattered, even more so than in our case, with $\Delta t$ up to 10 min and with a mean value of about two minutes, which is in accordance with our results. From Figure 11b (see rug plot), we certainly have the largest grouping between 1–4 min, which is also the case with the results of Hayes et al. [38] i.e., the results are in accordance. Certainly, there are other results in the literature such as from the paper of Basak & Chakrabarti [39], but our results and also the recent findings of Hayes et al. [38] differ from findings of Basak & Chakrabarti, which surely does not affect the main goal of the present work.

The conclusion is that the maximum of the signal, and consequently the electron density, is shifted by an average value of three minutes in relation to the maximum of the flux during the flare event due to ionosphere sluggishness. In addition, detailed statistics could have been performed but the main goal was to obtain a useful and easy to use expression for $N_e$.

Variation in X-ray flux (upper panel), measured by GOES-15, and $N_e$ (h = 74 km) as a function of UT during two successive flares on 12 June 2014 (lower panel) are presented in Figure 12. The red line in the lower panel shows results acquired by approximative Equation (5). The circles present values of electron density $N_e$ obtained in this research by the method mentioned above using Equation (3). One can see that the results are in good agreement except the post-flare wings ($N_e$ shape is more stretched). It can be noted that due to the sluggishness of the ionosphere, the shape of electron density over time does not totally follow the solar flux shape and it returns more slowly (post-flare wings) to a calm state due to the D-region relaxation time.

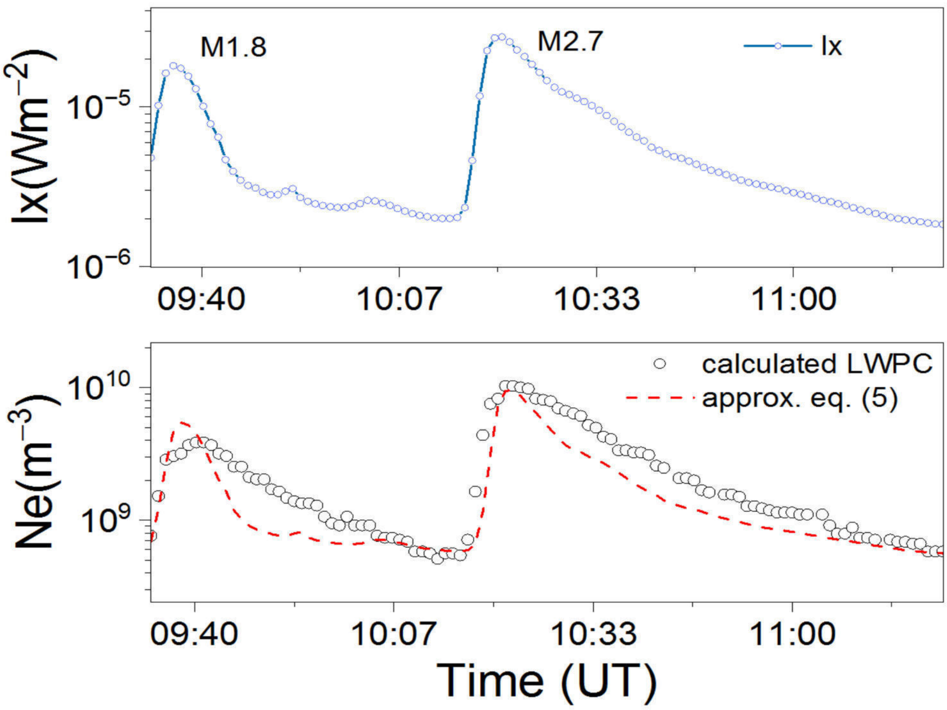


**Figure 12.** X-ray flux from GOES-15, and $N_e$ ($h$ = 74 km) as a function of UT during two M-class SFs on 12 June 2014. The dashed red line shows results acquired by approximative Equation (5). $N_e$ obtained by the above-mentioned method is presented by circles.

In [29], the database contains parameters $\beta$ and $H'$ for different values of $I_x$, i.e., different classes of solar flares (during the period of ascending phase and maximum of the solar cycle 24 and 25). Solar flares are monitored and analysed by VLF technique and parameters $\beta$ and $H'$ in database are obtained by method described in [20]. In https://github.com/sambolino/flarED (accessed on 19 September 2021) [29] for the input values of solar X-ray flux, Wait's parameters $\beta$ and $H'$ can be evaluated and altitude values of electron density for the low terrestrial ionosphere can be calculated.

Figure 13 presents a scatter plot of a pair of D-region parameters, $H'$ and $\beta$, for SID cases analysed in this study together with data obtained using methods from [29]. Calculated parameters $H'$ and $\beta$ are in the range of 60–74 km and 0.30–0.60 km$^{-1}$, respectively. Black circles represent data from present work and red circles are related to the data obtained using the flared method (see Section 2.2.2). In the bottom right corner (for M- and X-classes of SF) data are more scattered.

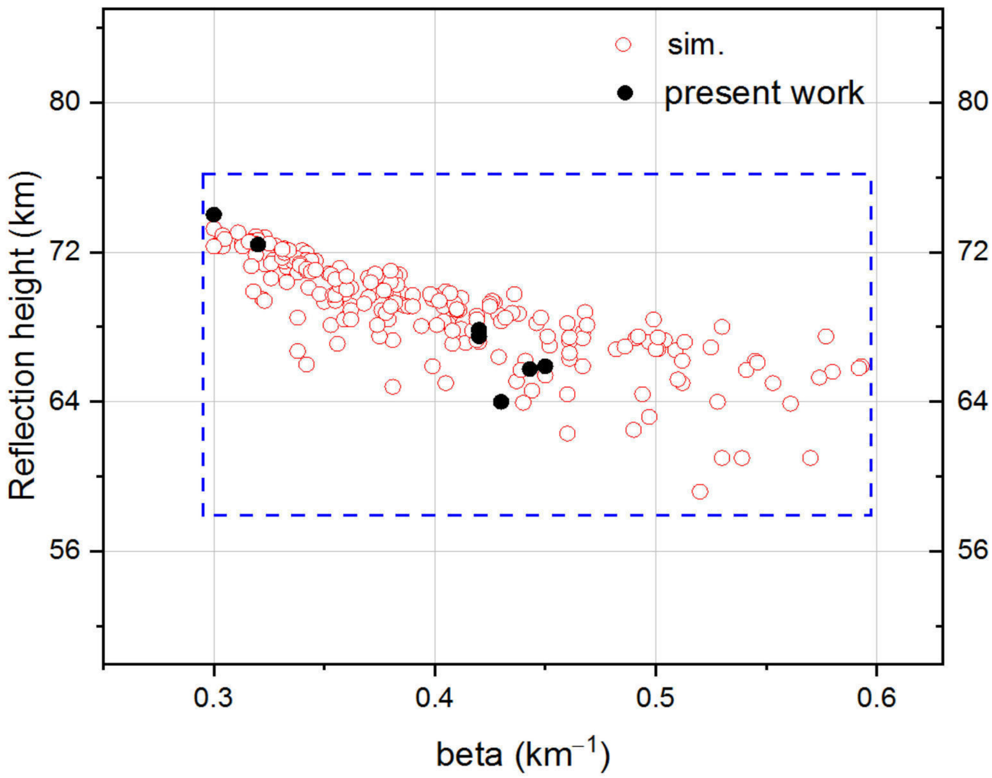


**Figure 13.** A scatter plot of a pair of D-region parameters, i.e., $H'$ versus $\beta$, is shown for SID cases analysed in this study using LWPC and two-component exponential model together with ones obtained using flared method from Github project [29].

### *3.3. Comparison of Results*

In Figure 14, we present the results from this investigation, i.e., paper (using three methods from Sections 2.2.1–2.2.3), which are either simulated, calculated, approximated or the data obtained from literature [16,37,40–42], for electron density $N_e$ at reference height as a function of X-ray flux. The area of importance is between the two red lines. It can be noticed that the results differ from each other in some cases by an order of magnitude or more. Although the data are scattered, especially for stronger flares (right side of the graph), they still tend to increase with the intensity of the X-ray radiation. As noted, our results were acquired on the basis of analysis of SID events on NAA/24.00 kHz signal and using methods described in the text. Electron density at reference height $h$ = 74 km changed from $N_e = 2.16 \times 10^8$ m$^{-3}$ to $N_e > 10^{11}$ m$^{-3}$. Additionally, we compared data with the $N_e$ data obtained using approximate Equation (5) (plus sign in Figure 14) and simulations (black star) using the flared method. The results are in fair agreement with previous studies. We can conclude that measurements over a long path give slightly higher slope, i.e., lower values of electron density than expected, but are quite satisfactory. This is important because most results concerning investigation in the D-region are scattered and vary in order of magnitude and we need to take into account all the data and correct the existing ones. During SIDs the time profile of electron density follows the solar X-ray flux variation.

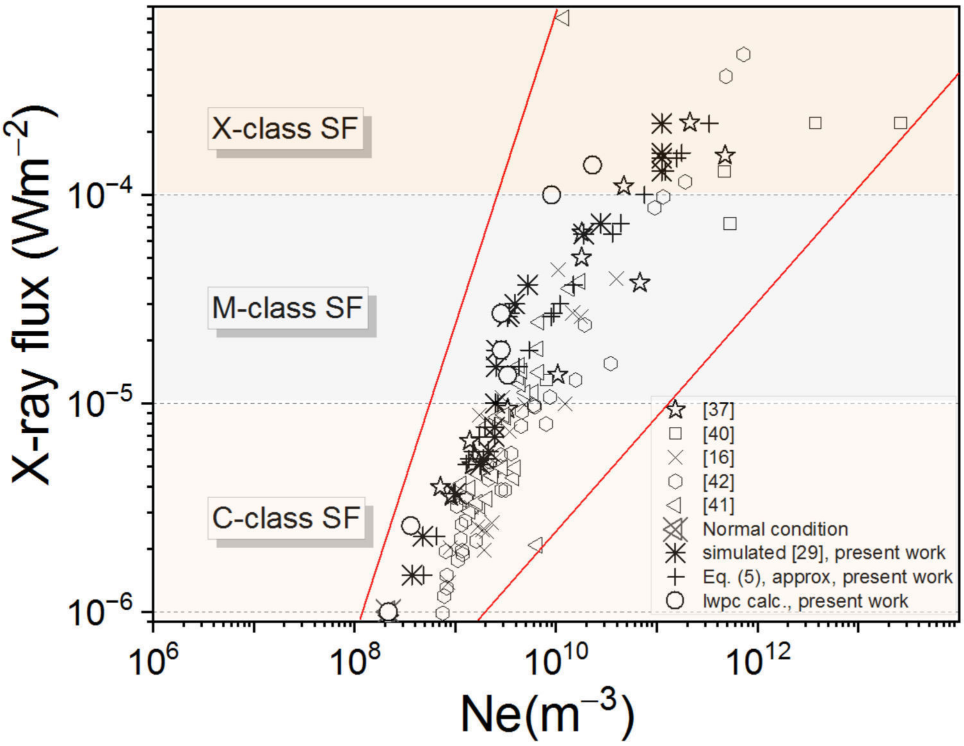


**Figure 14.** Electron-density data (calculated, simulated and approximated) at reference height $h$ = 74 km and maximum of $I_x$ flux during occurrence of different class SFs. The data are compared with results from [16,37,40–42]. Area of importance is between the two red lines.

## 4. Conclusions and Perspectives

In this paper we analysed SF events with extreme radiation in the X-spectral range. The perturbed VLF data were collected by monitoring the NAA/24.00 kHz VLF signal (transmitted in Maine, USA and then received in Belgrade, with GCP = 6540 km) and used together with GOES satellite data. The magnitude of impact of SFs on D-region and the consequences of these explosive events were analysed using measurements over a long path. The amplitude and phase data and ionosphere parameters during the enhancements of radiation due to the SF obtained in our study, are presented.

The GCP from the NAA transmitter to the Belgrade receiver is about 6540 km long and characterized as a long, dominantly sea path, and we studied cases when it is entirely sunlit. The data obtained here demonstrate the advantages of using these long-path measurements due to stable form of phase and amplitude variation caused by SID in contrast to the VLF perturbations on the short path which display more complexity and oscillations, including decreases and increases depending on the flare intensity. This is very important during the modelling process.

Furthermore, we conclude that the intensity of amplitude and phase perturbations on VLF kHz signal over a long path is in correlation with the size and shape of X-ray flux. This is in line with previous studies. The most effective influence on the enhancement of the ionization rate in the D-region during the observed SFs is due to the increased intensity of spectral lines in the X-ray spectra. Moreover, X-ray SFs with larger line intensities produce a larger increase in electron density. The computation was applied, and we obtained coefficients, i.e., sharpness, reflection height, and time delay needed for modelling this medium under increased radiation in the X-spectral range. One can notice that the intensified solar radiation in the X-spectral range changes D-region parameters and conducts an enhanced production rate, consequently deforming the VLF signal. The dependence of electron density on X-ray flux has slightly lower slope but is in fair agreement with previous studies.

The present manuscript offers an extension of the electron-density modeling in the daytime, SF-perturbed D-region of the ionosphere already introduced in [37]. In particular, the extension includes time delays from ionospheric sluggishness in $N_e$ modeling, making use of data over a long GC path that ensures enhanced stability of SID-induced variations in phase and amplitude shape. The construction of the associated flarED GitHub project is designed to be easily applicable.

Moreover, we introduce novel methods and provide a simple, modified expression for $N_e$ as a function of $I_x$, valid for unperturbed and perturbed conditions. We develop the expression by taking into account the delay time of the ionosphere response, making it more physical. The analysis and software are provided on GitHub under the MIT license.

In addition, the observed increase in the atmospheric aerosol number density after the event of SFs in February and March 2011, as well as high-level cloud formation in the upper atmosphere, reveal the importance of further investigation of SF and possible influence on particle-electrification mechanisms [43–45]. Recent studies [46] have introduced reconsideration of atmospheric aerosol–electricity interactions, which could improve theoretical understanding and simulations of the aerosol lifecycle, opening new horizons for weather and climate science. Future research will focus on a multidiscipline approach, investigating solar–geomagnetic activity effects on aerosol particles and on radiative transfer.

**Author Contributions:** Conceptualization, V.A.S. and D.M.Š.; writing—original draft preparation, V.A.S., Z.R.M.; writing—review and editing, V.A.S., D.M.Š., V.V., Z.R.M.; supervision, L.M.I. All authors have read and agreed to the published version of the manuscript.

**Funding:** This work was funded by the Institute of Physics Belgrade and University Union—Nikola Tesla Belgrade, through a grant by the Ministry of Education and Science of the Republic of Serbia. This article/publication is based upon work from COST Action CA17126—Towards understanding and modelling intense electronic excitation (TUMIEE), supported by COST (European Cooperation in Science and Technology).

**Institutional Review Board Statement:** Not applicable.

**Informed Consent Statement:** Not applicable.

**Data Availability Statement:** New dataset from this study is publicly available as well as python functions for calculating ionosphere parameters on GitHub: https://github.com/sambolino/flarED (accessed on 10 October 2021). Publicly available datasets were analysed in this study and can be found at https://satdat.ngdc.noaa.gov/sem/goes/data/avg (accessed on 2 September 2021).

**Acknowledgments:** We would like to express our appreciation to Ognyan Kounchev and Magdalena Christova for the shown attention to this paper and for a fruitful dialogue.

**Conflicts of Interest:** The authors declare no conflict of interest. The funders had no role in the design of the study; in the collection, analyses, or interpretation of data; in the writing of the manuscript, or in the decision to publish the results.

## References

1. Bothmer, V.; Daglis, I.A. *Space Weather: Physics and Effects*; Springer Science & Business Media: Berlin/Heidelberg, Germany, 2007.
2. Smith, H.J.; Smith, E.V.P. *Solar Flares*; Macmillan: New York, NY, USA, 1963.
3. Davidson, B. *Weatherman's Guide to the Sun*, 3rd ed.; Space Weather News, LLC.: New York, NY, USA, 2020.
4. Doschek, G.; Meekins, J.; Cowan, R.D. Spectra of solar flares from 8.5 Å to 16 Å. *Sol. Phys.* **1973**, *29*, 125–141. [CrossRef]
5. Tandberg-Hanssen, E.; Emslie, A.G. *The Physics of Solar Flares*; Cambridge University Press: Cambridge, UK, 2009.
6. Reames, D.V.; Murdin, P. Solar Wind: Energetic Particles. *Encycl. Astron. Astrophys.* **2002**, *2312*, 1–122.
7. Tandon, J.; Deshpande, S.; Bhatia, V. Electromagnetic radiation from solar flares. *Nature* **1968**, *220*, 1213–1214. [CrossRef]
8. Brasseur, G.P.; Solomon, S. Composition and chemistry. In *Aeronomy of the Middle Atmosphere: Chemistry and Physics of the Stratosphere and Mesosphere*; Springer: Berlin/Heidelberg, Germany, 2005; pp. 265–442.
9. Nina, A.; Čadež, V.; Srećković, V.; Šulić, D. The influence of solar spectral lines on electron concentration in terrestrial ionosphere. *Open Astron.* **2011**, *20*, 609–612. [CrossRef]
10. Valnicek, B.; Ranzinger, P. X-ray emission and D-region "sluggishness". *Bull. Astron. Inst. Czechoslov.* **1972**, *23*, 318.
11. Bain, W.C.; Hammond, E. Ionospheric solar flare effect observations. *J. Atmos. Sol. Terr. Phys.* **1975**, *37*, 573–574. [CrossRef]

12. Brasseur, G.P.; Solomon, S. Radiation. In *Aeronomy of the Middle Atmosphere: Chemistry and Physics of the Stratosphere and Mesosphere*; Springer: Berlin/Heidelberg, Germany, 2005; pp. 151–264.
13. Mitra, A.P. *Ionospheric Effects of Solar Flares*; Springer: Berlin/Heidelberg, The Netherlands, 1974. [CrossRef]
14. Nicolet, M.; Swider, W., Jr. Ionospheric conditions. *Planet. Space Sci.* **1963**, *11*, 1459–1482. [CrossRef]
15. Garcia, H.A. Temperature and emission measure from GOES soft X-ray measurements. *Sol. Phys.* **1994**, *154*, 275–308. [CrossRef]
16. Grubor, D.; Šulić, D.; Žigman, V. Classification of X-ray solar flares regarding their effects on the lower ionosphere electron density profile. *Ann. Geophys.* **2008**, *26*, 1731–1740. [CrossRef]
17. Wang, X.; Chen, Y.; Toth, G.; Manchester, W.B.; Gombosi, T.I.; Hero, A.O.; Jiao, Z.; Sun, H.; Jin, M.; Liu, Y. Predicting solar flares with machine learning: Investigating solar cycle dependence. *Astrophys. J.* **2020**, *895*, 3. [CrossRef]
18. Kelley, M.C. *The Earth's Ionosphere: Plasma Physics and Electrodynamics, ser. International Geophysics*, 2nd ed.; Academic Press: Cambridge, MA, USA, 2009.
19. Wah, W.P.; Abdullah, M.; Hasbi, A.M.; Bahari, S.A. Development of a VLF receiver system for sudden ionospheric disturbances (SID) detection. In Proceedings of the 2012 IEEE Asia-Pacific Conference on Applied Electromagnetics (APACE), Melaka, Malaysia, 11–13 December; pp. 98–103.
20. Šulić, D.; Srećković, V.; Mihajlov, A. A study of VLF signals variations associated with the changes of ionization level in the D-region in consequence of solar conditions. *Adv. Space Res.* **2016**, *57*, 1029–1043. [CrossRef]
21. Volland, H. On the solar flare effect of vlf-waves in the lower ionosphere. *J. Atmos. Sol.-Terr. Phys.* **1964**, *26*, 695–709. [CrossRef]
22. Šulić, D.; Srećković, V. A comparative study of measured amplitude and phase perturbations of VLF and LF radio signals induced by solar flares. *Serb. Astron. J.* **2014**, *188*, 45–54. [CrossRef]
23. Ferguson, A.J. *Computer Programs for Assessment of Long-Wavelength Radio Communications, Version 2.0: User's Guide and Source Files*; Space and Naval Warfare Systems Center: San Diego, CA, USA, 1998.
24. LWPC. Computer Programs for Assessment of Long-Wavelength Radio Communications, V2.1. 2018. Available online: https://github.com/space-physics/LWPC (accessed on 30 June 2021).
25. Nina, A.; Čadež, V.; Srećković, V.; Šulić, D. Altitude distribution of electron concentration in ionospheric D-region in presence of time-varying solar radiation flux. *Nucl. Instrum. Methods Phys. Res. B* **2012**, *279*, 110–113. [CrossRef]
26. Nina, A.; Čadež, V.; Šulić, D.; Srećković, V.; Žigman, V. Effective electron recombination coefficient in ionospheric D-region during the relaxation regime after solar flare from February 18, 2011. *Nucl. Instrum. Methods Phys. Res. B* **2012**, *279*, 106–109. [CrossRef]
27. Žigman, V.; Grubor, D.; Šulić, D. D-region electron density evaluated from VLF amplitude time delay during X-ray solar flares. *J. Atmos. Sol.-Terr. Phys.* **2007**, *69*, 775–792. [CrossRef]
28. Wait, J.R.; Spies, K.P. *Characteristics of the Earth-Ionosphere Waveguide for VLF Radio Waves, Technical Note 300*; US Department of Commerce, National Bureau of Standards: Boulder, CO, USA, 1964.
29. Vujčić, V.; Srećković, V.A. flarED Flare Electron Density. Available online: https://github.com/sambolino/flarED (accessed on 19 September 2021).
30. Da Silva, C.L.; Salazar, S.D.; Brum, C.G.; Terra, P. Survey of electron density changes in the daytime ionosphere over the Arecibo observatory due to lightning and solar flares. *Sci. Rep.* **2021**, *11*, 1–12. [CrossRef]
31. Kolarski, A.; Grubor, D. Sensing the Earth's low ionosphere during solar flares using VLF signals and goes solar X-ray data. *Adv. Space Res.* **2014**, *53*, 1595–1602. [CrossRef]
32. Kolarski, A.; Grubor, D. Comparative analysis of VLF signal variation along trajectory induced by X-ray solar flares. *J. Astrophys. Astron.* **2015**, *36*, 565–579. [CrossRef]
33. Nina, A.; Nico, G.; Mitrović, S.T.; Čadež, V.M.; Milošević, I.R.; Radovanović, M.; Popović, L.Č. Quiet Ionospheric D-Region (QIonDR) Model Based on VLF/LF Observations. *Remote Sens.* **2021**, *13*, 483. [CrossRef]
34. Palit, S.; Basak, T.; Mondal, S.; Pal, S.; Chakrabarti, S. Modeling of very low frequency (VLF) radio wave signal profile due to solar flares using the GEANT4 Monte Carlo simulation coupled with ionospheric chemistry. *Atmos. Chem. Phys.* **2013**, *13*, 9159–9168. [CrossRef]
35. Sezen, U.; Gulyaeva, T.L.; Arikan, F. Online international reference ionosphere extended to plasmasphere (IRI-Plas) model. In Proceedings of the 2017 XXXIInd General Assembly and Scientific Symposium of the International Union of Radio Science (URSI GASS), Montreal, QC, Canada, 19–26 August 2017; pp. 1–4.
36. Bilitza, D.; Altadill, D.; Truhlik, V.; Shubin, V.; Galkin, I.; Reinisch, B.; Huang, X. International Reference Ionosphere 2016: From Ionospheric Climate to Real-Time Weather Predictions. *Space Weather.* **2017**, *15*, 418–429. [CrossRef]
37. Srećković, V.A.; Šulić, D.M.; Ignjatović, L.; Vujčić, V. Low Ionosphere under Influence of Strong Solar Radiation: Diagnostics and Modeling. *Appl. Sci.* **2021**, *11*, 7194. [CrossRef]
38. Hayes, L.A.; O'Hara, O.S.; Murray, S.A.; Gallagher, P.T. Solar Flare Effects on the Earth's Lower Ionosphere. *Sol. Phys.* **2021**, *296*, 1–17. [CrossRef]
39. Basak, T.; Chakrabarti, S.K. Effective recombination coefficient and solar zenith angle effects on low-latitude D-region ionosphere evaluated from VLF signal amplitude and its time delay during X-ray solar flares. *Astrophys. Space Sci.* **2013**, *348*, 315–326. [CrossRef]
40. Gavrilov, B.; Ermak, V.; Lyakhov, A.; Poklad, Y.V.; Rybakov, V.; Ryakhovsky, I. Reconstruction of the Parameters of the Lower Midlatitude Ionosphere in M-and X-Class Solar Flares. *Geomagn. Aeron.* **2020**, *60*, 747–753. [CrossRef]

41. Pandey, U.; Singh, B.; Singh, O.; Saraswat, V. Solar flare induced ionospheric D-region perturbation as observed at a low latitude station Agra, India. *Astrophys. Space Sci.* **2015**, *357*, 1–11. [CrossRef]
42. Thomson, N.R.; Clilverd, M.A. Solar flare induced ionospheric D-region enhancements from VLF amplitude observations. *J. Atmos. Sol.-Terr. Phys.* **2001**, *63*, 1729–1737. [CrossRef]
43. Avakyan, S. Supramolecular physics of the solar-troposphere links: Control of the cloud cover by solar flares and geomagnetic storms. In Proceedings of the 11th Intl School and Conference "Problems of Geocosmos", St. Petersburg, Russia, 3–7 October 2016; pp. 187–191.
44. Goncharenko, Y.V.; Kivva, F. Evaluation of Size of the Atmospheric Aerosol Particles in the Reflecting Layers Occurring after Intense Solar Flares. *Telecommun. Radio Eng.* **2003**, *59*, 1–6.
45. McGrath-Spangler, E.L.; Denning, A.S. Global seasonal variations of midday planetary boundary layer depth from CALIPSO space-borne LIDAR. *J. Geophys. Res.* **2013**, *118*, 1226–1233. [CrossRef]
46. Mallios, S.A.; Daskalopoulou, V.; Amiridis, V. Orientation of non spherical prolate dust particles moving vertically in the Earth's atmosphere. *J. Aerosol. Sci.* **2021**, *151*, 105657. [CrossRef]

Atmospheric Environment 168 (2017) 46–54

Contents lists available at ScienceDirect

Atmospheric Environment

journal homepage: www.elsevier.com/locate/atmosenv

# Rainwater capacities for BTEX scavenging from ambient air

A. Šoštarić [a,*], S. Stanišić Stojić [b], G. Vuković [c], Z. Mijić [c], A. Stojić [c], I. Gržetić [d]

[a] Institute of Public Health Belgrade, Bulevar Despota Stefana 54a, 11000 Belgrade, Serbia
[b] Faculty of Physical Chemistry, University of Belgrade, Studentski Trg 12-16, 11000 Belgrade, Serbia
[c] Institute of Physics Belgrade, University of Belgrade, Pregrevica 118, 11080 Belgrade, Serbia
[d] Faculty of Chemistry, University of Belgrade, Studentski Trg 12-16, 11000 Belgrade, Serbia

## HIGHLIGHTS

- Potential of rainwater for BTEX scavenging from ambient air was examined.
- BTEX concentrations in rain samples exceeded the theoretically predicted values.
- BTEX retention could be associated with BTEX aerosol fraction.
- Random forest and instance based algorithms provide reliable enrichment predictions.
- Gas mixing ratios, rainwater characteristics and meteorology affect BTEX distribution.

## ARTICLE INFO

*Article history:*
Received 14 March 2017
Received in revised form
15 August 2017
Accepted 18 August 2017
Available online 23 August 2017

*Keywords:*
BTEX
Wet deposition
Rain
PTR-MS
Multivariate methods
Unmix

## ABSTRACT

The contribution of atmospheric precipitation to volatile organic compound (VOC) removal from the atmosphere remains a matter of scientific debate. The aim of this study was to examine the potential of rainwater for benzene, toluene, ethylbenzene and xylene (BTEX) scavenging from ambient air. To that end, air and rainwater samples were collected simultaneously during several rain events that occurred over two distinct time periods in the summer and autumn of 2015. BTEX concentrations in the gaseous and aqueous phases were determined using proton transfer reaction mass spectrometry. The results reveal that the registered amounts of BTEX in rainwater samples were higher than those predicted by Henry's law. Additional analysis, including physico-chemical characterization and source apportionment, was performed and a possible mechanism underlying the BTEX adsorption to the aqueous phase was considered and discussed herein. Finally, regression multivariate methods (MVA) were successfully applied (with relative errors from 20%) to examine the functional dependency of BTEX enrichment factor on gaseous concentrations, physico-chemical properties of rainwater and meteorological parameters.


## 1. Introduction

Benzene, toluene, ethylbenzene and the three xylene isomers, frequently referred to as BTEX, constitute a group of aromatic hydrocarbon species of particular environmental interest, commonly associated with the petrochemical industry and incomplete fossil fuel oxidation (Stojić et al., 2015a, 2015b). Besides being important photochemical precursors for tropospheric ozone and secondary organic aerosols (SOA) (Chatani et al., 2015), these hazardous air pollutants cause chronic toxicity even in small concentrations (Stojić et al., 2015c). According to the IARC data, benzene is recognized as a significant public health threat and classified as group I carcinogen, ethylbenzene is a suspected IIB carcinogen, while both toluene and the xylene isomers belong to group III neurotoxins (WHO, 1986, 1993, 1997; Durmusoglu et al., 2010).

In the atmosphere, volatile species are distributed between the gaseous, aqueous and particle phase (Matsumoto et al., 2010). In their biogeochemical cycle, it is believed that the role of atmospheric water is quite prominent, but this issue is still subject to continuous scientific debate (McNeill et al., 2012). The concentrations of BTEX in various forms of atmospheric water depend on various factors including their ambient gas mixing ratios, water solubility and Henry's law constant, frequency and intensity of precipitation events (Balla et al., 2014), gas-water surface interactions (Raja and Valsaraj, 2004), content and concentrations of other species in atmospheric water (Okochi et al., 2005; Sato et al.,

* Corresponding author.
*E-mail address:* andrej.sostaric@zdravlje.org.rs (A. Šoštarić).

http://dx.doi.org/10.1016/j.atmosenv.2017.08.045

2006; Allou et al., 2011), as well as the origin of air masses (Mullaugh et al., 2015). Previous studies, which primarily focused on wet deposition of BTEX and their partition between gaseous and aqueous phases, were relatively scarce and provided contradictory conclusions.

In the study aimed at investigating the capacity of rainwater for wet scavenging of BTEX, Okochi et al. (2004) reported that the concentrations of species detected in rain samples were higher than those predicted by Henry's law, and concluded that atmospheric precipitation might play significantly greater role in removing BTEX from ambient air than previously thought. Thereby, the observed supersaturation was assumed to be associated with the presence of surface-active agents in rain droplets, whereas the rainfall intensity appeared to be of negligible importance. Accordingly, our previous study confirmed a significant enrichment of BTEX in the aqueous phase in a dynamic equilibrium system designed to resemble the interactions between the gaseous and water phase during rainfall (Šoštarić et al., 2016). Conversely, recent findings of Mullaugh et al. (2015) indicate that BTEX were not efficiently scavenged from the atmosphere by wet deposition processes. Furthermore, the authors concluded that light-mediated reactions with OH· or nitrogen radicals remain the major atmospheric sink for BTEX. Nonetheless, it should be noted that this research was not based on the ambient air measurements, but it mainly relied on the previously published BTEX data from similar locations.

In order to better understand the fate of volatile species in atmospheric, terrestrial and aquatic systems, the present study examines the contribution of rainwater to wet scavenging of atmospheric BTEX, as well as the mechanisms related to their air-water distribution transfer.

## 2. Materials and methods

A total of 53 sample pairs of air and rainwater samples were collected simultaneously during several rain events that occurred over two distinct time periods in the summer and autumn season of 2015. The sampling was performed at the Institute of Physics (Belgrade, Serbia; 44°49′ N, 20°28′ E), located in the vicinity of the Danube river, in the suburban residential area, with a number of local fireboxes active during the heating season.

Rainwater sampling was performed using a custom-built precipitation collector with the effective sampling area of 9 $m^2$. The steep collecting panels (45°) were designed to reduce rainfall retention time and minimize possible BTEX volatilization. Such large sampling area enabled collecting a vast number of samples per each rain event. The panels were thoroughly rinsed with 18 MΩ ultrapure water (ELGA PURELAB maxima system) prior to each sampling campaign, and the rinsing water was collected and analyzed as a field blank control sample. No target compounds were detected in the field blank control samples. The samples were collected and stored directly into brown glass bottles of 1 300 mL. All bottles were washed with detergent, thoroughly rinsed with ultrapure water and dried in an oven for 2 h at 105 °C to remove any trace of contamination. During the sampling, the bottles were filled to the top to avoid headspace, and the sampling duration and sample temperature were recorded. Since sampling equipment enables collection of large volumes of rainwater within a short period, the last sample in each sampling campaign was collected in the bottle of 2600 mL and was split into two standard aliquots. The first aliquot was analyzed immediately, whereas the other one was examined after all other samples to determine whether the BTEX levels changed over time. No difference could be observed in the obtained quantity of double samples (Table S1, Supplementary material).

BTEX concentrations in both gas and water phases were measured using proton transfer reaction mass spectrometer (Standard PTR-quad-MS, Ionicon Analytik, GmbH, Austria), whose detailed description is given elsewhere (Lindinger et al., 1998). Since PTR-quad-MS is not capable of distinguishing isobaric ions, the signal detected at m/z 107 referred to $C_8$ aromatic hydrocarbons, ethylbenzene, o-, m-, and p-xylene. Signals detected at m/z 79 and m/z 93 referred to benzene and toluene, respectively (Warneke et al., 2003).

The air samples were collected as a side flow from a 1/8-inch teflon tube sampling line through which ambient air was drawn at the flow rate of about 50 L $min^{-1}$ to ensure short residence. The sample inlet was located 6 m above ground level with a sampling angle of 360°. Drift tube parameters included: pressure, ranging from 2.04 to 2.14 mbar; temperature, 60 °C; voltage, 600 V; E/N parameter, 145 Td providing reaction time of 90 μs? The count rate of $H_3O^+H_2O$ was 3–8% of the $9.2 \cdot 10^6$ counts $s^{-1}$ count rate of primary $H_3O^+$ ions. PTR-MS calibration was performed before and after each sampling campaign using an external standard five-point calibration, ranging from 0 to 26 ppbV, 0–25 ppbV and 0–80 ppbV for B, T and EX, respectively. For this purpose, 2.5 ppmV mixture of BTEX (BTEX in nitrogen, Messer Group GmbH) was diluted with high-purity synthetic air (CH free, Messer Group GmbH) by means of HORIBA ASGU 370-P system.

Determination of BTEX concentrations in rainwater was performed immediately after each sampling campaign. A liter of each unfiltered rainwater sample was transferred to the gas washing bottle (GWB) and purged out with synthetic air at a flow rate of 1L $min^{-1}$. Rainwater filtration was avoided due to potential adsorption of species on the filter. The GWB output was connected with PTR-MS inlet via T-piece, and further analytical procedure, calibration and data processing were conducted as described in Šoštarić et al. (2016). In brief, PTR-MS signal obtained during exsufflation was subject to baseline fitting. The exsufflation time was determined for each sample as the interval required for equilibrium to be achieved ($t_{eq}$). The obtained exsufflation time was used for determining the amounts of target compounds retained in the analyzed rainwater samples. The aqueous concentrations of analyzed species were calculated by multiplying the obtained amounts by the conversion factor (3.25; 3.83 and 4.41 for B, T and EX, respectively). The detection limits (DL) in rainwater were determined using HC free air and calculated as 10 nM, 10 nM and 20 nM for B, T and EX, respectively. The remaining portion of each rainwater sample was transferred to a 300-mL bottle and stored at 4 °C until further analysis, which included determination of the major inorganic anions ($F^-$, $Cl^-$, $SO_4^{2-}$, $NO_2^-$ and $NO_3^-$), dissolved cations ($Na^+$, $NH_4^+$, $K^+$, $Ca^{2+}$ and $Mg^{2+}$), total organic carbon, electrical conductivity, UV extinction, turbidity and pH, in accordance with the standard methods (US EPA 300.1:1993, EN ISO 14911:1998, ISO 8 245:1999, EN 27888:1993, SMEWW 19th method 5 910 B, US EPA 180.1:1993, EN ISO 10523:2008, respectively). More details of the methods and equipment applied for physico-chemical analysis conducted on rainwater samples are presented in Supplementary material.

In order to determine the extent to which Henry's law constant ($K_H$) describes BTEX distribution between the gaseous and aqueous phase, distribution coefficients ($D_{OBS}$) were calculated for each sample pair and each species, as the ratio of the corresponding experimentally derived rainwater concentrations in nM ($C_R$) and ambient gas phase mixing ratios in ppbV ($p_g$):

$$D_{OBS} = C_R \Big/ p_g \quad \left(M\ atm^{-1}\right) \tag{1}$$

Furthermore, the enrichment factors (EF) were calculated as the ratio of $D_{OBS}$ and $K_H$.

Considering the $K_H$ temperature dependence, EF were calculated using temperature corrected $K_HT$ for each rain sample by means of the following equation (Sander, 2015):

$$K_HT = K_H(298.15)exp\left\{\frac{-\Delta H}{R}\left(\frac{1}{298.15} - \frac{1}{T}\right)\right\} \quad (2)$$

where $K_H$ is the Henry's law constant at 298.15 K for pure water, $\Delta H$ is the enthalpy change of air-water transfer, $T$ is the rainwater temperature, and $R$ is the universal gas constant (8.314 J $K^{-1}$ $mol^{-1}$). Furthermore, to assess the representativeness of ground level conditions for the atmospheric conditions during rainfall, $K_HT$ and EF altitude profiles were calculated using the temperature profiles obtained from GDAS1 (Global Data Assimilation System, 2015), by replacing the rainwater temperature value by the temperature at the corresponding altitude.

Meteorological parameters during rain events (precipitation (accumulated rainfall, rain current and peak intensity, and the duration of a rain event), wind speed and direction, pressure, humidity and temperature) were measured by Vaisala Weather Transmitter WXT530 Series. Cloud information, including cloud height and type, was obtained from the airport “Nikola Tesla”, Belgrade, ICAO code LYBE, located 8.9 km SSW from the sampling site.

The relationships between enrichment factors (EF), physico-chemical characteristics and wind characteristics (wind speed and direction) were examined using the bivariate polar plot analyses (Carslaw and Beevers, 2013) implemented in the Openair package (Carslaw and Ropkins, 2012) within the statistical software environment R (Team, 2012).

The neutralization factors (NF) were calculated based on the study of Moreda-Piñeiro et al. (2014), Tiwari et al. (2016) and references therein in order to examine the potential of the cations to balance the rainwater acidic components:

$$[NF_{Ca^{2+}}] = \frac{[nssCa^{2+}]}{NO_3^- + [nssSO_4^{2-}]} \quad (3)$$

$$[NF_{Mg^{2+}}] = \frac{[nssMg^{2+}]}{NO_3^- + [nssSO_4^{2-}]} \quad (4)$$

$$[NF_{NH_4^+}] = \frac{[NH_4^+]}{NO_3^- + [nssSO_4^{2-}]} \quad (5)$$

$$[NF_{K^+}] = \frac{[nssK^+]}{NO_3^- + [nssSO_4^{2-}]} \quad (6)$$

To calculate the non-sea salt fraction of any particular ion (*nss*), we assumed that all Na originated from marine sources, and used it as a referent element. The nss contribution is given as:

$$[nss - X]_i = [X_i] - [Na^+]_i \left[\frac{[X]}{Na^+}\right]_{sea\ salt} \quad (7)$$

where $[nss - X]_i$ is the nss concentration of the selected ion in the sample $i$, $[X_i]$ is the total concentration of the ion X measured in the rainwater sample $i$, $[Na^+]$ is the total concentration of $Na^+$ measured in the rainwater sample, and $[[X][Na^+]^{-1}]_{seasalt}$ is the reference ratio determined in the seawater.

Potential remote source regions that might affect the observed BTEX mixing ratios were identified using HYSPLIT-derived 72-h back trajectories (Draxler and Rolph, 2014). The trajectories were computed for each hour UTC a day before and during each rain event, above the sampling location at the half of the planetary boundary layer height calculated from GDAS1 using MeteoInfo (Wang, 2014), as described in Stojić et al. (2016) and Stojić and Stanišić Stojić (2017).

Rainwater source apportionment was performed using Unmix (USEPA, 2007). The maximum number of species selected as input variables was chosen using the trial and error with the overall aim of yielding the most physically meaningful results. For concentrations below the DL, a value equal to the half of the DL was used.

Guided regularized random forest (GRRF) was applied (Deng and Runger, 2013) for the selection of features that are most relevant for EF. Random forest (RF) consists of a number of decision trees which every node represents a condition on a single variable designed to split the dataset in two parts so that similar response values end up in the same set. Variable importance measures how much each variable decreases the weighted impurity across all tress, a measure based on which the optimal condition is chosen. GRFF uses the importance scores from a preliminary RF to guide the feature selection of regularized random forest (RRF), and has several advantages as follows: it is more robust and computationally efficient than RRF, varSelRF and LASSO logistic regression; it can select compact feature subsets moderating the curse of dimensionality; it avoids the effort to analyze irrelevant or redundant features; and it has competitive accuracy performance. Variable importance presented herein was obtained by calculating the average value of 2000 GRRF runs. The appropriate number of trees was determined to assure out-of-bag error convergence. Method performance was tested by 100 times replicated 10-fold cross validation.

To analyze the relationship between EF and features that are considered most relevant for EF prediction, the following 24 regression MVA methods implemented in Weka 3.8 (Hall et al., 2009) were applied: Alternating Model Tree, Conjunctive Rule, Decision Stump, Decision Table, Elastic Net, Gaussian Processes, IBk, IBkLG, Isotonic Regression, K*, Least Median Squared, Linear Regression, Locally Weighted Learning, M5P, M5 Rules, Multilayer Perceptron, Pace Regression, Random Forest, Random Tree, Radial Base Function (RBF) Network, RBF Regressor, REP Tree, Simple Linear Regression and SMOreg Support Vector Machine. A brief description of the methods, including functions (neural network, support vector machine, etc.), clustering techniques, rules and trees, is provided in Supplementary material. Method performance was tested by 10 times replicated 10-fold cross-validation.

## 3. Results and discussion

Light showers, with occasional thunderstorms, constituted a considerable part of summer rain events. Scattered and broken clouds in the form of cumulonimbus or towering cumulus were observed at the height of 400–1 000 m. In the autumn campaign, the vast majority of rain events were light and sporadically followed by mist. Scattered clouds were registered at levels below 300 m, whereas broken clouds were observed from 100 to 900 m.

As expected, both aqueous and gaseous BTEX concentrations were higher during the cold part of the year. Lower BTEX concentrations in summer can be attributed to intense photochemical removal and washout effects associated with more sunny and rainy days (Lee et al., 2002), whereas higher concentrations of BTEX in autumn can be associated with individual combustion fireboxes widely spread in the vicinity of the sampling site. Furthermore, aqueous B concentrations in summer were below DL.

As can be seen in Fig. 1, each rain event was associated with air

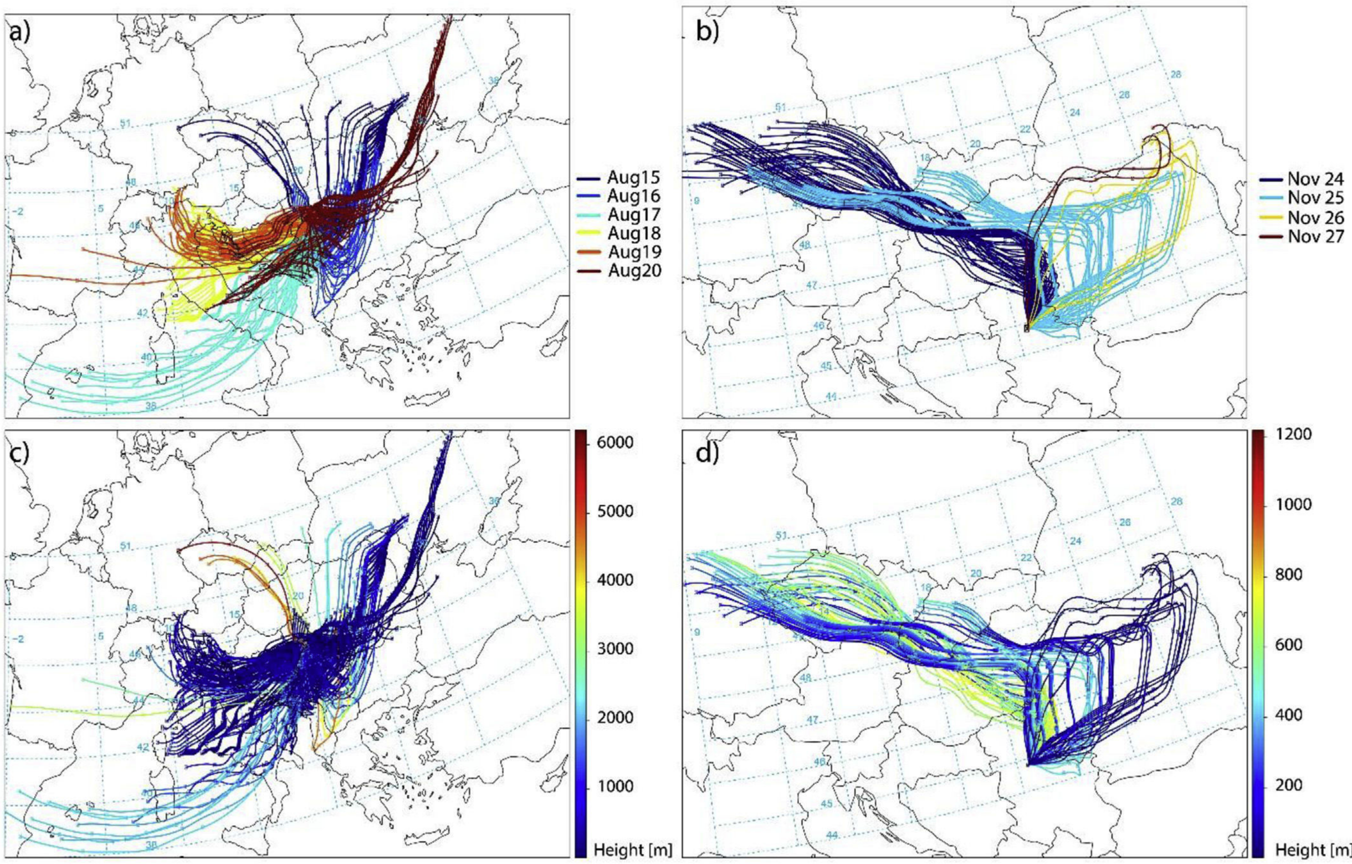


**Fig. 1.** Back trajectories a day before (August 15 and November 24) and during summer (a) and autumn (b) rain events and corresponding trajectory heights (c, d).

masses coming from different source regions and heights. During summer rain events, air flows from all directions were followed by significant variations in physico-chemical properties of rainwater, whereas N and NE air masses in autumn were associated with a more uniform rainwater composition. Gaseous concentrations of volatile species, particularly B, were relatively stable during rain events, which can be explained by the fact that the sampling site was dominated by local BTEX sources.

### 3.1. *Physico-chemical characteristics of rainwater*

Basic statistics for all rainwater parameters and BTEX concentrations is given in Table S2, Supplementary material. The average rainwater pH was 6.01, while the turbidity was below 10 NTU, indicating that the samples contained moderate amounts of suspended particles from the atmosphere. As illustrated in Fig. S1, conductivity, as well as high concentrations of most ions ($SO_4^{2-}$, $NO_3^-$, $Ca^{2+}$, $Mg^{2+}$, $K^+$ and $Na^+$) were influenced by the high-speed SW wind (20–30 m $s^{-1}$), while only $NH_4^+$ concentrations were increased with the wind of moderate speed (10 m $s^{-1}$) from NE direction.

The rainwater pH varied from 3.70 to 8.20 with the volume weighted mean of 6.01, which is mainly due to scavenging of alkaline species ($Ca^{2+}$ and $SO_4^{2-}$). The average pH value is also close to the 5-year-mean (6.1) obtained as a part of the regular air quality monitoring in Belgrade. The contribution of $SO_4^{2-}$ to the rainwater acidity was confirmed by ($Cl^-$ + $NO_3^-$) and ($SO_4^{2-}$) ratio below 1 (Tiwari et al., 2016). As shown, $Ca^{2+}$ was the dominant neutralization component, followed by $NH_4^+$, $Mg^{2+}$ and $K^+$, with mean of 77%, 14%, 7% and 2.3%, respectively.

As shown in Fig. S2, significant correlations were observed as follows: > 0.80 ($NO_3^-$ – $SO_4^{2-}$, $NH_4^+$ – aq. B, $NH_4^+$ – gas. B, $NH_4^+$ – $EF_B$); 0.70–0.80 ($F^-$ – $SO_4^{2-}$, $F^-$ – $NO_3^-$, $F^-$ – aq. B, $F^-$ – gas. B, $F^-$ – $EF_B$, $K^+$ – $Na^+$); and 0.60–0.70 ($NO_3^-$ – $Mg^{2+}$, $SO_4^{2-}$ – $Mg^{2+}$, $SO_4^{2-}$ – $EF_{EX}$, $Na^+$ – $Mg^{2+}$). Furthermore, high correlations were noted between aq. And gas. BTEX concentrations (≥0.80), as well as between aq. EX and aq. B (0.67) and aq. T (0.67), suggesting that these species might share the common source.

As can be seen in Tables S3, S4 and S5, four factors were derived using Unmix. With high contributions of volatile BTEX species (99%, 44.5% and 52.2%) and a relatively high share of UV extinction (33.3%), the first factor was recognized as organic compounds in the gaseous form. The second factor, characterized by the highest contribution of TOC (71.6%) and turbidity (79.7%), represented the solid fraction dissolved in the atmospheric water. Significant shares of $K^+$ (58.0%), $SO_4^{2-}$ (42.2%) and $NO_3^-$ (31.3%) were also apportioned to this factor, as a result of fossil fuel burning and traffic exhaust (Rao et al., 2016; Tiwari et al., 2016). The high shares of crustal-related elements, $Na^+$ (61.8%) and $Mg^{2+}$ (61.4%), were apportioned to the third factor (Cao et al., 2008; Sapek, 2014). Moderate to significant shares (>30%) of all species except $Na^+$, $K^+$ and B were apportioned to the fourth factor, being recognized as the aerosol fraction. Apart from gaseous oxides ($SO_2$ and $NO_2$), which react with ozone and OH· radicals in the presence of $Ca^{2+}$ and $Mg^{2+}$ (Seinfeld and Pandis, 2006), BTEX are susceptible to photo-oxidation that can also lead to SOA formation. BTEX reactions include oxidation with ozone and OH·, but also with $NO_x$ and $SO_2$, which results in multi-functional oxy products that are further deposited onto the existing aerosol or initiate the formation of SOA by self-nucleation. BTEX behave differently in the atmosphere due to differences in the methyl chain substituent and the alkyl chain length. Benzene is considered being extremely stable compared to T and EX (Słomińska et al., 2014), and it is less susceptible to the heterogeneous reactions and formation of SOA in the atmosphere.

The contributions of the gaseous organic- and aerosol-related factors were mostly associated with N wind of moderate speed (<10 m $s^{-1}$), which clearly reflects their local origin, while the solid- and crustal-related factors were associated with the air masses from SW direction and high wind speed (20–30 m $s^{-1}$) (Fig. S3). The contribution of the factor assigned to aerosols declined during rain events due to wet deposition, while similar behavior was not observed for other factors.

TEX air mixing ratios and rain concentrations decreased during the first 2 h of the rainfall, but tend to rise afterwards probably as a result of rainfall intensity decrease (Fig. S4, Supplementary material). The highest TEX enrichment, caused by air mixing ratio decrease, was detected during the second hour. Typical washout effect was observed for source contributions related to the rainwater aerosol and solid components, and was less pronounced for crustal factor. Unlike TEX, only a slight decrease in benzene air mixing ratios was noticeable, which is reflected in a constant $EF_B$ increase.

### 3.2. BTEX distribution between gaseous and aqueous phases

The exsufflation time required for the equilibrium to be achieved was different for rainwater samples and ultrapure water, which suggests that physico-chemical properties and BTEX content distributed between different phases have certain impact on the adsorption to the aqueous phase (Fig. 2, left). However, the correlations were registered only between the concentrations of B, and $F^-$ (−0.72) and $NH_4^+$ (0.83) (Fig. S2, Supplementary material). The impact of rainwater physico-chemical properties on the BTEX retention was further examined by insufflating 2 ppbV of BTEX in 10 pre-exsufflated rainwater samples, as described in our previous paper (Šoštarić et al., 2016). The results showed slightly longer exsufflation periods for rainwater samples compared to the pure water, indicating that physico-chemical properties are not the main contributor to the extended retention in the rainwater. The comparative qualitative analysis of rainwater and ultrapure water exsufflation time series obtained by real-time PTR-MS measurements showed that different capacities for BTEX retention can be mainly associated with BTEX aerosol fraction (Fig. 2, right).

Generally, due to very small $K_H$ values of aromatic compounds, BTEX concentrations in rainwater are expected to be low (Słomińska et al., 2014). However, according to the results, EF values were in the range from 61 to 128, from 8 to 209, and from 25 to 295 for B, T and EX, respectively, indicating that the BTEX amounts in the aqueous phase significantly exceeded the theoretically predicted levels. Both lower and higher EF values have been reported in the literature. According to the studies dealing with the distribution of chlorinated hydrocarbons and monocyclic aromatic hydrocarbons between air and rainwater, EF ranged from 2.4 to 34 for BTEX (Okochi et al., 2004; Sato et al., 2006), whereas the study of Valsaraj et al. (1993) reported several hundred to a thousand-fold enrichment of hydrophobic organic compounds in fog samples. The enhanced BTEX transfer to urban dew water was also shown by Okochi et al. (2005), with the reported EF values ranging from 7.87 to 20.2. Furthermore, Fries et al. (2007) showed that the concentrations of aromatic hydrocarbons including ethylbenzene, xylenes and 1,2,4-trimethylbenzene, have been significantly lower in rain (15–53 ng $L^{-1}$) than in snow (71–2 200 ng $L^{-1}$). In the later study,

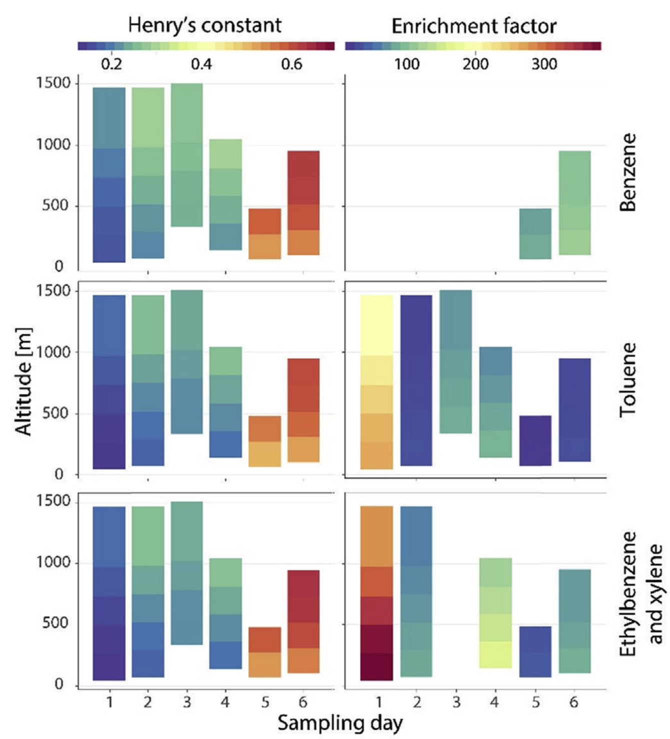


**Fig. 3.** Henry's constant and EF BTEX altitude distributions.

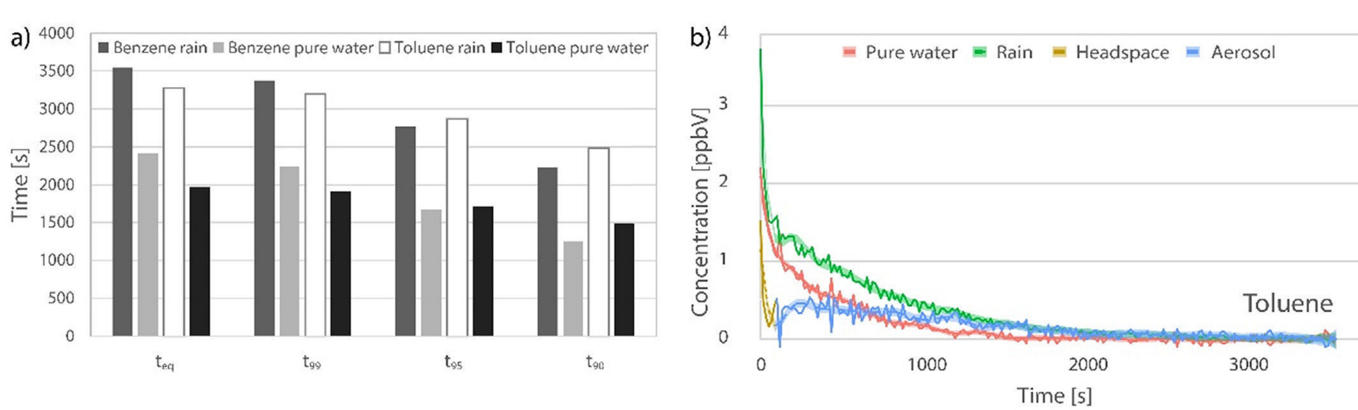


**Fig. 2.** The time required to reach equilibrium ($t_{eq}$) and 99, 95 and 90% quantity of benzene and toluene to be exsufflated (left), and toluene exsufflation from ultra-pure water and rainwater (right).

Fries et al. (2008) found that in-cloud scavenging could be a possible explanation for the occurrence of VOC in fallen snow.

Fig. 3 illustrates the $K_H$ and EF altitude distribution for BTEX. It should be mentioned that $K_H$ and EF for B and EX exhibit the similar pattern. As can be seen, $K_H$ and consequently EF, change as the raindrop falls to the ground. $K_H$ values calculated using the average temperature on the path of the raindrop differ ±20% from those obtained using the rainwater temperature. Such agreement indicates that the rainwater temperature measured at the ground level is a good indicator of atmospheric conditions under which reactions with BTEX takes place. Moreover, in the study of Lin et al. (2011), it was concluded that, at higher altitudes in locations with dominant local sources, VOC concentrations were generally lower, and hence, higher $K_H$ values would not be expected to affect $C_R$, nor calculated values of $D_{OBS}$ and EF.

As suggested by the field studies (Valsaraj et al., 1993; Goss, 1994; Okochi et al., 2004; Starokozhev et al., 2009), as well as the laboratory experiments (Bruant and Conklin, 2000, 2002; Raja et al., 2002; Raja and Valsaraj, 2004; Šoštarić et al., 2016), the interfacial adsorption might be the major mechanism associated with the enhanced VOC transfer to the aqueous phase.

Some previous studies have examined the composition of atmospheric water and the impact of different species, including nitric acid, anionic and nonionic surfactants, as well as the impact of salinity and pH on air-water VOC distribution (O'Sullivan et al., 1996; Vane and Giroux, 2000; Sato et al., 2006; Allou et al., 2011). The supersaturation of VOC in rain samples was explained by decreased rainwater polarity associated with the presence of different organic compounds (Sato et al., 2006). The presence of colloidal organic matter with its large binding capacity for many hydrophobic species was found in fog droplets (Valsaraj et al., 1993). Similarly, in the study of Okochi et al. (2005), the enhanced dissolution of VOC species in urban dew compared to rainwater was explained by the fact that dew forms near the ground and contain more humic-like substances that could lead to a decrease in water surface tension and consequently result in higher VOC enrichment.

The present study considers several factors that could contribute to BTEX enrichment in rainwater, including BTEX concentrations, rainwater physico-chemical properties, rainfall intensity, air masses origin, meteorological conditions and adsorption at the air/water interface.

As regards the physico-chemical characteristics of rainwater, only $F^-$ and $SO_4^{2-}$ can be considered important for the prediction of $EF_B$ (−0.73) and $EF_{EX}$ (0.62), respectively. The latter indicates that $SO_2$-rich coal burning emissions are also a significant source of EX, while the results for B should be taken with caution due to the small data size.

Higher rainwater T enrichment was mostly observed for low gaseous T concentrations, high TOC (8–12 mg $L^{-1}$) and turbidity (Supplementary file 1), although the strict link between rainwater enrichment and gaseous concentrations cannot be established. The exsufflation dynamics (Fig. 2) and the EF values suggest that prolonged BTEX retention could also be attributed to the adsorption to aerosol fraction. We have considered T partitioning, not only because T concentrations were in a relatively broad range, but also because of the significant number of samples collected in both seasons with comparable concentrations, despite the fact that similar findings were observed for the rainwater enrichment with EX (Supplementary file 2). As can be observed in Fig. 4 and Table S6 of the Supplementary material, higher T enrichment was mostly associated with a higher wind speed at the sampling site (up to 30 m $s^{-1}$) and air masses coming from SW area, whereas the lowest rainwater enrichment was registered under relatively stable atmospheric conditions (ws < 5 m $s^{-1}$). Similar associations were also observed for EX. Higher rainwater enrichment could be the result of the prolonged contact time between the aqueous and the gaseous phases, when strong wind-driven raindrops were falling obliquely.

According to GRRF results (Table S7, Supplementary material), physico-chemical rainwater properties and gaseous T concentrations appear to be of greater importance than meteorological factors for predicting T and EX rainwater enrichment. Furthermore, these findings also indicate that ground level gaseous concentrations have higher impact on the transfer of species to the aqueous phase than the polluted air masses coming from greater atmospheric heights.

Out of 24 examined MVA regression methods, some of which were previously successfully applied for prediction of $PM_{10}$ and VOC emissions (Stojić et al., 2015d; Perišić et al., 2017), it has been shown that RF, IBk and IBkLG can provide predictions of $EF_T$ and $EF_{EX}$ based on the variables of the highest importance derived by GRRF with relative errors of approx. 20%, *i.e.* 27%, and correlation coefficients around 0.95 and 0.87, respectively (Table 1). Conversely, the prediction of $EF_T$ and $EF_{EX}$ based on Unmix derived source contributions was less accurate (K*: 36.3% relative error and correlation coefficient 0.79). As can be concluded, functional description of $EF_T$ and $EF_{EX}$ can be based on certain rainwater properties and gaseous T concentrations. In addition to ambient and rainwater B concentrations, $EF_B$ is affected by meteorological conditions (sample and ambient temperature and Rh), but these results should be taken with caution due to the small B data size.

Fig. 5 represents EF for T and EX as a function of their ambient gas phase mixing ratios. As can be seen, EF values increased in summer, due to ambient air temperature, which is one of the most important factors for the decrease of the surface tension leading to enhanced interfacial adsorption (Bruant and Conklin, 2000, 2002). Another important feature of Fig. 5 is the power functional dependence of EF on ambient gas phase mixing ratios, as adsorption processes are generally more efficient for lower adsorbate concentrations and are characterized by the power functions. These findings are in compliance with the findings of Sato et al. (2006) who showed that rainwater enrichment is especially significant for the species with lower atmospheric concentrations.

## 4. Conclusions

The transfer of BTEX and other VOC from the atmosphere to various forms of atmospheric water is an important process that affects the global transport of air pollutants, environmental fate and enables the transfer of these species to terrestrial and aquatic systems. The purpose of this study was to investigate the scavenging potential of rainwater and consider the potential mechanisms and factors associated with this phenomenon.

As shown, BTEX concentrations observed in the aqueous phase exceeded the theoretically predicted values. Given that the interfacial adsorption is assumed to be the major mechanism underlying the enhanced rain scavenging of BTEX, the removal process was observed to be more efficient for lower gas mixing ratios, mainly due to equal surface available for smaller number of molecules and the prolonged contact time between the two phases when wind-driven rain drops were falling obliquely. Accordingly, theoretical predictions are probably more accurate in the area of larger gaseous concentrations, whereas in the case of lower concentrations, transfer to the aqueous phase is often underestimated. Furthermore, the results of the presented regression multivariate analysis suggest that multiple factors determine the spatio-temporal BTEX distribution in the environmental multiphase system, including ambient mixing ratios, physico-chemical properties of rainwater and meteorological data. More specifically, the functional description of $EF_T$ and $EF_{EX}$ can be based on certain rainwater properties.

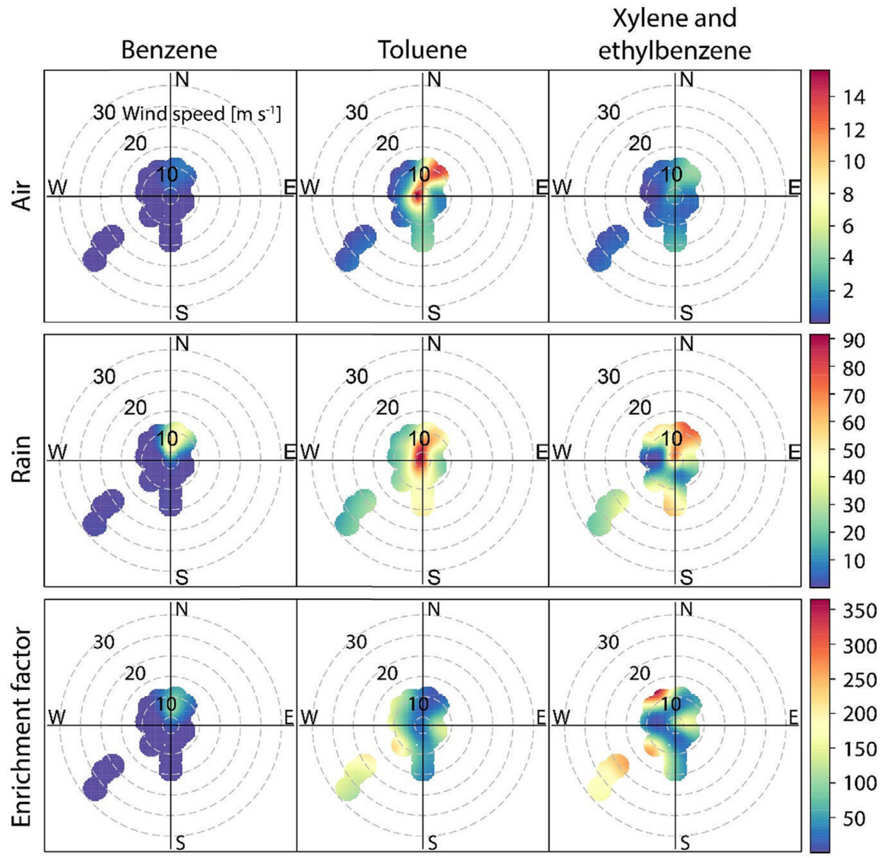


**Fig. 4.** The relationship between BTEX air mixing ratios (ppb), rain concentrations (nM) and enrichment factor and wind characteristics.

**Table 1**
MVA method performance comparison for enrichment factor prediction based on the measured parameters and Unmix-derived source contributions: absolute error, relative error and correlation coefficient (r).

| Method | $EF_T$ | | | | | | $EF_{EX}$ | | | | | |
|---|---|---|---|---|---|---|---|---|---|---|---|---|
| | Measured parameters | | | Unmix derived source contributions | | | Measured parameters | | | Unmix derived source contributions | | |
| | Abs. error | Rel. error | r | Abs. error | Rel. error | r | Abs. error | Rel. error | r | Abs. error | Rel. error | r |
| Alternating Model Tree | 18.5 | 34.8 | 0.88 | 40.8 | 76.4 | 0.67 | 33.8 | 42.0 | 0.78 | 59.2 | 111.0 | 0.53 |
| Conjunctive Rule | 26.1 | 48.9 | 0.64 | 32.0 | 59.9 | 0.40 | 39.2 | 48.7 | 0.55 | 43.4 | 81.2 | 0.41 |
| Decision Stump | 25.5 | 47.8 | 0.57 | 29.3 | 54.9 | 0.46 | 36.4 | 45.2 | 0.57 | 39.4 | 73.8 | 0.45 |
| Decision Table | 17.8 | 33.3 | 0.85 | 25.3 | 47.4 | 0.68 | 33.9 | 42.1 | 0.71 | 44.8 | 83.9 | 0.46 |
| Elastic Net | 15.2 | 28.5 | 0.88 | 22.3 | 41.9 | 0.77 | 29.4 | 36.5 | 0.74 | 38.6 | 72.4 | 0.62 |
| Gaussian Processes | 16.1 | 30.2 | 0.88 | 21.9 | 41.0 | 0.79 | 30.6 | 38.0 | 0.72 | 41.0 | 76.8 | 0.60 |
| IBk | 11.6 | 21.7 | 0.95 | 20.6 | 38.5 | 0.79 | 22.4 | 27.8 | 0.89 | 31.9 | 59.8 | 0.68 |
| IBkLG | 11.6 | 21.7 | 0.95 | 20.6 | 38.5 | 0.79 | 22.4 | 27.8 | 0.89 | 31.9 | 59.8 | 0.68 |
| Isotonic Regression | 13.7 | 25.7 | 0.93 | 31.4 | 58.9 | 0.54 | 34.9 | 43.3 | 0.62 | 39.5 | 74.0 | 0.58 |
| K* | 11.9 | 22.3 | 0.92 | 19.4 | 36.3 | 0.79 | 22.0 | 27.4 | 0.87 | 31.0 | 58.1 | 0.68 |
| Least MedSq | 17.4 | 32.7 | 0.87 | 35.6 | 66.8 | 0.67 | 52.7 | 65.4 | 0.29 | 47.4 | 88.8 | 0.50 |
| Linear Regression | 15.5 | 29.1 | 0.89 | 22.7 | 42.5 | 0.78 | 30.8 | 38.2 | 0.74 | 39.0 | 73.2 | 0.61 |
| LWL | 15.9 | 29.7 | 0.91 | 26.7 | 50.0 | 0.72 | 35.5 | 44.1 | 0.70 | 39.4 | 73.9 | 0.53 |
| M5P | 13.9 | 26.1 | 0.91 | 21.6 | 40.5 | 0.78 | 29.7 | 36.9 | 0.74 | 40.4 | 75.7 | 0.60 |
| M5Rules | 15.0 | 28.1 | 0.90 | 22.9 | 42.9 | 0.74 | 30.8 | 38.3 | 0.74 | 42.2 | 79.1 | 0.59 |
| Multilayer Perceptron | 17.7 | 33.1 | 0.92 | 24.2 | 45.4 | 0.80 | 37.5 | 46.5 | 0.74 | 49.5 | 92.7 | 0.55 |
| Pace Regression | 15.9 | 29.8 | 0.88 | 22.7 | 42.6 | 0.77 | 30.1 | 37.4 | 0.74 | 38.6 | 72.4 | 0.62 |
| Random Forest | 11.6 | 21.7 | 0.95 | 22.5 | 42.2 | 0.76 | 27.8 | 34.5 | 0.76 | 34.9 | 65.4 | 0.62 |
| Random Tree | 13.8 | 25.9 | 0.89 | 28.6 | 53.7 | 0.59 | 32.8 | 40.8 | 0.67 | 41.7 | 78.1 | 0.54 |
| RBF Network | 29.9 | 56.0 | 0.45 | 30.4 | 57.0 | 0.65 | 44.8 | 55.7 | 0.49 | 52.8 | 98.9 | 0.40 |
| RBF Regressor | 14.7 | 27.6 | 0.91 | 23.6 | 44.2 | 0.78 | 28.1 | 34.9 | 0.83 | 40.9 | 76.6 | 0.56 |
| REP Tree | 13.9 | 26.1 | 0.91 | 22.5 | 42.1 | 0.72 | 36.9 | 45.8 | 0.58 | 42.0 | 78.8 | 0.43 |
| Simple Linear Regression | 29.9 | 56.1 | 0.49 | 30.3 | 56.7 | 0.55 | 34.3 | 42.7 | 0.71 | 40.5 | 75.8 | 0.61 |
| SMOreg | 14.7 | 27.5 | 0.88 | 21.5 | 40.3 | 0.79 | 28.8 | 35.8 | 0.75 | 39.0 | 73.2 | 0.61 |

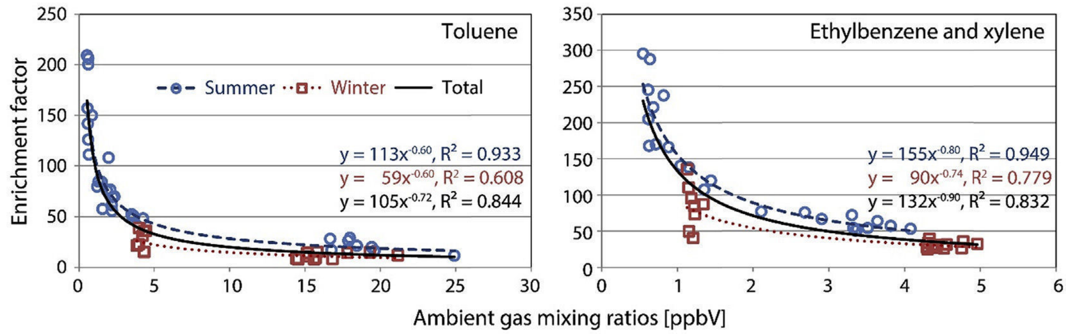


**Fig. 5.** The relationship between T and EX enrichment factors and their gaseous concentrations.

On the other hand, it has been shown that $EF_B$ is affected by meteorological conditions (sample and ambient temperature, and Rh), as well as B ambient and rainwater concentrations (however, these results should be interpreted with caution due to the small B data size).

## Acknowledgments

This paper was realized as part of projects No III43007 and No III41011, which were financed by the Ministry of Education, Science and Technological Development of the Republic of Serbia for the period 2011–17, and was supported by the Institute of Public Health of Belgrade, Serbia.

## Appendix A. Supplementary data

Supplementary data related to this article can be found at http://dx.doi.org/10.1016/j.atmosenv.2017.08.045.

## References


Allou, L., El Maimouni, L., Le Calve, S., 2011. Henry's law constant measurements for formaldehyde and benzaldehyde as a function of temperature and water composition. Atmos. Environ. 45, 2991–2998.

Balla, D., Papageorgiou, A., Voutsa, D., 2014. Carbonyl compounds and dissolved organic carbon in rainwater of an urban atmosphere. Environ. Sci. Pollut. Res. 21, 12062–12073.

Bruant Jr., R.G., Conklin, M.H., 2000. Dynamic determination of vapor/water interface adsorption for volatile hydrophobic organic compounds (VHOCs) using axisymmetric drop shape analysis: procedure and analysis of benzene adsorption. J. Phys. Chem. B 104, 11146–11152.

Bruant Jr., R.G., Conklin, M.H., 2002. Adsorption of benzene and methyl-substituted benzenes at the vapor/water interface. 3. finite binary-component VHOC adsorption. J. Phys. Chem. B 106, 2232–2239.

Cao, J.J., Chow, J.C., Watson, J.G., Wu, F., Han, Y.M., Jin, Z.D., An, Z.S., 2008. Size-differentiated source profiles for fugitive dust in the Chinese Loess Plateau. Atmos. Environ. 42, 2261–2275.

Carslaw, D.C., Beevers, S.D., 2013. Characterising and understanding emission sources using bivariate polar plots and k-means clustering. Environ. Model. Softw. 40, 325–329.

Carslaw, D.C., Ropkins, K., 2012. Openair - an R package for air quality data analysis. Environ. Model. Softw. 27, 52–61.

Chatani, S., Matsunaga, S.N., Nakatsuka, S., 2015. Estimate of biogenic VOC emissions in Japan and their effects on photochemical formation of ambient ozone and secondary organic aerosol. Atmos. Environ. 120, 38–50.

Deng, H., Runger, G., 2013. Gene selection with guided regularized random forest. Pattern Recognit. 46, 3483–3489.

Draxler, R.R., Rolph, G.D., 2014. HYSPLIT (HYbrid Single-particle Lagrangian Integrated).

Durmusoglu, E., Taspinar, F., Karademir, A., 2010. Health risk assessment of BTEX emissions in the landfill environment. J. Hazard. Mater 176, 870–877.

Fries, E., Starokozhev, E., Haunold, W., Jaeschke, W., Mitra, S.K., Borrmann, S., Schmidt, M.U., 2007. Laboratory studies on the uptake of aromatic hydrocarbons by ice crystals during vapor depositional crystal growth. Atmos. Environ. 41, 6156–6166.

Fries, E., Sieg, K., Püttmann, W., Jaeschke, W., Winterhalter, R., Williams, J., Moortgat, G.K., 2008. Benzene, alkylated benzenes, chlorinated hydrocarbons and monoterpenes in snow/ice at Jungfraujoch (46.6 N, 8.0 E) during CLACE 4 and 5. Sci. Total Environ. 391, 269–277.

Global Data Assimilation System, 2015. https://www.ready.noaa.gov/gdas1.php. (Accessed 27 December 2015).

Goss, K.U., 1994. Predicting the enrichment of organic compounds in fog caused by adsorption on the water surface. Atmos. Environ. 28, 3513–3517.

Hall, M., Frank, E., Holmes, G., Pfahringer, B., Reutemann, P., Witten, I.H., 2009. The WEKA data mining software: an update. SIGKDD Explor 11, 10–18.

Lee, S.C., Chiu, M.Y., Ho, K.F., Zou, S.C., Wang, X., 2002. Volatile organic compounds (VOCs) in urban atmosphere of Hong Kong. Chemosphere 48, 375–382.

Lin, C.C., Lin, C., Hsieh, L.T., Chen, C.Y., Wang, J.P., 2011. Vertical and diurnal characterization of volatile organic compounds in ambient air in urban areas. J. Air Waste. Manag. Assoc. 61, 714–720.

Lindinger, W., Hansel, A., Jordan, A., 1998. On-line monitoring of volatile organic compounds at pptv levels by means of Proton-Transfer-Reaction Mass Spectrometry (PTR-MS). Medical applications, food control and environmental research. Int. J. Mass Spectrom. Ion. Process 173, 191–241.

Matsumoto, K., Matsumoto, K., Mizuno, R., Igawa, M., 2010. Volatile organic compounds in ambient aerosols. Atmos. Res. 97, 124–128.

McNeill, V.F., Grannas, A.M., Abbatt, J.P., Ammann, M., Ariya, P., Bartels-Rausch, T., Domine, F., Donaldson, D.J., Guzman, M.I., Heger, D., Kahan, T.F., 2012. Organics in environmental ices: sources, chemistry, and impacts. Atmos. Chem. Phys. 12, 9653–9678.

Moreda-Piñeiro, J., Rodríguez, E.L., Pérez, C.M., Heras, G.B., Carou, I.T., Mahía, P.L., Lorenzo, S.M., Rodríguez, D.P., 2014. Influence of marine, terrestrial and anthropogenic sources on ionic and metallic composition of rainwater at a suburban site (Northwest Coast of Spain). Atmos. Environ. 88, 30–38.

Mullaugh, K.M., Hamilton, J.M., Avery, G.B., Felix, J.D., Mead, R.N., Willey, J.D., Kieber, R.J., 2015. Temporal and spatial variability of trace volatile organic compounds in rainwater. Chemosphere 134, 203–209.

O'Sullivan, D.W., Lee, M., Noone, B.C., Heikes, B.G., 1996. Henry's law constant determinations for hydrogen peroxide, methyl hydroperoxide, hydroxymethyl hydroperoxide, ethyl hydroperoxide, and peroxyacetic acid. J. Phys. Chem. 100, 3241–3247.

Okochi, H., Sugimoto, D., Igawa, M., 2004. The enhanced dissolution of some chlorinated hydrocarbons and monocyclic aromatic hydrocarbons in rainwater collected in Yokohama. Jpn. Atmos. Environ. 38, 4403–4414.

Okochi, H., Kataniwa, M., Sugimoto, D., Igawa, M., 2005. Enhanced dissolution of volatile organic compounds into urban dew water collected in Yokohama. Jpn. Atmos. Environ. 39, 6027–6036.

Perišić, M., Maletić, D., Stojić, S.S., Rajšić, S., Stojić, A., 2017. Forecasting hourly particulate matter concentrations based on the advanced multivariate methods. Int. J. Environ. Sci. Technol. 14, 1047–1054.

Raja, S., Valsaraj, K.T., 2004. Adsorption and transport of gas-phase naphthalene on micron-size fog droplets in air. Environ. Sci. Technol. 38, 763–768.

Raja, S., Yaccone, F.S., Ravikrishna, R., Valsaraj, K.T., 2002. Thermodynamic parameters for the adsorption of aromatic hydrocarbon vapors at the gas–water interface. J. Chem. Eng. Data 47, 1213–1219.

Rao, P.S.P., Tiwari, S., Matwale, J.L., Pervez, S., Tunved, P., Safai, P.D., Srivastava, A.K., Bisht, D.S., Singh, S., Hopke, P.K., 2016. Sources of chemical species in rainwater during monsoon and nonmonsoonal periods over two megacities in India and dominant source region of secondary aerosols. Atmos. Environ. 146, 90–99.

Sander, R., 2015. Compilation of Henry's law constants (version 4.0) for water as solvent. Atmos. Chem. Phys. 15, 4399–4981.

Sapek, B., 2014. Calcium and magnesium in atmospheric precipitation, groundwater and the soil solution in long-term meadow experiments. J. Eleme 19, 191–208.

Sato, E., Matsumoto, K., Okochi, H., Igawa, M., 2006. Scavenging effect of precipitation on volatile organic compounds in ambient atmosphere. Bull. Chem. Soc. Jpn. 79, 1231–1233.

Seinfeld, J.H., Pandis, S.N., 2006. Atmospheric Chemistry and Physics: from Air Pollution to Climate Change, second ed. J. Wiley & Sons, New York.

Šoštarić, A., Stojić, A., Stanišić, S.S., Gržetić, I., 2016. Quantification and mechanisms of BTEX distribution between aqueous and gaseous phase in a dynamic system. Chemosphere 144, 721–727.

Starokozhev, E., Fries, E., Cycura, A., Püttmann, W., 2009. Distribution of VOCs

between air and snow at the Jungfraujoch high alpine research station, Switzerland, during CLACE 5 (winter 2006). Atmos. Chem. Phys. 9, 3197–3207.
Stojić, A., Stanišić Stojić, S., 2017. The innovative concept of three-dimensional hybrid receptor modeling. Atmos. Environ. 164, 216–223.
Stojić, A., Stanišić, S.S., Šoštarić, A., Ilić, L., Mijić, Z., Rajšić, S., 2015a. Characterization of VOC sources in an urban area based on PTR-MS measurements and receptor modelling. Environ. Sci. Pollut. Res. 22, 13137–13152.
Stojić, A., Stojić, S.S., Mijić, Z., Ilić, L., Tomašević, M., Todorović, M., Perišić, M., 2015b. Comprehensive analysis of VOC emission sources in Belgrade urban area. Urban Built Environ. 55–88.
Stojić, A., Stojić, S.S., Mijić, Z., Šoštarić, A., Rajšić, S., 2015c. Spatio-temporal distribution of VOC emissions in urban area based on receptor modelling. Atmos. Environ. 106, 71–79.
Stojić, A., Maletić, D., Stojić, S.S., Mijić, Z., Šoštarić, A., 2015d. Forecasting of VOC emissions from traffic and industry using classification and regression multivariate methods. Sci. Total. Environ. 521, 19–26.
Stojić, A., Stanišić, S.S., Reljin, I., Čabarkapa, M., Šoštarić, A., Perišić, M., Mijić, Z., 2016. Comprehensive analysis of PM10 in Belgrade urban area on the basis of long term measurements. Environ. Sci. Pollut. Res. 23, 10722–10732.
Słomińska, M., Konieczka, P., Namieśnik, J., 2014. The fate of BTEX compounds in ambient air. Crit. Rev. Env. Sci. Tec. 44, 455–472.
Team, 2012. R: a language and environment for statistical computing. http://cran.case.edu/web/packages/dplR/vignettes/timeseries-dplR.pdf (Accessed 4 December 2015).
Tiwari, S., Hopke, P.K., Thimmiah, D., Dumka, U.C., Srivastava, A.K., Bisht, D.S., Rao, P.S.P., Chate, D.M., Srivastava, M.K., Tripathi, S.N., 2016. Nature and sources of ionic species in precipitation across the Indo-Gangetic Plains, India. Aerosol Air Qual. Res. 16, 943–957.
USEPA, 2007. EPA Unmix 6.0 Fundamentals and User Guide. USEPA Office of Research and Development.
Valsaraj, K.T., Thoma, G.J., Reible, D.D., Thibodeaux, L.J., 1993. On the enrichment of hydrophobic organic compounds in fog droplets. Atmos. Environ. 27, 203–210.
Vane, L.M., Giroux, E.L., 2000. Henry's law constants and micellar partitioning of volatile organic compounds in surfactant solutions. J. Chem. Eng. Data 45, 38–47.
Wang, Y.Q., 2014. MeteoInfo: GIS software for meteorological data visualization and analysis. Meteorol. Appl. 21, 360–368.
Warneke, C., De Gouw, J.A., Kuster, W.C., Goldan, P.D., Fall, R., 2003. Validation of atmospheric VOC measurements by proton-transfer-reaction mass spectrometry using a gas-chromatographic preseparation method. Environ. Sci. Technol. 37, 2494–2501.
WHO, 1986. Toluene Environmental Health Criteria, vol. 52. WHO (International Programme on Chemical Safety).
WHO, 1993. Benzene Environmental Health Criteria, vol. 150. WHO (International Programme on Chemical Safety).
WHO, 1997. Ethylbenzene Environmental Health Criteria, vol. 186. WHO (International Programme on Chemical Safety).

*universe*

MDPI

*Article*

# Ionospheric Response on Solar Flares through Machine Learning Modeling

**Filip Arnaut *, Aleksandra Kolarski , Vladimir A. Srećković and Zoran Mijić**

Institute of Physics Belgrade, University of Belgrade, Pregrevica 118, 11080 Belgrade, Serbia; aleksandra.kolarski@ipb.ac.rs (A.K.); vlada@ipb.ac.rs (V.A.S.); zoran.mijic@ipb.ac.rs (Z.M.)
* Correspondence: filip.arnaut@ipb.ac.rs

**Abstract:** Following solar flares (SF), the abrupt increase in X-radiation and EUV emission generates additional ionization and higher absorption of, e.g., electromagnetic waves in the sunlit hemisphere of the Earth's ionosphere. The modeling of the ionosphere under solar flares are motivated by new observations with spacecrafts, satellites, and ground-based measurements. The estimation of modeling parameters for the ionospheric D-region during SF events poses a significant challenge, typically requiring a trial-and-error approach. This research presents a machine learning (ML) methodology for modeling the sharpness (β) and reflection height ($H'$) during SF events occurred from 2008 to 2017. The research methodology was divided into two separate approaches: an instance-based approach, which involved obtaining SF parameters during the peak SF, and a time-series approach, which involved analyzing time-series data during SFs. The findings of the study revealed that the model for the instance-based approach exhibited mean absolute percentage error (MAPE) values of 9.1% for the β parameter and 2.45% for the $H'$ parameter. The findings from the time-series approach indicated that the model exhibited lower error rates compared to the instance-based approach. However, it was observed that the model demonstrated an increase in β residuals as the predicted β increased, whereas the opposite trend was observed for the $H'$ parameter. The main goal of the research is to develop an easy-to-use method that provides ionospheric parameters utilizing ML, which can be refined with additional and novel data as well as other techniques for data pre-processing and other algorithms. The proposed method and the utilized workflow and datasets are available at GitHub.

**Keywords:** regression; kernel density estimation; solar flares; ionospheric data; ionospheric parameters modeling



**Citation:** Arnaut, F.; Kolarski, A.; Srećković, V.A.; Mijić, Z. Ionospheric Response on Solar Flares through Machine Learning Modeling. *Universe* **2023**, *9*, 474. https://doi.org/10.3390/universe9110474

Academic Editor: Vladislav Demyanov

Received: 5 October 2023
Revised: 2 November 2023
Accepted: 3 November 2023
Published: 7 November 2023



## 1. Introduction

The low ionosphere, located between approx. 50 and 90 km above the Earth's surface [1], varies in ionization with the solar flow [2] and displays the effects of solar flares (SF) [3–5]. Crucial for its modeling, the ionosphere parameters are directly/indirectly measured with sounding rockets, which offer a single measuring point [6] and are associated with high operational costs [7–9]. Consequently, the utilization of the very low frequency (VLF) approach is commonly employed [10,11]. Usually, both the VLF signal's amplitude and phase display the impacts of SF occurrences that follow X-ray flux, in most cases often seen as increased values during such events, but with patterns highly influenced with VLF trace geometry [11–14]. The D-region of the ionosphere is defined by two parameters: sharpness (β) in $km^{-1}$ and reflection height ($H'$) in km [15], also known as Wait's parameters or waveguide ionospheric parameters. The electron density (ED) may be computed for both undisturbed and disturbed ionospheric conditions using an equation displayed by Wait and Spies [16]. Typically, the estimation of the ionospheric parameters is performed by the utilization of the Long Wavelength Propagation Capability (LWPC) software LWPC. Computer Programs for Assessment of Long-Wavelength Radio

Communications, V2.1. Available online: https://github.com/space-physics/LWPC (accessed on 2 February 2023). [17], which is a challenging task due to the complex nature of ionospheric modeling during disturbances, especially related to SF events of extreme intensity [18]. Figure 1 gives an example of one such energetic event, i.e., X17.2 SF that occurred on 28 October 2003 with peak soft X-ray Irradiance at 11:10UT, third in strength within the entire 23rd solar cycle. The response of the mid-latitude lower ionosphere over the Balkan region to this energetic SF, as recorded by BEL VLF station in Belgrade (Serbia), is given in Figure 2, together with the modeling results of the obtained electron density estimated by the use of a numerical procedure developed by Srećković et al. [19], relying on approximate equations for obtaining ionospheric parameters directly from measured X-ray data. In many cases of intense SFs, obtaining lower ionospheric response based on VLF signal technology indirectly from amplitude and phase perturbations of monitored VLF signals through classical approach using LWPC software can be problematic due to many factors, in first line including model limitations/restrictions and factors related to the geometry of Great Circle Paths of VLF signals. So, developing new approaches for retrieving necessary data for estimation of electron density profiles during such extreme events is of great importance.

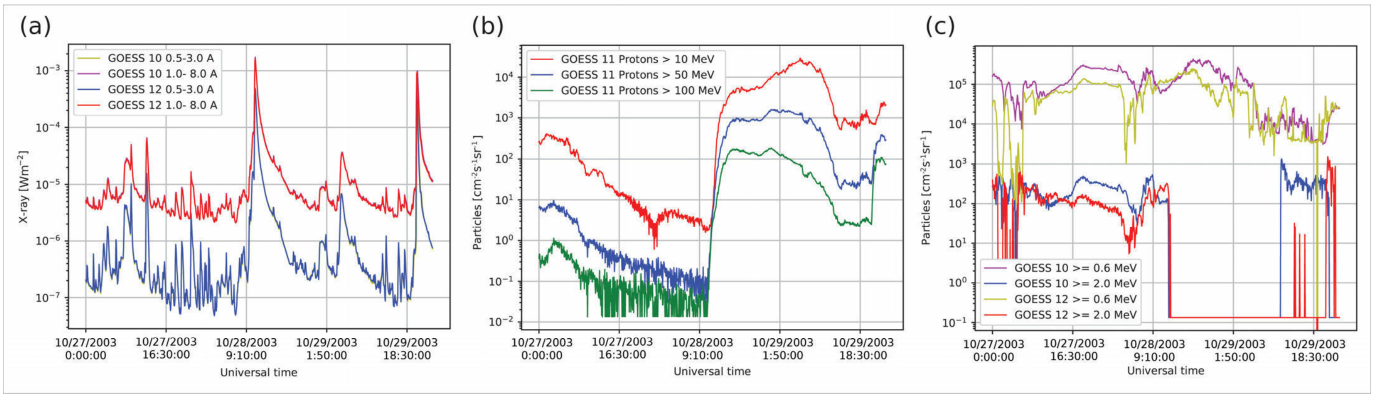


**Figure 1.** Measured data from GOES satellites for period 27–29 October 2003: variation in X-ray flux (**a**), proton flux (**b**), and electron flux (**c**) (data available at https://www.ncei.noaa.gov/data/goes-space-environment-monitor/access/avg, accessed: 2 February 2023).

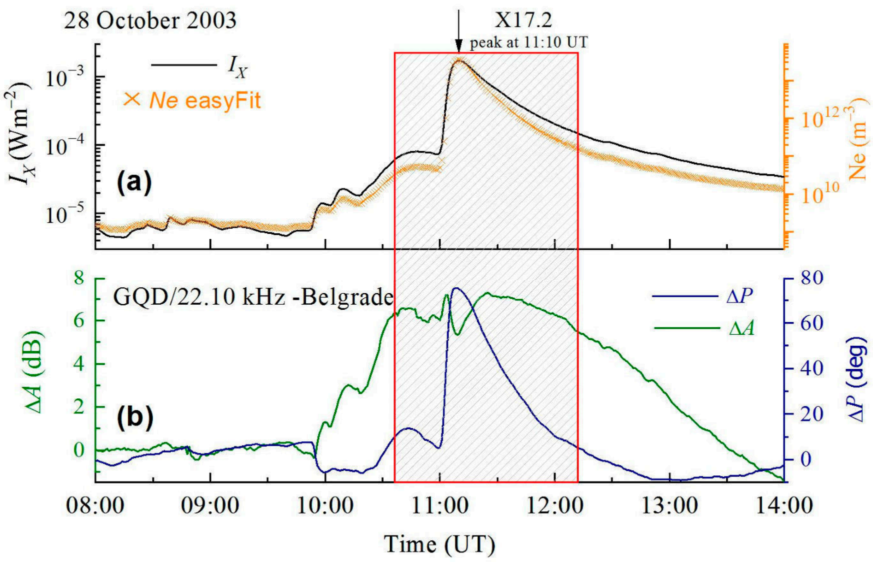


**Figure 2.** (**a**) Variation in X-ray flux from GOES-15 satellite (solid black line) and corresponding electron density (red crosses) at a reference height of 74 km versus universal time on 28 October 2003

during an extreme event of X17.2 class SF, obtained through the numerical procedure presented in Srećković et al. [20], (**b**) GQD signal amplitude and phase perturbations induced by X17.2 class SF, as recorded in Belgrade (Serbia).

Previous research has examined the estimation of ionospheric parameters by employing artificial neural networks (ANNs) and utilizing synthetic data created using the LWPC software [21]. Furthermore, Alpatov et al. [22] demonstrated that the inherent characteristics of the ionosphere necessitate the utilization of statistical and probabilistic approaches for effective ionospheric modeling. Gross and Cohen [21] developed an ANN target function that was designed to accept a single time-step of VLF amplitude and phase as the input and generate the waveguide parameters as the output. Subsequent research revealed that the model underwent expansion to encompass nighttime conditions [23]. In relation to the use of ANNs, the tuning of several hyperparameters, such as the number of epochs, learning rate, number of hidden layers, and number of nodes per hidden layer, presents challenges in the process of fine-tuning and renders them more vulnerable to overfitting. In this study, the primary focus will not be on ANNs. Instead, attention will be directed on comparatively simpler yet still-efficient ML models.

The research objectives have been divided into two distinct components. The initial step involves assessing the feasibility of deploying an ML model for the accurate prediction of β and $H'$ parameters. The primary objective can be categorized into two distinct methods: the instance-based approach and the time-series approach. In the instance-based approach, a specific set of features, such as X-ray irradiance, SF class, amplitude changes ($\Delta A$), and phase shifts ($\Delta P$), are utilized to effectively provide input to a ML regression model to determine the peak SF effect on waveguide parameters. On the other hand, the time-series approach involves training the model using a limited number of days' worth of X-ray irradiance and statistical data derived from X-ray irradiance. Afterwards, the model is tested on subsequent days to forecast waveguide parameters, i.e., to continuously determine waveguide parameters as a time-series. The secondary aim of this study is to determine the need for utilizing oversampling techniques with a post hoc analysis of oversampling. The advantages of employing an ML technique for the estimation of ionospheric parameters are evident in the (computationally) time consuming process involved in the LWPC modeling of those parameters. Four frequently employed ML algorithms are employed, namely, Random Forest (RF), Decision Tree (DT), K-nearest neighbors (KNN), and XGBoost (XGB). The datasets used in this study, along with certain components of the workflow, are available for access on GitHub (see Supplementary Material).

As ionospheric research focuses on radio signal propagation and influences on the great diversity of space-borne and ground-based technological systems [24–27], the overall aim of this study is to provide an alternative approach allowing the wider scientific community to obtain crucial ionospheric parameters being affected by SFs, promptly and efficiently. As existing and standard methods to determine ionospheric parameters are based on a trial-and-error process, e.g., the method presented in [17], there is a need to develop other methods to determine the β and $H'$ like easyFit [19] and FlareED [20]. Our aim is to develop a user-friendly method that can be refined with new data, other pre-processing techniques, and algorithms, etc. In future research, if the ML method provides satisfactory accuracy and stability, we can compare the ML method with the aforementioned methods (e.g., under different SF classes, etc.).

## 2. Materials and Methods

The research methodology was divided into two parts. The first part involved an instance-based approach, where instances of SF peaks and their associated features (such as $\Delta P$, $\Delta A$, X-ray irradiance, etc.) were provided. Based on these features, waveguide parameters were to be determined using ML techniques. The second methodology employed in this study involved the utilization of a time-series approach. Specifically, a time-series dataset of X-ray irradiance was provided, and various statistical features were computed based on the X-ray irradiance values. The determination of waveguide parameters was conducted using an ML model, based on the aforementioned features.

### 2.1. Instance-Based Approach

The data analysis initiated with the utilization of the original dataset, which contained 212 unique observations conducted throughout the course of various SF's. The initial dataset was utilized to generate synthetic data points in subsequent stages of the workflow. However, the validation data, consisting of an extra 45 data points, was excluded from the original dataset prior to the pre-processing phase (Figure 3). The initial dataset included observations pertaining to the X-ray irradiance, the difference between the amplitude and phase of the VLF signal, and the ionospheric parameters namely. The initial data cleaning process involved randomizing the data to obtain a representative sample and transforming the X-ray irradiance to assure accurate Kernel Density Estimation (KDE) without any errors, and subsequent de-transformation was performed before the ML modeling.


**Figure 3.** Data preparation, synthetic data preparation, and machine learning modeling workflow.

The KDE serves as the initial stage in the synthetic data preparation procedure, aiming to generate a more extensive collection of samples (in this case, 5000) to facilitate the training of the ML model. The KDE method is utilized to estimate the underlying distribution of the original data. Subsequently, multiple samples are generated from this estimated distribution, therefore producing an increased number of samples. In order to verify the accuracy of the KDE's estimation and sampling from the original data distribution, it is necessary to incorporate two more stages. This involves employing the Kolmogorov–

Smirnov test (KST), a non-parametric statistical test used to assess whether two datasets follow the same distributions [28]. The interpretation of the findings of the KST involves the evaluation of the $p$-value. If the $p$-value exceeds the predetermined significance level of 0.05, it is not possible to reject the null hypothesis, i.e., the two datasets originate from the same distribution, and vice versa [29]. The second stage validating the KDE involves doing a visual and statistical examination. This entails visualizing the distributions of both the original and synthetic data for all features and target variables, as well as calculating and comparing various statistical metrics such as the mean, median, mode, skewness, and kurtosis, etc.

If the results of the preceding statistical analysis are deemed to be valid, then the initial stage in data preparation for ML involves feature extraction. Feature extraction, also known as feature discovery, is a procedure in ML that involves adding to a dataset additional feature(s). This is performed with the objective of increasing the number of features available, hence potentially enhancing the performance of the ML model. In this particular instance, the sole addition made was the inclusion of the SF class, wherein solely the alphabetical component of the SF class (B, C, M, or X) was retained and afterwards converted into a numerical representation (e.g., 1, 2, 3, or 4).

The synthetic data for training and the original data for testing were used as inputs to the ML modeling process. Four distinct algorithms were employed in this study, namely, Random Forest (RF) [30], Decision Tree (DT) [31], K-nearest neighbors (KNN) [32,33], and XGBoost (XGB) [34]. With the exception of the DT algorithm, each of the algorithms applied in this study required the tuning of at least one hyperparameter (RF and KNN) or two hyperparameters (XGB). The hyperparameter that determines the performance of the RF model is the number of trees. Additionally, the number of trees is also a hyperparameter for the XGB algorithm. On the other hand, for the KNN algorithm, the hyperparameter is the value of K, i.e., the number of nearest neighbors. The XGB method has an extra hyperparameter known as the learning rate (LR). The hyperparameter values used for the algorithms employed are presented in Figure 3.

The outputs generated by all models were employed in order to choose the most optimal model, as determined by the mean and maximum percentage errors computed on the testing dataset. Following the selection of the optimal model based on the in-distribution training and testing, model validation was performed using the validation data, and, subsequently, an error analysis was carried out.

One noteworthy aspect of this study is the inclusion of an extra target variable. Unlike conventional regression or classification models that include $n$ features and a single target variable, this research incorporates two output variables, namely, ionospheric parameters (β and $H'$), as seen in Figure 4. The utilized methods incorporate SF class, $\Delta P$, $\Delta A$, and X-ray irradiance as their respective features, whereas the output parameters are waveguide parameters.

The evaluation metrics employed in this study to distinguish between models, specifically to determine which model performs better, are the mean absolute percentage error (MAPE) and the maximum absolute percentage error observed over all occurrences of the testing or validation datasets. Furthermore, the model's outputs may be further analyzed by displaying absolute errors, visual representations of predicted and true observations, etc.

### 2.2. Time-Series Approach

The time-series based approach necessitated minimal data pre-processing, specifically in terms of data cleaning and feature extraction, with the utilization of statistical features. The time-series based approach employed a methodology that closely resembled the instance-based approach. In this approach, the modeling process utilized the best model and (hyper)parameters determined from the instance-based approach. The dissemination of results exhibited similarities to the instance-based approach.

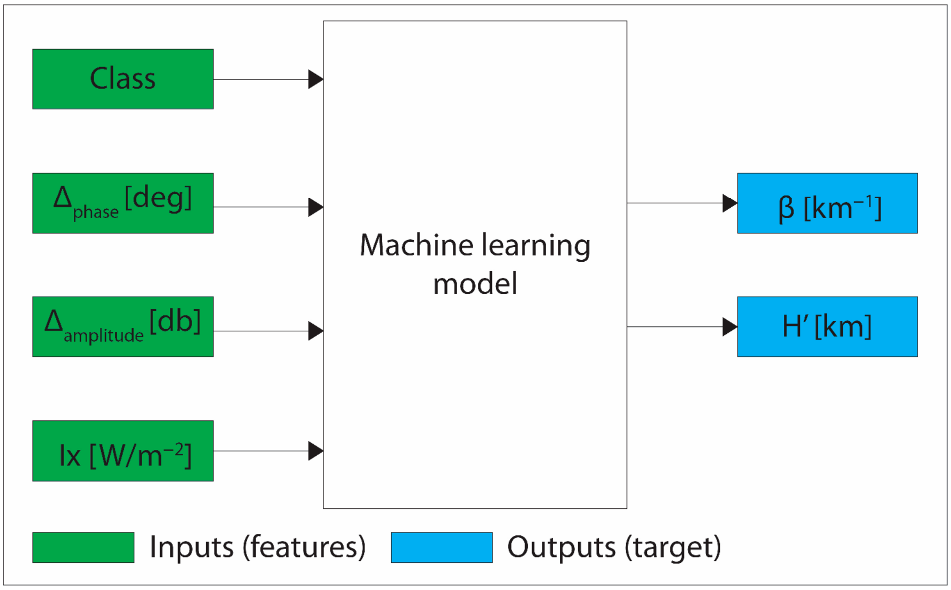


**Figure 4.** Diagram of features and targets for multi-output machine learning modeling.

## 3. Results and Discussion

### *3.1. Instance-Based Approach*

#### 3.1.1. Data Pre-Processing

The original dataset comprises 212 data points representing SF events from 2008 to 2017. Each data point includes the recorded time of measurement, transmitter information, X-ray irradiance, $\Delta A$ and $\Delta P$, ionospheric parameters, and the corresponding computed electron density. The validation dataset, initially removed from the original dataset and subsequently excluded from any subsequent analysis, was exclusively employed for model validation. It comprises 45 data points collected between 2004 and 2017, with a notable concentration of data points occurring during the periods of 2004–2006 and 2014–2017.

The comparison of SF intensities between the initial dataset used for ML model testing and the validation dataset reveals the distribution of each class of SF as a percentage. In the initial dataset, a small proportion of SFs belong to the X-class, specifically accounting for 1.89% (four occurrences). Conversely, in the validation dataset, this number significantly increases to 20% (nine instances). Similar observations can be made about the M-class SFs in the datasets. Approximately 18% (38 occurrences) of the original dataset consist of M-class SFs, but the validation dataset exhibits an almost doubled percentage of 35.56% (16 instances). The proportion of C-class SFs is larger in the original dataset (79%, 169 instances) compared to the validation dataset (42%, 19 instances). Ultimately, the B-class SFs in both datasets exhibit a similar level of outcomes, with a prevalence of 0.47% in the original dataset and 2.22% in the validation dataset. It is worth noting that both datasets contain only a single occurrence of B-class SFs.

The allocation of classes within the original dataset, specifically the testing and validation subsets, was conducted in a deliberate manner to ensure that the model undergoes initial testing with a distribution that is known and expected to yield higher performance. This approach allows for the selection of the most optimal model based on the original testing dataset. The aforementioned best model will then undergo further testing, using an unfamiliar distribution, i.e., the validation dataset. As a result, the evaluation metrics obtained from the validation dataset will accurately reflect the model's predictive performance.

The output of the KDE is a synthetic dataset that is drawn from the identical distribution as the original dataset, however, with an increased number of data points, namely, 5000 in this instance. The verification of the KDE was conducted using the KST. The results of the KST test demonstrated that the original dataset and the synthetic dataset exhibited similar distributions for all five parameters, namely, X-ray irradiance, $\Delta A$, $\Delta P$, β, and $H'$. Further examination was conducted by visually inspecting and comparing the two distributions (Figure 5).

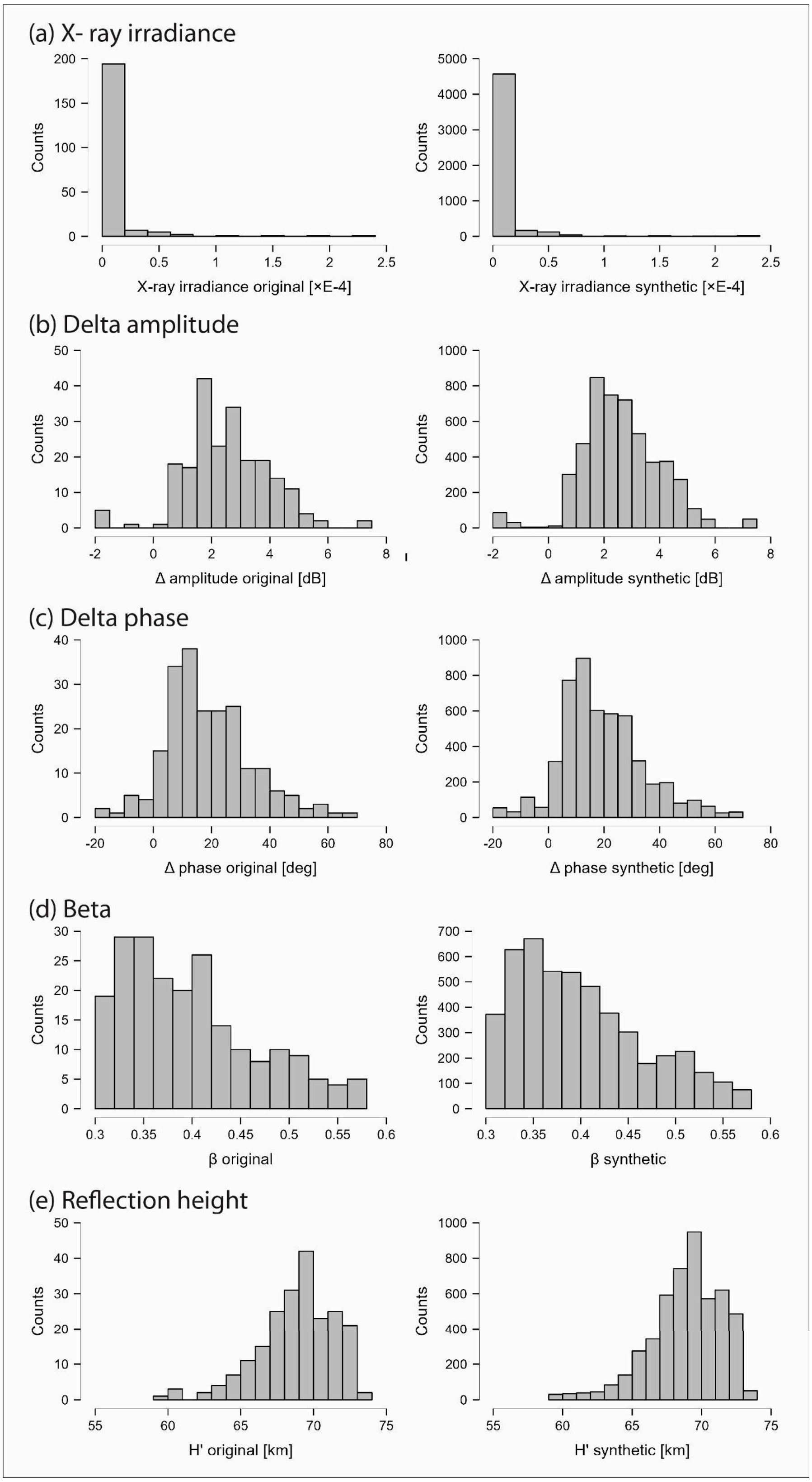


**Figure 5.** Comparison of original and synthetic data distributions for all features and targets for machine learning modeling.

Based on the analysis of Figure 5, it is apparent that all synthetic distributions exhibit a high degree of resemblance to the original distributions. The X-ray irradiance distribution in the original dataset had a pronounced skewness, with a tail extending towards positive values. As a result, the synthetic data also display a similar characteristic, with a severely skewed distribution towards positive values. This can also be expressed by using the skewness and kurtosis parameters. In the case of the original data, these parameters assume values of 6.178 and 42.932, respectively. Conversely, for the synthetic data distribution, the corresponding values are 6.22 and 42.622. These values, along with the KST, the visualization of the distribution, further confirm the efficacy of the KDE and the validity of the generated samples. A parallel analysis may be conducted on the target variables, such as the β parameter. In the original distribution, the mean value is 0.401, which is consistent with the value seen in the synthetic distribution. The median values for the original and synthetic distributions exhibit a little disparity, namely, 0.383 and 0.386, respectively. The $H'$ parameter exhibits comparable mean and median values between the original and synthetic distributions, which highlights that the synthetic data have been generated correctly.

Following the successful application of data oversampling techniques, the training dataset, i.e., the oversampled dataset, was prepared. Additionally, the testing dataset, which consists of the original, non-oversampled, measured data, and the validation dataset, comprising out-of-sample, measured data that was not utilized in the data pre-processing phase, were also finalized. These datasets were then employed for the purpose of ML modeling.

### 3.1.2. Initial Phase of Machine Learning Modeling

The first iteration of ML modeling involved the utilization of four distinct algorithms (RF, DT, KNN, and XGB). In all, a set of 16 models were created and evaluated. The evaluation metrics (MAPE) for both target variables is presented in Figure 6, with the upper panel representing the β parameter, and the lower panel representing the $H'$ parameter. Based on Figure 6, it is apparent that the algorithms DT and KNN, throughout all iterations, may be disregarded since they exhibit greater MAPE values compared to RF and XGB. On the other hand, both RF models and XGB models exhibit relatively comparable MAPE values. The RF models have constant MAPE values for both target variables. Consequently, additional analysis may be conducted to identify the most optimal RF model for exclusion. The model with 250 trees was selected as the optimal RF model across all iterations, based on the maximal percentage error observed for both target variables (11.5% for β and 1.1% for $H'$). In the initial round of modeling, the XGB model with 150 trees was identified as the most optimal choice. This particular model exhibited MAPE values of about 0.8 and 0.029% for the respective target variables. It is important to emphasize that the MAPE values should be interpreted cautiously due to the fact that the model was evaluated using the original dataset (in-sample model evaluation). When applying the model to new data (out-of-sample validation data), it is likely that the MAPE values will be higher. However, the purpose of this modeling is to identify the best overall model.

The XGB method was employed for the second stage of modeling because of the inclusion of an extra hyperparameter, specifically the LR. The XGB additional modeling was conducted using a predetermined number of trees (150) and a varying LR value ranging from 0.1 to 0.5, with increments of 0.1. A comparison was conducted between the optimal XGB model obtained in the initial phase of modeling, characterized by a learning rate of 0.3, and the model derived from the additional phase of XGB modeling, featuring a learning rate of 0.2. The MAPE values indicate that both models exhibit comparable error rates. Specifically, the LR = 0.3 model has MAPE values of 0.8 and 0.029 for β and $H'$, whereas the LR = 0.2 model shows MAPE values of 0.71 and 0.033 for β and $H'$, respectively. In contrast, there is a disparity in the maximal percentage error values between the LR = 0.3 model, which exhibits a maximal percentage value of 4.6% for the β parameter, and the LR = 0.2 model, which demonstrates a maximal percentage value of 3.29% for the same parameter. The XGB model with 150 trees and a LR value of 0.2 was selected as the optimal model, both within the XGB models and in comparison to the other models. A comparison was conducted between the optimal XGB model and the optimal RF model, revealing disparities in both the MAPE and the maximal percentage error. Specifically, the RF model exhibited maximal percentage errors of 11% for the β value, whereas the XGB model demonstrated values of 3%. This distinction was crucial in finding the most optimal model overall.

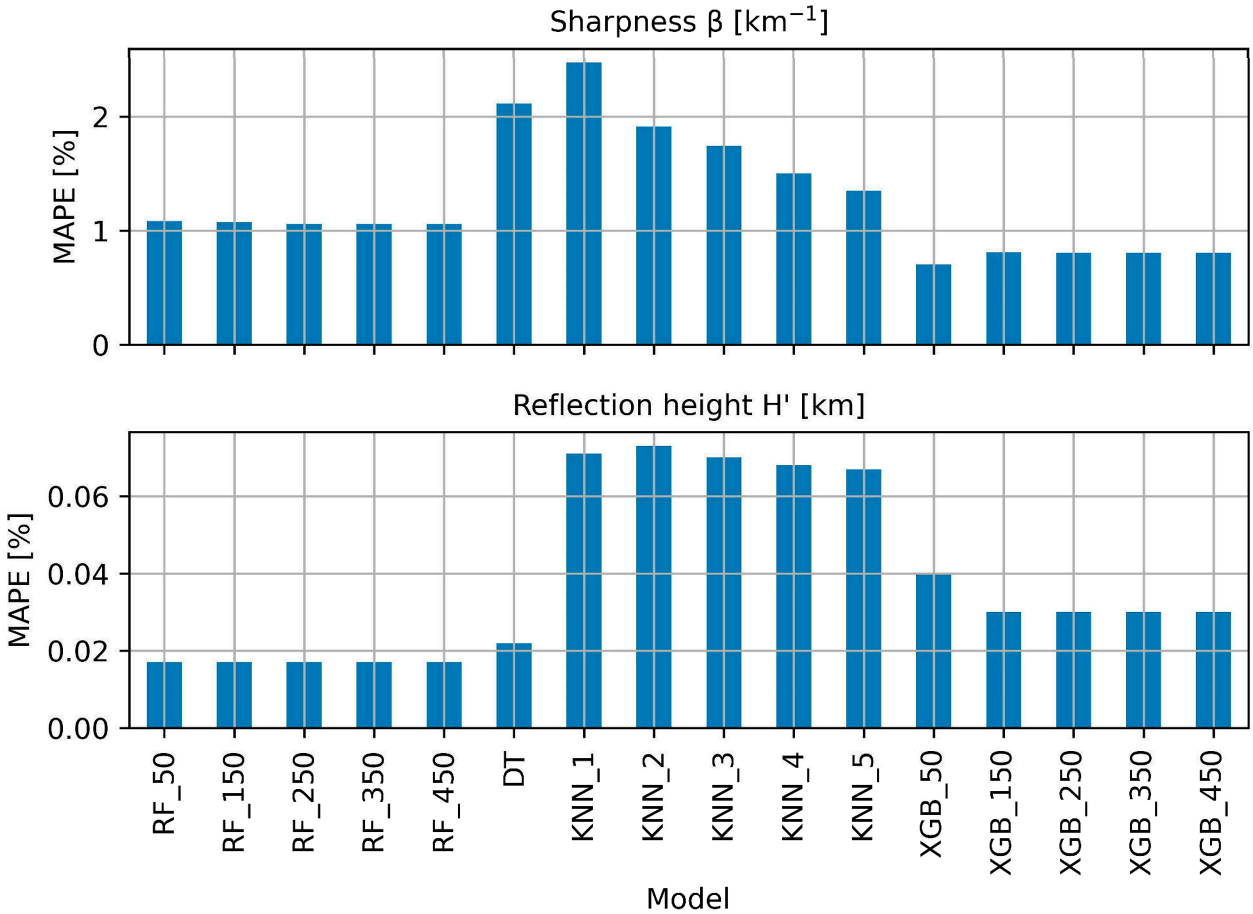


**Figure 6.** Mean absolute percentage errors for sharpness (**upper** panel) and reflection height (**lower** panel) for the initial phase of modeling; MAPE—Mean absolute percentage error; RF—Random Forest; DT—Decision tree; KNN—K-nearest neighbors; XGB—XGBoost; Adjacent number to model names (50–450 or 1–5) is the hyperparameter for the given model.

### 3.1.3. Model Validation

The process of model validation involved the utilization of an out-of-sample dataset that was initially omitted from the original dataset at the beginning of the analysis. MAPE values for both β and $H'$ exhibit greater values compared to the training dataset, as anticipated, with values of 9.1% and 2.45%, respectively. The maximum percentage error values for both parameters are around 38.8% and 12.2%, respectively. Figure 7 presents the error distribution for the parameters, denoted as Figure 7a,b, as well as the error distribution for the averaged error (Figure 7c), which is calculated as the average of both percentage errors.

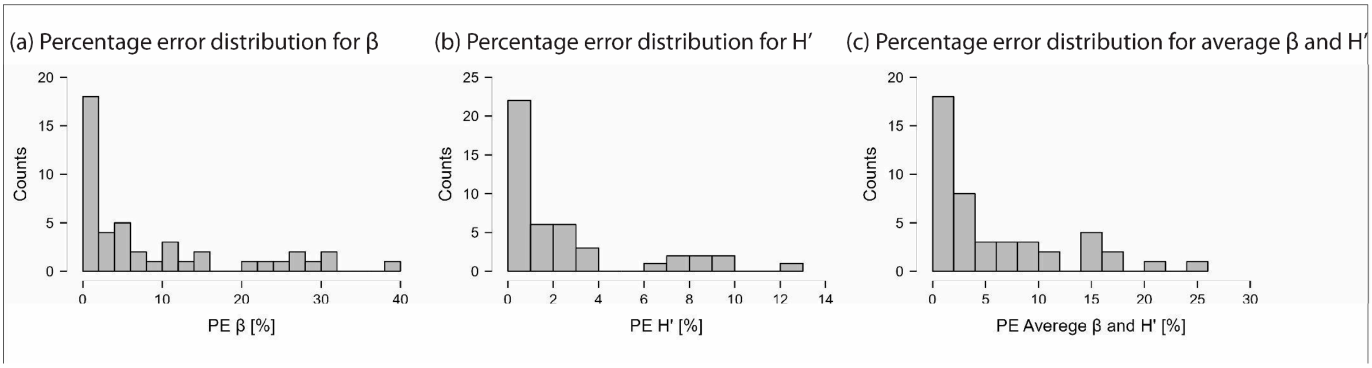


**Figure 7.** Model validation mean absolute percentage error distributions. (**a**) Sharpness; (**b**) Reflection height; (**c**) Averaged mean absolute percentage error for sharpness and reflection height; PE—Percentage error.

It is worth mentioning that the distributions for β and $H'$ exhibit a pronounced skew towards higher values, indicating that a majority of the values correspond to lower error rates. Approximately 66% of the data points pertaining to the β parameter exhibit a percentage error below 10%, whereas approximately 55% of the data points exhibit a percentage error below 5%. In contrast, it can be observed that around 97% of the data points exhibit an error rate of less than 10% for the $H'$ parameter, whereas 82% of the data points have error rates below 5%. This suggests that the MAPE is significantly impacted by a small number of high percentage errors. This observation is supported by the fact that there are nine occurrences where the percentage error values for β exceed 20%, and three cases where they exceed 30%. In contrast, the $H'$ parameter exhibits a single outlier, namely, the outlier characterized by a percentage inaccuracy of over 12%. This indicates that the model can produce relatively satisfactory β and $H'$ values, with the exception of a few significantly exaggerated errors, especially in the β parameter case. It is important to acknowledge the absolute range of errors generated by this method (MAE). The MAE for the β value is around 0.039 km$^{-1}$, whereas, for the $H'$ value, the MAE is around 1.64 km.

Further model validation may be conducted by visually analyzing the predicted and real data for both parameters, as seen in Figure 8. Linear fit line was used to construct a line of best fit across the predicted and observed data. The coefficient of determination (CD) for the β parameter was about 0.67, whereas, for the $H'$ parameter, the fit was greater at 0.8. The CD had values that were reasonably satisfactory. Significant outlier data points are evident in both cases. For instance, a notable outlier for the β parameter is observed (upper panel on Figure 8, green rectangle), where the predicted value was about 0.38 km$^{-1}$, whereas the real value was approximately 0.53 km$^{-1}$, resulting in an error rate of almost 28%. The observed data point can be associated with a C4.8 SF event, characterized by a very modest $\Delta A$ of around 0.06 dB, whereas the $\Delta P$ measured around 26 degrees. In the given case, the $H'$ parameter exhibited a minimal percentage error of 0.82%, with a true value of 70 km and a predicted value of 70.6 km. Another noteworthy example is observed in the lower section of Figure 8 (green rectangle), where a C9.6 SF yielded a $\Delta A$ measurement of 5.13 dB and a $\Delta P$ measurement of 50.04 degrees. The predicted value was 61.4 km, whereas the actual value was 70 km. In a prior case, there was an incorrect prediction of the β parameter, but the $H'$ parameter was predicted with a significantly low error rate. In the current circumstance, we observe a similar scenario where the β parameter was predicted with a minimal error rate of 1.2% (0.57 km$^{-1}$ reality against 0.563 km$^{-1}$ predicted).

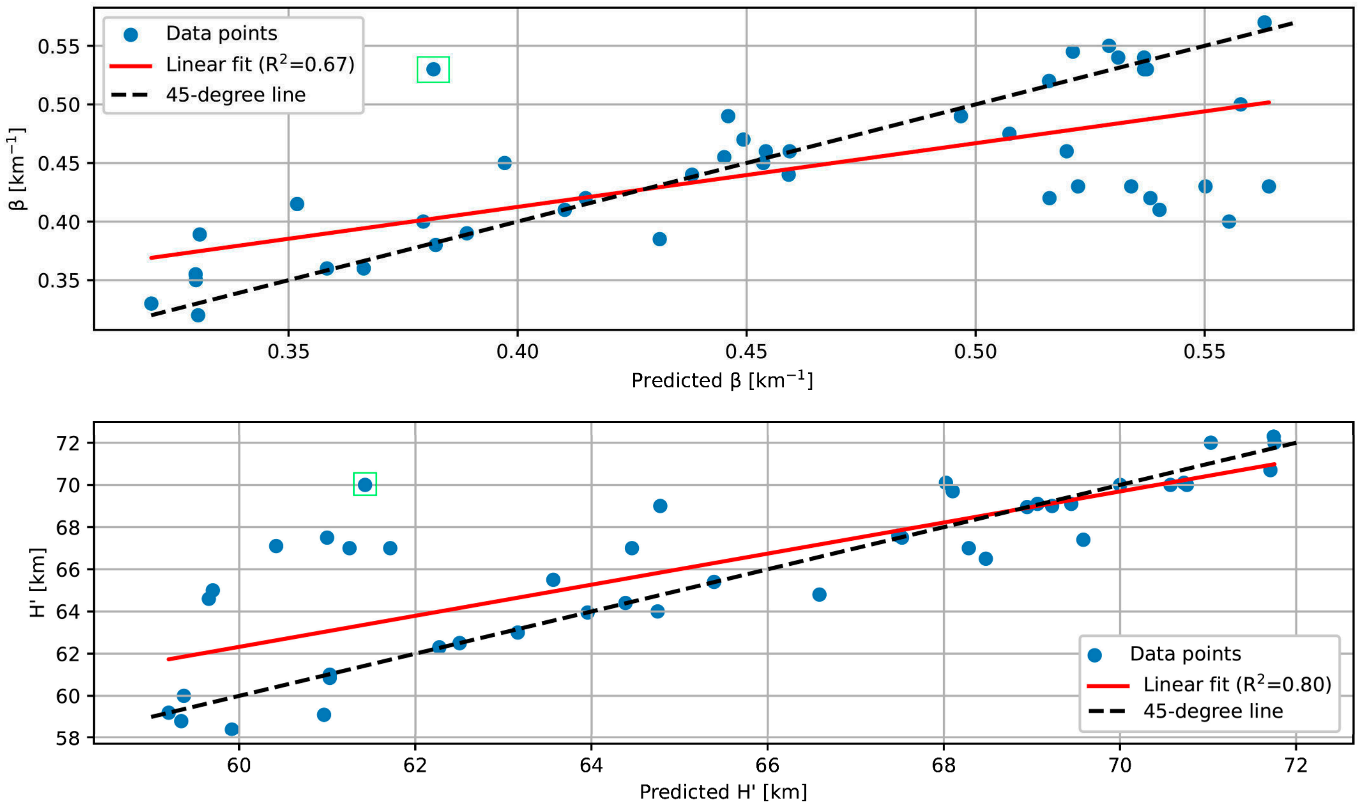


**Figure 8.** Predicted and observed value for sharpness (**upper** panel) and reflection height (**lower** panel) for the instance-based approach.

The inclusion of a residuals plot in conjunction with the predicted β and $H'$ values provide valuable insights into the predictive performance of the model (Figure 9). Specifically, the upper panel of Figure 9 which represents the residuals plot of the β parameter, does not exhibit any noticeable pattern, as well as the residual distribution is a normal distribution. Most of the residuals are concentrated within the range of −0.05 to 0.05 km$^{-1}$, with the largest outlier being the previously mentioned discrepancy of 0.14 km$^{-1}$, which is associated with a C4.8 SF. In contrast, the residuals plot for the $H'$ parameter exhibits a discernible pattern that aligns with a decrease in residuals as the predicted $H'$ parameter increases. The lower panel of Figure 9 reveals that the predicted value of 62 km and beyond exhibit residuals within the range of −2 to 2 km. However, before these values, the residuals are greater, ranging from −4 to 6 km. This suggests that the model's predictions of the $H'$ parameter over 62 km (with the exception of two cases) are associated with reduced error rates compared to its predictions of $H'$ values below 62 km. This observation is further substantiated by examining the average percentage error rates for predictions made below 62 km and those made beyond 62 km. The MAPE for predictions above 62 km is around 1.23%, but predictions below 62 km exhibit a greater MAPE value at 5.15%.

The XGB model exhibited a minor bias in its predictions of $H'$ parameters above a certain threshold value of 62 km. It is important to acknowledge, for future studies employing a similar methodology, that there exists a possible association between the SF class and the predicted $H'$ parameter. Specifically, among all the predictions in the validation dataset that are below 62 km, 8 out of 9 X-class solar flares are shown to have predictive values of $H'$ below 62 km. The observation can be understood as the model exhibiting elevated error rates when predicting ionospheric parameters on X-class SFs. This observation is supported by the fact that the validation dataset contains a significantly higher proportion of X-class SFs (20%) compared to the testing dataset (1.89%). The primary objective of the validation dataset was to serve as an out-of-sample test for the model, in which the original distribution of the SF classes is not present. In this regard, the validation dataset proved to be effective in achieving its intended purpose. The possible bias shown in this research might be mitigated by increasing the number of original samples and refraining from employing an oversampling approach.

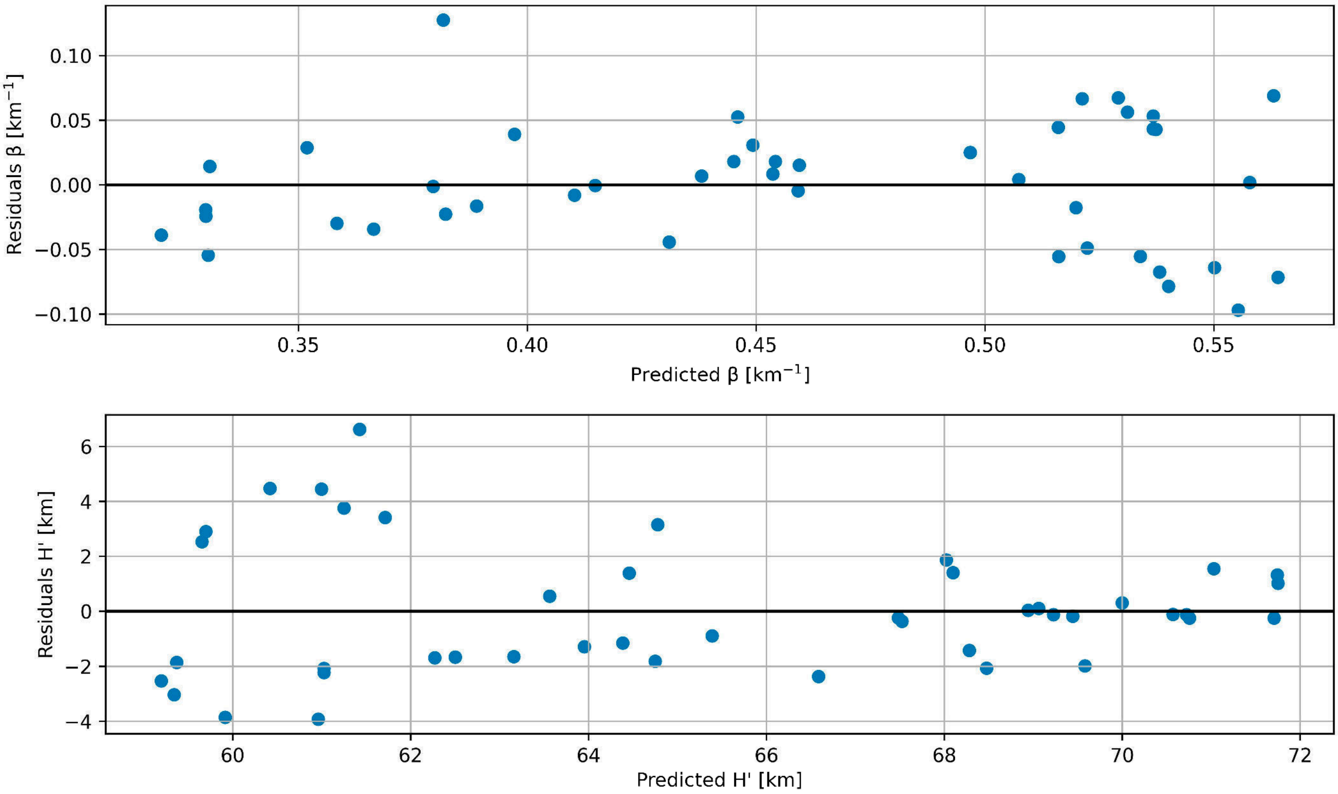


**Figure 9.** Residual and predicted plot for sharpness (**upper** panel) and reflection height (**lower** panel) for the instance-based approach.

A potential alternative approach, while hardly employed, is the balanced distribution of SF class features, ensuring an equal representation of X-, M-, and C-class SFs. The utilization of class balancing approaches in ML regression is not commonly employed, as these techniques are often utilized in ML classification tasks and are applied to the target variable. However, it may be worthwhile to investigate this approach further in future research, as the outcomes have the potential to alleviate potential model bias.

### 3.1.4. Post Hoc Analysis of the Sample Size

In ML tasks, the determination of the optimal number of samples is a challenging problem that often requires the researcher to engage in iterative experimentation. When granted permission, the collection of additional samples becomes advantageous until a specific threshold is reached, beyond which enlarging the sample size does not result in a reduction in the associated model error rate. In this study, we choose to augment the original dataset by oversampling through the utilization of KDE. This approach allows us to preserve the original data distribution while simultaneously expanding the sample size. The efficacy of the KDE approach was confirmed, and the oversampling technique yielded positive results. However, it would be advantageous for future research to conduct a concise assessment of the necessity for oversampling.

The test was conducted using both the original dataset and a synthetic dataset that shared the same distribution as the original. The datasets located between the original dataset and the synthetic dataset were acquired using the Random Undersampling (RUS) technique [35]. Afterwards, the KST was conducted to assess if these datasets exhibited the same distribution as the original dataset. The intermediate datasets were generated to represent various proportions of the synthetic dataset (e.g., 10%, 20%, etc.). The XGB method was employed for the modeling process, employing 150 trees and a LR value of 0.2. This LR value and the number of trees was previously established to be the optimal choice for the modeling process. The findings of the post hoc examination of the sample size are presented in Table 1.

**Table 1.** Post hoc analysis results for the sample size; MAPE—Mean absolute percentage error; PE—Percentage error; KST—Kolmogorov–Smirnov test; RUS—Random undersampling; T—True (passed the KST); NA—Not applicable.

| **Percentage of Synthetic Data** | **β (km$^{-1}$)** | | **$H'$ (km)** | | **Note** | **KST** |
|---|---|---|---|---|---|---|
| | **MAPE (%)** | **Max PE (%)** | **MAPE (%)** | **Max PE (%)** | | |
| 4.24 | 8.46 | 39.58 | 2.28 | 9.70 | Original dataset | NA |
| 10 | 9.24 | 36.45 | 2.36 | 11.38 | RUS | T |
| 20 | 9.61 | 38.57 | 2.45 | 11.52 | RUS | T |
| 30 | 9.94 | 46.13 | 2.52 | 12.17 | RUS | T |
| 40 | 10.39 | 49.20 | 2.44 | 12.31 | RUS | T |
| 50 | 9.13 | 35.78 | 2.48 | 11.91 | RUS | T |
| 60 | 10.07 | 49.05 | 2.54 | 12.01 | RUS | T |
| 70 | 9.28 | 40.48 | 2.31 | 11.82 | RUS | T |
| 80 | 9.04 | 47.01 | 2.64 | 12.61 | RUS | T |
| 90 | 9.47 | 43.95 | 2.35 | 11.08 | RUS | T |
| 100 | 9.08 | 38.83 | 2.46 | 12.25 | Full synthetic data | T |
| Minimum | 8.46 | 35.78 | 2.28 | 9.70 | | |
| Maximum | 10.39 | 49.20 | 2.64 | 12.61 | | |
| Range | 1.94 | 13.42 | 0.36 | 2.91 | | |

The post hoc examination of the sample size reveals that all intermediate samples, which constitute a portion of the synthetic sample, successfully passed the KST, thus they maintained the same distribution as the original and synthetic datasets. Both the β and $H'$ exhibit a MAPE range that is less than 2%, namely, 1.94% for β and 0.36% for $H'$. This suggests that expanding the sample size with the KDE did not result in any improvements for the model in terms of reducing the error rate. However, it is important to note that the highest percentage error for the β parameter does not exhibit the same trend, as it spans a range of 13.42%. Furthermore, the correlation analysis revealed that there was no significant association seen between the rise in the dataset and the decrease in the evaluation metric for both parameters. The observed maximum correlation coefficient was 0.49, indicating the relationship between the percentage of synthetic data and the maximal percentage error of the $H'$ parameter. However, this correlation coefficient does not reach a significant level, i.e., suggesting a lack of strong correlation intensity. Therefore, it may be inferred that the augmentation of the sample size, while preserving the initial distribution, did not confer any notable benefits for the ML model.

The examination of sample size in a post hoc analysis is a crucial aspect for future research, particularly when considering the utilization of oversampling techniques on smaller datasets, such as this one. This specific example demonstrates that even with a sample size of 212 data points from the original dataset, it is possible to attain error rates comparable to those observed with synthetic, oversampled data.

### *3.2. Time-Series Approach*

#### 3.2.1. Data Pre-Processing

The training data consisted of observations from 6 September 2017 to 9 September 2017, whereas the model testing was conducted using data from 10 September measured on a 1 min interval. The utilization of statistical attributes as features for modeling time-series ionospheric VLF data have been demonstrated in the study conducted by Arnaut et al. [36]. Similar statistical features were developed for the present research. Specifically, the characteristics encompassed rolling mean, median, and standard deviation statistics for different window sizes (5, 20, and 60 min). Additionally, it includes the first and second differential of the data and the percentage change between adjacent data points as well as lagged values in 1–5 min intervals. The identical model, specifically XGBoost with 150 trees and a LR of 0.2, was employed in a manner consistent with the instance-based approach.

3.2.2. Machine Learning Modeling for the Time-Series Approach

Figure 10 illustrates the training and testing datasets. Specifically, the training dataset showcases a prominent SF of X9.4 class that transpired on 6 September 2017. The training dataset contains a variety of smaller SF, which contributes to its suitability for training the model. In contrast, the testing dataset also exhibits a prominent SF of X8.2 class, which transpired on 10 September 2017. The objective of time-series-based modeling for β and $H'$ can be described as the determination of waveguide parameters during an extreme SF event, given the availability of a training dataset containing waveguide parameters for training the model. Further support for the utilization of such modeling can be derived from the observed correlation between X-ray irradiance data and both β and $H'$. Specifically, by employing the Spearman correlation coefficient, the correlations between X-ray irradiance and both β and $H'$ are found to be 0.804 and −0.876, respectively. The observed values of the correlation coefficient indicate a significant association between the waveguide parameters and X-ray irradiance, thereby suggesting their appropriateness for utilization in ML modeling.

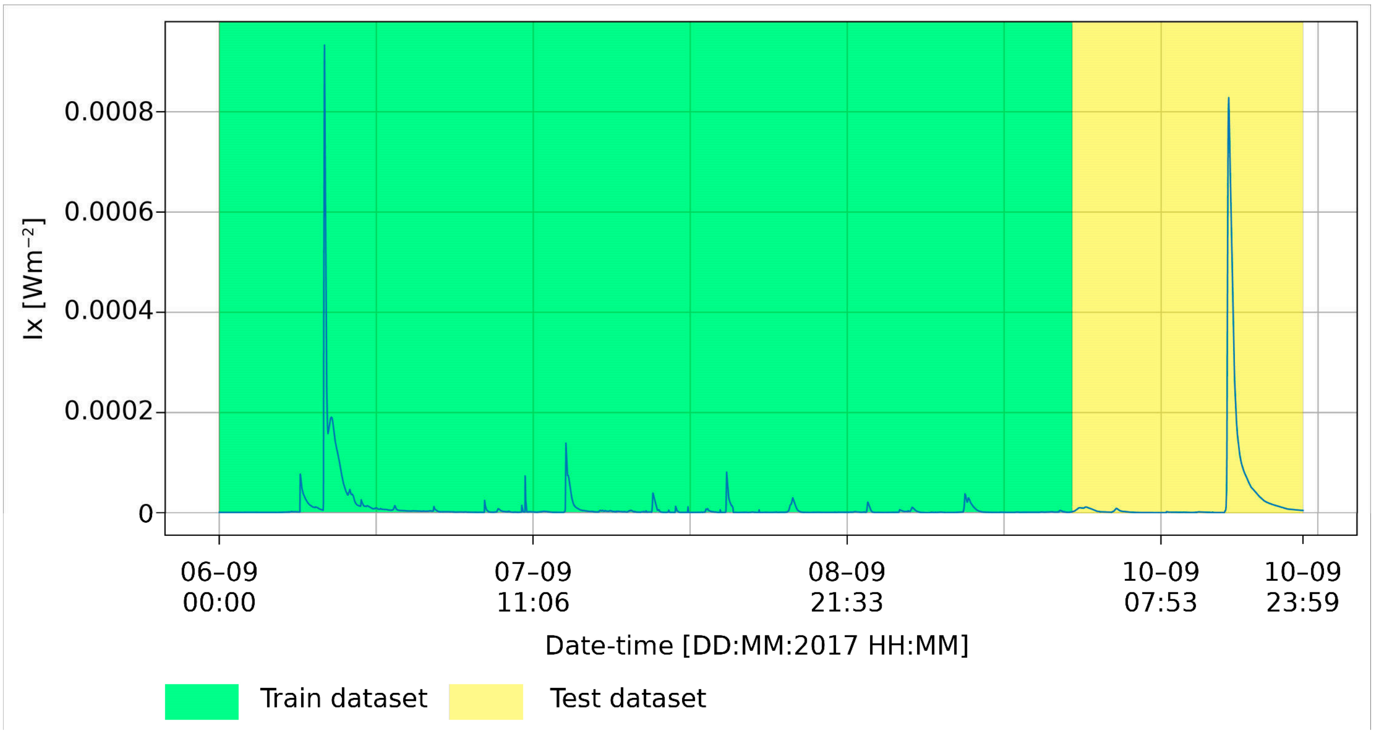


**Figure 10.** The training and testing dataset utilized for ML modeling of β and $H'$.

The outcomes of the modeling demonstrated significantly better results compared to those achieved through the instance-based approach. The MAPE value for the β parameter was 0.1%. Additionally, the maximum percentage error observed was 2.1%, corresponding to a maximum absolute error of 0.01 km$^{-1}$. In contrast, the findings pertaining to the $H'$ parameter reveal a MAPE of 0.04% and a maximum percentage error of 1.2%. The aforementioned values exhibit a correlation with MAE values of 0.02 km and 0.74 km, respectively. Additional analysis was conducted in the time-series based approach, similar to the instance-based approach, to validate the predicted values against the actual values

(Figure 11). The evaluation metrics were validated by comparing the predicted and actual values, with both variables yielding an $R^2$ score close to 1 (i.e., 100%), which signified a highly accurate regression model. In a similar vein, the linear regression analysis conducted on the data substantiated the alignment with the 45-degree line, thereby providing additional evidence of a highly accurate correspondence between the predicted and observed waveguide parameters.

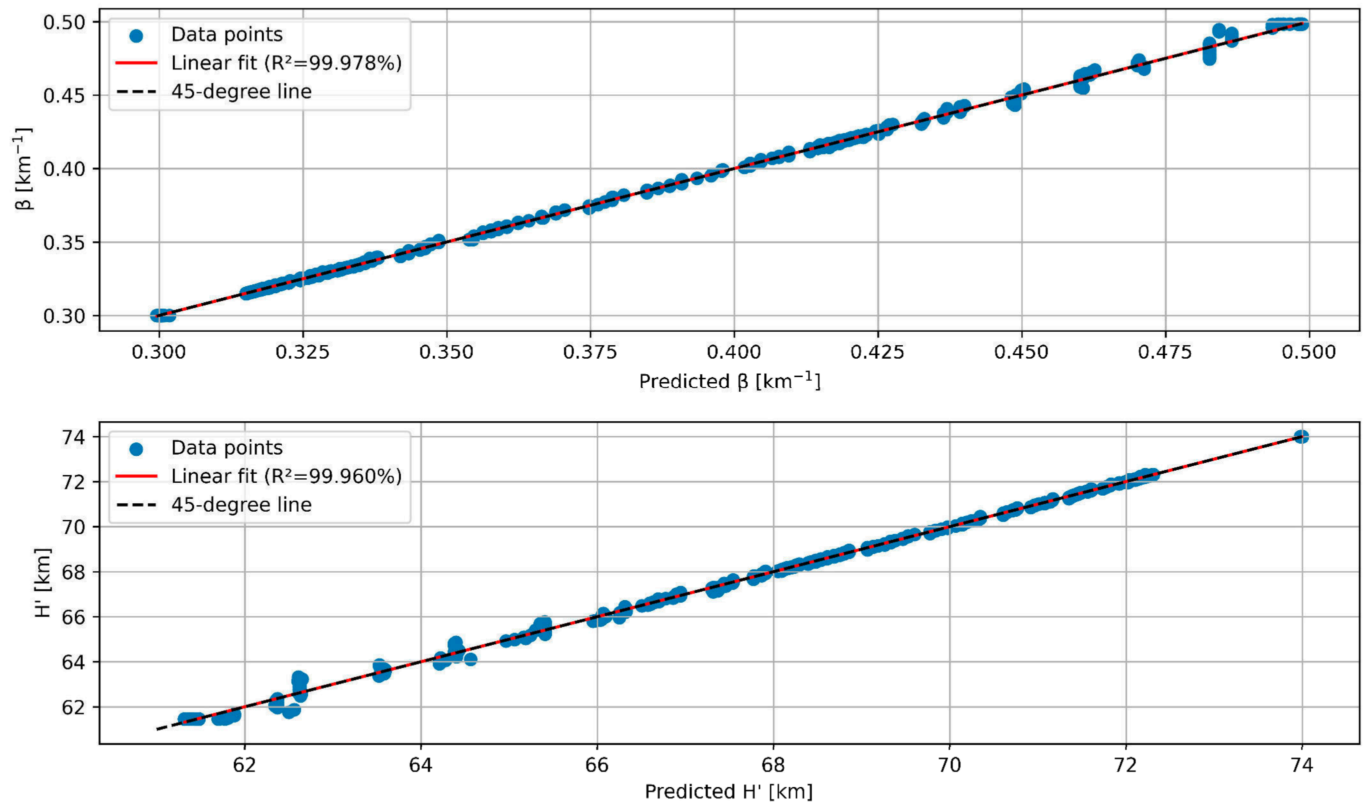


**Figure 11.** Predicted and observed value for sharpness (**upper** panel) and reflection height (**lower** panel) for the time-series approach.

Akin to the previous example involving the instance-based approach, an analysis of residuals was conducted for the time-series approach, as depicted in Figure 12. In contrast to the previous instance of residual analysis, the residuals observed in the time-series approach exhibited pronounced patterns. Specifically, in the upper panel of Figure 12, it is evident that the residuals increases as the predicted $\beta$ also increase. Additionally, there is a negative relationship between the predicted $H'$ and the corresponding residuals, indicating that as the predicted $H'$ increases, the residuals decrease. The $\beta$ predictions at a rate of 0.45 $km^{-1}$ exhibit a notable increase in residual values compared to the previous range of +0.005 to $-0.005$ $km^{-1}$. Similarly, for $H'$ values exceeding the predicted threshold of 66 km, the residuals fall within the range of +0.25 to $-0.25$ km.

The analysis of feature importance involved the ranking of features based on their informedness. Consistent with expectations, the X-ray irradiance feature exhibited the highest importance, accounting for approximately 89% of the overall feature importance. Following this, the rolling median statistic with a 5 min window demonstrated a significance of 8.38%. The collective contribution of additional features amounts to approximately 2.76% of the informedness for the model, suggesting that these features can be readily modified or eliminated to align with the researcher's requirements. One potential challenge faced by researchers is the exclusion of the initial 60 data points from the analysis due to the implementation of a rolling window statistic with a duration of 60 min. However, it is worth noting that from the information given by the feature importance analysis, these features can be disregarded without compromising the model's effectiveness, thus enabling the development of an equally proficient model.

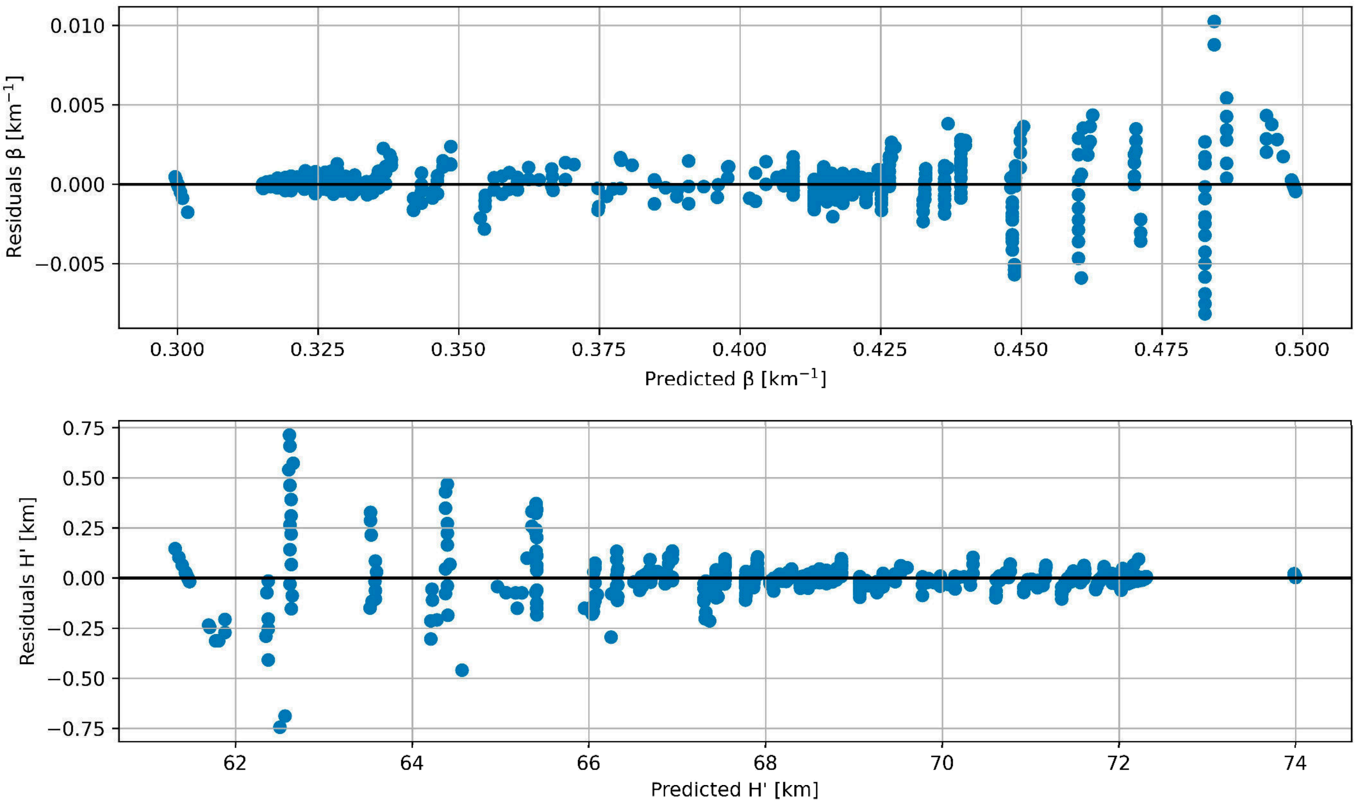


**Figure 12.** Residual and predicted plot for sharpness (**upper** panel) and reflection height (**lower** panel) for the time-series approach.

## 4. Conclusions

The employment of ML regression techniques on the provided SF data yielded significant insights into the feasibility of modeling ionospheric parameters without relying on the complicated and difficult to use software, e.g., LWPC software. One possible advantage of this approach, provided that the models are optimized, and the error rates are minimized, is the possibility of automatically determining ionospheric parameters in real-time or, at the very least, near-real time. Also, another potential benefit of such a model is the determination of the ED from the ionospheric parameters. The primary findings of this research can be summarized as:

- The utilization of synthetic data estimated using the KDE technique yielded datasets that were deemed adequate for ML modeling, as they closely adhered to the distribution of the original dataset. Further investigation is required to validate the outcomes of this study. Subsequent research should involve a more extensive dataset and, if feasible, refrain from relying on synthetic data, instead opting for a greater number of original samples. In relation to the present study, the utilization of synthetic data proved to be adequate, as the primary aim of this research was to determine the feasibility of employing ML regression techniques for the estimation of ionospheric parameters.
- The RF and XGB algorithms demonstrated adequate performance; however, the KNN and DT algorithms exhibited greater error rates compared to the aforementioned techniques. Subsequent investigations ought to integrate and prioritize the utilization of ANNs due to their benefits; however, they do necessitate careful hyperparameter tuning in order not overfit the model. Regarding XGB, it is worth noting that it possesses an additional hyperparameter compared to RF. This additional hyperparameter

allows for finer adjustments to the model, perhaps leading to improved predictions. Nevertheless, both RF and XGB are highly recommended as primary methodologies for investigating concepts that have not been completely explored.

- The residual analysis conducted in this study revealed that the final model had a possible minor bias towards predicting $H'$ values greater than 62 km, with a reduced error rate compared to predictions below 62 km.
- The results obtained from the time-series based approach exhibited a higher level of favorability compared to the instance-based approach, as indicated by the lower error rates. The model exhibited a potential bias in both the β and $H'$ parameters. Specifically, the β parameter demonstrated an increasing error rate as the predicted value increased, whereas the $H'$ parameter showed a decreasing error rate as the predicted value increased. Future research should consider placing more emphasis on a time-series based approach. This approach has shown the ability to efficiently present precise values of waveguide parameters over an extended period of time. Additionally, it has been observed that the features of this approach can be customized to meet the specific requirements of the researcher. Notably, it has been found that only two features contribute significantly to the informativeness of the model.
- Standard methods for determining ionospheric parameters are tedious and time-consuming, necessitating the development of other methods for determining such parameters. As to our knowledge, the literature and freely available methods for providing ionospheric parameters utilizing ML are not widely realized. Future comparison of the displayed ML method can be performed with methods such as easyFit and FlareED, where all the techniques can be tested and mutually compared under different SF classes and ionospheric perturbations.

The primary objective of this study is to employ an alternative approach for estimating low ionospheric parameters under the influence of SF events that enable easy modeling of this medium. An advantage of this method is the potential ability to streamline the process and obtain results in real-time or near-real time, as well as the potential to obtain parameters for the calculation of ED. However, further investigation is required to refine the methodology, investigate alternative algorithms, and explore additional pre-processing techniques. The wider statistical determination of the capabilities of the model for all SF classes can be enabled with additional data. As expected, the majority of the data fell within the C or M class, and future research is needed with more B- (barely detectable except in conditions of solar minimum) and X-class SFs. The research demonstrates the promise of the approach; nonetheless, additional comprehensive research is required to ensure its readiness for production.

**Supplementary Materials:** The training and testing data as well as parts of the workflow used in this study are available online at: https://github.com/arnautF/IR_SF_ML, accessed on 3 November 2023.

**Author Contributions:** Conceptualization, F.A. and A.K.; writing—original draft preparation, F.A. and A.K.; writing—review and editing F.A., A.K., V.A.S. and Z.M. All authors have read and agreed to the published version of the manuscript.

**Funding:** This work was funded by the Institute of Physics Belgrade, University of Belgrade, through a grant by the Ministry of Science, Technological Development and Innovations of the Republic of Serbia.

**Data Availability Statement:** In this study, publicly accessible datasets were examined. These data are accessible: https://hesperia.gsfc.nasa.gov/goes/goes_event_listings/, accessed on 9 April 2023, and https://www.ncei.noaa.gov/data/goes-space-environment-monitor/access/avg/, accessed on 7 May 2023.

**Acknowledgments:** The article is based upon work from COST Action CA22162—A transdisciplinary network to bridge climate science and impacts on society (FutureMed). Authors thank D. Šulić for fruitful discussions.

**Conflicts of Interest:** The authors declare no conflict of interest.

## References

1. Fedrizzi, M.; de Paula, E.R.; Kantor, I.J.; Langley, R.B.; Santos, M.C. Mapping the low-latitude ionosphere with GPS. *GPS WORLD* **2002**, *13*, 41–47.
2. Ahmedov, B.J.; Mirzaev, B.S.; Mamatov, F.M.; Khodzhaev, D.A.; Julliev, M.K. Integrating of gis and gps for ionospheric perturbations in d-And f-layers using vlf receiver. *InterCarto InterGIS* **2020**, *26*, 547–560. [CrossRef]
3. Kumar, S.I.; Kumar, A.; Menk, F.W.; Maurya, A.K.; Singh, R.; Veenadhari, B. Response of the low-latitude D region ionosphere to extreme space weather event of 14–16 December 2006. *J. Geophys. Res. Space Phys.* **2015**, *120*, 788–799. [CrossRef]
4. Mitra, A. The D-region of the ionosphere. *Endeavour* **1978**, *2*, 12–21. [CrossRef]
5. Ohya, H.; Nishino, M.; Murayama, Y.; Igarashi, K.; Saito, A. Using tweek atmospherics to measure the response of the low-middle latitude D-region ionosphere to a magnetic storm. *J. Atmos. Sol.-Terr. Phys.* **2006**, *68*, 697–709. [CrossRef]
6. Reddybattula, K.D.; Panda, S.K.; Sharma, S.K.; Singh, A.K.; Kurnala, K.; Haritha, C.S.; Wuyyuru, S. Anomaly effects of 6–10 September 2017 solar flares on ionospheric total electron content over Saudi Arabian low latitudes. *Acta Astronaut.* **2020**, *177*, 332–340. [CrossRef]
7. Ishisaka, K.; Okada, T.; Hawkins, J.; Murakami, S.; Miyake, T.; Murayama, Y.; Nagano, I.; Matsumoto, H. Investigation of electron density profile in the lower ionosphere by SRP-4 rocket experiment. *Earth Planets Space* **2005**, *57*, 879–884. [CrossRef]
8. Quan, L.; Cai, B.; Hu, X.; Xu, Q.; Li, L. Study of ionospheric D region changes during solar flares using MF radar measurements. *Adv. Space Res.* **2021**, *67*, 715–721. [CrossRef]
9. Richardson, D.; Cohen, M. Exploring the Feasibility of a Unified D-region Ionosphere Model. In Proceedings of the AGU Fall Meeting Abstracts, New Orleans, LA, USA, 13–17 December 2021; p. AE35B-1920.
10. Silber, I.; Price, C. On the Use of VLF Narrowband Measurements to Study the Lower Ionosphere and the Mesosphere–Lower Thermosphere. *Surv. Geophys.* **2017**, *38*, 407–441. [CrossRef]
11. Kolarski, A.; Veselinović, N.; Srećković, V.A.; Mijić, Z.; Savić, M.; Dragić, A. Impacts of Extreme Space Weather Events on September 6th, 2017 on Ionosphere and Primary Cosmic Rays. *Remote Sens.* **2023**, *15*, 1403. [CrossRef]
12. Grubor, D.; Šulić, D.M.; Žigman, V. Classification of X-ray solar flares regarding their effects on the lower ionosphere electron density profile. *Ann. Geophys.* **2008**, *26*, 1731–1740. [CrossRef]
13. Kolarski, A.; Grubor, D. Sensing the Earth's low ionosphere during solar flares using VLF signals and goes solar X-ray data. *Adv. Space Res.* **2014**, *53*, 1595–1602. [CrossRef]
14. Kolarski, A.; Grubor, D. Comparative Analysis of VLF Signal Variation along Trajectory Induced by X-ray Solar Flares. *J. Astrophys. Astron.* **2015**, *36*, 565–579. [CrossRef]
15. Thomson, N.R.; Clilverd, M.A.; McRae, W.M. Nighttime ionospheric D region parameters from VLF phase and amplitude. *J. Geophys. Res. Space Phys.* **2007**, *112*, A07304. [CrossRef]
16. Wait, J.R.; Spies, K.P. *Characteristics of the Earth-Ionosphere Waveguide for VLF Radio Waves*; US Department of Commerce, National Bureau of Standards: Washington, DC, USA, 1964; Volume 300.
17. Ferguson, J. *Computer Programs for Assessment of Long-Wavelength Radio Communications, Version 2.0: User's Guide and Source Files*; TD-3030, Space and Naval Warfare Systems Center: San Diego, CA, USA, 1998.
18. Bekker, S.Z.; Ryakhovsky, I.A.; Korsunskaya, J.A. Modeling of the Lower Ionosphere During Solar X-Ray Flares of Different Classes. *J. Geophys. Res. Space Phys.* **2021**, *126*, e2020JA028767. [CrossRef]
19. Srećković, V.A.; Šulić, D.M.; Vujčić, V.; Mijić, Z.R.; Ignjatović, L.M. Novel Modelling Approach for Obtaining the Parameters of Low Ionosphere under Extreme Radiation in X-Spectral Range. *Appl. Sci.* **2021**, *11*, 11574. [CrossRef]
20. Srećković, V.A.; Šulić, D.M.; Ignjatović, L.; Vujčić, V. Low Ionosphere under Influence of Strong Solar Radiation: Diagnostics and Modeling. *Appl. Sci.* **2021**, *11*, 7194. [CrossRef]
21. Gross, N.C.; Cohen, M.B. VLF Remote Sensing of the D Region Ionosphere Using Neural Networks. *J. Geophys. Res. Space Phys.* **2020**, *125*, e2019JA027135. [CrossRef]
22. Alpatov, V.V.; Bekker, S.Z.; Kozlov, S.I.; Lyakhov, A.N.; Yakim, V.V.; Yakubovsky, S.V. Analyzing existing applied models of the ionosphere to calculate radio wave propagation and a possibility of their use for radar-tracking systems. II. Domestic models. *Sol.-Terr. Phys.* **2020**, *6*, 60–66.
23. Richardson, D.K.; Cohen, M.B. Seasonal Variation of the D-Region Ionosphere: Very Low Frequency (VLF) and Machine Learning Models. *J. Geophys. Res. (Space Phys.)* **2021**, *126*, e29689. [CrossRef]
24. Berdermann, J.; Kriegel, M.; Banyś, D.; Heymann, F.; Hoque, M.M.; Wilken, V.; Borries, C.; Heßelbarth, A.; Jakowski, N. Ionospheric Response to the X9.3 Flare on 6 September 2017 and Its Implication for Navigation Services over Europe. *Space Weather* **2018**, *16*, 1604–1615. [CrossRef]
25. de Paula, V.; Segarra, A.; Altadill, D.; Curto, J.J.; Blanch, E. Detection of Solar Flares from the Analysis of Signal-to-Noise Ratio Recorded by Digisonde at Mid-Latitudes. *Remote Sens.* **2022**, *14*, 1898. [CrossRef]
26. Reddybattula, K.D.; Nelapudi, L.S.; Moses, M.; Devanaboyina, V.R.; Ali, M.A.; Jamjareegulgarn, P.; Panda, S.K. Ionospheric TEC Forecasting over an Indian Low Latitude Location Using Long Short-Term Memory (LSTM) Deep Learning Network. *Universe* **2022**, *8*, 562. [CrossRef]
27. Yasyukevich, Y.; Astafyeva, E.; Padokhin, A.; Ivanova, V.; Syrovatskii, S.; Podlesnyi, A. The 6 September 2017 X-Class Solar Flares and Their Impacts on the Ionosphere, GNSS, and HF Radio Wave Propagation. *Space Weather* **2018**, *16*, 1013–1027. [CrossRef] [PubMed]

28. Berger, V.W.; Zhou, Y. Kolmogorov–smirnov test: Overview. In *Wiley StatsRef: Statistics Reference Online*; John Wiley & Sons, Inc.: Hoboken, NJ, USA, 2014. [CrossRef]
29. Virtanen, P.; Gommers, R.; Oliphant, T.E.; Haberland, M.; Reddy, T.; Cournapeau, D.; Burovski, E.; Peterson, P.; Weckesser, W.; Bright, J.; et al. SciPy 1.0: Fundamental algorithms for scientific computing in Python. *Nat. Methods* **2020**, *17*, 261–272. [CrossRef] [PubMed]
30. Breiman, L. Random Forests. *Mach. Learn.* **2001**, *45*, 5–32. [CrossRef]
31. Breiman, L.; Friedman, J.H.; Olshen, R.A.; Stone, C.J. Classification and Regression Trees. *Biometrics* **1984**, *40*, 874.
32. Fix, E.; Hodges, J.L. Discriminatory analysis. Nonparametric discrimination: Consistency properties. *Int. Stat. Rev./Rev. Int. Stat.* **1989**, *57*, 238–247. [CrossRef]
33. Cover, T.; Hart, P. Nearest neighbor pattern classification. *IEEE Trans. Inf. Theory* **1967**, *13*, 21–27. [CrossRef]
34. Chen, T.; Guestrin, C. XGBoost: A Scalable Tree Boosting System. In Proceedings of the 22nd ACM SIGKDD International Conference on Knowledge Discovery and Data Mining, San Francisco, CA, USA, 13–17 August 2016; pp. 785–794.
35. Batista, G.E.A.P.A.; Prati, R.C.; Monard, M.C. A study of the behavior of several methods for balancing machine learning training data. *SIGKDD Explor. Newsl.* **2004**, *6*, 20–29. [CrossRef]
36. Arnaut, F.; Kolarski, A.; Srećković, V.A. Random Forest Classification and Ionospheric Response to Solar Flares: Analysis and Validation. *Universe* **2023**, *9*, 436. [CrossRef]

# MULTIVARIATE ANALYSIS OF TWO-YEAR RADON CONTINUOUS MONITORING IN GROUND LEVEL LABORATORY IN THE INSTITUTE OF PHYSICS BELGRADE

by

***Dimitrije M. MALETIĆ*** [1], ***Radomir M. BANJANAC*** [1], ***Dejan R. JOKOVIĆ*** [1], ***Aleksandar L. DRAGIĆ*** [1], ***Nikola B. VESELINOVIĆ*** [1], ***Mihailo R. SAVIĆ*** [1], ***Zoran R. MIJIĆ*** [1], ***Vladimir I. UDOVIČIĆ*** [1*], ***Svetlana D. ŽIVKOVIĆ-RADETA*** [2], ***and Jelena V. UDOVIČIĆ*** [2]

[1] Institute of Physics Belgrade, National Institute of the Republic of Serbia, University of Belgrade, Belgrade, Serbia
[2] Faculty of Applied Ecology Futura, Belgrade Metropolitan University, Belgrade, Serbia

Scientific paper
https://doi.org/10.2298/NTRP2304273M

**Multivariate classification and regression analysis of multiple meteorological variables and indoor radon activity concentration in Ground Level Laboratory in the Institute of Physics Belgrade, was performed and discussed. Meteorological variables used in this analysis were from radon active device, nearby meteorological station and finally from Global Data Assimilation System. Single variate analysis has identified variables with greatest value of Pearson's correlation coefficient with radon activity concentration and also, variables with greatest separation of events with increased radon activity concentration of over 200 Bqm$^{-3}$ and of events with radon level below this value. This initial analysis is showing the expected behavior of radon concentration with meteorological variables, with emphasis on data periods with or without air conditioning and with emphasis on indoor water vapor pressure, which was, in our previous research, identified as important variable in analysis of radon variability. This single variate analysis, including all data, proved that Global Data Assimilation System data could be used as a good enough approximate replacement for meteorological data from nearby meteorological station for multivariate analysis. Variable importance of Boosted Decision Trees with Gradient boosting multivariate analysis method are shown for all three periods and most important variables were discussed. Multivariate regression analysis gave good results, and can be useful to better tune the multivariate analysis methods.**

*Key words: continuous radon monitoring, multivariate analysis, Global Data Assimilation System, meteorological station*

## INTRODUCTION

Primarily, radon problem presents a health hazard [1]. The research of the dynamics of radon in various environments, living or working places, is of great importance in terms of protection against ionizing radiation and in designing of measures for its reduction. In the Low-Background Laboratory for Nuclear Physics extensive research on various radon fields has been done in the past, especially radon monitoring in the special designed low-background underground and ground level laboratory, with the aim of investigating the rare nuclear processes [2]. Besides radon monitoring in the laboratory, we work on several research topics regarding radon: using multivariate classification and regression methods, as developed for data analysis in high-energy physics [3], to study connection of climate variables and variations of radon concentrations, modelling of the indoor radon behaviour and national indoor radon mapping [4], taking interest in similar indoor radon mapping analysis in Montenegro [5], or by research of radon variability in a single dwelling [6], using advanced analysis tools, or performing continuous measurements in multi-store building [7] or laboratory space [8]. Indoor radon variability depends on many variables. Soil content, and building characteristics are very important. In case of researching of indoor radon variability, meteorological effects become the most important ones. With recent experiences with lowering the limits of indoor radon level, both in dwellings and working places, and the demand for decrease of public radon exposure, the need for more detailed knowledge on radon variability is increasing. Besides a possibility for improvement of mitigation

* Corresponding author, e-mail: udovicic@ipb.ac.rs

techniques, we could look into creating online warning pages, like we already have, for example, for UV radiation. These online warning pages, with information on radon concentration variations, could be interesting to people living in dwellings or working spaces with previously known radon problem, or dwellings with radon activity concentration close to 200 Bqm$^{-3}$ limit. These online warnings, could indicate a call for some temporary measures like starting of increased ventilation or reducing exposure. Local radon warning pages could be based on local meteorological station, but for larger regions, meteorological modeled data like Global Data Assimilation System (GDAS) could be used. In this paper we were looking into the possibility of using GDAS data in prediction of indoor radon variability, by jointly looking into GDAS and nearby meteorological station, and compare the results.

## DATA PREPARATION AND SELECTION

The radon continuous monitoring in ground level laboratory was performed with active device RadonEye Plus2 with time sampling of one hour. The device recorded variables: Rn-activity, indoor temperature and indoor humidity. The radon the measurement was done from November 2020 to November 2022. After looking into indoor temperature data, we decided to do three analysis, one with using all the data samples (whole period of measurement's), second using only data when air conditioning (AC) was operating, and third sample used for analysis was for periods when air conditioning was OFF (noAC).

Meteorological station located in Institute of Physics Belgrade yard, and maintained by Environmental Physics Laboratory [8], has being recording variables at 5 minute interval, and hourly values are used for this analysis. Variables are named by adding prefix outside; outside-cloudbase, outside-dew point, outside-humidity, outside-temp, outside-pressure and outside-rain.

The US National Centers for Environmental Prediction (NCEP) runs a series of computer analyses and forecasts operationally. One of the operational systems is the GDAS. At National Oceanic and Atmospheric Administration's (NOAA) Air Resources Laboratory (ARL), NCEP model output is used for air quality transport and dispersion modeling. The ARL archives GDAS output which contains basic fields, such as the temperature, pressure and humidity. Those GDAS data are very interesting since they are widely used by weather forecast groups worldwide, and our idea is that if we could use this freely accessed and frequently updated database, we could improve forecasting of some kind of *relative* indoor radon concentrations, and indicate by result of automatic online MVA regression analysis when to expect increased indoor radon concentrations based on meteorological variables. Because MVA methods are rather robust, and we wanted to see which, if any of GDAS variables are suited for our purpose, we included most of variables in our analysis. The GDAS1 data is available for integer values of latitude and longitude, so, for all variables', each data point was firstly 2-D linearly interpolated using variables' values on four integer latitudes and longitudes, surrounding latitude and longitude of our laboratory. The GDAS1 data is available for every three hours, so linear interpolation of each variable's data point was made in order that we can use hourly data. The GDAS1 variables used in our analysis can be identified as ones with prefix GDAS1; GDAS1-CAPE (convective available potential energy), GDAS1-CINH (convective inhibition), GDAS1-CPP6 (accumulated convective precipitation), GDAS1-CRAI (categorical rain), GDAS1-DSWF (downward short wave radiation flux), GDAS1-HCLD (high cloud cover), GDAS1-LCLD (low cloud cover), GDAS1-LHTF (latent heat net flux at surface), GDAS1-LIB4 (best 4-layer lifted index), GDAS1-LISD (standard lifted index), GDAS1-MCLD (middle cloud cover), GDAS1-PBLH (planetary boundary layer height), GDAS1-PRSS (pressure at surface), GDAS1-RH2M (relative humidity at 2m AGL), GDAS1-SHGT (geopotential height), GDAS1-SHTF (sensible heat net flux at surface), GDAS1-SOLM (volumetric soil moisture content), GDAS1-T02M (temperature at 2m AGL), GDAS1-TCLD (total cloud cover), GDAS1-TMPS (temperature at surface), GDAS1-TPP6 (accumulated precipitation), GDAS1-mofi-e (momentum flux intensity), GDAS1-mofd-e (momentum flux direction). In this analysis using GDAS data, we also could indicate if variables measured by local meteorological station do not differ too much from GDAS modeled and interpolated ones, that GDAS variables could be used in this kind of MVA analysis.

We included previously found interesting variable in radon research [6] and that is water vapor pressure in outdoor and indoor air, as well as the difference of the two. In order to calculate the water vapor pressure in air, we need to calculate the value of the saturation water vapor pressure

$$\mathrm{es}(T) = 0.6108 \cdot \mathrm{e}^{\frac{17.27 \cdot T}{T+237.3}} \tag{1}$$

In addition, the slope of the relationship between the saturation water vapor pressure (es [kPa]) and the air temperature $T$ [°C], is given in [9, 10], so including the slope, we get new formula for the saturation water vapor pressure

$$es(T) = \frac{4098 \cdot \left(0.6108 \cdot \mathrm{e}^{\frac{17.27 \cdot T}{T+237.3}}\right)}{(T+237.3)^2} \tag{2}$$

and since the formula used to calculate the relative humidity is

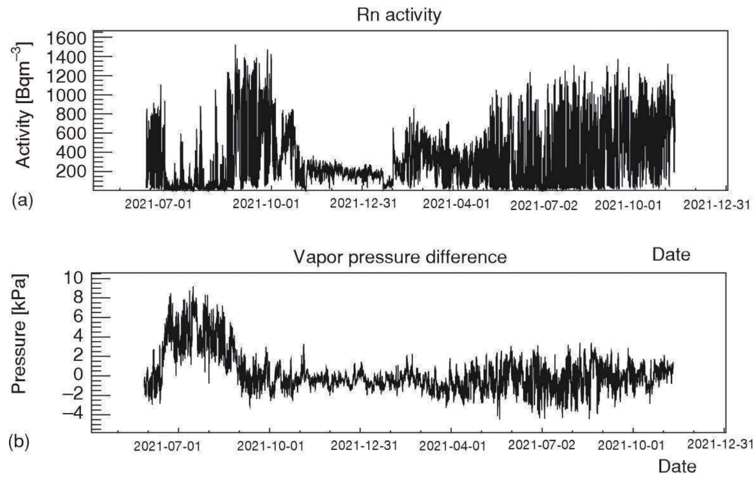


**Figure 1. The Rn activity indoor (a) and vapor pressure difference of outdoor and indoor (b). Note that with much greater outdoor water vapor pressure than indoor, comes influx of radon-free water vapor, and that results in significant decrease of indoor Rn activity**

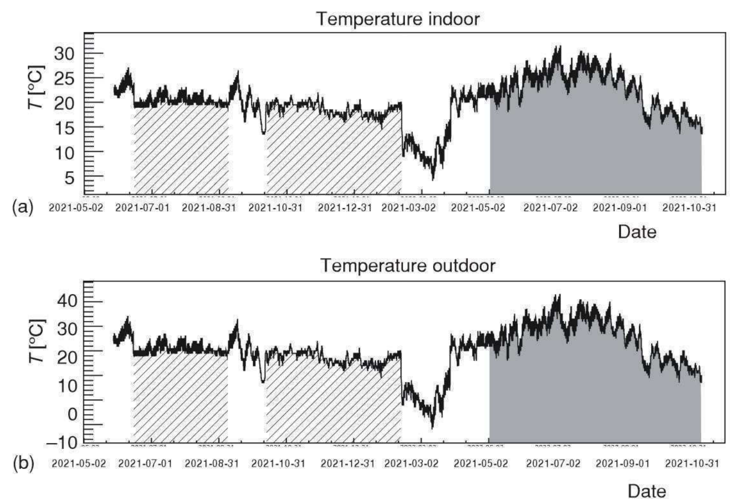


**Figure 2. Indoor temperature (a) and outdoor temperature (b) is shown. Indoor temperature which was used for analysis when air conditioning (AC) was on, is indicated in two line pattern areas, while gray shaded interval indicates period when air conditioning was off (noAC)**

$$\mathrm{RH} = \frac{\text{vapor pressure}}{\mathrm{es}(T)} \tag{3}$$

we get the formula to calculate the vapor pressure in air

$$\text{vapor pressure}(T, \mathrm{RH}) = \mathrm{RH} \cdot \frac{4098 \cdot \left(0.6108 \cdot \mathrm{e}^{\frac{17.27 \cdot T}{T + 237.3}}\right)}{(T + 237.3)^2} \tag{4}$$

Using this formula, we calculate four variables: indoor-vapor-press (vapor pressure from indoor-temperature and indoor-humidity data), outside-vapor-press (vapor pressure from outdoor outside-humidity, outside-temp data), diff-vapor-press (vapor pressure difference of outdoor and indoor) and gdas1-vapor-press (vapor pressure from GDAS1-T02M, GDAS1-RH2M data). On the bottom of fig. 1 the vapor pressure difference is shown, and it can be clearly seen that if the outer vapor pressure is much higher than the indoor vapor pressure, the indoor radon activity is lower fig. 1(a).

Out of two years of data taking, after merging all the data together to form a single hourly event with all the variables measured at that time, the number of useful hourly events was 12654. Table 1 shows the number of hourly events used for each of the three periods of analysis, which were split, firstly into signal and background events, where signal events are those for which Rn activity is more than 200 Bqm$^{-3}$, and background is less than that value, and then each set was split once more, into training and testing sample to be used in MVA analysis. Table 1 also shows the number of events used, and split, in periods with air condition operation on (AC), line pattern area on fig. 2(a), and air conditioning off (noAC) gray on fig. 2(a).

**Table 1. Summary table of number of hourly events used for specific part of analysis**

| | noAC | AC | All period |
|---|---|---|---|
| Signal training | 1343 | 912 | 3428 |
| Signal testing | 1343 | 912 | 3428 |
| Signal training and testing | 2686 | 1824 | 6856 |
| Background training | 942 | 1531 | 2899 |
| Background testing | 942 | 1531 | 2899 |
| Background training and testing | 1884 | 3062 | 5798 |

Before performing the multivariate (MVA) analysis, we have looked into single variable analysis, and the best way to see if variables could be useful for analysis is if they have, firstly, the greatest correlation with radon activity (concentration), and, secondly, which variable profiles for

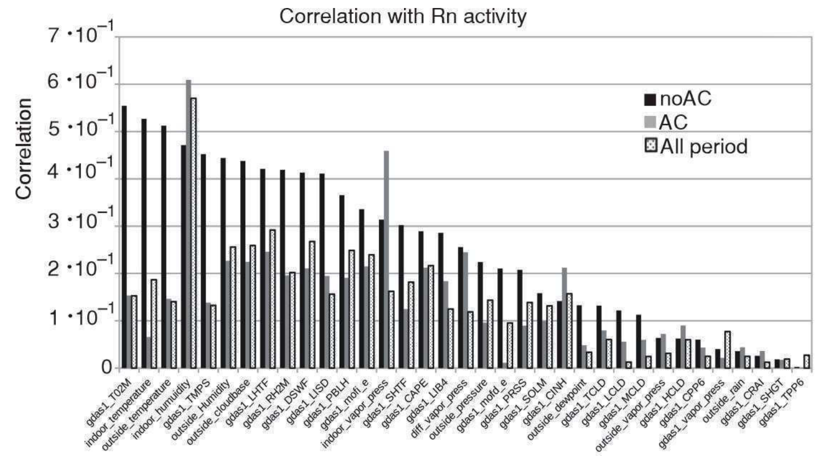


**Figure 3. The modulus of Pearson's correlation coefficients of radon activity with each of variables used in the analysis is shown. Note the decreasing of correlation with temperature variables, and increasing with humidity variables, when air conditioning (AC) was turned on**

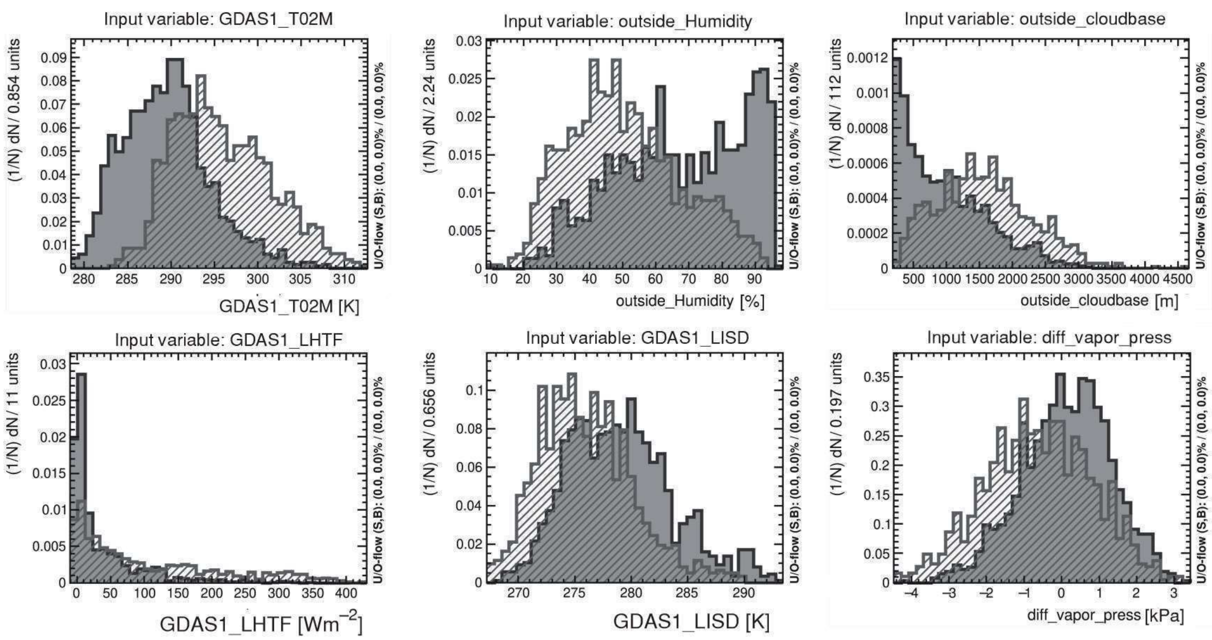


**Figure 4. For some variables there is a significant separation of distributions of variables' values for events with low and events with high radon activity. Variables shown are: temperature at height of 2 m above the ground (GDAS1-TO2M), outside relative air humidity, measure of lowest visible part of the cloud (cloudbase), latent heat net flux at the surface (LHTF), standard lifted index (LISD) and the difference of water vapor pressure from indoor and outdoor**

high Rn activity (signal) and low (background) data samples, have smallest overlap, meaning that they have greatest separation of high and low Rn activity samples. So, firstly, we are looking into modulus of Pearson's correlation coefficients for each of the variables used in this analysis with radon activity, fig. 3. Since the greatest variation of radon activity should give the best insight into correlation with variables, we are firstly looking into data with air condition off (noAC). To the variables with greatest modulus of Pearson's correlation coefficients with Rn activity (noAC) are temperature variables from all three sources of data GDAS, radonometar and meteorological station (GDAS1-T02M, indoor-temperature, outside-temperature, GDAS1-TMPS), than humidity (indoor-humidity, outside-humidity), outside-cloudbase, followed with GDAS variables: GDAS1-LHTF (latent heat net flux on surface) and GDAS1-DSWF (downward short wave radiation flux) and GDAS1-RH2M (relative humidity at height of 2 m), followed by indoor-vapor-pressure. When air conditioning is turned on, there is a change in correlation, where temperature variables correlations are decreasing, and there is an increase in correlation of humidity variables like indoor-humidity and indoor-vapor-pressure. We observe this change since temperature is now holding at approximately the same level by air conditioning, and any variation of radon activity we see does not come from approximately constant temperature. We noticed the similarity in modulus of Pearson's correlation coefficients of outside-T02M and outside-temperature with Rn activity of 55.4 % and 51.2 %, respectively, for noAC data, and 15.3 % and 14.6 %, respectively, for AC data. Also, outside-humidity and gdas1-RH2M with 44.4 % and 41.9 %, respectively, for noAC and 22.7 % and 19.6 % for AC data. When looking into pressure data, outside-pressure and GDAS1-PRSS have modulus of Pearson's correlation coefficients of 22.4 % and 20.8 %, respectively, for noAC data and 9.6 % and 9.0 % for AC data.

When looking into separation of variables for signal and background samples, fig. 4 shows selected

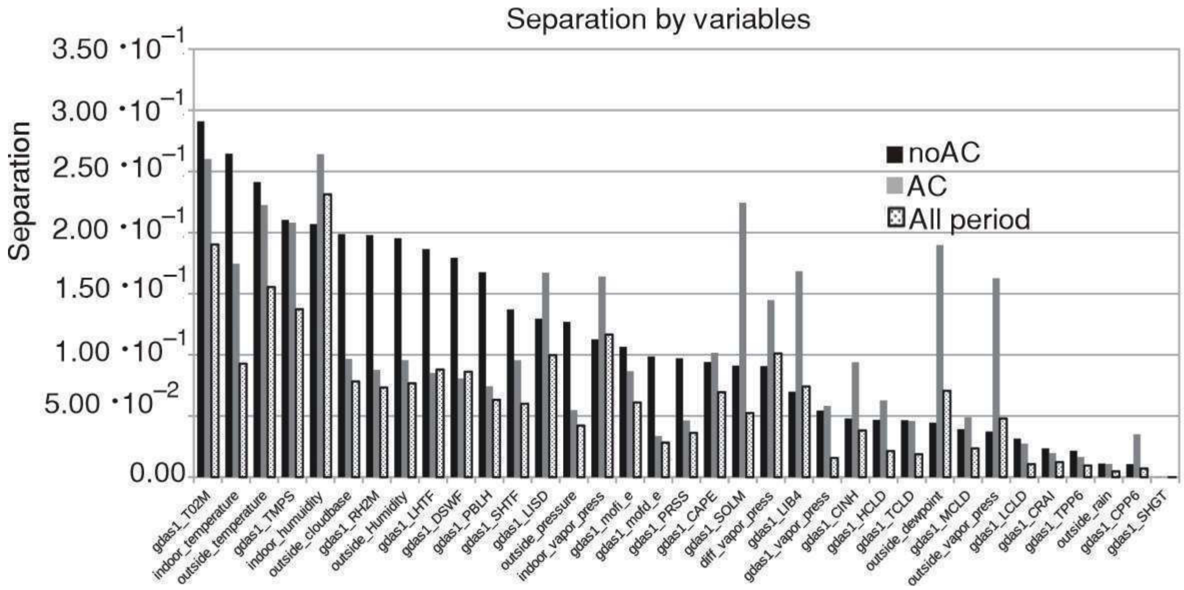


**Figure 5. Separation of events with low and high Rn activity by each variable**

variables, where separation can be seen with naked eye, and also, separations of high and low Rn activity for different variables can be roughly compared. But, we want to have more precise insight into separation, and for all three samples AC, noAC and samples of whole measurement period. This is shown in fig. 5 where we can see that for noAC, temperature variables have most significant separation values, as was the case with modulus of Pearson's correlation coefficients with Rn activity on fig. 3. With air conditioning turned on, the variables of humidity and vapor pressure gain in separation value, while indoor temperature is decreasing its separation value. Notice that the change is not so pronounced as was the case with correlation variables. Again, we noticed the similarity separation values of outside-T02M and outside-temperature 29.1 % and 24.1 %, respectively, for noAC data, and 26.0 % and 20.8 %, respectively, for AC data. Also, outside-humidity and GDAS1-RH2M with 19.8 % and 19.5 %, respectively, for noAC and 8.8 % and 9.6 % for AC data. When looking into pressure data, outside-pressure and GDAS1-PRSS have separation values of 12.7 % and 9.7 %, respectively, for noAC data and 5.5 % and 4.6 % for AC data.

## MULTIVARIATE CLASSIFICATION ANALYSIS

Toolkit for multivariate analysis (TMVA) [11] implemented in ROOT [12] framework for data analysis, has many of multivariate methods and tools implemented, which are frequently used for data analysis, as in High energy physics, also by data scientists in general. We will not get into details of wide spread of multivariate methods available, which can be found in TMVA manual [11]. The usage of those multivariate methods in TMVA is rather standardized. What is advantageous in using TMVA is that we could compare many of multivariate methods using the same training and testing sample. Also, the TMVA was used in many analyses, and is constantly under development, with many new methods implemented. The TMVA offers comparison of methods developed for other frameworks, like methods developed in programming langnages Python, or R, or modern methods like Deep and Convolutional Neural Networks, which is best to be run in multi-thread mode or on CPU or on GPU (graphical cards).

In MVA analysis, the data sample consists of events. Event is composed of data measured/recorded at the same time for each input variable. We can run MVA as Classification, Classification with category, and Regression. The MVA Classification is done when sample is divided into two samples (classes); signal and background. The MVA methods are trained to make the same classification using events they have not seen before, and their performance in classification is measured. Second MVA analysis is done as regression analysis. It is similar to classification, in the sense that the number of classes into which initial sample is divided is much bigger, and the value of classifier is not only 1 (signal) and 0 (background) but has much more values in between. Classification with category was not used, as the maximum performance of Classification is obtained when no other categorical values besides 1 (signal) and 0 (background) are used. Future performance tests could include categories like; very high, high, medium, low and very low radon concentrations.

When a sample is prepared, MVA classification needs some time to complete the training process for

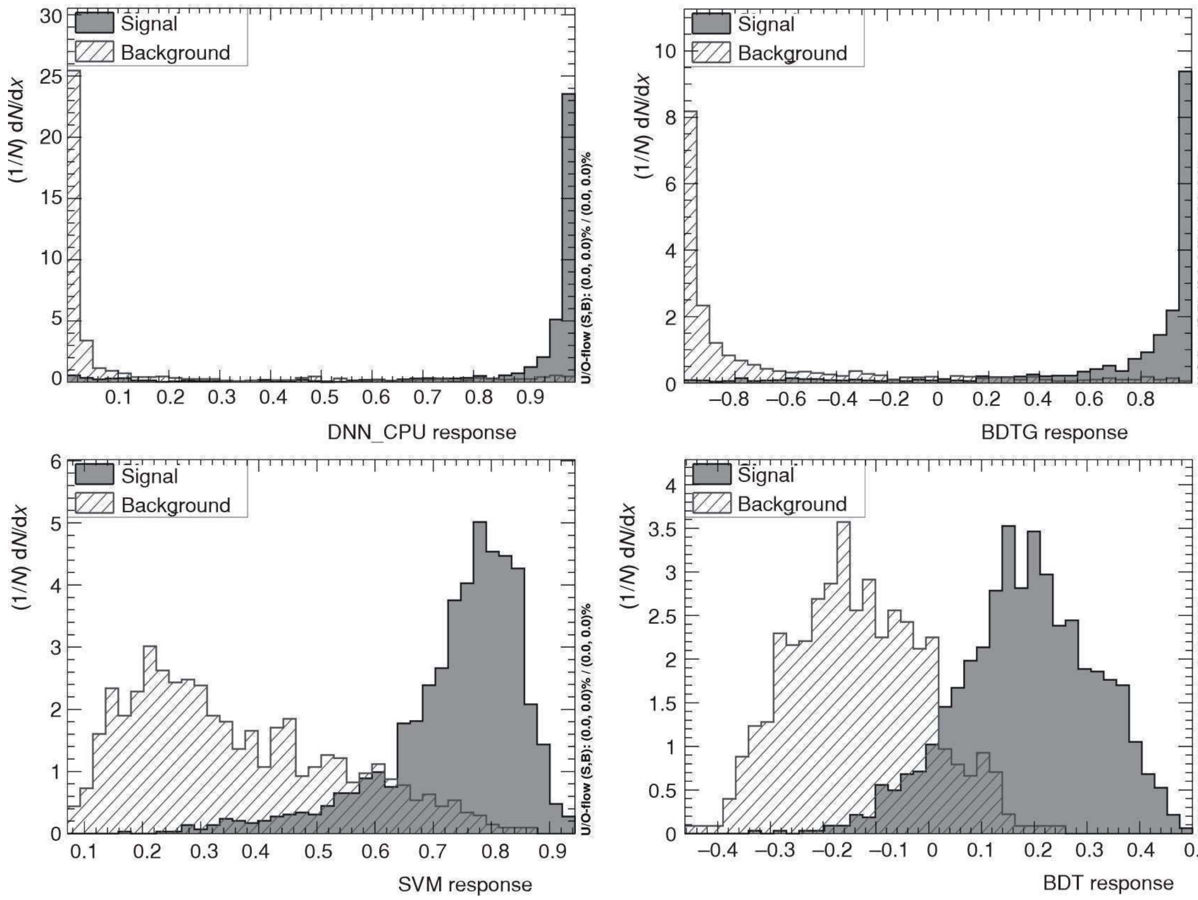


**Figure 6. Response of MVA methods to events with low and high Rn activity**

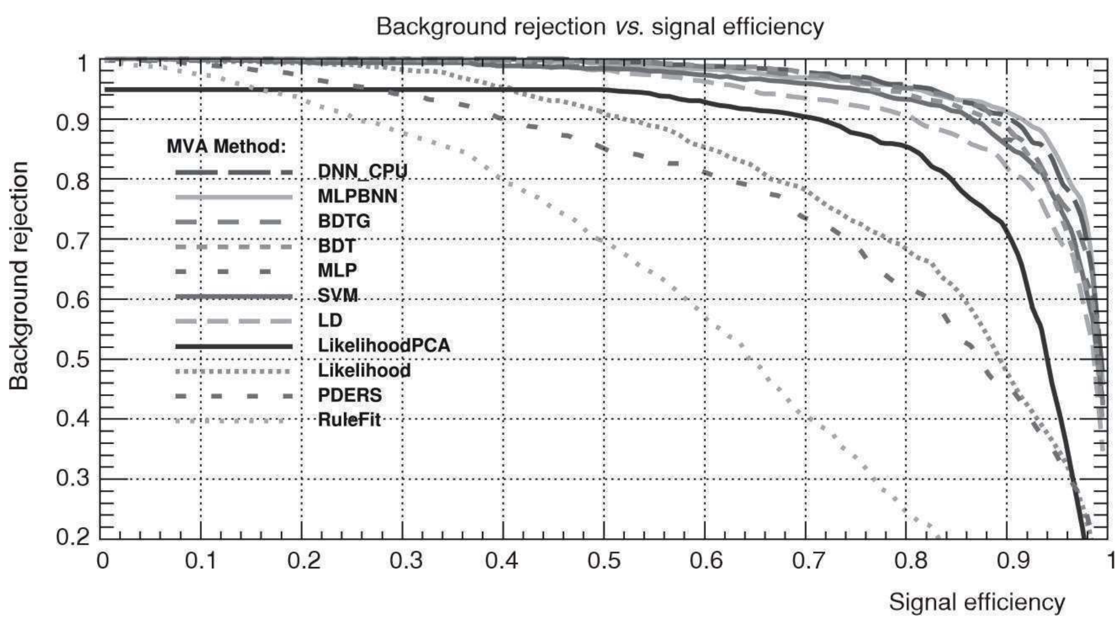


**Figure 7. The ROC curve for MVA methods for the time interval where air conditioning was off (noAC)**

each of MVA methods selected for comparison. Besides training, the sample of same number of events is used for evaluation, or testing, where MVA method is tested on samples not seen before (not used for training). The performance of some MVA method is expressed only using testing/evaluation sample.

The fig. 6 shows the response of best performing MVA methods, in analysis of noAC data, to events with low and high Rn activity, or signal and background. We can see, in fig. 7, that by looking into Receiver Operating Characteristic (ROC) curve comparison of all selected multivariate methods, that several

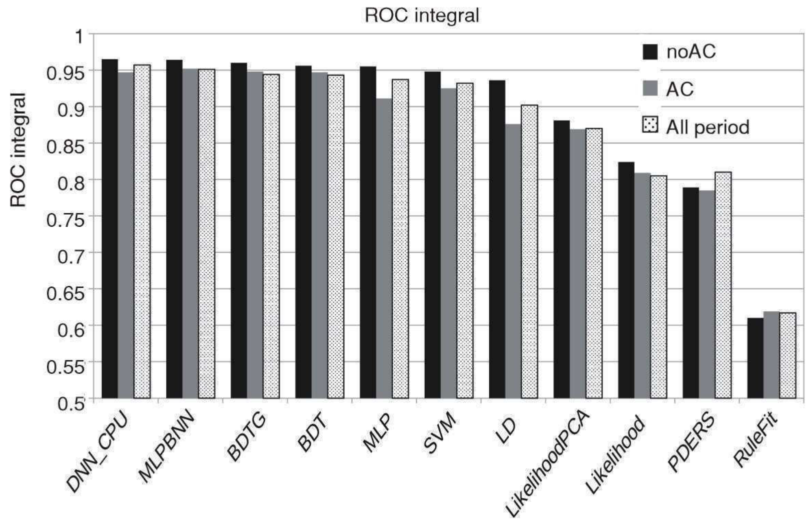


**Figure 8. Value of the ROC integral for MVA methods for the selected time intervals, AC and noAC, and for whole time interval**

methods have very good performances and also, very close performances. It is very good to have several methodologically very different multivariate methods performing in similar way, since this gives us confidence that classification is applicable. To illustrate this point, we can say that, very generally speaking, ANN are based on convolution of selected function to the resulting multivariate functional dependence, while Boosted Decision Trees are based on multidimensional space (cube) cuts, for approximation of multivariate functional dependence, and it is very good that both have very good performances in MVA classification.

The comparison of ROC curve integrals for best performing methods, for MVA classification analysis for all three intervals; noAC, AC and all-period analysis is shown at fig. 8. For five best performing methods, DNN-CPU (Deep Neural Network), MLPBNN (Multi-Layer Perceptron Bayesian regulator Neural Network), BDTG (Boosted Decision Trees with Gradient boosting), BDT (Boosted Decision Trees), and MLP (Multi-Layer Perceptron – an ANN), results are very similar, and also for all the three intervals, which is very important in sense that while variables' correlation with Rn activity vary greatly, this is easily overcome in MVA methods, adding very important property of robustness in variable selection. We should note that all the mentioned methods are ANN or DBT based multivariate methods.

The resulting trained multivariate methods are now ready to be included into some web applications, or used in variables' analysis. In web applications, Radon alarm could be constructed, when based on input variables, there is a great probability of increased indoor radon activity. For example, some places where it is known from previous measurements, like from participation in large indoor radon survey, that dwelling or working space has a problem with increased indoor radon concentration, some measures like increased ventilation or longer brakes from work, could be made. In variables' analysis, the simplification of MVA approximation of underlying multivariable function dependence could be made, not only with classification, but more effectively with regression methods.

The MVA methods which are trained and tested using full set of variables and all available data are ready to be used in some application. But, we can continue our work and try to modify something in our analysis chain to see if we can get better performance or method which uses lower number of input variables, without big loss in performance. We can make different selection of training data sets, like truncation of outlier data, we can change the number of input variables, or change parameters specific for each MVA method. For this purpose, it could be very useful to look into variable importance for specific MVA method, for example for BDTG in fig. 9, in order to look into the influence of variables on MVA decision. To show why this is useful we pay attention on Pearson's correlation coefficients of input variables and radon concentrations and notice that there could be several variables with high correlation coefficient with radon concentration, but highly inter-correlated with each other, which results in no gain in MVA method performance if we add several variables which are inter-correlated. So, we can exclude variables if their exclusion does not lower the MVA method performance. We choose to look into importance of variables on BDTG classification, for all time intervals. Again, we start with noAC intervals, where indoor radon activity was highest, and indoor temperature was not regulated. We start with two GDAS variables, GDAS1-SHTF (sensible heat net flux at surface) and GDAS1-SOLM (volumetric soil moisture content), followed by indoor-humidity and diff-vapor-pressure, and GDAS1-T02M at position 6, with some other variables similarly important as gdas momentum flux direction and gdas cloud cover variables.

When comparing data from meteorological station and gdas data, we cannot compare them in, for example, multivariate importance, since if one variable is chosen to be used in MVA training, similar variable in, for example Pearson's correlation coefficients or

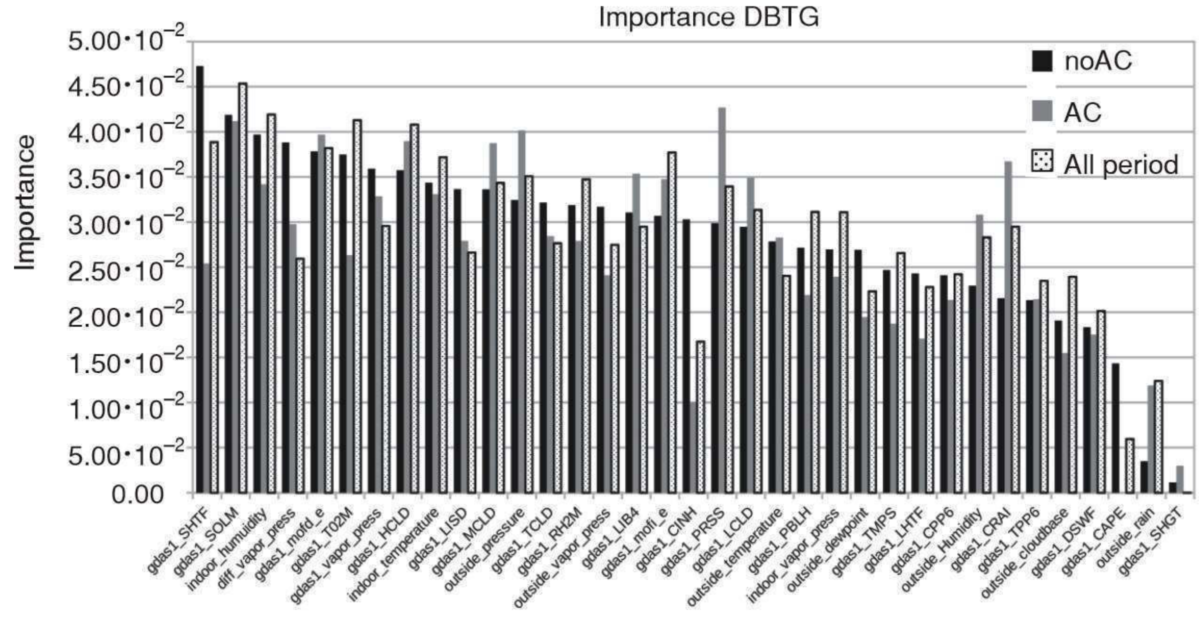


**Figure 9. Variable importance for MVA method BDTG for time intervals, AC and noAC, and for the whole time interval**

separation of variable for increased and for low Rn activity value, do not have power to make discrimination. Comparison can only be used when each variable is observed separately in a single variable analysis. Also, similar situation can happen with preparation of variables, where resulting variables are, de-correlated, and first variable is significant for further analysis but other, very similar variable before de-correlation, remains with negligible significance for further analysis.

## THE MVA REGRESSION

Regression analysis often fails if there is not a strong dependence of target variable, in our case Rn activity, on input variables. Reasoning is the following: Classification analysis has only two outputs, either it is signal (1) or background (0), but in case of regression, there are many more values between 0 and 1, and much more dependence, or events is needed to get positive results here. We ran MVA regression for three time intervals, noAC, AC and all-period. The BDTG and DNN-CPU show good prediction results after MVA regression training procedure, as a result of RMS of deviations of true and evaluated value of Rn activity are satisfyingly small, as is shown in fig. 10. The fig. 11 shows this in more detail for BDTG in noAC regression analysis, where the distribution of deviations is shown for each event in the testing sample.

## CONCLUSIONS

Single variate analysis of correlations of each of meteorological variable with indoor radon activity and Multivariate classification and regression analysis of all meteorological variables and radon activity was per-

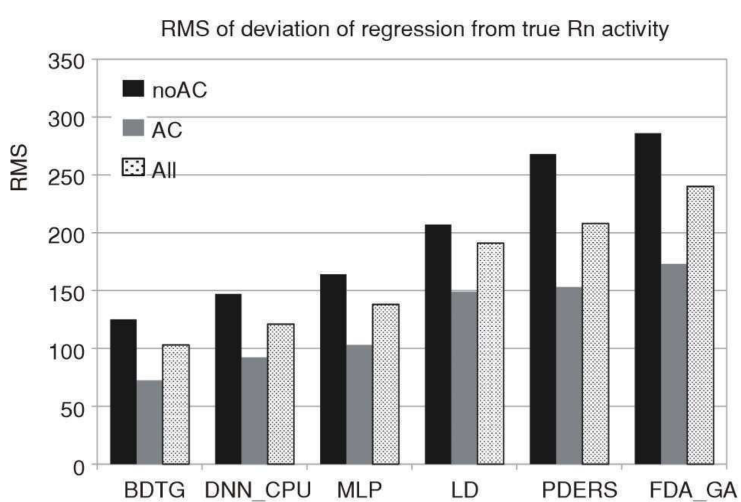


**Figure 10. The RMS of deviations of regressions from true value for selected time intervals, AC and noAC, and for the whole time interval, for several MVA regression methods**

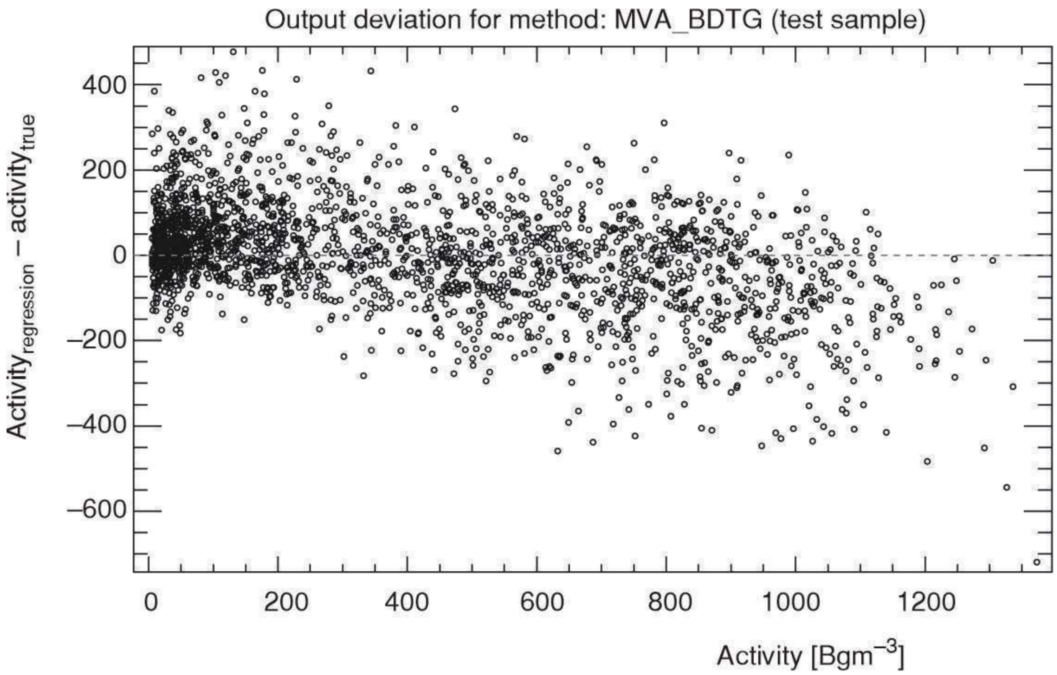


**Figure 11. Deviation of regression from true value for noAC period and BDTG MVA method**

formed and discussed. Meteorological variables used in this analysis were from radonometar device, then from a nearby meteorological station and finally from GDAS data. Single variate analysis has identified variables with greatest value of modulus of Pearson's correlation coefficient with Rn activity, and also variables with greatest separation of events with increased Rn activity of over 200 Bqm$^{-3}$ and of events with Rn activity below this value. This initial analysis and looking into variables were showing the expected behavior of Rn concentration with meteorological variables, with emphasis on data periods with or without air conditioning, and also with emphasis on previously found variable of indoor water vapor pressure. This single variate analysis and observing all the data proved also useful for conclusion that GDAS data could be used as a good enough approximate replacement for meteorological data from the nearby meteorological station for MVA analysis. The MVA classification analysis found several very well performing MVA methods which can be used in web application or for further detailed analysis of specific input variables. Variable importance of BDTG MVA method was shown for all three periods, and most important variables were discussed. Finally, MVA regression analysis gave also good results, and more quality measurements in this rarely accessed ground level laboratory would be useful to better tune the MVA methods, and do more detailed analysis.

## ACKNOWLEDGMENT

Authors thank the NOAA Air Resources Laboratory (https://www.arl.noaa.gov/) for GDAS data. (https://www.ready.noaa.gov/gdas1.php). Authors thank the Environmental Physics Laboratory (http://www.envpl.ipb.ac.rs/) for meteorological station data. The authors acknowledge funding provided by the Institute of Physics Belgrade, through grant by Ministry of Education, Science and Technological Development of the Republic of Serbia.

## AUTHORS' CONTRIBUTIONS

The original idea and draft were carried out by D. M. Maletić. The data provided by R. M. Banjanac, V. I. Udovičić and Z. Mijić. Statistical analysis was done by D. M. Maletić, D. R. Joković and A. L. Dragić. N. B. Veselinović, M. R. Savić, S. Živković-Radeta and J. V. Udovičić worked on data preparation and selection. All the authors analyzed and discussed the results and reviewed the manuscript.

## REFERENCES

[1] ***, WHO Handbook on Indoor Radon: A Public Health Perspective, World Health Organization, Switzerland, 94, 2009

[2] Dragić, A., *et al*., The New Set-Up in the Belgrade Low-Level and Cosmic-Ray Laboratory, *Nucl Technol Radiat, 26* (2011), 3, pp. 181-192

[3] Maletić, D., *et al*., Comparison of Multivariate Classification and Regression Methods for the Indoor Radon Measurements, *Nucl Technol Radiat, 29* (2014), 1, pp. 17-23

[4] Eremić-Savković, M., *et al.*, Results of the First National Indoor Radon Survey Performed in Serbia, *Journal of Radiological Protection, 40* (2020), 2, pp. N22-N30

[5] Vukotić, P., *et al*., Influence of Climate, Building, and Residential Factors on Radon Levels in Ground-Floor Dwellings in Montenegro, *Nucl Technol Radiat, 36* (2021), 1, pp. 74-84
[6] Udovičić, V., *et al*., Multiyear Indoor Radon Variability in a Family House – a Case Study in Serbia, *Nucl Technol Radiat, 33* (2018), 2, pp. 174-179
[7] Udovičić, V., *et al*., Radon Variability Due to Floor Level in Two Typical Residential Buildings in Serbia, *Nukleonika, 65* (2020), 2, pp. 121-125
[8] Maletić, D., *et al*., Correlative and Multivariate Analysis of Increased Radon Concentration in Underground Laboratory, *Radiation Protection Dosimetry, 162* (2014), 1-2, pp. 148-151
[9] Tetens, O., About Some Meteorological Terms (original: Über Einige Meteorologische Begriffe.) *Z. Geophys, 6* (1930) pp. 297-309
[10] Murray, W., On the Computation of Saturation Vapor Pressure, *J. Applied Meteorology, 6* (1967), pp. 203-204
[11] Hoecker, A., *et al*, TMVA – Toolkit for Multivariate Data Analysis. *PoS ACAT, 40* (2009), p. 12
[12] Brun, R., Rademakers, F., ROOT – An Object Oriented Data Analysis Framework, *Nucl. Inst. & Meth. in Phys. Res. A, 389* (1997), pp. 81-86

Received on December 18, 2023
Accepted on February 12, 2024

---

**Димитрије М. МАЛЕТИЋ, Радомир М. БАЊАНАЦ, Дејан Р. ЈОКОВИЋ, Александар Л. ДРАГИЋ, Никола Б. ВЕСЕЛИНОВИЋ, Михаило Р. САВИЋ, Зоран Р. МИЈИЋ, Владимир И. УДОВИЧИЋ Светлана Д. ЖИВКОВИЋ-РАДЕТА, Јелена В. УДОВИЧИЋ**

## МУЛТИВАРИЈАНТНА АНАЛИЗА ДВОГОДИШЊЕГ КОНТИНУАЛНОГ МОНИТОРИНГА РАДОНА У НАДЗЕМНОЈ ЛАБОРАТОРИЈИ У ИНСТИТУТУ ЗА ФИЗИКУ У БЕОГРАДУ

Приказана је мултиваријантна класификациона и регресиона анализа односа метеоролошких варијабли и концентрације радона у затвореној и ретко приступачној приземној лабораторији Института за физику Београд. Податке о метеоролошким варијаблама и концентрацији радона, коришћене у овој анализи, добијамо из активног уређаја за краткорочна мерења концентрације радона у затвореном простору, оближње метеоролошке станице и из података Глобалног система асимилације података. Једно-варијантном анализом идентификоване су варијабле са највећом вредношћу модула Пирсоновог коефицијента корелације са концентрацијом радона, као и варијабле са највећом моћи раздвајања догађаја са повећаном концентрацијом радона више од (200 Bqm$^{-3}$) и догађаја са нижом концентрацијом од ове вредности. Ова почетна анализа и сагледавање варијабли показују очекивану везу концентрације радона и метеоролошких варијабли, са нагласком на анализу података из различитих временских интервала, када је у лабораторији радила и када није радила климатизација, као и са нагласком на варијаблу разлика унутрашњег и спољњег притиска водене паре. Ова једно-вариантна анализа доводи до закључка да се подаци Глобалног система асимилације података могу користити као довољно добра приближна замена за метеоролошке податке из оближње метеоролошке станице за мултиваријантну анализу. Мултиваријантном класификационом анализом пронађено је неколико веома добрих мултиваријантних метода које се могу користити у некој веб апликацији или за даљу детаљну анализу специфичних улазних варијабли. Приказана је важност варијабли за мултиваријантни метод стабла одлучивања за сва три периода мерења, а разматране су и најважније варијабле. Коначно, мултиваријантна регресиона анализа је такође дала добре резултате, што може да буде корисно при оптимизацији класификационих мултиваријантних метода.

*Кључне речи: континуирани радон мониторинг, мултиваријантна анализа, Глобални систем асимилације података, метеоролошка станица*

Journal of Atmospheric and Solar-Terrestrial Physics 171 (2018) 250–259

Contents lists available at ScienceDirect

Journal of Atmospheric and Solar-Terrestrial Physics

journal homepage: www.elsevier.com/locate/jastp

# Changes of atmospheric properties over Belgrade, observed using remote sensing and in situ methods during the partial solar eclipse of 20 March 2015

L. Ilić [a,*], M. Kuzmanoski [a], P. Kolarž [a], A. Nina [a], V. Srećković [a], Z. Mijić [a], J. Bajčetić [b], M. Andrić [b]

[a] Institute of Physics Belgrade, University of Belgrade, Pregrevica 118, 11080, Belgrade, Serbia
[b] University of Defence, Military Academy, Generala Pavla Jurišića Šturma 33, 11000, Belgrade, Serbia

ARTICLE INFO

*Keywords:*
Solar eclipse
Lidar
Planetary boundary layer
Ground based observations

ABSTRACT

Measurements of atmospheric parameters were carried out during the partial solar eclipse (51% coverage of solar disc) observed in Belgrade on 20 March 2015. The measured parameters included height of the planetary boundary layer (PBL), meteorological parameters, solar radiation, surface ozone and air ions, as well as Very Low Frequency (VLF, 3–30 kHz) and Low Frequency (LF, 30–300 kHz) signals to detect low-ionospheric plasma perturbations. The observed decrease of global solar and UV-B radiation was 48%, similar to the solar disc coverage. Meteorological parameters showed similar behavior at two measurement sites, with different elevations and different measurement heights. Air temperature change due to solar eclipse was more pronounced at the lower measurement height, showing a decrease of 2.6 °C, with 15-min time delay relative to the eclipse maximum. However, at the other site temperature did not decrease; its morning increase ceased with the start of the eclipse, and continued after the eclipse maximum. Relative humidity at both sites remained almost constant until the eclipse maximum and then decreased as the temperature increased. The wind speed decreased and reached minimum 35 min after the last contact. The eclipse-induced decrease of PBL height was about 200 m, with minimum reached 20 min after the eclipse maximum. Although dependent on UV radiation, surface ozone concentration did not show the expected decrease, possibly due to less significant influence of photochemical reactions at the measurement site and decline of PBL height. Air-ion concentration decreased during the solar eclipse, with minimum almost coinciding with the eclipse maximum. Additionally, the referential Line-of-Sight (LOS) radio link was set in the area of Belgrade, using the carrier frequency of 3 GHz. Perturbation of the receiving signal level (RSL) was observed on March 20, probably induced by the solar eclipse. Eclipse-related perturbations in ionospheric D-region were detected based on the VLF/LF signal variations, as a consequence of Lyα radiation decrease.

## 1. Introduction

Abrupt change in the incoming solar radiation flux during solar eclipse induces disturbances in different atmospheric layers (Gerasopoulos et al., 2008; Aplin et al., 2016). These disturbances are not necessarily similar to those during sunset/sunrise, because of different time scales and initial conditions. They depend on a number of factors, including the percentage of sun obscuration, latitude, season, time of the day, synoptic conditions, terrain complexity and surface properties. Since solar energy impacts the atmosphere primarily by convection of heat from the ground, lower atmospheric layers are more influenced by changes in solar radiation. The layer of the atmosphere in direct interaction with the surface, thus directly influenced by the Earth's surface forcing, is called the planetary boundary layer (PBL). Since surface is also a source of humidity and pollutants, turbulence within the PBL is responsible for mixing and dispersion of pollutants, while air pollution concentrations in the PBL are generally higher than those in the free troposphere (Stull, 1988).

A number of studies have focused on the effect of solar eclipse on various atmospheric properties, mainly in PBL. Changes in meteorological parameters near the ground level were most extensively investigated, for several eclipse events (Anderson, 1999; Ahrens et al., 2001; Kolarž

* Corresponding author.
*E-mail address:* luka@ipb.ac.rs (L. Ilić).

https://doi.org/10.1016/j.jastp.2017.10.001
Received 31 March 2017; Received in revised form 16 August 2017; Accepted 3 October 2017
Available online 4 October 2017
1364-6826/

et al., 2005; Founda et al., 2007; Nymphas et al., 2009). The studies reported decrease in temperature and wind speed, changes in wind direction and increase in relative humidity, as a result of solar eclipse. The magnitude of these changes varied in different studies. Decrease in height of the PBL during solar eclipse was also observed (Kolev et al., 2005; Amiridis et al., 2007). The PBL quickly responds to surface forcing and its height can range from as low as a few hundred meters to a few kilometers. Diurnal cycle of the PBL height starts with the sunrise by heating of the surface and development of a convective boundary layer (CBL), reaching a steady state in the afternoon. The CBL remains as a residual layer until the development of a new mixing layer on the following day. A region of statically stable layer – the entrainment zone forms at the top of the PBL. It closely follows the PBL development, being shallow in the morning and thickening during the day due to intense turbulence and vigorous convection (Stull, 1988). During a solar eclipse, the change in the incoming radiation is more abrupt and affects the evolution of the PBL (Amiridis et al., 2007; Kolev et al., 2005), thus providing opportunity for investigating mechanisms involved in PBL evolution.

Some studies investigated eclipse-related changes in ozone concentration (Zerefos et al., 2001; Kolev et al., 2005; Zanis et al., 2001, 2007), due to its strong dependence upon the magnitude of UV flux (Bian et al., 2007). Tropospheric ozone ($O_3$)is the result of chemical reactions, mostly between nitrogen oxides (NOx), carbon monoxide (CO) and volatile organic compounds (VOCs), helped with UV radiation via process of photo-dissociation of $O_3$. Surface ozone concentrations were reported in literature to decrease during solar eclipse, with exception of unpolluted sites (Zanis et al., 2001, 2007).

Reported observations suggest increase in air ion (Kolarž et al., 2005; Aplin and Harrison, 2003 and references therein) and air radon concentrations (Gaso et al., 1994 and references therein) during solar eclipse, mainly attributed to PBL height decrease. Air ions are natural constituents of the atmosphere produced mostly by cosmic rays (20% of overall ionization) and natural radioactivity from soil (gamma decay of $^{40}$K)and the air ($^{222}$Rn). The first two ionization sources mentioned above are nearly constant in time, and consequently changes of air ion generation areprimarily related to changes in Rn concentration. The background concentration of cluster air ions in lower troposphere vary from a few hundred to a few thousand ions $cm^{-1}$, with an average near-ground ionization rate of 10 ion pairs $cm^{-3}s^{-1}$. Air ions are neutralized mostly by ion-to-ion recombination and ion-aerosol attachment (Dolezalek, 1974). Their concentration changes diurnally: during the night, when the boundary layer conditions are stable concentrations are high, with maximum at dawn. During the day, with the development of convective boundary layer, air ion concentration decreases with minimum in the afternoon (Blaauboer and Smetsers, 1996). Radon and aerosol-carried Rn progenies are powerful air ionizers (energy of α particle decay is more than 5 MeV, while average ionization energy of air is 34 eV/ion pair) and thus the main source of cluster air ion pair production in the troposphere. Radon exhalation from the ground is determined by concentration of uranium, diffusion coefficients and porosity of soil layers on the way to surface (Ishimori et al., 2013). Average Rn concentration over the continents is 10 Bq $m^{-3}$ (UNSCEAR, 1993).

The solar eclipse also influences ionosphere. In the upper part of this area variations in plasma frequencies are detected (Verhulst et al., 2016). Also, there are detected plasma variations in the lower ionosphere (see e.g. Guha et al., 2010; Maurya et al., 2014). One of the ways to register the variations of solar radiation impact within upper atmosphere is based on technology of radio waves which are reflected in ionosphere during propagation between emitters and receivers. Namely, the signal reflection height in the ionosphere and, consequently, parameters describing signal characteristics (propagation geometry, altitude distributions of refractive index and attenuation) depend on local plasma properties (primarily on electron density) (Bajčetić et al., 2015). Electron density declines during solar eclipse, similarly to sunset, resulting in increase of the reflection height of radio signals reflected on relevant atmospheric layer (Guha et al., 2010), as well as the occurrence of hydrodynamic waves (Nina and Čadež, 2013; Maurya et al., 2014). Because of that, the registered wave variations reflect the non-stationary physical and chemical conditions in the medium, along the considered wave trajectories, in real time. In addition to plasma parameters related to low ionosphere, several parameters describing signal propagation, like distance between transmitter and receiver, influence temporal changes in recorded signal characteristics. Because of that, the electron density decrease (or increase) can result in either increase and decrease of recorded amplitude (Grubor et al., 2008). Thus, only variation from the expected values is important for detection of influences of an event on low ionosphere.

The aim of this paper is to study atmospheric disturbances detected in Belgrade, induced by partial solar eclipse (51% coverage of solar disc) on March 20, 2015. Focusing on troposphere (mainly PBL) and ionosphere (D-region). For that purpose, four experimental setups were used to collect data, including lidar (Light Detection and Ranging) for measurement of PBL height and heights of elevated layers, AWESOME (Atmospheric Weather Electromagnetic System for Observation Modelling and Education) VLF/LF receiver (Cohen et al., 2010) and instruments for measurements solar radiation, meteorological parameters, concentrations of ozone, air ions and radon, and propagation of radio signals in troposphere.

The paper is organized as follows. In Section 2 we describe measurements and methods used in the study, and give overview of background conditions. The results are described in Section 3, and a conclusion of this study is given in Section 4.

## 2. Measurements and methods

### 2.1. UVradiation, ozone and air-ion measurements

UV-B erythemal radiation was measured using 501 biometer made by Solar light company, USA. Instrument was set on the roof of the Institute of Physics Belgrade (IPB), so that no obstacles entered the field of view. During the eclipse, data acquisition was set to 10 min. Global Sun radiation was measured by Republic Hydro-meteorological Service in Belgrade using Kipp&Zonen CMP6 pyranometer (http://www.kippzonen.com/Product/12/CMP6-Pyranometer), with 1-min data acquisition. Surface ozone measurements were conducted using Aeroqual monitor, series 500 (http://aeroqual.com/product/series-500-portable-air-pollution-monitor), made in New Zealand. The instrument was placed near UV 501 biometer and acquisition was set to 6 min. Air ions, temperature, pressure and relative humidity were measured using a Cylindrical Detector and Ion Spectrometer CDIS (Kolarž et al., 2011), made at IPB. The CDIS was placed 1 m above grassy surface (where the soil allows the radon exhalation), at IPB (44.86° N, 20.39° E, 89 m a.s.l.). Only positive air ion concentrations were measured since they have lower mobility than negative ions and consequently lower ion-to-aerosol attachment coefficient. Thus, they are less sensitive to air pollution and provide better picture of atmosphere processes. Radon was measured using continual radon measuring instrument RAD7, Durridge company, USA. Quality of continual Rn measurements is related to level of radon concentration and measuring period, i.e. counting events. The instrument was placed next to CDIS at the same level.

### 2.2. Measurements of meteorological parameters

The meteorological measurements were obtained at two semi-urban sites in Belgrade. One measurement site was located at IPB. At the site, temperature, relative humidity and atmospheric pressure at altitude 1 m above ground were measured. The meteorological measurements were also available from an automatic weather station collocated with a SYNOP station at Košutnjak, Belgrade (WMO no. 13275, 203 m a.s.l.), about 10 km away from the IPB site.

### 2.3. Detection of PBL height

A variety of methods can be used to quantify the PBL height, depending on available measurements (Emeis et al., 2008). Differences between PBL and free troposphere can be observed using vertical profiles of thermodynamic quantities and wind from radiosounding measurements. Lidar observations, using atmospheric aerosol as a tracer, can be used to determine heights of both PBL and elevated aerosol layers if present in the atmosphere.

In this study radiosounding and lidar measurements were used to determine PBL height. While radiosoudings are regularly available at 00UTC and 12UTC at the WMO station, providing meteorological data on mandatory and significant pressure levels, the advantage of lidar measurements is that they can be performed continuously with high vertical andtemporal resolutions. Data derived from lidarmeasurements can be used for detection and characterization of aerosols and PBL evolution, and allow for the detection of abrupt and smaller scale changes in the layer structure.

The lidar system at IPB, is a bi-axial system with combined elastic and Raman detection designed to perform continuous measurements of suspended aerosol particles in the PBL and the lower free - troposphere. It is based on the third harmonic frequency of a compact, pulsed Nd:YAG laser, emitting pulses of 65 mJ output energy at 355 nm with a 20 Hz repetition rate. The optical receiver is a Cassegrain reflecting telescope with a primary mirror of 250 mm diameter and a focal length of 1,250 mm. Photomultiplier tubes are used to detect elastic backscatter lidar signal at 355 nm and Raman signal at 387 nm. The detectors are operated both in the analog and photon-counting mode and the spatial raw resolution of the detected signals is 7.5 m. Averaging time of the lidar profiles during the March 2015 solar eclipse case was 1 min corresponding to 1,200 laser shots.

Lidar measurements can be used to estimate PBL height using different approaches (Sicard et al., 2006; Baars et al., 2008). In this study, the gradient method was used to determine the position of the strongest gradient of the aerosol vertical distribution, associated with the PBL height (Flamant et al., 1997). The height of a strong negative peak which can be identified as the absolute minimum of the range corrected signal's (RCS) derivative, determines the PBL top height. A strong negative gradient in lidar RCS is a result of decrease in aerosol backscatter due to decrease in aerosol concentration and humidity (Matthias et al., 2004). Our estimate of PBL height is based on lidar measurements at 355 nm. However, when available, measurements at larger wavelengths (i.e. 532 nm and 1,064 nm) are more appropriate for analysis of PBL height due to smaller relative contribution of molecular backscatter compared to 355 nm. Other local minima in the signal derivative, with absolute values above a specified threshold and with transition intervals including a minimum of five points, are associated with elevated aerosol layer top heights in the free troposphere (Flamant et al., 1997).

The Richardson number is used for PBL height estimation from radiosounding measurements. Radiosoundings are performed two times each day, at 00 and 12 UTC, at a weather station (Belgrade Košutnjak, WMO number 13275), 10 km away from the lidar measurement site at 203 m altitude. The Richardson number is defined as (Stull, 1988):

$$R_{ib} = \frac{g[z - z_0][\theta(z) - \theta(z_0)]}{\theta(z)\left[u(z)^2 + v(z)^2\right]} \tag{1}$$

where $g$ is acceleration due to gravity, $z_0$ is the altitude of the weather station, $\theta(z)$ is the potential temperature and $u(z)$ and $v(z)$ are zonal and meridional components of the wind. The layers in which $R_{ib}$ is above a critical value of 0.21 (Vogelezang and Holtslag, 1996; Menut et al., 1999) are considered to be above the PBL.

Since the data are available at discrete heights, at standard and significant pressure levels, the bulk Richardson number is used (Stull, 1988). Successful estimation of the PBL height from radiosounding measurements from stations in the WMO network, has been previously reported (Jeričević and Grisogono, 2006; Amiridis et al., 2007). Average uncertainty of the PBL height was estimated for March for a 10-year period from 2006 to 2015, from radiosounding profiles retrieved at 12 UTC. Typical resolutions varied from 100 m to 1,000 m, and the uncertainty of PBL height $H$ was estimatedusing the following formula:

$$H = H_{estimated} \pm \frac{\Delta z}{2} \tag{2}$$

where $\Delta z$ is the measurement resolution (Jeričević and Grisogono, 2006). It was calculated to be 180 m corresponding to the average vertical resolution of 350 m. On the eclipse day, the resolution and the uncertainty were estimated to be 150 m and 80 m, respectively.

### 2.4. Terrestrial line-of-sight radio communication measurement setup

The referential Line-of-Sight (LOS) radio link was set in the area of Belgrade, using the carrier frequency of 3 GHz, with the purpose of investigating solar eclipse contribution to receiving signal level (RSL) instability.

The transmitter was emitting non-modulated carrier, having the radio frequency (RF) output power level of 0 dBm. LOS link was established at the distance of 70 m. The signal was transmitted using the signal generator with the frequency stability of TCXO $\leq \pm 0.5$ ppm and signal level stability $\leq \pm 0.7$ dB which was housed at constant temperature. Antenna emitted horizontally polarized electromagnetic (EM) wave. The receiving system (Rx) was formed with Tektronix SA2600 spectrum analyser that was programmed to perform 1 kHz width spectral recording into 500 points. In this way, the generated signal spectrum at the receiving side could be reconstructed with an accuracy of 2 Hz, which made it possible to monitor temporal changes in the level of the received signal peak.

The measuring samples of the received signal level were recorded every 45 s equidistantly during continuous operation of the LOS link. On 20 March 2015, we made 480 recordings through 6 h, includingthe solar eclipse period.

### 2.5. Ionospheric observations

Global experimental setup for the low ionospheric observation is based on continuously emitting and receiving the VLF/LF signals by numerous worldwide-distributed VLF/LF transmitters and receivers, respectively. In this study, we based our analysis on D-region monitoring using the 37.5 kHz LF signal emitted by the NRK transmitter located in Grindavik (Iceland) and received at IPB by the AWESOMEVLF/LF receiver. This transmitter was chosen because the path of this signal passes through an area that was affected by a total eclipse.

### 2.6. Background conditions

The eclipse on March 20, 2015 started at 8:40 UTC, ended at 10:58 UTC, reaching maximum coverage of 51% at 9:48 UTC. In the days prior to the eclipse, the synoptic conditions were influenced by a cyclone moving to the east, over Balkans, followed by an increase in geopotential. Wind field was characterized by northwesterly flow shifting to northerly. On the day of the eclipse surface conditions were influenced by weak-gradient anticyclonic field. On the previous day, overcast skies with light rain in the evening were reported. From the morning of the March 20 and during the day, the sky was clear. The calm meteorological conditions provided good opportunity to observe possible eclipse-related changes in meteorological parameters near surface.

## 3. Results

### 3.1. Global and UV radiation

Primary effect of solar eclipse is reduction of solar radiation reaching the surface. In Fig. 1 diurnal variation of global sun radiation and UV-B erythemalradiation are shown for the day of the solar eclipse, and for three clear days after the eclipse. Solar eclipse on March 20 occurred during morning increase of both global and UV-B radiation due to sun elevation. Their attenuation was 48%, slightly smaller than the obscuration of the solar disc (51%). This difference could be due to diffuse solar irradianceknowing that UV-B radiation is the shortest wavelength reaching the surface and thus most prone to scattering. While the direct solar irradiance is reduced proportionally to the obscuration of solar disc during the eclipse, the diffuse irradiance is less affected due to contribution of multiple scattering from less shadowed part of the sky (Zerefos et al., 2001). They reported that the difference in reduction of diffuse and direct irradiance was more pronounced at shorter wavelengths.

### 3.2. Meteorological parameters

Meteorological measurements were analyzed to investigate the response of the air temperature, relative humidity and pressure at near-surface level to the eclipse. As mentioned in the previous section, the meteorological measurements were conducted at two locations: at IPB lidar measurement site and at Košutnjakstation, about10 km away. Diurnal cycle of the temperature was interrupted by the eclipse at both measurement sites (Fig. 2). Change in temperature increase rate was observed at both sites, with similar delay after the first contact. Higher temperatures were measured, and temperature decrease was more pronounced at IPB station, probably due to lower altitude and as a result of lower measurement height above ground. At this station, the temperature decreased during the eclipse, by 2.6 °C, at the rate of 0.043 °Cmin$^{-1}$, reaching minimum about 15 min after the maximum of the eclipse. At Košutnjakstation the temperature was almost constant after the first contact until the maximum of the eclipse, with an increase rate of 0.003 °wCmin$^{-1}$. After the eclipse maximum, it started increasing with increased downward radiation, at a higher rate of0.03 °C/min.To further investigate the effect of the eclipse on temperature, measurements available from Košutnjakstation on days following the eclipse were used. The rate of temperature change during the eclipse was compared to the rates recorded during the same period of day on three cloud-free days after the eclipse – March 21, 23 and 24. Increasing trend of maximum daily temperature was measured in this period. On the eclipse day, the increase rate from the first contact to the eclipse maximum (0.003 °Cmin$^{-1}$)was very low in comparison to the rates of 0.016 °C min$^{-1}$, 0.025 °Cmin$^{-1}$ and 0.032 °Cmin$^{-1}$ for the same period on March 21, 23 and 24, respectively. After the eclipse maximum until the end of the eclipse, temperature increase rate of 0.025 °Cmin$^{-1}$was comparable to the corresponding rates on the three following days. Total increase in temperature during the eclipse was 2.0 °C, while the corresponding measured increase on March 21, 23 and 24, was 2.3 °C, 3.3 °C and 4.0 °C, respectively.

Relative humidity showed decreasing trend, typical for the beginning of the day and morning increase of temperature. During the eclipse, humidity was almost constant until the maximal obscuration of solar disc, and then it decreased by 10% at both locations (IPB and Košutnjak), in consistence with temperature increase. Until the maximal obscuaration, at IPB, the temperature was decreasing while the relative humidity was almost constant. It remains unclear whether its behaviour is an effect of eclipse.

The wind speed measured at the Košutnjak station followed atypical diurnal cycle, until the maximum of the eclipse, when both wind speed and gustiness dropped, and started increasing after the event (Fig. 3). Wind speed decreased from a maximum of 2.7 ms$^{-1}$ to about 1.1 ms$^{-1}$at the end of the eclipse. The absolute minimum of wind speed and gusts was reached about 35 min after the last contact. Wind direction changed from northerly to northeasterly for the duration of the eclipse.

Pressure drop during the eclipse at Košutnjak station was 0.9 hPa (not shown here), which is most probably the consequence of the temperature

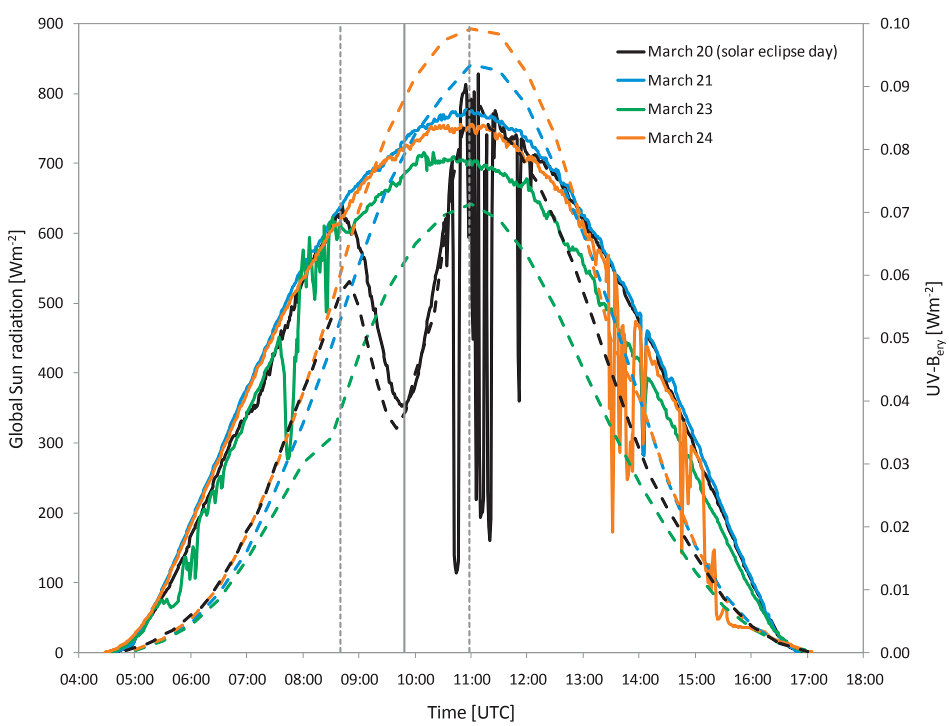


**Fig. 1.** Global Sun radiation (solid lines) and UV-B erythemal radiation (dashed lines) during partial Solar eclipse (March 20, 2015) and three clear days after the eclipse. Dotted vertical lines indicate beginning, maximum and end of the eclipse.

drop (Fig. 2). The pressure minimum was reached about 30 min after the eclipse maximum. Additional data, from radiosounding, provided information on vertical profiles of meteorological variables 1 h after the event. Up to the top of the PBL, the northerly wind speeds were relatively low, from 2 to 3.5 $ms^{-1}$. Air in the PBL was not very humid, with relative humidity of 35–60%.

These observed changes are generally in agreement with those reported in previous studies, related to eclipse events with larger obscuration of solar disc. The exception is relative humidity, which was almost constant until the eclipse maximum in this work, while it was reported to increase in previous studies. Anderson (1999) compiled data on near-surface temperature during selected total eclipse events, given in literature. These data showed temperature decrease of 2.0–3.6 °C, with minimal value coinciding with mid-eclipse (in one case), or reached with the time lag of 7–17 min. Foundaet al. (2007) presented observations at several sites in Greece, with different degrees of sun obscuration (74–100%) during solar eclipse in March 2007. Their results showed that temperature (measured at altitudes varying from 1.5 m to 17 m at different sites) decreased by 1.6–2.7 °C (3.9 °C at a site affected by low clouds), reaching minimal value 12–14 min after the mid-eclipse. Following the temperature response, the relative humidity was reported to increase by about 20% (Founda et al., 2007; Kolev et al., 2005). A decline in wind speed, after mid-eclipse, as a result of cooling the boundary layer and reduction of turbulent transport (Girard-Ardhuin et al., 2003) was also reported in literature (Anderson, 1999; Founda et al., 2007).

### 3.3. PBL evolution assessment from meteorological and lidar measurements

The presence of the residual layer, evolution of the PBL and aerosol layers in the free troposphere during the solar eclipse were observed using lidar measurements in Belgrade. For that purpose, the vertical profiles of the range-corrected analog signal at 355 nm, obtained from 10:15 UTC until 15:25 UTC with temporal resolution of 1 min, were analyzed, using the gradient method. The time series of range corrected signal (RCS) vertical profiles, along with heights of PBL and elevated aerosol layers are presented in Fig. 4.

The eclipse occurred before local noon, during the development of the mixing layer. In the morning, with surface heating, PBL started increasing from 600 m height to about 800 m above ground during the time period of about 2 h until the start of the eclipse at 8:40 UTC. The increase of the PBL height before the eclipse was steady and gradual. During this period, a layer was identified at height of about 1 km. This layer can be identified as the residual layer. With the beginning of the eclipse, the amount of solar radiation reaching the surface started

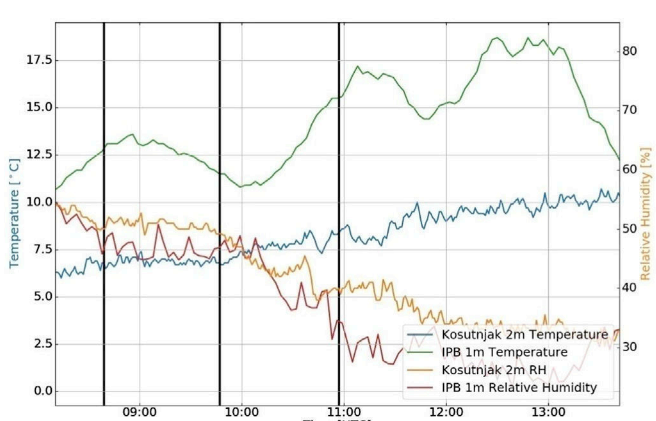


**Fig. 2.** Temperature and relative humidity. Vertical lines indicate beginning, maximum and end of the eclipse.

decreasing (Fig. 1). This affected the change in surface temperature (Fig. 2), and therefore convective motion, with the effects diminishing with height. The PBL height decreased by about 200 m during the solar eclipse, reaching minimum 20 min after the maximum of the eclipse. This decrease in PBL height is similar to those reported in previous research (Amiridis et al., 2007; Kolev et al., 2005), for solar eclipse with larger solar disc obscuration. With passing of the eclipse, the PBL started gaining height until reaching the height of about 1700 m around 13 UTC. Stronger variations of PBL height observed after the eclipse can be attributed to stronger convective motions. In first minutes after the eclipse, shallow cumulus clouds formed with their base at the top of the PBL. A peak in PBL height, coinciding with peaks in temperature and wind speed measurements was observed during the later phase of the event. Depth of the entrainment zone followed the development of the PBL. It showed gradual increase before the eclipse, from low values of about 30 m, to variations in height of several tens of meters after the eclipse as a result of strong convective motions.

The PBL height value calculated as an hourly average around 12 UTC (soon after the end of the eclipse), was 1 500 $\pm$ 100 m, in agreement with the one estimated from radiosounding:1 600 $\pm$ 80 m.Small differences of results obtained from radiosounding and lidar measurements can be due to local effects at two measurement sites and differences in the methods used. The gradient method uses gradient in lidar RCS due to decrease in aerosol backscatter while the bulk Richardson number approach relies on thermodynamic properties. Different surface properties and elevations of measurement sites influence the heat and momentum fluxes contributing to the PBL development. Lidar is operated on a fixed location during the whole measurement period, providing information on vertical column of air directly above the instrument. Radiosounding profiles are affected by the horizontal drift of the instrument caused by wind and depend on whether the ascent is made in a thermal or between thermals (Stull, 1988). To further estimate impact of eclipse on PBL height we compared these values with the PBL heights calculated for March for a 10-year period from 2006 to 2015 from the radiosounding profiles taken at 12 UTC (excluding the profile on the day of the eclipse). The values estimated both from lidar (around 12 UTC) and radiosounding measurements made on the day of the eclipse fall within the inter-quartile range of the values for the 10-year reference period (Fig. 4).

The lidar measurements during solar eclipse also showed presence of aerosol layers in free troposphere, at altitudes up to 4 km.

### 3.4. Ozone and air-ion concentrations

Surface ozone measurements showed no significant decrease, as opposed to most other measured parameters, possibly indicating less significant influence of photochemical reactions at the IPB semi-urban measurement site (see Fig. 5). While a decrease of surface ozone concentration during solar eclipse is expected, this effect could be missing in less polluted areas, or it could be masked by air transport or decline of PBL height (Zanis et al., 2001, 2007). For an urban station in Thessaloniki, Zanis et al. (2001) reported that surface ozone concentration decreased by 10–15 ppbv during the solar eclipse in August 1999 (maximum sun obscuration 90%), with a half-hour delay in starting time of the decrease after the first contact. However, they did not observe any effect on surface ozone in an elevated rural station at Hohenpeissenberg (99.4% sun coverage). Measurements during the solar eclipse in March 2006, conducted in Greece, showed decrease of 5–10 ppb surface ozone in an urban site in Thessaloniki (about 70% sun obscuration), while no effect was observed in relatively unpolluted sites in Finokalia and Kastelorizo, with 82% and 86% solar obscuration, respectively (Zanis et al., 2007). In our study, the measurements were taken at semi-urban site, during solar eclipse event with 51% sun obscuration. It is also noteworthy that measurements conducted for few other days, after the solar eclipse, in the present study showed high time lag of ozone concentration peaks compared to UV radiation peak. This was also reported in Tie et al. (2007) and Bian et al. (2007).

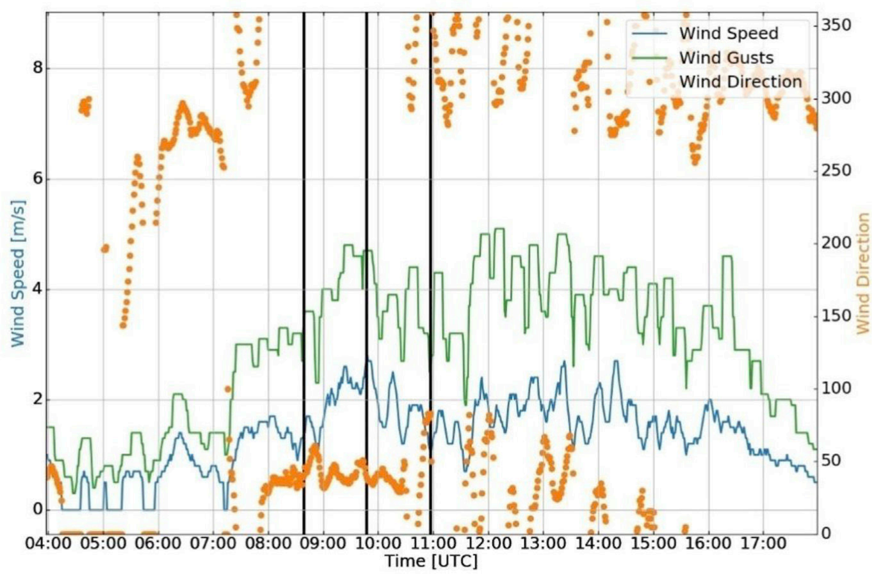


**Fig. 3.** Wind speed, gusts and direction. Vertical lines indicate beginning, maximum and end of the eclipse.

Radon concentrations measured during the eclipse (not shown here) were in the range between 0 and 15 Bq $m^{-3}$ which is typical background for this part of the day. As shown in Fig. 6, air ion concentration decreased during the course of the day. The decrease was more intensive during the eclipse. After the eclipse, air ion concentration returned to its usual diurnal path to afternoon minimum. This could be explained by decrease of diffusion processes that are responsible for radon exhalation from the soil, as a result of cease of heating the surface during the eclipse. Differences were noted in air ion change during the eclipse in 1999 (97.7% sun obscuration), described in Kolarž et al. (2005) and that described in this study (51% sun obscuration).

### 3.5. Line-of-Sight radio communication receiving signal change

The observed RSL change during the time of solar eclipse was compared with the RSL change in few following days. The usual change of RSL in morning hours presented in Bajčetić et al. (2013) was confirmed during regular days, while, the pattern of signal level variation was quite different during the solar eclipse (Fig. 7, left panel).

Additionally, the observed meteorological variables were used to calculate the value of the air refractivity parameter ($R$) using (3), with the aim of the correlation between variation of that parameter and microwave RSL change (Fig. 7, right panel).

$$R = 77,6\frac{P}{T} + 3,73{\cdot}10^5\frac{P_{vp}}{T^2}. \tag{3}$$

$R$ is the value which describes the overall influence of the tropospheric medium on the radio wave propagation and depends on relative air pressure $P$, absolute temperature $T$ and partially on water vapour pressure $P_{vp}$ (Debye, 1957; Falodun and Ajewole, 2006).

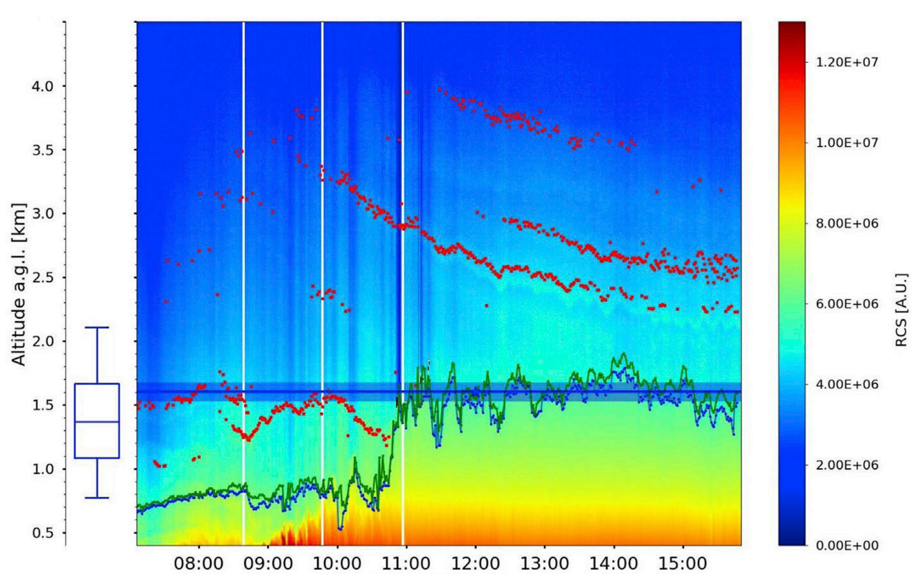


**Fig. 4.** Temporal evolution of PBL (blue line) and elevated aerosol layers (red dots). Colormaps represent the lidar RCS at 355 nm on March 20, 2015. White vertical lines indicate beginning, maximum and end of the eclipse. Box plot shows the median, first and third quartiles and 5th and 95th percentiles of PBL heights in March for period 2006–2015. (For interpretation of the references to colour in this figure legend, the reader is referred to the web version of this article.)

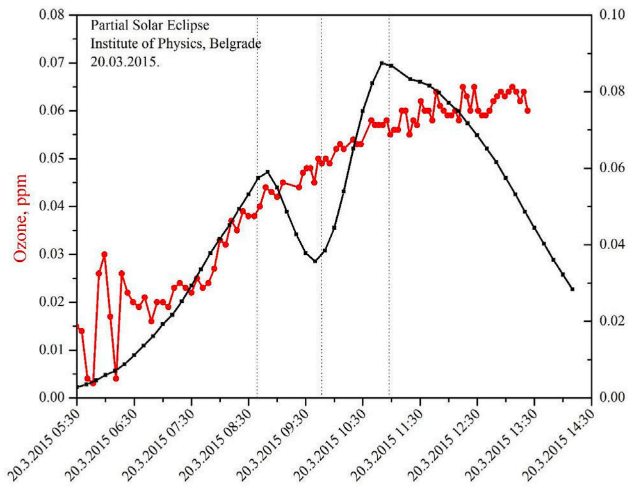


**Fig. 5.** Ozone and UV-B erythemal radiation during partial solar eclipse. Dotted vertical lines indicate beginning, maximum and end of the eclipse.

We normalized the measured values $R_{xi}$ (i = 1,…, 480) of the air refractivity parameterto its mean value during the related day ($\overline{R}_x$), using Eq.2measured values $R_{xi}$ of the air refractivity parameter, in order to emphasize the level of variation.

$$RSL = 100 \cdot \frac{R_{xi} - \overline{R}_x}{|\overline{R}_x|}. \tag{4}$$

Following the presented data in Fig. 8, it can be seen that there was meaningful correlation between RSL and R during the days after the solar eclipse, while their values change fairly independently on the day of the solar eclipse.

Analysing data presented in Fig. 8, it can be seen that before the period of solar eclipse, the disturbance manifested through the unusual *R* constant value until 08:40 is well correlated with the constant value of *RSL*. At the moment of solar eclipse maximum, the considerable *R* disturbance can be noticed, while this phenomenon does not reflect to the *RSL*. From 10:00, until the end of the solar eclipse, value of *R* varied within expected usual values, however *RSL* changed unusually.

This unusual RSL variation was possibly triggered by the solar eclipse event. In ordinary periods of measurements, the relative air pressure, absolute temperature and partially the pressure of the water vapour directly influence the permittivity of the air, causing the refraction of the electromagnetic wave, so the effects are noticeable as the RSL variation. However, during a solar eclipse event, it is not possible to consequently relate RSL and R. Considering the absolute amplitude variation of RSL, which was in the domain of 2,5 dB for the presented time periods, the sudden not so intense air permittivity perturbation within the area where LOS link was established did not have direct influence on the radio propagation at 3 GHz frequency. While RSLwas evidently slightly perturbedduring solar eclipse, there is not clear evidence that this perturbation is related to solar eclipse. The observed phenomena are not well presented in the literature for this particular scenario, and will be a subject of future analyses.

### 3.6. Effects on the ionosphere and LF radio signal propagation

The ionospheric perturbations were detected as variations of recorded NRK signal from Iceland. Generally, the temporal evolution of recorded signal can be used for detection of low ionospheric plasma perturbations; these changes in medium through which signal propagates affect wave reflection height, and consequently, propagation geometry and attenuation, resulting in variations of recorded signal characteristics.

The shapes of the temporal change depend on numerous parameters. Namely, in addition to periodic and sudden variations in the ionospheric plasma conditions, characteristics of signals like mutual locations of transmitter and receiver, power of transmitted signal, and geographical area through which the signal propagates, affect the recorded signal properties. For these reasons the dependencies between the ionospheric changes of electron density induced by radiation increase and VLF/LF signal amplitude are not monotonous, e.g. growth in the electron density does not necessarily cause amplification of recorded signal amplitudes (for detailed explanation see Nina et al., 2017). Thus, for detection of some sudden perturbationit is sufficient toobservechanges in temporal

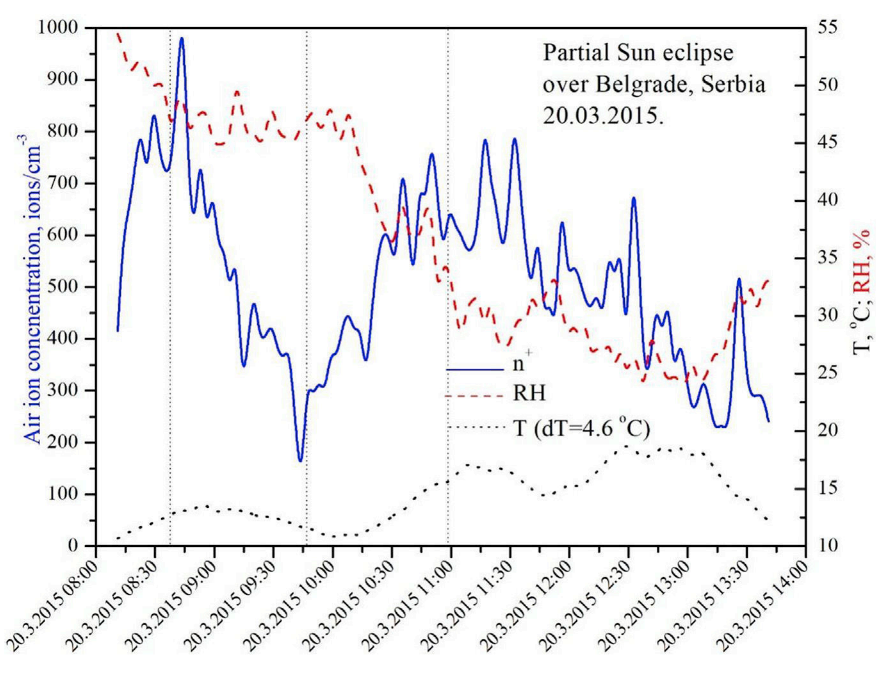


**Fig. 6.** Air ion concentration, temperature and relative humidity during partial solar eclipse. Dotted vertical lines indicate beginning, maximum and end of the eclipse.

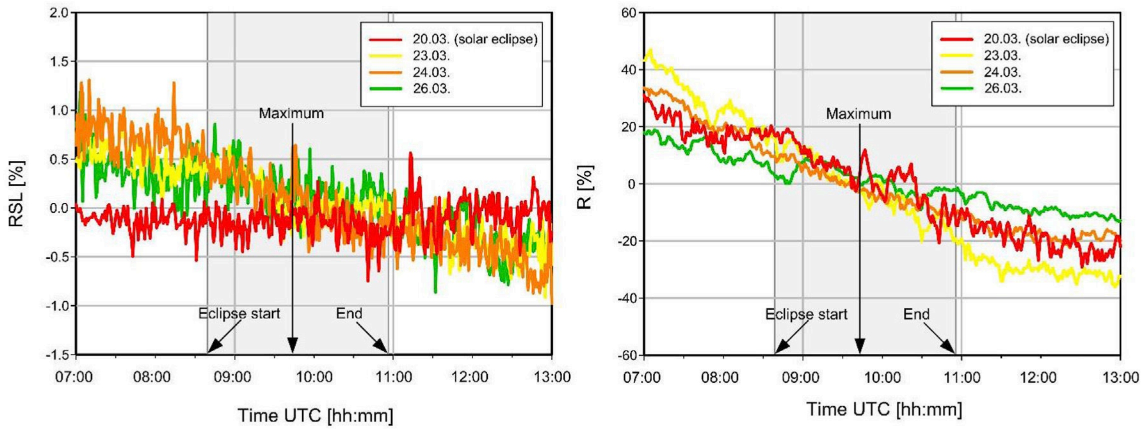


**Fig. 7.** Receiving signal level (*RSL*) and refractivity (R) variation. Shaded domains represent the time period when eclipse occurred.

evolution of signal characteristics.

Fig. 9 shows temporal variations of amplitude difference from its initial considered values, recorded by the AWESOME system at the Belgrade station on March 20, 2015 when solar eclipse occurred, and three days after that. The additional days are shown to visualize amplitude variation in solar eclipse period with respect to its shapes in other relevant periods without influence of the eclipse. The reason for choosing these particular days was relatively quiet conditions without significant traveling ionospheric disturbance resulting from atmospheric lightnings, and solar flares among other events. While amplitude variations are pronounced during the solar eclipse, they are practically within noise domains on the other three days. In the first period, a decrease in amplitude was observed, with the minimum occurring before the eclipse maximum. Further, the amplitude increased, exceeded the amplitude values during the first contact and reached the larger value approximately coincidently with the eclipse maximum time (indicated by a vertical line). Finally, it returned to the expected values, which are around initial values (this can be concluded from the three referent signals).

As explained in Section 1, electron density variation is most important for changes of plasma parameters which influence signal propagation. Its time variations depend on different electron gain and loss processes. The constituents of the low ionosphere can be ionized by γ, X and a part of UV photons. The most important solar influences on the ionization processes in the D-region in absence of large radiation increase, primarily as consequence of solar X-flares (Nina et al., 2012a,b) is coming from the

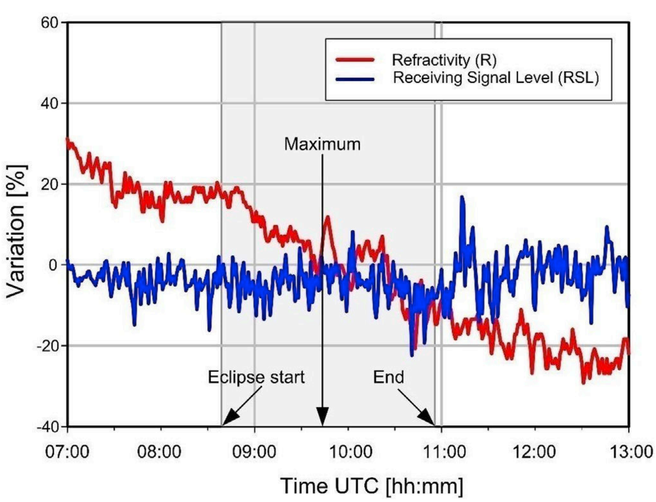


**Fig. 8.** *RSL* and R variation during solar eclipse. Shaded domains represent the time period when eclipse occurred.

solar Lyα line (121.6 nm) radiation (Swamy, 1991) whose presence is periodically intensified during the day. Bearing in mind that satellites did not register significant increase of intensity of X radiation, we can conclude that the signal variations are a consequence of Lyα radiation decrease. http://en.wikipedia.org/wiki/Solar_eclipse.

## 4. Conclusions

Changes in atmospheric properties were observed during a partial solar eclipse (51%) on March 20, 2015 in Belgrade. For that purpose, four experimental setups were used to collect data, including lidar to derive PBL height and heights of elevated layers, AWESOME VLF/LF receiver (Cohen et al., 2010) and instruments for measurements of solar radiation, meteorological parameters, concentrations of ozone, air ions and radon and propagation of radio signals in troposphere. Although the solar eclipse was only partial, its influence on atmospheric properties in troposphere and ionosphere was noticeable. The detected changes in atmospheric parameters were generally similar, but weaker in intensity, to those reported in literature for solar eclipse events with larger obscuration of solar disc.

In troposphere, the influence of the eclipse was observed in meteorological surface parameters, and it was evident up to the top of the PBL. Eclipse-induced decrease in PBL height was 200 m, comparable to that reported in literature, with minimal value occurring 20 min after the eclipse maximum. The PBL height determined from 12 UTC radiosounding measurements (soon after the eclipse), showed that it was within the usual values for this location at that time of year. The meteorological parameters showed similar behavior at two measurement sites Košutnjak and IPB, respectively. The temperature change was more pronounced and abrupt at the –IPB station, probably due to lower measurement height, where it decreased by 2.6 °C, reaching minimum 15 min after the eclipse maximum. This temperature change is similar to those reported in literature for solar eclipse with larger obscuration of solar disc. At the Košutnjakstation the temperature was almost constant, until the eclipse maximum. Relative humidity was almost constant at both sites from the first contact until the eclipse maximum, as opposed to the increase reported in literature. The diurnal cycle then continued, with the increase in temperature and decrease in relative humidity at both sites. The 10-m wind speed and gusts decreased, reaching a minimum about 30 min after the eclipse. The wind direction changed from northerly to northeasterly for the duration of the event. Decrease of PBL height and the entrainment zone thickness were also observed during the eclipse, as a result of diminished surface heating. Ozone concentrations showed no decrease, as opposed to most results reported in literature, except for those reported for rural measurement sites. The possible reasons are less significant influence of photochemical reactions, decrease in PBL height or advection by changing wind during the event. Measured

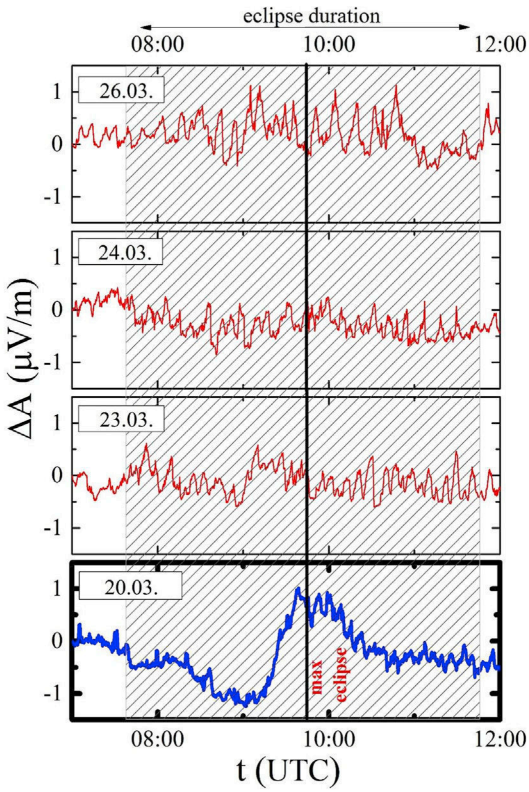


**Fig. 9.** The variations of amplitude difference from its initial considered values against the universal time (UT), recorded by the AWESOME system at the Belgrade station on March 20, 2015 when solar eclipseoccurred (lower panel) and three days after that (top panels). Shaded domains represent the time period when eclipse occurred (here we consider a whole period of eclipse because of long signal propagation path from Iceland to Serbia).

radon concentrations were typically low for this time of the day, while the air ion concentration sharply decreased.

The referential Line-of-Sight (LOS) radio link was set in the area of Belgrade, in order to investigate influence of the event on RSL instability. During the solar eclipse, an unusual pattern of the signal level variation was observed and different relationship between the RSL and the air refractivity parameter (R). Further analysis is needed to clearly relate the perturbation with solar eclipse which affected the atmospheric variables and therefore R.

Impact of the solar eclipse on the ionosphere was registered through changes of characteristics of radio waves which are reflected in ionosphere. The amplitude variations, were pronounced during the solar eclipse, and were at the expected values on the days after the event. Since satellite measurements did not show significant increase of intensity of X radiation, it was concluded that the signal variations are consequence of Lyα radiation decrease.

## Acknowledgements

This research was realized as a part of projects no. III43007, no. III41011, no. III44002, no. 176002, no. P171020, no. III45003 financed by the Ministry of Education, Science and Technological Development of the Republic of Serbia within the framework of integrated and interdisciplinary research for the period 2011–2017. Also, this study is made within the COST project TD1403 and VarSITY project.

## References

Ahrens, D., Moses, G.I., Lutz, J., Andreas, M., Helmut, M., 2001. Impacts of the solar eclipse of 11 August, 1999 on routinely recorded meteorological and air quality data in South-West Germany. Meteorol. Z. 10 (3), 215–223.

Amiridis, V., Melas, D., Balis, D.S., Papayannis, A., Founda, D., Katragkou, E., Giannakaki, E., Mamouri, R.E., Gerasopoulos, E., Zerefos, C., 2007. Aerosol Lidar observations and model calculations of the planetary boundary layer evolution over Greece, during the March 2006 total solar eclipse. Atmos. Chem. Phys. 7, 6181–6189. https://doi.org/10.5194/acp-7-6181-2007.

Anderson, J., 1999. Meteorological changes during a solar eclipse. Weather 54 (7), 207–215.

Aplin, K.L., Harrison, R.G., 2003. Meteorological effects of the eclipse of 11 August 1999 in cloudy and clear conditions. Proc. R. Soc. Lond. A 459, 353–371.

Aplin, K.L., Scott, C.J., Gray, S.L., 2016. Atmospheric changes from solar eclipses. Philosophycal Trans. R. Soc. A 374, 20150217.

Baars, H., Ansmann, A., Engelmann, R., Althausen, D., 2008. Continuous monitoring of the boundary-layer top with lidar. Atmos. Chem. Phys. 8, 7281–7296. https://doi.org/10.5194/acp-8-7281-2008.

Bajčetić, J., Andrić, M., Todorović, B., Pavlović, B., Suša, V., 2013. The correlation of geomagnetic component disturbances and 5 GHz LOS received signal daily variation. Microw. Rev. 19 (1).

Bajčetić, J.B., Nina, A., Čadež, V., Todorović, B.M., 2015. Ionospheric D-region temperature relaxation and its influences on radio signal propagation after solar X-flares occurrence. Therm. Sci. 19 (Suppl. 2), S299–S309.

Bian, H., Han, S., Tie, X., Sun, M., Liu, A., 2007. Evidence of impact of aerosols on surface ozone concentration in Tianjin, China. Atmos. Environ. 41, 4672–4681.

Blaauboer, R.O., Smetsers, R.C.G.M., 1996. Outdoor concentrations of the equilibrium-equivalent decay products of $^{222}$Rn in The Netherlands and the effect of meteorological variables. Radiat. Prot. Dosim. 69, 7–18.

Cohen, M.B., Inan, U.S., Paschal, E.W., 2010. Sensitive broadband ELF/VLF radio reception with the AWESOME instrument. IEEE Trans. Geosci. Remote. 48, 3–17.

Debye, P., 1957. Polar Molecules. Dover Publications, New York.

Dolezalek, H., 1974. Electrical Processes in Atmospheres, Springer Verlag, Electrical Processes in Atmospheres. Springer Verlag.

Emeis, S., Schafer, K., Munkel, C., 2008. Surface-based remote sensing of the mixing-layer height – A review. Meteorol. Z. 17 (5), 621–630.

Falodun, S.E., Ajewole, M.O., 2006. Radio refractive index in the lowest 100-m layer of the troposphere in Akure, South Western Nigeria. J. Atmos. Sol.-Terr. Phys 236–243.

Flamant, C., Pelon, J., Flamant, P.H., Durand, P., 1997. Lidar determination of the entrainement zone thickness at the top of the unstable marine atmospheric boundary-layer. Boundary-Layer Meteorol. 83, 247–284.

Founda, D., Melas, D., Lykoudis, S., Lisaridis, I., Gerasopoulos, E., Kouvarakis, G., Petrakis, M., Zerefos, C., 2007. The effect of the total solar eclipse of 29 March 2006 on meteorological variables in Greece. Atmos. Chem. Phys. 7, 5543–5553. https://doi.org/10.5194/acp-7-5543-2007.

Gaso, M.I., Cervantes, M.L., Segovia, N., Espindola, V.H., 1994. Atmospheric radon concentration levels. Radiat. Meas. 23, 225–230.

Gerasopoulos, E., Zerefos, C.S., Tsagouri, I., Founda, D., Amiridis, V., Bais, A.F., Belehaki, A., Christou, N., Economou, G., Kanakidou, M., Karamanos, A., Petrakis, M., Zanis, P., 2008. The total solar eclipse of March 2006: overview. Atmos. Chem. Phys. 8, 5205–5220.

Girard-Ardhuin, F., Bénech, B., Campistron, B., Dessens, J., Jacoby-Koaly, S., 2003. Remote sensing and surface observations of the response of the atmospheric boundary layer to a solar eclipse. Boundary-Layer Meteorol. 106, 93–115.

Grubor, D.P., Šulić, D.M., Žigman, V., 2008. Classification of X-ray solar flares regarding their effects on the lower ionosphere electron density profile. Ann. Geophys. 26 (7), 1731–1740.

Guha, A., De, B.K., Roy, R., Choudhury, A., 2010. Response of the equatorial lower ionosphere to the total solar eclipse of 22 July 2009 during sunrise transition period studied using VLF signal. J. Geophys. Res. 115, A11302. https://doi.org/10.1029/2009JA015101.

Ishimori, Y., Lange, K., Martin, P., Mayya, Y.S., Phaneuf, M., 2013. Measurement and Calculation of Radon Releases from NORM Residues. International Atomic Energy Agency, Vienna.

Jeričević, A., Grisogono, B., 2006. The critical bulk richardson number in urban areas: verification and application in a numerical weather prediction model. Tellus A 58, 19–27. https://doi.org/10.1111/j.1600-0870.2006.00153.x.

Kolarž, P., Šekarić, J., Marinković, B.P., Filipović, D.M., 2005. Correlation between some of the meteorological parameters measured during the partial solar eclipse, 11 August, 1999. J. Atmos. Sol. Terr. Phys. 67, 1357–1364.

Kolarž, P., Miljković, B., Ćurguz, Z., 2011. Air-ion counter and mobility spectrometer. Nucl. Instrum. Methods Phys. Res. B 279, 219–222.

Kolev, N., Tatarov, B., Grigorieva, V., Donev, E., Simenonov, P., Umlensky, V., Kaprielov, B., Kolev, I., 2005. Aerosol Lidar and in situ ozone observations of the planetary boundary layer over Bulgaria during the solar eclipse of 11 August 1999. Int. J. Remote Sens. 26, 3567–3584.

Matthias, V., Balis, D., Bosenberg, J., Eixmann, R., Iarlori, M., Komguem, L., Mattis, I., Papayannis, A., Pappalardo, G., Perrone, M.R., Wang, X., 2004. Vertical aerosol distribution over Europe: statistical analysis of Raman lidar data from 10 European aerosol research lidar network (EARLINET) stations. J. Geophys. Res. 109, D18201. https://doi.org/10.1029/2004JD004638.

Maurya, Ajeet K., Phanikumar, D.V., Rajesh, Singh, Sushil, Kumar, Veenadhari, B., Kwak, Y.-S., Abhikesh, Kumar, Singh Abhay, K., Niranjan, Kumar K., 2014. Low-mid latitude D region ionospheric perturbations associated with 22 July 2009 total solar eclipse: wave-like signatures inferred from VLF observations. J. Geophys. Res. Space Phys. 119 (10), 8512–8523.

Menut, L., Flamant, C., Pelon, J., Flamant, P.H., 1999. Evidence of interaction between synoptic and local scales in the surface layer over the Paris area. Bound. Layer. Meteorol. 93, 269–286. https://doi.org/10.1023/A:1002013631786.

Nina, A., Čadež, V.M., 2013. Detection of acoustic-gravity waves in lower ionosphere by VLF radio waves. Geophys. Res. Lett. 4018, 4803–4807.

Nina, A., Čadež, V., Srećković, V., Šulić, D., 2012a. Altitude distribution of electron concentration in ionospheric D-region in presence of time-varying solar radiation flux. Nucl. Instrum. Methods. B 279, 110–113.

Nina, A., Čadež, V., Šulić, D., Srećković, V., Žigman, V., 2012b. Effective electron recombination coefficient in ionospheric D-region during the relaxation regime after solar flare from February 18, 2011. Nucl. Instrum. Methods. B 279, 106–109.

Nina, A., Čadež, V.M., Popović, Č.L., Srećković, A.V., 2017. Diagnostics of plasma in the ionospheric D-region: detection and study of different ionospheric disturbance types. Eur. Phys. J. D 71 (7). https://doi.org/10.1140/epjd/e2017-70747-0, 189, 1-12.

Nymphas, E.F., Adeniyi, M.O., Ayoola, M.A., Oladiran, E.O., 2009. Micrometeorological measurements in Nigeria during the total solar eclipse of 29 March, 2006. J. Atmos. Sol. Terr. Phys. 71 (12), 1245–1253.

Sicard, M., Pérez, C., Rocadenbosch, F., Baldasano, J.M., García-Vizcaino, D., 2006. Mixed-layer depth determination in the Barcelona Coastal area from regular lidar measurements: methods, results and limitations. Bound. Layer Meteorol. 119 (1), 135–157. https://doi.org/10.1007/s10546-005-9005-9.

Stull, R.B., 1988. An Introduction to Boundary Layer Meteorology. Kluwer Acad., Dordrecht, The Netherlands.

Swamy, A.B., 1991. A new technique for estimating D-region effective recombination coefficients under different solar flare conditions. Astrophys. Space Sci. 185 (1), 153–164.

Tie, X., Madronich, S., Li, G.H., Ying, Z.M., Zhang, R., Garcia, A., Lee-Taylor, J., Liu, Y., 2007. Characterizations of chemical oxidants in Mexico City: a regional chemical/dynamical model (WRF-Chem) study. Atmos. Environ. 41, 1989–2008.

United Nations Scientific Committee on the Effects of Atomic Radiation (UNSCEAR), 1993. Report to the General Assembly, with Scientific Annexes. New York.

Verhulst, T.G.W., Sapundjiev, D., Stankov, S.M., 2016. High-resolution ionospheric observations and modeling over Belgium during the solar eclipse of 20 March 2015 including first results of ionospheric tilt and plasma drift measurements. Adv. Space Res. 57 (No.11), 2407–2419. https://doi.org/10.1016/j.asr.2016.03.009.

Vogelezang, D.H.P., Holtslag, A.A.M., 1996. Evolution and model impacts of alternative boundary layer formulations. Bound. Layer. Meteorol. 81, 245–269. https://doi.org/10.1007/BF02430331.

Zanis, P., Zerefos, C.S., Gilge, S., Melas, D., Balis, D., Ziomas, I., Gerasopoulos, E., Tzoumaka, P., Kaminski, U., Fricke, W., 2001. Comparison of measured and modeled surface ozone concentrations at two different sites in Europe during the solar eclipse on August 11, 1999. Atmos. Environ. 35, 4663–4673.

Zanis, P., Katragkou, E., Kanakidou, M., Psiloglou, B., Karathanasis, S., Vrekoussis, M., Gerasopoulos, E., Lysaridis, I., Markakis, K., Poupkou, A., Amiridis, V., Melas, D., Mihalopoulos, N., Zerefos, C., 2007. Effects on surface atmospheric photo-oxidants over Greece during the total solar eclipse event of 29 March 2006. Atmos. Chem. Phys. Discuss. 7, 11399–11428.

Zerefos, C.S., Balis, D.S., Zanis, P., Meleti, C., Bais, A.F., Tourpali, K., Melas, D., Ziomas, I., Galani, E., Kourtidis, K., Papayannis, A., Gogosheva, Z., 2001. Changes in surface UV solar irradiance and ozone over the Balkans during the eclipse of 11 August 1999. Adv. Space Res. 27 (12), 1955–1963.

Contrib. Astron. Obs. Skalnaté Pleso **55/2**, 88 – 94, (2025)
https://doi.org/10.31577/caosp.2025.55.2.88

# The strongest solar flares of Solar Cycle 25 and their subionospheric impact: data and modeling

**V.A. Srećković[1,2], A. Kolarski[1], M. Langović[1], F. Arnaut[1], S. Jevremović[1,2] and Z.R. Mijić[1]**

[1] *University of Belgrade, Institute of Physics Belgrade, PO Box 57, (E-mail: vlada@ipb.ac.rs, kolarski@ipb.ac.rs, langovic@ipb.ac.rs, zoran.mijic@ipb.ac.rs)*

[2] *Scientific Society "Isaac Newton", Volgina 7, 11160 Belgrade, Serbia (E-mail: iniscientificsociety@gmail.com)*

Received: November 15, 2024; Accepted: November 30, 2024

**Abstract.** Solar flares, which are powerful explosions on the Sun's surface, are well recognized driving forces that have a significant impact on the near-Earth environment, causing extra ionization within the sunlit Earth's atmospheric layers. Based on how they affect the lower ionosphere and its electron density profile, X-ray solar flares can be categorized. In order to forecast the effects of potential solar occurrences during the waning phase of Solar Cycle 25, this study focuses on the disturbances caused by X-ray solar flares. In this paper we examined Solar Cycle progression i.e. solar activity of highest intensity (strongest 50 solar flares) during the ascending phase of Solar Cycle 25 by conducting numerical ionospheric modeling based on the Geostationary Operational Environmental Satellite (GOES) database on solar X-ray radiation.

**Key words:** Space weather – Solar activity – Solar X-ray flares – radio signal perturbations – GOES – data – modeling – electron density

## 1. Introduction

Strong explosions of electromagnetic radiation that come from the Sun's surface are known as solar flares (SFs) (Bothmer et al., 2007; Kahler, 1982; Tandberg-Hanssen & Emslie, 2009; Davidson, 2020; Riley & Love, 2017). The SF classifications range from A to X-class (see e.g. Grubor et al., 2008; Hayes et al., 2021, and references therein). Strong flares have the ability to impair communication and navigation systems and can cause disturbances in the ionosphere, affecting terrestrial communication. SFs emit powerful X-ray and ultraviolet radiation that can ionize the upper atmosphere, resulting in extra free electrons (Khodairy et al., 2020; Le et al., 2013; Šulić et al., 2016; Curto, 2020; Barta et al., 2022). These unbound electrons can affect radio wave propagation by changing the ionosphere's refractive characteristics (Thomson & Clilverd, 2000; Šulić & Srećković, 2014; Kolarski & Grubor, 2014; Srećković, 2023). The density of the ionosphere briefly increases, affecting radio signals going through it (McRae & Thomson, 2004; Kelly, 2009; Nina et al., 2019; Srećković et al., 2024, 2017).

To forecast the impacts of potential solar occurrences during the declining phase of Solar Cycle 25, this study focuses on the disruptions induced by X-ray solar flares. In this paper, we investigated Solar Cycle progression, i.e. solar activity of highest intensity (strongest 50 solar flares) during the ascending phase of Solar Cycle 25 using numerical ionospheric modeling and the Geostationary Operational Environmental Satellite (GOES) (Aschwanden, 1994; Woods et al., 2024) database on solar X-ray radiation (`https://data.ngdc.noaa.gov/platforms/solar-space-observing-satellites/goes`).

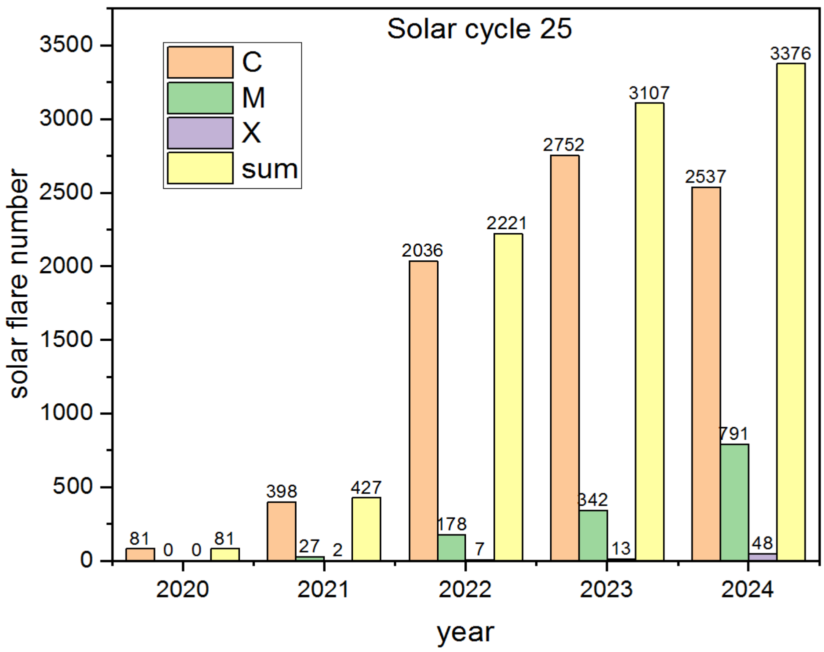


**Figure 1.** The graph shows the number of C, M and X-class solar flares that were produced during Solar Cycle 25 during the accessing phase, presented by year.

This study's findings may help to improve forecasting models (Gorney, 1990; Lean, 2010; Georgieva & Shiokawa, 2018; Bilitza et al., 2012, 2022), allowing for greater prediction and preparedness for ionospheric disruptions produced by high class SFs. The study of high-class SFs during Solar Cycle 25 and their impact on the ionosphere emphasizes the importance of ongoing research and monitoring of such occurrences to improve our understanding of space weather phenomena and protect technological infrastructure from potential disruptions.

The paper is organized as follows. This Section describes the current state and an introduction to the research problem. Section 2 provides results and analysis concerning the strongest solar flares of Solar Cycle 25 and their subionospheric impact, whereas Section Sec. 3 presents the conclusions and future perspectives of research.

## 2. Results and discussion

In this paper focus is on the further use of numerical method, so called easyFit that were developed by Srećković et al. (2021a,b) on the cases of high intensity SFs i.e. the strongest ones. We note that initially easyFit methods were developed for SF events of mid to high intensity (upper C-, M- and lower X-class SFs, see e.g. papers Srećković et al. (2021b); Kolarski et al. (2022)).

Datasets from this paper provide an overview of the results obtained by applying the numerical methods easyFit to the examples chosen for investigation, namely the top 50 SF of Solar Cycle 25 from X1.2 to X9. Solar X-ray flux was obtained from the Geostationary Operational Environmental Satellite (GOES) archive database (`https://data.ngdc.noaa.gov/platforms/solar-space-observing-satellites/goes`).

Figure 1 shows the number of C, M and X-class solar flares that were produced during the ascending branch of Solar Cycle 25 presented by year from 2020 to the end of 2024. We observe that, beginning in 2020 and reaching their peak at the end of 2024, the frequency of solar flares is clearly rising. It can be noted that on Jul 3, 2021 X1.59 - class flare occurred as the first X-class flare of Solar Cycle 25 and the first X-class solar flare since September 10, 2017.

Figure 2 upper panel shows sunspot number that were produced during the accessing phase of Solar Cycle 25 presented by year. We note that the number of sunspots is visibly increasing starting from 2020 and reaches its current maximum at the end of 2024. From the listed cases, differences in X-ray flux are associated with solar activity. Lower panel of Figure 2 shows the 50 strongest solar flares of Solar Cycle 25 (black circles) and corresponding reference height ionospheric D-region electron density (red circles). The left axis of the lower panel of Figure 2 shows the soft X-ray flux, while the right axis shows the perturbed values of the ower ionospheric electron density due to solar flares. The electron density is obtained by the easyFit method that was developed by Srećković et al. (2021a,b). One can observe a correlative behavior of increasing solar activity with increasing electron density.

Examining Solar Cycle progression we note that ionospheric disturbances and its parameters are correlated with solar activity during the ascending phase of Solar Cycle 25. These results will allow us to predict and model the ionosphere and its parameters during the waning phase of the Solar Cycle 25.

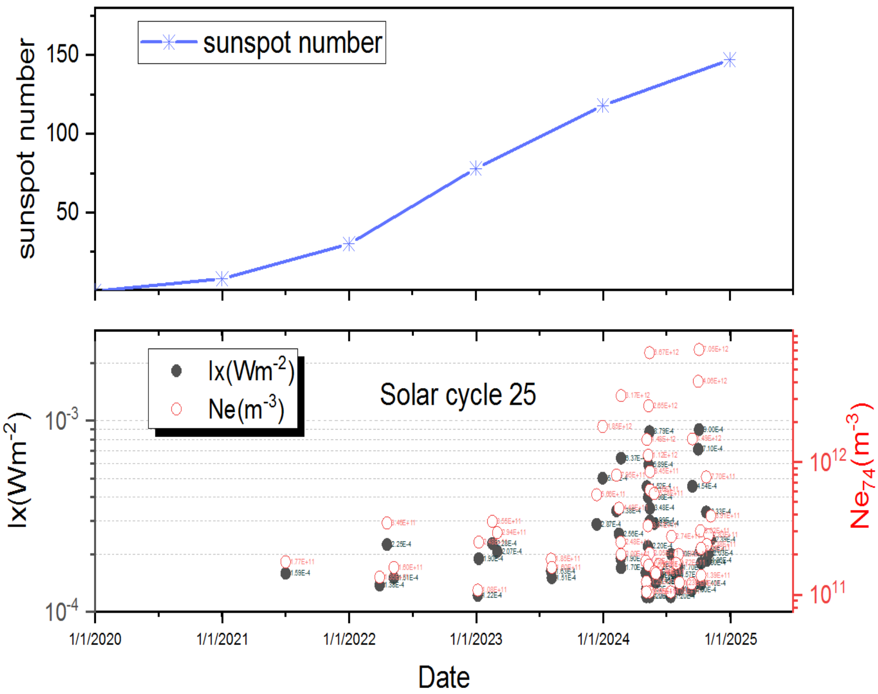


**Figure 2.** Upper panel: The graph shows sunspot number that were produced during Solar Cycle 25 by year; lower panel: The graph shows the 50 strongest solar flares of Solar Cycle 25 (black circles) and corresponding reference height ionospheric electron density (red circles).

## 3. Summary and future development

Solar flares, which are powerful explosions on the Sun's surface, are well recognized driving forces that have a significant impact on the near-Earth environment, causing extra ionization within the sunlit Earth's atmospheric layers. In order to forecast the effects of potential solar occurrences during the whole Solar Cycle 25, this study focuses on the disturbances caused by X-ray solar flares from 2020 to the end of 2024.

In this contribution, we investigated Solar Cycle progression, i.e. solar activity of highest intensity (strongest 50 solar flares) during the ascending phase of Solar Cycle 25, using numerical ionospheric modeling and the Geostationary Operational Environmental Satellite (GOES) database on solar X-ray radiation. Numerical method easyFit were applied to research impact of SFs of highest intensity ranging from X1 to X9 during 2020-2024 i.e. the ascending phase of Solar Cycle 25, with the aim to obtain parameters of perturbed lower ionosphere.

The results of this work could aid in the development of forecasting models, enabling better anticipation and readiness for ionospheric disturbances brought on by high-class SFs (see e.g. Gopalswamy, 2022). In order to better understand space weather events and safeguard technological infrastructure from potential disruptions, it is crucial to conduct continuous research and monitoring of high-class SFs during Solar Cycle 25 and their effects on the ionosphere.

**Acknowledgements.** This work has been supported by the Institute of Physics Belgrade through funds from the Ministry of Science, Technological Development and Innovations of the Republic of Serbia.

## References

Aschwanden, M. J., Irradiance observations of the 1-8 A solar soft X-ray flux from GOES. 1994, *Solar Physics (ISSN 0038-0938), vol. 152, no. 1, p. 53-59*, **152**, 53, DOI:10.1007/BF0147318

Barta, V., Natras, R., Srećković, V., et al., Multi-instrumental investigation of the solar flares impact on the ionosphere on 05–06 December 2006. 2022, *Frontiers in Environmental Science*, **10**, DOI:10.3389/fenvs.2022.904335

Bilitza, D., Brown, S. A., Wang, M. Y., Souza, J. R., & Roddy, P. A., Measurements and IRI model predictions during the recent solar minimum. 2012, *Journal of Atmospheric and Solar-Terrestrial Physics*, **86**, 99, DOI:10.1016/j.jastp.2012.06.010

Bilitza, D., Pezzopane, M., Truhlik, V., et al., The International Reference Ionosphere Model: A Review and Description of an Ionospheric Benchmark. 2022, *Reviews of Geophysics*, **60**, e2022RG000792, DOI:10.1029/2022RG000792

Bothmer, V., Daglis, I. A., & Bogdan, T. J., Space Weather: Physics and Effects. 2007, *Physics Today*, **60**, 59, DOI:10.1063/1.2825074

Curto, J. J., Geomagnetic solar flare effects: a review. 2020, *Journal of Space Weather and Space Climate*, **10**, 27, DOI:10.1051/swsc/2020027

Davidson, B. 2020, *Weatherman's Guide to the Sun, 3rd ed.* (Space Weather News, LLC.: New York, NY, USA)

Georgieva, K. & Shiokawa, K., Variability of the sun and its terrestrial impacts. 2018, *Journal of Atmospheric and Solar-Terrestrial Physics*, **180**, 1, DOI:10.1016/j.jastp.2018.09.008

Gopalswamy, N., The Sun and Space Weather. 2022, *Atmosphere*, **13**, DOI:10.3390/atmos13111781

Gorney, D. J., Solar cycle effects on the near-earth space environment. 1990, *Reviews of Geophysics*, **28**, 315, DOI:10.1029/RG028i003p00315

Grubor, D., Šulić, D., & Žigman, V., Classification of X-ray solar flares regarding their effects on the lower ionosphere electron density profile. 2008, *Annales Geophysicae*, **26**, 1731, DOI:10.5194/angeo-26-1731-2008

Hayes, L. A., O'Hara, O. S. D., Murray, S. A., & Gallagher, P. T., Solar Flare Effects on the Earth's Lower Ionosphere. 2021, *Solar Physics*, **296**, 157, DOI:10.1007/s11207-021-01898-y

Kahler, S. W., The role of the big flare syndrome in correlations of solar energetic proton fluxes and associated microwave burst parameters. 1982, *Journal of Geophysics Research*, **87**, 3439, DOI:10.1029/JA087iA05p03439

Kelly, M. C. 2009, *The Earth's Ionosphere: Plasma Physics and Electrodynamics, Second Edition* (Academic Press, USA)

Khodairy, S., Sharaf, M., Awad, M., Abdel Hamed, R., & Hussein, M., Impact of solar activity on Low Earth Orbiting satellites. 2020, in Journal of Physics Conference Series, Vol. **1523**, *Journal of Physics Conference Series* (IOP), 012010

Kolarski, A. & Grubor, D., Sensing the Earth's low ionosphere during solar flares using VLF signals and goes solar X-ray data. 2014, *Advances in space research*, **53**, 1595, DOI:10.1016/j.asr.2014.02.022

Kolarski, A., Srećković, V. A., & Mijić, Z. R., Monitoring solar activity during 23/24 solar cycle minimum through VLF radio signals. 2022, *Contributions of the Astronomical Observatory Skalnate Pleso*, **52**, 105, DOI:10.31577/caosp.2022.52.3.105

Le, H., Liu, L., Chen, Y., & Wan, W., Statistical analysis of ionospheric responses to solar flares in the solar cycle 23. 2013, *Journal of Geophysical Research (Space Physics)*, **118**, 576, DOI:10.1029/2012JA017934

Lean, J. L., Cycles and trends in solar irradiance and climate. 2010, *WIREs Climate Change*, **1**, 111, DOI:10.1002/wcc.18

McRae, W. M. & Thomson, N. R., Solar flare induced ionospheric D-region enhancements from VLF phase and amplitude observations. 2004, *Journal of Atmospheric and Solar-Terrestrial Physics*, **66**, 77, DOI:10.1016/j.jastp.2003.09.009

Nina, A., Srećković, V. A., & Radovanović, M., Multidisciplinarity in research of extreme solar energy influences on natural disasters. 2019, *Sustainability*, **11**, 974, DOI:10.3390/su11040974

Riley, P. & Love, J. J., Extreme geomagnetic storms: Probabilistic forecasts and their uncertainties. 2017, *Space Weather*, **15**, 53, DOI:10.1002/2016SW001470

Srećković, V. A., New Challenges in Exploring Solar Radiation: Influence, Consequences, Diagnostics, Prediction. 2023, *Applied Sciences*, **13**, 4126, DOI:10.3390/app13074126

Srećković, V. A., Dimitrijević, M. S., & Mijić, Z. R., Data in Astrophysics and Geophysics: Novel Research and Applications. 2024, *Data*, **9**, DOI:10.3390/data9020032

Srećković, V. A., Šulić, D. M., Ignjatović, L., & Vujčić, V., Low Ionosphere under Influence of Strong Solar Radiation: Diagnostics and Modeling. 2021a, *Applied Sciences*, **11**, 7194, DOI:10.3390/app11167194

Srećković, V. A., Šulić, D. M., Vujčić, V., Jevremović, D., & Vyklyuk, Y., The effects of solar activity: Electrons in the terrestrial lower ionosphere. 2017, *J. Geogr. Inst. Jovan Cvijic SASA*, **67**, 221, DOI:10.2298/IJGI1703221S

Srećković, V. A., Šulić, D. M., Vujčić, V., Mijić, Z. R., & Ignjatović, L. M., Novel Modelling Approach for Obtaining the Parameters of Low Ionosphere under Extreme Radiation in X-Spectral Range. 2021b, *Applied Sciences*, **11**, 11574, DOI:10.3390/app112311574

Tandberg-Hanssen, E. & Emslie, A. G. 2009, *The Physics of Solar Flares* (Cambridge University Press, UK)

Thomson, N. R. & Clilverd, M. A., Solar cycle changes in daytime VLF subionospheric attenuation. 2000, *Journal of Atmospheric and Solar-Terrestrial Physics*, **62**, 601, DOI:10.1016/S1364-6826(00)00026-2

Šulić, D. M. & Srećković, V. A., A Comparative Study of Measured Amplitude and Phase Perturbations of VLF and LF Radio Signals Induced by Solar Flares. 2014, *Serbian Astronomical Journal*, **188**, 45, DOI:10.2298/SAJ1488045S

Šulić, D. M., Srećković, V. A., & Mihajlov, A. A., A study of VLF signals variations associated with the changes of ionization level in the D-region in consequence of solar conditions. 2016, *Advances in Space Research*, **57**, 1029, DOI:10.1016/j.asr.2015.12.025

Woods, T. N., Eden, T., Eparvier, F. G., et al., GOES-R Series X-Ray Sensor (XRS): 1. Design and pre-flight calibration. 2024, *Journal of Geophysical Research: Space Physics*, **129**, e2024JA032925, DOI:10.1029/2024JA032925

Contrib. Astron. Obs. Skalnaté Pleso **53/3**, 163 – 175, (2023)
https://doi.org/10.31577/caosp.2023.53.3.163

# Data quality assurance for atmospheric probing and modeling: characterization of Belgrade Raman lidar station

**Z. Mijić[1], L. Ilić[1,2] and M. Kuzmanoski[1]**

[1] *Institute of Physics Belgrade, Pregrevica 118, 11080 Belgrade, Serbia, (E-mail: zoran.mijic@ipb.ac.rs, maja.kuzmanoski@ipb.ac.rs)*

[2] *now at Barcelona Supercomputing Center, Plaça Eusebi Güell, 1-3, 08034 Barcelona, Spain, (E-mail: luka.ilic@ipb.ac.rs)*

Received: September 30, 2023; Accepted: November 2, 2023

**Abstract.** Using the lidar (Light Detection And Ranging) technique atmospheric probing and observations of atmospheric aerosol optical properties may be conducted remotely with high spatial and temporal resolution. As an EARLINET (the European Aerosol Research LIdar Network) joining lidar station, Belgrade Raman lidar system has provided aerosol profiling data for potential atmospheric and climatological studies as well as assessment of planetary boundary layer evolution and conducting dedicated measurements during airborne hazard. A comprehensive quality-assurance program and self-testing check-up tools have been developed to examine the performance and temporal stability of a lidar system. The capabilities of the Belgrade Raman lidar system, as well as its experimental characterization related to zero bin assessment, analog to photon-counting signal delay, Rayleigh-fit and telecover tests to evaluate system accuracy, are presented in this study.

**Key words:** Remote sensing – Atmosphere – Optical properties – Data – Quality assurance

## 1. Introduction

For more accurate weather predictions and a better understanding of climate change and solar influence, it is essential to quantify the impact that clouds and atmospheric aerosols play in the Earth's radiation budget (Stocker et al., 2013; Boucher et al., 2013). Depending on aerosol composition and size distribution the amount of scattered and absorbed radiation (both incoming solar and outgoing terrestrial) can differ significantly. Aerosol radiative forcing has been identified as one of the biggest climate change unknowns due to its short lifespan and high spatial and temporal variability (Stocker et al., 2013). To quantify the influence of aerosols on the climate system using an integrated approach of ground-level and airborne in-situ measurements, ground-based remote sensing, and space-based observations combined with numerical modeling are required.

Change in the incoming solar radiation flux induces disturbances in different atmospheric layers (Aplin & Harrison, 2003; Maurya et al., 2014). Several studies have investigated the effect of solar eclipse on various atmospheric properties (Ilić et al., 2018; Kolarž et al., 2005; Nymphas et al., 2009). Atmospheric lidar (Light Detection And Ranging) can be used to determine heights of planetary boundary layer (PBL) using aerosols as tracers, providing opportunity to investigate PBL evolution-based processes. Decrease in height and evolution change of PBL during a solar eclipse have been observed (Ilić et al., 2018; Amiridis et al., 2007; Kolev et al., 2005).

Lidar, an active remote sensing technique, has proved itself to be the optimal tool for profiling height-resolved atmospheric aerosol optical parameters. Various aerosol lidar techniques have been developed during the last several decades operating at one or multiple wavelengths. The lidar principle is based on laser emission of short-duration light pulses into the receiver field of view. The intensity of the light backscattered by atmospheric molecules and particles is measured versus time (through the telescope receiver, collimating optics, a bandpass filter for daylight suppression) by an appropriate detector. The signal profile is recorded by an analog-to-digital converter or by a photon-counting device and accumulated for a selected integration period spanning time intervals from seconds to minutes. In order to establish a comprehensive and quantitative statistical data base of the horizontal and vertical distribution of aerosols on the continental scale the lidar network called EARLINET (the European Aerosol Research LIdar Network) was founded in 2000 (Pappalardo et al., 2014). The development of the quality assurance strategy (Freudenthaler et al., 2018), the optimization of instruments and data processing (Wandinger et al., 2016), and the dissemination of data have contributed to significant improvement of the network towards a more sustainable observing system. With the addition of new stations EARLINET has significantly enhanced its observation capacity during the past few years. Additionally, the Single Calculus Chain (SCC) was developed eliminating inconsistencies in the optical products retrieval processes and in the signal error calculation, automating the data evaluation, and enabling near real time (NRT) data processing (D'Amico et al., 2015, 2016; Papagiannopoulos et al., 2020; Mattis et al., 2016). Such network development allowed its contribution to calibration and validation of optical products retrieval from satellite missions (Abril-Gago et al., 2022).

In this study the capabilities of the EARLINET joining Belgrade Raman lidar system combined with its experimental characterization using self-testing check-up tools developed across the network to evaluate system accuracy are presented. Aerosol optical properties retrieved from such lidar measurements can be used to evaluate aerosol satellite measurements, e.g., Earth Clouds, Aerosols and Radiation Explorer (EARTHCARE) mission (Illingworth et al., 2015), and to improve aerosol representation in climate models.

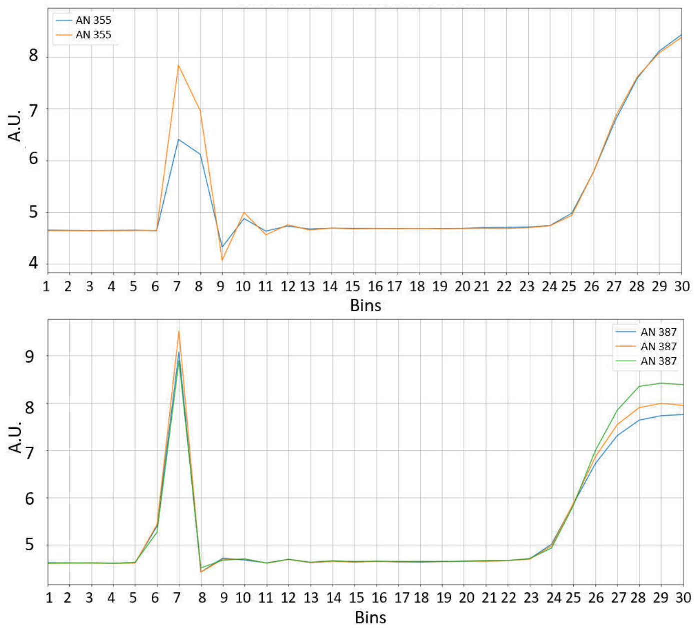


**Figure 1.** Zero bin assessment for elastic 355 nm (above) and Raman 387 nm (below) channels. Different color lines represent successive average signals from diffuse reflections of twenty laser shots.

## 2. Methodology

Raman lidar system at the Institute of Physics Belgrade (IPB), Serbia (44.860 N, 20.390 E) is bi-axial lidar system (telescope-laser axes distance is 200 mm) with combined elastic and Raman detection designed to perform continuous measurements of aerosols in the lower free troposphere (Ilić et al., 2018). Transmitter unit is based on the third harmonic frequency of a water cooled, pulsed Nd:YAG laser, emitting pulses of 65 mJ output energy at 355 nm with a 20 Hz repetition rate. In order to improve the maximum range and the precision of the system the beam expander is used to reduce the laser beam divergence (0.33 mrad) expanding the beam's diameter by 3 times. The optical receiving unit consists of two sub-units, a receiving telescope and wavelength separation unit. The optical receiver is a Cassegrain reflecting telescope with a primary mirror of 250 mm diameter and a focal length of 1250 mm. Photomultiplier tubes Hamamatsu R9880U-110 (PMT) are used to detect elastic backscatter lidar signal at 355 nm and Raman signal at 387 nm (Nitrogen vibrational scattering).

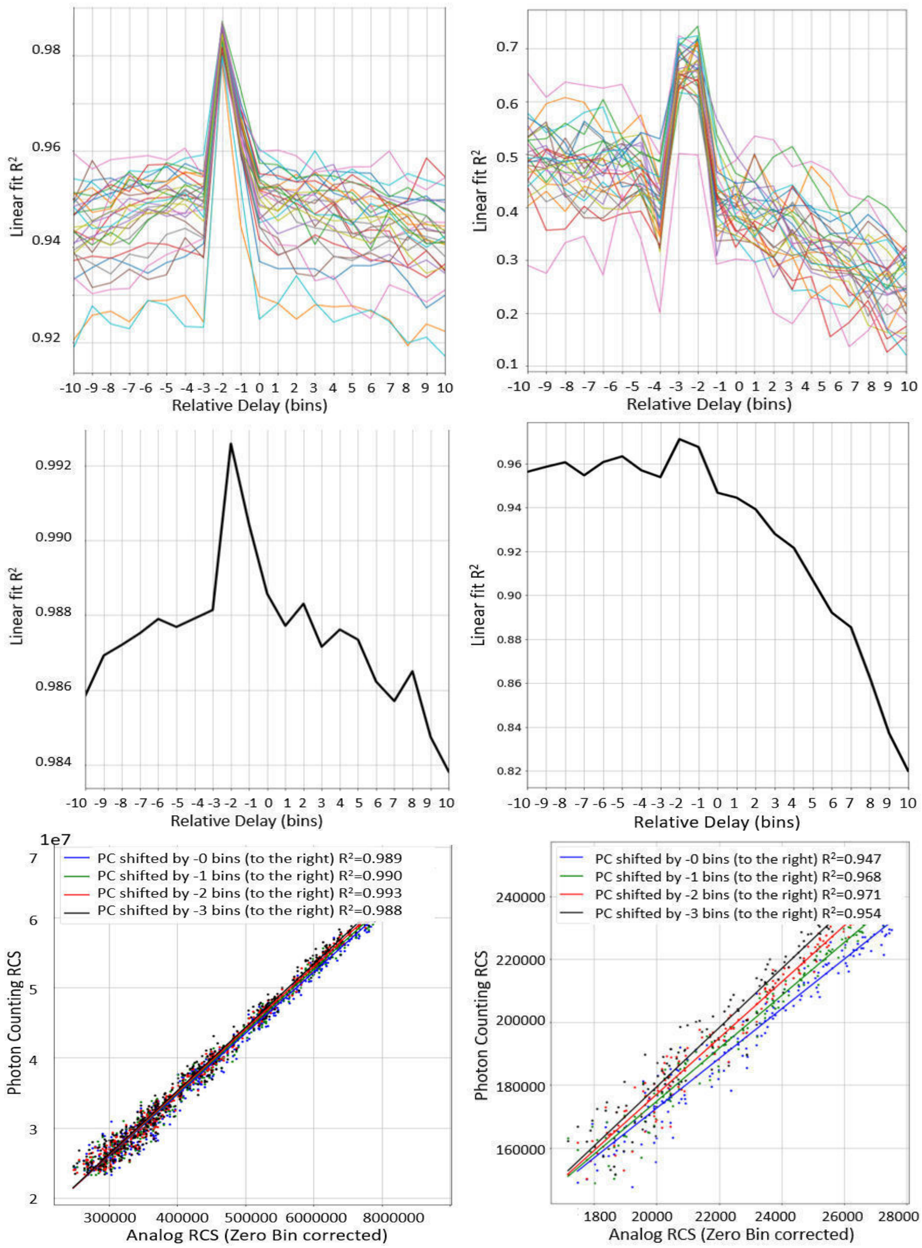


**Figure 2.** Analysis of the relative delay between zero-bin-corrected analog RCS and the PC RCS for 355 nm (left column) and 387 nm (right column) channels. Measurements of 30 1-minute profiles with 1200 shots each were used. A linear regression between AN and PC data was performed in the gluing region. Correlation coefficient as a function of relative delay between analog and photon counting signals (above). Correlation coefficient as a function of relative delay between analog and photon counting mean signals (center). Fit between the PC RCS and AN RCS channels (below).

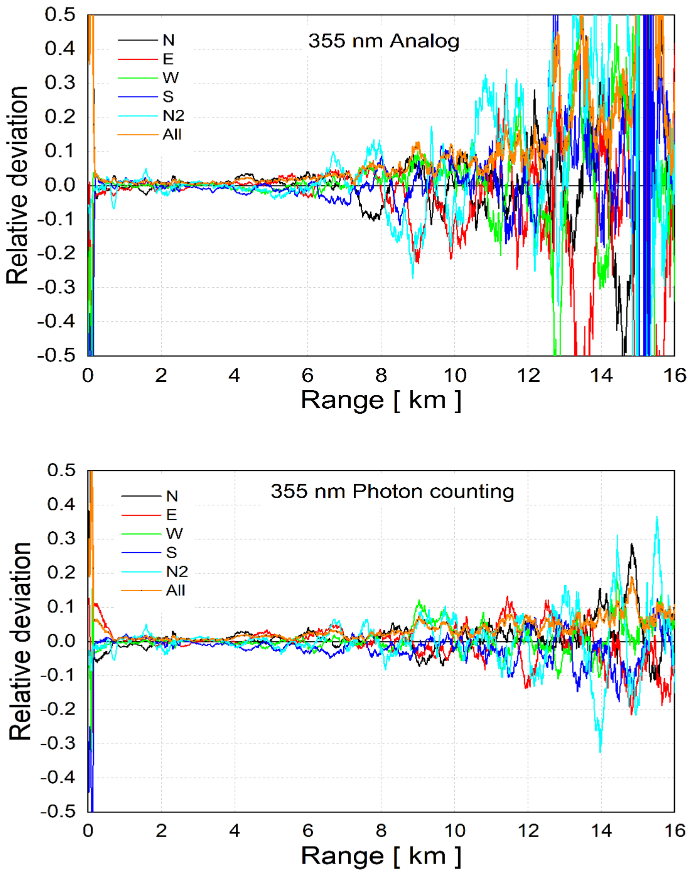


**Figure 3.** Relative deviations of signals collected in the four telescope sectors compared to the mean analog (above) and photon counting 355 nm signal (below), normalized in the 1500-2500 m range.

Interference filters with 0.96 nm and 0.45 nm FWHM before each PM tube are used to reduce the background noise. The detectors are operated both in the analog and photon-counting mode and the spatial raw resolution of the detected signals is 7.5 m. Averaging time of the lidar profiles is of the order of 1 min corresponding to 1200 laser shots. The Licel transient recorder is comprised of a fast transient digitizer with on board signal averaging, a discriminator for single photon detection and a multichannel scaler combined with preamplifiers for both systems. For analog detection, the signal is amplified according to the input range selected and digitized by a 12-Bit-20 MHz A/D converter. At the same time the signal part in the high frequency domain is amplified and a 250 MHz fast discriminator detects single photon events above the selected threshold voltage.

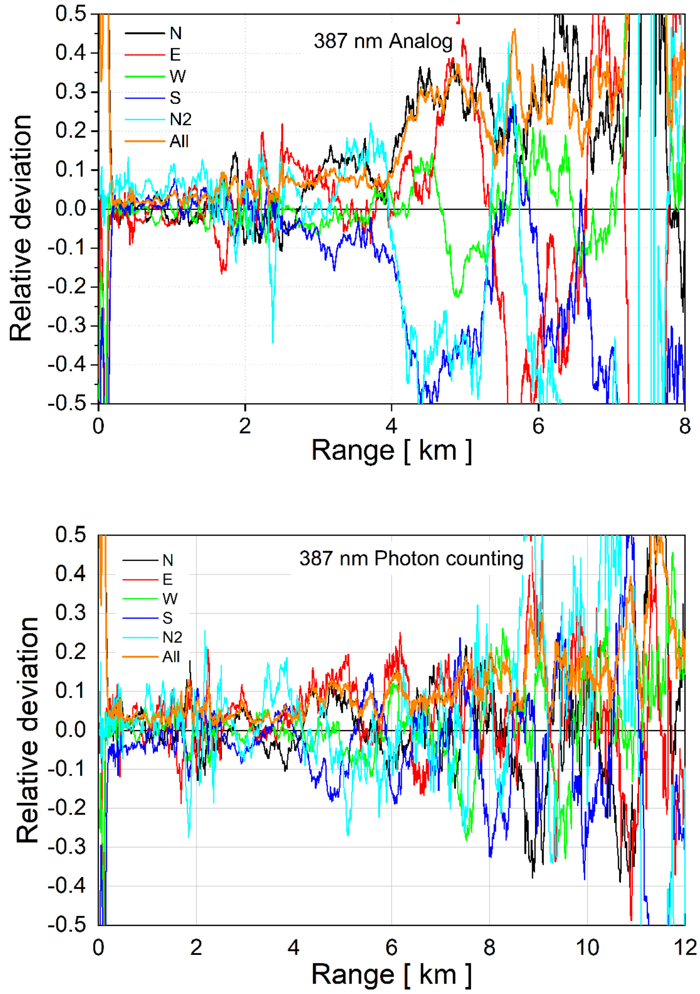


**Figure 4.** Relative deviations of signals collected in the four telescope sectors compared to the mean analog (above) and photon counting (below) 387 nm signal, normalized in the 1500-2500 m range.

In order to monitor and improve the quality of the lidar systems and their optical products, the quality assurance methods for both hardware and retrieval algorithms (Freudenthaler et al., 2018; D'Amico et al., 2015, 2016) have been established through the lidar network. System alignment is one of the fundamental setup tests because the partial overlap between the laser beam and the receiver field of view has a substantial impact on lidar measurements of particle optical characteristics (Freudenthaler et al., 2018). The fact that the ray bundles from various telescopic aperture regions go through the optical setup in various ways and with various incidence angles on the optical components can be used to assess the lidar system alignment i.e., full overlap between laser beam and telescope field of view. It is necessary to do a series of measurements using a telescope that is only partially covered so that each measurement actually represents the collection of backscattered light by a specific sector of the telescope in order to evaluate the alignment. Following the procedure described in Freudenthaler et al. (2018), a version of so-called telecover test using the set up of the telescope with four sectors was conducted in this study. For the fine alignment of the system in the far field, the range-corrected lidar signal is compared to the attenuated Rayleigh backscatter coefficient at a range interval which is considered aerosol free. To determine the lidar signal distortions due to the electronic noise the so-called dark measurement was performed. Dark signal was measured with fully covered telescope so that no light from the atmosphere and laser backscattered pulses could be detected. The lidar signals were preprocessed taking into the account 3 min dark signal (for both analog and photon counting channels) corresponding to 3600 laser shots. Such temporal averaged dark measurement with sufficient signal-to-noise ratio was subtracted from the lidar signals to improve the accuracy. In addition, experimental verification of the zero range of the signal detection was conducted (Barbosa et al., 2014).

## 3. Results and Discussion

### 3.1. Zero bin test

A trigger-delay between the actual laser pulse emission and the backscatter signal recording's presumed zero range (zero bin) can introduce notable inaccuracies in the near range signal. Particularly, the inversion of Raman signals can be significantly distorted since the signal slope in the near range varies considerably when the zero bin for range correction is changed (Freudenthaler et al., 2018). The signal peaks obtained from light reflected from a diffuse scattering target placed right above the emission part of the lidar system in order to block the laser path are presented in Figure 1. In order to prevent signal saturation the telescope was covered so that only a portion of the diffused light can enter the telescope. The first bin of the signal peak is the assessed zero bin. Since the analog to photon counting (AN-PC) signal delay might be different among LICEL transient recorder modules, the AN-PC delay should be further calculated for each module separately. In this paper the cross-correlation of the two range corrected signals was used to calculate the analog-pc delay (Barbosa et al., 2014). Analysis of the relative delay between zero-bin-corrected analog RCS and the PC RCS signals is presented in Figure 2 with the same system alignment as in Figure 3. For measurement of this delay, 30 profiles of 1200 shots each were used. A linear regression between AN and PC data was performed as a function of time delay from -10 to 10 bins. A distinct peak at -2 relative delay bins is clearly exhibited for elastic channel (with respect to zero-bin-corrected

AN signal). The main peaks for relative delay in the case of Raman channel are distributed between two range-bins, but the best assessment for relative delay corresponds also to -2 bins.

### 3.2. Telecover test

To check the laser-telescope alignment the telecover test using quarters of the telescope was used. This quadrant test used four sectors named North (N)-oriented from the telescope optical axis towards the laser optical axis, East (E), West (W) and South (S). The North2 (N2) signals were acquired using the same telecover sector as the N signals, but at the end of the measurement time sequence, thus deviations in the N and N2 signals reveal the effect of the changing environment during the measurements. Figure 3 and Figure 4 show relative deviations of signals collected with quadrant telescope sectors under stable atmospheric conditions on April 27, 2020 for both 355 nm and 387 nm channels, respectively. Signals obtained with a partly covered telescope are examined in terms of each sector deviation relative to the average of all signals in order to verify lidar response in the near field. The threshold for the accepted relative deviation of each sector signal is adopted to be 0.05. From the obtained results it can be seen that the Raman lidar response in the near field is below threshold and well alligned starting from 300 m. Although the telecover test is useful for the assessment of the far range response of the lidar system usually the additional test called Rayleigh fit should be applied.

### 3.3. Rayleigh fit test

To test the lidar alignment in the far range the Rayleigh fit procedure was used. For that purpose, the fitting of normalized lidar signal to the calculated attenuated Rayleigh backscatter coefficient ($\beta_m^{attn}$) in a range where we assume clean conditions (aerosol-free atmosphere) was performed. In Figure 5 and Figure 6 Rayleigh fit and corresponding relative deviations from the calculated Rayleigh signal for the elastic 355 nm and Raman 387 nm channels are presented. The 30 min measurements were performed during the night on the same day and with the lidar setup as presented in Figure 3. Molecular signals were calculated from the obtained Global Data Assimilation System (GDAS) profiles for the same day at 23UT following Bucholtz (1995)(Bucholtz, 1995). From Figure 5 it can be seen that the lidar system is well aligned up to the 14 km for elastic channel with the relative error less than 1% of the attenuated Rayleigh backscatter signal while Raman channel signal to noise ratio is acceptable up to the 8 km. Once the system is properly aligned it can be used for systematic aerosol measurements.

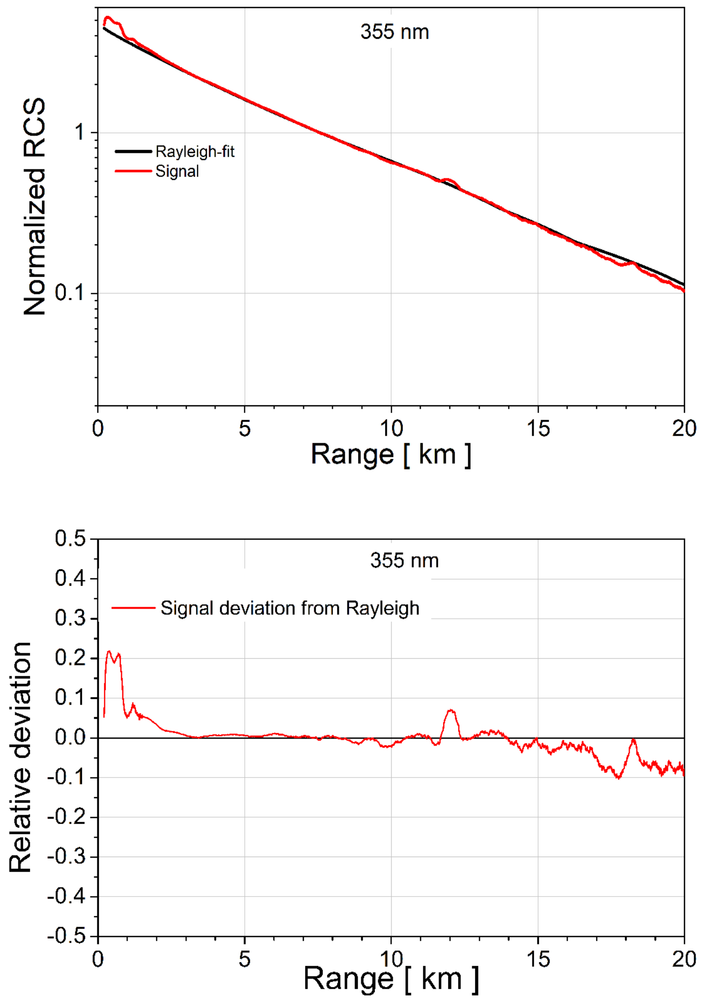


**Figure 5.** Photon counting 355 nm lidar signal (red) averaged over 30 minutes and calculated Rayleigh signal (black) from local radiosonde data of the same night, both normalised between 5 and 10 km range (above). Relative deviation from the calculated Rayleigh signal (below).

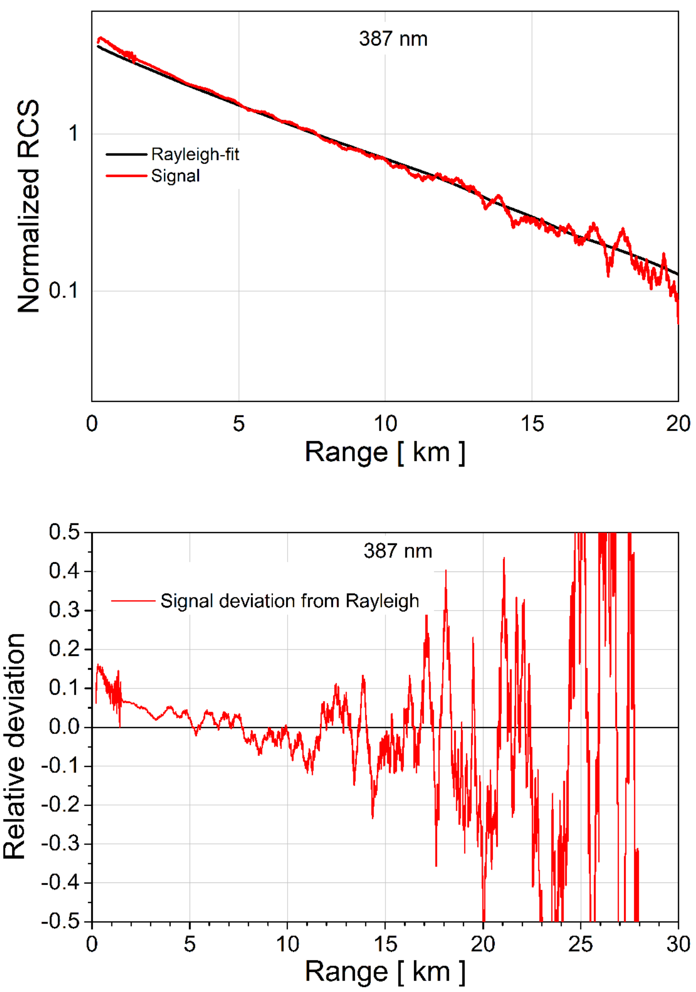


**Figure 6.** Photon counting 387 nm lidar signal (red) averaged over 30 minutes and calculated Rayleigh signal (black) from local radiosonde data of the same night, both normalised between 5 and 10 km range (above). Relative deviation from the calculated Rayleigh signal (below).

## 4. Summary

Lidar systems are optimal tools for providing range-resolved aerosol optical parameters and information on the atmospheric structure not only for climatological purposes but also in emergency situations when near real time delivery of the data and fast data processing is required. Although several lidar instrument intercomparison campaigns have been conducted within the network, it is not possible to evaluate all systems in their specific setup due to the constant technological development and subsequently systems upgrade together with improving measurements experiences. To overcome limited capacity for providing direct intercomparisons a complementary quality-assurance procedures and tools have been developed for regular internal system check-ups across the lidar network. In this paper the capabilities of the Belgrade Raman lidar system is assessed and characterization related to zero bin assessment, analog to photon-counting signal delay, Rayleigh-fit and telecover tests to evaluate system accuracy, are presented. Under described system setup the full overlap of the telescope field of view and laser beam is measured and the system alignment is assessed in the near field starting from 300 m. In the far range the Rayleigh fit procedure for elastic 355 nm channel exhibited good signal to noise ratio and alignment up to 14 km, but Raman channel at 387 nm demonstrated significant signal noise above 8 km. In addition, the cross correlation of the two range corrected analog and photon count signals was used to assess the analog-pc delay characteristic for each transient record module.

As a unique system in the region capable to perform remote monitoring of atmospheric aerosols it is expected to perform systematic measurements on a regular schedule in the near future and contribute to the collection of aerosol vertical distribution database in Europe. Lidar measurements of aerosol optical properties can be used for model evaluation (Meier et al., 2012; Binietoglou et al., 2015). Furthermore, the assimilation of lidar observations of aerosol vertical distribution (Cheng et al., 2019) can improve model estimation of aerosol impact on climate. In addition, changes in atmospheric properties caused by specific events, like solar eclipse-induced planetary boundary layer height changes or airborne particles transport can be observed. Having in mind geographical distribution of currently active lidar stations in Europe, Belgrade Raman lidar station can provide valuable data for intercomparison and validation of optical products for future satellite missions, but automatization of the measurement process and the upgrade to the multiwavelength lidar system are essential to develop in the future.

**Acknowledgements.** The authors acknowledge funding provided by the Institute of Physics Belgrade, through the grant by the Ministry of Science, Technological Development and Innovations of the Republic of Serbia. The financial support for EARLINET in the ACTRIS Research Infrastructure Project by the European Union's Horizon 2020 research and innovation programme under grant agreement No. 654109 and previously under the grants No. 262254 in the 7th Framework Programme (FP7/2007-2013) is gratefully acknowledged.

## References

Abril-Gago, J., Guerrero-Rascado, J. L., Costa, M. J., et al., Statistical validation of Aeolus L2A particle backscatter coefficient retrievals over ACTRIS/EARLINET stations on the Iberian Peninsula. 2022, *Atmospheric Chemistry and Physics*, **22**, 1425, DOI: 10.5194/acp-22-1425-2022

Amiridis, V., Melas, D., Balis, D. S., et al., Aerosol Lidar observations and model calculations of the Planetary Boundary Layer evolution over Greece, during the March 2006 Total Solar Eclipse. 2007, *Atmospheric Chemistry and Physics*, **7**, 6181, DOI: 10.5194/acp-7-6181-2007

Aplin, K. & Harrison, R., Meteorological effects of the eclipse of 11 August 1999 in cloudy and clear conditions. 2003, *Proceedings of the Royal Society of London. Series A: Mathematical, Physical and Engineering Sciences*, **459**, 353, DOI: 10.1098/rspa.2002.1042

Barbosa, H. M. J., Barja, B., Pauliquevis, T., et al., A permanent Raman lidar station in the Amazon: description, characterization, and first results. 2014, *Atmospheric Measurement Techniques*, **7**, 1745, DOI: 10.5194/amt-7-1745-2014

Binietoglou, I., Basart, S., Alados-Arboledas, L., et al., A methodology for investigating dust model performance using synergistic EARLINET/AERONET dust concentration retrievals. 2015, *Atmospheric Measurement Techniques*, **8**, 3577, DOI: 10.5194/amt-8-3577-2015

Boucher, O., Randall, D., Artaxo, P., et al. 2013, *Clouds and aerosols* (Cambridge, UK: Cambridge University Press), 571–657

Bucholtz, A., Rayleigh-scattering calculations for the terrestrial atmosphere. 1995, *Appl. Opt.*, **34**, 2765, DOI: 10.1364/AO.34.002765

Cheng, Y., Dai, T., Goto, D., et al., Investigating the assimilation of CALIPSO global aerosol vertical observations using a four-dimensional ensemble Kalman filter. 2019, *Atmospheric Chemistry and Physics*, **19**, 13445, DOI: 10.5194/acp-19-13445-2019

D'Amico, G., Amodeo, A., Baars, H., et al., EARLINET Single Calculus Chain – overview on methodology and strategy. 2015, *Atmospheric Measurement Techniques*, **8**, 4891, DOI: 10.5194/amt-8-4891-2015

D'Amico, G., Amodeo, A., Mattis, I., Freudenthaler, V., & Pappalardo, G., EARLINET Single Calculus Chain – technical – Part 1: Pre-processing of raw lidar data. 2016, *Atmospheric Measurement Techniques*, **9**, 491, DOI: 10.5194/amt-9-491-2016

Freudenthaler, V., Linné, H., Chaikovski, A., Rabus, D., & Groß, S., EARLINET lidar quality assurance tools. 2018, *Atmospheric Measurement Techniques Discussions*, **2018**, 1, DOI: 10.5194/amt-2017-395

Ilić, L., Kuzmanoski, M., Kolarž, P., et al., Changes of atmospheric properties over Belgrade, observed using remote sensing and in situ methods during the partial solar eclipse of 20 March 2015. 2018, *Journal of Atmospheric and Solar-Terrestrial Physics*, **171**, 250, DOI: https://doi.org/10.1016/j.jastp.2017.10.001, vertical Coupling in the Atmosphere-Ionosphere System: Recent Progress

Illingworth, A. J., Barker, H. W., Beljaars, A., et al., The EarthCARE Satellite: The Next Step Forward in Global Measurements of Clouds, Aerosols, Precipitation, and Radiation. 2015, *Bulletin of the American Meteorological Society*, **96**, 1311 , DOI: https://doi.org/10.1175/BAMS-D-12-00227.1

Kolarž, P., Šekarić, J., Marinković, B., & Filipović, D., Correlation between some of the meteorological parameters measured during the partial solar eclipse, 11 August 1999. 2005, *Journal of Atmospheric and Solar-Terrestrial Physics*, **67**, 1357, DOI: https://doi.org/10.1016/j.jastp.2005.07.016

Kolev, N., Tatarov, B., Grigorieva, V., et al., Aerosol Lidar and in situ ozone observations of the planetary boundary layer over Bulgaria during the solar eclipse of 11 August 1999. 2005, *International Journal of Remote Sensing*, **26**, 3567, DOI: 10.1080/01431160500076939

Mattis, I., D'Amico, G., Baars, H., et al., EARLINET Single Calculus Chain - technical - Part 2: Calculation of optical products. 2016, *Atmospheric Measurement Techniques*, **9**, 3009, DOI: 10.5194/amt-9-3009-2016

Maurya, A. K., Phanikumar, D. V., Singh, R., et al., Low-mid latitude D region ionospheric perturbations associated with 22 July 2009 total solar eclipse: Wave-like signatures inferred from VLF observations. 2014, *Journal of Geophysical Research: Space Physics*, **119**, 8512, DOI: https://doi.org/10.1002/2013JA019521

Meier, J., Tegen, I., Mattis, I., et al., A regional model of European aerosol transport: Evaluation with sun photometer, lidar and air quality data. 2012, *Atmospheric Environment*, **47**, 519, DOI: https://doi.org/10.1016/j.atmosenv.2011.09.029

Nymphas, E., Adeniyi, M., Ayoola, M., & Oladiran, E., Micrometeorological measurements in Nigeria during the total solar eclipse of 29 March, 2006. 2009, *Journal of Atmospheric and Solar-Terrestrial Physics*, **71**, 1245, DOI: https://doi.org/10.1016/j.jastp.2009.04.014

Papagiannopoulos, N., D'Amico, G., Gialitaki, A., et al., An EARLINET early warning system for atmospheric aerosol aviation hazards. 2020, *Atmospheric Chemistry and Physics*, **20**, 10775, DOI: 10.5194/acp-20-10775-2020

Pappalardo, G., Amodeo, A., Apituley, A., et al., EARLINET: towards an advanced sustainable European aerosol lidar network. 2014, *Atmospheric Measurement Techniques*, **7**, 2389, DOI: 10.5194/amt-7-2389-2014

Stocker, T. F., Qin, D., Plattner, G.-K., et al. 2013, *Technical summary* (Cambridge, UK: Cambridge University Press), 33–115

Wandinger, U., Freudenthaler, V., Baars, H., et al., EARLINET instrument intercomparison campaigns: overview on strategy and results. 2016, *Atmospheric Measurement Techniques*, **9**, 1001, DOI: 10.5194/amt-9-1001-2016

Contrib. Astron. Obs. Skalnaté Pleso **52/3**, 105 – 115, (2022)
https://doi.org/10.31577/caosp.2022.52.3.105

# Monitoring solar activity during 23/24 solar cycle minimum through VLF radio signals

**A. Kolarski, V.A. Srećković and Z.R. Mijić**

*Institute of Physics Belgrade, University of Belgrade, Pregrevica 118, 11080 Belgrade, Serbia (E-mail: aleksandra.kolarski@ipb.ac.rs)*

Received: July 20, 2022; Accepted: October 2, 2022

**Abstract.** Solar activity during solar minimum between $23^{rd}$ and $24^{th}$ solar cycle was inspected, based on solar X-ray radiation listings from Geostationary Operational Environmental Satellite (GOES) database. Periods of quiet solar conditions with low background X radiation are particularly favourable for analysis and exploration of low intensity solar flare events and their effects on lower ionosphere. Low intensity solar flare events were monitored and examined through Very Low Frequency (VLF) radio signals (3-30 kHz), recorded by the use of Absolute Phase and Amplitude Logger system (AbsPAL) operating at the Institute of Physics Belgrade, Serbia. For the purposes of numerical modeling of low ionospheric response to low class solar flare events, the Long Wave Propagation Capability (LWPC) software, based on Wait's theory, was applied. Main results are presented in this paper.

**Key words:** Solar activity – Solar X-ray flares – radio signal perturbations

## 1. Introduction

During quiet solar conditions, ionization i.e. production of electron content within lower ionospheric D-region, within altitude range 50-90 km, is in general related to photoionization processes caused by UV Lyman-$\alpha$ spectral line 121.6 nm, EUV spectral lines ranging from 102.7 nm to 118.8 nm and galactic cosmic rays. One of frequent extraterrestrial causing agents, that become major source of electron density perturbations within D-region, are X-ray solar flare events (0.1-0.8 nm) (Whitten & Poppoff, 1965; Wang et al., 2020; Hayes et al., 2021). Due to additional ionization, electron density height profile of the lower ionosphere changes (Mitra, 1974). Such perturbations affect propagation of Very Low Frequency (VLF) radio signals within Earth-ionosphere waveguide, causing deviations from their regular propagation patterns stable at unperturbed solar conditions (Thomson, 1993; McRae & Thomson, 2000). Since electron production rate coefficients can be considered directly proportional to intensity of incident X-radiation (Ratcliffe et al., 1972), perturbations of VLF radio signals induced by solar flares can be used as diagnostic tool for exploration of lower ionospheric electron content behavior during such events (see Barta et al., 2022, and references therein).

Utilization of VLF radio signals, as the remotesensing technique for exploration of the lower ionosphere (Thomson et al., 2011; McRae & Thomson, 2000; McRae & Thomson, 2004; Thomson et al., 2005), is widely adopted and extensively used by many research groups over several decades, e.g. (Silber & Price, 2017) and references therein. Response of the lower ionosphere to analyzed solar flare events, numerically was modeled by the use of Long Wave Propagation Capability (LWPC) (Ferguson, 1998) software relying on application of Wait's theory (Wait & Spies, 1964).

Effects of low intensity solar flare events of C and B classes, during 23/24 solar minimum, between descending branch of $23^{rd}$ and ascending branch of $24^{th}$ solar cycle, were inspected by monitoring recordings of VLF radio signals recorded in Belgrade (44.85 N, 20.38 W) Serbia, within time period from 2008 to 2010. Data related to solar X-rays is obtained from Geostationary Operational Environmental Satellite (GOES) archive database (`https://satdat.ngdc.noaa.gov/sem/goes/data/avg/`).

## 2. Observations

Periods of quiet solar activity, like during solar minimums, are of great interest for studying quiet ionospheric conditions and accompanying quiet i.e. unperturbed states within Earth-ionosphere waveguide related to VLF radio signals' transmission. In addition, since solar background X radiation during such periods is of small amount, low class solar flare events, like those of lower C class and moderate B class, when occur, are easily noticeable and recognizable, clearly distinguishing themselves from surrounding sections of unperturbed VLF radio signals. This gives a unique opportunity to examine characteristics of low class solar flare events, which are otherwise masked by high solar background X radiation during periods of usual more intense solar activity. An example of active Sun during solar maximum in April 2014 and quiet Sun during solar minimum in December 2019 are given in Figure 1, left and right, respectively. In 23/24 solar minimum, during 2008 there were 8 C class and 1 M class solar flare events reported, with X-ray background flux up to A8.1, while during 2009 there were 28 C class solar flare events reported, with X-ray background flux up to B1.4 (Figure 2).

VLF radio signal recordings obtained from the Absolute Phase and Amplitude Logger receiving station (AbsPAL), located and operating at the Institute of Physics in Belgrade, Serbia, was used as instrumental setup. Within inspected time period from 2008 to 2010, several VLF radio signals were simultaneously recorded by AbsPAL station in Belgrade. Geographical position and transmitter's characteristics of VLF radio signals propagating towards Belgrade are given in Table 1.

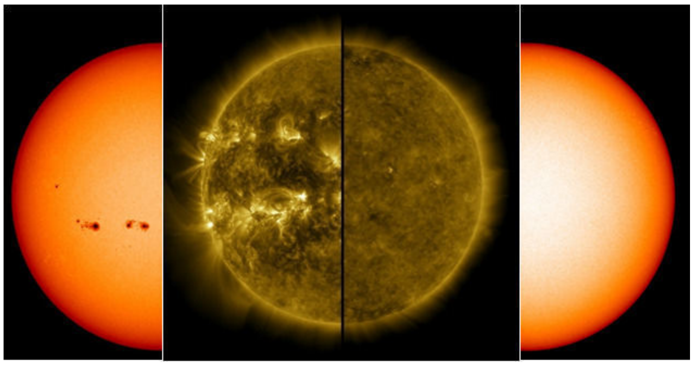

**Figure 1.** Active Sun during solar max. in April 2014 (left) and quiet Sun during solar min. in December 2019 (right) (taken from https://www.nasa.gov/).

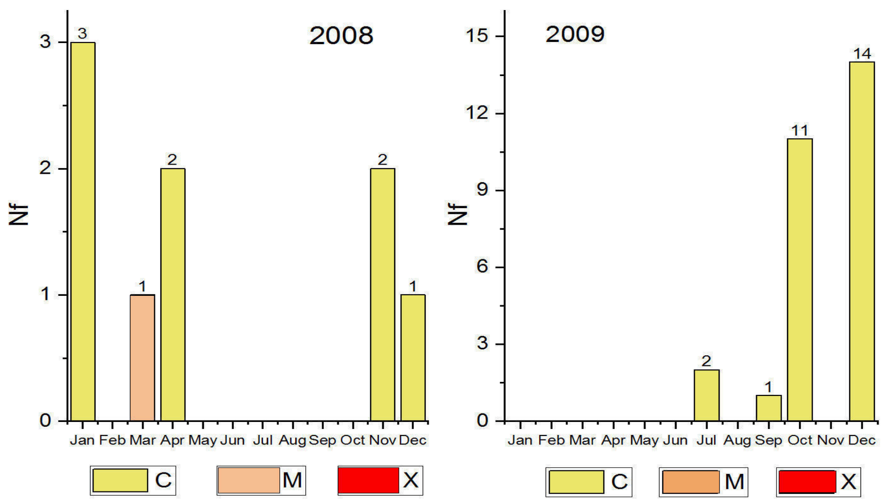


**Figure 2.** Solar flare events reported in period 2008-2010.

## 3. Results and discussion

Inspection of low intensity solar flare events of C and B class, on recorded VLF radio signals, was done according to provided solar X radiation listings from GOES database. During inspected period 2008-2010, low class solar flare events exhibited expected behavior, with amplitude perturbations of absolute amount in general of several tenth parts of dB up to few dB and with phase delay perturbations of absolute amount of few degrees to up to $16^{o}$. Some typical

**Table 1.** VLF radio signals registered in Belgrade during 23/24 solar cycle minimum.

| VLF signal (kHz) | Transmitter | Broadcast Power (kW) | GCP* Distance (km) |
|---|---|---|---|
| GQD/22.1 | Skelton, UK (54.72N; 2.88W) | 500 | 1982 |
| NAA/24.0 | Maine, USA (44.63N; 67.28W) | 1000 | 6547 |
| NWC/19.8 | H. E. Holt, Australia (27.2S; 114.98E) | 1000 | 11975 |
| DHO/23.4 | Rhauderfehn, Germany (53.08N; 7.62E) | 800 | 1301 |
| ICV/20.27 | Isola di Tavolara, Italy (NATO) (40.92N; 9.73E) | 20 | 970 |
| HWU/18.3 | Rosnay, France (NATO) (46.71N; 1.24E) | 400 | 1493 |

*Great Circle Path (GCP)

examples of low intensity solar flare events and accompanied VLF radio signal perturbations registered in Belgrade are given in Figures 3-4. However, in some cases, relatively weak solar flare events induced amplitude perturbations of as much as 5 dB and 13$^o$, while from relatively stronger ones, perturbations reached as much as 5 dB and 15$^o$ (Figures 5-8). Particularly interesting case was solar flare event of B class B8.35 which induced amplitude perturbation in NAA/24.0 kHz radio signal of 1.5 dB and phase delay perturbation of 10$^o$ (Figures 9-10, rounded by oval and enlarged in Figures 11-12).

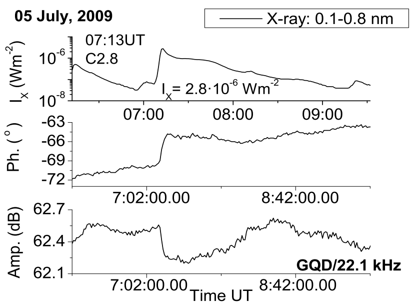


**Figure 3.** GQD signal perturbation during C2.8 class X-ray solar flare event.

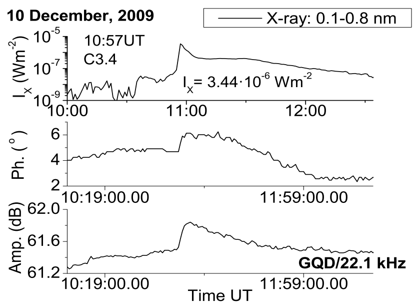


**Figure 4.** GQD signal perturbation during C3.4 class X-ray solar flare event.

Electron density height profile within Earth's lower ionosphere changes due to the incident solar X-ray radiation during solar flare events, causing in general descending and "sharpening" of the ionospheric lower boundary. Model of VLF radio signals propagation within Earth-ionosphere waveguide (Wait & Spies, 1964), that describes the electron density by reflecting edge sharpness,

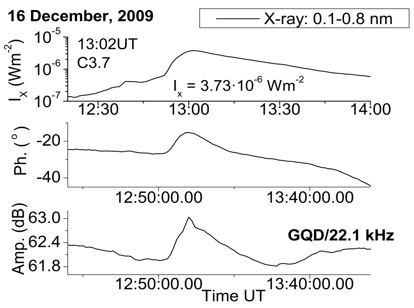


**Figure 5.** GQD signal perturbation during C3.7 class X-ray solar flare event.

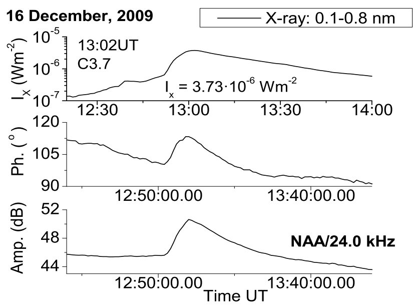


**Figure 6.** NAA signal perturbation during C3.7 class X-ray solar flare event.

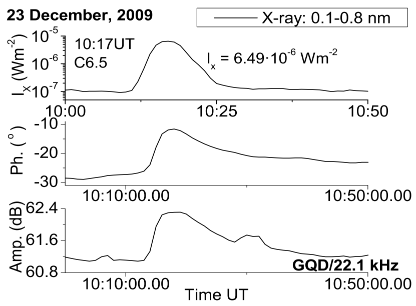


**Figure 7.** GQD signal perturbation during C6.5 class X-ray solar flare event.

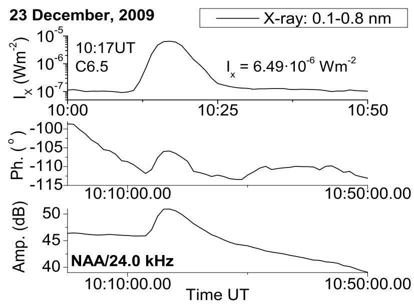


**Figure 8.** NAA signal perturbation during C6.5 class X-ray solar flare event.

denoted by $\beta$ (km$^{-1}$) and reflecting edge height, denoted by $H'$ (km), was used for purposes of numerical simulations of VLF radio signal propagation through Earth-ionosphere waveguide. Obtained results through simulations are in good agreement with VLF signal amplitude and phase delay data measured in Belgrade. Electron density height profiles $N_e$(z), within altitude range 50-90 km, were obtained through the equation (Wait & Spies, 1964):

$$N_e(z, H', \beta) = 1.43 \cdot 10^{13} e^{-0.15H'} e^{(\beta-0.15)(z-H')} \ . \quad (1)$$

Numerical simulations were conducted for the entire time evolution of chosen solar flare events, with parameter pairs ($\beta/H'$) held constant along VLF radio signal's GCPs, depicting "average" ionospheric conditions within waveguide. VLF radio signal's amplitude and phase delay perturbations $\Delta A$ (dB) and $\Delta P$ (°), were determined by comparing measured perturbed to the measured

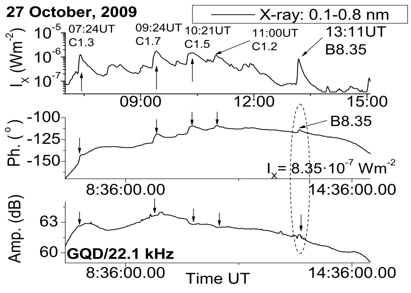


Figure 9. GQD signal perturbations during October $27^{th}$, 2009.

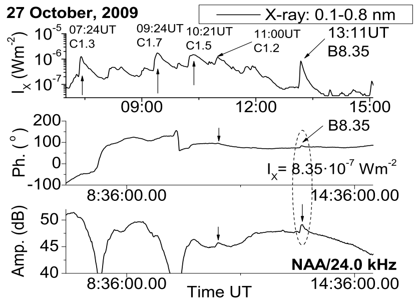


**Figure 10.** NAA signal perturbations during October $27^{th}$, 2009.

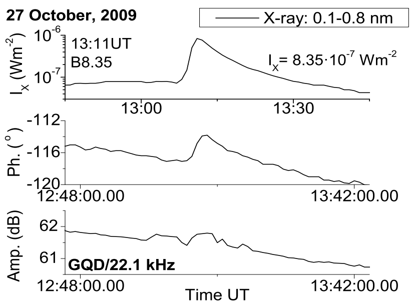


**Figure 11.** GQD signal perturbation during B8.35 class X-ray solar flare event.

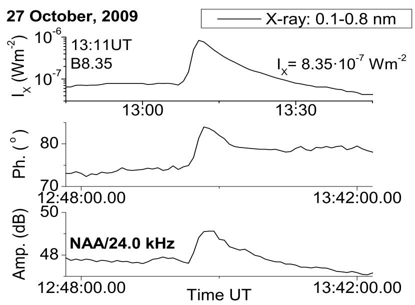


**Figure 12.** NAA signal perturbation during B8.35 class X-ray solar flare event.

unperturbed amplitude and phase delay values and are calculated as: $\Delta A = A_{flare}$ - $A_{unpert}$ and $\Delta P = P_{flare}$ - $P_{unpert}$. During simulations through iterative process, the goal was to achieve as close as possible to measured data, both absolute values of simulated amplitude and phase delay and relative amount of perturbations. Results obtained through numerical simulations are in good agreements with measured data. Calculated electron density height profiles during maximum of X-ray solar irradiance, in case of NAA/24.0 kHz signal trace, are given in (Figure 13), for some chosen examples of solar flare events: a) low intensity C class solar flare event C3.7 that occurred on December $16^{th}$, 2009, at 13:02UT with $I_{max} = 3.73 \cdot 10^{-6}$ Wm$^{-2}$, with measured $\Delta A_{flare}$=5 dB and $\Delta P_{flare}$=13$^{\rm o}$ and through simulations obtained parameter pair ($\beta/H'$) (0.43 km$^{-1}$/69.7 km) with calculated electron density $N_e$(74 km)=1.37·10$^9$ m$^{-3}$, b) moderate intensity C class solar flare event C6.5 that occurred on December

$23^{rd}$, 2009, at 10:17UT with $I_{max} = 6.49 \cdot 10^{-6}$ Wm$^{-2}$ with measured $\Delta A_{flare}$=5 dB and $\Delta P_{flare}$=6° and through simulations obtained parameter pair $(\beta/H')$ (0.43 km$^{-1}$/70.1 km) with calculated electron density $N_e$(74 km)=1.17·10$^9$ m$^{-3}$ and c) moderate intensity B class solar flare event B8.35 that occurred on October $27^{th}$, 2009, at 13:11UT with $I_{max} = 8.35 \cdot 10^{-7}$ Wm$^{-2}$ with measured $\Delta A_{flare}$=1.5 dB and $\Delta P_{flare}$=10° and through simulations obtained parameter pair $(\beta/H')$ (0.33 km$^{-1}$/72.3 km) with calculated electron density $N_e$(74 km)=3.79·10$^8$ m$^{-3}$. Obtained electron density height profiles in flare state, with $N_e$(74 km) increase of about one order of magnitude in case of C class flares, with slight increase of about 75% in case of B class flare, are realistic and in line with other studies (Žigman et al., 2007; Grubor et al., 2008; McRae & Thomson, 2004; Kolarski et al., 2011; Nina et al., 2011, 2012; Kolarski & Grubor, 2014; Kolarski et al., 2022; Srećković et al., 2021a,b).

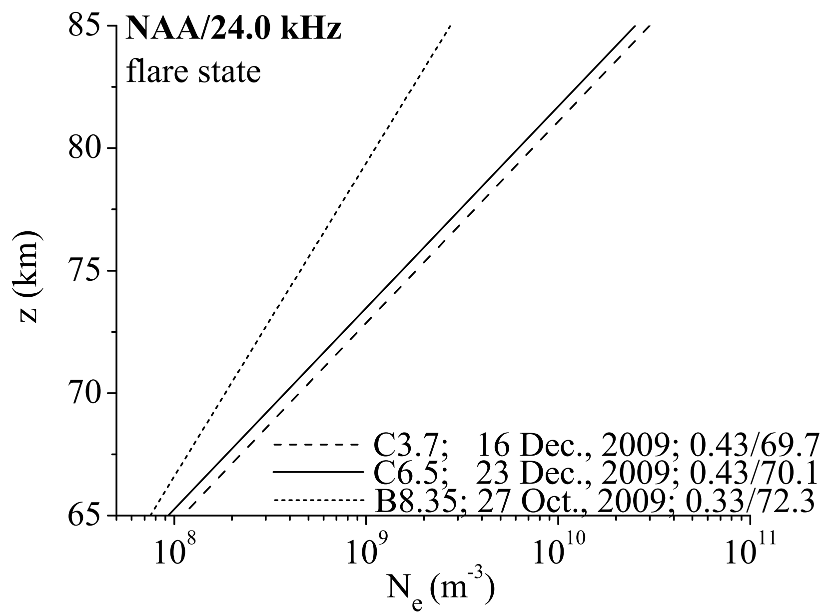


**Figure 13.** Electron density height profiles during C3.7 (dashed line), C6.5 (solid line) and B8.35 (dotted line) class X-ray solar flare events.

It is possible to draw conclusions about the intensity of the causing X-ray solar flare events, based upon perturbation amounts obtained from VLF radio signal recordings, when taking into consideration single VLF radio signal trace.

However, same solar flare event can produce perturbations different both in pattern and in intensity, when observed on different VLF radio signal traces. Typical examples are in general perturbations induced by solar flare events of moderate and lower intensity classes as recorded in Belgrade during active solar periods on NAA and GQD radio signals. In such cases, NAA signal's both amplitude and phase delay follow in pattern incident X-ray solar irradiance, while in case of GQD signal, amplitude and phase delay follow incident X-ray solar irradiance in pattern, but like mirrored images and only in some cases of higher class solar flare events this feature is more or less mitigated (Žigman et al., 2007; Grubor et al., 2008; Kolarski & Grubor, 2014). Aside to main factor of solar flare intensity (Grubor et al., 2008; Kolarski & Grubor, 2014), this behavior is also strongly under the influence of VLF GCP trace characteristics (Kolarski & Grubor, 2015; Šulić & Srećković, 2014; Šulić et al., 2016). For example, measured absolute perturbation as observed on GQD radio signal trace, in case of C3.7 solar flare event was $\Delta A_{flare}$=1 dB and $\Delta P_{flare}$=11.5$^o$, in case of C6.5 solar flare event was $\Delta A_{flare}$=1.2 dB and $\Delta P_{flare}$=15.5$^o$ and in case of B8.35 solar flare event it was $\Delta A_{flare}$=0.4 dB and $\Delta P_{flare}$=3.3$^o$.

## 4. Summary

Two year time period of VLF radio signal recordings from Belgrade AbsPAL database, corresponding to 23/24 solar minimum, was examined in order of getting better insight of effects that low intensity solar flare events of C and B classes have on the lower ionospheric region and transmission of VLF radio signals within Earth-ionosphere waveguide. According to GOES database, during inspected period 2008-2010, 38 solar flare events of C and M class were reported, with X-ray background flux in range up to A8.1 for 2008 and B1.4 for 2009. Low intensity solar flare events of C and B class were monitored on all recorded VLF radio signals. Depending on solar flare occurrence time and VLF radio signal's GCP towards Belgrade receiver station, some flares were simultaneously observed on several VLF radio signals, however, detailed analysis in this paper was conducted for cases of NAA/24.0 kHz and GQD/22.1 kHz signal traces.

As expected, majority of low class solar flare events in general revealed perturbations of absolute amount of several tenth parts of dB up to few dB and of few degrees to up to 16$^o$, following the manner of incident solar X-ray flux. However, there were also cases that fall out of the pattern, when relatively weak solar flare events such as C3.7, produced perturbations of 5 dB and 13$^o$, while relatively stronger ones, such C6.5 gave perturbations of similar amount, as 5 dB and 15$^o$. Due to low X-ray background flux, in some cases even B class solar flare events induced noticeable perturbations, as in case of B8.35 with perturbation of 1.5 dB and 10$^o$.

Numerical simulations were conducted using LWPC software package, with goal of achieving simulated VLF data as close as possible to measured VLF data in Belgrade, both in case of absolute values and in case of relative amount of perturbations. Results obtained through iterative numerical simulations are in good agreements with real VLF data measured in Belgrade (Žigman et al., 2007; Grubor et al., 2008; Kolarski et al., 2011; Nina et al., 2011). In case of NAA/24.0 kHz signal, perturbations induced by low class solar flare events produced "sharpening" and descending of the lower ionospheric boundary, as in cases of presented solar flare events reflection height went from unperturbed value of 74 km to 72.3, 70.1 and 69.7 km, while become "sharper" compared to unperturbed value of 0.3 km$^{-1}$ reaching 0.33 and 0.44 km$^{-1}$. Estimated $N_e$(74 km) are realistic and in line with other studies (McRae & Thomson, 2004; Nina et al., 2012; Kolarski & Grubor, 2014; Kolarski et al., 2022; Srećković et al., 2021a,b).

**Acknowledgements.** Authors thank D. Šulić for instrumental setup. This work was funded by the Institute of Physics Belgrade through a grant by the Ministry of Education, Science, and Technological Development of the Republic of Serbia. Authors appreciate comments expressed by referees, which improved this paper.

## References

Barta, V., Natras, R., Srekovi, V., et al., Multi-instrumental investigation of the solar flares impact on the ionosphere on 0506 December 2006. 2022, *Frontiers in Environmental Science*, **10**, DOI: 10.3389/fenvs.2022.904335

Ferguson, J. 1998, Computer programs for assessment of long-wavelength radio communications, version 2.0: User's guide and source files, Tech. rep., Space and naval warfare systems center San Diego CA

Grubor, D., Šulić, D., & Žigman, V., Classification of X-ray solar flares regarding their effects on the lower ionosphere electron density profile. 2008, *Annales Geophysicae*, **26**, 1731, DOI: 10.5194/angeo-26-1731-2008

Hayes, L. A., O'Hara, O. S. D., Murray, S. A., & Gallagher, P. T., Solar Flare Effects on the Earth's Lower Ionosphere. 2021, *Solar Physics*, **296**, 157, DOI: 10.1007/s11207-021-01898-y

Kolarski, A. & Grubor, D., Sensing the Earths low ionosphere during solar flares using VLF signals and goes solar X-ray data. 2014, *Advances in space research*, **53**, 1595, DOI: 10.1016/j.asr.2014.02.022

Kolarski, A. & Grubor, D., Comparative analysis of VLF signal variation along trajectory induced by X-ray solar flares. 2015, *Journal of Astrophysics and Astronomy*, **36**, 565, DOI: 10.1007/s12036-015-9361-x

Kolarski, A., Grubor, D., & Šulić, D., Diagnostics of the Solar X-Flare Impact on Lower Ionosphere through the VLF-NAA Signal Recordings. 2011, *Open Astronomy*, **20**, 591, DOI: 10.1515/astro-2017-0342

Kolarski, A., Srećković, V. A., & Mijić, Z. R., Response of the Earths Lower Ionosphere to Solar Flares and Lightning-Induced Electron Precipitation Events by Analysis of VLF Signals: Similarities and Differences. 2022, *Applied Sciences*, **12**, 582, DOI: 10.3390/app12020582

McRae, W. M. & Thomson, N. R., VLF phase and amplitude: Daytime ionospheric parameters. 2000, *Journal of Atmospheric and Solar-Terrestrial Physics*, **62**, 609, DOI: 10.1016/S1364-6826(00)00027-4

McRae, W. M. & Thomson, N. R., Solar flare induced ionospheric D-region enhancements from VLF phase and amplitude observations. 2004, *Journal of Atmospheric and Solar-Terrestrial Physics*, **66**, 77, DOI: 10.1016/j.jastp.2003.09.009

Mitra, A. P. 1974, *Ionospheric effects of solar flares* (Springer, Berlin/Heidelberg)

Nina, A., Čadež, V., Srećković, V., & Šulić, D., The influence of solar spectral lines on electron concentration in terrestrial ionosphere. 2011, *Open Astronomy*, **20**, 609, DOI: 10.1515/astro-2017-0346

Nina, A., Čadež, V., Srećković, V., & Šulić, D., Altitude distribution of electron concentration in ionospheric D-region in presence of time-varying solar radiation flux. 2012, *Nuclear Instruments and Methods in Physics Research Section B: Beam Interactions with Materials and Atoms*, **279**, 110, DOI: 10.1016/j.nimb.2011.10.019

Ratcliffe, J. A. et al. 1972, *An introduction to ionosphere and magnetosphere* (CUP Archive, Cambridge, UK)

Silber, I. & Price, C., On the use of VLF narrowband measurements to study the lower ionosphere and the mesosphere–lower thermosphere. 2017, *Surveys in Geophysics*, **38**, 407, DOI: 10.1007/s10712-016-9396-9

Srećković, V. A., Šulić, D. M., Ignjatović, L., & Vujčić, V., Low Ionosphere under Influence of Strong Solar Radiation: Diagnostics and Modeling. 2021a, *Applied Sciences*, **11**, 7194, DOI: 10.3390/app11167194

Srećković, V. A., Šulić, D. M., Vujčić, V., Mijić, Z. R., & Ignjatović, L. M., Novel Modelling Approach for Obtaining the Parameters of Low Ionosphere under Extreme Radiation in X-Spectral Range. 2021b, *Applied Sciences*, **11**, 11574, DOI: 10.3390/app112311574

Thomson, N., Experimental daytime VLF ionospheric parameters. 1993, *Journal of Atmospheric and Terrestrial Physics*, **55**, 173, DOI: 10.1016/0021-9169(93)90122-F

Thomson, N. R., Rodger, C. J., & Clilverd, M. A., Large solar flares and their ionospheric D region enhancements. 2005, *Journal of Geophysical Research: Space Physics*, **110**, DOI: https://doi.org/10.1029/2005JA011008

Thomson, N. R., Rodger, C. J., & Clilverd, M. A., Daytime D region parameters from long-path VLF phase and amplitude. 2011, *Journal of Geophysical Research: Space Physics*, **116**, DOI: https://doi.org/10.1029/2011JA016910

Šulić, D. M. & Srećković, V. A., A Comparative Study of Measured Amplitude and Phase Perturbations of VLF and LF Radio Signals Induced by Solar Flares. 2014, *Serbian Astronomical Journal*, **188**, 45, DOI: 10.2298/SAJ1488045S

Šulić, D. M., Srećković, V. A., & Mihajlov, A. A., A study of VLF signals variations associated with the changes of ionization level in the D-region in consequence of solar conditions. 2016, *Advances in Space Research*, **57**, 1029, DOI: 10.1016/j.asr.2015.12.025

Wait, J. R. & Spies, K. P. 1964, *Characteristics of the Earth-ionosphere waveguide for VLF radio waves* (US Department of Commerce, National Bureau of Standards, Boulder, CO, USA)

Wang, X., Chen, Y., Toth, G., et al., Predicting Solar Flares with Machine Learning: Investigating Solar Cycle Dependence. 2020, *Astrophysical Journal*, **895**, 3, DOI: 10.3847/1538-4357/ab89ac

Whitten, R. & Poppoff, I. 1965, *Physics of the Lower Ionosphere* (Prentice-Hall, Englewood Cliffs, N. J.)

Žigman, V., Grubor, D., & Šulić, D., D-region electron density evaluated from VLF amplitude time delay during X-ray solar flares. 2007, *Journal of atmospheric and solar-terrestrial physics*, **69**, 775, DOI: 10.1016/j.jastp.2007.01.012

data

Editorial

# Data in Astrophysics and Geophysics: Novel Research and Applications

**Vladimir A. Srećković [1,*], Milan S. Dimitrijević [2,3] and Zoran R. Mijić [1]**

1 Institute of Physics Belgrade, University of Belgrade, Pregrevica 118, 11080 Belgrade, Serbia; zoran.mijic@ipb.ac.rs
2 Astronomical Observatory, Volgina 7, 11060 Belgrade, Serbia; mdimitrijevic@aob.rs
3 LERMA, Observatoire de Paris, Sorbonne Université, PSL University, CNRS, F-92190 Meudon, France
* Correspondence: vlada@ipb.ac.rs; Tel.: +381-(0)11-37-13-000

check for updates

**Citation:** Srećković, V.A.; Dimitrijević, M.S.; Mijić, Z.R. Data in Astrophysics and Geophysics: Novel Research and Applications. *Data* **2024**, *9*, 32. https://doi.org/10.3390/data9020032

Received: 14 December 2023
Accepted: 1 February 2024
Published: 8 February 2024



## 1. Introduction

Rapid development of communication technologies and constant technological improvements as a result of scientific discoveries require the establishment of specific databases. The associated challenges in the management of such databases are not only related to the size of the data but also to the rate at which they are obtained and made freely available to the broader scientific community.

One innovative approach is to develop cooperation and effective synergies between disciplines such as space exploration, atmospheric and Earth observations (EOs), laboratory and field experiments, and numerical modeling, where all of these have great potential for direct application in research on Earth and different planetary environments [1].

Modeling various atmospheres using supercomputers' capacity and diagnosing astrophysical and laboratory plasma using atomic and molecular datasets rely on the development and improvement of theoretical approaches and methods of the calculation of different data parameters such as collisional cross-sections, rate coefficients, Stark broadening parameters (the shape of atomic spectral lines in plasma contains information on the plasma's parameters and can be used as a diagnostic tool), etc. (see, e.g., [2–5]). Space and Earth's layers are permanently exposed to influences of numerous perturbations characterized by time- and space-dependent intensity. The detection of astrophysical and terrestrial events and their influences, as well as the development and application of various models, is based on observation data, where challenges related to data volume, variety, and data flow are similar in terms of astro- and geo-observations [6,7]. Recent achievements in remote sensing technology, including satellite observations, and the analysis of huge amounts of data using supercomputing and machine learning techniques have significantly supported the advancement of geophysical research, particularly climate change.

In order to address complex climate issues and corresponding impacts, multi-instrument and multi-disciplinary expertise is required [8,9]. Furthermore, the increasing volume of data indicates increased usage of automated instruments and retrieval algorithms. The new knowledge and retrieval products can be readily used for model evaluation, data assimilation, satellite validation, and studies of various processes in the atmosphere and on Earth.

This Special Issue, "2nd Edition of Data in Astrophysics & Geophysics: Research and Applications", as a continuation of a prior series [10], aims to encourage communication between disciplines by identifying and grouping relevant research solutions. Its goals are to engage a broad community of researchers to make new discoveries enabled by the growth of data and technology and to continue interdisciplinary exchanges of ideas and methodologies between fields. To this end, articles addressing, but not limited to, the following topics were invited to be submitted to this Special Issue: big data in astrophysics and geophysics, data processing, visualization and acquisition, atomic and molecular data in astrophysics, Earth observation data, climate data records, natural hazards and disasters, and remote sensing.

The compilation of published datasets should be useful to both end users, for practical applications, and researchers, for their further scientific studies.

## 2. Contributions to this Special Issue

This Special Issue encompasses 14 open access papers that present scientific studies covering a wide range of applications in terms of both measured and modeled data exploitation and processing methods used.

In the paper by López-Espinoza et al. (contribution 1), daily precipitation data records from 136 sites located within the Mexico City Metropolitan Area were systemized for the period 1930–2015. The obtained dataset covered the rainy months for each location for at least 20 years. Having high spatial resolution, the presented precipitation dataset could be useful for extreme event studies, and particularly atmospheric modeling. In addition, the development of applications for precipitation mapping and flood forecasting could be important to contribute to obtaining data, bearing in mind the vulnerability of this region to tropical weather events.

Besides playing an important role in many research fields, meteorological parameters also have a significant impact on vector diseases. In the paper by Musah et al. (contribution 2), the development of an early warning detection system and prediction of increased mosquito populations in two Brazilian cities previously exposed to the Zika virus epidemic are discussed. The authors evaluate the accuracy of weather forecasts of temperature and humidity from an online weather platform with respect to the actual measurements collected from weather stations in order to test whether historical and future weather forecasts can be used for the modeling and prediction of vector diseases.

Using any available database for further research must be handled carefully, taking into account the quality of the data. Usually, data included in a database are categorized into different levels, meaning that the files have to overcome basic quality controls (for example, the presence of technical problems in the data files), advanced quality control (checking the data from a physical point of view) or, in some cases, the climatological data obtained from the fully quality controlled data, providing useful combined information to end users. The importance of the quality control procedure on total precipitation measurements for Montane Valley and Ridge Sites in southwestern Alberta, Canada, was discussed in the paper by Bames et al. (contribution 3). The authors presented different procedures for quality control and measurement error corrections for totalizing precipitation gauge data. The obtained results pointed out that, after applying the QC procedure, the annual cumulative precipitation on the ridge differed from 39% to 49%, while in the valley these corrections were in a range from −4% to 1%.

Mitigation and adaption strategy related to climate change is one of the research fields that requires a huge amount of EO data. Among many other disciplines, assessing the performance of buildings under different climate scenarios and providing long-term effects in terms of sustainable development and energy efficiency have become two of the top priorities in recent years. In the study by Gaur et al. (contribution 4), the authors provided the necessary climate data for building simulations in Canada. The dataset contains climate data for the period 1991–2021, as well as for future periods corresponding to various levels of temperature increase. Besides practitioners in Canada who can use the obtained information for building characteristic evaluation, the results of the study will be useful for applications relating to other regional projections.

While climate change has a significant impact across many geophysical disciplines, agriculture is one of the most directly influenced sectors, especially in vulnerable regions such as Africa. Adaptation and mitigation strategies in such regions have become more challenging; thus, requirements for weather and climate data to support timely decisions with respect to different climate scenarios are needed. In the paper by Moeletsi et al. (contribution 5), a description of the weather station network in South Africa is presented together with relevant data retrieval and processing information, calibration, and maintenance protocols. Such a detailed documented database should lead to more efficient utilization of available datasets for application in this important area.

Climate change and precipitation also influence rivers' water resources; thus, many previous studies have used global and regional hydrological models to assess runoff predictions for the largest basins all over the world. In the paper by Ayzel (contribution 6), the simulated runoff for 425 river basins in Russia is presented, covering a period ranging from 1979 to 2016 and offering a prediction for the 2017–2099 period. Different climate scenarios were used in order to assess changes in river runoff and potential floods. The results can potentially be used for both research and mitigation strategy regarding climate change.

The mapping of terrestrial ecosystems, including vegetation index, soil typing, etc., is of particular interest. Previous as well as currently operating Earth observation satellite missions have provided freely available data which are useful in many applications. Each mission focuses on a specific aspect (land monitoring, atmospheric, oceanic) of Earth observation. By combining machine learning algorithms and high-resolution imagery from Sentinel-1 and Sentinel-2 missions in the paper by Abera et al. (contribution 7), the authors provided a land cover map of Taita Taveta County in southern Kenya. This specific region is part of one of the world's biodiversity hotspots. The obtained results can be used for the monitoring of land cover changes and future managing.

In Lemenkova's study (contribution 8), the processing of complex geophysical data related to the Bolivian Andes is presented. This region is known for its complex geological parameters, with high seismic activity and risk of earthquakes. The author demonstrated the usage of the Generic Mapping Tools (GMTs) and Geographic Information System (GIS) scripting tool set for complex data processing in an integrated framework. The study is based on available data mostly derived from remote sensing open sources and script-based techniques, providing more flexibility in data processing and analysis. The identification of the distribution and magnitude of earthquakes in this specific region in the context of the geologic, geophysical, and topographic situations is presented.

The ability to combine hyperspectral scans with 3D point cloud representations has expanded the mapping of various geological objects. Rapid progress in artificial intelligence and machine learning algorithm application in earth sciences has enabled fast and effective characterization of geological structures in a three-dimensional environment. Based on previously developed open-source software for processing non-nadir hyperspectral scenery with different corrections, Lorenz et al. (contribution 9) provided a three-dimensional, km-scale, hyperspectral dataset of a well-exposed mineral deposit—the Black Angel at Maarmorilik, West Greenland. Extended documentation on the data processing workflow could be useful for application in various disciplines.

Seismic monitoring data for the Italian region is provided in the paper by Megna et al. (contribution 10). The authors presented the seismic network operating in the area of Montefeltro from 2018. The data available from this mobile network should reveal, with high temporal resolution, regions with the seismic activities of lower-intensity, thus improving currently operating models.

Besides earthquakes, one of the most frequently occurring natural hazards is landslides. Improving the regional inventory of landslides has become particularly important not only from a scientific point of view but also for different communities, ranging from local/regional stakeholders to various industries. In the paper by Li et al. (contribution 11), the authors presented an inventory of landslides based on multi-temporal high-resolution remote sensing images for the area of Baoji City, Shaanxi Province, China. Datasets of each identified landslide in shp format are provided and will be useful for the better characterization of large-scale landslides in regions of interest.

In the paper by Papenmeier et al. (contribution 12), geomorphological data, including maps of bathymetry, depth, and slope angle of detonation craters in the Fehmarn Belt, Baltic Sea, were presented. Many explosives remaining in marine waters worldwide after the world's military conflicts have been recognized as a serious threat to marine traffic and ecosystems. Investigation of the impact on the environment of controlled blast-in-place is of particular interest for future monitoring and clearance strategies.

Besides the investigation of seafloor morphological changes in coastlines, modeling coastal change during extreme weather events has attracted increasing attention. In the study by Mickey and Passeri (contribution 13), the authors provided a dataset of seamless cross-shore sandy coast profiles of the U.S. Atlantic and the Gulf of Mexico based on lidar (Light Detection And Ranging)-derived topography and available bathymetry. The database, containing various morphological metrics, will be useful for broader geophysical studies.

Spectroscopy is widely used to study plasmas in a variety of fields, including astronomy, atmospheric research, and applied physics. The availability of spectroscopic information related to both atoms and ions is crucial for a wide range of processes, from astrophysical- to thermal- and plasma-related practices. In the paper by Srećković et al. (contribution 14), the spectral absorption rate coefficients and average cross-sections for small molecular ions $AlH^+$, $HeH^+$, and $HK^+$ under different conditions (temperatures and wavelengths) have been provided using a quantum mechanical method. The obtained results are useful for industry and technology application as well as for theoretical interdisciplinary studies, including the modeling of various atmospheric processes.

To sum up the presented studies, they have all introduced a relevant observed and modeling dataset related to astrophysics and geophysics with potential applications in wide research areas, from climate change to astronomy.

## 3. Conclusions and Future Research Initiatives

This Special Issue was open to scientists with expertise coming from various research areas and disciplines. All papers in this issue were subjected to thorough peer review and were evaluated by at least two reviewers. Considering all of the contributions, this Special Issue demonstrates the high benefit of using a multi-disciplinary approach to analyze various geophysical and astrophysical phenomena. We believe that the quality of the papers and open access dataset provided, followed by accompanied data descriptions, will ensure the success of this Special Issue. By publishing work from a vast community of academics, both users and contributors will benefit from new findings and this will trigger further interdisciplinary exchanges of ideas and approaches.

**Author Contributions:** Writing, review, and editing: V.A.S., M.S.D., and Z.R.M. All authors have read and agreed to the published version of the manuscript.

**Funding:** This work was funded by the Institute of Physics Belgrade, University of Belgrade, through a grant by the Ministry of Science, Technological Development, and Innovations of the Republic of Serbia.

**Acknowledgments:** We appreciate the opportunity to organize this Special Issue "2nd Edition of Data in Astrophysics & Geophysics: Research and Applications". We would also like to express our appreciation to all of the authors for contributing their ideas and research to this Special Issue, as well as to the referees for their objective evaluation and useful recommendations. Finally, we want to give special thanks to the editorial team of the *Data* journal for their continuous support, dedication, and assistance all the way throughout the publication process.

**Conflicts of Interest:** The authors declare no conflicts of interest.

**List of Contributions**

1. López-Espinoza, E.D.; Fuentes-Mariles, O.A.; Herrera-Moro, D.R.; Gómez-Ramos, O.; Novelo-Casanova, D.A.; Zavala-Hidalgo, J. Daily Precipitation Data for the Mexico City Metropolitan Area from 1930 to 2015. *Data* **2022**, *7*, 88. https://doi.org/10.3390/data7070088.
2. Musah, A.; Dutra, L.M.M.; Aldosery, A.; Browning, E.; Ambrizzi, T.; Borges, I.V.G.; Tunali, M.; Başibüyük, S.; Yenigün, O.; Moreno, G.M.M.; et al. An Evaluation of the OpenWeatherMap API versus INMET Using Weather Data from Two Brazilian Cities: Recife and Campina Grande. *Data* **2022**, *7*, 106. https://doi.org/10.3390/data7080106.
3. Barnes, C.; Hopkinson, C. Quality Control Impacts on Total Precipitation Gauge Records for Montane Valley and Ridge Sites in SW Alberta, Canada. *Data* **2022**, *7*, 73. https://doi.org/10.3390/data7060073.

4. Gaur, A.; Lacasse, M. Climate Data to Support the Adaptation of Buildings to Climate Change in Canada. *Data* **2022**, *7*, 42. https://doi.org/10.3390/data7040042.
5. Moeletsi, M.E.; Myeni, L.; Kaempffer, L.C.; Vermaak, D.; de Nysschen, G.; Henningse, C.; Nel, I.; Rowswell, D. Climate Dataset for South Africa by the Agricultural Research Council. *Data* **2022**, *7*, 117. https://doi.org/10.3390/data7080117.
6. Ayzel, G. Runoff for Russia (RFR v1.0): The Large-Sample Dataset of Simulated Runoff and Its Characteristics. *Data* **2023**, *8*, 31. https://doi.org/10.3390/data8020031.
7. Abera, T.A.; Vuorinne, I.; Munyao, M.; Pellikka, P.K.E.; Heiskanen, J. Land Cover Map for Multifunctional Landscapes of Taita Taveta County, Kenya, Based on Sentinel-1 Radar, Sentinel-2 Optical, and Topoclimatic Data. *Data* **2022**, *7*, 36. https://doi.org/10.3390/data7030036.
8. Lemenkova, P. Handling Dataset with Geophysical and Geological Variables on the Bolivian Andes by the GMT Scripts. *Data* **2022**, *7*, 74. https://doi.org/10.3390/data7060074.
9. Lorenz, S.; Thiele, S.T.; Kirsch, M.; Unger, G.; Zimmermann, R.; Guarnieri, P.; Baker, N.; Sørensen, E.V.; Rosa, D.; Gloaguen, R. Three-Dimensional, Km-Scale Hyperspectral Data of Well-Exposed Zn-Pb Mineralization at Black Angel Mountain, Greenland. *Data* **2022**, *7*, 104. https://doi.org/10.3390/data7080104.
10. Megna, A.; Cimini, G.B.; Marchetti, A.; Pagliuca, N.M.; Santini, S. A Waveform Dataset in Continuous Mode of the Montefeltro Seismic Network (MF) in Central-Northern Italy from 2018 to 2020. *Data* **2022**, *7*, 169. https://doi.org/10.3390/data7120169.
11. Li, L.; Xu, C.; Yang, Z.; Zhang, Z.; Lv, M. An Inventory of Large-Scale Landslides in Baoji City, Shaanxi Province, China. *Data* **2022**, *7*, 114. https://doi.org/10.3390/data7080114.
12. Papenmeier, S.; Darr, A.; Feldens, P. Geomorphological Data from Detonation Craters in the Fehmarn Belt, German Baltic Sea. *Data* **2022**, *7*, 63. https://doi.org/10.3390/data7050063.
13. Mickey, R.C.; Passeri, D.L. A Database of Topo-Bathy Cross-Shore Profiles and Characteristics for U.S. Atlantic and Gulf of Mexico Sandy Coastlines. *Data* **2022**, *7*, 92. https://doi.org/10.3390/data7070092.
14. Srećković, V.A.; Ignjatović, L.M.; Kolarski, A.; Mijić, Z.R.; Dimitrijević, M.S.; Vujčić, V. Data for Photodissociation of Some Small Molecular Ions Relevant for Astrochemistry and Laboratory Investigation. *Data* **2022**, *7*, 129. https://doi.org/10.3390/data7090129.

## References

1. Škoda, P.; Adam, F. *Knowledge Discovery in Big Data from Astronomy and Earth Observation*; Elsevier: Amsterdam, The Netherlands, 2020.
2. Vukalović, J.; Marinković, B.P.; Rosado, J.; Blanco, F.; García, G.; Maljković, J.B. Investigating theoretical and experimental cross sections for elastic electron scattering from isoflurane. *Phys. Chem. Chem. Phys.* **2024**, *26*, 985–991. [CrossRef] [PubMed]
3. Kupka, F.; Dubernet, M.-L. VAMDC as a Resource for Atomic and Molecular Data and the New Release of VALD. *Open Astron.* **2011**, *20*, 503–510. [CrossRef]
4. Itikawa, Y.; Mason, N. Cross Sections for Electron Collisions with Water Molecules. *J. Phys. Chem. Ref. Data* **2005**, *34*, 1–22. [CrossRef]
5. Pop, N.; Iacob, F.; Niyonzima, S.; Abdoulanziz, A.; Laporta, V.; Reiter, D.; Schneider, I.F.; Mezei, J.Z. Reactive collisions between electrons and BeT+: Complete set of thermal rate coefficients up to 5000 K. *At. Data Nucl. Data Tables* **2021**, *139*, 101414. [CrossRef]
6. Brasseur, G.; Solomon, S. Radiation. In *Aeronomy of the Middle Atmosphere: Chemistry and Physics of the Stratosphere and Mesosphere*; Springer: Berlin/Heidelberg, Germany, 2005; pp. 151–264.
7. Fang, Z.; Wang, D.; Wang, X.; Li, Y. Research and Application of Big Earth Data Distribution and Sharing System. In Proceedings of the 2021 IEEE 6th International Conference on Cloud Computing and Big Data Analytics (ICCCBDA), Chengdu, China, 24–26 April 2021; pp. 62–66.
8. Ilić, L.; Kuzmanoski, M.; Kolarž, P.; Nina, A.; Srećković, V.; Mijić, Z.; Bajčetić, J.; Andrić, M. Changes of atmospheric properties over Belgrade, observed using remote sensing and in situ methods during the partial solar eclipse of 20 March 2015. *J. Atmos. Sol.-Terr. Phys.* **2018**, *171*, 250–259. [CrossRef]
9. Amaechi, P.O.; Akala, A.O.; Oyedokun, J.O.; Simi, K.G.; Aghogho, O.; Oyeyemi, E.O. Multi-Instrument Investigation of the Impact of the Space Weather Events of 6–10 September 2017. *Space Weather* **2021**, *19*, e02806. [CrossRef]
10. Special Issue "Data in Astrophysics & Geophysics: Research and Applications". Available online: https://www.mdpi.com/journal/data/special_issues/Astro_Geophy?view=default&listby=date (accessed on 4 December 2023).

A&M DATA

IV Meeting on Astrophysical Spectroscopy:
A&M DATA - Atmosphere

**To Professor Zoran Mijić**

Belgrade, Serbia, April 2nd, 2022

Dear Professor Mijić,

On behalf of the Scientific and Organizing Committees, we have a pleasure to invite you to attend the *IV Meeting on Astrophysical Spectroscopy: A&M DATA – Atmosphere* and present an **Invited lecture**: "Review of atmospheric aerosol optical properties profiling and lidar station activities in Serbia".

The fourth Meeting on Astrophysical Spectroscopy will be held from May 30 to June 2, 2022 on Fruška Gora, Serbia. The details of the conference are available at official website: http://asspectro2022.ipb.ac.rs/

We look forward to seeing you at IV A&M Meeting.

Yours sincerely,

**Vladimir Srećković**
(Co-Chair of the Scientific Committee)

**Dimitrijević Milan**
(Co-Chair of the Scientific Committee)

Conference Organizer:
University of Belgrade, Institute of Physics Belgrade

Co-organizers:
Astronomical Observatory of Belgrade

A&M DATA

IV Meeting on Astrophysical Spectroscopy: A&M DATA - Atmosphere

# C E R T I F I C A T E

**With this certificate we declare and confirm that:**

**Dr Zoran Mijić**,

Presented an **Invited lecture** at the *IV Meeting on Astrophysical Spectroscopy: A&M DATA – Atmosphere, May 30 to June 2, 2022 on Fruška Gora, Serbia* on the topic:

Review of atmospheric aerosol optical properties profiling and lidar station activities in Serbia

**Co-Chairmen of the**
**Scientific Committee**:

**Vladimir Srećković**
(Co-Chair of the Scientific Committee)

**Dimitrijević Milan**
(Co-Chair of the Scientific Committee)

Conference Organizer:
University of Belgrade, Institute of Physics Belgrade

Co-organizers:
Astronomical Observatory of Belgrade

# IV Meeting on Astrophysical Spectroscopy - A&M DATA - Atmosphere

May 30 to June 2, 2022, Fruška Gora, Serbia

# BOOK OF ABSTRACTS AND CONTRIBUTED PAPERS

**Edited by Vladimir A. Srećković, Milan S. Dimitrijević,
Nikola Veselinović and Nikola Cvetanović**

A&M DATA

UNIVERSITY OF BELGRADE
INSTITUTE OF PHYSICS | BELGRADE
NATIONAL INSTITUTE OF
THE REPUBLIC OF SERBIA

Belgrade 2022

## Scientific Committee



## Local Organizing Committee



## Organizers:

Institute of Physics Belgrade, Serbia,
Astronomical Observatory Belgrade, Serbia and
Faculty of Sciences – University of Novi Sad, Serbia

Text arrangement by computer: Tanja Milovanov

ISBN 978-86-82441-57-1



Financially supported by the Ministry of Education, Science and Technological Development of Serbia

Production: Skripta Internacional, Mike Alasa 54, Beograd in 50 copies

# SCIENTIFIC RATIONALE

Spectroscopy is a powerful tool for the analysis of radiation from different plasmas in astronomy, laboratory, fusion research, atmospheric research and industry. Effective theoretical analysis, synthesis and modelling of stellar spectra as well as the spectra from other plasma sources, depends on atomic data and their sources. In particular, for the modelling of stellar atmospheres and opacity calculations a large amount of atomic data is needed, since we do not know *a priori* the chemical composition of a stellar atmosphere. Consequently, the development of databases with atomic data and astroinformatics is important for stellar spectroscopy.

The Conference is planned as an opportunity to consider above mentioned aspects of spectroscopic research on plenary sessions and then to work on the special mini-projects, which will result in common papers to be published in international astronomical journals after the Conference.

**Venue**

Fruška Gora (Ceptor, Andrevlje), Serbia

# CONTENTS

# Review of atmospheric aerosol optical properties profiling and lidar station activities in Serbia

**Zoran Mijić[1], Maja Kuzmanoski[1], Luka Ilić[1,2], Aleksander Kovačević[1] and Darko Vasiljević[1]**

*[1]Institute of Physics Belgrade, Pregrevica 118, 11080 Belgrade, Serbia*
*E-mail: zoran.mijic@ipb.ac.rs*
*[2]now at Barcelona Supercomputing Center, Plaça Eusebi Güell, 1-3, 08034 Barcelona, Spain*

## Abstract

An advanced laser remote sensing technique – LIDAR (Light Detection And Ranging) is the most appropriate tool for providing range-resolved atmospheric aerosol vertical distribution. LIDAR measurements of aerosol optical properties with high spatial and temporal resolution give detailed information on the occurrence and development of aerosol structures. In this study a brief introduction of a lidar system developed at the Institute of Physics Belgrade in the past and the new system currently operating, is presented together with several activities conducted within European lidar network. The capacity and the experience from measurement campaigns aiming to provide near real time data products and study the changes in the atmosphere is also discussed.

## Introduction

Clouds and atmospheric aerosols play an important role in the Earth's radiation budget, thus quantifying the role of aerosols in climate system is crucial for better weather forecasting and understanding climate change. The amount of scattered and absorbed radiation (both incoming solar and outgoing terrestrial) varies according to aerosol composition, size and shape distributions. The short lifetime and large variability in space and time further contribute to the identification of aerosol radiative forcing as one of the significant unknowns in our understanding of climate change (Stocker et al., 2013). The complexity of the aerosol interaction with the climate system makes it necessary to estimate its impact through the integrated use of ground-level and airborne *in-situ* measurements, ground-based remote sensing, and space-borne observations in combination with advanced numerical modelling. LIDAR (Light Detection And Ranging), an active remote sensing technique, has proved itself to be the optimal tool for profiling height-resolved atmospheric aerosol optical parameters. Various aerosol lidar techniques have been developed during the last several decades like backscatter lidar, Raman lidar, depolarization lidar, and high spectral resolution lidar. Each type of lidar can operate at one or multiple wavelengths. The LIDAR principle is based on laser emission of short-duration light pulses into the receiver field of view. The intensity of the light backscattered by atmospheric molecules and particles is measured versus time (through the telescope receiver, collimating optics, a bandpass filter for daylight suppression) by an appropriate detector. The signal profile is recorded by an analog-to-digital converter or by a photon-counting device and accumulated for a selected integration period, which may range from a few to thousands of individual laser shots – spanning time intervals from seconds to minutes. In order to establish a comprehensive and quantitative statistical data base of the horizontal and vertical distribution of aerosols at European scale the lidar network called EARLINET (the European Aerosol Research LIdar Network) was founded in 2000 (Pappalardo et al., 2014). The development of the quality assurance strategy, the optimization of instruments and data processing, and the dissemination of data have contributed to significant improvement of the network towards a more sustainable observing system. Currently, EARLINET contributes to the Aerosol, Clouds and Trace gases Research Infrastructure (ACTRIS), the pan-European research infrastructure producing high-quality data and information on short-lived atmospheric constituents. In this paper a brief review of atmospheric aerosol remote sensing capacity over the past period at the Institute of Physics Belgrade (IPB), Serbia, is presented together with short introduction on the methodology of elastic backscatter and Raman lidar systems. In addition, experience from several activities of IPB lidar station from dedicated measurement campaigns is described.

## Methodology

The lidar equation for return signal $P(\lambda)$ elastically backscattered by air molecules and aerosol particles is found to be

$$P(\lambda,r)=P_0(\lambda)C\frac{O(r)}{r^2}\beta(\lambda,r)\exp\left[-2\int_0^r\alpha(r')dr'\right] \quad (1)$$

where $P_0(\lambda)$ is the laser pulse power; $C$ is a system constant (taking into account the optics and electronics used); $O(r)$ denotes the unitless correction function that corrects the lack of coincidence of the laser beam and the receiver field of view for ranges below the complete overlap height; $r$ is the distance between the laser exit and the point of scattering in the atmosphere; $\alpha(\lambda,r)$ and $\beta(\lambda,r)$ denote the height (distance) and wavelength $(\lambda)$ dependent extinction and backscatter coefficients respectively. The extinction coefficient describes the ability of particles to scatter or absorb light at a given wavelength while the backscatter coefficient (scattering coefficient at $180^{\circ}$, normalized to the unit solid angle) refers only to scattering events. Backscattering and extinction are both caused by particles and molecules.

While the molecular scattering properties can be determined with sufficient accuracy from the available measurements of temperature and pressure profiles, the aerosol backscatter $\beta_a(\lambda,r)$ and extinction $\alpha_a(\lambda,r)$ coefficients remain to be retrieved. In lidar profiling, the most significant errors occur during signal inversion, when the optical parameters of the atmospheric aerosols are extracted from the lidar signals using a number of implicit premises and *a priori* assumptions. Two *a priori* assumptions are necessary to allow the retrieval of $\alpha_a(\lambda,r)$ and $\beta_a(\lambda,r)$ profiles from the elastic lidar measurement: an assumed value of the lidar ratio (aerosol extinction/backscatter value) and the reference range chosen such that the particle backscatter coefficient is negligible compared to the known molecular backscatter coefficient value. The main drawback of this method is the fact that the extinction profile is estimated from the determined backscatter coefficient profile.

The first elastic backscatter lidar system at the IPB was developed in 2008 as bi-axial lidar system with transmitter unit based on a water-cooled, pulsed Nd:YAG laser, emitting pulses of 100 mJ and 50 mJ output energy at 1064 and 532 nm respectively, with a 20 Hz repetition rate (Fig .1). The optical receiver was the Schmidt–Cassegrain telescope with a primary mirror of 304.8 mm diameter. Si PIN photodiode FD5N was used to detect elastic backscatter lidar signal at 532 nm. An interference filter with 3 nm bandwidth was used to select the lidar wavelengths and to reject the atmospheric background radiation during daytime operation. For analog detection, the signal was amplified according to the input range selected and digitized by an A/D converter NI5124.

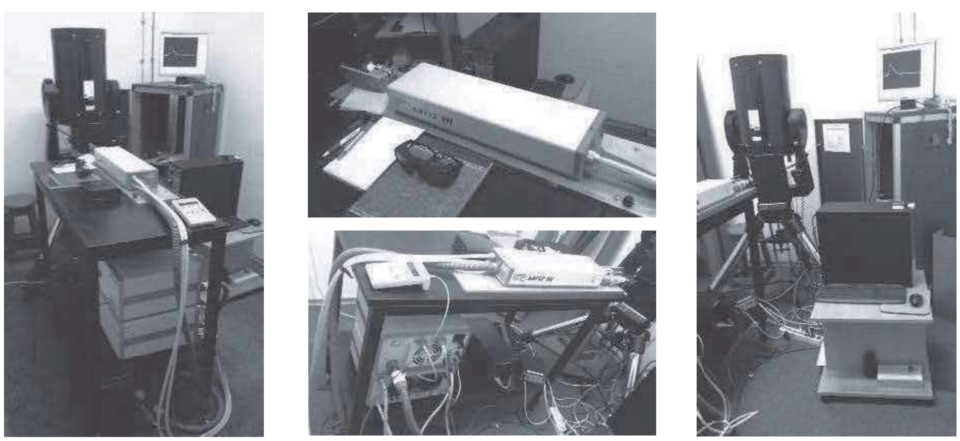

Fig. 1. Elastic backscatter lidar system developed at IPB.

The described system was the first lidar system of that kind used for aerosol profiling in Serbia. To overcome the limitation of elastic backscatter lidar technique the so-called Raman lidar technique can be used and the profile of particle extinction coefficient can directly be determined. Raman lidar measures lidar return signals elastically backscattered by air molecules and particles and inelastically (Raman) backscattered usually by nitrogen molecules. Whereas the elastic backscatter lidar is operational both at day and night, the Raman lidar is mainly used during nighttime, due to the strong daylight sky background. The determination of the particle extinction coefficient from molecular backscatter signals is rather straightforward since neither lidar ratio nor other critical assumptions are needed (Kovalev, 2015).

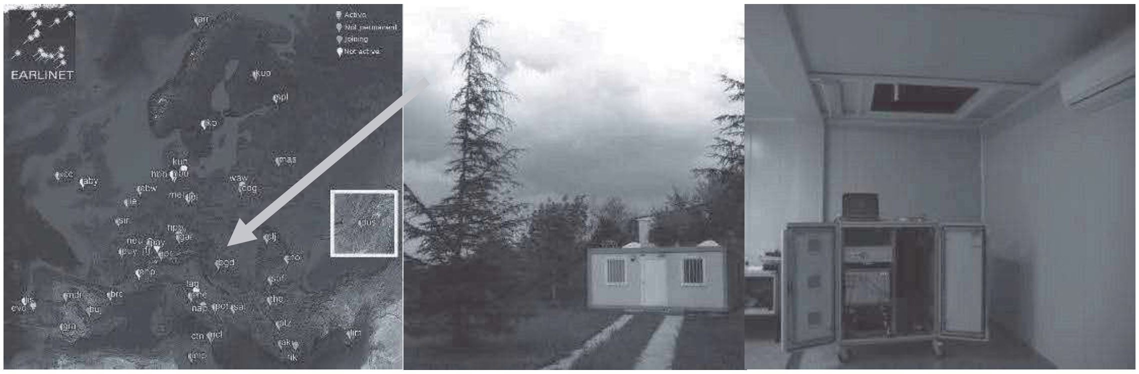


Fig. 2. IPB Raman EARLINET joining lidar station.

In 2014 Raman lidar operating at 355 nm and 387 nm ($N_2$) was set up at IPB, establishing Serbian EARLINET joining lidar station (Fig. 2). The basic characteristics of IPB Raman lidar are summarized in Table 1.

Table 1. IPB Raman lidar system components

| Emitter | | Receiver | Detection Unit |
|---|---|---|---|
| Pulse laser source: | Nd:YAG (Quantel CFR200) | Telescope type: Cassegrain, model Raymetrics DK250 | LICEL TR20-160 (12 bit at 20 MS/s), 250 MHz fast photon |
| Wavelength | 1064, 532, 355 nm | Telescope aperture: diameter: 250 mm | Detectors: Photomultiplier Tubes (Licel-Hamamatsu-R9880U-110) |
| Energy/pulse | 105/45/65 mJ | Field of view:0.5- 3 mrad (variable) | Detection mode: Analog and photon counting |
| Pulse duration and repetition | 5 ns<br>20 Hz | Fieldstop type: Circular - Iris Diaphragm, 3mm user selectable | Spatial resolution (raw): 7.5 m |
| Laser beam diameter: | 15 mm (expanded) | Elastic wavelength 355 nm | Full overlap: 250 m |
| Laser beam divergence: | 0.33 mrad | Raman wavelength: 387 nm ($N_2$) | Effective range: 0.05 – 16 km |

As a joining lidar station, systematic aerosol profiling has started in 2014 mostly for providing data for potential climatological studies as well as conducting dedicated measurements during Saharan dust intrusions or assessment of planetary boundary layer evolution (PBL) (Ilić et al., 2018). An example of such measurement performed on February 19, 2014 is presented in Fig 3. together with aerosol backscatter coefficient profile retrieved and dust load simulated by Dust REgional Atmospheric Model (DREAM) (Ničković et. al, 2011).

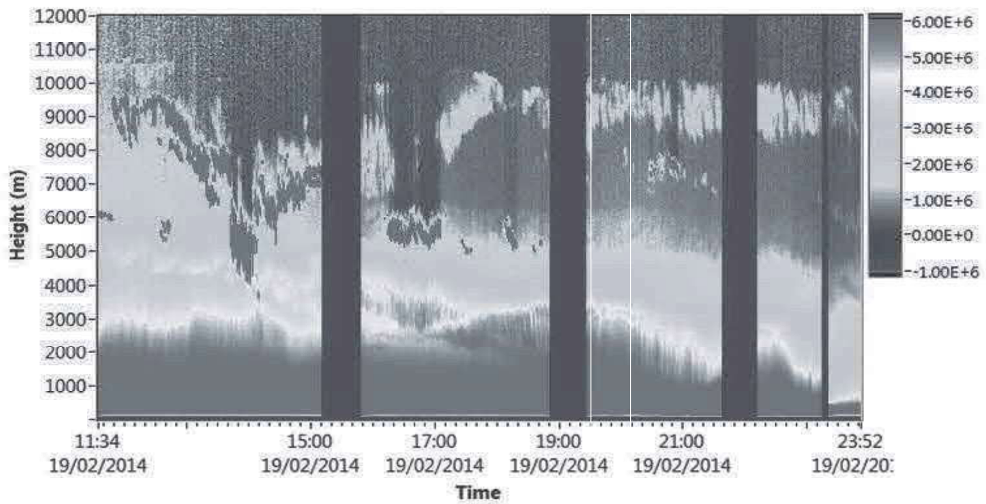


Emission wavelength: 355 nm Detection wavelength: 355 nm
Detection mode: an+pc, Temporal resolution: 60 s, Spatial resolution:

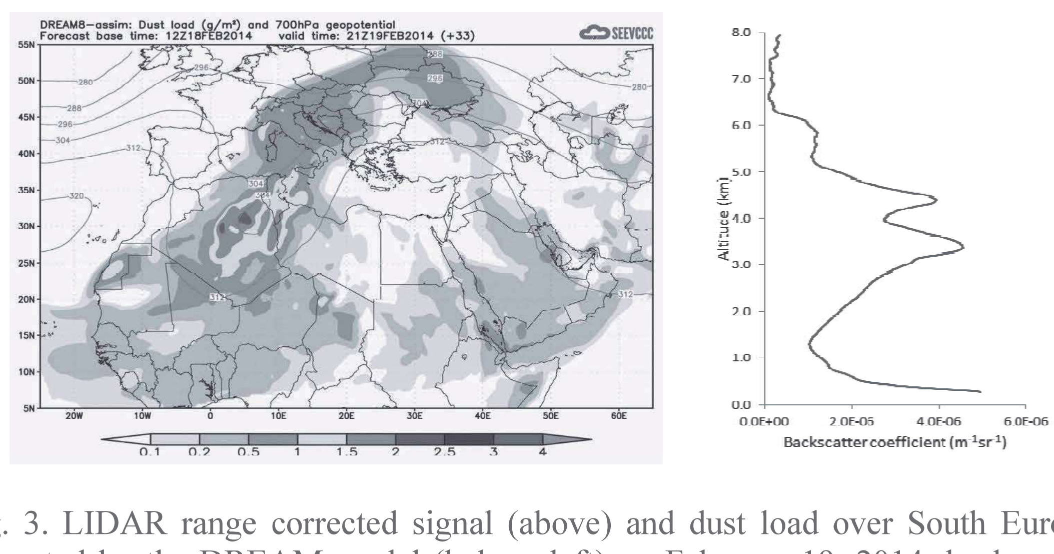


Fig. 3. LIDAR range corrected signal (above) and dust load over South Europe estimated by the DREAM model (below, left) on February 19, 2014; backscatter coefficient profile (below, right) retrieved for the selected time period (white rectangle).

## Activities of the IPB lidar station

In addition to regular aerosol profiling mostly performed at the very beginning after official joining the lidar network, several studies were conducted related to the application of gradient method for the identification of aerosol layer, as well as the evolution of PBL height (Ilić et al., 2018). The IPB lidar station also actively participated in several measurement campaigns organized through the EARLINET network.

## The EUNADICS-AV experiment for NRT alerts

Following the existing needs, the methodology providing a tailored aerosol products for aviation hazards based on high-resolution lidar data was developed with the aim to provide the EARLINET early warning system (EWS) for the fast alerting of airborne hazards (Papagiannopoulos et al., 2020). The application of the EWS and the timely delivery of the EARLINET data were tested in real time during the EUNADICS-AV exercise in March 2019. Each station submitted raw lidar data to the Single Calculus Chain (SCC) server every hour, which were automatically available on the EARLINET Quicklook Interface (https://quicklooks.earlinet.org/, last access: May 2022). The SCC is a tool created inside the EARLINET network for the automatic analysis of aerosol lidar observations (D'Amico et al., 2015). The primary goal of SCC is to offer a data processing chain that allows all EARLINET stations to retrieve aerosol products like backscatter and extinction profiles (measures of aerosol load) completely automatically. The raw lidar data were processed in less than 30 min after the measurement, enabling the timely delivery of the lidar data and the tailored product. When the raw data was submitted to the SCC server, it was instantly processed and made publicly available through the EARLINET portal in order to launch the alert distribution. The exercise revealed the network's strength, which, if activated immediately, can permit measurements in the event of natural threats for aviation.

## COVID-19 Campaign

A dedicated EARLINET measurement campaign was organized as part of the ACTRIS initiative to study the changes in the atmosphere during the COVID-19 lockdown period in May 2020, in order to monitor the atmosphere's structure during the lockdown and early relaxation period in Europe, and to identify possible changes due to decreased emissions by comparison to the aerosol climatology in Europe. The EARLINET near real time functioning was proven throughout the campaign, based on earlier experience from the EUNADICS-AV exercise. The IPB lidar station, along with 21 EARLINET stations, participated in the campaign by providing vertical aerosol profiles twice per day (minimum two hours measurements at noon, and minimum two hours after sunset). The measurements were submitted and analyzed in near-real time by SCC. The first analysis was based on the data processed by the SCC and directly published on the THREDDS server in NRT. The preliminary analysis made on aerosol lidar data shows that simple comparison of the observed backscatter values with the climatological values from 2000-2015 is not sufficient to extract a clear conclusion on how much the COVID-19 lock-down has impacted the aerosols in the atmosphere, but a certain effect in the lower troposphere can be seen.

## Conclusions

Lidar systems are optimal tools for providing range-resolved aerosol optical parameters and information on the atmospheric structure. The IPB lidar station is the only lidar station for aerosol profiling in Wester Balkans matching EARLINET quality control and quality assurance requirements. A brief description of the station capacity and activities in a few measurement campaigns are presented. Beyond the scientific goals of these campaigns, the actions organized by EARLINET/ACTRIS (NRT delivery of the data and fast analysis of the data products) proved that aerosol lidars are useful for providing information not only for climatological purposes, but also in emergency situations. Although the IPB lidar station is able to provide valuable data, automatization of the measurement process and the upgrade to the multiwavelength lidar system are required.

## Acknowledgments

The authors acknowledge funding provided by the Institute of Physics Belgrade, through the grant by the Ministry of Educations, Science, and Technological Development of the Republic of Serbia. The financial support for EARLINET in the ACTRIS Research Infrastructure Project by the European Union's Horizon 2020 research and innovation programme under grant agreement No. 654109 and previously under the grants No. 262254 in the 7th Framework Programme (FP7/2007-2013) and no 025991 in the 6th Framework Programme (FP6/2002-2006) is gratefully acknowledged.

## References

D'Amico, G., Amodeo, A., Baars, H., Binietoglou, I., Freudenthaler, V., Mattis, I., Wandinger, U., and Pappalardo, G., 2015, Atmos. Meas. Tech., 8, 4891-4916.

Freudenthaler, V., 2008, Proceedings of 24th International Laser Radar Conference, 23-27 June, Boulder, USA

Ilić, L., Kuzmanoski, M., Kolarž, P., Nina, A., Srećković, V., Mijić, Z., Bajčetić, J., Andrić, M., 2018, J.Atmos.Sol.-Terr. Phys.,171,250-259.

Kovalev, V. A., 2015, Solutions in lidar profiling of the atmosphere, John Wiley & Sons, Inc.

Ničković, S., Kallos, G., Papadopoulos, A., and Kakaliagou, O., 2001, J. Geophys. Res., 106, 18113- 18130.

Nicolae, D., Mona, L., Amodeo, A., D'Amico, G., Freudenthaler, V., Pietras, C., Baars, H. et.al. 2020, EARLINET/ACTRIS analysis of aerosol profilesduring the COVID-19 lock-down andrelaxation period -A preliminary study on aerosol properties in the low and high troposphere, Report, https://www.earlinet.org/index.php?id=covid-19-reports

Papagiannopoulos, N., D'Amico, G., Gialitaki, A., Ajtai, N., Alados-Arboledas, L., Amodeo, A., Amiridis, V., Baars, H., Balis, D., Binietoglou, I., Comerón, A., Dionisi, D., Falconieri, A., Fréville, P., Kampouri, A., Mattis, I., Mijić, Z., Molero, F., Papayannis, A., Pappalardo, G., Rodríguez-Gómez, A., Solomos, S., and Mona, L., 2020, Atmos. Chem. Phys., 20, 10775–10789.

Pappalardo, G., Amodeo, A., Apituley, A., Comeron, A., Freudenthaler, V., Linné, H., Ansmann, A., Bösenberg, J., D'Amico, G., Mattis, I., Mona, L., Wandinger, U., Amiridis, V., Alados-Arboledas, L., Nicolae, D., and Wiegner, M., 2014. Atmos. Meas. Tech., 7, 2389–2409.

Stocker,T. F., Qin D., Plattner,G.-K.Tignor, M., Allen,S. K., Boschung,J., A. Nauels, Xia,Y., Bex V., Midgley,P. M., 2013, IPCC: The Physical Science Basis, Contribution of Working Group I to the Fifth Assessment Report of the Intergovernmental Panel on Climate Change, Cambridge University Press, Cambridge, United Kingdom and New York, NY, USA.

# Certificate of Participation

## *Zoran Mijic, PhD*

Participated in the 1st International Conference on Physical Aspects of Environment (ICPAE2022, 31st March – 2nd April 2022, Zrenjanin, Serbia) as an invited lecturer with a paper titled

***Remote Sensing of Tropospheric Aerosols: Experience from Belgrade Raman Lidar Station***

Authored by
Zoran Mijic, Maja Kuzmanoski and Luka Ilic

Dean of the Technical Faculty "Mihajlo Pupin"
Dragica Radosav, PhD

Radosav Dragica

President of the Scientific Program Committee
Darko Radovancevic, PhD

Darko Radovančević

Zrenjanin, 2022

University of Novi Sad,
Technical Faculty
"Mihajlo Pupin",
Zrenjanin, Republic of Serbia

# International Conference on Physical Aspects of Environment ICPAE2022

Proceedings

**Zrenjanin, 31st March – 2nd April 2022**

University of Novi Sad,
Technical Faculty
"Mihajlo Pupin",
Zrenjanin, Republic of Serbia

# International Conference on Physical Aspects of Environment ICPAE2022

Proceedings

**Zrenjanin, 31st March – 2nd April 2022**

## Proceedings of the International Conference on Physical Aspects of Environment ICPAE2022

**Conference Organizer:**
Technical Faculty "Mihajlo Pupin", Zrenjanin, University of Novi Sad, Serbia

**Conference Co-Organizer:**
Faculty of Sciences and Mathematics, Nis, University of Nis, Serbia

**Publisher:**
Technical Faculty "Mihajlo Pupin", Zrenjanin, University of Novi Sad, Đure Đakovića bb, Zrenjanin, Serbia

**For Publisher:**
Dragica Radosav, Dean of Technical Faculty "Mihajlo Pupin", Zrenjanin, Serbia

**Editor:**
Darko Radovančević, Technical Faculty "Mihajlo Pupin", Zrenjanin, Serbia

**Co-Editor:**
Ljubiša Nešić, Faculty of Sciences and Mathematics, Nis, Serbia

**Technical Support:**
Milan Marković,Technical Faculty "Mihajlo Pupin", Zrenjanin, Serbia

CIP - Каталогизација у публикацији
Библиотеке Матице српске, Нови Сад

502(082)

**INTERNATIONAL Conference on Physical Aspects of Environment ICPAE2022 (1 ; 2022 ; Zrenjanin)**
Proceedings [Elektronski izvor] / First International Conference on Physical Aspects of Environment ICPAE2022, Zrenjanin, 31st March – 2nd April 2022 ; [editor Darko Radovančević]. - Zrenjanin : Technical Faculty "Mihajlo Pupin", 2022

Način pristupa (URL):
http://www.tfzr.uns.ac.rs/icpae/conference%20program/ICPAE2022.pdf. - Opis zasnovan na stanju na dan 21.6.2022. - Nasl. sa naslovnog ekrana. - Bibliografija uz svaki rad.

ISBN 978-86-7672-354-6

а) Животна средина -- Заштита -- Зборници

COBISS.SR-ID 69366025

**Scientific Program Committee:**

- Darko Radovančević, University of Novi Sad, Technical Faculty "Mihajlo Pupin", Zrenjanin, Serbia – President
- Ljubiša Nešić, University of Nis, Faculty of Sciences and Mathematics, Nis, Serbia - Vice President
- Saša Jovanović, University of Novi Sad, Technical Faculty "Mihajlo Pupin", Zrenjanin, Serbia
- Snežana Komatina, University of Novi Sad, Technical Faculty "Mihajlo Pupin", Zrenjanin, Serbia
- Bogdana Vujić, University of Novi Sad, Technical Faculty "Mihajlo Pupin", Zrenjanin, Serbia
- Višnja Mihajlović, University of Novi Sad, Technical Faculty "Mihajlo Pupin", Zrenjanin, Serbia
- Ljiljana Radovanović, University of Novi Sad, Technical Faculty "Mihajlo Pupin", Zrenjanin, Serbia
- Jelena Stojanov, University of Novi Sad, Technical Faculty "Mihajlo Pupin", Zrenjanin, Serbia
- Ljubiša Đorđević, University of Nis, Faculty of Sciences and Mathematics, Nis, Serbia
- Vesna Nikolić, University of Nis, Faculty of Occupational Safety, Nis, Serbia
- Tatjana Jovanović, University of Nis, Faculty of Medicine, Nis, Serbia
- Milan Pantić, University of Novi Sad, Faculty of Sciences, Novi Sad, Serbia
- Miodrag Krmar, University of Novi Sad, Faculty of Sciences, Novi Sad, Serbia
- Nataša Todorović, University of Novi Sad, Faculty of Sciences, Novi Sad, Serbia
- Jovana Nikolov, University of Novi Sad, Faculty of Sciences, Novi Sad, Serbia
- Nikola Jovančević, University of Novi Sad, Faculty of Sciences, Novi Sad, Serbia
- Dragan Markušev, Institute of Physics, Belgrade, Serbia
- Zoran Mijić, Institute of Physics, Belgrade, Serbia
- Robert Repnik, University of Maribor, Faculty of Natural Sciences and Mathematics, Maribor, Slovenia
- Vanja Radolić, Josip Juraj Strossmayer University of Osijek, Department of Physics, Osijek, Croatia
- Slavoljub Mijović, University of Montenegro, Faculty of Science and Mathematics, Podgorica, Montenegro

# INTRODUCTION

**The first International Conference on Physical Aspects of the Environment ICPAE2022**, took place from March 31 to April 2, 2022. It was organized by the Technical Faculty "Mihajlo Pupin" from Zrenjanin. The co-organizer was the Faculty of Sciences and Mathematics from Nis. Members of the scientific-program, advisory and organizational committee of the conference were prominent professors and researchers from the University of Novi Sad, University of Nis, Institute of Physics in Zemun, University of Maribor, Josip Juraj Strossmayer University of Osijek, University of Montenegro, Ss. Cyril and Methodius University from Skopje, University of Banja Luka and University of Sarajevo.

The conference was attended by a large number of renowned participants sharing the results of their research, ideas and achievements related to the burning issues in the field of geophysics, environmental modeling, air pollution, greenhouse effect, global warming, climate change, radiation and the environment, energy efficiency and sustainable development, environmental physics and education.

There were 32 papers for the presentation at the conference: 17 papers from abroad and 15 from Serbia.

Plenary presentations were given by:

- Slavoljub Mijović, University of Montenegro, Faculty of Science and Mathematics, Podgorica, Montenegro;
- Lambe Barandovski, Ss. Cyril and Methodius University, Faculty of Natural Sciences and Mathematics, Skopje, North Macedonia;
- Vanja Radolić, Josip Juraj Strossmayer University of Osijek, Department of Physics, Osijek, Croatia;
- Robert Repnik, University of Maribor, Faculty of Natural Sciences and Mathematics, Maribor, Slovenia;
- Abdulah Akšamović, University of Sarajevo, Faculty of Electrical engineering, Sarajevo, Bosnia and Herzegovina;
- Zoran Mijić, Institute of Physics, Belgrade, Serbia;
- Diana Mance, University of Rijeka, Department of Physics, Rijeka, Croatia;
- Tatjana Ivošević, University of Rijeka, Faculty of Maritime Studies, Rijeka, Croatia.

Zrenjanin, June 2022

President of the Scientific Program Committee
Darko Radovančević

# CONTENTS

## INVITED LECTURES



## LECTURES

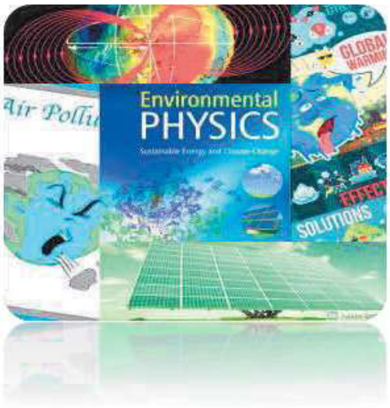


**First International Conference on Physical Aspects of Environment**

Technical Faculty "Mihajlo Pupin", University of Novi Sad, Zrenjanin, Serbia

Faculty of Sciences and Mathematics, University of Nis, Nis, Serbia

**31st March – 2nd April 2022**

---

# Invited Lectures

Conference Proceedings
ICPAE 2022, 31st March – 2nd April, Zrenjanin, Serbia
Technical Faculty "Mihajlo Pupin", Zrenjanin & Faculty of Sciences and Mathematics, Nis

# Remote Sensing of Tropospheric Aerosols: Experience from Belgrade Raman Lidar Station

Zoran Mijić[1*], Maja Kuzmanoski[1], Luka Ilić[1,2]

[1]*Institute of Physics Belgrade, Pregrevica 118, Belgrade, Serbia*
[2]*Now at Barcelona Supercomputing Center, Barcelona, Spain*
*zoran.mijic@ipb.ac.rs*

**Abstract.** Atmospheric aerosols are considered as one of the major uncertainties in climate forcing and atmospheric processes due to their short lifetime and the large variability. Lidar (LIght Detection And Ranging), an active remote sensing technique, represents the optimal tool to provide range-resolved aerosol optical parameters and information on the atmospheric structure and its dynamics. In order to create a quantitative, comprehensive, and statistically significant database for the horizontal, vertical, and temporal distribution of aerosols on a continental scale the European Aerosol Research Lidar Network (EARLINET) has been established. In this study the capacity of Belgrade Raman lidar system and the activities of lidar station within EARLINET will be presented together with the experience from measurement campaigns aiming to provide near real time (NRT) data products and study the changes in the atmosphere during the COVID-19 lockdown period.

**Keywords:** atmospheric aerosol, optical properties, remote sensing, lidar, air quality

## INTRODUCTION

Aerosols in the atmosphere play an important role in numerous atmospheric processes. Despite being a minor component of the atmosphere, they have a significant impact on the Earth's radiation budget, the water cycle and atmospheric chemistry, playing a crucial role in climate change and air quality. Due to their short lifetime and the large variability in space and time atmospheric aerosols are considered one of the major uncertainties in atmospheric processes [1]. As a result, vertically resolved studies of particle physical and optical parameters such as particle surface area concentration, volume and mass concentrations, mean particle size, and volume extinction coefficient are of particular interest. Long-term height-resolved measurements of atmospheric aerosol optical parameters can be carried out using lidar (Light Detection And Ranging), an active remote sensing technique. The observational lidar stations network called EARLINET (the European Aerosol Research Lidar Network) [2] was founded in 2000 to provide the long-term measurement series needed to build a climatology of aerosol optical properties at the continental scale. The main objectives of EARLINET are the establishment of a comprehensive and quantitative statistical data base of the horizontal and vertical distribution of aerosols at the European scale using a network of advanced laser remote sensing stations, and the use of these data for studies related to the impact of aerosols on a variety of environmental problems. In this paper the characteristics of Raman lidar system at the Institute of Physics Belgrade (IPB) [3], an EARLINET joining lidar station, is presented together with several quality tests in order to demonstrate the performance of a lidar system. In addition, preliminary findings and experience from a dedicated EARLINET measurement campaign organized in May 2020 in order to monitor the atmosphere's structure during the COVID-19 lockdown period in Europe is discussed.

## Methodolgy

### *Raman lidar*

Raman lidar system at the IPB (44.860 N, 20.390 E) is bi-axial lidar system with combined elastic and Raman detection designed to perform continuous measurements of aerosols in the planetary boundary layer and the lower free troposphere (Figure 1). Transmitter unit is based on the third harmonic frequency of a water cooled, pulsed Nd:YAG laser, emitting pulses of 65 mJ output energy at 355 nm with a 20 Hz repetition rate. The optical receiving unit consists of two sub-units, a receiving telescope and wavelength separation unit. The optical receiver is a Cassegrain reflecting telescope with a primary mirror of 250 mm diameter and a focal length of 1250 mm. Photomultiplier tubes are used to detect elastic backscatter lidar signal at 355 nm and Raman signal at 387 nm (nitrogen vibrational scattering). The detectors are operating both in the analog and photon-counting mode and the spatial raw resolution of the detected signals is 7.5 m. Averaging time of the lidar profiles is of the order of 1 min corresponding to 1200 laser shots. The Licel transient recorder comprises a fast transient digitizer with on board signal averaging, a discriminator for single photon detection and a multichannel scaler combined with preamplifiers for both systems. For analog detection, the signal is amplified according to the input range selected and digitized by a 12-Bit-20 MHz A/D converter. At the same time the signal part in the high frequency domain is amplified and a 250 MHz fast discriminator detects single photon events above the selected threshold voltage.

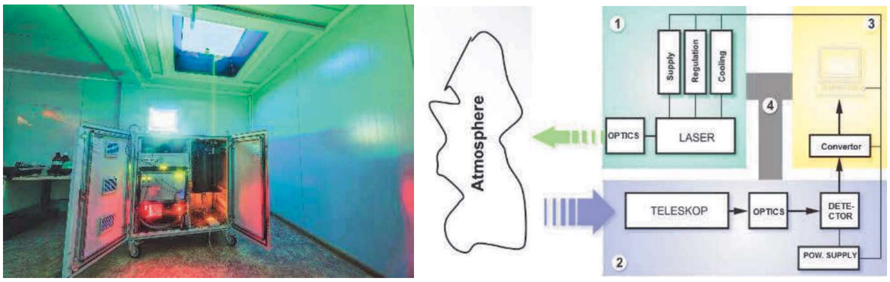


Figure 1. Raman lidar at IPB (left) and components of a lidar system (right)

### *COVID-19 Campaign*

The lockdown period provided a unique opportunity to examine the effects of reduced anthropogenic activities on changes in the atmospheric environment. As a part of the ACTRIS initiative for studying the changes in the atmosphere during the COVID-19 lockdown period in May 2020 a dedicated EARLINET measurement campaign was organized in order to monitor the atmosphere's structure and to identify possible changes due to decreased emissions by comparison to the aerosol climatology in Europe. During the campaign the near real time (NRT) operation of the EARLINET was demonstrated. The Belgrade lidar station participated in the campaign together with 21 EARLINET stations providing vertical aerosol profiles twice per day (minimum two hours measurements at noon, and minimum two hours after sunset). The measurements were submitted and processed by the Single Calculus Chain (SCC) in the near-real time. The SCC is a tool for the automatic analysis of aerosol lidar measurements developed within EARLINET network [4,5]. The main aim of SCC is to provide a data processing chain that allows all EARLINET stations to retrieve, in a fully automatic way, the aerosol backscatter and extinction profiles (measures of the aerosol load) together with other aerosol products. The first analysis was based on the data processed by the SCC and directly published on the THREDDS server in NRT.

## RESULTS AND DISCUSSION

A quality assurance scheme for both hardware and retrieval methods has been built within the lidar network. System alignment is one of the fundamental setup tests because the incomplete overlap between the laser beam and the receiver field of view has a substantial impact on lidar observations of particle optical characteristics. Thus, quality assurance of lidar measurements needs testing the lidar system's alignment following Freudenthaler's procedure [6]. It consists of a series of measurements with a partly covered telescope (four sectors labeled N, E, W, and S), such that each measurement represents a collection of backscattered light at a specific sector of the telescope. The variation of each sector signal from the average of all signals of less than 10% is required.

The Rayleigh fit method, which is based on normalizing of the lidar signal to the calculated Rayleigh backscatter coefficient in a range where we assume clean environment and where the calculated signal matches the lidar signal sufficiently well, can be used to ensure lidar alignment in the far range. As seen in Figure 2. IPB lidar system was accurately aligned up to 14 km. Once properly aligned, the device could be utilized for systematic aerosol measurements.

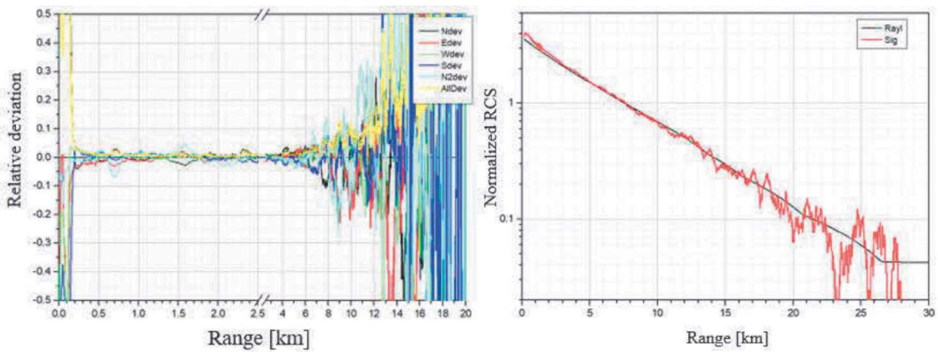


Figure 2. Deviations of signals collected with four telescope sectors compared to the mean signal (left) and Rayleigh fit for 355 nm elastic channel, Raman lidar at IPB, May 8$^{th}$, 2020

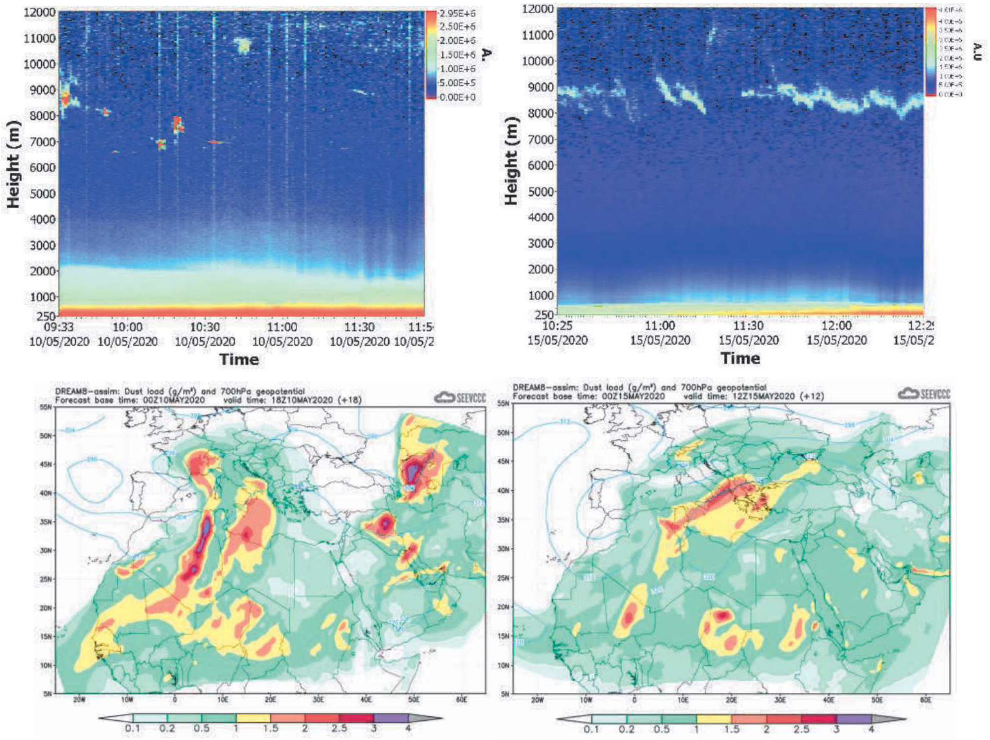


Figure 3.LIDAR range corrected signal (above) and dust load over South Europe estimated by the DREAM model (below) on 10th and 15th May, 2020

The preliminary analysis made on aerosol lidar data shows that by simply comparing the observed backscatter values with the climatological values from 2000-2015 was not sufficient to extract a clear conclusion on how much the COVID-19 lock-down has impacted the aerosols over Europe, but a certain effect for low troposphere was observed [7]. Generally, during the week of 15 – 21 May 2020, the aerosol backscatter coefficient values in both upper and lower troposphere were very close to the climatological values. On 15th of May, a certain tendency of higher than climatological values is observed because of the dust intrusion over the Southern Europe. Aerosol backscatter was significantly higher than in North and Central Europe, both in the low and high troposphere. Clear skies and high temperatures were observed in southern Europe accompanied with Saharan dust in the Balkans. In Figure 3 time evolution of lidar range-corrected signal at IPB, Belgrade on May 10th and 15th is shown indicating the presence of Saharan dust in lower troposphere that was also confirmed by the forecast of Dust Regional Atmospheric Model (DREAM) [8].

## CONCLUSION

Basic characteristics of Raman lidar system at IPB together with the results of few quality checks are presented showing the capacity for detection and monitoring aerosol layers' intrusion in Serbia. The action organized by EARLINET/ACTRIS (NRT delivery of the data and fast analysis of the data products) proved that aerosol lidars are useful for providing information not only for climatological purposes, but also in emergency situations. A more quantitative analysis based on re-analyzing additional data products is expected to be availabe soon in order to consolidate the conclusions on how much the COVID-19 lock-down has impacted the aerosols in the atmosphere.

## ACKNOWLEDGEMENTS

The authors acknowledge funding provided by the Institute of Physics Belgrade, through the grant by the Ministry of Educations, Science, and Technological Development of the Republic of Serbia. The financial support for EARLINET in the ACTRIS Research Infrastructure Project by the European Union's Horizon 2020 research and innovation programme under grant agreement no 654109 and previously under the grants no. 262254 in the 7th Framework Programme (FP7/2007-2013) and no 025991 in the 6th Framework Programme (FP6/2002-2006) is gratefully acknowledged.

## REFERENCES

1. T. F. Stocker, D. Qin, G.-K. Plattner, M. Tignor, S. K. Allen, J. Boschung, A. Nauels, Y. Xia, V. Bex, P. M. Midgley, 2013, IPCC: The Physical Science Basis, Contribution of Working Group I to the Fifth Assessment Report of the Intergovernmental Panel on Climate Change, Cambridge University Press, Cambridge, United Kingdom and New York, NY, USA.
2. G. Pappalardo, A. Amodeo, A. Apituley, A. Comeron, V. Freudenthaler, H. Linné, A.Ansmann, J. Bösenberg, G. D'Amico, I.Mattis, L. Mona, U. Wandinger, V Amiridis, L. Alados Arboledas, D. Nicolae, M. Wiegner, 2014, EARLINET: towards an advanced sustainable European aerosol lidar network, *Atmos. Meas. Tech.* **7**, 2389–2409
3. L. Ilić, M. Kuzmanoski, P. Kolarž, A. Nina, V. Srećković, Z. Mijić, J. Bajčetić, M. Andrić, 2018, Changes of atmospheric properties over Belgrade, observed using remote sensing and in situ methods during the partial solar eclipse of 20 March 2015,*J. Atmos. Sol. Terr. Phys.***171**, 250-259
4. G.D'Amico, A. Amodeo, H. Baars, I.Binietoglou, V.Freudenthaler, I.Mattis, U. Wandinger, G.Pappalardo, 2015, EARLINET Single Calculus Chain – overview on methodology and strategy, *Atmos. Meas. Tech.* 8, 4891-4916.
5. G.D'Amico, A.Amodeo, I.Mattis, V.Freudenthaler, G.Pappalardo, 2016, EARLINET Single Calculus Chaintechnical– Part 1: Pre-processing of raw lidar data, *Atmos. Meas. Tech.* 9, 491-507.
6. V.Freudenthaler, Proceedings of 24th International Laser Radar Conference, 23-27 June, Boulder, USA, 2008
7. D. Nicolae, L. Mona, A. Amodeo, G. D'Amico, V. Freudenthaler, C. Pietras, H. Baars *et.al.* 2020, EARLINET/ACTRIS analysis of aerosol profilesduring the COVID-19 lock-down andrelaxation period -A preliminary study on aerosol properties in the low and high troposphere, Report, https://www.earlinet.org/index.php?id=covid-19-reports
8. S.Nickovic, A.Papadopoulos, O. Kakaliagou, G.Kallos, 2001, Model for prediciton of desert dust cycle in theatmosphere. J. Geophys. Res., **106**, 18113-18129

University of Belgrade
Technical Faculty in Bor and
Mining and Metallurgy Institute Bor

# 49th International October Conference on Mining and Metallurgy

# PROCEEDINGS

**Editors:**
**Nada Štrbac**
**Ivana Marković**
**Ljubiša Balanović**

IOC 2017
International October Conference

**Bor Lake, Serbia**
**October 18-21, 2017**

**PROCEEDINGS,**
**49th INTERNATIONAL OCTOBER CONFERNCE**
**on Mining and Metallurgy**

**Editors:**
**Prof. dr Nada Štrbac**
**Doc. dr Ivana Marković**
**Doc. dr Ljubiša Balanović**
*University of Belgrade, Technical Faculty in Bor*

**Technical Editor:**
**M. Sc. Uroš Stamenković**
*University of Belgrade, Technical Faculty in Bor*

**Publisher:** University of Belgrade, Technical Faculty in Bor
**For the publisher:** Dean Prof. dr Nada Štrbac
**Circulation:** 200 copies

**Printed by "Happy trend DOO", Zaječar, 2017**

ISBN 978-86-6305-066-2

CIP - Каталогизација у публикацији - Народна библиотека Србије, Београд

622(082)
669(082)

**INTERNATIONAL October Conference on Mining and Metallurgy** (49 ; 2017 ; Bor Lake)
Proceedings / 49th International October Conference on Mining and Metallurgy - IOC 2017, Bor Lake, Serbia, October 18-21, 2017; [organized by] University of Belgrade, Technical Faculty Bor and Mining and Metallurgy Institute Bor; editors Nada Štrbac, Ivana Marković, Ljubiša Balanović. - Bor : University of Belgrade, Technical Faculty, 2017 (Zaječar : Happy trend). - XXIII, 664 str. : ilustr. ; 25 cm

Tiraž 200. - Bibliografija uz svaki rad. - Registar.

ISBN 978-86-6305-066-2

a) Рударство - Зборници b) Металургија - Зборници

COBISS.SR-ID 246349324

Bor Lake, Serbia, October 18-21, 2017

## SCIENTIFIC COMMITTEE

Prof. dr Nada Štrbac (Serbia) - president
Prof. dr Radoje Pantović (Serbia) - vice-president
Prof. dr Grozdanka Bogdanović (Serbia)- vice-president
Prof. dr Dragoslav Gusković (Serbia) - vice-president
Prof. dr Aleksandar Dimitrov (Macedonia)
Dr Ana Kostov (Serbia)
Dr Andrei Rotaru (Romania)
Prof. dr Anđelka Mihajlov (Serbia)
Prof. dr Batrić Pešić (USA)
Prof. dr Boštjan Markoli (Slovenia)
Prof. dr Boyan Boyanov (Bulgaria)
Prof. dr Branka Jordović (Serbia)
Prof. dr Carl Heinz Spitzer (Germany)
Prof. dr Costas Matis (Greece)
Prof. dr Dejan Tanikić (Serbia)
Prof. dr Desimir Marković (Serbia)
Prof. dr Dimitris Panias (Greece)
Prof. dr Dimitriu Sorin (Romania)
Prof. dr Dragan Manasijević (Serbia)
Prof. dr Duško Minić (Serbia)
Prof. dr Endre Romhanji (Serbia)
Prof. dr Fathi Habashi (Canada)
Prof. dr Guven Onal (Turkey)
Prof. dr György Kaptay (Hungary)
Prof. dr Heikki Jalkanen (Finland)
Prof. dr Iwao Katayama (Japan)
Prof. dr Jakob Lamut (Slovenia)
Prof. dr Jelena Penavin Škundrić (B&H)
Prof. dr Jožef Medved (Slovenia)
Prof. dr Karlo Raić (Serbia)
Prof. dr Kemal Delijić (Montenegro)
Prof. dr Krzystof Fitzner (Poland)
Prof. dr Luis Filipe Malheiros (Portugal)
Dr Magnus Ericsson (Sweden)
Prof. dr Milan Antonijević (Serbia)
Prof. dr Milan Trumić (Serbia)
Prof. dr Mile Dimitrijević ( Serbia)
Prof. dr Mirjana Rajčić Vujasinović (Serbia)
Prof. dr Mirko Gojić (Croatia)
Dr Mile Bugarin (Serbia)
Dr Milenko Ljubojev (Serbia)
Dr Mirjam Jan-Blažić (Slovenia)
Dr Miroslav Sokić (Serbia)
Prof. dr Mirsada Oruč (B&H)
Dr Nadežda Talijan (Serbia)
Prof. dr Nenad Radović (Serbia)
Prof. dr Nenad Vušović (Serbia)
Prof. dr Nobuyuki Masuda (Japan)
Prof. dr Onuralp Yucel (Turkey)
Prof. dr Petr M. Solozhenkin (Russia)
Prof. dr Rodoljub Stanojlović (Serbia)
Prof. dr Sanda Krausz (Romania)
Prof. dr Seshadri Seetharaman (Sweden)
Dr Slavomir Hredzak (Slovakia)
Prof. dr Snežana Šerbula (Serbia)
Prof. dr Stoyan Groudev (Bulgaria)
Prof. dr Sulejman Muhamedagić (B&H)
Prof. dr Svetlana Ivanov (Serbia)
Dr Srećko Stopić (Germany)
Prof. dr Tamara Holjevac Grgurić (Croatia)
Prof. dr Tatjana Volkov-Husović (Serbia)
Prof. dr Tomaš Havlik (Slovakia)
Prof. dr Velizar Stanković (Serbia)
Prof. dr Velimir Radmilović (USA)
Prof. dr Vitomir Milić (Serbia)
Dr Vladan Ćosović (Serbia)
Prof. dr Vladimir Krstić (Canada)
Prof. dr Vladislav Kecojević (USA)
Prof. dr Vlastimir Trujić (Serbia)
Prof. dr Yong Du (China)
Prof. dr Zoran Marković (Serbia)
Prof. dr Žarko Radović (Montenegro)
Prof. dr Željko Kamberović (Serbia)
Prof. dr Živan Živković (Serbia)
Dr Walter Valery (Australia)
Dr Zvonko Gulišija (Serbia)

## ORGANIZING COMMITTEE

Doc. dr Ivana Marković - president
Doc. dr Ljubiša Balanović - vice-president
Doc. dr Saša Stojadinović - vice-president
Prof. dr Svetlana Ivanov
Prof. dr Dragan Manasijević
Prof. dr Snežana Urošević
Dr Ana Kostov (IRM Bor)
Doc. dr Vesna Grekulović
Doc. dr Aleksandra Mitovski
Doc. dr Dejan Petrović
Doc. dr Milan Gorgievski
Doc. dr Ana Simonović
Doc.dr Tanja Kalinović
Doc.dr Marija Petrović Mihajlović
M.Sc. Uroš Stamenković
M.Sc. Oliver Marković
Slavica Stevanović, prof. engl.
Sandra Vasković, prof. engl.
Predrag Stolić, dipl. ing.
Dr Ana Radojević
M.Sc. Jelena Milosavljević

# RAMAN LIDAR FOR ATMOSPHERIC AEROSOL PROFILING IN SERBIA

**Zoran Mijić, Luka Ilić, Maja Kuzmanoski**

Institute of Physics Belgrade, University of Belgrade, Pregrevica 118, 11080 Belgrade, Serbia

**Abstract**
*Due to the large variability in space and time atmospheric aerosols are considered one of the major uncertainties in climate forcing and atmospheric processes affecting human health and environment. An advanced laser remote sensing technique – lidar is the most appropriate tool for providing range-resolved aerosol vertical distribution. Lidar measurements of aerosol optical properties with high spatial and temporal resolution give detailed information on the occurrence and development of aerosol structures. The characteristics of Raman lidar system at the Institute of Physics Belgrade and its potential for investigation of tropospheric aerosols will be discussed. Lidar case study measurements together with methodology for aerosol layer identification is presented.*

***Keywords:*** *remote sensing, Raman lidar, aerosol vertical distribution*

## 1. INTRODUCTION

Atmospheric aerosols influence the energy balance of the Earth, the water cycle and atmospheric chemistry, playing a crucial role in climate change and air quality. Due to their short lifetime and the large variability in space and time, atmospheric aerosols are considered one of the major uncertainties in climate forcing and atmospheric processes [1]. For radiative studies, it is necessary to measure aerosol optical properties, size, morphology and composition as a function of time and space, with a high resolution in both domains to account for the large variability. Lidar (Light Detection And Ranging), an active remote sensing technique, represents the optimal tool to provide range-resolved aerosol optical parameters. The first observational lidar stations network called EARLINET (the European Aerosol Research Lidar Network) [2] was founded in 2000 to provide the long-term measurement series needed to build a climatology of aerosol optical properties at the continental scale. The main objectives of EARLINET are the establishment of a comprehensive and quantitative statistical data base of the horizontal and vertical distribution of aerosols on the European scale using a network of advanced laser remote sensing stations, and the use of these data for studies related to the impact of aerosols on a variety of environmental problems. The developments for the quality assurance strategy, the optimization of instruments and data processing, and the dissemination of data have contributed to a significant improvement of the network towards a more sustainable observing system. Several lidar techniques are suitable for aerosol studies and in the last ten years rapid progress in laser technology, measurement techniques, and data acquisition systems has contributed to a much wider use of these techniques for aerosol remote monitoring. In this paper the characteristics of Raman lidar system at the Institute of Physics Belgrade (IPB), the EARLINET joining lidar station, is presented together with several quality tests in order to assess the performance of a lidar system. Case study measurement together with gradient method used to determine heights of both planetary boundary layer (PBL) and elevated aerosol layers is discussed.

## 2. EXPERIMENTAL

Atmospheric probing by lidar is able to obtain time dependent three dimensional pictures of aerosol distributions. Typical lidar system can be divided into the three main components, transmitter, receiving and data acquisition unit (Figure 1-left panel). Raman lidar system at the IPB (44.860 N, 20.390 E) is bi-axial lidar system with combined elastic and Raman detection designed to perform continuous measurements of aerosols in the planetary boundary layer and the lower free troposphere (Figure 1-right panel). Transmitter unit is based on the third harmonic frequency of a water cooled, pulsed Nd:YAG laser, emitting pulses of 65 mJ output energy at 355 nm with a 20 Hz repetition rate. In order to improve the maximum range and the precision of the system the beam expander is used to reduce the laser beam divergence expanding the beam's diameter by 3 times. The optical receiving unit consists of two sub-units, a receiving telescope and wavelength separation unit. The optical receiver is a Cassegrain reflecting telescope with a primary mirror of 250 mm diameter and a focal length of 1250 mm. Photomultiplier tubes are used to detect elastic backscatter lidar signal at 355 nm and Raman signal at 387 nm (Nitrogen vibrational scattering). The detectors are operated both in the analog and photon-counting mode and the spatial raw resolution of the detected signals is 7.5 m. Averaging time of the lidar profiles is of the order of 1 min corresponding to 1200 laser shots. The Licel transient recorder is comprised of a fast transient digitizer with on board signal averaging, a discriminator for single photon detection and a multichannel scaler combined with preamplifiers for both systems. For analog detection, the signal is amplified according to the input range selected and digitized by a 12-Bit-20 MHz A/D converter. At the same time the signal part in the high frequency domain is amplified and a 250 MHz fast discriminator detects single photon events above the selected threshold voltage.

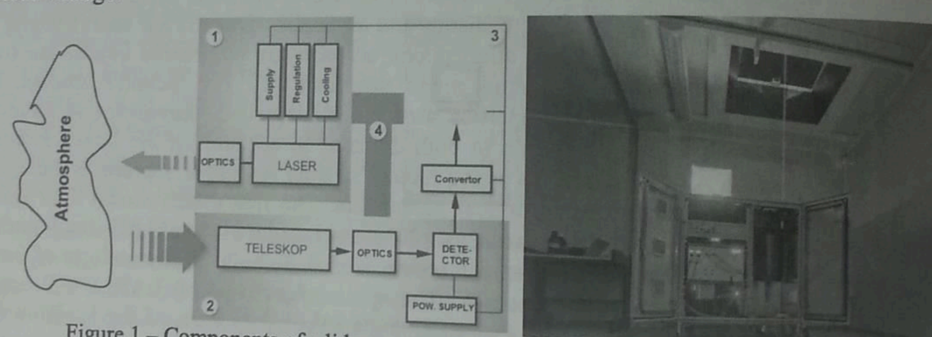


Figure 1 – Components of a lidar system (left) and Raman lidar at IPB (right)

Besides vertical profiles of aerosols backscatter and extinction coefficients lidar measurements can be used to estimate PBL height and aerosol elevated layers using different approaches [3]. In this study, the gradient method was used to determine the position of the strongest gradient of the aerosol vertical distribution, associated with the PBL height [4]. The height of a strong negative peak which can be identified as the absolute minimum of the range corrected signal's (RCS) derivative, determines the PBL top height. Other local minima in the signal derivative, with absolute values above a specified threshold and with transition intervals including a minimum of five points, are associated with elevated aerosol layer top heights in the free troposphere [4]. Differences between PBL and free troposphere can be also observed using vertical profiles of thermodynamic quantities and wind from radiosounding measurements. The bulk Richardson number is used for PBL height estimation from radiosounding measurements [5] at a weather station (Belgrade Košutnjak, WMO number 13275), 10 km away from the lidar measurement site.

## 3. RESULTS AND DISCUSSION

Within the lidar network, quality assurance program has been developed for both hardware and retrieval algorithms. One of the basic setup tests is system alignment since the incomplete overlap between the laser beam and the receiver field of view affects significantly lidar observations of particle optical properties.

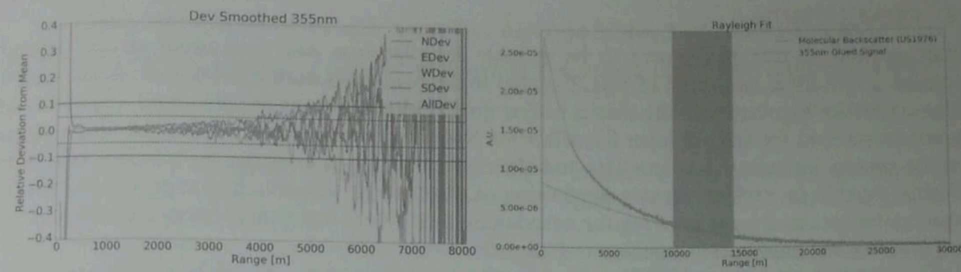


Figure 2 – Deviations of signals collected with four telescope sectors compared to the mean signal (left) and Rayleigh fit and fitting interval for 355 nm elastic channel, Raman lidar at IPB

Thus, quality assurance of the lidar measurement requires to test the alignment of the lidar system i.e. to determine overlap function. Procedure developed by Freudenthaler [6] involves a set of measurements with partially covered telescope (four sectors named N, E, W and S) so that each measurement is in fact collection of the backscattered light at a certain sector of the telescope. The deviation of each sector signal compared to the average of all signals below 10% is acceptable and from Figure 2 it is clear that the system is well aligned in the near field starting from 400 m. To assure lidar alignment in the far range the Rayleigh fit procedure can be used which is a normalization of the lidar signal to the calculated Rayleigh backscatter coefficient in a range where we assume clean conditions and where the calculated signal fits the lidar signal sufficiently good. From Figure 2–right panel it can be seen that the lidar system is well aligned up to the 12 km. Once the system is properly aligned it can be used for systematic aerosol measurements. In Figure 3 time series of RCS measured on July 6 2014 is presented.

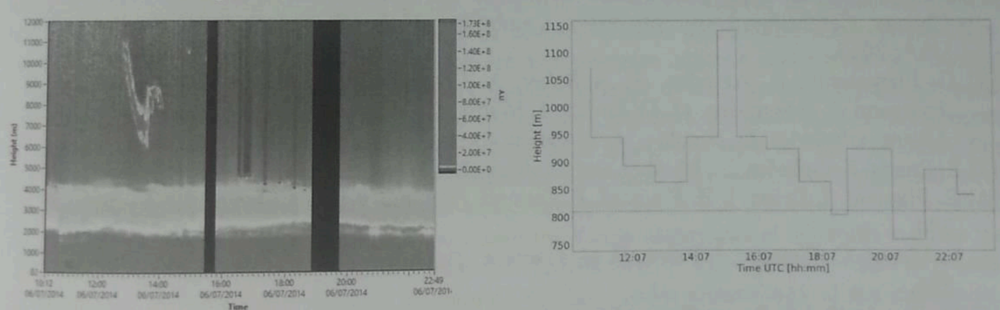


Figure 3 – Colormaps represent the lidar RCS at 355 nm on July 6 2014 (left). Hourly averaged PBL height (right). Horizontal red line represents PBL height retrieved from radiosounding at 00 UTC (dashed line) on July 7 2014

The gradient method was used to analyze the evolution of the PBL height during its diurnal cycle, and estimate elevated aerosol layer heights. Hourly averaged values of PBL show decrease of the PBL height from 1070 m to 860 m after the local noon (10 UTC). Significant increase in PBL height, reaching above 1100 m around 15 UTC can be attributed to strong convective motions which could have influenced formation of clouds between 16 UTC and 18 UTC, visible in the RCS plot. Gradient method shows decrease of the PBL heights until the end of the measurement period to about 840 m. This value, is similar to the one estimated from 00 UTC radiosounding – 810 m. Two elevated aerosol layers were identified, one with its top reaching height of 2 – 2.2 km in the morning and reducing its height to below 1800 m in the afternoon. Another layer with top height ranging from 3.1 to 3.5 km was present during the whole measurement period.

## 4. CONCLUSION

Raman lidar at IPB has shown to be suitable for detection and monitoring aerosol layers' intrusion in Serbia, evolution of PBL but also to describe their optical properties. Basic system characteristics together with the results of few quality checks results are presented. Capability of gradient method for aerosol layer identification has been demonstrated. Additional optimization of the system including data handling and algorithm tests are in progress. As a unique system in Serbia capable to perform remote monitoring of atmospheric aerosols it is expected to perform systematic measurements on a regular schedule in near future and contribute to the collection of aerosol vertical distribution database in Europe.

## ACKNOWLEDGEMENTS

*This paper was realized as a part of the project III43007 financed by the Ministry of Education and Science of the Republic of Serbia within the framework of integrated and interdisciplinary research for the period 2011-2017. The publication was supported by the project GEO-CRADLE (Coordinating and integRating state-of-the-art Earth Observation Activities in the regions of North Africa, Middle East, and Balkans and Developing Links with GEO related initiatives towards GEOSS), Grant Agreement No. 690133, funded under European Union Horizon 2020 Programme - Topic: SC5-18b-2015, Integrating North African, Middle East and Balkan Earth Observation capacities in GEOSS.*

## REFERENCES

[1] T. F. Stocker, D. Qin, G.-K. Plattner, M. Tignor, S. K. Allen, J. Boschung, A. Nauels, Y. Xia, V. Bex, P. M. Midgley, IPCC: The Physical Science Basis, Contribution of Working Group I to the Fifth Assessment Report of the Intergovernmental Panel on Climate Change, Cambridge University Press, Cambridge, United Kingdom and New York, NY, USA, 2013.

[2] G. Pappalardo, A. Amodeo, A. Apituley, A. Comeron, V. Freudenthaler, H. Linné, A. Ansmann, J. Bösenberg, G. D'Amico, I. Mattis, L. Mona, U. Wandinger, V Amiridis, L. Alados Arboledas, D. Nicolae, M. Wiegner. Atmos. Meas. Tech. 7 (2014) 2389.

[3] S. Emeis, K. Schafer, C., Munkel Meteorologische Zeitschrift, 17(5) (2008) 621-630.

[4] C. Flamant, J. Pelon, P.H. Flamant, P. Durand., Boundary-Layer Meteorol. 83 (1997) 247-284.

[5] L. Menut, C. Flamant, J. Pelon, P. H. Flamant., Boundary-Layer Meteorol. 93 (1999) 269–286.

[6] V. Freudenthaler, Proceedings of 24th International Laser Radar Conference, 23-27 June, Boulder, USA, 2008.

**University of Belgrade**
**Technical Faculty in Bor and**
**Mining and Metallurgy Institute Bor**

# 49th International October Conference on Mining and Metallurgy

# PROCEEDINGS

**Editors:**
**Nada Štrbac**
**Ivana Marković**
**Ljubiša Balanović**

IOC 2017
International October Conference

**Bor Lake, Serbia**
**October 18-21, 2017**

**PROCEEDINGS,**
**49th INTERNATIONAL OCTOBER CONFERNCE**
**on Mining and Metallurgy**

**Editors:**
**Prof. dr Nada Štrbac**
**Doc. dr Ivana Marković**
**Doc. dr Ljubiša Balanović**
*University of Belgrade, Technical Faculty in Bor*

**Technical Editor:**
**M. Sc. Uroš Stamenković**
*University of Belgrade, Technical Faculty in Bor*

**Publisher:** University of Belgrade, Technical Faculty in Bor
**For the publisher:** Dean Prof. dr Nada Štrbac
**Circulation:** 200 copies

**Printed by "Happy trend DOO", Zaječar, 2017**

ISBN 978-86-6305-066-2

CIP - Каталогизација у публикацији - Народна библиотека Србије, Београд

622(082)
669(082)

**INTERNATIONAL October Conference on Mining and Metallurgy** (49 ; 2017 ; Bor Lake)
Proceedings / 49th International October Conference on Mining and Metallurgy - IOC 2017, Bor Lake, Serbia, October 18-21, 2017; [organized by] University of Belgrade, Technical Faculty Bor and Mining and Metallurgy Institute Bor; editors Nada Štrbac, Ivana Marković, Ljubiša Balanović. - Bor : University of Belgrade, Technical Faculty, 2017 (Zaječar : Happy trend). - XXIII, 664 str. : ilustr. ; 25 cm

Tiraž 200. - Bibliografija uz svaki rad. - Registar.

ISBN 978-86-6305-066-2

a) Рударство - Зборници b) Металургија - Зборници

COBISS.SR-ID 246349324

Bor Lake, Serbia, October 18-21, 2017

# AIR MASS TRANSPORT OVER BALKANS REGION IDENTIFIED BY ATMOSPHERIC MODELING AND AEROSOL LIDAR TECHNIQUE

**Zoran Mijić, Mirjana Perišić, Luka Ilić, Andreja Stojić, Maja Kuzmanoski**

Institute of Physics Belgrade, University of Belgrade, Pregrevica 118, 11080 Belgrade, Serbia

**Abstract**
*This study combines atmospheric modeling with lidar measurements in order to assess the origin of aerosols traveling over Balkan region, having an impact on regional radiative budget and air quality. Particulate matter potential source regions and transport pathways were investigated using hybrid receptor modeling and mass concentrations measured in Belgrade, Serbia. In addition, the case study evidencing transport of Saharan dust particles simulated by the DREAM model was presented. The capability of the lidar technique to derive range-resolved vertical profiles of aerosol optical parameters was used to analyze the aerosol layers altitude and temporal evolution.*

***Keywords:*** *atmospheric modeling, transport, PM*

## 1. INTRODUCTION

Suspended particulate matter (PM) in the atmosphere, commonly known as aerosol, plays an important role in the climate system. Besides significant effect on climate change, air quality and human health, aerosols affect long-range transport and deposition of toxics and nutrients. The complexity of aerosol processes in the atmosphere leads to large uncertainties in understanding of their role in many of the major environmental issues [1]. The direct (scattering and absorbing incoming solar radiation) and indirect aerosol effects (as they act as a cloud condensation nuclei) make the two largest contributions to the total uncertainty of radiative forcing. Regarding the impact of aerosols on air quality, the same processes that govern the global distribution, control the aerosol properties on regional and local scales. While *in situ* measurements are most adequate for air quality monitoring at the ground level, the assessment of impact of remote sources and transformation processes requires aerosol vertical distribution observations. Key parameters to be observed for this purpose are the presence, altitude and extent of elevated aerosol layers, the height of the planetary boundary layer (PBL), aerosol type, and mass concentration. Since long-range transport occurs at elevated layers, surface-based measurements of aerosol properties, such as chemical composition and size distribution are not sufficient. For global coverage including all relevant parameters, an integrated approach including ground-level and airborne in-situ measurements, ground-based remote sensing, and space-borne observations in combination with advanced modeling is necessary. Large observational networks such as the European Aerosol Research Lidar Network (EARLINET) [2], provide the long-term measurement series needed to build an aerosol vertical profile climatology at the continental scale. The capability of the lidar system (Light Detection And Ranging) to derive range-resolved aerosol vertical profiles with high spatial and temporal resolution is used to identify layers altitude and temporal evolution of intrusions. Using altitudes as inputs in air mass back-trajectories tracing method identification of aerosol sources at large distances from the measurement point, if their contribution is important, can be conducted. In this study hybrid receptor models for identification of potential source regions of PM affecting air quality in Belgrade are presented together with a case study evidencing transport of Saharan dust particles.

## 2. METHODOLOGY

Lidar technique is an active remote sensing method based on laser emission of the short-duration light pulses to the atmosphere and the analysis of the return signal. The intensity of the light backscattered by atmospheric molecules and particles is measured versus time – through the telescope receiver, collimating optics, a bandpass filter for daylight suppression – by an appropriate detector. For vertical profiling and remote sensing of atmospheric aerosol layers, Raman lidar at the Institute of Physics Belgrade (44.860 N, 20.390 E) has been used. It is bi-axial system with combined elastic and Raman detection designed to perform continuous measurements of aerosols in the PBL layer and the lower free troposphere. It is based on the third harmonic frequency of a compact, pulsed Nd:YAG laser, emitting pulses of 65 mJ output energy at 355 nm with a 20 Hz repetition rate. The optical receiver is a Cassegrain reflecting telescope with a primary mirror of 250 mm diameter and a focal length of 1250 mm. Photomultiplier tubes are used to detect elastic backscatter lidar signal at 355 nm and Raman signal at 387 nm. The detectors are operated both in the analog and photon-counting mode with lidar profiles averaging time of the order of 1 min and the spatial raw resolution of the detected signals of 7.5 m. Lidar measurements can be used in synergy with numerical models in order to validate and compare information about aerosols. In this paper DREAM (Dust Regional Atmospheric Model) model, designed to simulate and/or forecast the atmospheric cycle of mineral dust aerosol [3], is used to analyze dust transport. To estimate potential PM remote emission sources and their impact at the receptor site, concentration weighted trajectory (CWT) hybrid receptor model [4] was applied to the data set comprised of hourly $PM_{10}$ mass concentrations obtained from Belgrade suburban location "Ovča" during the period 2012-14, and 72-h air masses back-trajectories, calculated according to Perišić et al. [5]. Furthermore, to obtain the vertical profile of PM, concentration weighted boundary layer (CWBL) hybrid receptor model [6], which uses a two-dimensional grid and a planetary boundary layer height, or any altitude in general, as a frame of reference, was used. Although the model can be applied for analyzing the pollutant concentration vertical distribution along the transport pathway, in this paper we present its usage for the receptor site solely.

## 3. RESULTS AND DISCUSSION

According to the CWT analysis, the most prominent $PM_{10}$ sources were located in neighboring countries and in the areas NW, E and S of Belgrade. Significant impact of Central and Eastern European sources was registered during the autumn season (Figure 1–left panel).

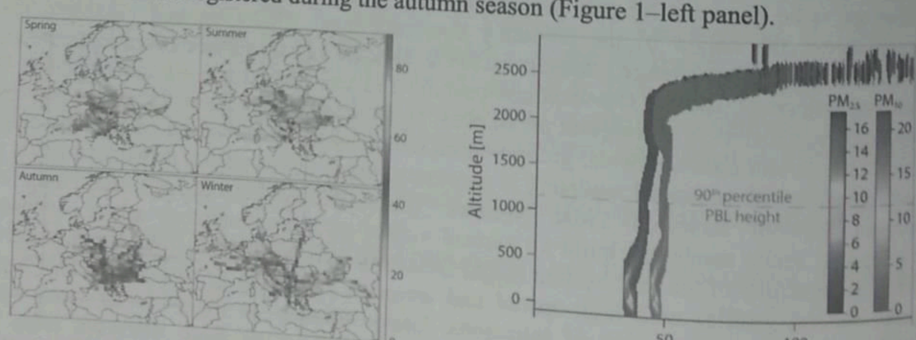


Figure 1 - CWT [µg m$^{-3}$] derived maps of $PM_{10}$ potential sources in Europe – seasonal variations (left), and CWBL derived PM altitude distribution above the receptor site (right) – color scales indicate the number of events

Very similar, almost constant PM altitude distribution over the receptor site was observed for both coarse and fine particles (Figure 1–right panel), and the most common PBL heights (within 90th percentile). However, given the number of events (colored scale), it can be seen that concentrations exhibit decreasing trend to the height of about 400 m because the species emitted or generated near the ground level are mostly trapped and concentrated within the PBL, whereas free atmosphere concentrations remain low. Large CWBL values at higher altitudes correspond to rare PBL fluctuations which are not statistically significant, so the model results cannot be taken into consideration.

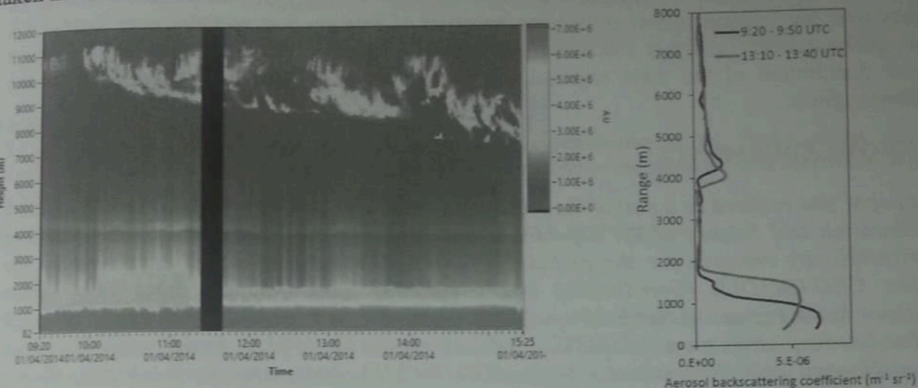


Figure 2 – Lidar range corrected signal (left) and backscatter coefficient at 355 nm (right) in Belgrade

Another aspect of aerosol climatology over Balkans region is related to the intrusions of Saharan dust which usually occurs during spring and summer periods. Such a case study evidencing transport of Saharan dust on 1st April 2014 is presented. From the RCS lidar time series (Figure 2), but also from the calculated backscatter coefficients profiles, the direct presence of an aerosol layer around 4-5 km altitude over Belgrade can been seen. This event was also successfully forecasted by DREAM model (Figure 3-left panel).

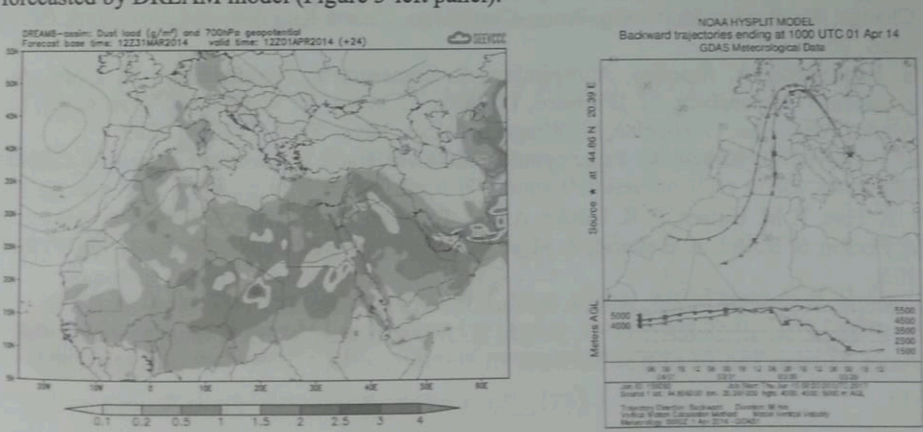


Figure 3 – Dust load over South Europe, estimated by the DREAM model (left) and air mass back-trajectories ending over Belgrade on 1st April, 2014 (righ)

Since the aerosols serve as a valuable tracer of air motion, using lidar observed altitudes of aerosol layer as inputs in the HYSPLIT [7] back-trajectory tracing method the source of aerosols was confirmed. As shown in Figure 3 (right panel) air masses reaching Belgrade traveled over

South Europe (Mediterranean Sea, Spain) and West Europe being influenced by continental pollution too.

## 4. CONCLUSION

The main advantage of lidar – real time observation of aerosol layering is that it can be used for air mass origin and path identification. Furthermore, in combination with statistical and numerical modeling, this technique can provide important information about aerosol type and distribution. In this paper we presented a case analysis of aerosol transport process affecting air quality over the Balkans region evidencing transport of Saharan dust particles over Serbia. Air mass back-trajectory analysis combined with hybrid receptor modeling were used to assess spatial distribution of the main regional sources for aerosols affecting air quality over the Balkans regions.

## ACKNOWLEDGEMENTS

*This paper was realized as a part of the projects III43007 and III41011 financed by the Ministry of Education and Science of the Republic of Serbia within the framework of integrated and interdisciplinary research for the period 2011-2017. The publication was supported by the project GEO-CRADLE (Coordinating and integRating state-of-the-art Earth Observation Activities in the regions of North Africa, Middle East, and Balkans and Developing Links with GEO related initiatives towards GEOSS), Grant Agreement No. 690133, funded under European Union Horizon 2020 Programme - Topic: SC5-18b-2015, Integrating North African, Middle East and Balkan Earth Observation capacities in GEOSS. The authors gratefully acknowledge the NOAA Air Resources Laboratory (ARL) for the provision of the HYSPLIT transport and dispersion model and/or READY website (http://www.ready.noaa.gov) used in this publication.*

## REFERENCES

[1] T. F. Stocker, D. Qin, G.-K. Plattner, M. Tignor, S. K. Allen, J. Boschung, A. Nauels, Y. Xia, V. Bex, P. M. Midgley, IPCC: The Physical Science Basis, Contribution of Working Group I to the Fifth Assessment Report of the Intergovernmental Panel on Climate Change, Cambridge University Press, Cambridge, United Kingdom and New York, NY, USA, 2013.

[2] G. Pappalardo, A. Amodeo, A. Apituley, A. Comeron, V. Freudenthaler, H. Linné, A. Ansmann, J. Bösenberg, G. D'Amico, I. Mattis, L. Mona, U. Wandinger, V. Amiridis, L. Alados Arboledas, D. Nicolae, M. Wiegner, Atmos. Meas. Tech. 7 (2014) 2389.

[3] S. Nickovic, G. Kallos, A. Papadopoulos, O. Kakaliagou, J. Geophys. Res. 106 (2001) 1813.

[4] Y. K. Hsu, T. M. Holsen, P. K. Hopke, Atmos. Environ. 37(4) (2003) 545-562.

[5] M. Perišić, S. Rajšić, A. Šoštarić, Z. Mijić, A. Stojić, Air Qual Atmos Health 10 (2017) 93-103.

[6] A. Stojić, S. Stanišić Stojić., Atmos. Environ. 164 (2017) 216-223.

[7] A. F. Stein, R. R. Draxler, G. D. Rolph, B. J. B. Stunder, M. D. Cohen, F. Ngan, Bull. Amer. Meteor. Soc. 96 (2015) 2059-2077.

# WeBIOPATR2017

# Particulate Matter: Research and Management

Proceedings from the 6th WeBIOPATR Workshop & Conference
Belgrade, Serbia
6.-8.9.2017

Milena Jovašević-Stojanović
and Alena Bartoňová, eds.

Belgrade 2019

WeBIOPATR

*The 6$^{th}$ WeBIOPATR Workshop and Conference,*
*Particulate Matter: Research and Management,*
***WEBIOPATR2017 is organized by:***

Vinča Institute of Nuclear Sciences, Serbia
Public Health Institute of Belgrade, Serbia
NILU Norwegian Institute for Air Research, Norway

*The 6$^{th}$ WeBIOPATR Workshop and Conference,*
*Particulate Matter: Research and Management,*
***WeBIOPATR2017 is supported by:***

Ministry of Education, Science and Technological Development of

Republic of Serbia

# PROCEEDINGS

The Sixth International WeBIOPATR Workshop & Conference
Particulate Matter: Research and Management
**WeBIOPATR2017**

6 - 8 September 2017
Belgrade, Serbia

*Editors*
Milena Jovašević-Stojanović
Alena Bartoňová

*Publisher*
Vinča Institute of Nuclear Sciences
Dr Zlatko Rakočević, Director
P.O. Box 522
11001 Belgrade, Serbia

*Printed by*
Vinča Institute of Nuclear Sciences

*Number of copies*
150

ISBN: 978-86-7306-152-8

Vinča Institute of Nuclear Sciences
www.vin.bg.ac.rs

**SCIENTIFIC COMMITTEE**

Dr Alena Bartoňová, Norway

Dr Bojan Radak, Serbia

Prof. Dr David Broday, Israel

Dr Med Elizabeta Paunović, Germany

Dr Maria Cruiz Min, Spain

Dr Milena Jovašević-Stojanović, Serbia

Prof. Dr Nenad Živković, Serbia

Prof. Dr Radim Šrám, Czech Republic

Dr Renata Kovačević, Serbia

Dr Slobodan Nićković, Serbia

Prof. Dr Simone Barreira Morais, Portugal

Zoran Mijić, Serbia

Prof. Dr Zoran Ristovski, Australia

Dr Zorana Jovanović-Andersen, Denmark

**ORGANIZING COMMITTEE**

*Vinča Institute of Nuclear Sciences, Belgrade: Serbia*
Dr Dragan Alavantić, Serbia
MS Ivan Lazović, Serbia
MS Maja Jovanović, Serbia (Secretary)
Dr Milena Jovašević-Stojanović (Co-chair)
Dr Miloš Davidović, Serbia (Secretary)
Dr Snežana Pašalić, Serbia

*NILU - Norwegian Institute for Air Research, Kjeller*
Dr Alena Bartoňová, Norway (Co-chair)

*Public Health Institute of Belgrade, Belgrade*
Dr Anka Cvetković, Serbia
MS Andrej Šoštarić, Serbia
Vesna Slapčević, Serbia

*Ministry of Environmental Protection of RS*
Ms Biljana Filipović, Serbia

*Serbian Environmental Protection Agency*
Mr Dejan Lekić, Serbia
Mr Tihomir Popović, Serbia

*National Institute of Public Health "Dr Milan Jovanović-Batut", Belgrade*
Dr Med Branislava Matić, Serbia

*Military Medical Academy, Belgrade*
Prof. Dr Jasmina Jović-Stošić, Serbia

*Institute of Physics, Belgrade*
Dr Mira Aničić Urošević, Serbia

*Faculty of Occupational Protection, University of Niš*
Prof. Dr Nenad Živković, Serbia

*Medical Faculty, University of Niš*
Prof. Dr Aleksandra Stanković, Serbia

*Institute of Metallurgy and Mining, Bor*
Dr Viša Tasić, Serbia

*Mechanical Faculty, University of Belgrade*
Prof. Dr Aleksandar Jovović, Serbia

## CONFERENCE TOPICS

| | |
|---|---|
| **ATMOSPHERIC PARTICULATE MATTER - PHYSICAL AND CHEMICAL PROPERTIES** | • *sources and formation of particulate matter*<br>• *particulate matter composition and levels outdoors and indoors*<br>• *environmental modeling*<br>• *nanoparticles in the environment* |
| **PARTICULATE MATTER AND HEALTH** | • *exposure to particulate matter*<br>• *health aspects of atmospheric particulate matter*<br>• *full chain approach* |
| **PARTICULATE MATTER AND REGULATORY ISSUES** | • *issues related to monitoring of particulate matter*<br>• *legislative aspects*<br>• *abatement strategies* |

# PREFACE

The International Workshop and Conference, Particulate Matter: Research and Management – WeBIOPATR is a biennial event held in Serbia since 2007. The conference addresses air quality in general and particulate matter specifically. Atmospheric particulate matter arises both from primary emissions and from secondary formation in the atmosphere. It is one of the least well-understood local and regional air pollutants, has complex implications for climate change, and is perhaps the pollutant with the highest health relevance. It also poses many challenges to monitoring.

By WeBIOPATR, we aim to link the research communities with relevance to particulate matter with the practitioners of air quality management on all administrative levels, in order to facilitate professional dialogue and uptake of newest research into practice. The workshops usually draw an audience of about 70, and attract media attention in Serbia. It enjoys support of the responsible authorities, Ministry of Health, Ministry of Environment, and the Serbian Environmental Agency whose sponsorship is indispensable and gratefully acknowledged. We enjoy also support of international bodies such as the WHO.

The 1st WeBIOPATR Workshop was held in Beograd, 20.-22. May 2007, associated with a project funded by the Research Council of Norway. The 2nd workshop was held in Mecavnik, Serbia, 28.8.-1.9. 2009. WeBIOPATR2011 was held in Beograd 14.-17. 11. 2011 and for the first time, included a dedicated student workshop. WeBIOPATR2013 was held in Beograd 2.-4. 10. 2013. It covered the traditional PM research and management issues, discussions on how to encourage citizens to contribute to environmental governance, and how to develop participatory sensing methods. WeBIOPATR2015 was held in Beograd 14.-16.10. 2015. Own sessions were devoted to sensor technologies for air quality monitoring, utilizing information and input from the EU FP7 funded project CITI-SENSE (http://co.citi-sense.eu) and the EU COST action EuNetAir (www.eunetair.it).

We have now the pleasure to present to you the proceedings of the 6th conference held in Beograd 6.-8.9. 2017. We are excited to have contributions from old friends and new acquaintances, and we are especially pleased with a wider than before Western Balkan participation. The contributions were reviewed. The language editing was performed by Dr Simon Smith, PhD, to whom we would like to extend out sincere thanks. Technical manuscript preparation was graciously done by Dr Milos Davidovic, PhD, to whom we are very grateful.

We are hoping that you, the reader, will extend your support to WeBIOPATR also in the future. The issues of atmospheric pollution, with their wide implications for climate change, human health and ecosystem services, are no less important today than before. Addressing them requires a strong scientific community and commitment of all societal actors. Your contribution will make a difference.

*Milena Jovašević-Stojanović and Alena Bartoňová*

# CONTENTS

## 5.3. A STUDY OF A DUST INTRUSION EVENT OVER BELGRADE, SERBIA

**M. Kuzmanoski, L. Ilić, M. Todorović, Z. Mijić**
*Institute of Physics Belgrade, University of Belgrade, Belgrade, Serbia*
*maja.kuzmanoski@ipb.ac.rs*

### ABSTRACT

This paper is to present the results of aerosol measurements from a dust intrusion episode in Belgrade during the period of July 5-7, 2014. A vertical profile of the aerosol backscattering coefficient, obtained from ground-based LIDAR measurements in Belgrade, showed a distinct elevated dust layer at altitudes of 2-5 km on July 5, 2014. The altitude of the layer decreased later in the episode, with its centre of mass decreasing from approximately 4 km to below 3 km. On the last day of the episode, an entrainment of the dust layer into the planetary boundary layer was observed, consistent with the observed change of $PM_{10}$ concentration at the surface level. The $PM_{10}$ concentration increased by 15-17 μg m$^{-3}$ at three monitoring sites in Belgrade, as the dust plume was settling down during the episode. The DREAM model simulations reproduced well the observed dust layer altitude. Dust surface concentrations from the model showed an increase of 11 μg m$^{-3}$ during the episode. The difference from observed $PM_{10}$ increase was attributed to contributions of other aerosol types to observations.

### INTRODUCTION

Mineral dust is one of the most abundant components of the global aerosol burden (Kinne et al., 2006). Saharan dust originates from the world's primary dust source region, and can be transported over long distances (Prospero, 1999; Ansmann et al., 2003). It mixes with other aerosol types along the transport path, affecting their physical, optical and radiative properties. Mineral dust affects the Earth's radiative budget by scattering and absorbing solar and terrestrial radiation (direct effect), by modifying cloud properties due to their role in cloud formation (indirect effect) or by changing the thermal structure of the atmosphere (semi-direct effect). However, there is significant uncertainty in estimating role of dust in the Earth's climate system (IPCC, 2013). Dust impacts air quality, even at locations distant from the source region (Prospero, 1999), and has harmful effects on human health (Giannadaki et al., 2014). To address these problems, it is important to improve the understanding of dust properties on temporal and spatial scales. This requires the synergistic use of ground-based and satellite measurements, along with a regional dust model, for the analysis of dust spatial and temporal variability.

Here we present a case study of a dust intrusion episode observed in Belgrade from July 5-7, 2014. The analysis of the temporal variability of the dust layer was based on ground-based LIDAR measurements in Belgrade, while satellite measurements were used in the discussion of the spatial distribution of dust. Furthermore, the impact of the dust intrusion episode on $PM_{10}$ concentrations in Belgrade was analysed. The measurement results were compared with results of Dust REgional Atmospheric Model DREAM (Ničković et al., 2001).

### METHODOLOGY

The aerosol backscattering coefficient at 355 nm was derived from LIDAR measurements in Belgrade. A combined Raman elastic backscatter LIDAR has been operating at the Institute of Physics Belgrade since February 2014. It is based on the Nd:YAG laser operating at a fundamental wavelength of 1064 nm, and second and third harmonics at 532 and 355 nm. The laser pulses of 5 nm duration are transmitted at repetition rate of 20 Hz, with the output energies of 105, 45 and 65 mJ at these three wavelengths. The receiver is based on a 250 mm Cassegrain telescope in a biaxial arrangement, with adjustable field of view in the range from 0.5 to 3 mrad. Photomultiplier tubes are used to detect the backscatter signal in photon counting and analogue mode. The signals are detected at 355 and 387 nm, with a vertical resolution of 7.5 m and a temporal resolution of 1 minute. In this work we analysed the elastic backscatter signal at 355 nm. The analysis of the LIDAR signal to obtain the aerosol backscattering coefficient was performed using Fernald-Klett retrieval method (Fernald, 1984; Klett, 1985), assuming a LIDAR ratio value of 50 sr. Due to incomplete overlap of the laser and telescope fields of view, the LIDAR signal registering below 500 m was not considered in the analysis.

Daily $PM_{10}$ mass concentrations at surface level, at three stations in Belgrade, were obtained from the State network for automatic monitoring of air quality (https://data.gov.rs/sr/datasets/kvalitet-vazdukha-u-republitsi-srbiji/).

Dust REgional Atmospheric Model DREAM (Ničković et al., 2001) embedded into the NCEP/NMME non-hydrostatic atmospheric model (Janjić et al., 2011) was used to provide horizontal and vertical distribution of dust concentration. The model domain covers Northern Africa, the Middle East and a large part of the European continent, with a horizontal resolution of 1/5° (~ 30 km) and 28 vertical levels. It uses 8 particle size bins within the 0.1-10 μm radius range.

Additionally, we used an aerosol optical depth (AOD) at 550 nm from combined Deep Blue and Dark Target algorithms and the Deep Blue Ångström exponent (AE) at 412-470 nm products from the MODIS (Moderate Resolution Imaging Spetroradiometer) instrument aboard the NASA Aqua satellite. We used Collection 6, Level 3 data products. It should be noted, that the increase in AOD indicates an increase in aerosol load, while the AE parameter is used as a qualitative measure of particle size (the smaller AE values indicate predominantly coarse particles).

CALIOP (Cloud-Aerosol Lidar with Orthogonal Polarization) on board the CALIPSO satellite, was used to obtain vertical profiles of aerosols and clouds. It is an elastic backscatter LIDAR operating at two wavelengths: 532 nm and 1064 nm, with a depolarization channel at 532 nm. Here we used Level 2 Vertical Feature Mask product, which provides information on the aerosol types present in the detected layers (Omar et al., 2009).

Air-mass back trajectories ending at different altitudes over the LIDAR measurement site were calculated using the Hybrid Single-Particle Lagrangian Integrated Trajectory (HYSPLIT) model (Draxler and Hess, 1998; http://ready.arl.noaa.gov/HYSPLIT.php), with meteorological input from the Global Data Assimilation System (GDAS). The backtrajectories were used to provide an indication of the origin and pathways of air-masses arriving at altitudes of interest over Belgrade.

## RESULTS AND DISCUSSION

We present an analysis of a dust episode that was observed over Belgrade from July 5-7, 2014. The beginning of the episode can be seen in MODIS data shown in Figure 1. MODIS values of AOD and AE indicate an increase of aerosol load and an increased contribution of coarse particles on July 5th compared to the previous day; this is typical for dust episodes.

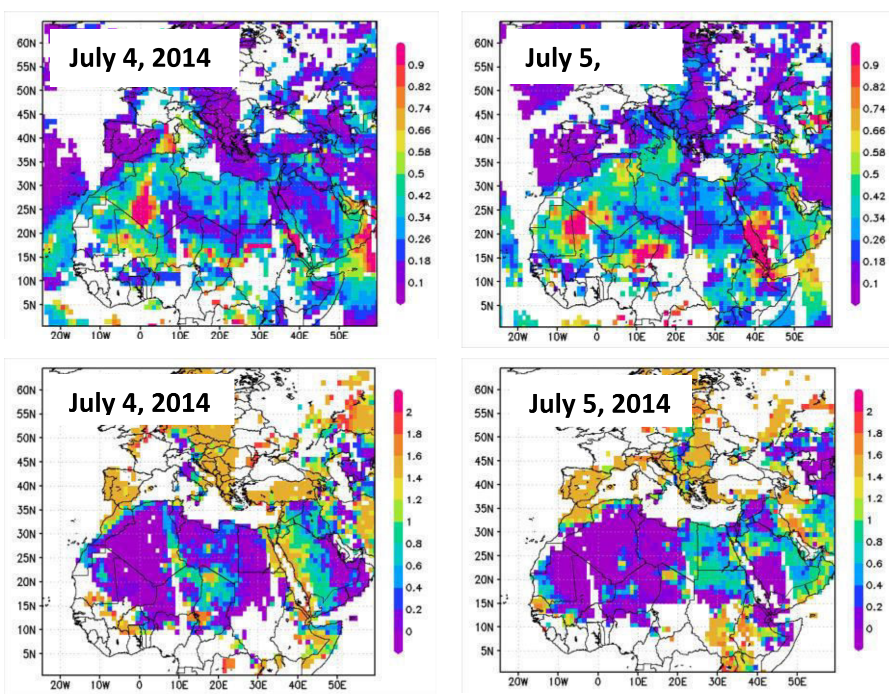


***Figure 1.*** *MODIS aerosol data for July 4-5, 2014: (upper panels) MODIS aerosol optical depth (AOD) at 550 nm from combined Deep Blue and Dark Target algorithms; (lower panels) Deep Blue Angström exponent (AE) at 412-470 nm.*

The observed AOD at 550 nm over Belgrade increased from below 0.1 on July 4th, to about 0.3 on July 5th (the first day of the dust episode), with a decrease in the AE value from 1.4 to 0.4. Moderate AOD values were observed over Belgrade during the dust episode. MODIS data also showed that the dust event affected parts of western and central Europe.

A close CALIPSO overpass over Belgrade occurred during the peak of the dust episode, on July 6th, at approximately 12 UTC. The CALIOP Vertical Feature Mask data, along the satellite ground track, is presented in Figure 2. We also showed the dust load over the area of interest and a vertical profile of the dust concentration along the CALIPSO ground track, resulting from DREAM model simulations. Both CALIOP data and the DREAM model results indicated that the dust plume extended north to Poland. The concentrations resulting from the model were largest around 40°N, at altitudes between 2 and 3 km, and decreased towards the north. At the part of the track within a 100 km distance from Belgrade, the DREAM model dust concentrations showeda maximum at a similar altitude range. CALIOP data suggested the presence of polluted dust (a mixture of pure dust with smoke or anthropogenic pollution) in this layer.

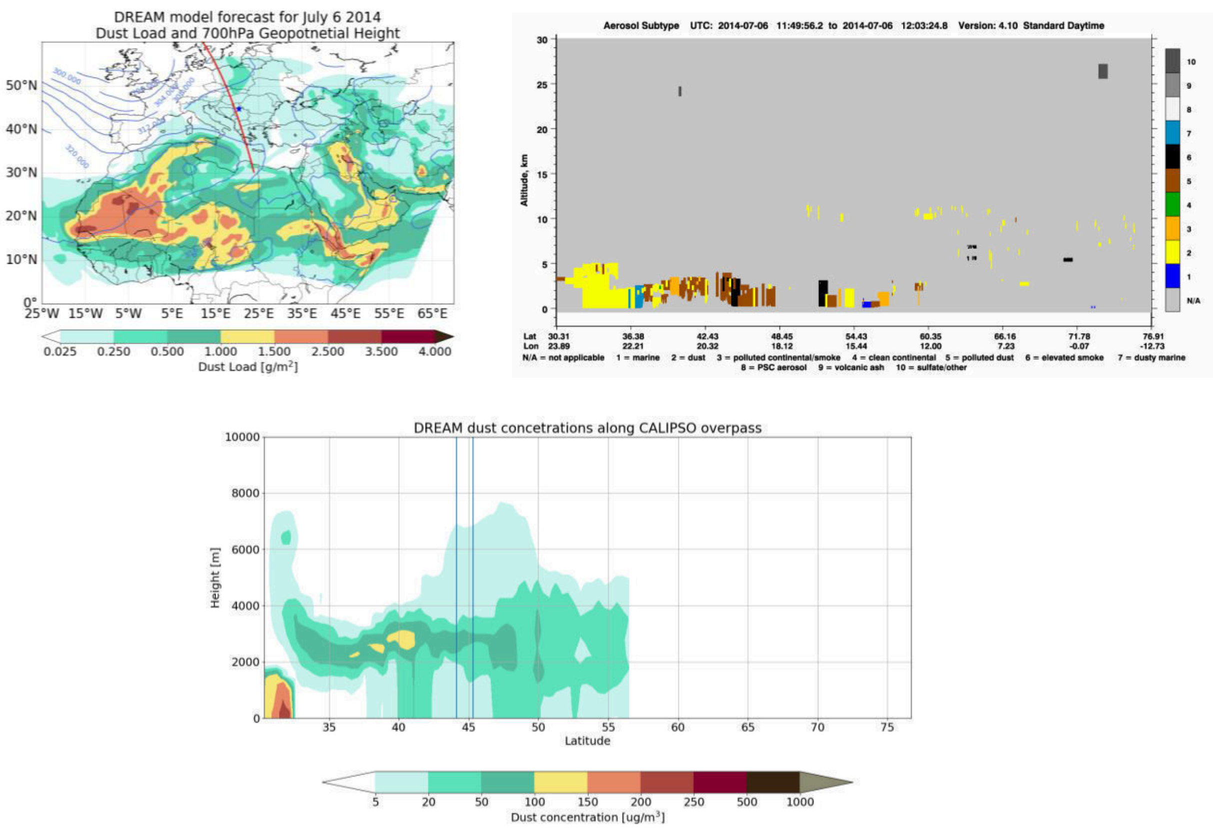


*__Figure 2.__ (upper panels) Map of dust load calculated from DREAM model on July 6, 2014 at 12 UTC, with CALIPSO ground track and Belgrade LIDAR station marked; and the corresponding results of CALIOP aerosol classification. (lower panel) Dust concentration vertical profiles along the CALIPSO ground track obtained from DREAM model. Data between the two vertical lines corresponds to the part of the track within 100 km distance from Belgrade LIDAR station.*

Ground-based LIDAR measurements in Belgrade were analyzed to characterize the aerosol vertical profile during the dust episode. The profile of the aerosol backscattering coefficient showed a distinctly elevated aerosol layer on July 5th, at altitudes between approximately 2 and 5 km, with a maximum at about 4.5 km. It was identified as a dust layer, based on the air-mass backtrajectory was calculated to find the corresponding aerosol source region. Selected vertical profiles of the aerosol backscattering coefficient, and of the corresponding profiles of dust mass concentration obtained from DREAM model simulations, are presented in Figure 3. It should be noted that their comparison is only qualitative as we did not attempt to calculate the backscattering coefficient from the DREAM model results due to its high sensitivity to aerosol chemistry. The averaging of LIDAR signals for the analysis of the presented data was performed in 30minute intervals centered at the time of the model result. The dust layer boundaries were determined following the procedure described by Mona et al. (2006). The backscattering coefficients showed that the layer descended during the course of the dust episode, and indicated an entrainment of dust into the PBL on July 7th. Dust mass concentrations resulting from the DREAM model showed a similar vertical pattern as the LIDAR measurements and a notable increase of dust concentration at altitudes below 2 km on July 7th.

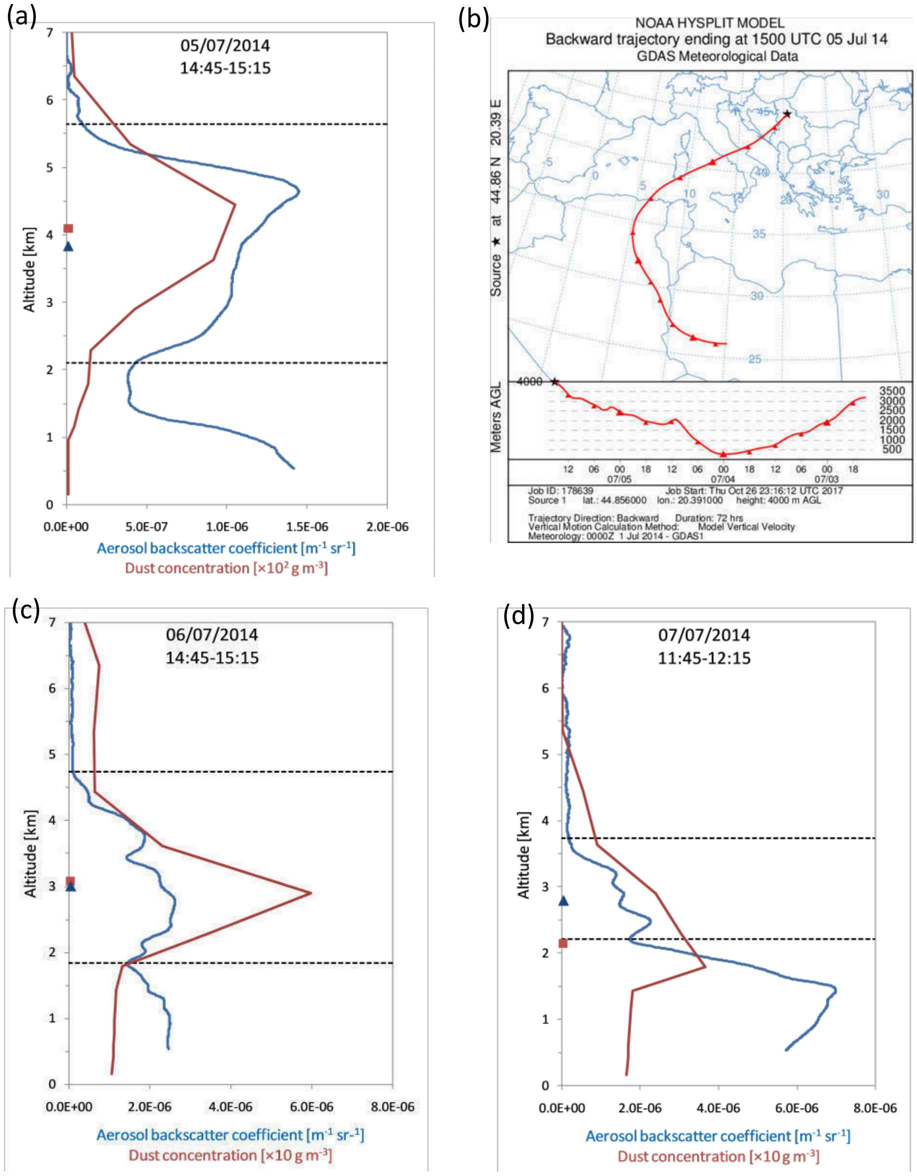


***Figure 3.*** *(a, c, d) Vertical profile of aerosol backscattering coefficient from LIDAR measurements in Belgrade (blue line) and the corresponding profile of dust concentration from the DREAM model (red line); horizontal lines indicate dust layer base and top, while symbols show the positions of the dust layer's center of mass as calculated from LIDAR measurements and the DREAM model (b) 72hour airmass backtrajectory arriving at a 4 km altitude over Belgrade on July 5, 2014, at 15 UTC (corresponding to profile (a)).*

Figure 3 also shows altitudes of the dust layer center of mass, based on LIDAR measurements and the DREAM model. In the case of LIDAR measurements, it was calculated as a backscattering-coefficient-weighted altitude, according to:

$$z_c = \frac{\int_{z_b}^{z_t} z \cdot \beta(z) dz}{\int_{z_b}^{z_t} \beta(z) dz}$$

where $z_b$ and $z_t$ are the altitudes of the base and the top of the dust layer and $\beta(z)$ is the aerosol backscattering coefficient at altitude $z$. To minimize the effect of anthropogenic pollution, the center of mass from the LIDAR measurements was calculated only for the elevated layer. The dust's centre of mass from the DREAM model was calculated taking into account the entire dust profile.

Daily mass concentration of $PM_{10}$ at ground level showed a similar trend at three air quality monitoring stations in Belgrade, with an increase during the dust episode (Figure 4). The increase started on July 6th, and the maximum was reached on July 7th, exceeding the 95th percentile of the summer (June, July and August) 2014 values. However, the daily limit value of 50 μg $m^{-3}$, set by the EU Air Quality Directive 2008/50/EC, was not exceeded. The increase of $PM_{10}$ concentration is in agreement with the results of the LIDAR measurements, and the DREAM model, which indicated a settling of the dust plume (as shown in Figure 3). For comparison, daily average dust mass concentrations at the surface, obtained from the DREAM model, are also shown in Figure 4. They showed a similar trend as measured $PM_{10}$ concentrations, increasing by 11 μg $m^{-3}$ during the dust episode, while measured $PM_{10}$ increased by 15 to 17 μg $m^{-3}$ at the three monitoring stations. Larger measured $PM_{10}$ concentrations, compared to surface dust concentrations from the model, were attributed to sources other than mineral dust.

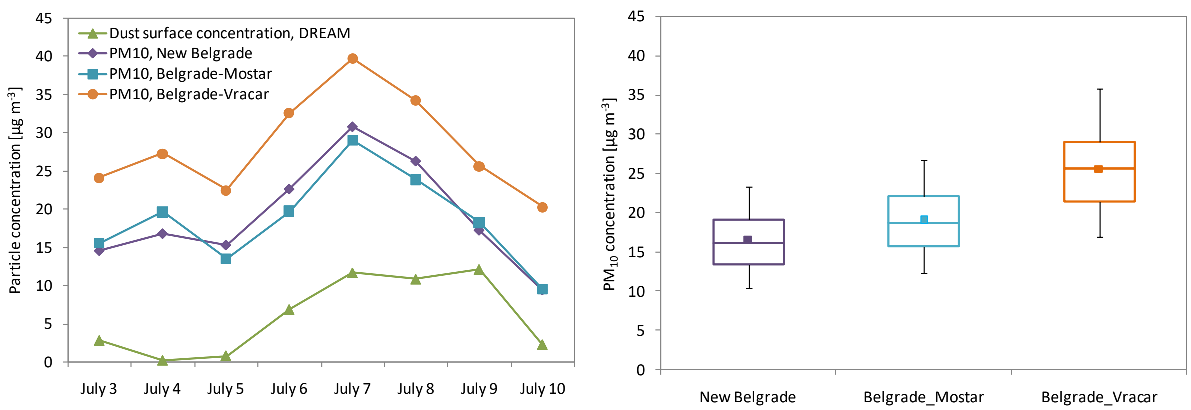


***Figure 4.*** *(left panel) Daily average dust surface concentration values from the DREAM model and $PM_{10}$ concentrations from three air quality monitoring stations in Belgrade. (right panel) Boxplot of $PM_{10}$ concentrations during summer (June, July, August) of 2014 at three monitoring stations in Belgrade; the extent of the box indicates the 25th and 75th percentiles, the central line represents the median value, while the whiskers indicate the 5th and 95th percentiles; the points represent the mean values.*

## CONCLUSION

We present analysis of a dust intrusion episode that was observed over Belgrade on July 5-7, 2014. The satellite measurements showed that the dust plume extended to western and central Europe. A distinctly elevated dust layer, extending at altitudes of approximately 2-5 km, was observed on July 5th using ground-based LIDAR in Belgrade. The layer altitude decreased during the dust episode, with the centre of mass altitude decreasing from approximately 4 km to below 3 km. The LIDAR measurements indicated entrainment of dust into the PBL on July 7th, the last day of the episode. The vertical distribution of dust and its temporal evolution over Belgrade was reproduced well by the DREAM model. The observed daily $PM_{10}$ concentrations at three monitoring stations in Belgrade showed an increase of 15-17 μg $m^{-3}$, while dust was settling down during the episode as indicated by LIDAR measurements. Dust surface concentrations obtained from the DREAM model showed the same trend as measured $PM_{10}$ concentrations, with a smaller increase (11 μg $m^{-3}$), during the episode: This difference was attributed to the contribution of other aerosol types to the observed $PM_{10}$ concentrations.

## ACKNOWLEDGEMENTS

This research was realized as a part of the project no. III43007, financed by the Ministry of Education, Science and Technological Development of the Republic of Serbia within the framework of integrated and interdisciplinary research for the period 2011-2020. The authors acknowledge support by the project GEO-CRADLE, Grant Agreement No. 690133, funded under European Union Horizon 2020 Programme. The authors gratefully acknowledge the NOAA Air Resources Laboratory (ARL) for the provision of HYSPLIT transport and dispersion

model and READY website (http://www.ready.noaa.gov), used in this publication. Analyses and visualizations of MODIS data used in this study were produced with the Giovanni online data system, developed and maintained by the NASA GES DISC. CALIPSO data were obtained from the NASA Langley Research Center Atmospheric Science Data Center.

## REFERENCES


1. Ansmann, A., Bösenberg J., Chaikovsky, A., Comeron, A., Eckhardt, S., Eixmann, S. et al., 2003. Long-range transport of Saharan dust to northern Europe: The 11-16 October 2001 outbreak observed with EARLINET, Journal of Geophysical Research 108, 4783, doi:10.1029/2003JD003757.
2. Draxler, R. R. and Hess, G. D., 1998. An overview of the HYSPLIT 4 modeling system for trajectories, dispersion, and deposition, Australian Meteorology Magazine, 47, 295-308.
3. Fernald, F. G., 1984. Analysis of atmospheric lidar observations: some comments, Applied Optics 23,652-653.
4. Giannadaki, D., Pozzer, A., Lelieveld, J., 2014. Modeled global effects of airborne desert dust on air quality and premature mortality, Atmospheric Chemistry and Physics 14, 957-968.
5. IPCC: Climate Change 2013: The physical science basis. Contribution of Working Group I to the Fifth Assessment Report of the Intergovernmental Panel on Climate Change, edited by: Stocker, T.F., Qin, D., Plattner, G.-K., Tignor, M., Allen, S.K., Boschung, J., Nauels, A., Xia, Y., Bex, V., Midgley, P.M., Cambridge University Press, Cambridge, UK and New York, USA.
6. Janjić, Z. I., Gerrity Jr, J. P., Ničković, S., 2011. An alternative approach to non-hydrostatic modelling, Monthly Weather Review 129, 1164-78.
7. Kinne, S., Schulz, M., Textor, C., Guilbert, S., Balkansky, Y., Bauer, S. E. et al., 2006. An AeroCom initial assessment - optical properties in aerosol component modules of global models, Atmospheric Chemistry and Physics 6, 1815-1834.
8. Klett, J. D. 1985. Lidar inversion with variable backscatter/extinction ratios, Applied Optics 24, 1638-1643.
9. Mona, L., Amodeo, A., Pandolfi, M., Pappalardo, G., 2006. Saharan dust intrusions in the Mediterranean area: Three years of Raman lidar measurements, Journal of Geophysical Research, 111, D16203, doi:10.1029/2005JD006569.
10. Ničković, S., Kallos, G., Papadopoulos, A., Kakaliagou, O., 2001. A model for prediction of desert dust cycle in the atmosphere, Journal of Geophysical Research 106, 18113-18130.
11. Omar, A. H., Winker, D. M., Kittaka, C., Vaughan, M. A., Liu, Z., Hu, et al., 2009. The CALIPSO automated aerosol classification and Lidar Ratio Selection Algorithm, Journal of Atmospheric and Oceanic Technology 26, 1994-2014, doi:10.1175/2009JTECHA1231.1.
12. Prospero, J. M., 1999. Long-term measurements of the transport of African mineral dust to the southeastern United States: Implications for regional air quality, Journal of Geophysical Research 104, 15917-15927, doi:10.1029/1999JD900072.

# 5.4. RELATIVE IMPORTANCE OF GASEOUS POLLUTANTS AND AEROSOL CONSTITUENTS FOR IDENTIFICATION OF $PM_{10}$ SOURCES OF VARIABILITY

**M. Perišić (1), G. Vuković (1), Z. Mijić (1), A. Šoštarić (2) and A. Stojić (1)**
*(1) Institute of Physics, University of Belgrade, Pregrevica 118, Serbia*
*(2) Institute of Public Health of Belgrade, Boulevard of Despot Stefan 54a, Belgrade, Serbia*
mirjana.perisic@ipb.ac.rs

## ABSTRACT

This study combines advanced statistical methods including time series decomposition, source apportionment and supervised learning algorithms, to identify the main sources of particulate matter ($PM_{10}$) variability in an urban area within Belgrade. The analyses indicated that the season, (i.e., meteorological conditions) strongly influenced daily and annual $PM_{10}$ variations particularly during the colder part of the year. A guided regularized random forest model estimated that As, Cd, BaP, CO, and benzene have the highest relative importance for the prediction of $PM_{10}$. Polar plot source apportionment revealed common sources of pollution at specific directions. Specifically, emissions of $PM_{10}$, CO and benzene could be attributed to heating and gasification processes, while processes in oil refineries and chemical industries produced $PM_{10}$ and toluene.

## INTRODUCTION

Due to adverse effects on human health and the increased risk of morbidity and mortality, particulate matter (PM) is one of the most studied atmospheric pollutants, and perhaps, the most pressing issue in worldwide air quality regulation (Fuzzi et al, 2015, Stanišić Stojić et al, 2016). Even though significant progress has been made through the integration of different scientific approaches, modelling of air pollution data remains a challenge due to the complexity and non-linear nature of atmospheric phenomena and processes (Pai et al, 2013). During the last decade, poor air quality in Belgrade, with many $PM_{10}$ limit value exceedances (Directive 2008/50/EC), has been identified as an important environmental risk factor (Perišić et al, 2015, 2017). Identification of factors affecting $PM_{10}$ concentration variability could provide better insight into the aerosol spatiotemporal distribution and source composition, revealing their dominant sources in an urban area (Stojić et al, 2016).

Apart from the commonly used methods for data analysis, this study adopts the advanced statistical classifier, guided regularized random forest (GRRF), widely applied in many fields for feature selection. Moreover, the study demonstrates the possibilities of source apportionment analysis, which combines correlation and regression statistics with the bivariate polar plot analysis, to offer considerably more insight into air pollution sources.

## METHODOLOGY

The analysed dataset, comprised of daily $PM_{10}$ and its constituent concentrations (As, Cd, Cr, Mn, Ni, Pb, BaP, $Cl^-$, $NO_3^-$, $NH_4^+$, $SO_4^{2-}$, $Na^+$, $K^+$, $Mg^{2+}$ and $Ca^{2+}$), and hourly $PM_{10}$ and gaseous pollutant concentrations (CO, $SO_2$, NO, $NO_2$, $NO_x$, benzene, toluene, o- and m, p xylene) have been obtained from an Institute of Public Health regular monitoring station located within an urban area in Belgrade (Longitude 20.470, Latitude 44.817) from 2011 - 2016. The time series of $PM_{10}$ concentrations was resolved into the additive components of the multi-year and seasonal trends, as well as the remainders using the Loess smoothing decomposition model (LSD) (Li et al, 2014). Daily, weekly and seasonal periodicity was analyzed by the use of Lomb-Scargle periodogram (*Lomb* package within the statistical software environment *R*) (Ruf, 1999; Team, 2014). Bivariate polar plot analysis was used for identification of the main $PM_{10}$ emission sources (Carslaw and Ropkins, 2012), while the advanced bivariate polar plots, coupled with pair-wise statistics, were applied to distinguish specific sources and to gain information about pollutant relationships. The model includes a weighted Pearson correlation, linear regression slope and Gaussian kernel to locally weight the statistical calculations on a wind speed-direction surface together with variable-scaling (Grange et al, 2016). Feature selection was implemented using a GRRF ensemble learning method (Deng and Runger, 2013). GRRF can select compact feature subsets revealing higher order variable interactions, thus moderating the problem of dimensionality and avoiding the effort to analyze irrelevant or redundant features.

## RESULTS AND DISCUSSION

Annual concentrations of $PM_{10}$ and BaP exceeded prescribed limit values of 50 $\mu g\ m^{-3}$ and 1 $ng\ m^{-3}$, respectively (Directive 2000/69/EC, Directive 2008/50/EC) every year of the period examined. The most abundant aerosol constituents were Cr, Pb and Mn (Figure 1), while $SO_4^{2-}$ and $NO_3^-$ were the ions with the highest concentrations.

In an urban area, the dominance of sulfate and nitrate ions is related to fossil fuel burning and traffic exhaust emission of $SO_2$ and $NO_x$, which, in the presence of water, transform into these ions. In addition, $NH_4^+$ and $Ca^{2+}$ cations are usually presented as neutralizing agents for $SO_4^{2-}$ and $NO_3^-$ in heterogeneous atmospheric chemical reactions.

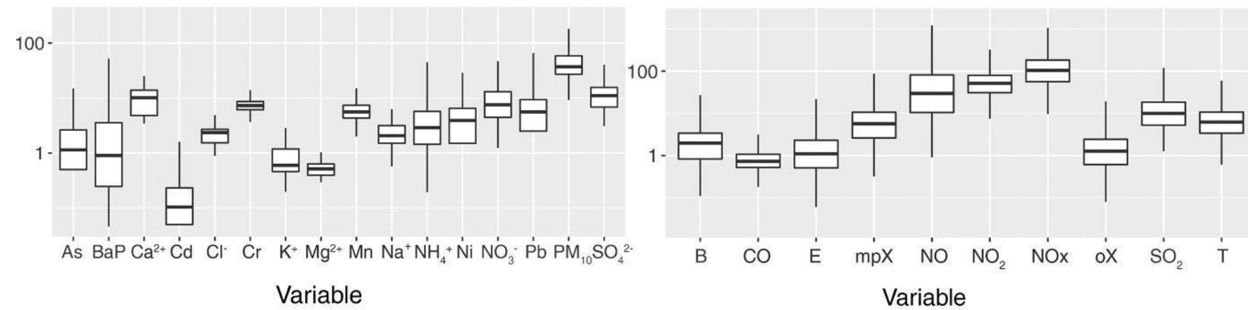


***Figure 1.*** *$PM_{10}$ concentration [$\mu g\ m^{-3}$], its chemical constituent (ions and BaP [$\mu g\ m^{-3}$], metals [$ng\ m^{-3}$]) (left) and gaseous pollutant [$\mu g\ m^{-3}$] (right) whisker plots*

Spectral analysis (Figure 2, left) reveals the highest normalized power values are attributed to the periods of 12 and 24 h, 7 days, and 1 and 3 months. This implies that meteorological conditions and anthropogenic emissions are strongly affected by aerosol daily and seasonal variations, and weekly periodicity, respectively (Bigi, 2016).

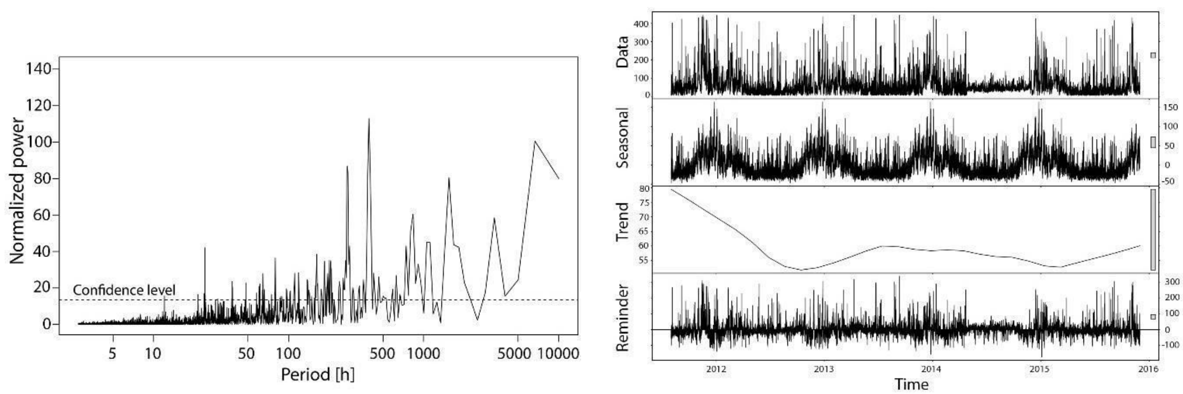


***Figure 2.*** *$PM_{10}$ Lomb-Scargle periodogram (left) and $PM_{10}$ time series decomposition [$\mu g\ m^{-3}$] (right)*

Decomposed $PM_{10}$ time series indicates a decreasing multi-year trend and significant impact of the seasonal component. Large variance of the remainder component possibly occurs as a result of short-term air pollution episodes (Figure 2, right). The conventional bivariate polar plot approach reveals the pronounced influence of both local and remote sources on $PM_{10}$ variability (Figure 3).

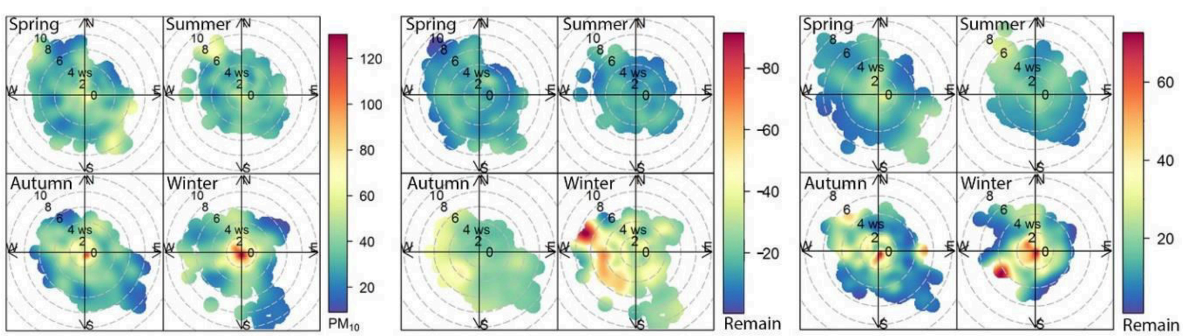


***Figure 3.*** *Bivariate polar plot of $PM_{10}$ concentrations (left) and its remainder components: negative (middle) and positive (right) [$\mu g\ m^{-3}$]*

Bivariate polar plot analysis of the remainder component, separately applied on positive and negative values, confirms that the episodes of the highest variations mainly occur during the colder part of the year. Positive variations related to SW and negative related to NW winds with speeds greater than 6 m $s^{-1}$.

The highest Pearson's correlation coefficients were obtained between concentrations of $PM_{10}$ and its constituents (BaP (0.83), As (0.81), Cd (0.79) and Pb (0.66)), as well as for the gaseous pollutants: CO (0.56), benzene (0.46), NO (0.35), and $NO_x$ (0.35). Similarly, the GRRF estimated the highest relative importance of As, Cd, BaP, CO and benzene for the prediction of $PM_{10}$, indicating that the environmental burden is mainly associated with fossil fuel combustion, particularly pronounced during the colder part of the year. An inconsistency between the correlation and GRRF analysis was observed for toluene. This compound had a higher importance for $PM_{10}$ prediction than $NO_x$, but its correlation coefficient was among the lowest (0.25).

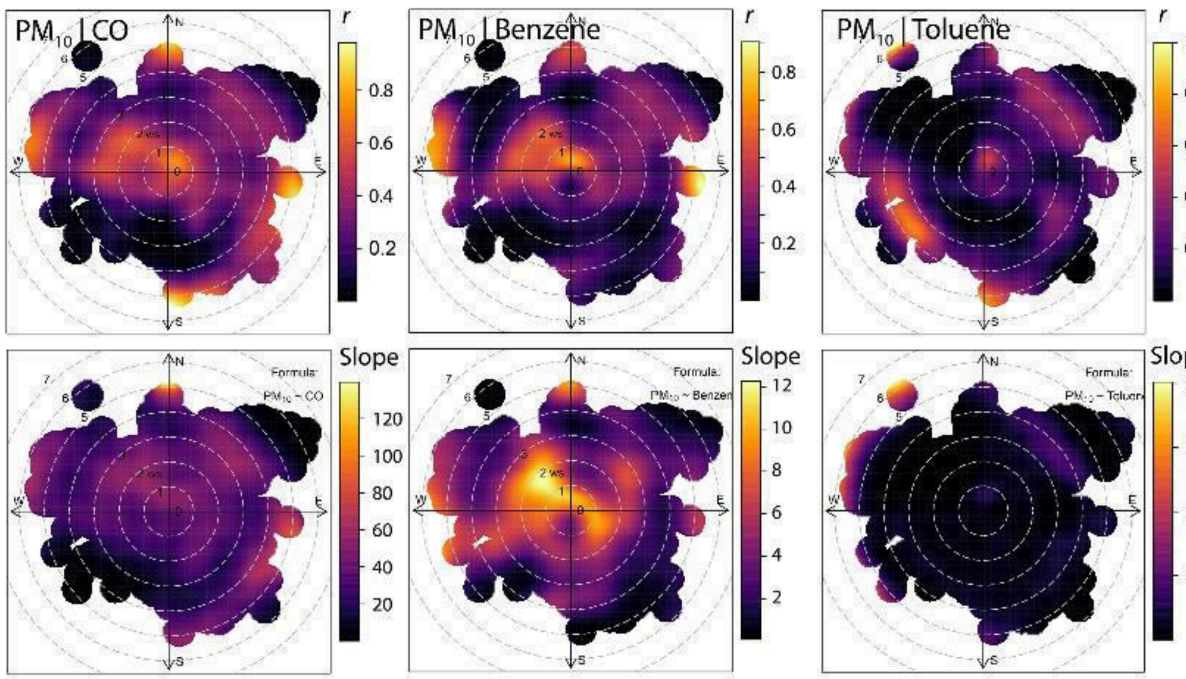


***Figure 4.*** *Bivariate polar source apportionment*

Even though Pearson's coefficients did not indicate a significant correlation between $PM_{10}$ and gaseous pollutants ($r < 0.6$), the bivariate polar source apportionment (Figure 4) showed that during episodes of north-westerly winds, concentrations of $PM_{10}$ and benzene and CO were more correlated ($r \approx 0.7$) probably because of several common sources in the vicinity of the sampling site. Source composition obtained from slope diagrams reveals a 1:0.1 and 1:12 contribution of $PM_{10}$, CO and benzene, respectively. This could be associated with various biomass combustion processes (traffic activities, heating plants and individual heating units) (Yokelson et al, 2007). Besides the vicinity of the sampling site, particulate matter and toluene shared prominent sources located in the SW, S, NE and SE directions ($r > 0.8$, wind speed > 4 m s-1). Unlike southern and western sources, characterized by $PM_{10}$ to toluene ratio of 1:1 which could be related to mineral oil and gas refineries, the source located on the north-east is characterized by the ratio of 1:6 indicating influences from the chemical industry, and chemical installations for production, on an industrial scale, of basic organic chemicals including aromatic hydrocarbons (European Commission, 2006).

## CONCLUSIONS

Due to the pronounced nonlinearity and complexity of atmospheric processes in the troposphere of an urban environment, the application of multivariate and nonlinear methods is required to gain reliable information for a better understanding of the underlying factors which determine the air pollution phenomena. Methods such as feature selection based on advanced supervised learning algorithms, advanced source apportionment techniques and time series decomposition and detailed component analysis, are capable of providing this information, particularly for characterization of variable pollution sources. Summarizing this study, it has been shown that locally emitted and transported pollution, as well as meteorological factors, have the highest impact on urban air quality.

## ACKNOWLEDGMENTS

This paper was completed as part of the project titled “Studying climate change and its influence on the environment: impacts, adaptation and mitigation" (III43007) financed by the Ministry of Education and Science of the Republic of Serbia within the framework of integrated and interdisciplinary research for the period 2011-2017. The publication was supported by the project GEO-CRADLE (Coordinating and integRating state-of-the-art Earth Observation Activities in the regions of North Africa, Middle East, and Balkans and Developing Links with GEO related initiatives towards GEOSS), Grant Agreement No. 690133, funded under European Union Horizon 2020 Programme - Topic: SC5-18b-2015, Integrating North African, Middle East and Balkan Earth Observation capacities in GEOSS.

## REFERENCES

1. Bigi, A. and Ghermandi, G. 2016. Trends and variability of atmospheric $PM_{2.5}$ and $PM_{10-2.5}$ concentration in the Po Valley, Italy. Atmospheric Chemistry and Physics 16, 15777-15788.
2. Carslaw, D.C., Ropkins, K. 2012. Openair - an R package for air quality data analysis. Environmental Modelling and Software 27-28, 52-61.
3. Deng, H. and Runger, G. 2013. Gene selection with guided regularized random forest. Pattern Recognition 46, 3483-3489.
4. Directive 2000/69/EC of the European Parliament and of the council of 16 November 2000 relating to limit values for benzene and carbon monoxide in ambient air. Official Journal of the European Communities L313, 12-21 (13/12/2000).
5. Directive 2008/50/EC of the European Parliament and of the Council of 21 May 2008 on ambient air quality and cleaner air for Europe. Official Journal of the European Union L152/3, 6-15 (11/06/2008).Fuzzi, S., Baltensperger, U., Carslaw, K., Decesari, S., Denier Van Der Gon, H., Facchini, M.C., Fowler, D., Koren, I., Langford, B., Lohmann, U. and Nemitz, E. 2015. Particulate matter, air quality and climate: lessons learned and future needs. Atmospheric Chemistry and Physics 15, 8217-8299.
6. European Commission, 2006. Guidance Document for the implementation of the European Pollutant Release and Transfer Register (E-PRTR).
7. Grange S.K., Lewis A. and Carslaw D. 2016. Source apportionment advances using polar plots of bivariate correlation and regression statistics. Atmospheric Environment 145, 128-134.
8. Li, L., Qian, J., Ou, C. Q., Zhou, Y. X., Guo, C. and Guo, Y. 2014. Spatial and temporal analysis of Air Pollution Index and its timescale-dependent relationship with meteorological factors in Guangzhou, China, 2001-2011. Environmental Pollution 190, 75-81.
9. Ruf, T. 1999. The Lomb-Scargle periodogram in biological rhythm research: analysis of incomplete and unequally spaced time-series. Biological Rhythm Research 30, 178-201.
10. Pai, T.Y., Hanaki, K., Chiou, R.J. 2013. Forecasting hourly roadside particulate matter in Taipei County of Taiwan based on firstorder and one-variable grey model. CLEAN Soil Air Water 41, 737-742.
11. Perišić, M., Rajšić, S., Šoštarić, A., Mijić, Z. and Stojić, A. 2017. Levels of $PM_{10}$-bound species in Belgrade, Serbia: spatio-temporal distributions and related human health risk estimation. Air Quality, Atmosphere and Health 10, 93-103.
12. Perišić, M., Stojić, A., Stojić, S. S., Šoštarić, A., Mijić, Z., and Rajšić, S. (2015). Estimation of required $PM_{10}$ emission source reduction on the basis of a 10-year period data. *Air Quality, Atmosphere & Health*, *8*(4), 379-389.
13. Stanišić Stojić, S., Stanišić, N., Stojić, A., and Šoštarić, A. 2016a. Single and combined effects of air pollutants on circulatory and respiratory system-related mortality in Belgrade, Serbia, Journal of Toxicology and Environmental Health, Part A 79, 17-27.
14. Stojić, A., Stojić, S. S., Reljin, I., Čabarkapa, M., Šoštarić, A., Perišić, M. and Mijić, Z. 2016. Comprehensive analysis of $PM_{10}$ in Belgrade urban area on the basis of long-term measurements. Environmental Science and Pollution Research 23, 10722-10732.
15. R Core Team, 2014. R: A language and environment for statistical computing. R Foundation for Statistical Computing, Vienna, Austria. http://www.R-project.org/.
16. Yokelson, R. J., Urbanski, S. P., Atlas, E. L., et. al, 2007. Emissions from forest fires near Mexico City. Atmospheric Chemistry and Physics 7, 5569-5584.

## 6.1. MULTISCALE MULTIFRACTAL ANALYSIS OF NONLINEARITY IN PARTICULATE MATTER TIME SERIES

**A. Stojić (1), S. Stanišić Stojić (2), M. Perišić (1), Z. Mijić (1)**

*(1) Institute of Physics, University of Belgrade, Belgrade, Serbia, (2) Faculty of Physical Chemistry, University of Belgrade, Belgrade, Serbia*

andreja.stojic@ipb.ac.rs

### ABSTRACT

In this study the multiscale multifractal method was used with aim of capturing the fractal behaviour of the particulate matter time series obtained from an urban area in Belgrade, Serbia, as well as investigating their persistence properties and heterogeneity features. As shown, the $PM_{2.5}$ time series exhibited persistency, slightly affected by the concentrations occurring randomly only at the level of small fluctuations and small scales. Compared to $PM_{2.5}$, $PM_{10}$ concentrations were shown to display more stochastic behaviour with more frequent random fluctuations being observed at small scales. The results herein presented contribute to the current understanding of the structural complexity of the temporal evolution of particulate matter and provide a theoretical background for enhanced air pollution modelling.

### INTRODUCTION

Comprehensive analyses, conducted over the past few years, of air pollutant emission sources, their subsequent distribution and relationship to mortality caused by circulatory, respiratory and malignant diseases suggest that the exposure to particulate matter (PM) has detrimental effects on human health in the Belgrade area (Stanišić Stojić et al, 2016a, 2016b). Besides the fact that PM levels in Serbia are higher than in most European cities, with a significant number of air quality standard exceedances, our studies have shown that suspended particles also contain high concentrations of carcinogenic contaminants, such as arsenic and benzo(a)pyrene (Stojić et al, 2015a, 2015b, 2016, Perišić et al, 2015, 2017).

Diverse methods have been implemented to provide relevant information for efficient air quality management, including deterministic models, statistical analysis, neural networks, fuzzy models, geographic information system, remote sensing and trend analysis (Yu et al, 2011). Multifractality is one of the inherent properties that can be recognized in physical, chemical, biological, social and other systems, that are described as very complex at different spatial and temporal scale levels (Glushkov et al, 2014). The atmosphere is a complex system that exhibits nonlinear behavior involving both deterministic and stochastic components (Lorenz and Haman, 1996). In previous studies, the multifractal approach has been applied to analyse average ozone concentrations (Kocak et al, 2000), nonlinearity in $NO_2$ and CO time series (Kumar et al, 2008) and the daily air pollution index (Sivakumar et al, 2007). The aim was to provide information essential to better understand the behaviour of pollution and to forecast the temporal evolution of the species (Dong et al, 2017). The multifractal method was used herein to reveal PM fluctuation properties, *i.e.* to investigate to what extent, and on which time scale, changes in $PM_{2.5}$ and $PM_{10}$ concentration levels can be considered random or persistent.

### METHODOLOGY

In this study, multiscale multifractal analysis (MMA) was used to investigate the presence of fractal behaviour in the complex time series of $PM_{2.5}$ and $PM_{10}$ concentrations. Data was obtained during a period of almost three years (2012-2014) of regular pollutant monitoring in Belgrade (suburban site Ovča, Longitude 20.528, Latitude 44.884, Serbia) provided by the Institute of Public Health Belgrade. MMA is a generalization of the standard multifractal detrended fluctuation analysis (MF-DFA), which adds the dependence on scale, providing a broader analysis of the fluctuation properties, as well as, more general and stable results (Gierałtowski et al, 2012).

### RESULTS AND DISCUSSION

Measured PM concentrations are presented in Figure 1. According to the results, multiscale multifractal derived Hurst surfaces confirmed the non-linear behavior of PM time series (Figure 2).

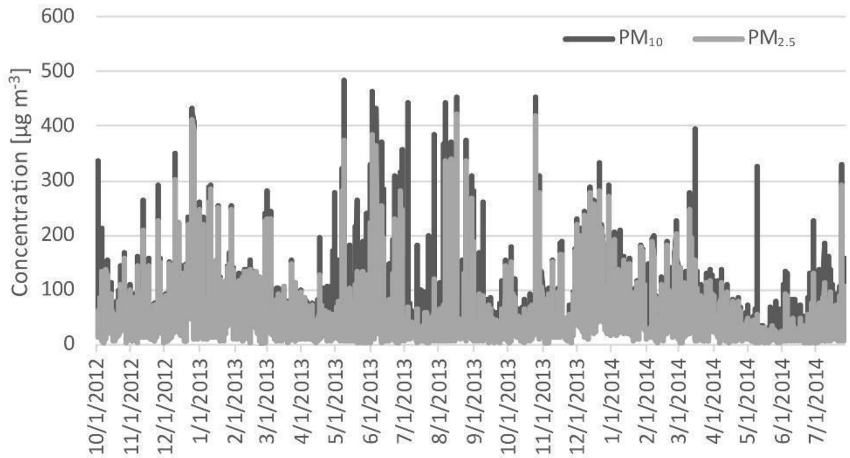


***Figure 1**. Measured $PM_{2.5}$ and $PM_{10}$ concentrations.*

For most of the scale and multifractal parameter values, the local Hurst exponent remains in the interval between 1 and 1.5 indicating persistency of the $PM_{2.5}$ time series, while slightly affected by the concentrations occurring randomly. Such random concentration values occur only at the level of small fluctuations for scales below 44, which corresponds to a period of about 2 days. At this scale, there emerges a clear crossover resulting from the different correlation properties. Given that the sampling site was not directly exposed to intense PM bursts, the occurrence of concentrations in narrow bands (Hurst exponent equals 2) was not recorded. The $PM_{10}$ Hurst surface reveals similar features, except that in the area of small variance and scales below 90, its growth to a maximum of approximately 1.9 is steeper, almost reaching black noise area values of local Hurst exponent. Compared to $PM_{2.5}$, the $PM_{10}$ Hurst structure around its maximum corresponds to visibly more pronounced peaks in the time series (Figure 1). However, unlike $PM_{2.5}$, the $PM_{10}$ Hurst surface shows no crossover.

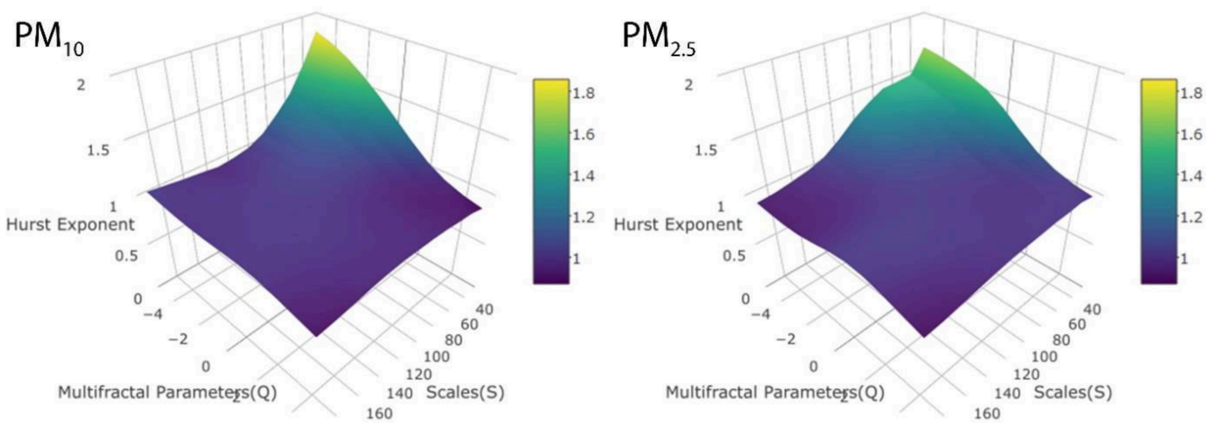


***Figure 2**. MMA derived particulate matter Hurst surfaces.*

In addition, the generalized distance coefficient (0.069) between Hurst surfaces of PM fractions is higher than the threshold value (0.065) and implies that the $PM_{2.5}$ and $PM_{10}$ time series must be considered statistically different. The difference is particularly pronounced in the area of small fluctuations and medium scales (Figure 3).

Furthermore, it is shown that the source of multifractality, examined by PM time series randomization, originates from both nonlinear correlations and a fat-tailed probability distribution (Figure 4).

The findings of Lalwani (2016) and Liu et al. (2015) confirmed the existence of multifractality in the PM time series and found that daily pollutant concentrations exhibited high persistence in a period of approximately one year. As argued, the persistence in the air pollutant concentrations over longer period of time may be governed by the impact of background levels, seasonal trend or intrinsic evolution of the system.

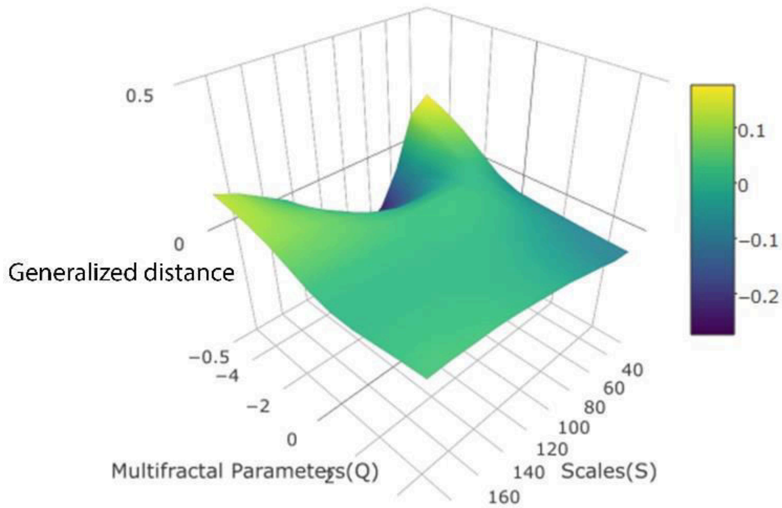


***Figure 3***. *Generalized $PM_{10}/PM_{2.5}$ Hurst surface distance.*

The difference in the behavior of the $PM_{2.5}$ and $PM_{10}$ time series was proven by Xue et al. (2015), who employed a multifractal analysis to explore temporal fluctuations and self-similarities within the PM time series and to understand their behaviour associated with diffusion, spreading and coagulation processes. Using the multifractal detrended fluctuation analysis method, the researchers registered the pronounced multifractality and long-term persistence of the $PM_{2.5}$ time-series, whereas the $PM_{10}$ time series were shown to have stochastic behaviour.

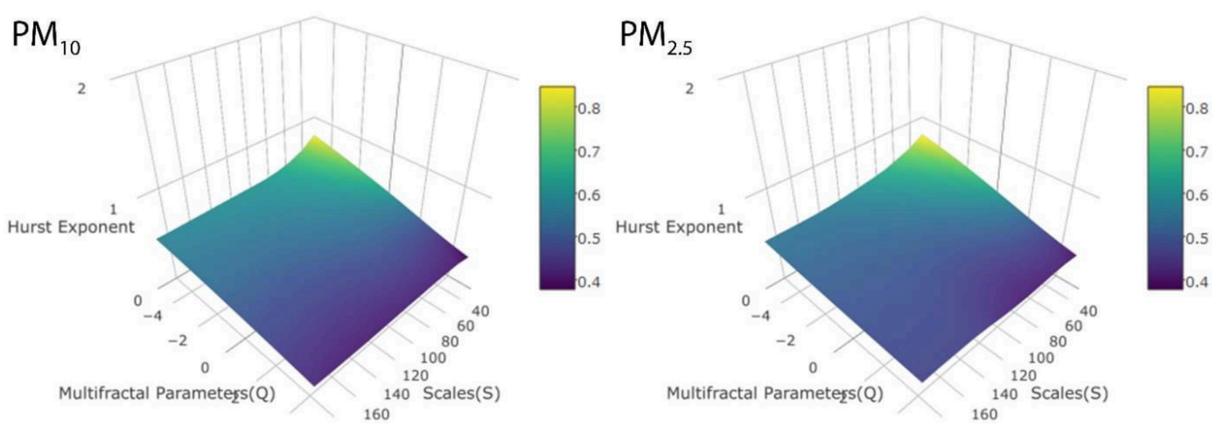


***Figure 4***. *MMA derived Hurst surfaces for randomized PM time series.*

**CONCLUSIONS**

In this study, the multifractal approach was used to analyse the temporal dynamics of $PM_{2.5}$ and $PM_{10}$ concentrations on the basis of a regular monitoring of data over a three-year period. As shown, the particulate matter time series possess a long-term memory of distant past events and require a large number of exponents, the so-called fractal dimensions, to be described. The presented analysis provides essential information for better understanding of the PM behaviour and the underlying factors, as well as for more accurate and reliable pollutant forecasting and efficient mitigation policy.


**ACKNOWLEDGEMENTS**

This study was performed as part of the projects Grant No III43007 and No III41011, which were supported by the Ministry of Education, Science and Technological Development of the Republic of Serbia within the framework of integrated and interdisciplinary research for the period 2011-2017. The publication was supported by the project GEO-CRADLE (Coordinating and integRating state-of-the-art Earth Observation Activities in the regions of North Africa, Middle East, and Balkans and Developing Links with GEO related initiatives towards GEOSS), Grant Agreement No. 690133, funded under European Union Horizon 2020 Programme - Topic: SC5-18b-2015, Integrating North African, Middle East and Balkan Earth Observation capacities in GEOSS.

## REFERENCES

1. Dong, Q., Wang, Y. and Li, P. 2017. Multifractal behaviour of an air pollutant time series and the relevance to the predictability, Environmental Pollution 222, 444-457.
2. Gierałtowski, J., Żebrowski, J. J. and Baranowski, R. 2012. Multiscale multifractal analysis of heart rate variability recordings with a large number of occurrences of arrhythmia, Physical Review E 85(2), 021915.
3. Glushkov, A. V., Svinarenko, A. A., Buyadzhi, V. V., Zaichko, P. A. and Ternovsky, V. B. 2014. Chaosgeometric attractor and quantum neural networks approach to simulation chaotic evolutionary dynamics during perception process, Advances in Neural Networks, Fuzzy Systems and Artificial Intelligence, Series: Recent Advances in Computer Engineering, Ed. J. Balicki. Gdansk, WSEAS Pub.
4. Koçak, K., Şaylan, L. and Şen, O. 2000. Nonlinear time series prediction of $O_3$ concentration in Istanbul, Atmospheric Environment 34(8), 1267-1271.
5. Kumar, U., Prakash, A. and Jain, V. K. 2008. Characterization of chaos in air pollutants: A Volterra-Wiener-Korenberg series and numerical titration approach, Atmospheric Environment 42(7), 1537-1551.
6. Lalwani, A. 2016. Long-Range Correlations in Air Quality Time Series: Effect of Differencing and Shuffling, Aerosol and Air Quality Research 16(9), 2302-2313.
7. Liu, Z., Wang, L. and Zhu, H. 2015. A time-scaling property of air pollution indices: a case study of Shanghai, China, Atmospheric Pollution Research 6(5), 886-892.
8. Lorenz, E. N. and Haman, K. 1996. The essence of chaos, Pure and Applied Geophysics 147(3), 598-599.
9. Sivakumar, B., Wallender, W. W., Horwath, W. R. and Mitchell, J. P. 2007. Nonlinear deterministic analysis of air pollution dynamics in a rural and agricultural setting, Advances in Complex Systems 10(04), 581-597.
10. Stojić, A., Stojić, S. S., Šoštarić, A., Ilić L., Mijić Z. and Rajšić S. 2015a. Characterization of VOC sources in an urban area based on PTR-MS measurements and receptor modelling, Environmental Science and Pollution Research 1-16.
11. Stojić, A., Stojić, S. S., Mijić, Z., Šoštarić, A. and Rajšić S. 2015b. Spatio-temporal distribution of VOC emissions in urban area based on receptor modelling, Atmospheric Environment 106, 71-79.
12. Stojić, A., Stojić, S. S., Reljin, I., Čabarkapa, M., Šoštarić, A., Perišić, M. and Mijić, Z. 2016. Comprehensive analysis of $PM_{10}$ in Belgrade urban area on the basis of long-term measurements, Environmental Science and Pollution Research 23(11), 10722-10732.
13. Stojić, S. S., Stanišić, N., Stojić, A., and Šoštarić, A. 2016a. Single and combined effects of air pollutants on circulatory and respiratory system-related mortality in Belgrade, Serbia, Journal of Toxicology and Environmental Health, Part A 79(1), 17-27.
14. Stojić, S. S., Stanišić, N., and Stojić, A. 2016b. Temperature-related mortality estimates after accounting for the cumulative effects of air pollution in an urban area, Environmental Health 15(1), 73.
15. Perišić, M., Stojić, A., Stojić, S. S., Šoštarić, A., Mijić, Z. and Rajšić, S. 2015. Estimation of required $PM_{10}$ emission source reduction on the basis of a 10-year period data, Air Quality, Atmosphere & Health 8(4), 379-389.
16. Perišić, M., Rajšić, S., Šoštarić, A., Mijić, Z. and Stojić, A. 2017. Levels of $PM_{10}$-bound species in Belgrade, Serbia: spatio-temporal distributions and related human health risk estimation, Air Quality, Atmosphere & Health 10(1), 93-103.
17. Xue, Y., Pan, W., Lu, W. Z. and He, H. D. 2015. Multifractal nature of particulate matters (PMs) in Hong Kong urban air, Science of the Total Environment 532, 744-751.
18. Yu, B., Huang, C., Liu, Z., Wang, H. and Wang, L. 2011. A chaotic analysis on air pollution index change over past 10 years in Lanzhou, Northwest China, Stochastic Environmental Research and Risk Assessment 25(5), 643-653.

CIP - Каталогизација у публикацији
Народна библиотека Србије, Београд

**502.3:502.175(082)**
**66.071.9(082)**
**613.15(082)**

**INTERNATIONAL WeBIOPATR Workshop Particulate Matter: Research and Management (6; 2017; Beograd)**

Proceedings [Elektronski izvor] /
The Sixth International WeBIOPATR Workshop & Conference
Particulate Matter: Research and Management, WeBIOPATR2017,
6-8 September 2017, Belgrade;
editors Milena Jovašević-Stojanović and Alena Bartoňová. –
Belgrade: Vinča Institute of Nuclear Sciences, 2019
(Belgrade: Vinča Institute of Nuclear Sciences). -
1 elektronski optički disk (CD-ROM); 12 cm

Sistemski zahtevi: Nisu navedeni. –
Nasl. sa naslovne strane dokumenta. -
Tiraž 150. –
Bibliografija uz svaki rad.

**ISBN 978-86-7306-152-8**

a) Ваздух - Контрола квалитета - Зборници

b) Отпадни гасови – Штетно дејство - Зборници

c) Здравље - Заштита - Зборници

**COBISS.SR-ID 278918412**

ISBN 978-86-7306-152-8

WeBIOPATR

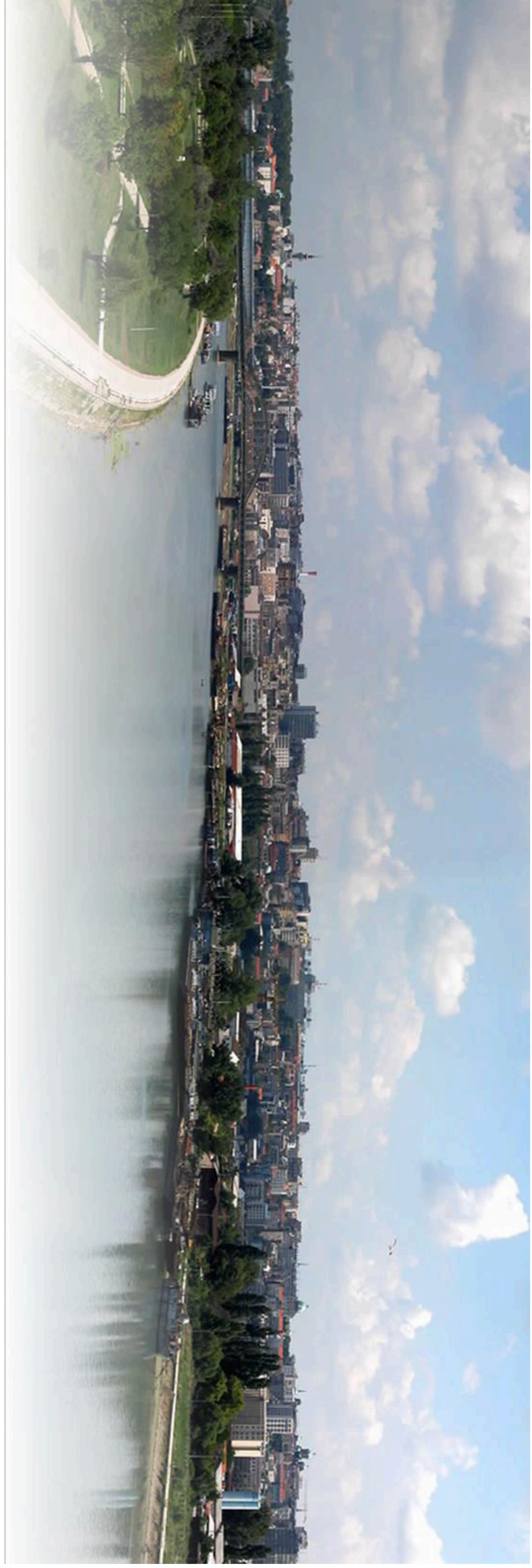

ПУБЛИКАЦИЈЕ АСТРОНОМСКОГ ДРУШТВА “РУЂЕР БОШКОВИЋ” Св. 20
PUBLICATIONS OF THE ASTRONOMICAL SOCIETY “RUDJER BOŠKOVIĆ” No. 20

# PROCEEDINGS
## OF THE XII SERBIAN-BULGARIAN ASTRONOMICAL CONFERENCE

**Sokobanja, Serbia, September 25-29, 2020**

**Eds. Luka Č. Popović, Vladimir A. Srećković, Milan S. Dimitrijević and Anđelka Kovačević**

SB 2020

**BELGRADE, 2020**

ПУБЛИКАЦИЈЕ АСТРОНОМСКОГ ДРУШТВА "РУЂЕР БОШКОВИЋ"
PUBLICATIONS OF THE ASTRONOMICAL SOCIETY "RUDJER BOŠKOVIĆ"

Св. 20 No. 20

# PROCEEDINGS OF THE XII SERBIAN-BULGARIAN ASTRONOMICAL CONFERENCE

**Sokobanja, Serbia, September 25-29, 2020**

**Eds. Luka Č. Popović, Vladimir A. Srećković,**

**Milan S. Dimitrijević and Anđelka Kovačević**

Б Е О Г Р А Д
2020

PUBL. ASTRON. SOC. "RUDJER BOŠKOVIĆ" No. 20, 1-192 BELGRADE, DECEMBER 2020

ORGANIZER:
Astronomical Observatory Belgrade, Serbia

Co-organizers:
Institute of Mathematics and Informatics - BAS, Sofia, Bulgaria
Institute of Physics Belgrade, Belgrade, Serbia
Faculty of Mathematics and Department of Astronomy, University of Belgrade, Serbia

Logo on the front cover: Saša Simić

Text arrangement by computer: Tatjana Milovanov


President of the Astronomical Society "Rudjer Bošković": Miodrag Dačić

Financially supported by the Ministry of Education, Science and Technological Development of Serbia

ISBN 978-86-89035-15-5

Production: Skripta Internacional, Mike Alasa 54, Beograd, in 100 copies

# CONTENTS

**Proceedings of the XII Serbian-Bulgarian Astronomical Conference**
**(XII SBAC) Sokobanja, Serbia, September 25-29, 2020**
**Editors: L. Č. Popović, V. A. Srećković, M. S. Dimitrijević and A. Kovačević**
**Publ. Astron. Soc. "Rudjer Bošković" No 20, 2020, 107-121**

# ACTIVITIES OF SERBIAN SCIENTISTS IN EUROPLANET

ALEKSANDRA NINA[1], MILAN RADOVANOVIĆ[2],
LUKA Č. POPOVIĆ[3], ANA ČERNOK[4], BRATISLAV P. MARINKOVIĆ[1],
VLADIMIR A. SREĆKOVIĆ[1], ANĐELKA KOVAČEVIĆ[5],
JELENA RADOVIĆ[6], VLADAN ČELEBONOVIĆ[1],
IVANA MILIĆ ŽITNIK[3], ZORAN MIJIĆ[1], NIKOLA VESELINOVIĆ[1],
ALEKSANDRA KOLARSKI[7] and ALENA ZDRAVKOVIĆ[8]

[1]*Institute of Physics Belgrade, University of Belgrade, Pregrevica 118, 11080 Belgrade, Serbia*
[2]*Geographical Institute Jovan Cvijić SASA, 11000 Belgrade, Serbia*
[3]*Astronomical Observatory, Volgina 7, 11060 Belgrade, Serbia*
[4]*Royal Ontario Museum, Center for the applied planetary mineralogy, Toronto, ON, Canada*
[5]*Department of astronomy, Faculty of Mathematics, University of Belgrade Studentski trg 16, 11000 Belgrade, Serbia*
[6]*Charles University, Faculty of Mathematics and Physics, Ke Karlovu 3, 12116, Prague 2*
[7]*Technical Faculty "Mihajlo Pupin", University of Novi Sad, 23000 Zrenjanin, Serbia*
[8]*Faculty of Mining and Geology, University of Belgrade, Belgrade*
E-mail: sandrast@ipb.ac.rs, bratislav.marinkovic@ipb.ac.rs, vlada@ipb.ac.rs, vladan@ipb.ac.rs, zoran.mijic@ipb.ac.rs, veselinovic@ipb.ac.rs
E-mail: m.radovanovic@gi.sanu.rs, lpopovic@aob.rs, ivana@aob.rs, acernok@rom.on.ca, andjelka@matf.bg.ac.rs, radovicj95@gmail.com, aleksandrakolarski@gmail.com, alena.zdravkovic@rgf.bg.ac.rs

**Abstract.** The Europlanet Society, an organization which promotes the advancement of European planetary science and related fields, has 10 hubs. The Serbian Europlanet Group (SEG) is included in the Europlanet South Eastern European Hub (ESEEH) and, currently, has 20 active scientists.

In this work, we present activities of SEG. Primarily, we describe two Europlanet workshops organized in the Petnica Science Center: "Geology and geophysics of the solar system bodies" and "Integrations of satellite and ground-based observations and multidisciplinarity in research and prediction of different types of hazards in Solar system" that occurred in 2018 and 2019, respectively, and the Europlanet session during XII Serbian-

Bulgarian Astronomical Conference that occurred in Sokobanja 2020. In addition, we present other activities that were primarily aimed at connecting SEG members coming from six institutions as well as the promotion of the Europlanet and ESEEH organizations.

## 1. INTRODUCTION

The Europlanet society is an organization which promotes the European planetary science and related fields. Its aims are to support the development of planetary science at a national and regional level, particularly in countries and areas that are currently under-represented within the community, and early career researchers who establish their network within the Europlanet: the Europlanet Early Career (EPEC) network (https://www.europlanet-society.org/early-careers-network/ ).

Two Europlanet projects (the Europlanet 2020 Research Infrastructure and the Europlanet 2024 Research Infrastructure (RI)) are funded through the European Commission's Horizon 2020 programme. The first one, lasting 4 years, ended 2020, while the second one runs for four years from February 2020 until January 2024. The latest is led by the University of Kent, UK, and has 53 beneficiary institutions from 21 countries in Europe and around the world, with a further 44 affiliated partners. It provides free access to the world's largest collection of planetary simulation and analysis facilities, data services and tools, a ground-based observational network and programme of community support activities.

The Europlanet consists of 10 Regional Hubs:

- Benelux
- Central Europe: Austria, Czech Republic, Hungary, Poland, Slovenia and Slovakia
- France
- Germany
- Ireland and UK
- Italy
- Northern Europe: Denmark, Estonia, Finland, Iceland, Latvia, Lithuania, Norway and Sweden
- Southeast Europe: Bulgaria, Croatia, Cyprus, Greece, Romania, and Serbia
- Spain and Portugal
- Switzerland

As one can see, Serbia is one of, current six countries included in the Southeast European Hub that is established in 2019.

More information about organization and activities of this society can be found at the website https://www.europlanet-society.org/.

## 2. SERBIAN EUROPLANET GROUP

The Serbian Europlanet Group (SEG) currently consists of 20 members from 6 institutions. Details of members and activities of SEG can be found at https://www.europlanet-society.org/europlanet-society/regional-hubs/southeast-europe/.

The main activities of Serbian scientists in the Europlanet were:
- Organization of two Europlanet meetings and one session,
- Establishing of SEG webpage,
- Participations in the Europlanet science congresses and meetings,
- Participations in the Europlanet NA1 Expert Exchange Program, and
- Participations in the Europlanet commities.

In this paper we describe these activities and present scientific research of SEG members related to the Europlanet fields.

## 3. EUROPLANET MEETING ORGANIZATIONS

Serbian scientist organized two Europlanet workshops in Petica Science Center near Valjevo in Serbia:
- "Geology and geophysics of the solar system bodies" (24 June– 1 July, 2018), and
- "Integrations of satellite and ground-based observations and multidisciplinarity in research and prediction of different types of hazards in the Solar system" (10-13 May, 2019),

and Europlanet session during the XII Serbian-Bulgarian Astronomical Conference (XII SBAC) in Sokobanja, Serbia 25-29 September, 2020.

### 3.1. Europlanet workshops

#### 3.1.1. Workshop in Geology and Geophysics of the Solar System

The workshop took place in Petnica Science Center, Petnica, Serbia (23 June – 1 July 2018) and further details can be found at http://petnica.rs/planetary2017. It was designed to cover a wide range of topics related to the formation, structure and dynamics of the Solar System and aimed to attract students and young researchers of various backgrounds and of different levels of experience in the fields of planetary sciences and space exploration. The workshop attended 43 participants, of which 24 PhD, 13 master and 6 undergraduate students. They were from 19 different home countries, including 15 from Eastern Europe, 3 from Russia and 4 from Northern Afrika. Other participants came from as far as India, Australia, and USA. The scientific organizers of the workshop were Dr. Katarina Miljkovic (Curtin University, Australia), Dr. Ana Cernok (The Open University, UK) and Dr. Matija Cuk (SETI Institute, USA), supported by the local organizers Dusan Pavlovic (Petnica Science Centre, Serbia) and Andrea Rajsic, deputy (University of Belgrade, Serbia). In total, there were 14 lecturers (7 female and 7 male). Although there was only one lecturer from a Serbian institution (University of Belgrade), there were 5 other lecturers (including the organizers) who were originally from Serbia. This planetary sciences workshop was supported by the Europlanet 2020 RI NA1 (Innovation through Science Networking) Task 5 (Coordination of ground-based observations) and Europlanet 2020 RI NA2 (Impact through outreach and engagement).

### 3.1.2. Workshop in Hazards in the Solar system

This workshop was focused on integrations of satellite and ground-based observations and multidisciplinarity in research and prediction of different types of hazards in the Solar system. The main of this meeting was connection of young researchers and scientists from under-represented countries, and experts in corresponding scientific fields. The organizer was the Geographical Institute "Jovan Cvijic" of Serbian Academy of Sciences and Arts. The chairs of the Scientific committee were Aleksandra Nina, Milan Radovanović from Serbia and Giovanni Nico from Italy. In this committee participated 11 scientists from 9 countries. Aleksandra Nina and Milan Radovanović were co-chairs, and Gorica Stanojević, Vladimir Čadež, Dejan Doljak, Vladimir Srećković and Dragoljub Štrbac were members of the Local Organizing Committee. The meeting attended 33 participants (of which 11 early career scientists) from 8 European countries: Bulgaria, Croatia, Greece, Hungary, Italy, Russia, Ukraine and Serbia. Their research fields relate to different theoretical and observation areas as well as to data sciences. In addition, two participants were from industry. This event was supported by the Europlanet 2020 RI NA1 - Innovation through Science Networking, Task 2: Scientific working groups (Europlanet 2020 RI has received funding from the European Union's Horizon 2020 research and innovation programme under grant No. 654208) and the Ministry for Education, Science and Technological Development of Republic of Serbia. More information about this event can be found at
http://www.gi.sanu.ac.rs/site/index.php/en/activities/conferences-organisation/998-hazards-sos.

### 3.3. Europlanet session organised by SEG

Serbian scientists organized a Europlanet session during XII Serbian-Bulgarian Astronomical Conference (SBAS 12) that was held in Sokobanja from 25-29 of September 2020 (see Popović et al. 2020). Several lectures were held, a discussion, as well as the report of work of our group in the previous period was presented. At this Europlanet special session and during SBAC 12, possible directions for expanding cooperation were discussed with Bulgarian colleagues and also with colleagues from Europlanet Southeast HUB countries.

### 3.4. Participations in the Europlanet Science Congresses

Serbian scientists participated at the Europlanet Science Congresses (EPSC). The number of participants from Serbia is increasing. 7 scientists from Serbia participated in the EPSC-2020 and presented 3 lectures.

**Figure 1:** Participants of the workshop “Integrations of satellite and ground-based observations and multidisciplinarity in research and prediction of different types of hazards in the Solar system” held in Petnica Science Center on 10-13 May, 2019 (photo: Veljko Vujičić). From left to right:
**Upper row:** Konstantinos Kourtidis (Greece) , Pál Gábor Vizi (Hungary), Jelena Petrović (Serbia), Anđelka Kovačević (Serbia), Duško Borka (Serbia), Gorica Stanojević (Serbia), Zorica Marinković (Serbia), Bratislav Marinković (Serbia) and Dejan Doljak (Serbia);
**Middle row:** Georgi Simeonov (Bulgaria), Inna Pulinets (Russia), Bozhidar Srebrov (Bulgaria), Dejan Vinković (Croatia), Yaroslav Vyklyuk (Ukraine), Pier Francesco Biagi (Italy), Aleksandra Kolarski (Serbia), Lelica Popović (Serbia), Nikola Veselinović (Serbia) and Zoran Mijić (Serbia);
**Bottom row:** Predrag Jovanović (Serbia), Vesna Borka Jovanović (Serbia), Sergey Pulinets (Russia), Milan Radovanović (Serbia), Aleksandra Nina (Serbia), Vladimir Srećković (Serbia), Giovanni Nico (Italy), Milan S. Dimitrijević (Serbia), Luka Č. Popović (Serbia), Nataša Todorović (Serbia), Slavica Malinović-Milićević (Serbia) and Dragoljub Štrbac (Serbia).

### 3.5. Participations in the Regional Hubs Meetings

On the 4$^{th}$ and 5$^{th}$ June 2019, in Hotel Gellért, Budapest the Regional Hubs Meeting was organized by Melinda Dósa from Wigner RCP with the presence of the representatives from the Europlanet Society, Benelux Hub (represented by Ann Carine Vandaele, vice-president of Europlanet Society), Central European Hub, France, Italy, Northern European Hub, Spain & Portugal and Southeast European Hub, in total there were 23 researchers present. After the participants introduced themselves, the talk by Anita Heward, communication officer, was given on the Role of the hubs in the Europlanet Society and building a sustainable future from Europlanet 2020 RI. Following discussion was about the importance of widen-ing.in Europlanet. The focus of the meeting was on Planetary science – technology – industry synergy: aims and possibilities & Towards a strategy definition. As a result of this meeting the participation and formal enrollment in Europlanet Society by Serbian researchers has been substantially increased.

### 3.6. Participation in the Europlanet NA1 Expert Exchange Program

Supported through the Europlanet NA1 Expert Exchange Program, Dr. Alena Zdravković, curator of the Mineral and Rock Collection of the Faculty of Mining and Geology in Belgrade, Serbia, visited The Open University in October 2017 to work with Dr. Ana Cernok and other experts in meteorite science. During this visit, six meteorite samples from the Marquis de Mauroy collection of the Mineral and Rock Collection (01. Lancon, 02. Bath, 03. Powder Mill Creek, 04.Morrisyown Hamblen, 05. Merceditas and 06. Hex River, with numbers representing a handing number at the Open University) were used for polished thin- and thick-section preparation at the Open University, Milton Keynes, UK. Lancon and Bath are fragmented chondrite meteorites, Powder Mill Creek and Morrisyown Hamblen are mesosiderites, and Merceditas and Hex River are iron meteorites. Since the meteorite samples belong to a very old collection, dating from 1899, due to inadequate equipment and unprecise preparation facilities in the laboratory of Faculty of Mining and Geology in Belgrade, those kind of samples were never used for utilizing cut and polishing preparations. This visit aimed at meteorite thin-section preparation was an important milestone for this Serbian collection. It was the first such opportunity to open and present the collection to an international scientific community. More importantly, those are the only thin sections of meteorite samples available at Belgrade University, and will therefore serve as precious teaching material for students educating, as well as for initiating meteorite research.

### 3.7. Participations in the Europlanet committees

As a member of the Southeastern European Hub Committee, Aleksandra Nina participated in two teleconferences and one meeting of the Selection committee for Europlanet funding.

### 3.8. Other activities

Lecture during XIX Serbian astronomical conference (19 SAC) held at the Serbian Academy of Sciences and Arts in Belgrade, from October 13 – 17, 2020 (see Kovačević et al. 2020).

## 4. SOME STUDIES OF SEG MEMBERS

SEG members are scientists in four research fields: astronomy, geophysics, physics and geography. Here we present a few research that are in Europlanet areas.

### 4.1. Astronomy

#### 4.1.1. The functional relation between mean motion resonances and Yarkovsky force on small eccentricities

We examined asteroid's motion with orbital eccentricity in the range (0.1, 0.2) across the 2-body mean motion resonance (MMRs) with Jupiter due to the Yarkovsky effect. We calculated time delays d*tr* caused by the resonance on the mobility of an asteroid with the Yarkovsky drift speed. We derived a functional relation that accurately describes dependence between the average time lead/lag d*tr*, the strength of the resonance *SR*, and the semimajor axis drift speed d*a*/d*t* with asteroids' orbital eccentricities in the range (0.1, 0.2). We analysed average values of d*tr* using this functional relation comparing with obtained values of d*tr* from the numerical integrations. On the basis of the obtained results and analyses, we conclude that our equation can be used for the 2-body MMRs with strengths in the range $[1.3\times10^{-8}, 2.2\times10^{-4}]$, for Yarkovsky drift speeds in the range $[2.6\times10^{-4}, 2\times10^{-3}]$ au/Myr and for asteroids' orbital eccentricities in the range (0.1, 0.2) (Milić Žitnik 2020a).

#### 4.1.2. The specific property of motion of resonant asteroids with very slow Yarkovsky drift speeds

We examined the specific characteristics of the motion of asteroids with very slow Yarkovsky drift speeds across the 2-body MMRs with Jupiter, whose strengths cover a wide range. It was found that the test asteroids with very small Yarkovsky drift speeds moved extremely rapidly across MMRs (order of magnitude $10^{-5}$ au/Myr or less). This result may indicate that, below a certain boundary value of d*a*/d*t* asteroids typically move quickly across MMRs. From the obtained results, it is concluded that the boundary value of the Yarkovsky drift speed is $7\times10^{-5}$ au/Myr (Milić Žitnik 2019).

### 4.1.3. The relationship between the 'limiting' Yarkovsky drift speed and asteroid families' Yarkovsky *V*-shape

We examined the relationship between asteroid families' *V*-shapes and the 'limiting' diameters in the ($a$, $1/D$) plane. Following the recently defined 'limiting' value of the Yarkovsky drift speed at $7\times10^{-5}$ au/Myr, we decided to investigate the relation between the asteroid family Yarkovsky *V*-shape and the 'limiting' Yarkovsky drift speed of asteroid's semi-major axes. We have used the known scaling formula to calculate the Yarkovsky drift speed in order to determine the inner and outer 'limiting' diameters (for the inner and outer *V*-shape borders) from the 'limiting' Yarkovsky drift speed. The method was applied to 11 asteroid families of different taxonomic classes, origin type and age, located throughout the Main Belt. Our main conclusion is that the 'breakpoints' in changing *V*-shape of the very old asteroid families, crossed by relatively strong MMRs on both sides very close to the parent body, are exactly the inverse of 'limiting' diameters in the a versus $1/D$ plane. This result uncovers a novel interesting property of asteroid families' Yarkovsky *V*-shapes (Milić Žitnik 2020b).

### 4.1.4. Improvement of modelling of atmospheres using A&M data

We continued to work on topics of modelling various atmospheres (using new software packages and supercomputers) and diagnostic of the astrophysical (terrestrial and space) and laboratory plasma using A&M datasets e.g. rate coefficients, Stark broadening parameters, line profiles (the shape of atomic spectral lines in plasmas contains information on the plasma parameters, and can be used as a diagnostic tool), etc. Results which are of interest for Europlanet community are presented in our recently published papers (see e.g. Ignjatović et al. 2019, Srećković et al. 2020, Majlinger et al. 2020, Dimitrijević et al. 2020) as well as in database MolD http://servo.aob.rs/mold (Marinković et al. 2019) hosted on SerVO at AOB.

### 4.1.5. Correlation of solar wind parameters with cosmic rays observed with ground station

It has been well known for more than half a century that solar activity has a strong influence on galactic cosmic ray (GCR) flux reaching Earth (anti-correlation). Coronal mass ejections (CMEs) structure and shockwave can additionally modulate GCRs, which could results in a transient decrease in observed GCR intensity, known as Forbush decrease (FD). These FDs can be detected even with ground muon detector (Savić et al. 2019). Variation of GCR can be analyzed correlating in situ measurement of the particles species present in solar wind with ground observations. Correlation between the 1-hour variations of GCR and several different one-hour averaged particle fluxes was found during FDs and it depends on energy of the particles of the solar wind as well as cut-off rigidities of secondary cosmic rays detectors on ground.

### 4.1.6. Habitability of exoplanets

Balbi, Hami and Kovačević (2020) present a new investigation of the habitability of the Milky Way bulge, that expands previous studies on the Galactic Habitable Zone. This work discusses existing knowledge on the abundance of planets in the bulge, metallicity and the possible frequency of rocky planets, orbital stability and encounters, and the possibility of planets around the central supermassive black hole. The paper focuses the two aspects that can present substantial differences with respect to the environment in the disk: (i) the ionizing radiation environment, due to the presence of the central black hole and to the highest rate of supernovae explosions and (ii) the efficiency of putative lithopanspermia mechanism for the diffusion of life between stellar systems. Authors devised analytical models of the star density in the bulge to provide estimates of the rate of catastrophic events and of the diffusion timescales for life over interstellar distances.

This article has been published as an invited contribution in the Special Issue "Frontiers of Astrobiology" edited by Manasvi Lingam.

Another concern for habitability is the presence of the supermassive black hole in the Galactic center, but also in nearby Active galactic nuclei, that could have resulted in a substantial flux of ionizing radiation during its past active phase, causing increased planetary atmospheric erosion and potentially harmful effects to surface life as shown by Wisłocka, Kovačević, Balbi (2019).

The goal of this paper is to improve our knowledge of the erosion of exoplanetary atmospheres through radiation from supermassive black holes (SMBHs) undergoing an active galactic nucleus (AGN) phase.

Authors extended the well-known energy-limited mass-loss model to include the case of radiation from AGNs. In the paper was calculated the possible atmospheric mass loss for 54 known exoplanets (of which 16 are hot Jupiters residing in the Galactic bulge and 38 are Earth-like planets, EPs) due to radiation from the Milky Way's (MW) central SMBH, Sagittarius A* (Sgr A*), and from a set of 107 220 AGNs generated using the 33 350 AGNs at z < 0.5 of the Sloan Digital Sky Survey database.

It was found that planets in the Galactic bulge might have lost up to several Earth atmospheres in mass during the AGN phase of Sgr A*, while the EPs are at a safe distance from Sgr A* (>7 kpc) and have not undergone any atmospheric erosion in their lifetimes. It was also found that the MW EPs might experience a mass loss up to 15 times the Mars atmosphere over a period of 50 Myr as the result of exposure to the cumulative extreme-UV flux FXUV from the AGNs up to z

= 0.5. This work was featured in famous *Forbes Magazine* in their section Innovation.

## 4.2. Geophysics

### 4.2.1. Investigation of a possible new type of lower ionosphere precursor of earthquakes

Analysis of the signal transmitted in Italy and received by the AbsPAL receiver in Belgrade in the period around the earthquake that occurred in the vicinity of Kraljevo on November 3, 2010 indicated a change in the amplitude of the signal less than an hour before this event. Although this change has not been reported in the literature, an additional study of several earthquakes indicates the existence of this change in other cases as well. The first study of this phenomenon is presented in Nina et al. (2020), and a broader statistical analysis is underway.

### 4.2.2. Modelling of solar X-ray flare influence on propagation of satellite signals

Due to the low electron density, the unperturbed D-region has practically no effect on the propagation of satellite signals. Therefore, it is generally not involved in modeling of signal propagation path or, if it is, its influence is given by analytical expressions based on observational data from higher altitudes. In Nina et al. (2020b), it is shown that during intense perturbations of this ionospheric layer due to the influence of solar X-ray flares (they do not perturb significantly higher ionospheric layers except when their intensity is very strong) it is necessary to include observational data for the D-region in modeling the propagation of satellite signals.

### 4.2.3. Satellite radar technique for atmospheric water vapor measurement and modelling effects of the ionospheric disturbances

Atmospheric water vapor measurement can be carried out in many different ways. One of the techniques for observing and measuring atmospheric water vapor is through satellite radars, precisely the Synthetic Aperture Radar (SAR) used and carried on the platform of many active satellites. In Radović (2020) are introduced four of such satellites and the water vapor modelling technique called SAR Interferometry is described as well. Along with the above mentioned in Radović (2020) it is demonstrated how neglecting the ionospheric disturbances that can occur during the satellite radar measurement of the water vapor can influence the modelling of certain parameters which are connected to the measured atmospheric water vapor.

#### 4.2.4. Remote sensing of the atmospheric aerosol

Atmospheric aerosol plays one of the most important roles in climate changes and environmental issues through direct (scattering and absorption of solar and terrestrial radiation) and indirect (modification of cloud condensation nuclei through aerosol-cloud interaction) effects. In Mijić and Perišić (2019), study the relationship between satellite aerosol optical depth (AOD) measurements by Moderate Resolution Imaging Spectroradiometer (MODIS) and PM (Particulate Matter) concentrations data set from the Belgrade region was investigated. The preliminary results showed that AOD retrieved from a satellite sensor can be considered as a good proxy for ground observed PM mass concentrations. Within the EARLINET (European Aerosol Research Lidar Network) network a stand-alone lidar-based method (Papagiannopoulos et al. 2020) for detecting airborne hazards for aviation in near real time (NRT) is developed. In addition, Belgrade lidar station has been involved in ESA ADM-Aeolus mission (the first high-spectral resolution lidar in space) Cal/Val activity through validation of L2A products of aerosol and cloud profiles of backscatter, extinction and lidar-ratio.

#### 4.2.5. Atmospheric disturbances due to severe stormy weather over Balkan region

Strong release of energy by atmospheric lightning discharges induced ionization changes along the propagation path of several Very Low Frequency (VLF) radio signals that had been received and recorded by Absolute Phase and Amplitude Logger (AbsPAL) system located in Belgrade (44.85$^{o}$ N, 20.38$^{o}$ E), at the Institute of Physics Belgrade, University of Belgrade, Serbia. Increased ionization is apparent in the perturbation of the signal amplitude and phase delay with respect to regular undisturbed ionospheric conditions. Integrated ground-based observations were performed with the aim to find coincidence and possible relationship between phenomena of VLF signal perturbations, optically documented Transient Luminous Events (TLEs) and documented lightning stroke events, during the stormy night of 27$^{th}$-28$^{th}$ of May, 2009. The survey enclosed data from three independent sources: 1) VLF signal records from Belgrade Institute for Physics database, 2) video records of sprite events from ITALIAN METEOR and TLE NETWORK (I.M.T.N.) database and 3) detected lightning strokes from European Cooperation for Lightning Detection (EUCLID) network database. In most cases, the correspondence between VLF perturbations and CG strokes and on the other hand, VLF perturbations and TLE events, was found. In some cases the correspondence between all three phenomena was found (Kolarski 2019, 2020).

### 4.3. Physics

**4.3.1.** V. Čelebonović has been working on the problem of impact craters on the surfaces of solid planetary and satellite bodies. He showed that using standard solid state physics and measured properties of the craters, one can derive various parameters of the impactors. The calculations were checked on several known examples, and the agreement is reasonable.
**4.3.2.** The role of electron induced dissociation in the comet's coma and the findings during Rosetta spacecraft mission have been the subject of investigation published in Marinković et al. (2017). Data needs for modelling electron processes in cometary coma and their influence on the interpretation of the observed data by Rosetta instruments, have been discussed together with the currently available data and databases, where BEAMDB (Belgrade Electron/Atom(Molecule) DataBase - http://servo.aob.rs/emol) is given as an example (Marinković et al. 2019).

### 4.4. Geography

**4.4.1.** Our research was devoted to the determination of the causal relationship between the flow of particles that are coming from the Sun and the hurricanes Irma, Jose, and Katia. As a result of the preliminary analysis, using 12,274,264 linear models by parallel calculations, six of them were chosen as best. The identified lags were the basis for refinement of models with the artificial neural networks. Multilayer perceptrons with back propagation and recurrent LSTM have been chosen as commonly used artificial neural networks. Comparison of the accuracy of both linear and artificial neural networks results confirmed the adequacy of these models and made it possible to take into account the dynamics of the solar wind. Sensitivity analysis has shown that F10.7 has the greatest impact on the wind speed of the hurricanes. Despite low sensitivity of pressure to change the parameters of the solar wind, their strong fluctuations can cause a sharp decrease in pressure, and therefore the appearance of hurricanes (Vyklyuk, et al. 2019).

**4.4.2.** Forest fires that occurred in Portugal on 18 June 2017 caused several tens of human casualties. The cause of their emergence, as well as many others that occurred in Western Europe at the same time remained unknown. Taking into account consequences, including loss of human lives and endangerment of ecosystem sustainability, discovering of the forest fires causes is the very significant question. The heliocentric hypothesis has indirectly been tested, according to which charged particles are a possible cause of forest fires. We must point out that it was not possible to verify whether in this specific case the particles by reaching the ground and burning the plant mass create the initial phase of the formation of the flame. Therefore, we have tried to determine whether during the critical period, i.e. from 15–19 June there is a certain statistical connection between certain parameters of the solar wind and meteorological elements. Based on the 2 hourly values of the charged particles flow, a correlation analysis was performed with hourly values of individual meteorological elements including time lag at Monte Real station. The application of the Adaptive Neuro Fuzzy Inference System models has shown that there is a high degree of connection between the flow of protons and the analysed meteorological elements in Portugal. However, further verification of this hypothesis requires further laboratory testing (Radovanović et al. 2019).

## 5. CONCLUSION

In this paper we present activities of Serbian scientists in the Europlanet. We describe two Europlanet workshops organized in the Petnica Science Center: "Geology and geophysics of the solar system bodies" and "Integrations of satellite and ground-based observations and multi-disciplinarity in research and prediction of different types of hazards in Solar system" that occurred in 2018 and 2019, respectively, and the Europlanet session during XII Serbian-Bulgarian Astronomical Conference that occurred in Sokobanja 2020. In addition, we present other activities that were primarily aimed at connecting SEG members coming from six institutions as well as the promotion of the Europlanet and ESEEH organizations. Several studies relevant for the Europlanet research fields are presented in the second part of this paper.

## Acknowledgments

This research is supported by the Europlanet. The authors acknowledge funding provided by the Institute of Physics Belgrade, Astronomical Observatory (the contract 451-03-68/2020-14/200002), Faculty of Mathematics University of Belgrade (the contract 451-03-68/2020-14/200104) through the grants by the Ministry of Education, Science, and Technological Development of the Republic of Serbia.

## References

Balbi A., Hami M., Kovačević A.: 2020, The Habitability of the Galactic Bulge, *Life*, 10, 132-145.

Čelebonović V.: 2020, The origin of impact craters, some ideas. *Bulg. Astron. J*, 33, 21.

Drimitrijević M. S., Srećković V. A., Ignjatović Lj. M., Marinković B. P.: 2021, The role of some collisional processes in AGNs: rate coefficients needed for modeling, *New Astronomy*, 84, 101529.

Ignjatović Lj. M., Srećković V. A., Dimitrijević M. S.: 2019. The collisional atomic processes of Rydberg alkali atoms in geo-cosmical plasmas. *Monthly Notices of the Royal Astronomical Society*, 483(3), 4202-4209.

Kolarski A.: 2019, *Atmospheric disturbances due to severe stormy weather*, Book of Abstracts, "Integrations of satellite and ground-based observations and multi-disciplinarity in research and prediction of different types of hazards in Solar system", Petnica, Science Center, May 10-13, 2019, Valjevo, Serbia, Geographical Institute "Jovan Cvijić" SASA, Belgrade, Serbia, p. 42.

Kolarski A.: 2020, *Storm activity over Balkan region during May 2009*, Book of Abstracts, “XII Serbian-Bulgarian Astronomical Conference (XII SBAC)” September 25-29, 2020, Sokobanja, Serbia, Astronomical Observatory, Belgrade, Serbia, p. 75.

Kovačević A., Kovačević Dojčinović A., Marčeta D., Onić D: 2020, Book of abstracts XIX Serbian Astronomical Conference October 13 - 17, 2020, Belgrade, Serbia.

Majlinger Z., Dimitrijević M. S., Srećković V. A.: 2020, Stark broadening of Co II spectral lines in hot stars and white dwarf spectra, *Monthly Notices of the Royal Astronomical Society*, 496(4), 5584-5590.

Marinković B. P., Bredehöft J. H., Vujčić V., Jevremović D., Mason N. J.: 2017, Rosetta Mission: Electron Scattering Cross Sections - Data Needs and Coverage in BEAMDB Database, *Atoms*, 5(4), 46 [18pp].

Marinković B. P., Srećković V. A., Vujčić V., Ivanović S., Uskoković N., Nešić M., Ignjatović Lj. M., Jevremović D., Dimitrijević M. S., Mason N. J.: 2019, BEAMDB and MOLD – Databases at the Serbian Virtual Observatory for collisional and radiative processes, *Atoms*, 7(1), 11 [14pp].

Mijić Z., Perišić M.: 2019, *Comparison of Modis aerosol observations and ground-based PM measurement for the Belgrade region*, Book of abstracts, “Integrations of satellite and ground-based observations and multi-disciplinarity in research and prediction of different types of hazards in Solar system”, pp.51-52, Petnica Science Center, 10-13 May, 2019, Geographical Institute "Jovan Cvijić" SASA, Belgrade.

Milić Žitnik I.: 2019, The specific property of motion of resonant asteroids with very slow Yarkovsky drift speeds, *MNRAS*, 486, 2435-2439.

Milić Žitnik I.: 2020a, The functional relation between mean motion resonances and the Yarkovsky force for small eccentricities, *MNRAS*, 498(3), 4465-4471.

Milić Žitnik I.: 2020b, The relationship between the 'limiting' Yarkovsky drift speed and asteroid families' Yarkovsky V-shapes, *SAJ*, 200, 25-41.

Nina A., Radovanović M., Srećković V. A.: 2019, Book of abstracts, “Integrations of satellite and ground-based observations and multi-disciplinarity in research and prediction of different types of hazards in Solar system”, Petnica Science Center, 10-13 May, 2019, Geographical Institute "Jovan Cvijić" SASA, Belgrade.

Nina A, Pulinets S., Biagi P. F., Nico G., Mitrović S. T., Radovanović M., Popović L. Č.: 2020a, *Sci. Total Environ*., 710, 136406.

Nina A., Nico G, Odalović O., Čadež M., V., Todorović Drakul M., Radovanović M., Popović L. Č.: 2020b, *IEEE Geosci. Remote Sens. Lett*., 17(7), 1198 – 1202.

Papagiannopoulos N., D'Amico G., Gialitaki A., Ajtai N., Alados-Arboledas L., Amodeo A., Amiridis V., Baars H., Balis D., Binietoglou I., Comerón A., Dionisi D., Falconieri A., Fréville P., Kampouri A., Mattis I., Mijić Z., Molero F., Papayannis A., Pappalardo G., Rodríguez-Gómez A., Solomos S., Mona L.: 2020, An EARLINET early warning system for atmospheric aerosol aviation hazards, *Atmos. Chem. Phys.*, 20, 10775–10789.

Popović L. Č., Srećković V. A., Dimitrijević M. S., Kovačević A.: 2020, *Book of Abstracts,* “XII Serbian-Bulgarian Astronomical Conference (XII SBAC)” September 25 - 29, 2020, Sokobanja, Serbia, Astronomical Observatory, Belgrade, Serbia

Radovanović M. M, Vyklyuk Y, Stevančević T, M, Milenković Đ. M, Jakovljević D, Petrović M, Malinović Milićević S, Vuković N, Vujko A, Yamashkin A, Sydor P, Vuković D, Škoda M.: 2019, Forest fires in Portugal — case study, 18 June 2017, *Thermal Science*, 23(1), 73-86.

Radović J.: 2020, *Satellite radar technique for atmospheric water vapor measurement and modelling effects of the ionospheric disturbances*, Master thesis, Faculty of Physics, University of Belgrade, Serbia.

Savić M., Veselinović N., Dragić A., Maletić D., Joković D., Banjanac R., Udovičić V.: 2019, Rigidity dependence of Forbush decreases in the energy region exceeding the sensitivity of neutron monitors, *Advances in Space Research*, 63(4), 1483-1489.

Srećković V. A., Dimitrijević M. S., Ignjatović Lj. M.: 2020, The influence of collisional-ionization and recombination processes on spectral line shapes in stellar atmospheres and in the hydrogen clouds in broad-line region of AGNs, *Contrib. Astron. Obs. Skalnaté Pleso*, 50, 171-178.

Vyklyuk Y, Radovanović M. M, Milovanović B, Milenković M, Petrović M, Doljak D, Malinovic Milićević S, Vuković N, Vujko A, Matsiuk N, Mukherjee S.: 2019, Space weather and hurricanes Irma, Jose and Katia, *Astrophys Space Sci,* 364, 154.

Wisłocka A. M., Kovačević A. B., Balbi A.: 2019, Comparative analysis of the influence of Sgr A* and nearby active galactic nuclei on the mass loss of known exoplanets, *Astron. Astrophys*., 624, A71 [17 pp].

**IV Meeting on Astrophysical Spectroscopy -**

**A&M DATA - Atmosphere**

May 30 to June 2, 2022, Fruška Gora, Serbia

# BOOK OF ABSTRACTS AND CONTRIBUTED PAPERS

**Edited by Vladimir A. Srećković, Milan S. Dimitrijević,**

**Nikola Veselinović and Nikola Cvetanović**

A&M DATA

UNIVERSITY OF BELGRADE
INSTITUTE OF PHYSICS | BELGRADE
NATIONAL INSTITUTE OF THE REPUBLIC OF SERBIA

Belgrade 2022

## Scientific Committee

Milan S. Dimitrijević, **Co-Chairman**
Vladimir A. Srećković, **Co-Chairman**

Nebil Ben Nessib, Saudi Arabia
Nikolay Bezuglov, Russia
Magdalena Christova, Bulgaria
Nikola Cvetanović, Serbia
Stevica Djurović, Serbia
Saša Dujko, Serbia
Rafik Hamdi, Tunisia
Darko Jevremović, Serbia
Bratislav Marinković, Serbia
Zoran Mijić, Serbia
Aleksandra Nina, Serbia
Bratislav Obradović, Serbia
Luka Č. Popović, Serbia
Branko Predojević, Republic of Srpska
Maja Rabasović, Serbia
Sylvie Sahal-Bréchot, France

## Local Organizing Committee

Vladimir A. Srećković (Chair), Institute of Physics Belgrade

Nikola Veselinović, Institute of Physics Belgrade
Lazar Gavanski, Faculty of Sciences – University of Novi Sad
Nataša Simić, Faculty of Sciences – University of Novi Sad
Veljko Vujčić, Astronomical Observatory, Belgrade
Radomir Banjanac, Institute of Physics Belgrade
Aleksandra Kolarski, Institute of Physics Belgrade
Milan S. Dimitrijević, Astronomical Observatory, Belgrade

## Organizers:

Institute of Physics Belgrade, Serbia,
Astronomical Observatory Belgrade, Serbia and
Faculty of Sciences – University of Novi Sad, Serbia

Text arrangement by computer: Tanja Milovanov

ISBN 978-86-82441-57-1



Financially supported by the Ministry of Education, Science and Technological Development of Serbia

Production: Skripta Internacional, Mike Alasa 54, Beograd in 50 copies

# Data analysis on Serbian participation in COST Actions: Celebrating 50 years of research networks

**Bratislav P. Marinković[a], Stefan Ivanović[b] and Zoran Mijić[c]**

*Institute of Physics Belgrade, Pregrevica 118, 11080 Belgrade, Serbia*
*[a]E-mail: bratislav.marinkovic@ipb.ac.rs Member of COST Committee of Senior Officials (CSO)*
*[b]E-mail: stefan.ivanovic992@gmail.com; data analyst*
*[c]E-mail: zoran.mijic@ipb.ac.rs; COST National Coordinator (CNC)*

## Abstract

Last year COST celebrated 50 years of the existence and successful networking activities. Although it does not finance the research itself, it already has become an inevitable part of each European country's community of researchers and innovators since it is devoted to both excellence and widening priorities of European Research Area. Here, we have briefly analyzed data of Serbian participation in COST Actions by tackling the issues of the rate and extent of involvement, presenting its interdisciplinary, organization of info-days and some success stories such as chairing the Actions.

## Introduction

The European Cooperation in Science and Technology (COST) is the oldest intergovernmental funding organization in Europe created in the year 1971 with the aim to establish the research networks among scientists and innovators across Europe. Among 19 founding countries at that time there was Yugoslavia, whose researchers took active role in projects called *Actions*. In 2001, June 7$^{th}$, Serbia (Federal Republic of Yugoslavia) rejoins COST and nowadays is one of 40 member countries together with one cooperating country that all form COST Association. Average number of countries participating in one Action was between 8 and 12 in the period of the first 20 years of COST establishment. Since then, this number is growing every year hitting the value of 31 and it is assumed to grow further in the forthcoming years (COST Brochure 2021).

COST organization experienced several transformations during its long history. It was established prior the start of Framework programs (FP), the first FP covering three years from 1984 to 1987. European Science Foundation, ESF, was an implementing agency via which EU financed COST organization from 2003

(Milutinović 2006). After the end of the 7th FP (2007-2013) and on the beginning of the Horizon 2020 (2014-2020), COST organization became COST Association, an entity functioning under Belgian law and directly financed by EU via Special Agreement. At the end of 2021 there were 289 running Actions, Serbian researchers participated in 93.8% (271) of them. In an Open Call for 2021 there were 22 638 proposers, among them 451 from Serbia, out of which 278 (61.6%) are female and 150 (33.3%) young researchers (COST Statistics 2021). They are called *secondary proposers* and they have a priority in the nomination for Management Committee (MC) of Action which has decision powers for governing of the COST Action in order to implement activities and manage the budget in the view of achieving the Action objectives.

Main decision body of COST Association is the COST Committee of Senior Officials (CSO) that forms the general assembly in which every country has two representative members. The COST National Coordinators (CNC) are the national contact points and they are responsible to appoint the national MC members to COST Actions. The COST Scientific Committee (SC) advises the COST Association about the Open Call, the procedures related to the submission, evaluation, and selection of proposals and it conducts the monitoring and final assessment of COST Actions. Serbian CNCs and CSO members were Prof. Dr Dragan Milutinović (2001-2006), Prof. Dr Biljana D. Stojanović (2006-2014), Prof. Dr Goran S. Đorđević (2014-2015), Dr Bratislav P. Marinković (2015-2021). At present Serbian CNC is Dr Zoran Mijić, CSO members are Dr B. P. Marinković and Ms Željka Dukić. Members of the SC are Prof. Dr Jovanka Lević (2013-2017) and Prof. Dr Viktor Nedović (2017-present).

**COST info-days and COST connect events**

A number of info-days have been organized in Serbia, where distinguished guests from COST have been participating, while the attendance of Serbian researchers always has been above 100 participants. These info-days have been always organized with the support of Ministry for Education, Science and Technological Development. The first info-day was organized by Prof. Dr Dragan Milutinović on 13th September 2001 with more than 300 participants. Mr Gösta Diehl, chairman of CSO, and Mr Erwin van Rij, head of COST Secretariat at the Commission of EU, visited "Vinča" institute and gave a presentation to an assembly of interested scientists at the Faculty of Mechanical Engineering (Milutinović 2006). On 14th March 2007 an info-day was organized by Prof. Dr. Biljana Stojanović (CNC and CSO member) and Ms Jasmina Milenković (CSO member). At this occasion a high delegation from COST was present: Prof. Dr Francesco Fedi, COST CSO President, Dr Martin Grabert, Director of COST office and Mr Peippo, Head of COST Secretariat-Council of the European Union. On September 2nd 2009 Prof. Dr Biljana Stojanović organized a seccesful info-day at which Prof. Dr. John G. Bartzis, Vice-President of CSO gave a lecture entitled

"COST: Past, Present and Future". On 25th March 2015, an info-day was organized with guests from COST, Dr. Ángeles Rodriguez-Peña, COST President and Ms Katalin Alföldi, Policy officer for excellence and inclusiveness of COST programme. The Serbian representation in 245 COST Actions within 9 Domains was summarized by Prof. Dr. Goran Đorđević, while the participant's experience was shared by Dr. Bratislav Marinković. During the info-day on 23rd March 2018 Acad. Sierd Cloetingh, COST President, Prof. Eva Kondorosi, Vice President of ERC and Chair of the Working Group on Widening European Participation, Mr Bart Veys, Policy officer and Mr Christer Halen, Policy administrator gave talks on COST, while Dr. Bratislav Marinković, Prof. Dr. Zorica Srdjević and Prof. Dr. Slobodan Cvejić presented Serbian experience in COST (https://mpn.gov.rs/vesti/u-rektoratu-univerziteta-u-beogradu-odrzan-cost-info-dan/ ).

On 10th October 2018 "COST Connect event" on *Sustainable Energy in the Danube Region* was held in Belgrade, organized by COST members Dr Ronald de Bruin, COST Director, Mr Bart Veys, Policy officer and Dr Elwin Reimink, Data and impact analysis officer, while the Serbian delegation was led by Prof. Dr Viktor Nedović, State secretary, Ms Željka Dukić, CSO member and Dr Bratislav Marinković, CNC and CSO member (https://mpn.gov.rs/vesti/u-beogradu-odrzana-konferencija-cost-connect/ ). COST Connect is a thematic event that brings COST Actions, policymakers and stakeholders together to exchange their ideas.

The info-day held on 29th March 2019 brought COST delegation (Dr Ronald de Bruin, Dr Elwin Reimink and Mr Christer Halen) in Belgrade. This info-day was combined with the presentations of Marie Skłodowska-Curie Actions, EURAXESS Serbia and EIT-Climate-KIC, European Institute of Innovation & Technology, while Serbian experience in COST was shared by Prof. Dr Bojan Blagojević from Faculty of Agriculture and Chair of COST Action CA18105 and by Dr Tijana Lainović from Medical Faculty, School of Dentistry, University of Novi Sad, MC member of COST Action CA16124. There was a large interest for this info-day at which 146 researchers participated.

**Chairing COST Actions**

The very first Chair of one COST Action was Prof. Dr Biljana Stojanović from the Institute for Multidisciplinary Research, University of Belgrade. She proposed the consorcium and chaired the Action 539 - Electroceramics from Nanopowders Produced by Innovative Methods (ELENA) which main objective was to improve the physical and electronic properties of advanced electroceramics and thick films produced by chemical, physical and mechanical synthesis techniques focusing on the polymeric precursors, sol-gel, spray pyrolysis, microemulsion, ultrasonic and freezedrying methods (Stojanović 2009). The Action started in 2005 and ended in 2009 with total number of 22 member and 6 non-COST countries involved. During the life of the Action there were organized 7 MC meetings, 11 working group (WG) meetings, 35 Short-term scientific missions (STMS), 7 Workshops and 2

Training Schools. More than 300 publications were published, while at the conferences more than 150 contributions were presented (Stojanović 2009).

During the first open call in 2018 the proposal by Prof. Dr Bojan Blagojević was successful and COST Action CA18105 - Risk-based meat inspection and integrated meat safety assurance (RIBMINS) was approved. The Action started in 2019 with the main aim to combine and strengthen European-wide research efforts on modern meat safety control systems. It will last till 2023, it is organized in 5 WG with researchers from 35 countries. This was the first time when Serbian institution holds a position of a Grant Holder.

The open call in 2019 was very productive, 3 of 45 Actions were approved in which the main proposer was from Serbia. Those Actions are: CA19110 - Plasma applications for smart and sustainable agriculture (PlAgri) with Dr Nevena Puač from the Institute of Physics Belgrade as a Chair; CA19128 Pan-European Network for Climate Adaptive Forest Restoration and Reforestation (PEN-CAFoRR) chaired by Prof Vladan Ivetić, Faculty of Forestry, University of Belgrade; CA19135 Connecting Education and Research Communities for an Innovative Resource Aware Society (CERCIRAS) chaired by Dr Gordana Rakić, Faculty of Sciences, University of Novi Sad. These Actions started in 2020 and will last 4 years.

The open call in 2020 brought one chairing position for Serbian scientist. It is the Action CA20108 FAIR NEtwork of micrometeorological measurements (FAIRNESS) proposed by Dr Branislava Lalić from Faculty of Agriculture, University of Novi Sad. The action intends to improve standardization and integration between databases/sets of micrometeorological measurements that are part of research projects or local/regional observational networks established for special purposes (agrometeorology, urban microclimate monitoring).

**Success stories highlighted in the booklet on COST 50 years**

One of the COST success stories is the Action TD1308 - Origins and evolution of life on Earth and in the Universe (ORIGINS). Prof. Didier Queloz, a member of this Action received Nobel prize in Physics in 2019 for discovery of 'an exoplanet orbiting a solar-type star'. Serbian representatives in this Action that lasted from May 2014 till May 2018 were Prof. Dr Zorica Svirčev from University of Novi Sad, Faculty of Sciences and Dr Branislav Vukotić from Astronomical Observatory Belgrade.

In the special edition of COST booklet "*50 years of research networks*" (COST Brochure 2021) an article named "Doors Opening Across Europe Thanks to Tree Talk" highlights the research of Prof. Dr Saša Orlović, at the Faculty of Agriculture and Head of the Institute of Lowland Forestry and Environment at the University of Novi Sad and Dr Dejan Stojanović, also at the Institute of Lowland Forestry and Environment. In the article it has been pointed out how cross border collaboration is helping scientists in Serbia to open the doors of cooperation with their colleagues around Europe. Prof. Dr Saša Orlović is a very active participant in COST Actions, being either MC member or MC substitue in nine past Actions (E42, E47, E52, FP0903, FP1106, FP1201, FP1204, ES1308, FP1403) and two running Actions (CA18134 and CA18201).

A testimony by Goran Tmušić, PhD student and research assistant at the Faculty of Sciences of the University of Novi Sad has been recorded by mentioning his experience as a participant of the COST Action CA16219 - *Harmonization of UAS techniques for agricultural and natural ecosystems monitoring* (https://50years.cost.eu/stories/goran-tmusic/ ). Member of MC of the Action CA16219 are Prof. Dr. Jasna Plavšić from the Faculty of Civil Engineering, University of Belgrade and Dr. Jugoslav Joković from the Faculty of Electronic Engineering, University of Niš.

The statement of Dr Ana Milojević from the Faculty of Political Sciences, University of Belgrade was posted at the COST website on the occasion of 50 years celebration: “All COST Actions are about getting people together. I collaborated with many excellent scholars, which I believe is one of the strongest points of COST”. Dr Ana Milojević is MC member of CA17132 and MC substitute of IS1308 Action.

**Analysis of Serbian participation in COST Actions**

Involvement of Serbian researchers in COST Actions is constantly increasing as well as their share of total COST budget that is covering their activities. In 2020, Serbia participated in 270 Actions out of 291 Actions running at any time of the year (92.8%). In 2020, a total of 243 participants from Serbia were reimbursed by COST for their participation in COST Action networking activities (meetings, STSM, Training Schools) and our share in relation to the total budget of the Actions was 4.8% (in 2018 and 2019 these shares were 3.6%). In 2020, 58 participants from Serbia were involved in STSM, 34 trainees and 5 trainers were involved in Training Schools. There were also 12 Conference Grant participants from Serbia. In 2020, 45% of the participants from Serbia in networking activities holding a PhD were Early Career Investigators (ECI up to 8 years after obtaining PhD), while the average for all COST countries was 25% (COST Statistics 2021). However, the absolute figures for 2020 when compared to 2019 are significantly lower what is the consequence of covid-19 pandemic situation that reflected strongly on network activities.

Currently we are undergoing the statistical analysis of Serbian participation in COST Actions trying to achieve the how many of Serbian researchers and innovators have been participating in COST, how many of them have been in MC or at some other leading positions such as vice-chairs, WG leaders, STSM, grant awarding or science communication coordinators and Grant holder representatives.

The Actions that were approved in 2014 and before were distributed across different domains, each domain was covered by domain committee which could approve certain number of Actions in proportion of the number of proposals. On the 163$^{rd}$ CSO meeting in Reading, UK, in November 2005 a decision of major restructuring of COST was taken. From June 2006 till 2014 there were 9 domains: Biomedicine and Molecular Biosciences (BMBS), Chemistry and Molecular Sciences and Technologies (CMST), Earth System Science and Environmental Management (ESSEM), Food and Agriculture (FA), Forests, their Products and Services (FPS), Information & Communication Technologies (ICT), Individuals, Society, Culture and Health (ISCH), Materials, Physical and Nanosciences (MPNS), Transport and Urban Development (TUD) and one Transdisciplinary Domain (TD). At that time, Serbia country rate participation in COST Actions was 21.9% out of 228 running Actions any time of the year (Annual Report 2006). The participation rates were 30.6% (of 222) (Annual Report 2007), 33.2% (out of 238) (Annual Report 2008), 32.2% (out of 255) in 2007, 2008 and 2009, respectively. In 2010 the percentage was 42% (Annual Report 2010). Participation of Serbian researchers was gradually but thoroughly increasing during the years: 50% of 301 Actions in 2012; 56% of 349 in 2013; 66% of 370 in 2014; 74% of 347 in 2015; 81% of 352 in 2016; 83% of 339 in 2017; 89% of 291 in 2018 and 92% of 292 in 2019 (COST Statistics 2020).

**Interdisciplinary in COST research**

Analysis of interdisciplinary of COST Actions is carried out in the view of 6 main OECD scientific fields, each field consists of several subfields. It covers the Actions from the period of open calls 2015-1 till the 2020-1. The summary result is given in Fig. 1. On the graph the first columns in blue represent data from the 7 open calls (2015-2018) while the second columns in grey are those from all 9 open calls (2015-2020). The methodology of representing data is the same as presented in (Marinković 2019). In every Memorandum of Understanding (MoU) it is mandatory to state to which scientific field and subfield the Action belongs to. Those data have been aggregated for each open call and results have been presented by the SC and COST data analysts. If the degree of interdisciplinarity of the proposals have been measured based on the key expertise defined in OECD Fields of Science and Technology (OECD DSTI/EAS/STP/NESTI(2006)19/ FINAL Document, 2007) selected by the main proposers when submitting the proposal, then the results show that almost half of all proposals are interdisciplinary, covering two, three or more disciplines. This interdisciplinary degree persists in COST open calls.

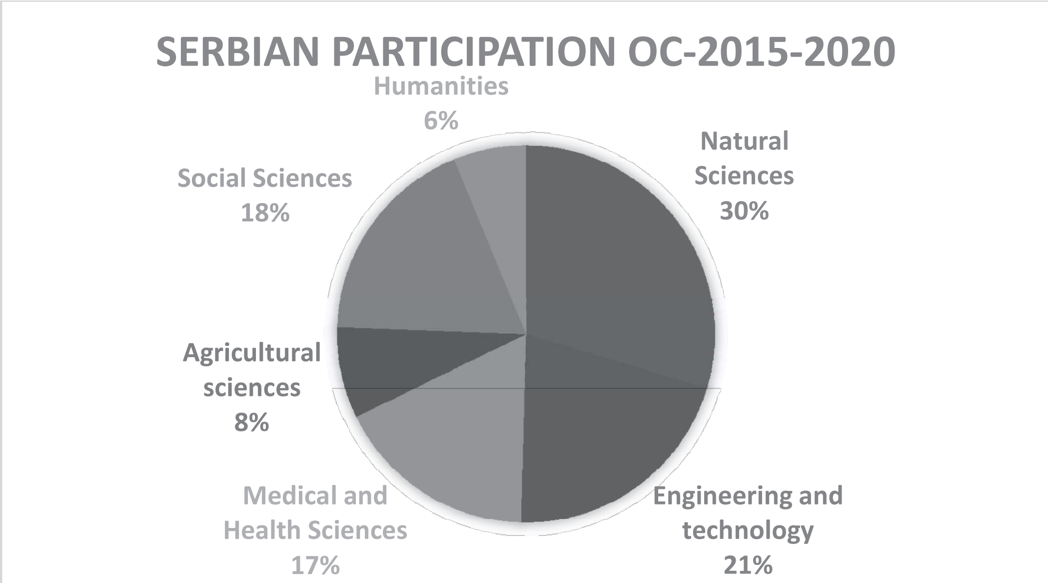


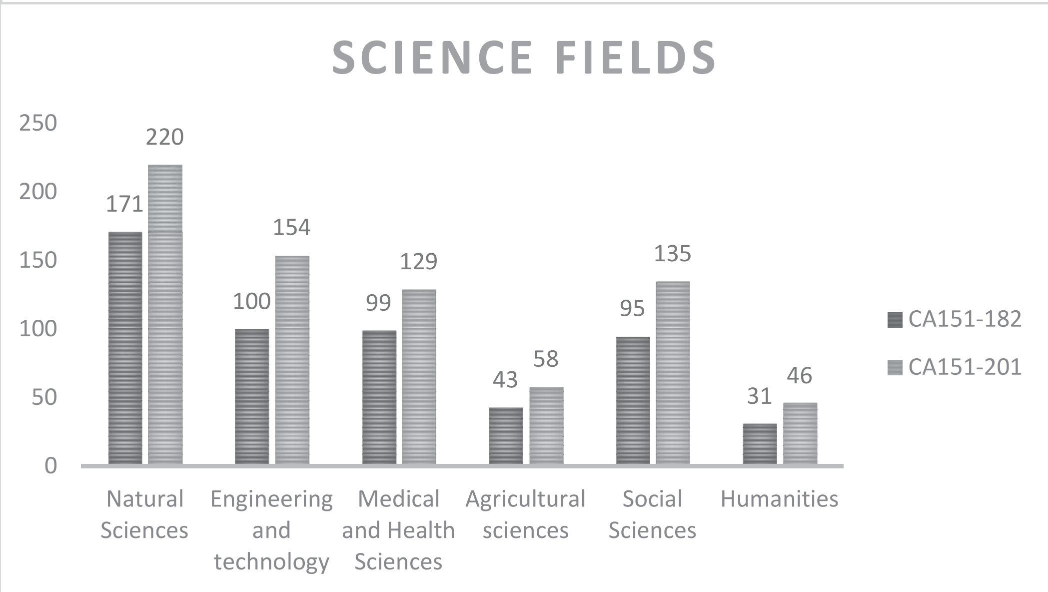


Fig. 1. Distribution of 6 main OECD scientific fields among Serbian research community in period 2015-2020: a) percentages; b) numbers in the first columns (blue) represent data from the 7 open calls (2015-2018), while the second columns (grey) are those from all 9 open calls (2015-2020).

**Conclusions**

Serbian participation in COST activities is significantly growing. We are taking part almost in all new Actions, e.g., in 39 out of 40 Actions launched in the latest open call OC-2020-1. That is showing the versatility of Serbian science and also its incorporation into European Research Area (ERA). But it also shows that there are not enough national programs and calls that support research community. During covid-19 pandemic time (years 2020 and 2021) many traditional ways of research have changed and been transformed to adopt more distant access to facilities and networking. Also COST, on April 2021, launched new Virtual Networking Tools (VTNs) with two novel instruments, the Virtual Networking Support (VNS) Grant in order to stimulate virtual collaboration among the members of a COST Action, and the Virtual Mobility (VM) Grant(s) for strengthening the individual activities. The rules and principles related to the submission, running and monitoring COST Actions have been recently simplified together with the guidelines for COST Action Proposal Submission, Evaluation, Selection and Approval documentation (COST Documents and Guidelines 2022). Accordingly, the national rules for joining and proposing new Actions have changed. All changes have been presented at the national COST webpages (http://mail.ipb.ac.rs/~ncc-serbia/). The procedure for applying for the MC position can be finished by direct upload of the required documents via dedicated link (https://survey.ipb.ac.rs/index.php/666713?lang=sr). The great challenge is ahead our COST and research and innovation community to make a participation in new 70 Actions that are envisaged to be approved at the end of May 2022, together with the new 70 Actions within newest call OC-2022-1 that will be closed on 22nd October 2022. On the same time, it will be a great opportunity for Serbian science to be more extensively integrated in ERA.

**Acknowledgments**

Author thanks Profs. Drs Dragan Milutinović, Biljana Stojanović, Goran Đorđević and Ms Željka Dukić for useful comments and providing us with the relevant documentation. Thanks are due to the Ministry of Education, Science and Technological Development of the Republic of Serbia.

**References**

Annual Report, 2006, COST Association
Annual Report, 2007, COST Association
Annual Report, 2008, COST Association
Annual Report, 2010, COST Association
COST Brochure, 2021, 50 years of research networks, COST Association https://www.cost.eu/uploads/2021/05/COST_50-years_brochure-210503.pdf
COST Statistics, 2020, Serbia - Participation in COST Activities: Overview 2012-2019, COST Association
COST Documents and Guidelines, 2022, COST Association https://www.cost.eu/funding/documents-guidelines/
COST Statistics, 2021, Serbia - Participation in COST Activities: Overview 2020, COST Association

Marinković, B. P., 2019, "COST Actions as a wide network of researchers and innovators across Europe", Proc. The Seventh Conference on Information Theory and Complex Systems (TINKOS 2019), Belgrade 15-16 October 2019, Book of Abstracts, Eds. Ilić, V. and Mitrović Dankulov, M. (Mathematical Institute of the SASA and Institute of Physics Belgrade, University of Belgrade, Belgrade, 2019)

Milutinović, D., 2006, Report of the National COST Coordinator for the p eriod July 2001 to July 2006

OECD DSTI/EAS/STP/NESTI(2006)19/FINAL Document, 2007, Revised field of science and technology (FOS) classification in the Frascati Manual: https://www.oecd.org/sti/inno/38235147.pdf

Stojanović, B.D., 2009, COST Action 539 - Final Evaluation Report - Electroceramics from Nanopowders Produced by Innovative Methods (ELENA) 2005-2009 https://www.cost.eu/actions/539/

# Statistics of Management Committee Members from Serbia in COST Actions

**Zoran R. Mijić[1] and Bratislav P. Marinković[2]**

*Institute of Physics Belgrade, Pregrevica 118, 11080 Belgrade, Serbia*
*[1]E-mail: zoran.mijic@ipb.ac.rs COST National Coordinator (CNC)*
*[2]E-mail: bratislav.marinkovic@ipb.ac.rs Member of COST Committee of Senior Officials (CSO)*

## Abstract

COST (European Cooperation in Science and Technology) provides researchers and innovators access to the top scientific and technology networks in Europe and beyond. In order to increase Europe's capacity to solve scientific, technical, and social concerns it connects academics and innovators by providing funding for excellence-driven and multidisciplinary pan-European networks (COST Actions). Each Action is managed by a Management Committee composed of COST Member representatives. In this paper the basic analysis of Serbian representatives in active COST Actions is presented.

## Introduction

COST Actions are open, bottom-up networks of researchers and innovators that facilitate pan-European collaboration in a range of scientific and technological domains (Marinković, 2019). COST Action proposals are evaluated on the basis of excellence and can be submitted via an open call procedure. Participants at various stages of their careers collaborate in a field of science and technology of mutual interest to at least seven COST Full Members. The number of countries per Action has increased by 27% in the last seven years, mostly as a result of more Inclusiveness Target Countries (ITCs) joining COST Actions.

COST Action is managed by a Management Committee (Action MC) composed of Action MC Members (COST documents guideline, 2021). The COST National Coordinators (CNCs) is the national contact point in the COST Member responsible for the nomination in the Action MC. The selection of maxima two MC members per Action representing the COST Member state is based on national rules and procedures. Following the good practice, the consultation from Action Main Proposer/Chair prior nomination of MC is required to ensure that the profile of the proposed Action MC Member matches the aims and objectives of the COST Action and, where possible, brings diversity and interdisciplinarity in the Action MC.

An Action starts officially on the date of the first Action MC meeting (MC1) that should take place not earlier than 4 months and not later than 9 months after COST Committee of Senior Officials (CSO - main decision body of COST Association) approval.

Before the start of the Action, nominated persons will automatically become Action MC Members, but after the Action MC1 meeting, new Action MC Members must be validated by the Action MC. Validation occurs implicitly, that is, without any action on the part of the Action MC. An Action MC decision, on the other hand, might clearly approve or reject the nomination. The refusal must be supported by a formal reason submitted within four weeks of the nomination. If no express rejection decision is made within four weeks following nomination, the nomination is confirmed (Annotated Rules for COST actions, 2021).

The Action MC Members should actively participate to the work of at least one Working Group (WG) and represent their COST Member community in order to coordinate the input to the Action and disseminate opportunities arising within the Action at national level. The basic information and data related to the Serbian representatives in active Actions are presented below.

**Statistics of MC members from Serbia**

The official data obtained by COST Association in May 2022 provide the information on nomination and MC member's statistics for all COST Members (COST statistics, 2022). Fig 1. depicts the average days needed for MC member nomination (for Action secondary proposers) after the official CSO approval. Serbia, with 61 days needed for nomination, is in the middle range with respect to all other countries.

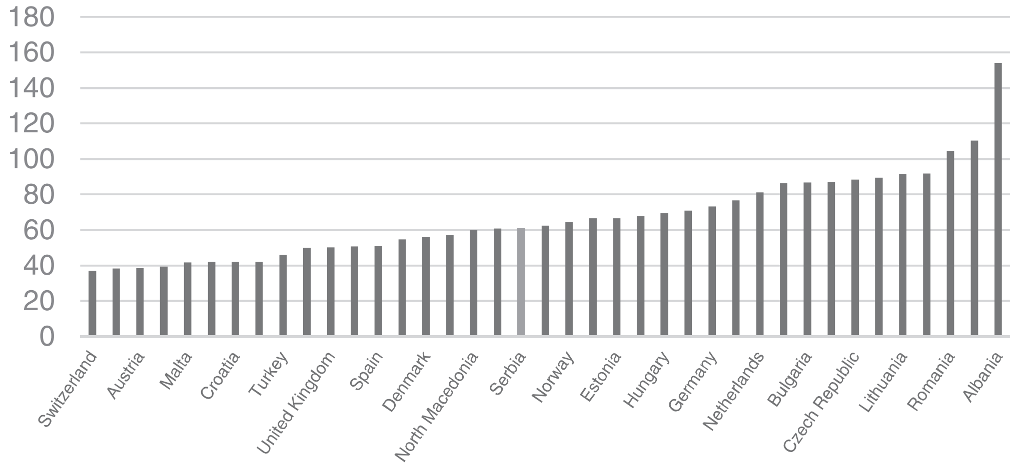


Fig. 1. Days between CSO approval and MC delegate nomination for Actions proposers.

On the other hand 123 days in average is needed for nominations of non-secondary proposers (Fig 2.) indicating the necessity to improve the information sharing on new Actions approval and promotion of benefits for non-secondary proposers to join COST Actions.

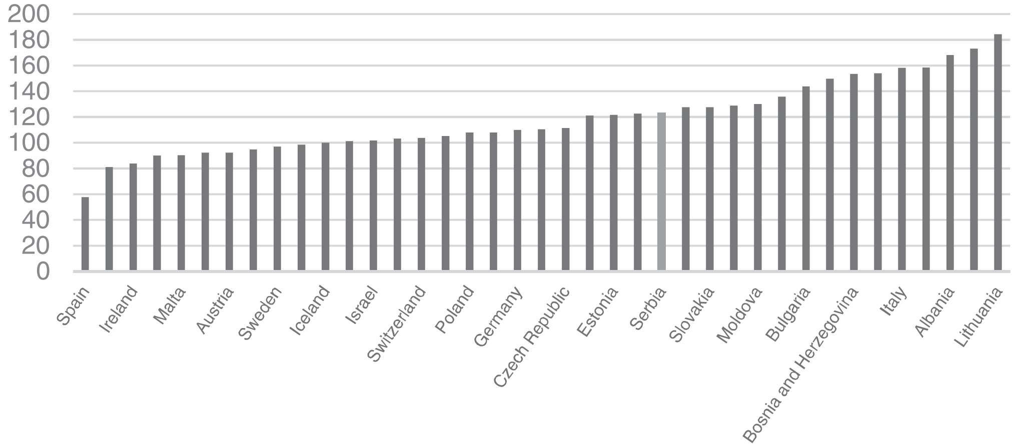


Fig. 2. Days between CSO approval and MC delegate nomination for Actions non-proposers.

The percentage of the nominated MC members at least 1 month before the MC1 meeting is 88.2% for secondary proposers (Fig. 3) and 52.6% for non-proposers (Fig. 4).

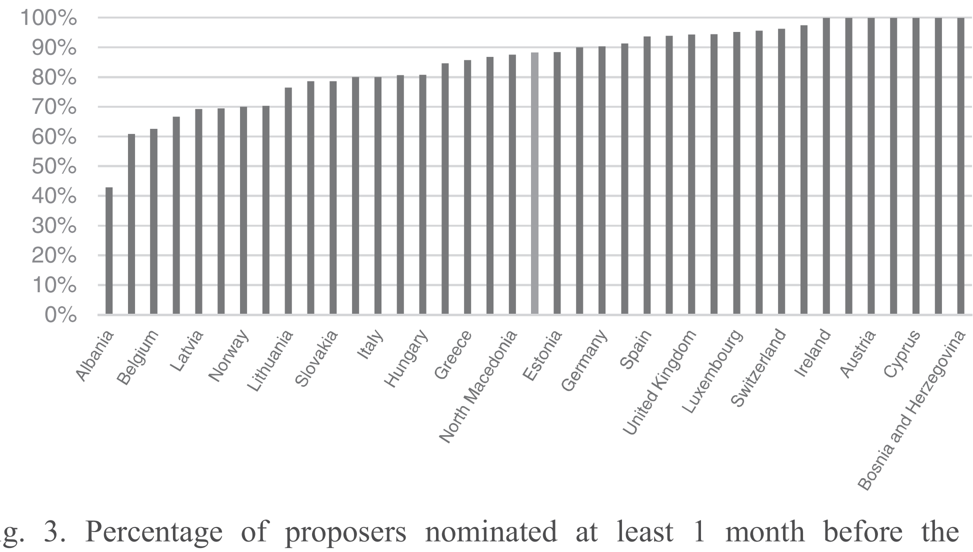


Fig. 3. Percentage of proposers nominated at least 1 month before the first Management Committee meeting.

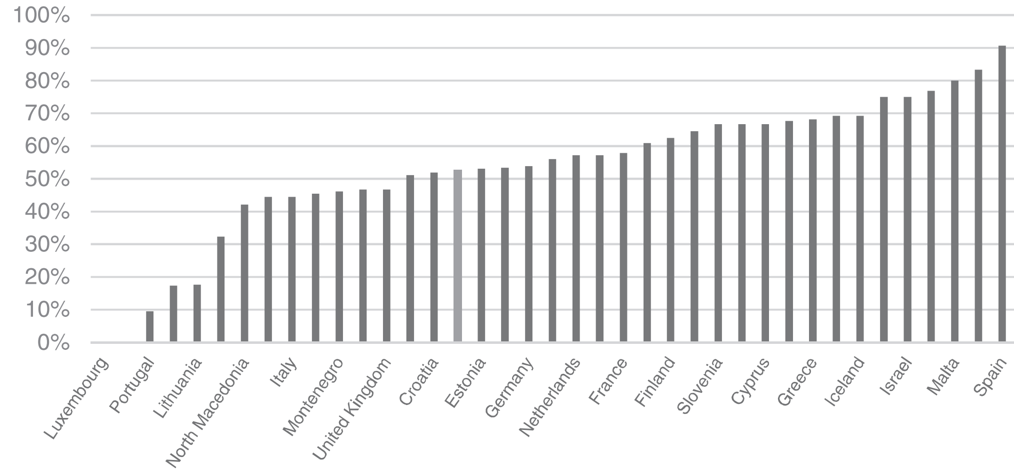


Fig. 4. Percentage of non-proposers nominated at least 1 month before the first Management Committee meeting.

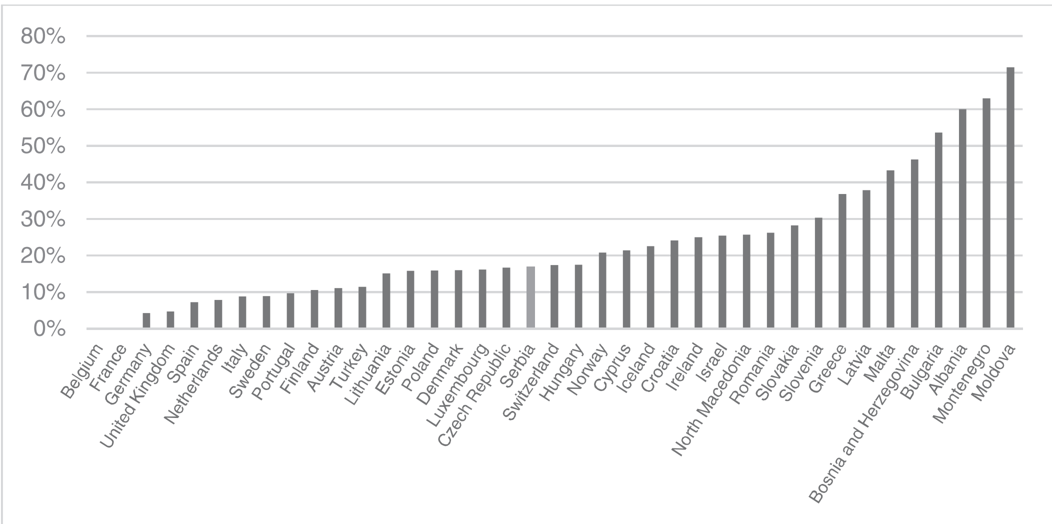


Fig. 5. Percentage of nominated MC Members already active in another Action.

According to the national rule one researcher can participate as MC Member in two active Actions. Such restriction aims to stimulate researcher, especially younger researchers coming from wider scientific community, for joining COST activities by taking one of the leading positions. As a result 16.9% of nominated MC Members are already active in another Action (Fig. 5) allowing pretty high opportunity for other researcher to take an active role. Equal access to leadership positions, notably with regard to empowerment of young researchers and innovators (researcher or innovator under the age of 40) is one of the key component of The Openness and Inclusiveness COST Principle (The COST Mission, 2021). Serbia, with 46.5% relative mobilization of younger researchers is the leading country in this domain.

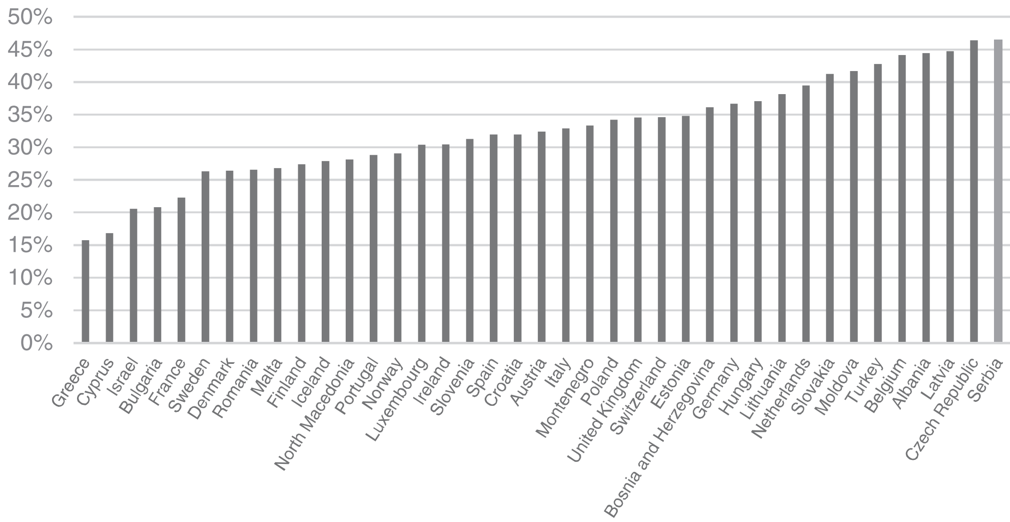


Fig. 6. Relative mobilization of younger researchers.

In addition, gender balance is regarded as an important component of COST's aim to being open and accessible to all categories of researchers. It is consistently emphasized as an essential aspect for COST Actions while organizing their activities. 54.9% of MC members from Serbia are females showing that Serbia reaches pretty fair gender balance (Fig. 7).

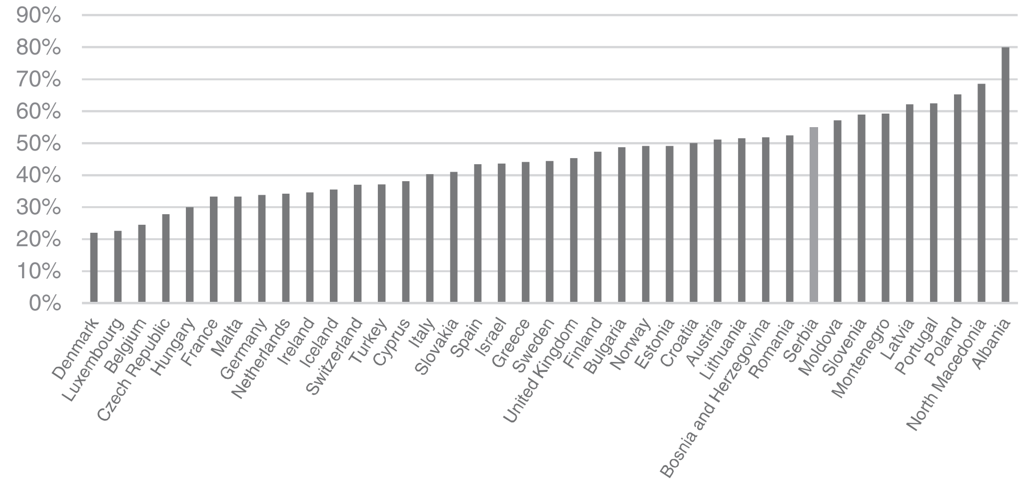


Fig. 7. Percentage of female MC Members.

## Conclusions

COST Association provides nomination and MC statistics annually for each country participating in active Actions. Since the nomination procedure and collaborative potential for joining COST Actions are specific for each country there are no common target values which should be achieved, but rather recommendations. The obtained parameters should be useful for national COST office and CNC as indicators what kind of the procedures could be improved in order to attract more participants assuring effective networking activities. Although MC members from Serbia have already significant involvement in COST Actions, national COST office constantly works on improvement of the national nomination procedures. Dedicated national web site and online application form (Serbian COST office, 2022) is expected to further accelerate and facilitate the MC nomination procedure.

## Acknowledgments

Thanks are due to The Ministry of Education, Science and Technological Development of the Republic of Serbia and the Institute of Physics Belgrade for national COST office support.

## References

Annotated Rules for COST actions (Level C – COST Actions), 2021, available at https://www.cost.eu/uploads/2022/02/COST-094-21-Annotated-Rules-for-COST-Actions-Level-C-2022-02-15.pdf

COST documents guidelines 2021, available a https://www.cost.eu/funding/documents-guidelines/

COST Statistics - Serbia - Participation in COST Activities, Overview 2021 (May 2022).

Marinković, B. P., 2019, "COST Actions as a wide network of researchers and innovators across Europe", Proc. The Seventh Conference on Information Theory and Complex Systems (TINKOS 2019), Belgrade 15-16 October 2019, Book of Abstracts, Eds. Ilić, V. and Mitrović Dankulov, M., Mathematical Institute of the SASA and Institute of Physics Belgrade, University of Belgrade, Serbia

Serbian COST office, 2022, national website available at http://mail.ipb.ac.rs/~ncc-serbia/

The COST Mission, 2021, available at https://www.cost.eu/about/cost-mission/

UNIVERSITY "UNION - NIKOLA TESLA"

Nikola Tesla

# THE SECOND INTERNATIONAL CONFERENCE ON SUSTAINABLE ENVIRONMENT AND TECHNOLOGIES

# PROCEEDINGS

"Creating sustainable commUNITy"

INTERNATIONAL CONFERENCE ON SUSTAINABLE ENVIRONMENT AND TECHNOLOGIES

23-24 SEPTEMBER 2022

CARA DUŠANA 62-64, BELGRADE, SERBIA

UNIVERSITY "UNION - NIKOLA TESLA"

THE SECOND INTERNATIONAL CONFERENCE ON
SUSTAINABLE ENVIRONMENT AND TECHNOLOGIES

# PROCEEDINGS

23-24 SEPTEMBER 2022
CARA DUSANA 62-64,BELGRADE,SERBIA

## PARTNERS:

"GRADITELJ INŽENJERING" D.O.O.

UNIVERSITY OF PRIŠTINA, KOSOVSKA MITROVICA

INSTITUTE OF MINING AND METALLURGY

FACULTY OF SCIENCES AND MATHEMATICS IN KOSOVSKA MITROVICA

INSTITUTE OF AGRICULTURAL ECONOMICS

PETROLEUM-GAS UNIVERSITY OF PLOIEŞTI, ROMANIA

INSTITUTE FOR PROTECTION AND ECOLOGY OF THE REPUBLIC OF SRPSKA (IPERS)

SERBIAN WATER PROTECTION SOCIETY

The Secend International Conference on Sustainable Environment and Technologies

*“Creating sustainable commUNiTy”*

**Organizer of the Conference:** University „Union Nikola Tesla”, Belgrad, Serbia

**Editors:**

Ph.D Sanja Mrazovac Kurilić

Ph.D Ljiljana Nikolić Bujanović

**Publisher:** University „Union-Nikola Tesla”, Belgrade, Serbia

**For publisher:**

Ph.D Nebojša Zakić

**Design:**

MSc. Arh. Dunja Bujanović

Mateja Đurić, student

**Printed in:** Dobrotoljublje, Belgrade

**ISSBN 978-86-89529-38-8**

Conference is financially supported by
The Ministry of Education, Science and Technological
Development of the Republic of Serbia

## ORGANIZING COMMITTEE

PHD LJILJANA NIKOLIĆ BUJANOVIĆ
PHD SANJA MRAZOVAC KURILIĆ
PHD SLOBODAN ANĐELKOVIĆ
PHD NATAŠA SIMIĆ
PHD MARINA BUGARČIĆ
DRAGANA DUDIĆ
OLJA KRČADINAC

## SCIENTIFIC COMMITTEE („UNION-NIKOLA TESLA“)

PHD NEBOJŠA ZAKIĆ
PHD LJILJANA NIKOLIĆ BUJANOVIĆ
PHD SANJA MRAZOVAC KURILIĆ
PHD MARINA MILOVANOVIĆ
PHD DEJAN BELJAKOVIĆ
PHD ALEKSANDAR MILAJIĆ
PHD TATJANA KOSIĆ
PHD DARINKA GOLUBOVIĆ –MATIĆ
PHD DRAGANA VASILSKI
PHD MIŠA STOJADINOVIĆ
PHD IVAN PETROVIĆ
PHD JUGOSLAV ANIČIĆ
PHD VESNA PETROVIĆ
PHD JASMINA PERIŠIĆ
PHD VIOLETA CIBULIĆ
PHD RUŽICA BOGDANOVIĆ

## INTERNATIONAL SCIENTIFIC COMMITTEE

PHD PIETRO ELISEI - ITALY
PHD ANDREY VLADIMIROVICH BARANOV - RUSSIA
PHD ТАТЬЯНА ЛОХОВА - RUSSIA
PHD AMELA JERIČEVIĆ- CROATIA
PHD GORAN GAŠPARAC- CROATIA
PHD SANJA KAPELJ - CROATIA
PHD PREDRAG ILIĆ - BOSNIA AND HERZEGOVINA
PHD SUZANA GOTOVAC ATLAGIĆ - BOSNIA AND HERZEGOVINA
PHD HEIDI HUNTREISER - GERMANY
PHD ANKE ROIGER - GERMANY
PHD MIRJANA VOJINOVIĆ MILORADOV - SERBIA
PHD ANJA JOKIĆ- SERBIA
PHD GORDANA GOJGIĆ CVIJOVIĆ - SERBIA
PHD ZORAN NIKIĆ- SERBIA
PHD BENIAMINO MURGANTE - ITALY
PHD SONJA RADOVIĆ JELOVAC – MONTENEGRO
PHD ALEKSANDAR PAVIĆ- UNITED KINGDOM
PHD FERID SKOPLJAK - BOSNIA AND HERZEGOVINA
PHD MAJA ROSO POPOVAC - BOSNIA AND HERZEGOVINA
PHD ZORAN CEKIĆ – SERBIA
PHD SINIŠA TRKULJA –SERBIA
PHD SRĐAN REDŽEPAGIĆ – FRANCE
PHD LIDIJA STEFANOVSKA – NORTH MACEDONIA
PHD SONJA LEPITKOVA – NORTH MACEDONIA
PHD JAKA VADNJAL- SLOVENIA
PHD JASMINA STARC – SLOVENIA
PHD FRANC VIDIC – SLOVENIA
PHD JEAN VASILE ANDREI – ROMANIA
PHD JONEL SUBIĆ- SERBIA
PHD BRANKO LATINOVIĆ- BOSNIA AND HERZEGOVINA
PHD ŽELJKO STANKOVIĆ- SERBIA

# LIST OF CONTENT

## *PLENARY LECTURES*



## *LECTURES*

# A NEW MODELING METHOD FOR DETERMINING PLASMA PARAMETERS IN THE LOW IONOSPHERE UNDER X-RAY RADIATION

**Desanka M. Šulić [1]*, Vladimir A. Srećković [2] and Z. Mijić [2]**

[1] University Union – Nikola Tesla, 11000 Belgrade, Serbia
[2] Institute of Physics Belgrade, University of Belgrade, Pregrevica 118, 11080 Belgrade, Serbia

vlada@ipb.ac.rs

## Abstract

Intense radiation can generate additional ionization in the Earth's atmosphere and change its structure. This extreme solar radiation and activity create sudden ionospheric disturbances and consequently affect electronic equipment on the ground and signals from space, potentially induce various natural disasters and influence on sustainable development. The aim of this work is to present our study, on few examples, of sudden ionospheric disturbances induced by the large solar flares. All data are recorded by VLF Belgrade station systems and the model computation is used to obtain the daytime atmosphere parameters induced by this extreme solar radiation. We analyzed in details physics of the D-region during consecutive huge solar flares which continuously perturbed this layer. We give perturbed ionospheric D-region simple approximative formula for electron density.

**Keywords:** observations; solar radiation; Sun activity; atmosphere; disturbances; dataset; modeling, sustainable development

## INTRODUCTION

In today's science, special attention is paid to the extreme weather events, climate change, preservation and protection, because they have been identified as important for sustainable development in our century. Consequently, a very important question nowadays in modern society is - can we predict the magnitude of impact of explosive solar events (such as solar flares) on Earth, humans, electronic equipment and on nature generally. This question is difficult and complex, and the answer is not so simple. By analysis we cannot with certainty predict the event itself but we can statistically estimate the consequences of these explosive events on ionospheric parameters, perhaps predict dam-age to electronic equipment, predict disruption of GPS, etc.

Ionosphere as a huge segment of atmosphere has a tendency to be constantly separated in different regions D, E, and F, with different physical characteristics and chemistry (Brasseur & Solomon, 2005; Mitra, 1974; Nicolet & Aikin, 1960) which depend on incident radiation. At the time of solar flares and consequently during sudden ionospheric disturbances (SID) events the increase of the ionospheric electron concentration at all altitudes is noticeable. As a result of radiation effects, the solar-induced SID and plasma irregularities causes perturbations in the received amplitude and phase of Very Low Frequency (VLF in narrow band 3 -30 kHz) radio signals - in narrow band 3 -30 kHz- mainly in the D region which is located between the Earth's lower atmosphere with dense air and its strongly conducting ionosphere. Nowadays, special attention is paid to the extreme weather events, climate change, preservation and protection, because they have been identified as important for sustainable development in our century. Consequently, a very important question in modern society is can we predict the magnitude of impact of explosive solar events such as solar flares on the Earth, humans, electronic equipment and on nature generally and can we estimate the consequence of these catastrophic events?

In this contribution we focus on amplitude and phase data of worldwide transmitters of radio signals recorded by Belgrade VLF stations (Scherrer et al., 2008; Šulić & Srećković, 2014).VLF signals from the emitters located all over the world are constantly recoded by this equipment. Events of X-ray solar flares monitored by GOES satellites are further identified using radio stations system of receivers. For these events, VLF wave enhancements are measured and analyzed for the daytime atmosphere. Our research aims to improve the knowledge on the importance of extreme events and space weather for the overall sustainable development.

## RESULTS

In this research we have studied the amplitude ($A$) and phase ($P$) data, obtained by monitoring VLF radio signals emitted by worldwide transmitters during solar-induced SIDs. All the data were registered by receiver systems at a Belgrade site. The receivers can simultaneously record several signals emitted by different emitters (located at different countries and territories) at the fixed frequencies. The time resolution of the recorded data can be in range from 0.001

to 1 s, which is applicable for detection of various SIDs from very short-term disturbances lasting several ms to very long perturbation. The technicalities and description of the Belgrade site are presented in (Šulić & Srećković, 2014).

Here we present the study of sudden ionospheric disturbances induced by the large flares. The monitoring and investigation of VLF data has been carried out simultaneously with the examination of the correlative incoming solar X-ray fluxes collected from Geostationary Operational Environmental Satellite (GOES) (Garcia, 1994). For our study the most important are registered data of incoming solar radiation X-ray flux in the XRS band of 0.1-0.8 nm.

In the presence of SIDs, a standard numerical procedure for the estimation of plasma parameters is based on comparison of the recorded changes of amplitude and phase with the matching values acquired in simulations by the Long-Wave Propagation Capability (LWPC) numerical software package (Ferguson, 1998) as explained in (Nina, Čadež, Srećković, & Šulić, 2012; Nina, Čadež, Šulić, Srećković, & Žigman, 2012; Šulić, Srećković, & Mihajlov, 2016).

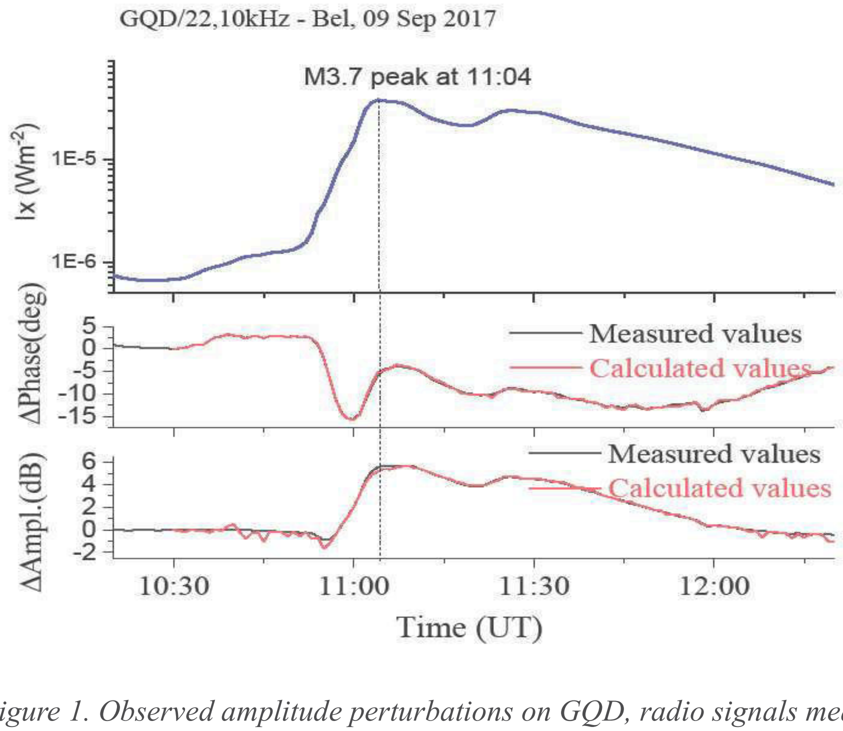


*Figure 1. Observed amplitude perturbations on GQD, radio signals measured at Belgrade and calculated one. (middle panel) Observed and calculated phase perturbations. (lower panel) Time variation of X-ray irradiance measured by GOES-15 satellite on 09 Sep 2017. Simultaneous variations of X-ray flux, delta amplitude and phase of GQD/22.10 signal against universal time during occurrence of M3.7 class solar flare on 09 Sep 2017 (upper panel)*

M3.7 class SF occurred on 09 Sep 2017 is an illustrative example of long lasting intense solar radiation (~ 60 min) which induced SID and caused variation in VLF signal. Also, this example is good for showing the methodology of our analysis. In Figure 1 is presented simultaneous variations of X-ray flux, amplitude and phase of GQD/22.10 kHz signals against universal time during occurrence of M3.7 class SF on 09 Sep 2017. Lower panel shows observed amplitude perturbations on GQD, radio signals measured at Belgrade station with calculated values (red line), and in the middle panel there are presented observed and calculated phase perturbations (red line). Time variation of X-ray flux measured by GOES-15 satellite on 09 Sep 2017 is on the upper panel. One can see that shapes VLF signal parameters are stretched and similar to the shape of the X-ray flux.

The daytime exponential profile of electron density in general use for VLF modeling (Wait and Spies, 1964) is given by:

$$N_e(h,H',\beta) = 1.43\cdot 10^{13}\exp(-0.15\cdot H')\exp[(\beta-0.15)\cdot(h-H')] \quad \mathrm{m}^{-3} \quad (1)$$

where $\beta$ in km$^{-1}$ is time-dependent parameters of sharpness and *H'* a reference height in km. Here *Ne (h,H',β)* and *h* are given in m$^{-3}$ and km, respectively. Electron densities can be obtained from the observed amplitude and phase perturbations by a trial-and-error method where the density profile is adjusted until the simulated amplitude and phase (using LWPC code) match with observed data. In this way, the obtained Wait's parameters $\beta$ and *H'* can be used in Equation (1) for further simulations.

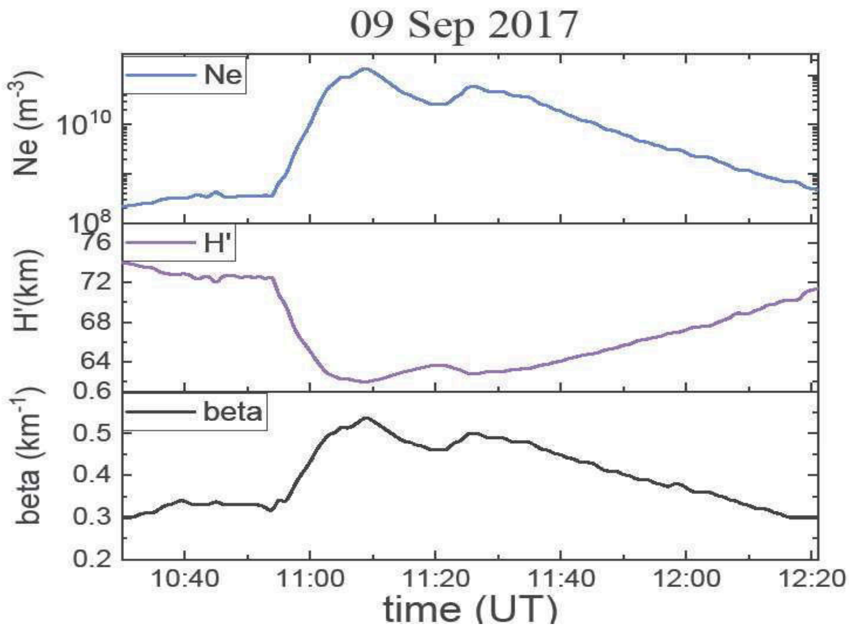


*Figure 2. Effective reflection height H', the sharpness β and electron density at reference height h=74 km during occurrences of M3.7 class solar flare on 09 Sep 2017 from lower to upper panel, respectively.*

In Figure 2 calculated parameters are shown: time dependent effective reflection height H', sharpness β and electron density at reference height during occurrences of M3.7 class solar flare on 09 Sep 2017 from lower to upper panel, respectively.

**Approximative expressions:**

To enable the better and more adequate use of data, we give electron density results obtained using simple and accurate fitting formula based on a least-squares method, which is logarithmic and represented by a second-degree polynomial with height dependent coefficients a1(h), a2(h), a3(h):

$$\log Ne(h, Ix) = \mathrm{a}_1(h) + \mathrm{a}_2(h) \cdot \log Ix + \mathrm{a}_3(h) \cdot (\log Ix)^2 \qquad (2)$$

Here Ix is solar X-ray flux ($Wm^{-2}$), and h is height (km).

Figure 3 shows variation of X-ray flux, as measured by GOES-15 satellite, and the corresponding electron density evaluated at reference height 74 km versus universal time UT during five successive flares on 10 Jun 2014. The red line presents results obtained using simple and accurate fitting formula (2). With circles are presented Ne obtained by the mentioned above method Eq. (1). For this explosive X class solar flares electron density grows for almost two orders of magnitude.

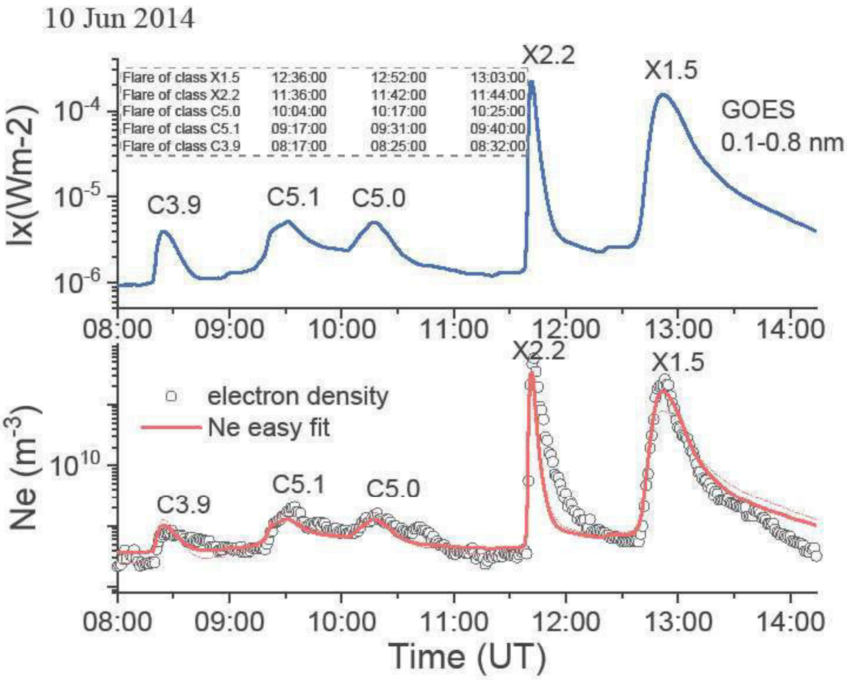


*Figure 3. Variation of X-ray flux, as measured by GOES-15 satellite, and the corresponding electron density evaluated at reference height 74 km versus universal time UT during five successive flares on 10 Jun 2014. The red line presents results obtained using simple and accurate formula (2) based on a least-squares method. With circles are presented Ne obtained by the mentioned above method.*

## CONCLUSION

The magnitude of impact of solar flares on Earth and consequences of these explosive events is analyzed. The VLF radio data and important ionosphere parameters, during the enhancements of X-ray flux due to the flare, are presented and obtained in our study. The computation is applied to the altitude profile of electron density of the perturbed D region, during occurrences of solar flares. It can be noticed that the intense solar radiation, namely solar extreme events lead to an increased electron production rate and can increase electron density up to few orders of magnitude depending on flare intensity with distortion of the amplitude and phase VLF signal. Also, we give a simple approximative and accurate formula for altitude electron density profile which is valid for non-perturbed and also for perturbed D-region.

The results confirmed the advantageous usage of the presented method for investigation solar-terrestrial coupling processes and detecting and analyzing space weather phenomena such as solar explosive events. This study advances knowledge about the extreme radiation, as an undoubted requirement for understanding space weather and sustainable development.

Notably, the data and its complexity in analysis and research of D region and space weather highlight the interdisciplinary nature of study.

## ACKNOWLEDGEMENTS

This work was funded by the University Union – Nikola Tesla and Institute of Physics Belgrade, through the grant by the Ministry of Education and Science of the Republic of Serbia.

## LITERATURE:

Brasseur, Guy P, & Solomon, Susan. (2005). *Aeronomy of the middle atmosphere: Chemistry and physics of the stratosphere and mesosphere* (3rd ed. Vol. 32). Dordrecht, The Netherlands: Springer Science & Business Media.

Ferguson, A.J. (1998). Computer Programs for Assessment of Long-Wavelength Radio Communications, Version 2.0: User's Guide and Source Files. San Diego CA: Space and Naval Warfare Syst. Cent. .

Garcia, Howard A. (1994). Temperature and emission measure from GOES soft X-ray measurements. *Sol. Phys., 154*(2), 275-308. doi: 10.1007/BF00681100

Mitra, Ashesh Prasad. (1974). *Ionospheric Effects of Solar Flares*. Dordrecht, Holland: Springer.

Nicolet, Marcel, & Aikin, A.C. (1960). The formation of the D region of the ionosphere. *J. Geophys. Res., 65*(5), 1469-1483. doi: 10.1029/JZ065i005p01469

Nina, A, Čadež, V, Srećković, V, & Šulić, D. (2012). Altitude distribution of electron concentration in ionospheric D-region in presence of time-varying solar radiation flux. *Nucl. Instrum. Methods Phys. Res. B, 279*, 110-113. doi: 10.1016/j.nimb.2011.10.019

Nina, A, Čadež, V, Šulić, D, Srećković, V, & Žigman, V. (2012). Effective electron recombination coefficient in ionospheric D-region during the relaxation regime after solar flare from February 18, 2011. *Nucl. Instrum. Methods Phys. Res. B, 279*, 106-109. doi: 10.1016/j.nimb.2011.10.026

Scherrer, Deborah, Cohen, Morris, Hoeksema, Todd, Inan, Umran, Mitchell, Ray, & Scherrer, Philip. (2008). Distributing space weather monitoring instruments and educational materials worldwide for IHY 2007: The AWESOME and SID project. *Adv. Space Res., 42*(11), 1777-1785. doi: 10.1016/j.asr.2007.12.013

Šulić, DM, & Srećković, VA. (2014). A comparative study of measured amplitude and phase perturbations of VLF and LF radio signals induced by solar flares. *Serb. Astron. Jour., 188*(188), 45-54. doi: 10.2298/SAJ1488045S

Šulić, DM, Srećković, VA, & Mihajlov, AA. (2016). A study of VLF signals variations associated with the changes of ionization level in the D-region in consequence of solar conditions. *Adv. Space Res., 57*(4), 1029-1043. doi: 10.1016/j.asr.2015.12.025

University of Novi Sad,
Technical Faculty
"Mihajlo Pupin",
Zrenjanin, Republic of Serbia

# International Conference on Physical Aspects of Environment ICPAE2022

Proceedings

Zrenjanin, 31st March – 2nd April 2022

University of Novi Sad,
Technical Faculty
"Mihajlo Pupin",
Zrenjanin, Republic of Serbia

# International Conference on Physical Aspects of Environment ICPAE2022

Proceedings

Zrenjanin, 31st March – 2nd April 2022

# Proceedings of the International Conference on Physical Aspects of Environment ICPAE2022

**Conference Organizer:**
Technical Faculty "Mihajlo Pupin", Zrenjanin, University of Novi Sad, Serbia

**Conference Co-Organizer:**
Faculty of Sciences and Mathematics, Nis, University of Nis, Serbia

**Publisher:**
Technical Faculty "Mihajlo Pupin", Zrenjanin, University of Novi Sad, Đure Đakovića bb, Zrenjanin, Serbia

**For Publisher:**
Dragica Radosav, Dean of Technical Faculty "Mihajlo Pupin", Zrenjanin, Serbia

**Editor:**
Darko Radovančević, Technical Faculty "Mihajlo Pupin", Zrenjanin, Serbia

**Co-Editor:**
Ljubiša Nešić, Faculty of Sciences and Mathematics, Nis, Serbia

**Technical Support:**
Milan Marković,Technical Faculty "Mihajlo Pupin", Zrenjanin, Serbia

CIP - Каталогизација у публикацији
Библиотеке Матице српске, Нови Сад

502(082)

**INTERNATIONAL Conference on Physical Aspects of Environment ICPAE2022 (1 ; 2022 ; Zrenjanin)**
Proceedings [Elektronski izvor] / First International Conference on Physical Aspects of Environment ICPAE2022, Zrenjanin, 31st March – 2nd April 2022 ; [editor Darko Radovančević]. - Zrenjanin : Technical Faculty "Mihajlo Pupin", 2022

Način pristupa (URL):
http://www.tfzr.uns.ac.rs/icpae/conference%20program/ICPAE2022.pdf. - Opis zasnovan na stanju na dan 21.6.2022. - Nasl. sa naslovnog ekrana. - Bibliografija uz svaki rad.

ISBN 978-86-7672-354-6

a) Животна средина -- Заштита -- Зборници

COBISS.SR-ID 69366025

**Scientific Program Committee:**

- Darko Radovančević, University of Novi Sad, Technical Faculty "Mihajlo Pupin", Zrenjanin, Serbia – President
- Ljubiša Nešić, University of Nis, Faculty of Sciences and Mathematics, Nis, Serbia - Vice President
- Saša Jovanović, University of Novi Sad, Technical Faculty "Mihajlo Pupin", Zrenjanin, Serbia
- Snežana Komatina, University of Novi Sad, Technical Faculty "Mihajlo Pupin", Zrenjanin, Serbia
- Bogdana Vujić, University of Novi Sad, Technical Faculty "Mihajlo Pupin", Zrenjanin, Serbia
- Višnja Mihajlović, University of Novi Sad, Technical Faculty "Mihajlo Pupin", Zrenjanin, Serbia
- Ljiljana Radovanović, University of Novi Sad, Technical Faculty "Mihajlo Pupin", Zrenjanin, Serbia
- Jelena Stojanov, University of Novi Sad, Technical Faculty "Mihajlo Pupin", Zrenjanin, Serbia
- Ljubiša Đorđević, University of Nis, Faculty of Sciences and Mathematics, Nis, Serbia
- Vesna Nikolić, University of Nis, Faculty of Occupational Safety, Nis, Serbia
- Tatjana Jovanović, University of Nis, Faculty of Medicine, Nis, Serbia
- Milan Pantić, University of Novi Sad, Faculty of Sciences, Novi Sad, Serbia
- Miodrag Krmar, University of Novi Sad, Faculty of Sciences, Novi Sad, Serbia
- Nataša Todorović, University of Novi Sad, Faculty of Sciences, Novi Sad, Serbia
- Jovana Nikolov, University of Novi Sad, Faculty of Sciences, Novi Sad, Serbia
- Nikola Jovančević, University of Novi Sad, Faculty of Sciences, Novi Sad, Serbia
- Dragan Markušev, Institute of Physics, Belgrade, Serbia
- Zoran Mijić, Institute of Physics, Belgrade, Serbia
- Robert Repnik, University of Maribor, Faculty of Natural Sciences and Mathematics, Maribor, Slovenia
- Vanja Radolić, Josip Juraj Strossmayer University of Osijek, Department of Physics, Osijek, Croatia
- Slavoljub Mijović, University of Montenegro, Faculty of Science and Mathematics, Podgorica, Montenegro

# INTRODUCTION

**The first International Conference on Physical Aspects of the Environment ICPAE2022**, took place from March 31 to April 2, 2022. It was organized by the Technical Faculty "Mihajlo Pupin" from Zrenjanin. The co-organizer was the Faculty of Sciences and Mathematics from Nis. Members of the scientific-program, advisory and organizational committee of the conference were prominent professors and researchers from the University of Novi Sad, University of Nis, Institute of Physics in Zemun, University of Maribor, Josip Juraj Strossmayer University of Osijek, University of Montenegro, Ss. Cyril and Methodius University from Skopje, University of Banja Luka and University of Sarajevo.

The conference was attended by a large number of renowned participants sharing the results of their research, ideas and achievements related to the burning issues in the field of geophysics, environmental modeling, air pollution, greenhouse effect, global warming, climate change, radiation and the environment, energy efficiency and sustainable development, environmental physics and education.

There were 32 papers for the presentation at the conference: 17 papers from abroad and 15 from Serbia.

Plenary presentations were given by:

- Slavoljub Mijović, University of Montenegro, Faculty of Science and Mathematics, Podgorica, Montenegro;
- Lambe Barandovski, Ss. Cyril and Methodius University, Faculty of Natural Sciences and Mathematics, Skopje, North Macedonia;
- Vanja Radolić, Josip Juraj Strossmayer University of Osijek, Department of Physics, Osijek, Croatia;
- Robert Repnik, University of Maribor, Faculty of Natural Sciences and Mathematics, Maribor, Slovenia;
- Abdulah Akšamović, University of Sarajevo, Faculty of Electrical engineering, Sarajevo, Bosnia and Herzegovina;
- Zoran Mijić, Institute of Physics, Belgrade, Serbia;
- Diana Mance, University of Rijeka, Department of Physics, Rijeka, Croatia;
- Tatjana Ivošević, University of Rijeka, Faculty of Maritime Studies, Rijeka, Croatia.

Zrenjanin, June 2022

President of the Scientific Program Committee
Darko Radovančević

Conference Proceedings
ICPAE 2022, 31st March – 2nd April, Zrenjanin, Serbia
Technical Faculty "Mihajlo Pupin", Zrenjanin & Faculty of Sciences and Mathematics, Nis

# A Physically-Based Numerical Model for Pollen Forecast

Slobodan Ničković[1,2*], Luka Ilić[1,3], Slavko Petković[2], Goran Pejanović[2], Alberto Huete[4], Zoran Mijić[1]

*[1*]Institute of Physics Belgrade, Pregrevica 118, Belgrade, Serbia*
*[2]Republic Hydrometeorological Service of Serbia, Kneza Višeslava 66, Belgrade, Serbia*
*[3]Barcelona Supercomputing Center, Barcelona, Spain*
*[4]University of Technology Sydney, A School of Life Sciences, Sydney, Australia*
*nickovic@gmail.com*

**Abstract.** One of the largest healthcare issues is the emergence of allergies, which is frequently triggered by pollen particles. Inhaled pollen grains released by trees, grasses, and ragweed are the most significant risk factors for developing asthma. Establishing a forecasting system with the objective to issue early warnings for high concentration pollen episodes is of particular interest but still challenging task. Over the last decade several pollen models have been developed to predict the atmospheric pollen process. In this study the characteristics of newly developed physically-based numerical pollen model PREAM (Pollen Regional Atmospheric Model) is presented. The potential of the model to correctly mimic extreme pollen events in Melbourne, Australia will be demonstrated.

**Keywords:** pollen, numerical simulation, forecasting

## INTRODUCTION

More than 300 million people worldwide have asthma [1] resulting, at the global scale, in approximately 180,000 deaths annually, most of which are preventable. Approximately 50% of adults and 90% of children with asthma had an allergic form of the disease [2]. The allergy occurrence is often caused by pollen and has today increased to such an extent that is regarded as one of the major current healthcare problems. The strongest risk factors for developing asthma are inhaled substances and particles that may provoke allergic reactions; pollen grains emitted by trees, grasses, and ragweed are among the most commonly present particles. The pollen dispersion process is mainly driven by atmospheric conditions. It starts with the pollen emission which depends on plant phenology, the diurnal plant physiological cycle, and on near-surface atmospheric conditions. When a plant reaches the pollination period, pollen emission is triggered by sufficiently strong near-ground turbulence associated often with stormy weather. Emitted pollen is then dispersed by vertical air mixing and by free-atmospheric horizontal transport. In the final phase of the pollen atmospheric process, pollen grains settle down to the Earth surface by wet deposition (due to precipitation) and by dry deposition (due to gravity and near-surface turbulence). In order to predict and/or study the atmospheric pollen process, several pollen numerical models have been developed over the last decade: e.g., SILAM, COSMO-ART models [3,4]. Of particular interest is the question whether models can predict extreme pollen episodes generated by thunderstorm processes which can affect human health dangerously. Thunderstorm-cased asthma, usually called 'thunderstorm asthma' (TA) is a striking event in which patients could experience life-threatening asthma attacks caused by extreme numbers of pollen grains [5]. During thunderstorms, a local-to-mesoscale atmospheric circulation usually generates formation of a cold-air downburst with strong surface winds, associated with a cold-air outflow front. If a thunderstorm occurs during a pollen season, favorable conditions for intense pollen uptake and transport (such as convection, cold-air outflow) are fulfilled.

The objective of this study is to examine the capacity of the PREAM (Pollen Regional Atmospheric Model) pollen model to predict excessive TA events such as the Melbourne case. PREAM is a version of the DREAM regional dust aerosol atmospheric model [6] modified in our study to predict pollen dispersion. It is an online model driven by the atmospheric NCEP WRF Nonhydrostatic Mesoscale Model, referred onwards as WRF-NMM and developed to be easily applicable over different geographical domains and with arbitrary spatial resolution.

## METHODOLOGY

The atmospheric WRF-NMM model component has prognostic variables distributed horizontally over the Arakawa semi-staggered E-grid. In the vertical, the terrain-following hybrid pressure-sigma coordinate is used. The atmospheric large-scale transport is based on the horizontal advection numerical scheme which preserves energy and enstrophy. The non-hydrostatic atmospheric processes, becoming important for horizontal scales finer than approximately 10 km, are introduced in the model through an add-on non-hydrostatic module that can be turned on/off, depending on the resolution. The vertical diffusion is handled by the surface layer scheme and by the turbulence scheme. For horizontal transport of positive-definite scalars, the WRF-NMM mass conservative positive-definite advection scheme is used which permits no formation of new false concentration maxima and reduces to a minimum the numerical dispersion. The scheme is applied for the horizontal advection of pollen concentration, specific humidity, and cloud water and turbulence kinetic energy.

PREAM simulates all major components of atmospheric pollen processes such as emission, horizontal and vertical turbulent mixing, long-range transport and pollen wet and dry deposition. It numerically solves the following Euler-based pollen mass conservation equation:

$$\begin{aligned}\frac{\partial C}{\partial t} + u\frac{\partial C}{\partial x} + v\frac{\partial C}{\partial y} + \nabla_h(K_H\nabla_h C) + \frac{\partial}{\partial z}\left(K_v\frac{\partial C}{\partial z}\right) + \left(w - v_g\right)\frac{\partial C}{\partial z} \\ - \left(\frac{\partial C}{\partial t}\right)_{SR} + \left(\frac{\partial C}{\partial t}\right)_{SN} = 0\end{aligned} \tag{1}$$

Here, C is the pollen concentration; u, v and w are horizontal and vertical velocity components; $v_g$ is the pollen gravitation settling velocity; $\nabla_h$ is the horizontal gradient operator; $K_H$ and $K_V$ are the lateral and vertical mixing coefficients; subscripts SR and SN indicate pollen sources and sinks, respectively. During the model integration, the calculation of a pollen grain emission is made over model grid-point cells declared as pollen potential sources. Once emitted into the atmosphere, the pollen aerosol is driven by turbulent vertical mixing, by horizontal and vertical advection and by deposition processes. The parameterization of the pollen source is based on the WRF-NMM approach of mass emissions from the surface-atmosphere interface. The emission is dependent on the near-surface turbulent state and its level intensity is regulated by a thin viscous sub-layer inserted between the model surface and the first model layer [7].

The dry deposition of pollen is parameterized following the scheme including gravitational settling, Brownian and turbulent deposition at the air-surface interface, and interception and impaction at the surface roughness elements [6]. The scheme takes into account properties of the depositing particles (size, density), features of the depositing surfaces (roughness, land cover, land texture) and conditions of the lower atmosphere. Different parameterizations are used for the following two groups of surfaces: a) bare soil, ice and sea, and b) land covered by vegetation. The wet removal of the concentration by precipitation is predicted by the atmospheric model where at each model time step the removal is calculated using a constant washout parameter [7].

## RESULTS AND DISCUSSION

Following the objective of our study to examine the capability of the pollen model to predict extreme thunderstorm asthma conditions such as the 2016 Melbourne event, we specify the model domain to cover the south-western part of Australia. In the vertical, there are 28 model levels spanning from the surface to 50 hPa. The horizontal resolution is set to 1/20 deg, leading to approximately 8 km grid distance within the model domain. With this, vertical velocities originating from the non-hydrostatic dynamics are enhanced and the convective processes more realistically represented. The model's basic time step is set to 18 s. The pollen advection and lateral diffusion are computed every 2 time steps, the pollen emission and vertical diffusion are updated every 4 time steps, and the convection and large scale precipitation are calculated every 8 time steps. The model was run over the period 14-22 November 2016. The initial and boundary conditions for the atmospheric model part are specified using weather prediction parameters of the ECMWF global model. Since there are no satisfactory three-dimensional pollen concentration observations to be assimilated, the initial state of pollen concentration in the model is defined by the 24-hour forecast from the previous day model run. Only at the ‘‘cold start’’ of the model on 00:00 UTC 14 November 2016 the initial pollen concentration was set to zero. The geographical distribution of potential sources of grass pollen was represented using the Australian Land Use and Management (ALUM) classification data (ABARES, 2017) at 50 m horizontal resolution.

The model accurately predicted the cold front passage over Melbourne and the surface pollen counts combined with 10 m wind streamlines (Figure 1). The model confirms that northerly winds associated with the cold front lifted the pollen from the pastures near Melbourne. Hot dry northerly winds at 16:00ADT contributed to increased airborne pollen concentration. Cold air downdraft circulation brought pollen down to the ground level. A mixture of humid air and high airborne pollen concentration approaching Melbourne is considered to be a cause for pollen grains rupturing which made them easier to penetrate deep into the lower human lung airways. However, the current PREAM model version does not yet parameterize pollen grain rupturing process. During the TA event in the wider Melbourne area, thousands of patients with respiratory distress asked for medical assistance.

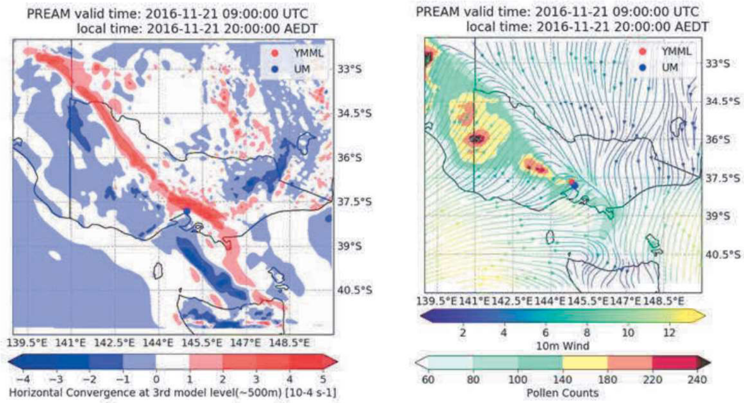


Figure 1. Model predictions at 20 ADT on 21 November 2016. The model near-surface horizontal wind convergence indicating the movement of the thunderstorms (left); the model surface pollen concentration (right)

Figure 3 shows the time evolution of predicted and observed pollen concentrations during the Melbourne TA event. Grass pollen concentrations are daily averages observed at the University of Melbourne, Parkville site during 16-27 November. The available daily-averaged measurements [8] indicate occurrence of a weaker pollen event during 16-17 November. The model simulated this pollen event by predicting of 102 grains/m$^3$ in 1hr values on 17 November. The model daily average for the same period shows 30 grains/m$^3$ compared to the observed 77 grains/m$^3$. The timing of the daily averaged peak for this secondary event was accurately predicted.

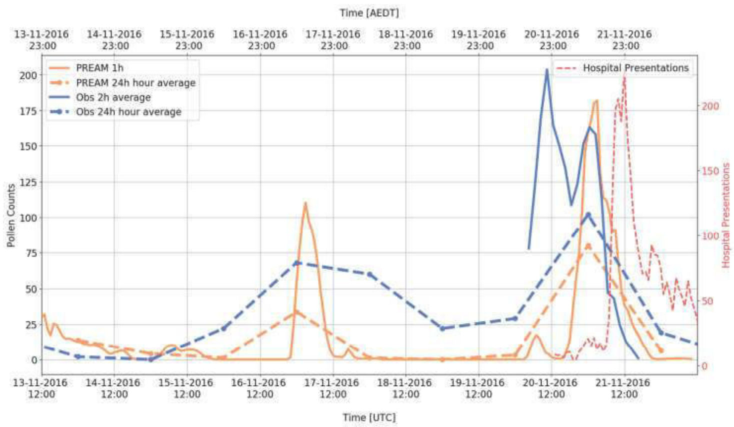


Figure 2. Time evolution of the pollen counts and hospital presentations for the Melbourne TA event during the period 13-22 November.

On 21 November 2h-averaged observations show a two-fold maximum of which the second peak of 160 grains/m$^3$ actually triggered the TA event. The model correctly predicted the timing and values the second maximum. As a result of these extreme concentrations, the number of hospital presentations as shown in the Figure 2 abruptly increased over the next few hours.

## CONCLUSION

The world's largest and most catastrophic epidemic thunderstorm asthma event occurred in Melbourne on 21 November 2016, Australia. In this study we implemented a regional Euler-type pollen prediction model over the Australian state of Victoria in order to explore its capability to predict the Melbourne pollen event. The model simulation covering the period 16-22 November 2016 was verified against available pollen counts observed at a Melbourne site. The model correctly identified the increased pollen concentrations from the weaker observed peak on 16 November. More importantly, the extreme pollen concentrations on the 21st November, which triggered the epidemic asthma, was quite well represented by the model, in terms of both timing and location. However, whether the proposed prediction system can reasonably perform over longer (e.g. seasonal) time frames will require further research. Ongoing research is also related to the parameterization of the pollen grain rupturing process in the model, which is considered as one of the key component for developing successful TA early warning system.

## ACKNOWLEDGEMENTS

The European Centre for Medium-Range Forecasting (ECMWF) forecasts are used for initial and boundary conditions in the model. ZM and LI acknowledge funding provided by the Institute of Physics Belgrade, through the grant by the Ministry of Education, Science, and Technological Development of the Republic of Serbia.

## REFERENCES

1. T. To, S. Stanojevic, G. Moores, A.S. Gershon, E.D. Bateman, A.A Cruz, L. Boulet, 2012. Global asthma prevalence in adults: findings from the cross-sectional world health survey. *BMC Public Health*. 12:204
2. Ó. Palomares, S. Sánchez-Ramón, I. Dávila, L. Prieto, L. Pérez de Llano, M. Lleonart, et al. 2017. dIvergEnt: How IgE Axis Contributes to the Continuum of Allergic Asthma and Anti-IgE Therapies. *Int. J. Mol. Sci.* 18(6):E1328.
3. P. Siljamo, M. Sofiev, E. Filatova, L. Grewling, S. Ja¨ger, E. Khoreva, , et al. 2013. A numerical model of birchpollen emission and dispersion in the atmosphere. Modelevaluation and sensitivity analysis. *Int. J. Biometeorol* 57, 125-136
4. K. Zink, H. Vogel, B. Vogel, D. Magyar, C. Kottmeier, 2012. Modeling the dispersion of Ambrosia artemisiifolia L. pollen with themodel system COSMO-ART. *Int. J. Biometeorol*. vol. 56, 669–680.
5. P. E. Taylor, H Jonsson, 2004. Thunderstorm Asthma. *Curr. Allergy. Asthm*. R. 4, 409–413
6. S. Nickovic, G. Kallos, A. Papadopoulos, O. Kakaliagou, 2001. A model for prediction of desert dust cycle in the atmosphere. *J. Geophys. Res*. 106, 18113-18130.
7. Z. Janjic,1994. The step-mountain eta coordinate model: further developments of the convection, viscous sublayer, and turbulence closure schemes, *Mon. Weather Rev*. 122, 927–945

8. Thien, F., Beggs, P. J, Csutoros, D., Darvall, J., Hew, M., et al. 2018. The Melbourne epidemic thunderstorm asthma event 2016: an investigation of environmental triggers, effect on health services, and patient risk factors, *Lancet Planet. Health* 2, e255–263

University of Belgrade, Technical Faculty in Bor


# 30th International Conference Ecological Truth & Environmental Research 2023

# Proceedings


Editor
Prof. Dr Snežana Šerbula

University of Belgrade, Technical Faculty in Bor

# 30 EcoTER

## 30th International Conference Ecological Truth & Environmental Research 2023

# Proceedings


Editor
Prof. Dr Snežana Šerbula

**PROCEEDINGS**

**30th INTERNATIONAL CONFERENCE**

**ECOLOGICAL TRUTH AND ENVIRONMENTAL RESEARCH – EcoTER'23**

**Editor:**

**Prof. Dr Snežana Šerbula**

University of Belgrade, Technical Faculty in Bor

**Editor of Student section:**

**Prof. Dr Maja Nujkić**

University of Belgrade, Technical Faculty in Bor

**Technical editors:**

**Jelena Milosavljević, PhD,** University of Belgrade, Technical Faculty in Bor

**Asst. prof. Dr Ana Radojević**, University of Belgrade, Technical Faculty in Bor

**Sonja Stanković**, **MSc**, University of Belgrade, Technical Faculty in Bor

**Cover design:**

**Aleksandar Cvetković**, **BSc**, University of Belgrade, Technical Faculty in Bor

**Publisher:** University of Belgrade, Technical Faculty in Bor

**For the publisher:** Prof. Dr Dejan Tanikić, Dean

**Printed:** University of Belgrade, Technical Faculty in Bor, 100 copies, electronic edition

**Year of publication:** 2023



ISBN 978-86-6305-137-9

CIP - Каталогизација у публикацији
Народна библиотека Србије, Београд

502/504(082)(0.034.2)
574(082)(0.034.2)

**INTERNATIONAL Conference Ecological Truth & Environmental Research (30 ; 2023)**
Proceedings [Elektronski izvor] / 30th International Conference Ecological Truth & Environmental Research - EcoTER'23, 20-23 June 2023, Serbia ; organized by University of Belgrade, Technical faculty in Bor (Serbia) ; co-organizers University of Banja Luka, Faculty of Technology – Banja Luka (B&H) ... [et al.] ; [editor Snežana Šerbula]. - Bor : University of Belgrade, Technical faculty, 2023 (Bor : University of Belgrade, Technical faculty). - 1 elektronski optički disk (CD-ROM) ; 12 cm

Sistemski zahtevi: Nisu navedeni. - Nasl. sa naslovne strane dokumenta. - Preface / Snežana Šerbula. - Tiraž 100. - Bibliografija uz svaki rad.

ISBN 978-86-6305-137-9

а) Животна средина -- Зборници б) Екологија – Зборници

COBISS.SR-ID 118723849
----------------------------------

# 30th International Conference
# Ecological Truth and Environmental Research – EcoTER'23

*is organized by:*

**UNIVERSITY OF BELGRADE**
**TECHNICAL FACULTY IN BOR (SERBIA)**

*Co-organizers of the Conference:*

**University of Banja Luka, Faculty of Technology, Banja Luka (B&H)**

**University of Montenegro, Faculty of Metallurgy and Technology, Podgorica (Montenegro)**

**University of Zagreb, Faculty of Metallurgy, Sisak (Croatia)**

**University of Pristina, Faculty of Technical Sciences, Kosovska Mitrovica**

**Association of Young Researchers Bor (Serbia)**

## HONORARY COMMITTEE

## SCIENTIFIC COMMITTEE

## ORGANIZING COMMITTEE

# INFLUENCES OF EXTREME SOLAR ACTIVITY ON EARTH ENVIRONMENT – CASE STUDY

**Aleksandra Kolarski[1], Vladimir Srećković[1], Zoran Mijić[1*]**
[1]Institute of Physics Belgrade, University of Belgrade, Pregrevica 118, 11080 Belgrade, SERBIA
*zoran.mijic@ipb.ac.rs

## Abstract
*The changes in the Earth environment triggered by the Solar activity can have a significant impact on the functionality of spaceborne and ground-based systems and services, potentially putting human wellbeing at risk. Recent assessment of the European Space Agency pointed out that a single extreme space weather event might have a huge socioeconomic impact on Europe society with its tendency to become even more sensitive in the future years. Many studies indicated significant direct influence of space weather events such as geomagnetic storms and solar flares on human health. As a result, systematic monitoring, and investigation of changes in the atmosphere caused by solar flares have become extremely important over the last decades. The aim of this case study is to investigate the solar flare effects on the ionosphere focusing on the changes that occurred above the European region on 6 September 2017, when one of the strongest solar flares occurred. Simultaneous monitoring of Very Low Frequency radio signals propagation at the Institute of Physics Belgrade station in regular and perturbed ionospheric conditions, enabled retrieving of propagation parameters of sharpness and reflection height during perturbed ionospheric conditions. In addition, numerical simulations reveal changes in electron density profiles showing the increase of several orders of magnitude compared to unperturbed conditions. Obtained findings could be useful for investigation of both atmospheric plasma properties, and prediction of extreme weather impacts on human activities.*

**Keywords**: solar flare, radio signal, environmental impact, atmospheric perturbation.

## INTRODUCTION

Through solar-terrestrial interactions between solar activity events of electromagnetic (EM) and corpuscular nature and our planet's outer protective magnetospheric shield, Sun in a great matter influences the near-surface Earth environment. Some of the main inducing agents originating from the Sun are powerful events such as solar flares (SFs), coronal mass ejections (CMEs), energetic proton and electron events etc. Such energetic space weather events can potentially be hazardous to human health [1] and activities, causing radio communication and navigation disturbances such as radio wave blackout [2], directly affecting human crews on space missions and space-born instruments and also producing geomagnetic storms [3].

Energy released during solar flare events, powerful bursts of electromagnetic energy, is well known to penetrate deep into the Earth's atmosphere. Aside from the Lyman-alpha component, soft-range X-rays with wavelengths of 0.1–0.8 nm reach the lowest of ionospheric regions, the D-region spreading between 50 and 90 km in height that overlaps with mesospheric region of the atmosphere [4]. Additional incident EM radiation during SFs changes plasma properties within lower ionosphere causing electron density height profile to change as well, following in behaviour input X-ray radiation. Investigation of changes in the atmosphere caused by solar flares and related impacts on the environment have attracted more attention over the last decades. In this paper characteristics of one of the strongest SF events observed are analysed and its impact on lower ionospheric perturbations discussed.

## MATERIALS AND METHODS

Case study presented in this work covers X-class SF event X9.3 occurred on September 6th, 2017 (Figure 1) and accompanying CMEs directed towards Earth through ionospheric influences within the near Earth environment. Technology for remote sensing of the lower ionosphere employing artificial man-made Very Low Frequency (VLF) radio signals of frequency range 3–30 kHz is applied [5,6]. Analysis is conducted on data recorded by BEL VLF systems located at the Institute of Physics Belgrade, while X-ray data were taken from GOES database [7]. Retrieving of propagation parameters of sharpness and reflection height during perturbed ionospheric conditions was done according to measured VLF signal perturbations related to X9.3 inducing agent through numerical simulations, with electron density height profile variation during this event obtained based on Wait's empirical approach [6].

*a)* *b)* *c)*

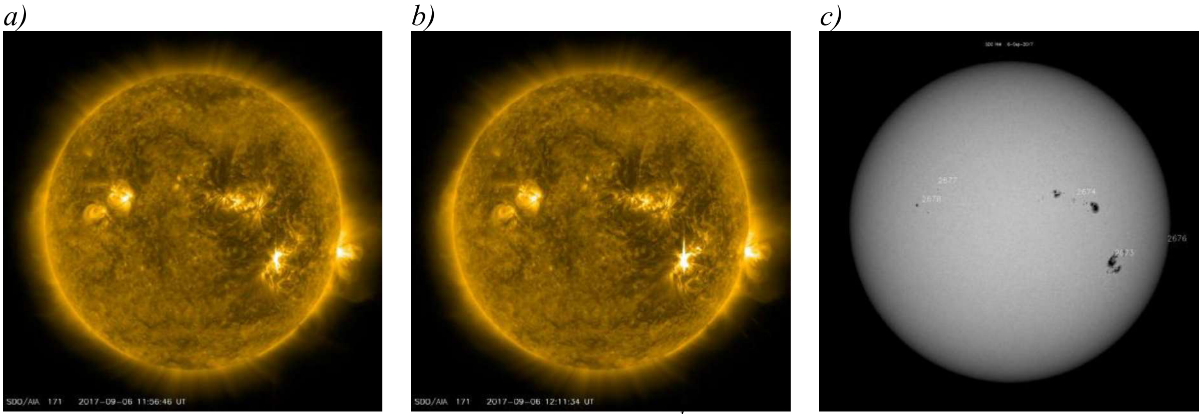


***Figure 1*** *X-class SF event X9.3 occurred on September $6^{th}$, 2017, started at 11:53UT, reached peak at 12:02UT with $Ix_{max} = 9.3293 \cdot 10^{-4}$ Wm$^{-2}$, and ended at 12:10UT, which originated from active region 2673, as captured by one of NASA's Solar Dynamics Observatory telescopes: two successive frames of this SF and its active region a) frame at 11:56UT left; b) frame at 12:11UT in the middle; c) active regions on September $6^{th}$ 2017 (taken from https://www.nasa.gov/)*

Absolute Phase and Amplitude Logger (AbsPAL) station, located in Belgrade (44.85°N; 20.38°E), provided the VLF data used in this analysis. Amplitude and phase perturbations related to case study event of X9.3 SF, were monitored on VLF signal emitted from military transmitter in Skelton (54.72°N; 2.88°W), UK on frequency 22.1 kHz, with code name GQD, arriving in Belgrade from west with Great Circle Path (GCP) in length of about 2 Mm (Figure 2). Methodology used relies on subionospheric VLF signal propagation within Earth-ionosphere waveguide, with lower ionosphere as the upper boundary and Earth's surface as the lower boundary of this waveguide, and hop-wave theory of radio signal transmitting within the waveguide [5,6,8,9]. Approach involves multi-signal simultaneous monitoring of VLF signals' amplitude and phase in regular and perturbed ionospheric conditions, enabling to retrieve properties of perturbation from measured VLF data, through comparison between unperturbed and perturbed states, using numerical procedures for modelling of ionospheric plasma properties [10–20].

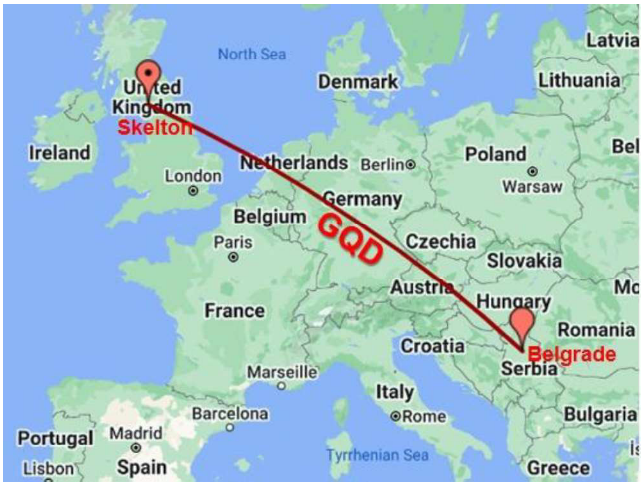


***Figure 2*** *Great Circle Path (red) of VLF radio signal GQD/22.1 kHz, transmited from Skelton (UK) and registered in Belgrade (Serbia)*

## RESULTS AND DISCUSSION

Amplitude and phase perturbations observed on GQD signal recorded in Belgrade during X9.3 SF, with incident soft X-ray irradiance as recorded by GOES-15 satellite, are presented in Figure 3, on middle, lower and upper panel, respectively.

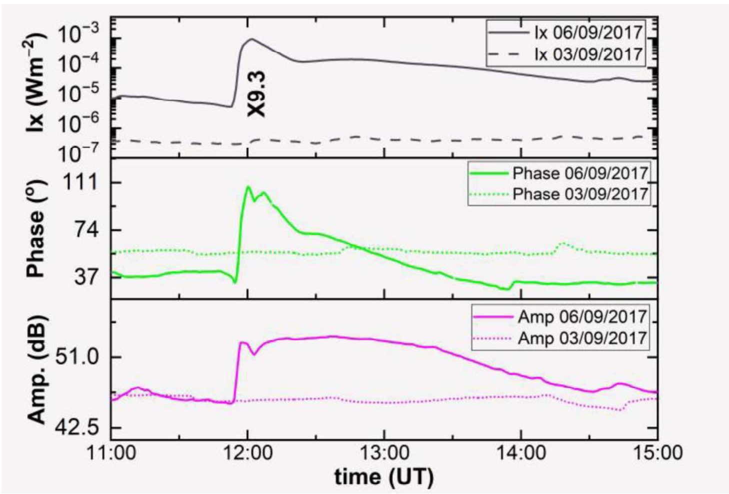


***Figure 3*** *Simultaneous variations of X-ray flux (perturbed and quiet days in solid and dashed gray, respectively) recorded by GOES-15 satelite, perturbed phase (solid green) and amplitude (solid pink) and quiet signals (dotted green and pink) of GQD/22.10 kHz VLF radio signal during X9.3 SF occurred on September 6$^{th}$, 2017, recorded by Belgrade VLF station (from upper to lower panel)*

Amplitude and phase perturbations on monitored VLF signals are of relatively simple morphology and pattern, following inducing X-radiation agent with time delay corresponding to the sluggishness of the ionosphere [21,22]. Recorded amplitude and phase perturbation on monitored GQD signal as induced by SF event X9.3 on September 6th, 2017, reached maximal increase of 7.09 dB in amplitude and 52.03° in phase compared to unperturbed values during September 3rd, 2017, corresponding to the peak activity of soft X-ray flux.

Based on amplitude and phase perturbations during X9.3 SF, modelling of ionospheric plasma properties was done through numerical simulations, using Long Wavelength Propagation Capability (LWPC) software [23] and the FlarED' Method and Approximate Analytic Expression application [4,17]. Estimated values of analysed VLF signals' amplitude and phase obtained during modelling through both applied numerical procedures are in good agreement with real values measured by BEL VLF receiving system.

LWPC software utilisation based on Wait's theory application, rely on Wait's parameters β ($km^{-1}$) and *H'* (km) (lower ionospheric boundary sharpness and VLF signal's reflection height), determined for daytime ionospheric conditions using Equation (1) [6]. Electron densities calculated at the reflection height, when $h = H'$ give profile throughout D-region altitude range (Figure 4).

$$N_e(h, H', \beta) = 1.43 \cdot 10^{13} \cdot e^{(-0.15 \cdot H')} \cdot e^{[(\beta - 0.15) \cdot (h - H')]}, \quad (m^{-3}) \qquad (1)$$

FlarED' Method and Approximate Analytic Expression application, designed for obtaining VLF signal propagation parameters β and *H'* from incident solar X-ray irradiance, gave electron density profiles (Figure 5) calculated by using polynomial Equation (2) [4,17].

$$\log Ne(h, Ix) = a_1(h) + a_2(h) \cdot \log Ix + a_3(h) \cdot (\log Ix)^2 \qquad (2)$$

Estimated electron densities at reference height of 74 km, obtained by both numerical approaches are within one order of magnitude. Obtained results are in line with results from other studies dealing with high class SF events and conducted by observation from mid-latitudinal located VLF receivers [4,15,16,18,24,25].

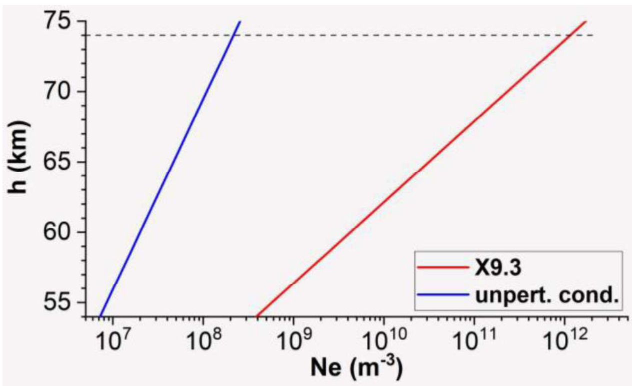


***Figure 4** Electron density height profile for GQD signal at peak intensity of X9.3 SF (red) obtained using Equation (1) and in unperturbed ionospheric conditions (blue); reference height 74 km is indicated by dotted black line*

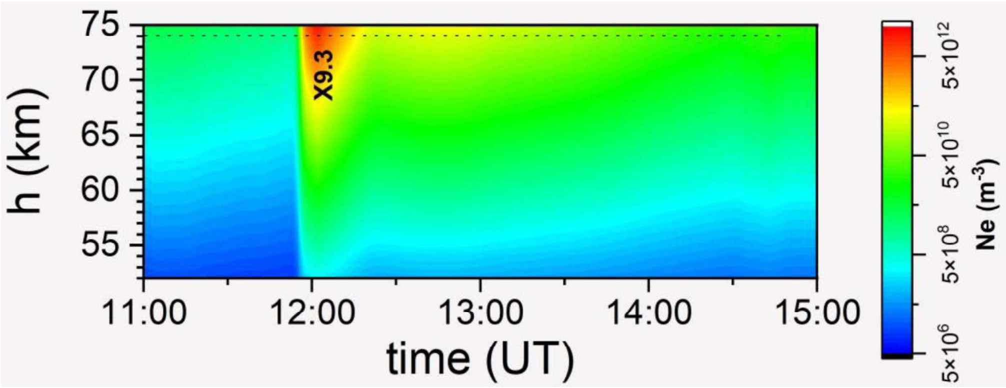


***Figure 5*** *Electron density height profiles for GQD signal during four hours including peak intensity of X9.3 SF obtained through application of approximative Equation (2); reference height 74 km is indicated by dotted black line*

## CONCLUSION

Solar flare events are well-known extraterrestrial driver for lower ionospheric perturbations, inducing change of plasma properties in near Earth environment, that can affect human health and cause serious damage to electronically dependent modern society, causing satellite operation breakdowns, communication blackouts, flight risks especially over polar regions, etc. Ionospheric D-region, as medium for VLF signal propagation in a way “mirrors” disturbances of its plasma properties onto propagation parameters of VLF signals, forcing them to deviate from their regular propagation patterns characteristic for unperturbed ionospheric conditions. In this manner caused amplitude and/or phase perturbations make VLF technique as very efficient and as the technique of choice for this region remote sensing exploration. Lower ionospheric disturbance related to X9.3 solar flare event that occurred on September 6$^{th}$, 2017, caused perturbations in propagation parameters of VLF signals, that as recorded by Belgrade VLF system and observed on GQD signal, reached several dB in amplitude and few tens of degrees in phase, compared to unperturbed signal on September 3$^{rd}$, 2017. Accordingly, electron density profiles also changed, following the incident soft X-ray radiation, showing the increase of several orders of magnitude compared to their unperturbed values at the reference height of 74 km, as obtained through conducted numerical simulations.

## ACKNOWLEDGEMENT

*This work was funded by the Institute of Physics Belgrade, University of Belgrade, through a grant by the Ministry of Science, Technological Development and Innovations of the Republic of Serbia.*

## REFERENCES

[1] Alabdulgader A., McCraty R., Atkinson M., *et al*., Sci. Rep. (2018) 2663.

[2] Yasyukevich Y., Astafyeva E., Padokhin A., *et al*., Space Weather (2018) 1013–1027.

[3] Riley P., Love J. J., Space Weather (2017) 53–64.

[4] Srećković V. A., Šulić D. M., Ignjatović Lj., *et al*., Appl. Sci. 11 (2021) 7194.

[5] Mitra A. P., Lonospheric Effects of Solar Flares; Springer, Berlin/Heidelberg (1974), p.305, ISBN: 978-90-277-0467-2.

[6] Wait J. R, Spies K. P., Characteristics of the Earth-Ionosphere Waveguide for VLF Radio Waves; US Department of Commerce, National Bureau of Standards, Gaithersburg MD, (1964), p.110.

[7] NOAA National Centre's for Environmental Information, *Available on the following link*: https://satdat.ngdc.noaa.gov/sem/goes/data/avg/.

[8] Budden K., Radio Waves in the Ionosphere, Cambridge University Press, Cambridge (1961), p.542, ISBN: 052111439X.

[9] Wait J. R., Electromagnetic Waves in Stratified Media, Pergamon Press, Oxford (1970), p.620, ISBN: 9781483184258.

[10] Silber I., Price C., Surv. Geophys. 38 (2017) 407–441.

[11] Žigman V., Kudela K., Grubor D., Adv. Space Res. 53 (2014) 763–775.

[12] Nina A., Remote Sens. 14 (2022) 54.

[13] Šulić D., Nina A., Srećković V., arXiv (2014) arXiv:1405.3783.

[14] Grubor D., Šulić D., Žigman V., Ann. Geophys. 26 (2008) 1731–1740.

[15] Kolarski A., Srećković V. A., Mijić Z. R., Appl. Sci. 12 (2022) 582.

[16] Barta V., Natras R., Srećković V., *et al*., Front. Environ. Sci. 10 (2022) 904335.

[17] Srećković V.A., Šulić D.M., Vujčić V., *et al*., Appl. Sci. 11 (2021) 11574.

[18] Kolarski A., Veselinović N., Srećković V. A., *et al*., A. Remote Sens. 15 (2023) 1403.

[19] Kolarski A., Grubor D., Adv. Space Res. 53 (2014) 1595–1602.

[20] Kolarski A., Srećković V. A., Mijić Z. R., Contrib. Astron. Obs. Skaln. Pleso 52 (2022) 105.

[21] Appleton E. V., J. Atmos. Sol.-Terr. Phy. 3 (1953) 282–284.

[22] Žigman V., Grubor D., Šulić D., J. Atmos. Sol.-Terr. Phys. 69 (2007) 775–792.

[23] Ferguson, J. Computer Programs for Assessment of Long-Wavelength Radio Communications, Version 2.0: User's Guide and Source Files, Space and Naval Warfare Systems Center, San Diego (1998).

[24] Thomson N. R., Rodger C. J., Clilverd M. A., J. Geophys. Res. Space Phys. (2005) A06306.

[25] McRae W. M., Thomson N. R., J. Atmos. Sol.-Terr. Phys. 66 (2004) 77–87.

# NOVEL APPROACH IN AIRBORNE POLLEN DISPERSION MODELLING

**Slobodan Ničković[1,2], Luka Ilić[1,3], Slavko Petković[2], Goran Pejanović[2], Alfredo Huete[4], Zoran Mijić[1*]**

[1]Institute of Physics Belgrade, University of Belgrade, Pregrevica 118, 11080 Belgrade, SERBIA

[2]Republic Hydrometeorological Service of Serbia, 11000 Belgrade, SERBIA

[3]now at Barcelona Supercomputing Center, Plaça Eusebi Güell, 1–3, 08034 Barcelona, SPAIN

[4]School of Life Sciences, University of Technology Sydney, Sydney, NSW, AUSTRALIA

[*]*zoran.mijic@ipb.ac.rs*

## Abstract

*When exposed to high atmospheric humidity, pollen grains rupture and release large numbers of small allergenic particles. Unlike whole pollen grains, these submicron particles easily enter deep into lungs and can cause a serious asthmatic response. Current operating pollen models predict the concentration of intact (whole) pollen grains but not respirable allergenic fragmented particles. We tested a novel numerical pollen model that predicts the formation and dispersion of sub-pollen allergenic granules released after pollen grains burst in the moist air. We evaluated the model for the case of the November 2016 Melbourne thunderstorm asthma epidemic, which resulted in 10 deaths and thousands of hospital admittances. This episode was triggered by intact grass pollen transported toward the city by a severe storm weather system followed by a 5 hour lag in the arrival of the finer, sub-pollen granules into the city, with a spike in hospital presentations shortly after. The model accurately predicted the observed times, locations and quantities of both fragmented and intact pollen concentrations. The presented modelling system, if operationally implemented, can be used as a prognostic tool for early warning alerts on asthma epidemic occurrences.*

**Keywords**: pollen, numerical modeling, thuderstorm asthma, sub-pollen particles.

## INTRODUCTION

Thunderstorms occurring during the pollen season are often associated with an increased number of sub-pollen particles. The conceptual model of thunderstorm asthma (asthma episodes associated with thunderstorms) assumes that a thunderstorm circulation transports the emitted pollen grains into a cloud where grains rupture due to high atmospheric moisture. Each pollen grain release almost one thousand sub-pollen particles [1]. Recently presented direct measurements of sub-pollen concentrations performed for the first time with a novel fluorescence spectroscopic technique show that fragments remain airborne for several hours after pollen rupturing by thunderstorms [2]. These fragmented particles are small enough to enter deep into the lungs and to cause severe asthmatic reaction [3].

During the 21 November 2016, the asthma epidemic episode in Melbourne (Australia), ryegrass pollen was transported to the city from widespread pastures in the region by a strong wind gusts ahead of fast-moving thunderstorm squall-line front [4]. The city recorded ten asthma-related deaths and almost 500 admissions to the hospital over a short time after this event. The number of hospital visits increased by 992% within 30 h [5]. The Melbourne episode was the worldwide largest asthma epidemic coinciding with pollen presence. Many people had breathing difficulties occurred in such a short interval that it caused extreme pressure on the health system. The sudden increase in observed ruptured pollen counts associated with the frontal passage was assumed to be the major cause of the epidemic [6]. High levels of intact pollen concentrations, observed a day earlier on 20 November from nearby local grass emissions did not cause an asthma epidemic, since stable synoptic conditions prevailing that day were not favourable for pollen fragmentation. In response to the 21 November thunderstorm asthma episode, the local Victorian government recommended the development of a physical pollen model as a key priority in order to fulfil societal needs for a more reliable early warning system.

Currently several physical models available in the community provide short-term prediction of the intact pollen concentration embedded into numerical weather prediction systems [7,8]. However, parameterization of pollen rupturing and dispersion of sub-pollen allergenic particles is still challenging task. In this paper the results of sub-pollen particles prediction obtained by numerical simulation are presented using a novel parameterization scheme for pollen rupturing.

## MATERIALS AND METHODS

The numerical model called DREAM-POLL have been developed to predict not only the intact pollen concentration but also the production and dispersion of allergens released from ruptured pollen grains. DREAM-POLL is an Euler-type model in which prognostic pollen concentration equation is embedded on-line into a high-resolution non-hydrostatic weather prediction model. The on-line modelling approach allows the atmospheric and pollen processes to be synchronously simulated. DREAM-POLL mathematically describes the major phases of the atmospheric pollen cycle, including the emission of pollen, its vertical and horizontal transport, and pollen turbulent mixing and deposition.

The model starts emitting pollen from a pre-specified source when near-ground turbulence exceeds a threshold at that source. The emitted pollen is further directed by the turbulence and large-scale dynamics of the atmospheric model driver. At the end of their atmospheric cycle, pollen particles are settled to the ground by precipitation and by near-surface dynamics as predicted by the atmospheric driver. In the newly developed pollen rupturing parameterization, we calculate in every model time step the number of fragmented particles released from ruptured pollen grains whenever the atmospheric humidity of the driver model exceeds a pre-specified threshold of 60% [9]. The intact, ruptured and fragmented particles are driven by the same atmospheric dynamics in the model, except that intact pollen elements are emitted from the ground, and the other two particle categories originate in high moisture cloud conditions. Model experiments presented in this study were performed with horizontal grid spacing of approximately 5 km. At this resolution, convective and non-hydrostatic atmospheric processes are explicitly resolved in the model, which is essential for appropriate simulation of pollen dynamics under thunderstorm conditions. The 50-m resolution Australian

Land Use and Management (ALUM) classification data was used to specify the grass fraction used in the model as potential pollen sources. We tested the model performance by executing it in a real-time prognostic mode for the Melbourne episode, validating its results against available pollen observations.

DREAM-POLL represents a modified version of the DREAM regional dust aerosol atmospheric model [10]. The model domain in this study covers the southwestern region of Australia, and there are 28 model vertical levels spanning from the surface to 50 hPa. The horizontal grid distance is set to 1/20 deg (approximately 5 km). The pollen advection and lateral diffusion are computed every 35 sec, the emission and vertical diffusion are updated every 70 sec, and the convection and large-scale precipitation are calculated every 140 sec.

The model was run over the period 19–22 November 2016 during which the Melbourne episode happened. The initial and boundary conditions for the atmospheric model component were specified using weather prediction parameters of the European Centre for Medium-range Weather Forecast (ECMWF) global model. Since there are no satisfactory three-dimensional pollen concentration observations to be assimilated, the initial state of pollen concentration in the model was defined by the 24-h forecast from the previous day model run. Only for the "cold start" of the model at 00:00 UTC 19 November 2016, the initial pollen concentrations were set to zero.

## RESULTS AND DISCUSSION

The synoptic situation on 21 November was characterized by the presence of a cold front over southeast Australia. Northerly winds ahead of the front swept ryegrass pollen from pastures north of Melbourne. A multi-cell thunderstorm squall-line heading the cold front passed the city area between 17:00 and 18:30 AEDT (AEDT – Australian Eastern Daylight Time is the local time, which is UTC+11:00), when surface meteorological parameters abruptly changed their values. From the early afternoon onwards, the observed intact and ruptured pollen concentrations increased as well. At 16:00 AEDT, the simulated horizontal wind convergence line approached the wider city area. The convergence line separated the warmer air on the Melbourne side from the colder maritime air southward. Previously emitted intact pollen north of the city was lifted by warm updrafts to zones of moist air, while cold downdrafts prevailed behind the squall-line. The predicted location, orientation, and intensity of the squall-line agree with satellite data. Its circulation pattern is consistent with conceptual models of squall-line thunderstorm systems. After entering the moist air, pollen rupturing was triggered, but at this time the ruptured grains had not reach the surface. At 22:00 AEDT, after the thunderstorm line moved away from Melbourne, the predicted intact pollen concentrations were reduced to zero (Figure 1a). However, about this time, the surface concentration of ruptured particles achieved its maximum (Figure 1b).

Figure 2 shows the spatio-temporal evolution of the intact and fragmented particles as predicted for the pollen measurement site Burwood (the Deakin University, Melbourne). Being lighter in weight, the fragmented particles progressed much slower than the heavier intact pollen grains, with most sub-pollen particles arriving at the city on 21 November about 5 h later than intact pollen. A time delay of several hours is observed during asthma thunderstorm episodes in the USA as well [2].

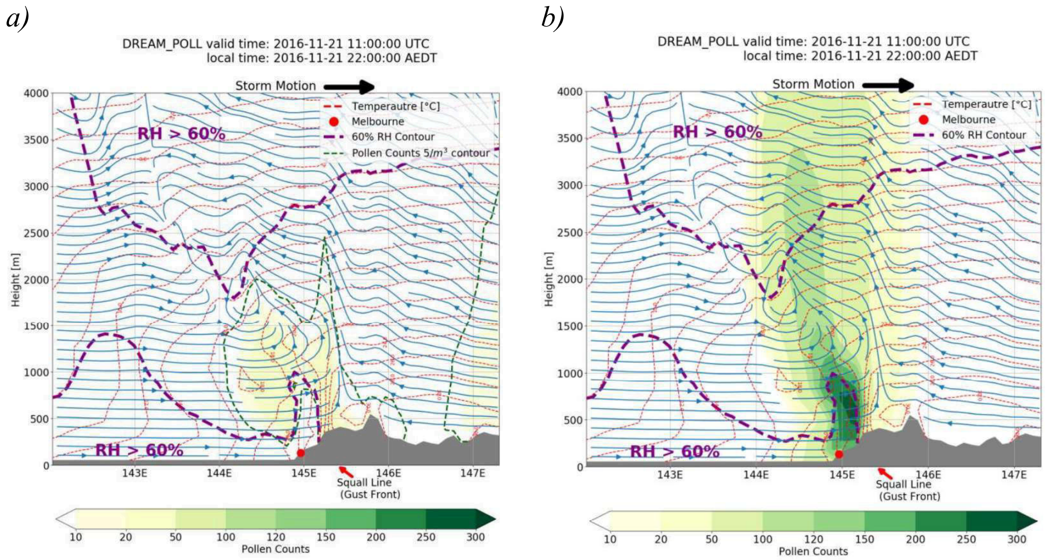


***Figure 1*** *Predicted intact and ruptured pollen concentration at 22:00 AEDT on 21 November; Vertical cross sections along the normal to the front, with pollen concentration (yellow-to-green palette), streamlines and contours of 60% relative humidity (dashed purple lines); a) intact; b) ruptured pollen; Melbourne is represented by a red dot in each panel.*

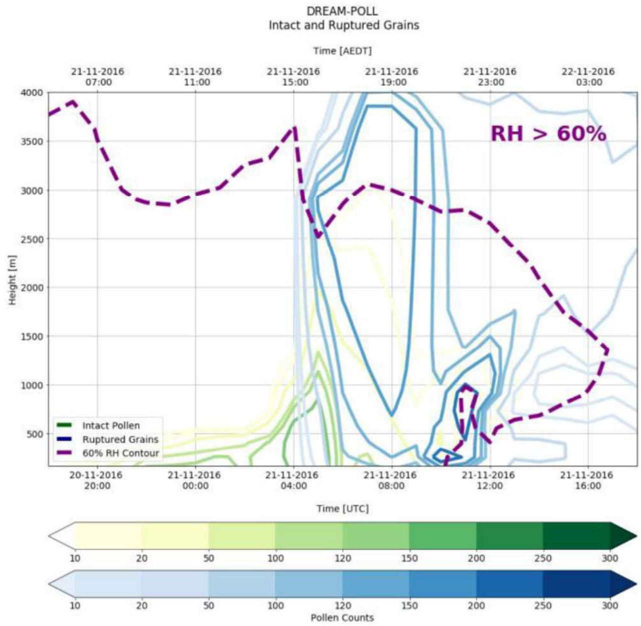


***Figure 2*** *Predicted intact and ruptured pollen grains above Melbourne; 60% relative humidity contour*

There are two peaks of intact pollen concentrations observed in Melbourne during the 20–21 November period (Figure 3). The first peak on the 20th is attributed to pollen probably emitted from nearby urban sources. During this day, there were no significant ruptured pollen numbers recorded, which indicates that particle fragmentation did not occur under the prevailing stable synoptic conditions. However, on the 21 November both observations and model results show increased numbers of intact and ruptured pollen particles linked with the passage of the wind gust front. Affected by the passing front, the largest decrease/increase of predicted intact/ruptured particle numbers occurred at approximately 18:00 AEDT. Significant increase in the observed ruptured-to-intact grain ratio after the front passage was reproduced by the model as well.

The predicted intact pollen achieved its largest number several hours before the thunderstorm arrived in Melbourne. Later that afternoon, the arrival of the squall front coincided with a short-term precipitation event [5]. From 15:00 AEDT onwards, the predicted number of pollen fragments (represented with the size of 3.03 μm in the model) started to increase, reaching the maximum concentration of 97,500 particles per $m^3$ at 21:00 AEDT. This value is within an order of observed magnitudes [2]. A decline in intact pollen before and an increase in fragment numbers after the frontal passage we simulated are consistent with a recently published characterization of airborne pollen dynamics during several thunderstorms [2]. The maximum number of allergenic pollen fragments was predicted to have occurred 2 h before the highest recorded number of asthma-related hospital presentations.

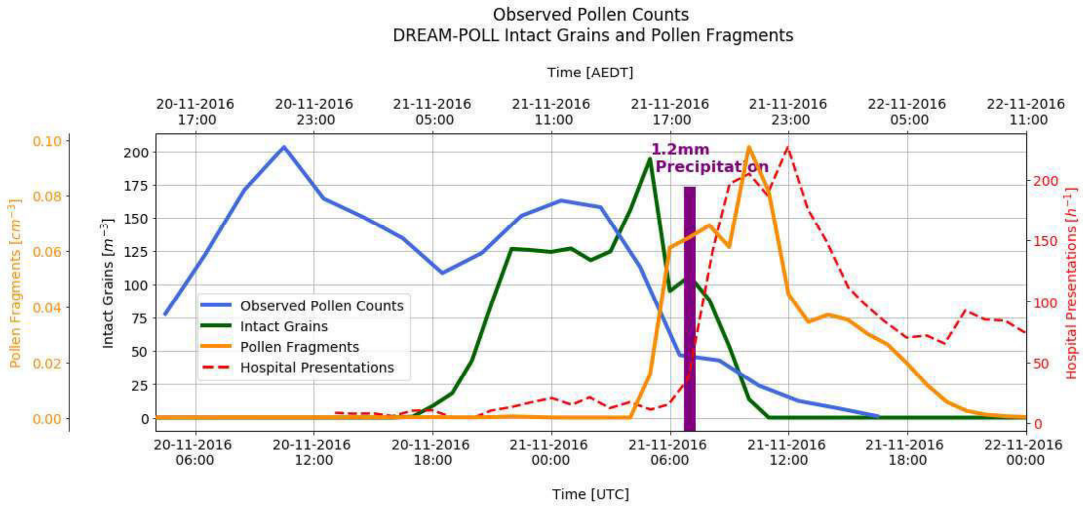


***Figure 3*** *Pollen concentrations in Melbourne: Observed pollen counts (blue); predicted intact grains (green) and sub-pollen particles (orange); observed 1.2 mm precipitation (purple bar); 1-h hospital presentations (dashed red line)*

## CONCLUSION

We presented in this study a numerical modelling approach that enables the prediction of concentration of respirable sub-pollen fragments several days in advance. We demonstrated the effectiveness of this approach by forecasting the Melbourne thunderstorm asthma event 48 h earlier. The proposed method can play a crucial component in an early warning system dedicated to predict time and location of asthma-related outbreaks. DREAM-POLL can be implemented with different model resolutions, over specified geographical domains and for a given pollen type. The availability of such an early-warning system would allow civil authorities to react in a timely manner to asthma epidemics and thus significantly diminish pressure on health services and reduce fatalities and illnesses due to respiratory problems.

However, a numerical parameterization scheme for sub-pollen particles formation from whole grains can be further improved taking into the account not only high humidity but other effects of convective thunderstorm conditions.

## ACKNOWLEDGEMENT

*The authors acknowledge Prof. Ed Newbigin and Jeremy Silver (the University of Melbourne, Australia) for supplying the pollen observation data and Dr. Elizabeth E. Ebert (Weather and Environmental Prediction, Bureau of Meteorology Melbourne, Australia) for useful discussions. L. Ilic and Z. Mijic acknowledge funding provided by the Institute of Physics Belgrade, through a grant by the Ministry of Education, Science and Technological Development of the Republic of Serbia. Partial support has also been provided by the Republic Hydrometeorological Service of Serbia.*

## REFERENCES

[1] Taylor P. E., Jonsson H., Curr. Allergy. Asthm. (2004) 409–413.

[2] Hughes D. D., Mampage C. B. A., Jones L. M., *et al*., Environ. Sci. Technol. Lett. 7 (2020) 409–414.

[3] D'Amato G., Annesi Maesano, I., Molino, A., *et al*., J. Allergy Clin. Immunol. 139 (2017) 1786-1787.

[4] Grundstein A., Shepherd M., Miller P., *et al*., J. Appl. Meteorol. Clim. 56 (2017) 1337–1343.

[5] Thien F., Beggs P. J, Csutoros D., *et al*., Lancet Planet Health 2 (2018) e255–263.

[6] Lindstrom J.S., Silver D., Sutherland F., Med. J. Aust. 207 (2017) 235–237.

[7] Siljamo P., Sofiev M., Filatova E., *et al*., Int. J. Biometeorol. 57 (2013) 125–136.

[8] Sofiev M., Siljamo P., Ranta H., *et al*., Int. J. Biometeorol. 57 (2013) 45–58.

[9] Wozniak M.C., Solmon F., Steiner A. L., Geophys. Res. Lett. 45 (2018) 7156–7164.

[10] Nickovic S., Kallos G., Papadopoulos A., *et al*., J. Geophys. Res. 106 (2001) 18113–18130.


eco.tfbor.bg.ac.rs

ISBN 978-86-6305-137-9

tfbor.bg.ac.rs

University of Belgrade, Technical Faculty in Bor


# 30th International Conference Ecological Truth & Environmental Research 2023

# Proceedings

Editor
Prof. Dr Snežana Šerbula

University of Belgrade, Technical Faculty in Bor


# 30th International Conference Ecological Truth & Environmental Research 2023

# Proceedings

Editor
Prof. Dr Snežana Šerbula

**PROCEEDINGS**

**30th INTERNATIONAL CONFERENCE**

**ECOLOGICAL TRUTH AND ENVIRONMENTAL RESEARCH – EcoTER'23**


**Editor:**

**Prof. Dr Snežana Šerbula**

University of Belgrade, Technical Faculty in Bor

**Editor of Student section:**

**Prof. Dr Maja Nujkić**

University of Belgrade, Technical Faculty in Bor

**Technical editors:**

**Jelena Milosavljević, PhD,** University of Belgrade, Technical Faculty in Bor

**Asst. prof. Dr Ana Radojević**, University of Belgrade, Technical Faculty in Bor

**Sonja Stanković**, **MSc**, University of Belgrade, Technical Faculty in Bor

**Cover design:**

**Aleksandar Cvetković**, **BSc**, University of Belgrade, Technical Faculty in Bor

**Publisher:** University of Belgrade, Technical Faculty in Bor

**For the publisher:** Prof. Dr Dejan Tanikić, Dean

**Printed:** University of Belgrade, Technical Faculty in Bor, 100 copies, electronic edition

**Year of publication:** 2023





ISBN 978-86-6305-137-9

CIP - Каталогизација у публикацији
Народна библиотека Србије, Београд

502/504(082)(0.034.2)
574(082)(0.034.2)

**INTERNATIONAL Conference Ecological Truth & Environmental Research (30 ; 2023)**
Proceedings [Elektronski izvor] / 30th International Conference Ecological Truth & Environmental Research - EcoTER'23, 20-23 June 2023, Serbia ; organized by University of Belgrade, Technical faculty in Bor (Serbia) ; co-organizers University of Banja Luka, Faculty of Technology – Banja Luka (B&H) ... [et al.] ; [editor Snežana Šerbula]. - Bor : University of Belgrade, Technical faculty, 2023 (Bor : University of Belgrade, Technical faculty). - 1 elektronski optički disk (CD-ROM) ; 12 cm

Sistemski zahtevi: Nisu navedeni. - Nasl. sa naslovne strane dokumenta. - Preface / Snežana Šerbula. - Tiraž 100. - Bibliografija uz svaki rad.

ISBN 978-86-6305-137-9

а) Животна средина -- Зборници б) Екологија – Зборници

COBISS.SR-ID 118723849

----------------------------------

# 30th International Conference
# Ecological Truth and Environmental Research – EcoTER'23

*is organized by:*

**UNIVERSITY OF BELGRADE**
**TECHNICAL FACULTY IN BOR (SERBIA)**

*Co-organizers of the Conference:*

**University of Banja Luka, Faculty of Technology, Banja Luka (B&H)**

**University of Montenegro, Faculty of Metallurgy and Technology, Podgorica (Montenegro)**

**University of Zagreb, Faculty of Metallurgy, Sisak (Croatia)**

**University of Pristina, Faculty of Technical Sciences, Kosovska Mitrovica**

**Association of Young Researchers Bor (Serbia)**

## HONORARY COMMITTEE

## SCIENTIFIC COMMITTEE

## ORGANIZING COMMITTEE

**Prof. Dr Snežana Šerbula, *President***

**Prof. Dr Snežana Milić, *Vice President***

**Prof. Dr Đorđe Nikolić, *Vice President***

Prof. Dr Marija Petrović Mihajlović

Prof. Dr Milan Radovanović

Prof. Dr Milica Veličković

Prof. Dr Danijela Voza

Prof. Dr Maja Nujkić

Prof. Dr Žaklina Tasić

Dr Ana Simonović

Dr Tanja Kalinović

Dr Ana Radojević

Dr Jelena Kalinović

Dr Jelena Milosavljević

Sonja Stanković, MSc

Miljan Marković, MSc

Vladan Nedelkovski, MSc

Aleksandar Cvetković, BSc

# INFLUENCES OF EXTREME SOLAR ACTIVITY ON EARTH ENVIRONMENT – CASE STUDY

**Aleksandra Kolarski[1], Vladimir Srećković[1], Zoran Mijić[1*]**
[1]Institute of Physics Belgrade, University of Belgrade, Pregrevica 118, 11080 Belgrade, SERBIA
*zoran.mijic@ipb.ac.rs*

## Abstract
*The changes in the Earth environment triggered by the Solar activity can have a significant impact on the functionality of spaceborne and ground-based systems and services, potentially putting human wellbeing at risk. Recent assessment of the European Space Agency pointed out that a single extreme space weather event might have a huge socioeconomic impact on Europe society with its tendency to become even more sensitive in the future years. Many studies indicated significant direct influence of space weather events such as geomagnetic storms and solar flares on human health. As a result, systematic monitoring, and investigation of changes in the atmosphere caused by solar flares have become extremely important over the last decades. The aim of this case study is to investigate the solar flare effects on the ionosphere focusing on the changes that occurred above the European region on 6 September 2017, when one of the strongest solar flares occurred. Simultaneous monitoring of Very Low Frequency radio signals propagation at the Institute of Physics Belgrade station in regular and perturbed ionospheric conditions, enabled retrieving of propagation parameters of sharpness and reflection height during perturbed ionospheric conditions. In addition, numerical simulations reveal changes in electron density profiles showing the increase of several orders of magnitude compared to unperturbed conditions. Obtained findings could be useful for investigation of both atmospheric plasma properties, and prediction of extreme weather impacts on human activities.*

**Keywords**: solar flare, radio signal, environmental impact, atmospheric perturbation.

## INTRODUCTION

Through solar-terrestrial interactions between solar activity events of electromagnetic (EM) and corpuscular nature and our planet's outer protective magnetospheric shield, Sun in a great matter influences the near-surface Earth environment. Some of the main inducing agents originating from the Sun are powerful events such as solar flares (SFs), coronal mass ejections (CMEs), energetic proton and electron events etc. Such energetic space weather events can potentially be hazardous to human health [1] and activities, causing radio communication and navigation disturbances such as radio wave blackout [2], directly affecting human crews on space missions and space-born instruments and also producing geomagnetic storms [3].

Energy released during solar flare events, powerful bursts of electromagnetic energy, is well known to penetrate deep into the Earth's atmosphere. Aside from the Lyman-alpha component, soft-range X-rays with wavelengths of 0.1–0.8 nm reach the lowest of ionospheric regions, the D-region spreading between 50 and 90 km in height that overlaps with mesospheric region of the atmosphere [4]. Additional incident EM radiation during SFs changes plasma properties within lower ionosphere causing electron density height profile to change as well, following in behaviour input X-ray radiation. Investigation of changes in the atmosphere caused by solar flares and related impacts on the environment have attracted more attention over the last decades. In this paper characteristics of one of the strongest SF events observed are analysed and its impact on lower ionospheric perturbations discussed.

## MATERIALS AND METHODS

Case study presented in this work covers X-class SF event X9.3 occurred on September 6th, 2017 (Figure 1) and accompanying CMEs directed towards Earth through ionospheric influences within the near Earth environment. Technology for remote sensing of the lower ionosphere employing artificial man-made Very Low Frequency (VLF) radio signals of frequency range 3–30 kHz is applied [5,6]. Analysis is conducted on data recorded by BEL VLF systems located at the Institute of Physics Belgrade, while X-ray data were taken from GOES database [7]. Retrieving of propagation parameters of sharpness and reflection height during perturbed ionospheric conditions was done according to measured VLF signal perturbations related to X9.3 inducing agent through numerical simulations, with electron density height profile variation during this event obtained based on Wait's empirical approach [6].

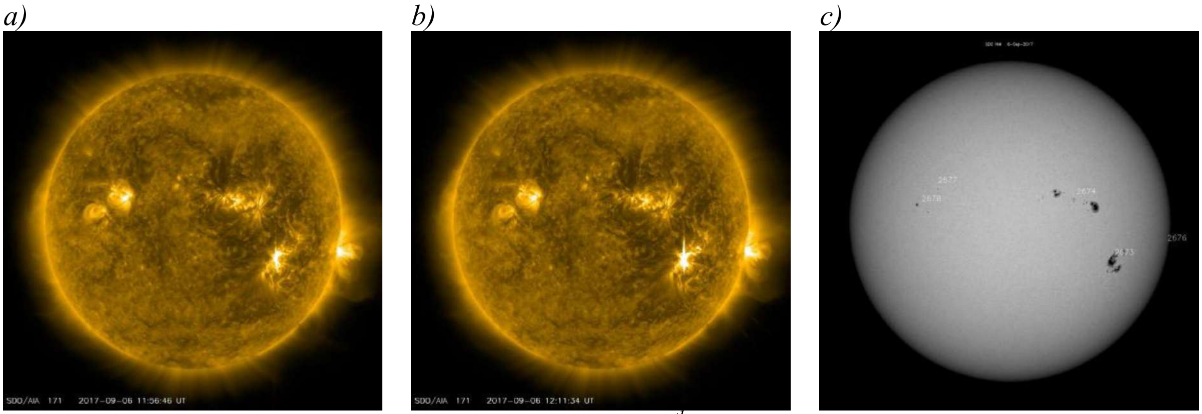


***Figure 1*** *X-class SF event X9.3 occurred on September 6th, 2017, started at 11:53UT, reached peak at 12:02UT with* $Ix_{max} = 9.3293 \cdot 10^{-4}$ Wm$^{-2}$, *and ended at 12:10UT, which originated from active region 2673, as captured by one of NASA's Solar Dynamics Observatory telescopes: two successive frames of this SF and its active region a) frame at 11:56UT left; b) frame at 12:11UT in the middle; c) active regions on September 6th 2017 (taken from https://www.nasa.gov/)*

Absolute Phase and Amplitude Logger (AbsPAL) station, located in Belgrade (44.85°N; 20.38°E), provided the VLF data used in this analysis. Amplitude and phase perturbations related to case study event of X9.3 SF, were monitored on VLF signal emitted from military transmitter in Skelton (54.72°N; 2.88°W), UK on frequency 22.1 kHz, with code name GQD, arriving in Belgrade from west with Great Circle Path (GCP) in length of about 2 Mm (Figure 2). Methodology used relies on subionospheric VLF signal propagation within Earth-ionosphere waveguide, with lower ionosphere as the upper boundary and Earth's surface as the lower boundary of this waveguide, and hop-wave theory of radio signal transmitting within the waveguide [5,6,8,9]. Approach involves multi-signal simultaneous monitoring of VLF signals' amplitude and phase in regular and perturbed ionospheric conditions, enabling to retrieve properties of perturbation from measured VLF data, through comparison between unperturbed and perturbed states, using numerical procedures for modelling of ionospheric plasma properties [10–20].

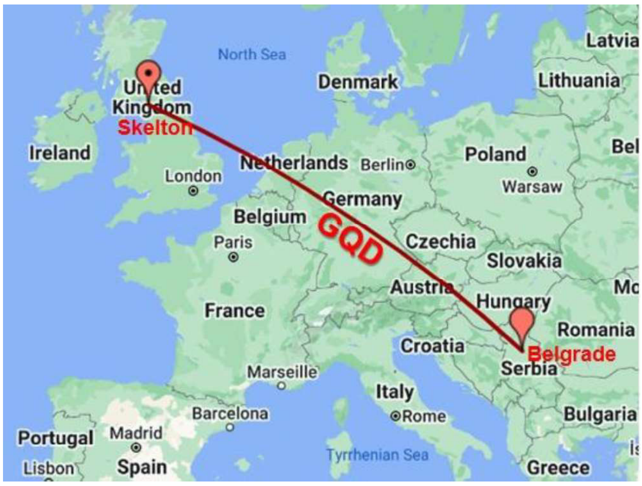


***Figure 2*** *Great Circle Path (red) of VLF radio signal GQD/22.1 kHz, transmited from Skelton (UK) and registered in Belgrade (Serbia)*

## RESULTS AND DISCUSSION

Amplitude and phase perturbations observed on GQD signal recorded in Belgrade during X9.3 SF, with incident soft X-ray irradiance as recorded by GOES-15 satellite, are presented in Figure 3, on middle, lower and upper panel, respectively.

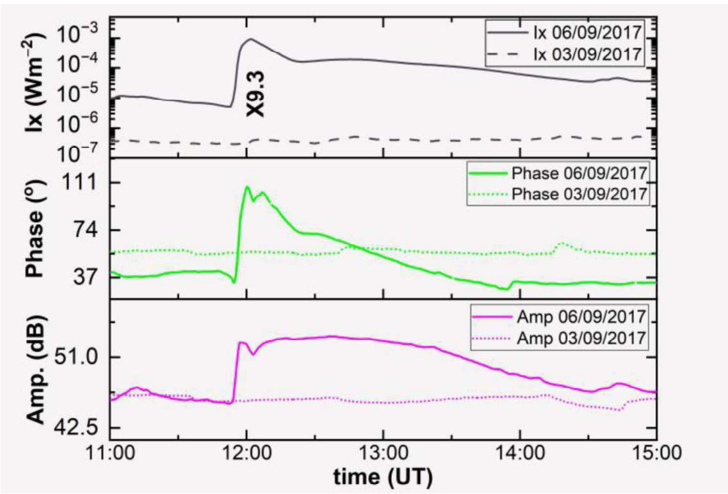


***Figure 3*** *Simultaneous variations of X-ray flux (perturbed and quiet days in solid and dashed gray, respectively) recorded by GOES-15 satelite, perturbed phase (solid green) and amplitude (solid pink) and quiet signals (dotted green and pink) of GQD/22.10 kHz VLF radio signal during X9.3 SF occurred on September 6$^{th}$, 2017, recorded by Belgrade VLF station (from upper to lower panel)*

Amplitude and phase perturbations on monitored VLF signals are of relatively simple morphology and pattern, following inducing X-radiation agent with time delay corresponding to the sluggishness of the ionosphere [21,22]. Recorded amplitude and phase perturbation on monitored GQD signal as induced by SF event X9.3 on September 6th, 2017, reached maximal increase of 7.09 dB in amplitude and 52.03° in phase compared to unperturbed values during September 3rd, 2017, corresponding to the peak activity of soft X-ray flux.

Based on amplitude and phase perturbations during X9.3 SF, modelling of ionospheric plasma properties was done through numerical simulations, using Long Wavelength Propagation Capability (LWPC) software [23] and the FlarED' Method and Approximate Analytic Expression application [4,17]. Estimated values of analysed VLF signals' amplitude and phase obtained during modelling through both applied numerical procedures are in good agreement with real values measured by BEL VLF receiving system.

LWPC software utilisation based on Wait's theory application, rely on Wait's parameters β ($km^{-1}$) and *H'* (km) (lower ionospheric boundary sharpness and VLF signal's reflection height), determined for daytime ionospheric conditions using Equation (1) [6]. Electron densities calculated at the reflection height, when $h = H'$ give profile throughout D-region altitude range (Figure 4).

$$N_e(h, H', \beta) = 1.43\cdot 10^{13}\cdot e^{(-0.15\cdot H')}\cdot e^{[(\beta-0.15)\cdot(h-H')]}, \quad (m^{-3}) \tag{1}$$

FlarED' Method and Approximate Analytic Expression application, designed for obtaining VLF signal propagation parameters β and *H'* from incident solar X-ray irradiance, gave electron density profiles (Figure 5) calculated by using polynomial Equation (2) [4,17].

$$\log Ne(h, Ix) = a_1(h) + a_2(h)\cdot \log Ix + a_3(h)\cdot(\log Ix)^2 \tag{2}$$

Estimated electron densities at reference height of 74 km, obtained by both numerical approaches are within one order of magnitude. Obtained results are in line with results from other studies dealing with high class SF events and conducted by observation from mid-latitudinal located VLF receivers [4,15,16,18,24,25].

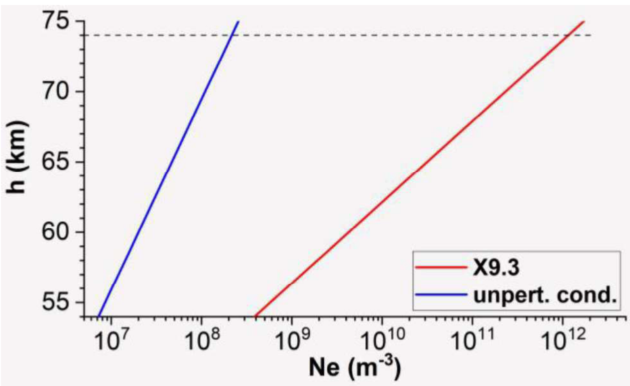


***Figure 4*** *Electron density height profile for GQD signal at peak intensity of X9.3 SF (red) obtained using Equation (1) and in unperturbed ionospheric conditions (blue); reference height 74 km is indicated by dotted black line*

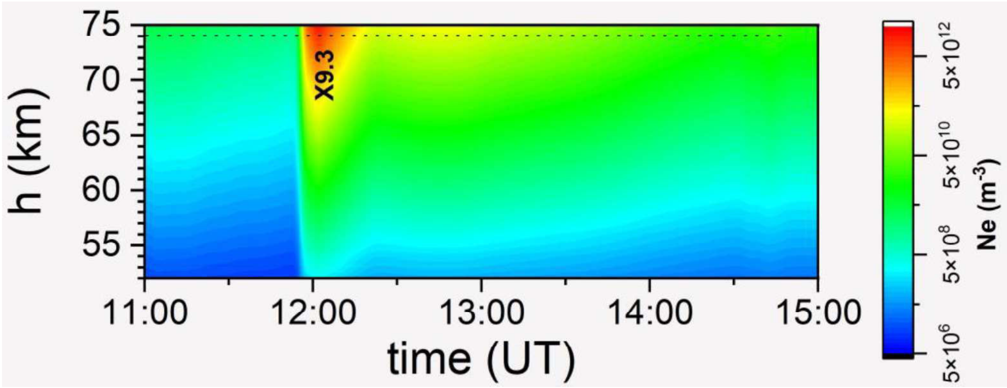


***Figure 5*** *Electron density height profiles for GQD signal during four hours including peak intensity of X9.3 SF obtained through application of approximative Equation (2); reference height 74 km is indicated by dotted black line*

## CONCLUSION

Solar flare events are well-known extraterrestrial driver for lower ionospheric perturbations, inducing change of plasma properties in near Earth environment, that can affect human health and cause serious damage to electronically dependent modern society, causing satellite operation breakdowns, communication blackouts, flight risks especially over polar regions, etc. Ionospheric D-region, as medium for VLF signal propagation in a way “mirrors” disturbances of its plasma properties onto propagation parameters of VLF signals, forcing them to deviate from their regular propagation patterns characteristic for unperturbed ionospheric conditions. In this manner caused amplitude and/or phase perturbations make VLF technique as very efficient and as the technique of choice for this region remote sensing exploration. Lower ionospheric disturbance related to X9.3 solar flare event that occurred on September 6$^{th}$, 2017, caused perturbations in propagation parameters of VLF signals, that as recorded by Belgrade VLF system and observed on GQD signal, reached several dB in amplitude and few tens of degrees in phase, compared to unperturbed signal on September 3$^{rd}$, 2017. Accordingly, electron density profiles also changed, following the incident soft X-ray radiation, showing the increase of several orders of magnitude compared to their unperturbed values at the reference height of 74 km, as obtained through conducted numerical simulations.

## ACKNOWLEDGEMENT

*This work was funded by the Institute of Physics Belgrade, University of Belgrade, through a grant by the Ministry of Science, Technological Development and Innovations of the Republic of Serbia.*

## REFERENCES

[1] Alabdulgader A., McCraty R., Atkinson M., *et al*., Sci. Rep. (2018) 2663.

[2] Yasyukevich Y., Astafyeva E., Padokhin A., *et al*., Space Weather (2018) 1013–1027.

[3] Riley P., Love J. J., Space Weather (2017) 53–64.

[4] Srećković V. A., Šulić D. M., Ignjatović Lj., *et al*., Appl. Sci. 11 (2021) 7194.

[5] Mitra A. P., Lonospheric Effects of Solar Flares; Springer, Berlin/Heidelberg (1974), p.305, ISBN: 978-90-277-0467-2.

[6] Wait J. R, Spies K. P., Characteristics of the Earth-Ionosphere Waveguide for VLF Radio Waves; US Department of Commerce, National Bureau of Standards, Gaithersburg MD, (1964), p.110.

[7] NOAA National Centre's for Environmental Information, *Available on the following link*: https://satdat.ngdc.noaa.gov/sem/goes/data/avg/.

[8] Budden K., Radio Waves in the Ionosphere, Cambridge University Press, Cambridge (1961), p.542, ISBN: 052111439X.

[9] Wait J. R., Electromagnetic Waves in Stratified Media, Pergamon Press, Oxford (1970), p.620, ISBN: 9781483184258.

[10] Silber I., Price C., Surv. Geophys. 38 (2017) 407–441.

[11] Žigman V., Kudela K., Grubor D., Adv. Space Res. 53 (2014) 763–775.

[12] Nina A., Remote Sens. 14 (2022) 54.

[13] Šulić D., Nina A., Srećković V., arXiv (2014) arXiv:1405.3783.

[14] Grubor D., Šulić D., Žigman V., Ann. Geophys. 26 (2008) 1731–1740.

[15] Kolarski A., Srećković V. A., Mijić Z. R., Appl. Sci. 12 (2022) 582.

[16] Barta V., Natras R., Srećković V., *et al.*, Front. Environ. Sci. 10 (2022) 904335.

[17] Srećković V.A., Šulić D.M., Vujčić V., *et al.*, Appl. Sci. 11 (2021) 11574.

[18] Kolarski A., Veselinović N., Srećković V. A., *et al.*, A. Remote Sens. 15 (2023) 1403.

[19] Kolarski A., Grubor D., Adv. Space Res. 53 (2014) 1595–1602.

[20] Kolarski A., Srećković V. A., Mijić Z. R., Contrib. Astron. Obs. Skaln. Pleso 52 (2022) 105.

[21] Appleton E. V., J. Atmos. Sol.-Terr. Phy. 3 (1953) 282–284.

[22] Žigman V., Grubor D., Šulić D., J. Atmos. Sol.-Terr. Phys. 69 (2007) 775–792.

[23] Ferguson, J. Computer Programs for Assessment of Long-Wavelength Radio Communications, Version 2.0: User's Guide and Source Files, Space and Naval Warfare Systems Center, San Diego (1998).

[24] Thomson N. R., Rodger C. J., Clilverd M. A., J. Geophys. Res. Space Phys. (2005) A06306.

[25] McRae W. M., Thomson N. R., J. Atmos. Sol.-Terr. Phys. 66 (2004) 77–87.

# NOVEL APPROACH IN AIRBORNE POLLEN DISPERSION MODELLING

**Slobodan Ničković[1,2], Luka Ilić[1,3], Slavko Petković[2], Goran Pejanović[2], Alfredo Huete[4], Zoran Mijić[1*]**

[1]Institute of Physics Belgrade, University of Belgrade, Pregrevica 118, 11080 Belgrade, SERBIA

[2]Republic Hydrometeorological Service of Serbia, 11000 Belgrade, SERBIA

[3]now at Barcelona Supercomputing Center, Plaça Eusebi Güell, 1–3, 08034 Barcelona, SPAIN

[4]School of Life Sciences, University of Technology Sydney, Sydney, NSW, AUSTRALIA

[*]*zoran.mijic@ipb.ac.rs*

## Abstract

*When exposed to high atmospheric humidity, pollen grains rupture and release large numbers of small allergenic particles. Unlike whole pollen grains, these submicron particles easily enter deep into lungs and can cause a serious asthmatic response. Current operating pollen models predict the concentration of intact (whole) pollen grains but not respirable allergenic fragmented particles. We tested a novel numerical pollen model that predicts the formation and dispersion of sub-pollen allergenic granules released after pollen grains burst in the moist air. We evaluated the model for the case of the November 2016 Melbourne thunderstorm asthma epidemic, which resulted in 10 deaths and thousands of hospital admittances. This episode was triggered by intact grass pollen transported toward the city by a severe storm weather system followed by a 5 hour lag in the arrival of the finer, sub-pollen granules into the city, with a spike in hospital presentations shortly after. The model accurately predicted the observed times, locations and quantities of both fragmented and intact pollen concentrations. The presented modelling system, if operationally implemented, can be used as a prognostic tool for early warning alerts on asthma epidemic occurrences.*

**Keywords**: pollen, numerical modeling, thuderstorm asthma, sub-pollen particles.

## INTRODUCTION

Thunderstorms occurring during the pollen season are often associated with an increased number of sub-pollen particles. The conceptual model of thunderstorm asthma (asthma episodes associated with thunderstorms) assumes that a thunderstorm circulation transports the emitted pollen grains into a cloud where grains rupture due to high atmospheric moisture. Each pollen grain release almost one thousand sub-pollen particles [1]. Recently presented direct measurements of sub-pollen concentrations performed for the first time with a novel fluorescence spectroscopic technique show that fragments remain airborne for several hours after pollen rupturing by thunderstorms [2]. These fragmented particles are small enough to enter deep into the lungs and to cause severe asthmatic reaction [3].

During the 21 November 2016, the asthma epidemic episode in Melbourne (Australia), ryegrass pollen was transported to the city from widespread pastures in the region by a strong wind gusts ahead of fast-moving thunderstorm squall-line front [4]. The city recorded ten asthma-related deaths and almost 500 admissions to the hospital over a short time after this event. The number of hospital visits increased by 992% within 30 h [5]. The Melbourne episode was the worldwide largest asthma epidemic coinciding with pollen presence. Many people had breathing difficulties occurred in such a short interval that it caused extreme pressure on the health system. The sudden increase in observed ruptured pollen counts associated with the frontal passage was assumed to be the major cause of the epidemic [6]. High levels of intact pollen concentrations, observed a day earlier on 20 November from nearby local grass emissions did not cause an asthma epidemic, since stable synoptic conditions prevailing that day were not favourable for pollen fragmentation. In response to the 21 November thunderstorm asthma episode, the local Victorian government recommended the development of a physical pollen model as a key priority in order to fulfil societal needs for a more reliable early warning system.

Currently several physical models available in the community provide short-term prediction of the intact pollen concentration embedded into numerical weather prediction systems [7,8]. However, parameterization of pollen rupturing and dispersion of sub-pollen allergenic particles is still challenging task. In this paper the results of sub-pollen particles prediction obtained by numerical simulation are presented using a novel parameterization scheme for pollen rupturing.

## MATERIALS AND METHODS

The numerical model called DREAM-POLL have been developed to predict not only the intact pollen concentration but also the production and dispersion of allergens released from ruptured pollen grains. DREAM-POLL is an Euler-type model in which prognostic pollen concentration equation is embedded on-line into a high-resolution non-hydrostatic weather prediction model. The on-line modelling approach allows the atmospheric and pollen processes to be synchronously simulated. DREAM-POLL mathematically describes the major phases of the atmospheric pollen cycle, including the emission of pollen, its vertical and horizontal transport, and pollen turbulent mixing and deposition.

The model starts emitting pollen from a pre-specified source when near-ground turbulence exceeds a threshold at that source. The emitted pollen is further directed by the turbulence and large-scale dynamics of the atmospheric model driver. At the end of their atmospheric cycle, pollen particles are settled to the ground by precipitation and by near-surface dynamics as predicted by the atmospheric driver. In the newly developed pollen rupturing parameterization, we calculate in every model time step the number of fragmented particles released from ruptured pollen grains whenever the atmospheric humidity of the driver model exceeds a pre-specified threshold of 60% [9]. The intact, ruptured and fragmented particles are driven by the same atmospheric dynamics in the model, except that intact pollen elements are emitted from the ground, and the other two particle categories originate in high moisture cloud conditions. Model experiments presented in this study were performed with horizontal grid spacing of approximately 5 km. At this resolution, convective and non-hydrostatic atmospheric processes are explicitly resolved in the model, which is essential for appropriate simulation of pollen dynamics under thunderstorm conditions. The 50-m resolution Australian

Land Use and Management (ALUM) classification data was used to specify the grass fraction used in the model as potential pollen sources. We tested the model performance by executing it in a real-time prognostic mode for the Melbourne episode, validating its results against available pollen observations.

DREAM-POLL represents a modified version of the DREAM regional dust aerosol atmospheric model [10]. The model domain in this study covers the southwestern region of Australia, and there are 28 model vertical levels spanning from the surface to 50 hPa. The horizontal grid distance is set to 1/20 deg (approximately 5 km). The pollen advection and lateral diffusion are computed every 35 sec, the emission and vertical diffusion are updated every 70 sec, and the convection and large-scale precipitation are calculated every 140 sec.

The model was run over the period 19–22 November 2016 during which the Melbourne episode happened. The initial and boundary conditions for the atmospheric model component were specified using weather prediction parameters of the European Centre for Medium-range Weather Forecast (ECMWF) global model. Since there are no satisfactory three-dimensional pollen concentration observations to be assimilated, the initial state of pollen concentration in the model was defined by the 24-h forecast from the previous day model run. Only for the "cold start" of the model at 00:00 UTC 19 November 2016, the initial pollen concentrations were set to zero.

## RESULTS AND DISCUSSION

The synoptic situation on 21 November was characterized by the presence of a cold front over southeast Australia. Northerly winds ahead of the front swept ryegrass pollen from pastures north of Melbourne. A multi-cell thunderstorm squall-line heading the cold front passed the city area between 17:00 and 18:30 AEDT (AEDT – Australian Eastern Daylight Time is the local time, which is UTC+11:00), when surface meteorological parameters abruptly changed their values. From the early afternoon onwards, the observed intact and ruptured pollen concentrations increased as well. At 16:00 AEDT, the simulated horizontal wind convergence line approached the wider city area. The convergence line separated the warmer air on the Melbourne side from the colder maritime air southward. Previously emitted intact pollen north of the city was lifted by warm updrafts to zones of moist air, while cold downdrafts prevailed behind the squall-line. The predicted location, orientation, and intensity of the squall-line agree with satellite data. Its circulation pattern is consistent with conceptual models of squall-line thunderstorm systems. After entering the moist air, pollen rupturing was triggered, but at this time the ruptured grains had not reach the surface. At 22:00 AEDT, after the thunderstorm line moved away from Melbourne, the predicted intact pollen concentrations were reduced to zero (Figure 1a). However, about this time, the surface concentration of ruptured particles achieved its maximum (Figure 1b).

Figure 2 shows the spatio-temporal evolution of the intact and fragmented particles as predicted for the pollen measurement site Burwood (the Deakin University, Melbourne). Being lighter in weight, the fragmented particles progressed much slower than the heavier intact pollen grains, with most sub-pollen particles arriving at the city on 21 November about 5 h later than intact pollen. A time delay of several hours is observed during asthma thunderstorm episodes in the USA as well [2].

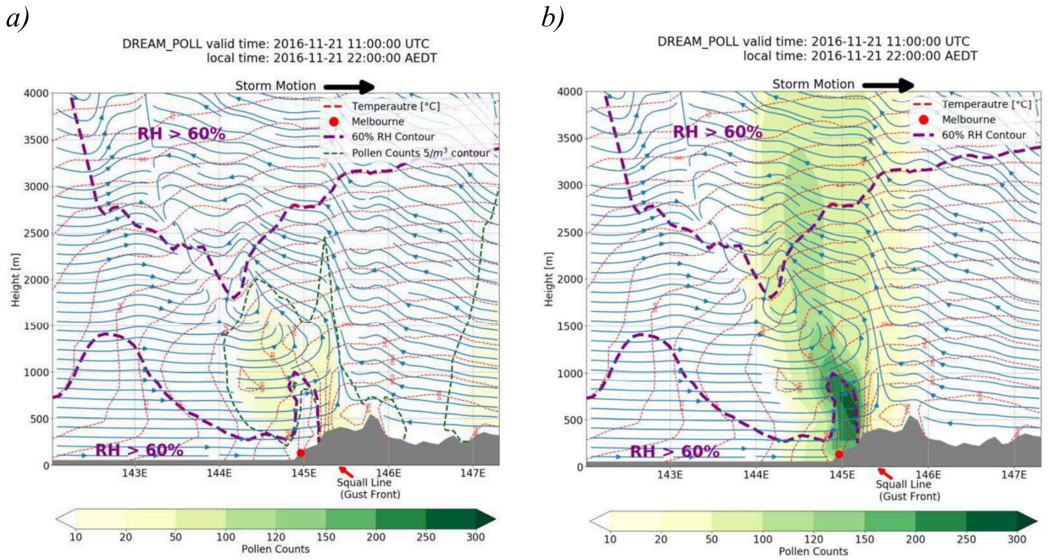


***Figure 1** Predicted intact and ruptured pollen concentration at 22:00 AEDT on 21 November; Vertical cross sections along the normal to the front, with pollen concentration (yellow-to-green palette), streamlines and contours of 60% relative humidity (dashed purple lines); a) intact; b) ruptured pollen; Melbourne is represented by a red dot in each panel.*

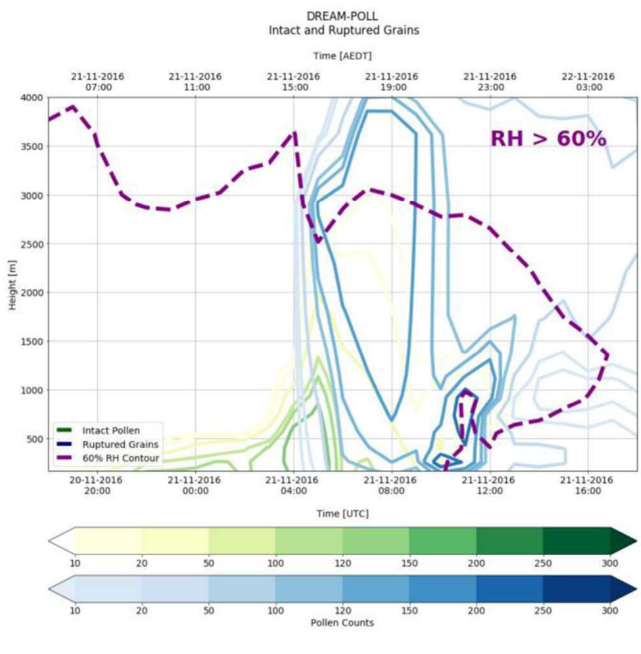


***Figure 2** Predicted intact and ruptured pollen grains above Melbourne; 60% relative humidity contour*

There are two peaks of intact pollen concentrations observed in Melbourne during the 20–21 November period (Figure 3). The first peak on the 20th is attributed to pollen probably emitted from nearby urban sources. During this day, there were no significant ruptured pollen numbers recorded, which indicates that particle fragmentation did not occur under the prevailing stable synoptic conditions. However, on the 21 November both observations and model results show increased numbers of intact and ruptured pollen particles linked with the passage of the wind gust front. Affected by the passing front, the largest decrease/increase of predicted intact/ruptured particle numbers occurred at approximately 18:00 AEDT. Significant increase in the observed ruptured-to-intact grain ratio after the front passage was reproduced by the model as well.

The predicted intact pollen achieved its largest number several hours before the thunderstorm arrived in Melbourne. Later that afternoon, the arrival of the squall front coincided with a short-term precipitation event [5]. From 15:00 AEDT onwards, the predicted number of pollen fragments (represented with the size of 3.03 μm in the model) started to increase, reaching the maximum concentration of 97,500 particles per m$^3$ at 21:00 AEDT. This value is within an order of observed magnitudes [2]. A decline in intact pollen before and an increase in fragment numbers after the frontal passage we simulated are consistent with a recently published characterization of airborne pollen dynamics during several thunderstorms [2]. The maximum number of allergenic pollen fragments was predicted to have occurred 2 h before the highest recorded number of asthma-related hospital presentations.

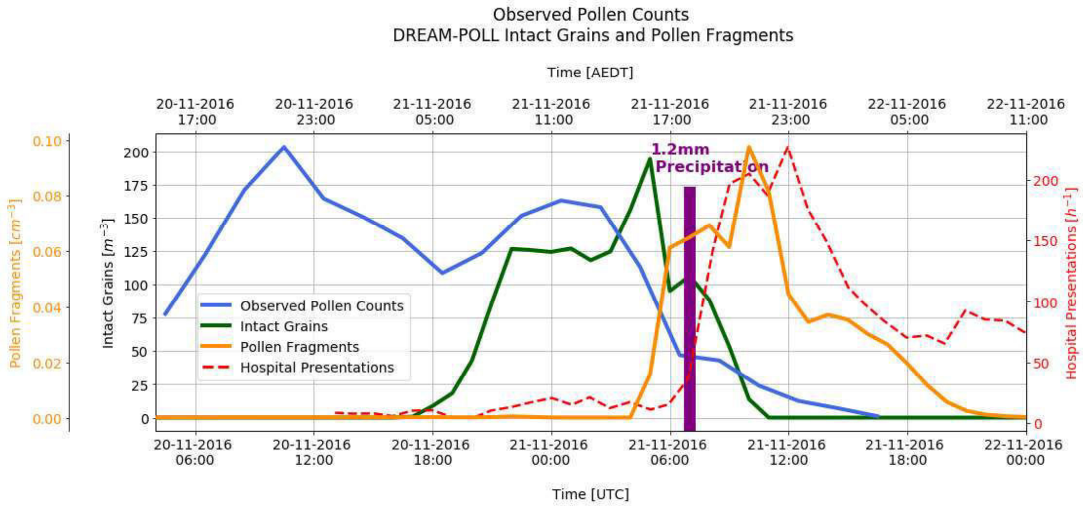


***Figure 3*** *Pollen concentrations in Melbourne: Observed pollen counts (blue); predicted intact grains (green) and sub-pollen particles (orange); observed 1.2 mm precipitation (purple bar); 1-h hospital presentations (dashed red line)*

## CONCLUSION

We presented in this study a numerical modelling approach that enables the prediction of concentration of respirable sub-pollen fragments several days in advance. We demonstrated the effectiveness of this approach by forecasting the Melbourne thunderstorm asthma event 48 h earlier. The proposed method can play a crucial component in an early warning system dedicated to predict time and location of asthma-related outbreaks. DREAM-POLL can be implemented with different model resolutions, over specified geographical domains and for a given pollen type. The availability of such an early-warning system would allow civil authorities to react in a timely manner to asthma epidemics and thus significantly diminish pressure on health services and reduce fatalities and illnesses due to respiratory problems.

However, a numerical parameterization scheme for sub-pollen particles formation from whole grains can be further improved taking into the account not only high humidity but other effects of convective thunderstorm conditions.

**ACKNOWLEDGEMENT**

*The authors acknowledge Prof. Ed Newbigin and Jeremy Silver (the University of Melbourne, Australia) for supplying the pollen observation data and Dr. Elizabeth E. Ebert (Weather and Environmental Prediction, Bureau of Meteorology Melbourne, Australia) for useful discussions. L. Ilic and Z. Mijic acknowledge funding provided by the Institute of Physics Belgrade, through a grant by the Ministry of Education, Science and Technological Development of the Republic of Serbia. Partial support has also been provided by the Republic Hydrometeorological Service of Serbia.*

**REFERENCES**

[1] Taylor P. E., Jonsson H., Curr. Allergy. Asthm. (2004) 409–413.

[2] Hughes D. D., Mampage C. B. A., Jones L. M., *et al*., Environ. Sci. Technol. Lett. 7 (2020) 409–414.

[3] D'Amato G., Annesi Maesano, I., Molino, A., *et al*., J. Allergy Clin. Immunol. 139 (2017) 1786-1787.

[4] Grundstein A., Shepherd M., Miller P., *et al*., J. Appl. Meteorol. Clim. 56 (2017) 1337–1343.

[5] Thien F., Beggs P. J, Csutoros D., *et al*., Lancet Planet Health 2 (2018) e255–263.

[6] Lindstrom J.S., Silver D., Sutherland F., Med. J. Aust. 207 (2017) 235–237.

[7] Siljamo P., Sofiev M., Filatova E., *et al*., Int. J. Biometeorol. 57 (2013) 125–136.

[8] Sofiev M., Siljamo P., Ranta H., *et al*., Int. J. Biometeorol. 57 (2013) 45–58.

[9] Wozniak M.C., Solmon F., Steiner A. L., Geophys. Res. Lett. 45 (2018) 7156–7164.

[10] Nickovic S., Kallos G., Papadopoulos A., *et al*., J. Geophys. Res. 106 (2001) 18113–18130.


eco.tfbor.bg.ac.rs ISBN 978-86-6305-137-9 tfbor.bg.ac.rs

# Book of abstracts

# PHOTONICA2017

The Sixth International School and Conference on Photonics

& COST actions: MP1406 and MP1402

&H2020-MSCA-RISE-2015 CARDIALLY workshop

28 August – 1 September 2017

Belgrade, Serbia


*Editors*

Marina Lekić and Aleksandar Krmpot

Institute of Physics Belgrade, Serbia



Belgrade, 2017

ABSTRACTS OF TUTORIAL, KEYNOTE, INVITED LECTURES, PROGRESS REPORTS AND CONTRIBUTED PAPERS

of

# The Sixth International School and Conference on Photonics PHOTONICA2017

28 August – 1 September 2017
Belgrade Serbia

*Editors*
Marina Lekić and Aleksandar Krmpot

*Technical assistance*
Marko Nikolić and Danica Pavlović

*Publisher*
Institute of Physics Belgrade
Pregrevica 118
11080 Belgrade, Serbia

*Printed by*
Serbian Academy of Sciences and Arts

*Number of copies*
300

ISBN 978-86-82441-46-5

PHOTONICA 2017 (The Sixth International School and Conference on Photonica - www.photonica.ac.rs) is organized by Institute of Physics Belgrade, University of Belgrade (www.ipb.ac.rs), Serbian Academy of Sciences and Arts (www.sanu.ac.rs), and Optical Society of Serbia (www.ods.org.rs).

Other institution that helped the organization of this event are: Vinča Institute of Nuclear Sciences, University of Belgrade (www.vinca.rs), Faculty of Electrical Engineering, University of Belgrade (www.etf.bg.ac.rs), Institute of Chemistry, Technology and Metallurgy, University of Belgrade (www.ihtm.bg.ac.rs), Faculty of Technical Sciences, University of Novi Sad (www.ftn.uns.ac.rs), Faculty of Physics, University of Belgrade (www.ff.bg.ac.rs), and Faculty of Biology, University of Belgrade (www.bio.bg.ac.rs).

PHOTONICA 2017 is organized under auspices and with support of the Ministry of Education, Science and Technological Development, Serbia (www.mpn.gov.rs). PHOTONICA 2017 is supported and recognized by The Integrated Initiative of European Laser Research Infrastructures LaserLab-Europe (www.laserlab-europe.eu) and European Physical Society (www.eps.org).

**The support of the sponsors of PHOTONICA 2017 is gratefully acknowledged:**

# Committees

## Scientific Committee

Aleksandar Krmpot, Serbia
Antun Balaž, Serbia
Arlene D. Wilson-Gordon, Israel
Bojan Resan, Switzerland
Boris Malomed, Israel
Branislav Jelenković, Serbia
Dejan Gvozdić, Serbia
Detlef Kip, Germany
Dragan Indjin, United Kingdom
Edik Rafailov, United Kingdom
Feng Chen, China
Francesco Cataliotti, Italy
Giannis Zacharakis, Greece
Goran Isić, Serbia
Goran Mašanović, United Kingdom
Isabelle Philippa Staude, Germany
Jelena Radovanović, Serbia
Jerker Widengren, Sweden
Jovana  Petrović, Serbia
Laurent Sanchez, France
LjupčoHadžievski, Serbia
Marco Santagiustina, Italy
Milan Mashanović, United States of America
Milan Trtica, Serbia
Miloš Živanov, Serbia
Milutin Stepić, Serbia
Milivoj Belić, Qatar
Nikola Stojanović, Germany
Pavle Anđus, Serbia
Peđa Mihailović, Serbia
Radoš Gajić, Serbia
Schaaf Peter, Germany
Sergei Turitsyn, United Kingdom
Suzana Petrović, Serbia
Ticijana Ban, Croatia
Vladana Vukojević, Sweden
Zoran Jakšić, Serbia
Željko Šljivančanin, Serbia

## Organizing Committee

Aleksandar Krmpot, (Chair)
Marina Lekić (Secretary)
Stanko Nikolić (webmaster)
Marko Nikolić,
Vladimir Veljić
Danica Pavlović

## Technical Organizer

PanaComp
Wonderland Travel
Serbia

## 11. Other topics in photonics

# Vertical Raman LIDAR profiling of atmosphericaerosol optical properties over Belgrade

Z. Mijić, L. Ilić and M. Kuzmanoski
*Institute of Physics,Belgrade, Serbia*
e-mail:luka.ilic@ipb.ac.rs

The direct radiative effect due to aerosol–radiation interactions is the change in radiative flux caused by the combined scattering and absorption of radiation by anthropogenic and natural aerosols. Due to their short lifetime and the large variability in space and time atmospheric aerosols are considered one of the major uncertainties in climate forcing and atmospheric processes [1]. For radiative studies it is necessary to measure aerosol optical properties, size, morphology and composition as a function of time and space, with a high resolution in both domains to account for the large variability. Lidar (Light Detection And Ranging), an active remote sensing technique, represents the optimal tool to provide range-resolved aerosol optical parameters. Large observational networks such as the European Aerosol Research Lidar Network (EARLINET) [2], the Aerosol Robotic Network (AERONET), provide the long-term measurement series needed to build a climatology of aerosol optical properties at the continental and global scales.
In order to assess the origin and type of aerosols which travel over Balkan region, having an impact on modification of the regional radiative budget, case studies combining measurements at the EARLINET joining lidar station in Belgrade with atmospheric modeling have been analyzed. For vertical profiling and remote sensing of atmospheric aerosol layers the Raman lidar system at the Institute of Physics Belgrade (44.860 N, 20.390 E) has been used. It is bi-axial system with combined elastic and Raman detection designed to perform continuous measurements of aerosols in the planetary boundary layer and the lower free troposphere. It is based on the third harmonic frequency of a compact, pulsed Nd:YAG laser, emitting pulses of 65 mJ output energy at 355 nm with a 20 Hz repetition rate. The optical receiver is a Cassegrain reflecting telescope with a primary mirror of 250 mm diameter and a focal length of 1250 mm. Photomultiplier tubes are used to detect elastic backscatter lidar signal at 355 nm and Raman signal at 387 nm. The detectors are operated both in the analog and photon-counting mode and the spatial raw resolution of the detected signals is 7.5 m. Averaging time of the lidar profiles is of the order of 1 min corresponding to 1200 laser shots. Lidar measurements can be used in synergy with numerical models in order to validate and compare information about aerosols. In this paper DREAM (Dust Regional Atmospheric Model) model, designed to simulate and/or predict the atmospheric cycle of mineral dust aerosol [3], will be used to analyze dust transport. The capability of the lidar technique to derive range-resolved vertical profiles of aerosol optical parameters (backscatter and extinction coefficient) with very high spatial and temporal resolution will be used to identify the altitude of layers and the temporal evolution of intrusions. Using these altitudes as inputs in air mass trajectory model, the source of aerosols can be identified. The additional techniques (satellite remote sensing) will be also discussed for selected case-studies.

REFERENCES

[1] IPCC: The Physical Science Basis, Contribution of Working Group I to the Fifth Assessment Report of the Intergovernmental Panel on Climate Change, edited by: Stocker, T. F., Qin, D., Plattner, G.-K., Tignor, M., Allen, S. K., Boschung, J., Nauels, A., Xia, Y., Bex, V., and Midgley, P. M., Cambridge University Press, Cambridge, United Kingdom and New York, NY, USA, (2013).
[2] G. Pappalardo, A. Amodeo, A. Apituley, A. Comeron, V. Freudenthaler, H. Linné, A.Ansmann, J. Bösenberg, G. D'Amico, I.Mattis, L. Mona, U. Wandinger, V Amiridis, L. Alados Arboledas, D. Nicolae, and M. Wiegner,: EARLINET: towards an advanced sustainable European aerosol lidar network, Atmos. Meas. Tech. 7, 2389 (2014).
[3] S. Nickovic, G. Kallos, A. Papadopoulos, O. Kakaliagou, J. Geophys. Res. 106, 1813 (2001).

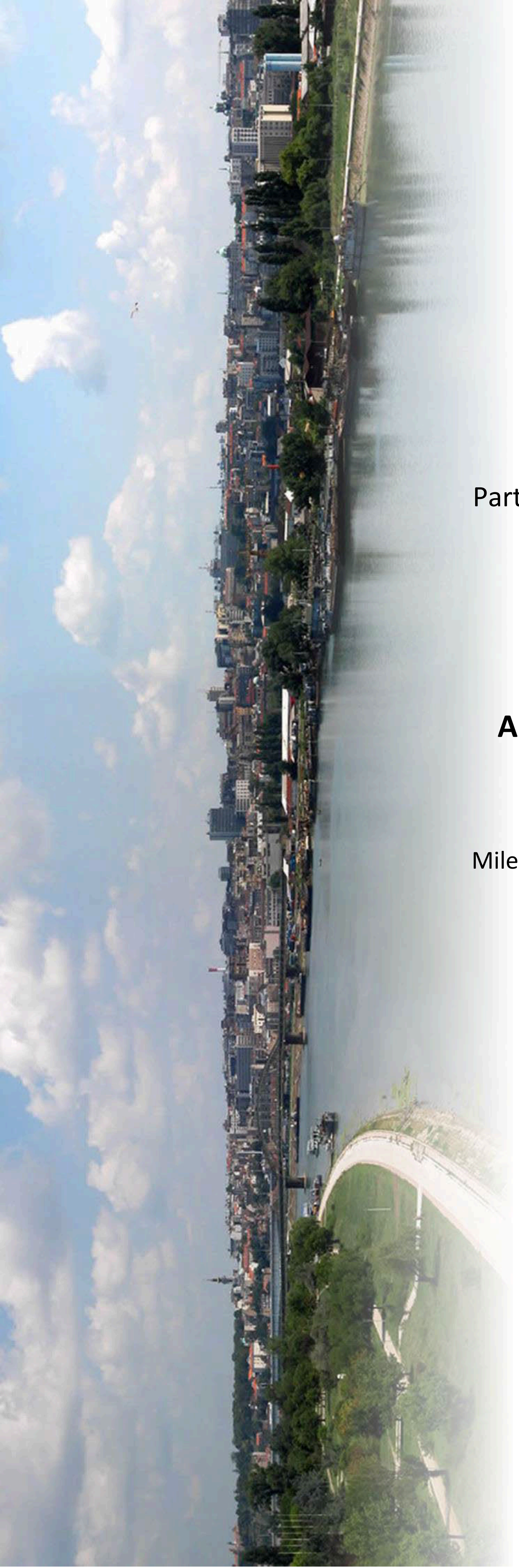

# WeBIOPATR 2019

The Seventh International WEBIOPATR
Workshop & Conference
Particulate Matter: Research and Management

**Abstracts of Keynote Invited Lectures
and Contributed Papers**

Milena Jovašević-Stojanović and Alena Bartoňová, Eds

Public Health Institute of Belgrade

Belgrade 2019

# ABSTRACTS OF KEYNOTE INVITED LECTURES AND CONTRIBUTED PAPERS

The Seventh International WeBIOPATR Workshop & Conference

Particulate Matter: Research and Management

**WeBIOPATR 2019**

1st to 3rd October, 2019

Belgrade, Serbia

*Editors*

Milena Jovašević-Stojanović

Alena Bartoňová

*Publisher*

Public Health Institute of Belgrade

Prof. Dr Dušanka Matijević, Director

Boulevar Despota Stefana 54a

Serbia, 11000 Belgrade

*Printed by*

Printing office of the Public Health Institute of Belgrade

*Number of copies*

150

ISBN 978-86-83069-56-9



www.zdravlje.org.rs

## SCIENTIFIC COMMITTEE

Aleksandar Jovović, Serbia

Alena Bartoňová, Norway

Antonije Onjia, Serbia

David Broday, Israel

Dikaia Saraga, Greece

Griša Močnik, Slovenia

Ivan Gržetić, Serbia

María Cruz Minguillón, Spain

Milena Jovašević-Stojanović, Serbia

Radim J. Šrám, Czech Republic

Renata Kovačević, Serbia

Selahattin Incecik, Turkey

Slobodan Ničković, Serbia

Simone Barreira Morais, Portugal

Zoran Mijić, Serbia

Zoran Ristovski, Australia

Zorana Jovanović-Andersen, Denmark

## ORGANIZING COMMITTEE

Aleksandra Stanković, Serbia

Alena Bartoňová, Norway

Andrej Šoštarić, Serbia

Anka Cvetković, Serbia

Biljana Filipović, Serbia

Branislava Matić, Serbia

Dejan Lekić, Serbia

Dragan Alavantić, Serbia

Ivan Lazović, Serbia

Jasmina Jović-Stošić, Serbia

Maja Jovanović (Secretary), Serbia

Marija Živković (Secretary), Serbia

Milena Jovašević-Stojanović, Serbia

Miloš Davidović, Serbia

Mira Aničić Urošević, Serbia

Mirjana Perišić, Serbia

Nenad Živković, Serbia

Tihomir Popović, Serbia

Vesna Slepčević, Serbia

Viša Tasić, Serbia

## CONFERENCE TOPICS

1. **Atmospheric Particulate Matter - Physical and Chemical Properties**
    i. Sources and formation of particulate matter
    ii. Particulate matter composition and levels outdoors and indoors
    iii. Environmental modeling
    iv. Nanoparticles in the environment
2. **Particulate Matter and Health**
    i. Exposure to particulate matter
    ii. Health aspects of atmospheric particulate matter
    iii. Full chain approach
3. **Particulate Matter and Regulatory Issues**
    i. Issues related to monitoring of particulate matter
    ii. Legislative aspects
    iii. Abatement strategies

*Organizers*

Vinča Institute of Nuclear Sciences, Serbia
Public Health Institute of Belgrade, Serbia
NILU Norwegian Institute for Air Research, Norway

*The Seventh WeBIOPATR Workshop and Conference,*
*Particulate Matter: Research and Management, WEBIOPATR 2019*
*is supported by:*
*Ministry of Education, Science and Technological Development of Republic of Serbia*

# PREFACE

The International Workshop and Conference, Particulate Matter: Research and Management – WeBIOPATR is a biennial event held in Serbia since 2007. The conference addresses air quality in general and particulate matter specifically. Atmospheric particulate matter arises both from primary emissions and from secondary formation in the atmosphere. It is one of the least well understood local and regional air pollutants, has complex implications for climate change, and is perhaps the pollutant with the highest health relevance. It also poses many challenges to monitoring.

By WeBIOPATR, we aim to link the research communities with relevance to particulate matter with the practitioners of air quality management on all administrative levels, in order to facilitate professional dialogue and uptake of newest research into practice. The workshops usually draw an audience of about 70, and attract media attention in Serbia. It enjoys support of the responsible authorities: Ministry of Education, Science and Technological Development, Ministry of Health, Ministry of Environment, and the Serbian Environmental Agency whose sponsorship is indispensable and gratefully acknowledged. We enjoy also support of international bodies such as the WHO.

The 1$^{st}$ WeBIOPATR Workshop was held in Beograd, 20.-22. May 2007, associated with a project funded by the Research Council of Norway. The 2$^{nd}$ workshop was held in Mecavnik, Serbia, 28.8.-1.9. 2009. WeBIOPATR2011 was held in Beograd 14.-17. 11. 2011 and for the first time, included a dedicated student workshop. WeBIOPATR2013 was held in Beograd 2.-4. 10. 2013. It covered the traditional PM research and management issues, discussions on how to encourage citizens to contribute to environmental governance, and how to develop participatory sensing methods. WeBIOPATR2015 was held in Beograd 14.-16.10. 2015. Own sessions were devoted to sensor technologies for air quality monitoring, utilizing information and input from the EU FP7 funded project CITI-SENSE (http://co.citi- sense.eu ) and the EU COST action EuNetAir (www.eunetair.it). WeBIOPATR2017, the 6$^{th}$ conference, was held in Beograd 6.-8.9. 2017, with a wider than before Western Balkan participation.

WeBIOPATR2019 will be held 1.-3 -10-2019 in the Mechanical Faculty, University of Belgrade. It has attracted a record 58 contributions, and is bringing together scientists from 12 countries, documenting that the issues of atmospheric pollution, with their wide implications for climate change, human health and ecosystem services, are no less important today.

We are grateful to our unrelenting national and international partners for their support for this event.

Welcome to Beograd, and have a stimulating and productive time!

*Milena Jovašević-Stojanović and Alena Bartoňová*

## TABLE OF CONTENTS

## 10.2. A CLIMATOLOGY OF SATELLITE DERIVED AEROSOL OPTICAL DEPTH OVER BELGRADE REGION, SERBIA

**Z. Mijić, A. Jovanović, M. Kuzmanoski, L. Ilić**
*(1) Institute of Physics Belgrade, University of Belgrade, Belgrade, Serbia,*
zoran.mijic@ipb.ac.rs

Suspended particulate matter (PM) in the atmosphere, commonly known as atmospheric aerosol plays one of the most important roles in climate change, air quality, and human health. Atmospheric aerosol affects climate through the direct (scattering and absorption both solar and terrestrial radiation) and indirect effects (modification of cloud through aerosol-cloud interaction) introducing one of the major uncertainty in our quantitative understanding of the radiative forcing (IPCC, 2007). Numerous studies have shown a significant association between particle matter concentrations and health risk especially airborne particle matter with diameter less than 10 μm ($PM_{10}$) and 2.5 μm ($PM_{2.5}$) (Yang et al. 2018). As the evidence base for the association between PM and short-term, as well as long-term, health effects has become much larger and broader, it is important to regularly update the guidelines for PM and PM-bound components limit values. Usually ground-based monitoring networks are used for PM assessment but still with no adequate spatial and time coverage. For the last decade various studies have been conducted to overcome this problem and to get PM estimates from satellite measurements (Kumar et al. 2007, Li et al. 2015). One of the most important aerosol products retrieved from satellite measurement is aerosol optical depth (AOD) which is the integration of the aerosol extinction coefficient from the Earth's surface to the top of the atmosphere, and it represents the attenuation of solar radiation caused by aerosols. The relationship between AOD and surface PM concentrations depends on various factors, including aerosol vertical distribution, aerosol type and its chemical composition, as well as its spatial and temporal variability, which are governed by spatio-temporal distribution of emissions and meteorological conditions (Kong et al., 2016). Due to their short lifetime and the large variability in space and time it is necessary to establish a climatology of the aerosol distribution both on regional and global scale thus satellite-retrieved AOD has become an important indicator of ground-level PM and aerosol burden in the atmosphere. The Moderate Resolution Imaging Spectroradiometer (MODIS) is aboard two polar orbiting satellites Terra and Aqua and measures the upwelling radiance from the Earth–atmosphere system at 36 wavelength bands, ranging from 0.4 to 14 μm. MODIS provides a daily near-global distribution of AOD over both ocean and land (Sayer et al., 2013). In this study long-term temporal variation and trend of AOD over Belgrade region are presented. Monthly mean values of MODIS aerosol optical depth at 550 nm were examined for the 10 year period 2005–2015. The MOD08 Combined Dark Target and Deep Blue AOD data products from MODIS Terra platform (Collection 6.1, Level 3 AOD data downloaded through NASA GIOVANNI web portal https://giovanni.gsfc.nasa.gov/giovanni/) at 1 degree spatial resolution were utilized. Frequency distributions of the AOD values were examined together with monthly and seasonal variations. The annual AOD mean was 0.17 with standard deviation of 0.07 over ten year period. AOD values exhibited seasonal annual mean variation and slightly negative trend. Significant monthly AOD variability is observed with maximum in August (~0.28) and a minimum in winter months (~0.06). Analysis of long term time series of AOD data could reveal how AOD regarding ground-based PM measurement in Belgrade changes over time. The aerosol climatology can be useful in the climate change assessment, weather and environmental monitoring over Belgrade region with the potential for further application in particle matter estimates from satellite measurement.

### REFERENCES

IPCC. 2007c. Climate Change 2007: Impacts, Adaptation and Vulnerability. Contribution of Working Group II to the Fourth Assessment Report of the IPCC. In M.L. Parry, M., Canziani, O., Palutikof, J., van der Linden, and Hanson, C.E. University Press, Cambridge, UK, pp 976.

Kong, L., Xin, J., Zhang, W., Wang, Y. 2016. The empirical correlations between PM2.5, PM10 and AOD in the Beijing metropolitan region and the PM2.5, PM10 distributions retrieved by MODIS, Environmental Pollution 216, 350-360.

Kumar, N., Chu, S.A., Foster A. 2007. An empirical relationship between PM2.5 and aerosol optical depth in Delhi Metropolitan, Atmospheric Environment 41, 4492-4503.

Li., J., Carlson, E. B., Lacis, A. A., 2015. How well do satellite AOD observations represent the spatial and temporal variability of PM2.5 concentration for the United States?,Atmospheric Environment 102, 260-273.

Sayer, A. M., N. C. Hsu, C. Bettenhausen, and M.-J. Jeong, 2013. Validation and uncertainty estimates for MODIS Collection 6 "Deep Blue" aerosol data, Journal of Geophysics Researh Atmosphere 118, 7864–7872.

Yang, Y., Vivian, C. Pun., Shengzhi, S., Hualiang L., Tonya, G., M., Hong, Q., 2018. Particulate matter components and health: a literature review on exposure assessment, Journal of Public Health and Emergency 2, 14.

## 10.8. CASE STUDY OF THE VERTICAL DISTRIBUTION OF SAHARAN DUST OVER BELGRADE

**A. Jovanović, L. Ilić, M. Kuzmanoski, Z. Mijić**
*Institute of Physics Belgrade, University of Belgrade, Belgrade, Serbia*
*aleksandar.jovanovic@ipb.ac.rs*

Mineral dust aerosol is ubiquitous in the troposphere around the globe, and dominant in terms of mass concentration (Grini et al., 2005). Sahara is the largest source of dust emission and atmospheric dust loading in the world (Choobari et al., 2014). Strong low-level winds and convection can uplift mineral dust particles into the free troposphere, where they are transported over large distances even at intercontinental scales (Goudie and Middleton, 2001). Dust aerosols have a direct impact on the global radiative budget of the atmosphere by scattering and absorbing shortwave and longwave radiation. Also, dust aerosols can change the microphysical characteristics of clouds and precipitation due to their role in the nucleation of cloud ice and droplets (Rosenfeld et al., 2001). Furthermore, dust impacts air quality even at locations distant from its source region (Prospero, 1999). To improve understanding of these effects, it is important to characterize dust horizontal and vertical distribution, as well as meteorological conditions that lead to dust outbreaks in region of interest.

In this study, four episodes of long-range transport of Saharan dust to Balkans will be investigated based on results of numerical model and available ground-based measurements. Synoptic circulation patterns and airmass backtrajectories during these events will also be analyzed. For dust forecast, we used the Dust Regional Atmospheric Model – DREAM. The model was developed to predict the concentration of dust aerosol in the troposphere, and includes processes of dust emission, dust horizontal and vertical turbulent mixing, long-range transport and dust deposition (Ničković et al., 2001). Modeled dust concentration vertical profiles and concentrations at surface level during the selected events will be discussed. A qualitative comparison of modeled dust vertical profiles and results of LIDAR (Light Detection and Ranging) measurements in Belgrade will be presented. Furthermore, comparison of modeled dust surface concentrations with the measurements of $PM_{10}$ particle mass concentration in two urban background stations in Belgrade will be shown, to give insight into the effect of dust on air quality during these dust episodes.

### REFERENCES

Choobari, O. A., Zawar-Reza, P., and Sturman, A., 2014. The global distribution of mineral dust and its impacts on the climate system: A review, Atmospheric Research, 138, 152–165.

Goudie, A. S. and Middleton, N. J., 2001. Saharan dust storms: nature and consequences, Earth-Science Reviews, 56, 179–204.

Grini, A., Myhre, G., Zender, C. S., and Isaksen, I. S. A., 2005. Model simulations of dust sources and transport in the global atmosphere: Effects of soil erodibility and wind speed variability, Journal of Geophysical Research, 110, D02205.

Ničković, S., Kallos, G., Papadopoulos, A., Kakaliagou, O., 2001. A model for prediction of desert dust cycle in the atmosphere, Journal of Geophysical Research 106, 18113-18130.

Prospero, J. M., 1999. Long-term measurements of the transport of African mineral dust to the southeastern United States: Implications for regional air quality, Journal of Geophysical Research 104, 15917–15927.

*Rosenfeld, D., Y. Rudich, and R. Lahav 2001. Desert dust suppressing precipitation: A possible desertification feedback loop, Proceedings of the National Academy of Sciences of the United States of America, 98, 5975–5980.*

CIP - Каталогизација у публикацији
Народна библиотека Србије, Београд

502.3:502.175(048)
613.15(048)
66.071.9(048)

**INTERNATIONAL WeBIOPATR Workshop & Conference,**
**Particulate Matter: Research and Management (7 ; 2019 ; Beograd)**

Abstracts of keynote invited lectures and contributed papers /
The Seventh International WeBIOPATR Workshop & Conference
Particulate Matter: Research and Management, WeBIOPATR 2019,
1st to 3rd October, 2019 Belgrade, Serbia ;
[organizers Vinča Institute of Nuclear Sciences, Serbia,
[and] Public Health Institute of Belgrade, Serbia
[and] NILU Norwegian Institute for Air Research, Norway] ;
editors Milena Jovašević-Stojanović, Alena Bartoňová.
- Belgrade : Public Health Institute, 2019
(Belgrade : Printing Office of the Public Health Institute). - 104 str. : ilustr. ; 30 cm

Tiraž 150.
- Str. 7: Preface / Milena Jovašević-Stojanović and Alena Bartoňová.
- Bibliografija uz većinu apstrakata. – Registar

ISBN 978-86-83069-56-9

1. Conference Particulate Matter: Research and Management (7 ; 2019 ; Beograd)
а) Ваздух -- Контрола квалитета -- Апстракти
б) Здравље -- Заштита -- Апстракти
в) Отпадни гасови -- Штетно дејство -- Апстракти

COBISS.SR-ID 279772172

ISBN 978-86-83069-56-9

ISBN 978-86-83069-56-9

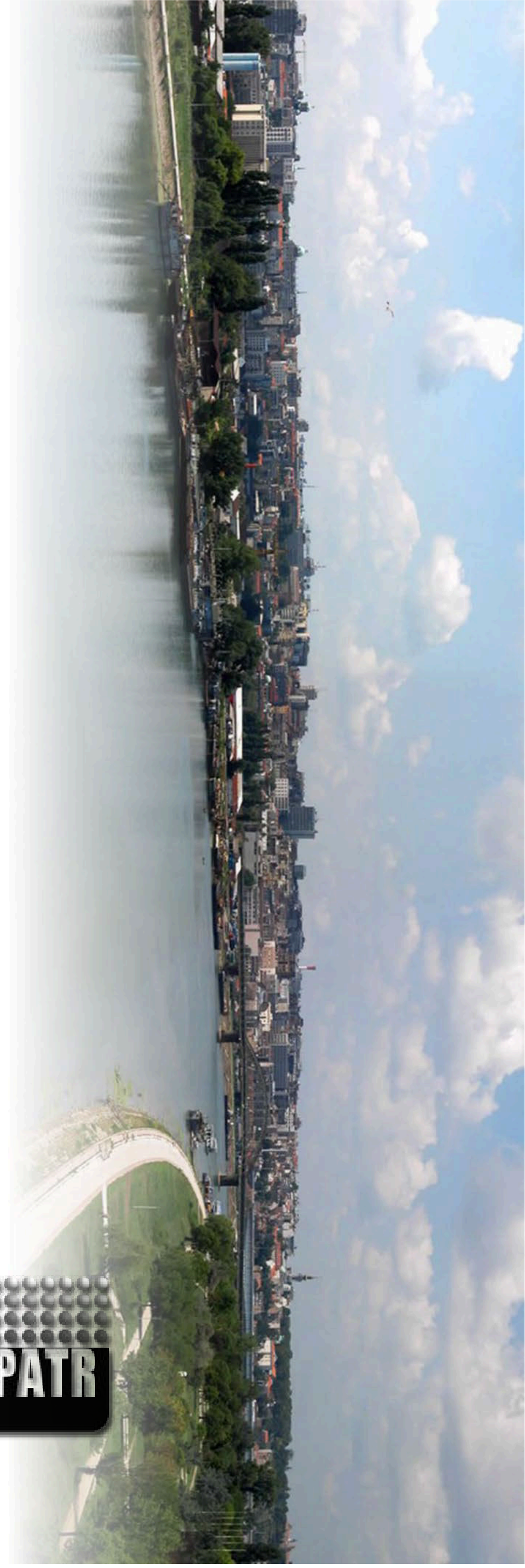

WeBIOPATR

# Integrations of satellite and ground-based observations and multi-disciplinarity in research and prediction of different types of hazards in Solar system

May 10-13, 2019, Petnica Science Center, Valjevo, Serbia

# BOOK OF ABSTRACTS

**Edited by Aleksandra Nina, Milan Radovanović and Vladimir A. Srećković**


europlanet NA1 – Innovation Through Science Networking
Task 2 – Scientific Working Groups

Geographical Institute "Jovan Cvijić"
SERBIAN ACADEMY OF SCIENCES AND ARTS

## Scientific Committee

Aleksandra Nina, Institute of Physics Belgrade, University of Belgrade, Belgrade, Serbia (co-chair)

Milan Radovanović, Geographical Institute "Jovan Cvijić" of the Serbian Academy of Sciences and Arts, Belgrade, Serbia (co-chair)

Giovanni Nico, Instituto per le Applicazioni del Calcolo (IAC), Consiglio Nazionale delle Ricerche (CNR), Bari, Italy (co-chair)

Pier Francesco Biagi, Università di Bari, Physics Department, Bari, Italy

Mihai Datcu, DLR Institute of Remote Sensing Technology, Wessling, Germany

Melinda Dosa, Hungarian Academy of Science, Department of Space Physics, Budapest, Hungary

Darko Jevremović, Astronomical Observatory, Belgrade, Serbia

Ognyan Kounchev, Institute of Mathematics and Informatics, Bulgarian Academy of Sciences, Sofia, Bulgaria

Konstantinos Kourtidis, Department of Environmental Engineering, School of Engineering Democritus University of Thrace, Xanthi, Greece

Slavica Malinović-Milićević, ACIMSI - University Center for Meteorology and Environmental Modelling, University of Novi Sad, Novi Sad, Serbia

Bratislav P. Marinković, Institute of Physics Belgrade, University of Belgrade, Serbia

Luka Č. Popović, Astronomical Observatory, Belgrade, Serbia

Sergey Pulinets, Space Research Institute (IKI) of the Russian Academy of Sciences, Moscow, Russia

Vladimir A. Srećković, Institute of Physics Belgrade, University of Belgrade, Serbia

Dejan Vinković, Hipersfera Ltd., Zagreb, Croatia

Yaroslav Vyklyuk, Bukovinian University, Chernivtsi, Ukraine

## Local Organizing Committee

Aleksandra Nina, Institute of Physics Belgrade, University of Belgrade, Serbia (co-chair)

Milan Radovanović, Geographical Institute "Jovan Cvijić" of the Serbian Academy of Sciences and Arts, Belgrade, Serbia (co-chair)

Gorica Stanojević, Geographical Institute "Jovan Cvijić" of the Serbian Academy of Sciences and Arts, Belgrade, Serbia

Vladimir M. Čadež, Astronomical Observatory, Belgrade, Serbia

Dejan Doljak, Geographical Institute "Jovan Cvijić" of the Serbian Academy of Sciences and Arts, Belgrade, Serbia

Vladimir A. Srećković, Institute of Physics Belgrade, University of Belgrade, Serbia

Dragoljub Štrbac, Geographical Institute "Jovan Cvijić" of the Serbian Academy of Sciences and Arts, Belgrade, Serbia

**Venue:** Petnica Science Center, Valjevo, Serbia

**Organizers:** Europlanet 2020 RI NA1 – Innovation through Science Networking and Geographical Institute "Jovan Cvijić" of Serbian Academy of Sciences and Arts

**Published by:** Geographical Institute "Jovan Cvijić" of Serbian Academy of Sciences and Arts, 2019

The publication of this issue is financially supported by the Ministry for Education, Science and Technological Development of Serbia

Picture on the first cover: Aleksandra Nina

ISBN 978-86-80029-77-1

**Printed by:** Skripta Internacional, Mike Alasa 54, Beograd
Number of copies: 50

# CONTENTS

## Abstracts of Invited Lectures

## Abstracts of Progress Reports

## Abstracts of Posters

*Poster*

# COMPARISON OF MODIS AEROSOL OBSERVATIONS AND GROUND-BASED PM MEASUREMENT FOR THE BELGRADE REGION

*Zoran Mijić*[1], *Mirjana Perišić*[1]

[1] Institute of Physics Belgrade, University of Belgrade, Serbia;
e-mail: zoran.mijic@ipb.ac.rs, mirjana.perisic@ipb.ac.rs

Suspended particulate matter in the atmosphere, commonly known as atmospheric aerosol, plays one of the most important role in climate changes and environmental issues. Numerous epidemiological studies in recent years have shown detrimental effects of aerosol pollution on human health, causing respiratory and cardiovascular disease and even premature death (Kim, Oh, Park, & Cheong, 2018). Additionally, scattering and absorption of solar and terrestrial radiation as direct, and modification of cloud condensation nuclei through aerosol-cloud interaction as indirect effects of aerosols, make the largest contribution to the total uncertainty of the radiative forcing (Intergovernmental Panel on Climate Change, 2007).

Assessment of air quality primarily relies on ground-based measurements of the concentrations of airborne particulate matter (PM) with aerodynamic diameter less than 10 μm ($PM_{10}$) and 2.5 μm ($PM_{2.5}$), and for this purpose, all European countries were established regulatory monitoring networks. Because this kind of observation provides limited spatial PM information, various studies have been conducted to obtain PM estimates from satellite measurements (Kumar, Chu, & Foster, 2007; Li, Carlson, & Lacis, 2015). Aerosol optical depth (AOD) is one of the most important aerosol product retrieved from satellite measurements, and represent the attenuation of solar radiation caused by aerosols. The relationship between AOD (integration of the aerosol extinction coefficient from the Earth's surface to the top of the atmosphere) and surface PM concentrations depends on various factors: aerosol type and its chemical composition, vertical distribution, spatial and temporal variability - all governed by emissions and meteorological conditions (Kong, Xin, Zhang, & Wang, 2016; Sayer, Hsu, Bettenhausen, & Jeong, 2013).

In this study, we investigated the relationship between AOD and, $PM_{2.5}$ and $PM_{10}$ concentrations data set from the Belgrade region. We obtained Level 2 AOD data at 0.55 μm based on measurements by Moderate Resolution Imaging Spectroradiometer (MODIS) aboard *Terra* (MOD04) and *Aqua (*MYD04) platforms with the resolution of 10x10 $km^2$ for three years period 2012-2014. Hourly average $PM_{2.5}$ and $PM_{10}$ mass concentrations for the investigating period were obtained from urban and suburban monitoring stations of the Institute of Public Health Belgrade. The analyses included the impact of ambient relative humidity (RH) on PM concentration due to the hygroscopic growth of aerosol particles, as well as vertical correction of AOD with respect to the mixing layer height (MLH). The preliminary results showed that AOD retrieved from satellite sensor can be considered as a good proxy for ground observed PM mass concentrations. It is found that the relationship between AOD and PM is practically linear and strongly influenced by RH and MLH. The increase in the correlation coefficient (of around 20%) is indicative for vertical corrected AOD parameter and dry PM. Further investigation should examined influences of the other

meteorological parameters, different season and types of monitoring stations at the examined PM-AOD relationship. Also, the study based on the analyses of satellite aerosol products and ground-based measured pollutants concentrations may be used for air quality assessment and PM prediction in the region of the City of Belgrade.

**Acknowledgments**

This paper was realized as a part of the projects III43007 and III41011 financed by the Ministry of Education and Science of the Republic of Serbia within the framework of integrated and interdisciplinary research for the period 2011-2019. The MODIS data were obtained from NASA Atmosphere Archive and Distribution System (LAADS) at the Goddard Space Flight Center (GSFC) and we would like to thanks MODIS team for developing the AOD product.

**References**

Intergovernmental Panel on Climate Change. (2007). Climate Change 2007: The Physical Science Basis. Contribution of Working Group I to the Fourth Assessment Report of the Intergovernmental Panel on Climate Change. Cambridge, UK; New York, NY: Cambridge University Press.

Kim, J.-H., Oh, I.-H., Park, J.-H., & Cheong, H.-K. (2018). Premature Deaths Attributable to Long-term Exposure to Ambient Fine Particulate Matter in the Republic of Korea. *Journal of Korean Medical Science, 33*(37). https://doi.org/10.3346/jkms.2018.33.e251

Kumar, N., Chu, A., & Foster, A. (2007). An empirical relationship between PM2. 5 and aerosol optical depth in Delhi Metropolitan. *Atmospheric Environment, 41*(21), 4492–4503. https://doi.org/10.1016/j.atmosenv.2007.01.046

Li, J., Carlson, B. E., & Lacis, A. A. (2015). How well do satellite AOD observations represent the spatial and temporal variability of PM2. 5 concentration for the United States? *Atmospheric Environment, 102*, 260–273. https://doi.org/10.1016/j.atmosenv.2014.12.010

Kong, L., Xin, J., Zhang, W., & Wang, Y. (2016). The empirical correlations between PM2. 5, PM10 and AOD in the Beijing metropolitan region and the PM2. 5, PM10 distributions retrieved by MODIS. *Environmental pollution, 216*, 350–360. https://doi.org/10.1016/j.envpol.2016.05.085

Sayer, A. M., Hsu, N. C., Bettenhausen, C., & Jeong, M. J. (2013). Validation and uncertainty estimates for MODIS Collection 6 "Deep Blue" aerosol data. *Journal of Geophysical Research: Atmospheres, 118*(14), 7864–7872. https://doi.org/10.1002/jgrd.50600

# PROGRAMME

## Friday, May 10

13:00 - 15:00 **Arrival, registration and lunch**

**Chairs:** Aleksandra Nina and Milan Radovanović
15:30 – 15:45 **Opening ceremony**

**Chair:** Sergey Pulinets
15:45 – 16:30 **Darko Jevremović:** *SOLAR SYSTEM OBJECTS IN THE LSST ERA (ASSESSING THE HAZARDS)*
16:30 – 17:00 **Pál Gábor Vizi, Péter Szutor, Szaniszló Bérczi, Szilárd Csizmadia, Tibor Hegedűs:** *TRAJECTORY AND ANALYSIS OF LOCAL FIREBALL-METEORITE EVENTS AND EXTENDED METEOR HUNTING WITH SMARTPHONES AS 'SKY EVENT' CAMERAS*

18:00 – 19:30 **Welcome cocktail**
20:00 – Dinner time

## Saturday, May 11

**Chair:** Bratislav P. Marinković
9:00 – 9:45 **Sergey Pulinets, Dimitar Ouzounov:** *INTEGRATION OF SATELLITE AND GROUND-BASED OBSERVATIONS AND MULTI-DISCIPLINARITY IN EARTHQUAKE AND VOLCANO ERUPTION FORECAST BASED ON THE LAIC PHYSICAL MODEL*
9:45 – 10:30 **Pier Francesco Biagi:** *THE INFREP VLF/LF RADIO NETWORK: PRESENT SITUATION AND RECENT RESULTS*

10:30 – 11:00 Coffee break

**Chair:** Pier Francesco Biagi
11:00 – 11:45 **Konstantinos Kourtidis, Veronika Barta, Jozsef Bor, Evgeny Mareev, Christina Oikonomou, Colin Price, Sergey Pulinets:** *WORK WITHIN THE COST ACTION ELECTRONET ON THE COUPLING OF THE ATMOSPHERIC ELECTRIC CIRCUIT TO EARTHQUAKES, LIGHTNING AND THE SUN-EARTH ENVIRONMENT*
11:45 – 12:30 **Aleksandra Nina, Giovanni Nico, Luka Č. Popović, Vladimir M. Čadež, Milan Radovanović:** *NATURAL DISASTERS AND LOW IONOSPHERIC DISTURBANCES DETECTED BY BELGRADE VLF/LF RECEIVER STATION*

**Chair:** Ognyan Kounchev

| | |
|---|---|
| 12:30 – 14:00 | **Discussions – integration of observation methods and models in research of earthquakes and volcanoes** |
| 14:00 – 15:00 | Lunch break |

**Chair:** Luka Č. Popović

| | |
|---|---|
| 15:00 – 15:45 | **Giovanni Nico, Weike Feng, Olimpia Masci, Motoyuki Sato, Luciano Garramone:** *RADAR INTERFEROMETRY AS A NEW TOOL FOR EARTHQUAKE GEOTECHNICAL ENGINEERING* |
| 15:45 – 16:30 | **Nikola Veselinović, Mihailo Savić, Aleksandar Dragić, Dimitrije Maletić, Dejan Joković, Radomir Banjanac, Vladimir Udovičić, David Knežević:** *CORRELATION OF SOLAR WIND PARAMETERS WITH COSMIC RAYS OBSERVED WITH GROUND STATION* |
| 16:30 – 17:00 | **Sergey Pulinets:** *THE ROLE OF GALACTIC COSMIC RAYS IN DYNAMICS OF HURRICANES AND TYPHOONS AND GLOBAL CHANGE* |
| 17:00 – 17:30 | Coffee break |

**Chair:** Darko Jevremović

| | |
|---|---|
| 17:30 – 18:15 | **Dejan Vinković, Maria Gritsevich:** *THE CHALLENGES OF HYPERVELOCITY MICROPHYSICS RESEARCH IN METEOROID IMPACTS INTO THE ATMOSPHERE* |
| 18:15 – 19:00 | **Bozhidar Srebrov, Ognyan Kounchev, Georgi Simeonov:** *ANALYSIS OF BIG DATA IN GEOMAGNETISM VIA WAVELET ANALYSIS* |
| 20:00 – | **Meeting dinner** |

## Sunday, May 12

**Chair:** Konstantinos Kourtidis

| | |
|---|---|
| 9:00 – 9:30 | **Slavica Malinović-Milićević, Zoran Mijatović, Ilija Arsenić, Zorica Podraščanin, Ana Firanj Sremac, Milan Radovanović, Nusret Drešković:** *THE IMPORTANCE OF GROUND-BASED AND SATELLITE OBSERVATIONS FOR MONITORING AND ESTIMATION OF UV RADIATION IN NOVI SAD, SERBIA* |
| 9:30 – 10:00 | **Nataša Todorović:** *DYNAMICAL ORIGIN OF TWO POTENTIALLY HAZARDOUS ASTEROIDS* |
| 10:00 – 10:30 | Coffee break |

**Chair:** Giovanni Nico

| | |
|---|---|
| 10:30 – 12:00 | **Discussions – integration of observation methods and models in research of hurricanes, meteors and climatic changes** |
| 12:00 | **Meeting photo** |
| 12:05 – 14:00 | **Guided tour of Petnica's vicinity** |
| 14:00 – 15:00 | Lunch break |

**Chair:** Milan S. Dimitrijević

| | |
|---|---|
| 15:15 – 16:00 | **Yaroslav Vyklyuk, Milan Radovanović, Slavica Malinović-Milićević**: *DEEP LEARNING LSTM RECURRENT NEURAL NETWORK FOR CONSEQUENCE FORECASTING OF THE SOLAR WIND DISTURBANCE* |
| 16:00 – 16:30 | **Andjelka B. Kovačević**: *PLANETARY ATMOSPHERES EROSION DUE TO Sgr A AND (z<0.5) ACTIVE GALACTIC NUCLEI RADIATION* |
| 16:30 – 17:00 | **Dušan Marčeta, Bojan Novaković**: *STARDUST-RELOADED: THE ASTEROID AND SPACE DEBRIS NETWORK* |
| 17:00 – 17:30 | Coffee break |
| 17:30 – 19:00 | **Posters** |
| 19:00 – | Dinner time |
| 20:30 – | **Networking event** |

## Monday, May 13

**Chair:** Yaroslav Vyklyuk

| | |
|---|---|
| 9:00 – 9:45 | **Milan S. Dimitrijević**: *MILUTIN MILANKOVIĆ AND CLIMATE CHANGES LEADING TO ICE AGES* |
| 9:45 – 10:30 | **Aleksandar Valjarević, Nikola Bačević, Marko Ivanović**: *DIGITAL AND NUMERICAL METHODS IN ESTIMATION OF A HAZARD FLOODS IN THE MUNICIPALITY OF OBRENOVAC* |
| 10:30 – 10:45 | Closing ceremony |
| 11:15 – | Departure |

## LIST OF POSTERS

**P1. Veljko Vujčić, Darko Jevremović:** *NEO DETECTION USING COMPLEX EVENT PROCESSING*

**P2. Aleksandra Kolarski:** *ATMOSPHERIC DISTURBANCES DUE TO SEVERE STORMY WEATHER*

**P3. Jelena Petrović, Snežana Dragović:** *RADON AS POTENTIAL EARTHQUAKE PRECURSOR*

**P4. Predrag Jovanović, Duško Borka, Vesna Borka Jovanović:** *CONSTRAINING YUKAWA GRAVITY FROM PLANETARY MOTION IN THE SOLAR SYSTEM*

**P5. Bratislav P. Marinković, Stefan Ivanović, Nebojša Uskoković, Milutin Nešić:** *ELECTRON-IMPACT CROSS SECTIONS FOR THOLINS: COVERAGE WITHIN BEAMDB DATABASE*

**P6. Milan Radovanović, Aleksandra Nina, Vladimir A. Srećković:** *EXTREME SOLAR RADIATION AND NATURAL DISASTERS: CROSS DISCIPLINARY APPROACHES*

**P7. Vladimir A. Srećković:** *SOLAR ACTIVITY, NATURAL HAZARDS, LOW IONOSPHERIC PERTURBATIONS AND SATELLITE AND GROUND-BASED OBSERVATIONS*

**P8. Zoran Mijić, Mirjana Perišić:** *COMPARISON OF MODIS AEROSOL OBSERVATIONS AND GROUND-BASED PM MEASUREMENT FOR THE BELGRADE REGION*

CIP - Каталогизација у публикацији - Народна библиотека Србије, Београд

523:504.4(048)

INTEGRATIONS of satellite and ground-based observations and multi-disciplinarity in research and prediction of different types of hazards in Solar system (2019 ; Valjevo)
Book of abstracts / Integrations of satellite and ground-based observations and multi-disciplinarity in research and prediction of different types of hazards in Solar system, May 10-13, 2019, Valjevo, Serbia ; edited by Aleksandra Nina, Milan Radovanović, and Vladimir A. Srećković. - Belgrade : Geographical Institute "Jovan Cvijić" SASA, 2019 (Beograd : Skripta Internacional). - 59 str. : ilustr. ; 24 cm

Tiraž 50.

ISBN 978-86-80029-77-1

a) Сунчев систем - Безбедност - Апстракти b) Природне катастрофе - Апстракти
COBISS.SR-ID 275944460

**III Meeting on Astrophysical Spectroscopy - A&M DATA**

December 6 to 9, 2021, Palić, Serbia

# BOOK OF ABSTRACTS AND CONTRIBUTED PAPERS

**Edited by Vladimir A. Srećković, Milan S. Dimitrijević and Nikola Cvetanović**

Belgrade 2021

## Organizers:

Institute of Physics Belgrade, Serbia and
Astronomical Observatory Belgrade, Serbia

Text arrangement by computer: Tanja Milovanov

ISBN 978-86-82441-54-0



Financially supported by the Ministry of Education, Science and Technological Development of Serbia

Production: Skripta Internacional, Mike Alasa 54, Beograd in 50 copies

# Lower ionosphere under high-energy events: observations and model parameters

**Aleksandra Kolarski [1], Vladimir A. Srećković[2] and Zoran R. Mijić[2]**

[1]*Technical Faculty Mihajlo Pupin, University of Novi Sad, Đure Đakovića bb, 23000 Zrenjanin, Serbia*
*E-mail: aleksandra.kolarski@tfzr.rs*
[2]*Institute of Physics Belgrade, University of Belgrade, PO Box 57, 11000 Belgrade, Serbia*
*E-mail: vlada@ipb.ac.rs, zoran.mijic@ipb.ac.rs*

Analysis of lower ionospheric response and electron density altitude profile variations in lower ionosphere induced by high-energy events during daytime and during nighttime was carried out. Sudden events induced changes in ionosphere and consequently electron density height profile. All data are recorded by BEL radio stations system and the model computation is used to obtain the atmospheric parameters induced by these perturbations. According to perturbed conditions, variation of estimated parameters, sharpness and reflection height differ for analyzed cases. The data and results are useful for Earth observation, telecommunication and other applications in modern society.

## References

[1] Šulić, D. M., Srećković, V. A., & Mihajlov, A. A. (2016). A study of VLF signals variations associated with the changes of ionization level in the D-region in consequence of solar conditions. *Advances in Space Research*, 57(4), 1029-1043.

[2] Srećković, V. A., Šulić, D. M., Ignjatović, L., & Vujčić, V. (2021). Low Ionosphere under Influence of Strong Solar Radiation: Diagnostics and Modeling. *Applied Sciences*, *11*(16), 7194.

# Demonstration of the EARLINET Capacity to Provide Near Real Time Data

**Zoran Mijić**

*Institute of Physics Belgrade, University of Belgrade, Pregrevica 118, 11080 Belgrade, Serbia*

The European Aerosol Research Lidar Network, EARLINET, was established in 2000 with the goal of creating a quantitative, comprehensive, and statistically significant database for the horizontal, vertical, and temporal distribution of aerosols on a continental scale [1]. EARLINET is part of ACTRIS (Aerosols, Clouds and Trace gases Research Infrastructure) a pan-European initiative consolidating actions amongst European partners producing high-quality observations of atmospheric aerosols, clouds and trace gases. Aerosol lidars with their high temporal and vertical resolution, provide reliable information on the atmospheric structure, its dynamics, and its optical properties. The Belgrade lidar station [2] participated in the several campaigns providing vertical aerosol profiles measurements which were submitted and processed by the Single Calculus Chain (SCC) in the near-real time (NRT). The SCC is a tool for the automatic analysis of aerosol lidar measurements developed within EARLINET network [3,4]. The main aim of SCC is to provide a data processing chain that allows all EARLINET stations to retrieve, in a fully automatic way, the aerosol backscatter and extinction profiles together with other aerosol products. Beyond the scientific goals of this campaign, the actions organized by EARLINET/ACTRIS (NRT delivery of the data and fast analysis of the data products) proved that aerosol lidars are useful for providing information not only for climatological purposes, but also in emergency situations [5].

## References

[1] Pappalardo, G., Amodeo, A., Apituley, A., Comeron, A., Freudenthaler, V., Linné, H., Ansmann, A., Bösenberg, J., D'Amico, G., Mattis, I., Mona, L., Wandinger, U., Amiridis, V., Alados-Arboledas, L., Nicolae, D., and Wiegner, M., 2014. EARLINET: towards an advanced sustainable European aerosol lidar network, Atmospheric Measurement Techniques 7, 2389–2409.

[2] Ilić, L., Kuzmanoski M., Kolarž P., Nina A., Srećković V., Mijić Z., Bajčetić J., Andrić M., 2018. Changes of atmospheric properties over Belgrade, observed using remote sensing and in situ methods during the partial solar eclipse of 20 March 2015, Journal of Atmospheric and Solar-Terrestrial Physics171,250-259.

[3] D'Amico, G., Amodeo, A., Baars, H., Binietoglou, I., Freudenthaler, V., Mattis, I., Wandinger, U., and Pappalardo, G., 2015. EARLINET Single Calculus Chain – overview on methodology and strategy, Atmospheric Measurement Techniques 8, 4891-4916.
[4] D'Amico, G., Amodeo, A., Mattis, I., Freudenthaler, V., and Pappalardo, G., 2016. EARLINET Single Calculus Chaintechnical– Part 1: Pre-processing of raw lidar data, Atmospheric Measurement Techniques 9, 491-507.
[5] Papagiannopoulos, N., D'Amico, G., Gialitaki, A., Ajtai, N., Alados-Arboledas, L., Amodeo, A., Amiridis, V., Baars, H. et al., 2020. An EARLINET early warning system for atmospheric aerosol aviation hazards, Atmospheric Chemistry and Physics 20, 10775–10789.

# Usage of High-Resolution Satellite Products in Atmospheric modeling

**Zoran Mijić**

*Institute of Physics Belgrade, University of Belgrade, Pregrevica 118, 11080 Belgrade, Serbia*

Aerosol optical depth (AOD) is one of the most important aerosol products retrieved from satellite measurements, and represent the attenuation of solar radiation caused by aerosols. The direct radiative effect due to aerosol–radiation interactions is the change in radiative flux caused by the combined scattering and absorption of radiation by anthropogenic and natural aerosols. Due to their short lifetime and the large variability in space and time atmospheric aerosols are considered one of the major uncertainties in climate forcing and atmospheric processes [1]. The relationship between AOD (integration of the aerosol extinction coefficient from the Earth's surface to the top of the atmosphere) and surface aerosol concentrations depends on various factors: aerosol type and its chemical composition, vertical distribution, spatial and temporal variability. In this study the potential of Level 2 AOD data at 0.55 μm based on measurements by Moderate Resolution Imaging Spectroradiometer (MODIS) aboard Terra (MOD04) and Aqua (MYD04) platforms for PM modeling will be discussed [2]. In addition, recently lunched ESA Aeolus mission products intended for assimilation in Numerical Weather Prediction (NWP) models in Near-Real-Time together with its optical products will be introduced.

## References

[1] IPCC (2007), IPCC Fourth Assessment Report Climate Change 2007 - The Physical Science Basis Contribution of Working Group I to the Fourth Assessment Report of the IPCC

[2] Fu, D., Xia, X., Wang, J. et al. Synergy of AERONET and MODIS AOD products in the estimation of PM2.5 concentrations in Beijing. Sci Rep 8, 10174 (2018).

CIP - Каталогизација у публикацији
Народна библиотека Србије, Београд

52-355.3(048)
533.92:537.228.5(048)
539.184.27(048)

**MEETING on Astrophysical Spectroscopy - A&M DATA (3 ; 2021 ; Palić)**
Book of abstracts and contributed papers / III Meeting on Astrophysical Spectroscopy - A&M DATA, December 6 to 9, 2021, Palić, Serbia ; edited by Vladimir A. Srećković, Milan S. Dimitrijević and Nikola Cvetanović. - Belgrade : Institute of Physics, 2021 (Beograd : Skripta Internacional). - 56 str. ; 24 cm

Tiraž 50. - Registar.

ISBN 978-86-82441-54-0

a) Астрофизика - Апстракти b) Плазма - Спектрална анализа - Апстракти
c) Штарков ефекат - Апстракти

COBISS.SR-ID 52784137

# WeBIOPATR 2021

The Eighth International WEBIOPATR
Workshop & Conference
Particulate Matter: Research and Management

## Abstracts of Keynote Invited Lectures and Contributed Papers

Milena Jovašević-Stojanović,

Alena Bartoňová,

Miloš Davidović and Simon Smith, Eds

Vinča Insitute of Nuclear Sciences

Vinča, Belgrade 2021

# ABSTRACTS OF KEYNOTE INVITED LECTURES AND CONTRIBUTED PAPERS

The Eighth WeBIOPATR Workshop & Conference

Particulate Matter: Research and Management

**WeBIOPATR 2021**

29th November to 1st December 2021

Vinča, Belgrade, Serbia

*Editors*

Milena Jovašević-Stojanović

Alena Bartoňová

Miloš Davidović

Simon Smith

*Publisher*

Vinča Institute of Nuclear Sciences

Prof. Dr Snežana Pajović, Director

P.O.Box 522

11001 Belgrade, Serbia

*Printed by*

Vinča Institute of Nuclear Sciences

ISBN 978-86-7306-164-1



www.vin.bg.ac.rs/

## SCIENTIFIC COMMITTEE

Aleksandar Jovović, Serbia

Alena Bartoňová, Norway

Antonije Onjia, Serbia

David Broday, Israel

Dikaia Saraga, Greece

Griša Močnik, Slovenia

Ivan Gržetić, Serbia

María Cruz Minguillón, Spain

Milena Jovašević-Stojanović, Serbia

Miloš Davidović, Serbiac

Saverio de Vito, Italy

Selahattin Incecik, Turkey

Slobodan Ničković, Serbia

Simone Barreira Morais, Portugal

Zoran Mijić, Serbia

Zoran Ristovski, Australia

Zorana Jovanović-Andersen, Denmark

## ORGANIZING COMMITTEE

Aleksandra Stanković, Serbia

Alena Bartoňová, Norway

Andrej Šoštarić, Serbia

Anka Cvetković, Serbia

Biljana Filipović, Serbia

Branislava Matić, Serbia

Lidija Marić-Tanasković, Serbia

Uzahir Ramadani, Serbia

Ivan Lazović, Serbia

Sonja Dmitrašinović (Secretary), Serbia

Marija Živković (Secretary), Serbia

Milena Jovašević-Stojanović, Serbia

Miloš Davidović, Serbia

Mira Aničić Urošević, Serbia

Mirjana Perišić, Serbia

Nenad Živković, Serbia

Tihomir Popović, Serbia

Vesna Slepčević, Serbia

Viša Tasić, Serbia

## CONFERENCE TOPICS

1. **Atmospheric Particulate Matter - Physical and Chemical Properties**
   i. Sources and formation of particulate matter
   ii. Particulate matter composition and levels outdoors and indoors
   iii. Environmental modeling
   iv. Nanoparticles in the environment
2. **Particulate Matter and Health**
   i. Exposure to particulate matter
   ii. Health aspects of atmospheric particulate matter
   iii. Full chain approach
   iv. COVID-19 and particulate matter
3. **Particulate Matter and Regulatory Issues**
   i. Issues related to monitoring of particulate matter
   ii. Legislative aspects
   iii. Abatement strategies

*Organizers*

Vinča Institute of Nuclear Sciences, Serbia

Public Health Institute of Belgrade, Serbia

NILU Norwegian Institute for Air Research, Norway

*The 8th WeBIOPATR Workshop and Conference,*

*Particulate Matter: Research and Management, WEBIOPATR 2021*

*is supported by:*

EC H2020 Framework Program for Research and Innovation, area "Spreading excellence and widening participation", VIDIS project (2020-2023) coordinated by Vinca Institute of Nuclear Sciences, Grant agreement number 952433.

*Ministry of Education, Science and Technological Development of Republic of Serbia*

# PREFACE

Dear Colleagues,

Welcome to the 8th WeBIOPATR Conference, to be held at the premises of the Vinca Institute of Nuclear Sciences, Serbia, 29.11.–1.12.2021, as a combination of online and face-to-face event.

The International Workshop and Conference, Particulate Matter: Research and Management – WeBIOPATR is a biennial event held in Serbia since 2007. The conference addresses air quality in general and particulate matter specifically. Atmospheric particulate matter arises both from primary emissions and from secondary formation in the atmosphere. It is one of the least well understood local and regional air pollutants, has complex implications for climate change, and is perhaps the pollutant with the highest health relevance. It also poses many challenges to monitoring.

By WeBIOPATR, we aim to link the research communities with relevance to particulate matter with the practitioners of air quality management on all administrative levels, in order to facilitate professional dialogue and uptake of newest research into practice. The workshops usually draw an audience of about 70 and attract media attention in Serbia. It enjoys support of the responsible authorities, Ministry of Education, Science and Technological Development, Ministry of Health, Ministry of Environment, and the Serbian Environmental Agency whose sponsorship is indispensable and gratefully acknowledged. We also enjoy support of international bodies such as the WHO.

The 1st WeBIOPATR Workshop was held in Beograd, 20.-22. May 2007, associated with a project funded by the Research Council of Norway. The 2nd workshop was held in Mećavnik, Serbia, 28.8.-1.9.2009. WeBIOPATR2011 was held in Beograd 14.-17.11.2011 and for the first time, included a dedicated student workshop. WeBIOPATR2013 was held in Beograd 2.-4.10. 2013. It covered the traditional PM research and management issues, discussions on how to encourage citizens to contribute to environmental governance, and how to develop participatory sensing methods. WeBIOPATR2015 was held in Beograd 14.-16.10. 2015. Dedicated sessions were devoted to sensor technologies for air quality monitoring, utilizing information and input from the EU FP7 funded project CITI-SENSE (http://co.citi-sense.eu) and the EU COST action EuNetAir (www.eunetair.it). WeBIOPATR2017, the 6th conference, was held in Beograd 6.-8.9. 2017, with a wider than before Western Balkan participation. The 7th WeBIOPATR2019 was held 1.-4.10. 2019 at the Mechanical Faculty, University of Belgrade. It has attracted a record of over 50 contributions, and brought together scientists from 12 countries, documenting that the issues of atmospheric pollution, with their wide implications for climate change, human health and ecosystem services, are no less important today. This year's event will be with similar number of contributions that have been accepted.

In the past two years, all our lives were affected by the COVID-19 pandemic. We have adapted our ways of life and work – and now we hope that the new format of the conference will be a success, for the participants physically present as well as for those who will participate online.

We are very grateful to our unrelenting national and international partners for their financial and scientific support for this event. In addition, WeBIOPATR2021 is supported by the VIDIS project, https://vidis-project.org/, funded by the EC H2020 Framework Programme for Research and Innovation, area "Spreading excellence and widening participation". VIDIS (2020-2023) is coordinated by Vinca Institute, Grant agreement number 952433.

Welcome to Vinca and online and have a stimulating and productive time!

*Milena Jovašević-Stojanović and Alena Bartoňová*

**TABLE OF CONTENTS**

## 5.4 A NUMERICAL MODEL FOR POLLEN PREDICTION: THUNDERSTORM ASTHMA CASE STUDY

**S. Ničković (1,2), L. Ilić(1), S. Petković (2), G. Pejanović (2), A. Huete (3), Z. Mijić (1)**

*(1) Institute of Physics Belgrade, University of Belgrade, Belgrade, Serbia, (2) Republic Hydrometeorological Service of Serbia, Belgrade, Serbia, (3) School of Life Sciences, University of Technology Sydney, Sydney,NSW Australia, zoran.mijic@ipb.ac.rs*

More than 300 million people worldwide have asthma - resulting, at the global scale, in approximately 180,000 deaths annually (To et al., 2012). Approximately 50% of adults and 90% of children with asthma had an allergic form of the disease (Palomares et al., 2017). The allergy occurrence is often caused by pollen, representing one of the major healthcare problems. The strongest risk factors for developing asthma are inhaled particles; pollen grains emitted by trees, grasses, and ragweed are among the most commonly present particles. The pollen dispersion process starts with the pollen emission which depends on plant phenology and on near-surface atmospheric conditions. Emitted pollen is dispersed by vertical air mixing and by free-atmospheric horizontal transport. In the final phase of the pollen atmospheric process, pollen grains settle down to the Earth's surface by wet and by dry deposition (due to gravity and near-surface turbulence). In order to predict the atmospheric pollen process, several pollen models have been developed over the last decade (e.g., Siljamo et al., 2013; Luvall et al., 2013). The prediction of extreme pollen episodes generated by thunderstorm processes is of particular interest. Thunderstorm-caused asthma, usually called "thunderstorm asthma" (TA) is a striking event in which patients could experience life-threatening asthma attacks caused by extreme numbers of pollen grains. If a thunderstorm occurs during a pollen season, favourable conditions for intense pollen uptake and transport are fulfilled. In the TA Melbourne case occurred on November 21st 2016, high near-surface concentrations of grass pollen caused instant allergic reactions in predisposed persons. As a result, within 30 hours there was a 672% increase in visits to emergency services due to respiratory difficulties, and a 992% increase of asthma-related hospital admissions compared with the occurrences in previous 3 years (Thien et al., 2018). In this study, the capacity of the PREAM (Pollen Regional Atmospheric Model) model to predict excessive TA events is examined. PREAM is a version of the DREAM regional dust aerosol atmospheric model (Ničković et al., 2001) modified in our study to predict pollen dispersion. In our study we implemented a regional Euler-type pollen prediction model over the Australian state of Victoria in order to explore its capability to predict the Melbourne pollen event. We set up the model with a horizontal resolution below 10km, sufficiently fine to confidently resolve pollen sources and to adequately represent atmospheric features essential for pollen storm generation (such as non-hydrostatic and convection processes). Furthermore, we introduced an advanced pollen emission scheme which takes into account different near-surface turbulence conditions. The model simulation covering the period 16-22 November 2016 was verified against available pollen counts observed at a Melbourne site. The model correctly identified the increased pollen concentrations from the weaker observed peak on 16th November. The extreme pollen concentrations on the 21st November, which triggered the epidemic asthma, was quite well represented by the model, in terms of both timing and location, thus demonstrating its high potential to successfully simulate extreme pollen events.

### REFERENCES

Luvall, J. C., NASA/MSFC, Huntsville, AL; and W. A. Sprigg, E. Levetin, A. Huete, S. Ničković, et.al., 2013. Use of MODIS Satellite Data to Evaluate Juniperus spp. Pollen Phenology to Support a Pollen Dispersal Model, PREAM, to Support Public Health Allergy Alerts Earth Observation Systems and Applications for Public Health Models and Decisions, 93rd American Meteorological Society Annual Meeting January 05 – 10.

Palomares Ó, Sánchez-Ramón S, Dávila I, Prieto L, Pérez de Llano L, Lleonart M, et al. 2017. dIvergEnt: How IgE Axis Contributes to the Continuum of Allergic Asthma and Anti-IgE Therapies, International Journal of Molecular Sciences 18(6):E1328.

Ničković, S., Kallos, G., Papadopoulos, A., Kakaliagou, O., 2001. A model for prediction of desert dust cycle in the atmosphere. Journal of Geophysical Research 106, 18113-18130.

Siljamo, P., Sofiev, M., Filatova, E., Grewling, L., Jager, S., Khoreva, E., et al. 2013. A numerical model of birch pollen emission and dispersion in the atmosphere Model evaluation and sensitivity analysis, International Journal of Biometeorology 57, 125-136.

Thien, F., Beggs, P. J, Csutoros, D., Darvall, J., Hew, M., et al. 2018. The Melbourne epidemic thunderstorm asthma event 2016: an investigation of environmental triggers, effect on health services, and patient risk factors, Lancet Planet Health 2, e255–263.

To, T., Stanojevic, S., Moores, G., Gershon, A.S., Bateman, E.D., Cruz, A.A., Boulet, L., 2012. Global asthma prevalence in adults: findings from the cross-sectional world health survey, BMC Public Health. 12:204.

## 8.3 A STUDY ON TROPOSPHERIC AEROSOLS CHANGE DURING THE COVID-19 LOCK-DOWN PERIOD: EXPERIENCE FROM EARLINET MEASUREMENT CAMPAIGN

**Z. Mijić, M. Kuzmanoski, L. Ilić**
*Institute of Physics Belgrade, University of Belgrade, Belgrade, Serbia*
*zoran.mijic@ipb.ac.rs*

To slow down the rate of spread of corona virus, most of the countries in Europe have followed partial-to-complete lockdown measures in 2020. The lockdown period provided a unique opportunity to examine the effects of reduced anthropogenic activities on changes in the atmospheric environment. Aerosol lidars with their high temporal and vertical resolution, provide reliable information on the atmospheric structure, its dynamics, and its optical properties. The European Aerosol Research Lidar Network, EARLINET, was established in 2000 as a research project with the goal of creating a quantitative, comprehensive, and statistically significant database for the horizontal, vertical, and temporal distribution of aerosols on a continental scale (Pappalardo et al., 2014). EARLINET is part of ACTRIS (Aerosols, Clouds and Trace gases Research Infrastructure) a pan-European initiative consolidating actions among European partners producing high-quality observations of aerosols, clouds and trace gases.

As a part of the ACTRIS initiative for studying the changes in the atmosphere during the COVID-19 lockdown period in May 2020 a dedicated EARLINET measurement campaign was organized in order to: monitor the atmosphere's structure during the lockdown and early relaxation period in Europe, and to identify possible changes due to decreased emissions by comparison to the aerosol climatology in Europe. During the campaign the near-real-time (NRT) operation of the EARLINET was demonstrated following previous experience from the EUNADICS-AV exercise (Papagiannopoulos et al., 2020). The Belgrade lidar station (Ilić et al., 2018) participated in the campaign together with 21 EARLINET stations providing vertical aerosol profiles twice per day (minimum two hours measurements at noon, and minimum two hours after sunset). The measurements were submitted and processed by the Single Calculus Chain (SCC) in the near-real-time. The SCC is a tool for the automatic analysis of aerosol lidar measurements developed within EARLINET network (D'Amico et al., 2015, D'Amico et al., 2016). The main aim of SCC is to provide a data processing chain that allows all EARLINET stations to retrieve, in a fully automatic way, the aerosol backscatter and extinction profiles (measures of the aerosol load) together with other aerosol products. This first analysis was based on the data processed by the SCC and directly published on the THREDDS server in NRT. The preliminary analysis made on aerosol lidar data shows that by simply comparing the observed backscatter values with the climatological values from 2000-2015 is not sufficient to extract a clear conclusion on how much the COVID-19 lock-down has impacted the aerosols in the atmosphere, but a certain effect for low troposphere can be seen. Beyond the scientific goals of this campaign, the actions organized by EARLINET/ACTRIS (NRT delivery of the data and fast analysis of the data products) proved that aerosol lidars are useful for providing information not only for climatological purposes, but also in emergency situations. A more quantitative analysis based on re-analyzing additional data products will be made to consolidate the conclusions.

### REFERENCES

Pappalardo, G., Amodeo, A., Apituley, A., Comeron, A., Freudenthaler, V., Linné, H., Ansmann, A., Bösenberg, J., D'Amico, G., Mattis, I., Mona, L., Wandinger, U., Amiridis, V., Alados-Arboledas, L., Nicolae, D., and Wiegner, M., 2014. EARLINET: towards an advanced sustainable European aerosol lidar network, Atmospheric Measurement Techniques 7, 2389–2409.

D'Amico, G., Amodeo, A., Baars, H., Binietoglou, I., Freudenthaler, V., Mattis, I., Wandinger, U., and Pappalardo, G., 2015. EARLINET Single Calculus Chain – overview on methodology and strategy, Atmospheric Measurement Techniques 8, 4891-4916.

D'Amico, G., Amodeo, A., Mattis, I., Freudenthaler, V., and Pappalardo, G., 2016. EARLINET Single Calculus Chaintechnical– Part 1: Pre-processing of raw lidar data, Atmospheric Measurement Techniques 9, 491-507.

Ilić, L., KuzmanoskiM., KolaržP., NinaA., SrećkovićV., MijićZ., BajčetićJ., AndrićM., 2018. Changes of atmospheric properties over Belgrade, observed using remote sensing and in situ methods during the partial solar eclipse of 20 March 2015,Journal of Atmospheric and Solar-Terrestrial Physics171,250-259.

Papagiannopoulos, N., D'Amico, G., Gialitaki, A., Ajtai, N., Alados-Arboledas, L., Amodeo, A., Amiridis, V., Baars, H. et al., 2020. An EARLINET early warning system for atmospheric aerosol aviation hazards, Atmospheric Chemistry and Physics 20, 10775–10789.

CIP - Каталогизација у публикацији
Народна библиотека Србије, Београд

ISBN 978-86-7306-164-1

9 788673 061641

WeBIOPATR

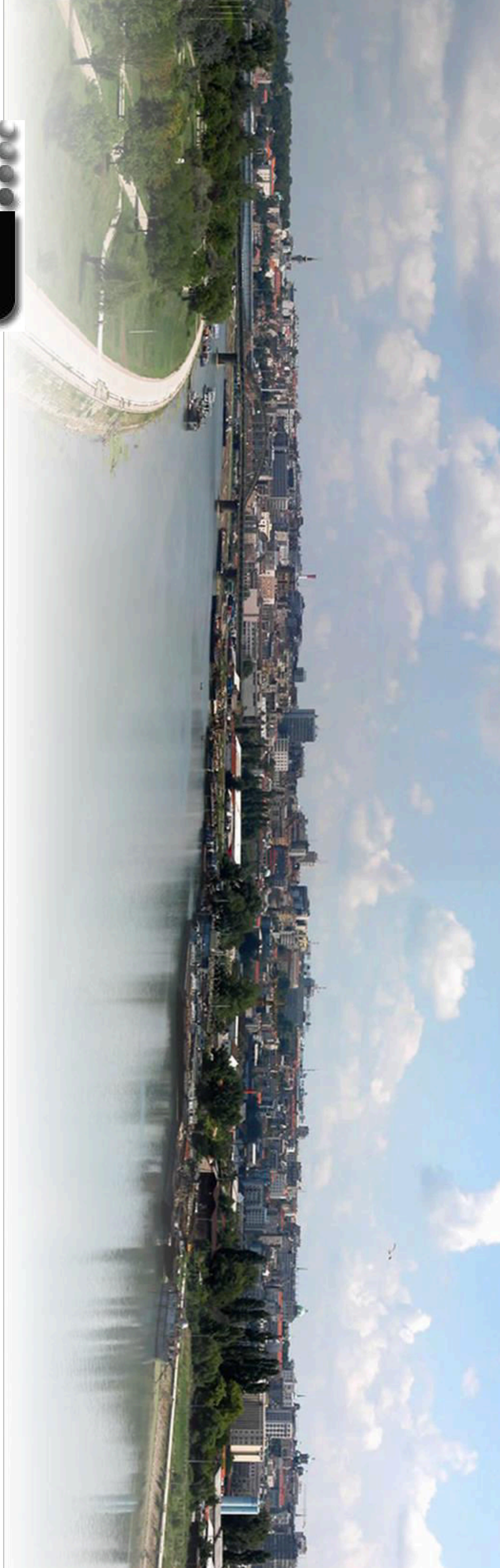

# XIV Serbian Conference on Spectral Line Shapes in Astrophysics

June 19 - 23, 2023 Bajina Bašta, Serbia

# BOOK OF ABSTRACTS

Eds. Luka Č. Popović, Nataša Bon, Edi Bon
and Sylvie Sahal-Bréchot

Astronomical Observatory
Belgrade, 2023

# XIV Serbian Conference on Spectral Line Shapes in Astrophysics

June 19 - 23, 2023 Bajina Bašta, Serbia




Organized by: Astronomical Observatory Belgrade, Serbia

Co-organizer: Faculty of Mathematics, University of Belgrade, Serbia

Published by: Observatory Belgrade, Volgina 7, 11060 Belgrade, Serbia

The publication of this issue is financially supported by the Ministry of Science, Technological Development and Innovation of the Republic of Serbia

Website: http://servo.aob.rs/scslsa/

Cover image design: Sladjana Marčeta Mandić

Computer text design: Sladjana Marčeta Mandić

ISBN 978-86-82296-04-1

Printed by: Skripta Internacional, Mike Alasa 54, Beograd

Number of copies: 70

# XIV Serbian Conference on Spectral Line Shapes in Astrophysics

# BOOK OF ABSTRACTS

**Editors: Luka Č. Popović, Nataša Bon, Edi Bon and Sylvie Sahal-Bréchot**

**Belgrade, 2023**

# CONTENTS

# THE INFLUENCE OF SOLAR X RAYS: MODELING ATMOSPHERE

**A. Kolarski[1], V. A. Srećković[1] and Z. Mijić[1]**

[1]*Institute of Physics Belgrade, UB, Pregrevica 118, 11080 Belgrade, Serbia*

*E-mail: aleksandra.kolarski@ipb.ac.rs, vlada@ipb.ac.rs, zoran.mijic@ipb.ac.rs*

The atmosphere of the sunlit Earth is mostly influenced from outside by solar radiation, mainly in soft-range X-ray section of the electromagnetic spectrum. The ionosphere's photo-ionization rate is influenced by composite particles and the solar radiation spectrum at the altitude under consideration. Data on some solar spectral lines, especially as Lyman-alpha, and radiation could be very useful in studying solar flares. In this contribution we statistically analyzed the influence of solar flares i.e. radiation on Very Low Frequency VLF signals and atmosphere composition.

# MULTI-INSTRUMENTAL INVESTIGATION OF THE POWERFUL SOLAR FLARES IMPACT ON THE IONOSPHERE: CASE STUDY

**A. Kolarski[1], N. Veselinović[1], V. A. Srećković[1], Z. Mijić[1], M. Savić[1] and A. Dragić[1]**

[1]*Institute of Physics Belgrade, UB, Pregrevica 118, 11080 Belgrade, Serbia*

*E-mail: aleksandra.kolarski@ipb.ac.rs, nikola.veselinovic@ipb.ac.rs, vlada@ipb.ac.rs, zoran.mijic@ipb.ac.rs, mihailo.savic@ipb.ac.rs, aleksandar.dragic@ipb.ac.rs*

Case study of energetic solar events which included strongest solar flare of the previous solar cycle, X9.3 from 6 September 2017 and accompanying Coronal Mass Ejections (CMEs) directed towards Earth is presented through ionospheric and primary cosmic rays implications. Conducted analysis and numerical simulations were done both on data from ground-based Belgrade Very Low Frequency (VLF) and Cosmic Ray (CR) stations and space-borne satellite platforms of GOES and SOHO missions. Some of the main findings regarding related disturbances of ionospheric parameters and on primary cosmic rays are presented in this work.

V Meeting on Astrophysical Spectroscopy -

A&M DATA - Astronomy & Earth Observations

September 12 - 15, 2023, Palić, Serbia

# BOOK OF ABSTRACTS AND CONTRIBUTED PAPERS

Edited by Vladimir A. Srećković, Milan S. Dimitrijević, Aleksandra Kolarski, Zoran R. Mijić and Nikola B. Veselinović

A&M DATA

UNIVERSITY OF BELGRADE
INSTITUTE OF PHYSICS | BELGRADE
NATIONAL INSTITUTE OF THE REPUBLIC OF SERBIA

Belgrade 2023

## Scientific Committee

Vladimir A. Srećković, **Co-Chairman,** Serbia
Milan S. Dimitrijević, **Co-Chairman,** Serbia

Nikolay Bezuglov, Russia
Nebil Ben Nessib, Saudi Arabia
Vesna Borka Jovanović, Serbia
Nikola Cvetanović, Serbia
Saša Dujko, Serbia
Stevica Đurović, Serbia
Zoran Grujić, Serbia
Rafik Hamdi, Tunisia
Magdalena D. Christova, Bulgaria
Dragana Ilić, Serbia
Milivoje Ivković, Serbia
Darko Jevremović, Serbia
Ognyan Kounchev, Bulgaria
Bratislav P. Marinković, Serbia
Zoran R. Mijić, Serbia
Aleksandar Milosavljević, France
Aleksandra Nina, Serbia
Bratislav M. Obradović, Serbia
Nicolina Pop, Romania
Luka Č. Popović, Serbia
Branko Predojević, Republic of Srpska, BiH
Sylvie Sahal-Bréchot, France
Igor Savić, Serbia
Sanja Tošić, Serbia
Nikola B. Veselinović, Serbia

## Local Organizing Committee

Aleksandra Kolarski (Co-Chair), Institute of Physics Belgrade
Vladimir A. Srećković (Co-Chair), Institute of Physics Belgrade
Nikola B. Veselinović (Secretary), Institute of Physics Belgrade
Zoran R. Mijić, Institute of Physics Belgrade
Nenad M. Sakan, Institute of Physics Belgrade
Veljko Vujčić, Astronomical Observatory, Belgrade
Nikola Cvetanović, University of Belgrade, Faculty of Transport and Traffic Engineering

**Organizers:**

Institute of Physics Belgrade, Serbia,

Text arrangement by computer: Tanja Milovanov

ISBN 978-86-82441-61-8



Financially supported by the Ministry of Science, Technological Developement and Innovation of Serbia

Production: Skripta Internacional, Mike Alasa 54, Beograd in 50 copies

# Aerosol vertical profiles in Belgrade, Serbia, associated with different surface PM10 concentrations

**Maja Kuzmanoski[1], Zorica Podraščanin[2], Ana Ćirišan[3] and Zoran R. Mijić[1]**

*[1]Institute of Physics Belgrade, University of Belgrade, Belgrade, Serbia*
*E-mail: maja.kuzmanoski@ipb.ac.rs*
*[2]Department of Physics, Faculty of Sciences, University of Novi Sad, Novi Sad, Serbia*
*[3]Faculty of Ecology and Environmental Protection, Union-Nikola Tesla University, Belgrade, Serbia*

The height of the atmospheric boundary layer (ABLH) is an important parameter in studies of air pollution, as it determines the volume available for dispersion of pollutants. Aerosol lidar provides information on temporal changes of ABLH (using aerosols as tracers) and vertical structure of aerosol layer. Coupled with measurements of meteorological parameters, this information is valuable in interpretation of particulate matter (PM) observations at ground level. Knowledge of the temporal changes of aerosol vertical profile is helpful in understanding the formation of PM air pollution and the impact of long-range transport to surface PM concentrations.

Aerosol lidar measurements performed in Belgrade during 2018-2020, were used to derive vertical profiles of aerosol backscatter coefficient at 355 nm (Klett, 1981; Fernald, 1984) and the temporal evolution of ABLH (Ilić et al., 2018). In this study, selected cases of aerosol layer vertical structure, under different thermodynamic stability conditions of ABL and different levels of PM pollution, are discussed.

## References

Fernald, F. G., 1984, Appl. Opt. 23, 652-653.
Ilić, L., Kuzmanoski, M., Kolarž, P., Nina, A., Srećković, V., Mijić, Z., Bajčetić, J. Andrić, M.., 2018, J. Atmos. Sol. Terr. Phys., 171, 250-259.
Klett, J. D., 1981, Appl. Opt., 24, 1638-1643.

# Multi-instrumental investigation of extreme space weather events in September 2017: Data and modeling

**Nikola B. Veselinović, Aleksandra Kolarski, Vladimir A. Srećković, Zoran R. Mijić, Mihailo R. Savić and Aleksandar L. Dragić**

*Institute of Physics Belgrade, Pregrevica 118, 11080 Belgrade, Serbia*
*E-mail: veselinovic@ipb.ac.rs*

Strong Solar activity during September 2017, despite being in the declining phase of cycle 24, produced several solar flares, accompanied by a series of coronal mass ejections that led to complex and geoeffective plasma structures in the heliosphere (Luhmann et al., 2020). These events, involving interactions between plasma structures (Albert et al., 2020), as well as their influence on Earth's environment are very difficult to forecast.

A number of studies used different approaches to analyze influence of Solar activity on particular phenomena either in heliosphere (Kozev et al., 2022, Savić et al., 2023) or ionosphere responses (Kolarski et al., 2022, Srećković at al., 2021). Recently, several investigations based on multi-instrumental measurements and numerical simulations show more comprehensive insight into the ionospheric responses and change of primary cosmic rays' flux due to the extreme Solar activity (Kolarski et al., 2023, Barta et al., 2022).

The focus of this research is to investigate the phenomena induced by the extreme event in near-Earth space and Earth's atmosphere during September 2017, with an emphasis on studying and modeling the variations in cosmic ray flux and disturbances in the lower ionosphere in correlation with Solar activity. The investigation is based on ground-based measurements such as from neutron monitors, very low-frequency (VLF) radio wave stations, and cosmic ray detectors, as well as in situ measurements from different space probes.

The results of this study show that the ionospheric atomic and molecular data like sharpness and effective reflection height and electron density obtained from Belgrade VLF data measurements, are in correlation with incident X-ray flux while time series of cosmic rays' flux measured at Belgrade muon station correspond to disturbance of near-Earth heliospheric conditions.

The multi-instrumental approach accompanied with numerical modeling of specific space weather events additionally contribute to better understanding of solar-terrestrial coupling processes.

## References

Albert, D., Antony, B., Ba, Y. A., Babikov, Y. L., et al., 2020, Atoms, 8, 76
Barta, V., Natras, R., Srećković, V., Koronczay, D., et al., 2022, Front. Environ. Sci. 10:904335.
Kolarski, A., Veselinović, N., Srećković, V. A., Mijić, Z., et al., 2023, Remote Sens. 15, 1403
Kolarski, A., Srećković, V. A., Mijić, Z. R., 2022, Appl. Sci. 12, 582
Kozarev, K., Nedal, M., Miteva, R., Dechev, M. and Zucca, P., 2022, Front. Astron. Space Sci. 9:801429.
Luhmann, J. G., Gopalswamy, N., Jian, L. K. et al., 2022, Sol Phys 295, 61
Savić, M., Veselinović, N., Dragić, A., et al., 2023, Adv. Sp. Research, 71,4
Srećković, V. A., Šulić, D. M., Vujčić, V., Mijić, Z. R., et al., Appl. Sci. 2021, 11, 11574

# COST programme role within the Serbian multilateral collaboration in science and innovation framework

**Bratislav P. Marinković and Zoran R. Mijić**

*Institute of Physics Belgrade, Pregrevica 118, 11080 Belgrade, Serbia*
*E-mail: bratislav.marinkovic@ipb.ac.rs*

COST – Cooperation in Science and Technology is a networking programme fully financed by the European Horizon frameworks (H2020 and HE) with the aim to foster collaboration of researchers and innovators within European countries and to contribute to the creation of European Research Area (ERA). Its main priorities are to promote and spread excellence, to foster interdisciplinary research through breakthrough science and to empower and retain young researchers and innovators. Although COST programme does not finance the research itself (it is lean on the national funding schemas of all 41 participating countries) it enables wide collaboration and networking through general or working group meetings, short term scientific missions, training schools and management meetings.

In 2022 Serbian researchers performed an individual participation in more than 750 COST Action activities. COST Actions generally last for four years, up to now, Serbian researchers chaired and co-chaired 23 Actions and participated in total of 928 Actions (https://www.cost.eu/about/members/serbia/). The broader statistics of Serbian participation in COST Actions can be found in Marinković et al. (2022).

## Acknowledgements

Thanks are due to The Ministry of Science, Technological Development and Innovation of the Republic of Serbia and the Institute of Physics Belgrade for national COST office support.

## References

Marinković, Bratislav P., Ivanović, Stefan and Mijić, Zoran, “Data analysis on Serbian participation in COST Actions: Celebrating 50 years of research networks”, IV Meeting on Astrophysical Spectroscopy - A&M DATA - Atmosphere, May 30 to June 2, 2022, Fruška Gora, Serbia, Book of Abstracts and Contributed Papers, Eds: V. A. Srećković, M. S. Dimitrijević, N. Veselinović and N. Cvetanović, (Institute of Physics Belgrade, Belgrade, 2022), Progress report, pp.49-57. ISBN: 978-86-82441-57-1

# Interdisciplinary research in the European Cooperation in Science and Technology – advantage or disadvantage?

**Zoran R. Mijić and Bratislav P. Marinković**

*Institute of Physics Belgrade, Pregrevica 118, 11080 Belgrade, Serbia*
*E-mail: zoran.mijic@ipb.ac.rs*

Collaboration is at the heart of modern science while interdisciplinary research plays a very important role in addressing some of the most important and complex problems. The European Cooperation in Science and Technology – COST is the oldest intergovernmental funding organization in Europe with the aim to establish the research networks among scientists and innovators. Two years ago, COST celebrated 50 years of the existence and successful networking activities. During that period COST has become one of the best mechanisms to promote science cooperation in the world. For establishing a collaboration proximity is particularly important, but once a collaboration is in place scientists manage to continue a collaboration despite a large distance. COST Actions support a variety of networking tools enabling spatial and social proximity thus increasing the level of scientific production.

In this paper review of available data on the effects of participating in a COST Action on the level of scientific production i.e., scientific co-publications between active members of an Action is given (Seeber et al., 2022a). In addition, the interdisciplinary nature of co-publications and involvement of researchers from inclusive target countries as well as young researcher is discussed. Since researcher from Serbia are involved in almost 96% of active Actions (Mijić and Marinković, 2022) it is particularly important to assess whether these effects persist after the life time of the Action.

Regarding the multidisciplinarity of the new Actions approved in 2023, 54% of them cover at least two fields of science and technology, while 11% cover at least three fields. Natural sciences are represented in 49% of the Actions leading the way as the most represented field of science. Therefore, additional discussion will be given for better understanding whether Actions proposals' degree of interdisciplinarity and the relative proportion of different scientific fields, may be disadvantage or not in the project evaluation procedure in the COST research framework (Seeber et al., 2022b).

**Acknowledgements**

Thanks are due to The Ministry of Science, Technological Development and Innovation of the Republic of Serbia and the Institute of Physics Belgrade for national COST office support.

**References**

Mijić, Z., Marinković, B., 2022, IV Meeting on Astrophysical Spectroscopy - A&M DATA - Atmosphere, Book of Abstracts and Contributed Papers, Eds: V. A. Srećković, M. S. Dimitrijević, N. Veselinović and N. Cvetanović, pp.74-80.

Seeber, M., Vlegels, J., Seeber, M., 2022a, 26th International Conference on Science and Technology Indicators, Proceedings, Eds: N. Robinson-Garcia, D. Torres-Salinas, W. Arroyo-Machado, sti2239

Seeber, M., Vlegels, J., Cattaneo, M., 2022b, J. Assoc. Inf. Sci. Technol. 73, 1106

# Data quality assurance and characterization of Belgrade Raman lidar station

**Zoran R. Mijić[1*], Maja Kuzmanoski[1] and Luka Ilić[1,2]**

[1]*Institute of Physics Belgrade, Pregrevica 118, 11080 Belgrade, Serbia*
[2]*now at Barcelona Supercomputing Center, Plaça Eusebi Güell, 1-3, 08034 Barcelona, Spain*
[*]*E-mail: zoran.mijic@ipb.ac.rs*

Atmospheric probing and the observations of atmospheric aerosol particles can be performed remotely with high spatial and temporal resolution using LIDAR (Light Detection And Ranging) technique. Aerosol optical characteristics provide extensive information on the existence and development of atmospheric aerosol structures. As an EARLINET (the European Aerosol Research LIdar Network) (Pappalardo et al., 2014) joining lidar station, Belgrade Raman lidar system has provided aerosol profiling data for potential climatological studies as well as assessment of planetary boundary layer evolution (Ilić et al., 2018) and conducting dedicated measurements during potential airborne hazards events (e.g., volcanic ash, desert dust, biomass burning). To provide a quality controlled and homogeneous analysis of raw lidar data across the network, a centralized analysis tool, called the Single Calculus Chain (SCC), has been released within EARLINET (Mattis et al., 2016). In order to assess the performance and the temporal stability of a lidar system a rigorous quality-assurance (QA) program and self-testing check-up tools have been developed. In this paper a description of the Belgrade Raman lidar system capabilities, and its experimental characterization related to zero bin, analog to photon-counting signal delay, the Rayleigh-fit and telecover tests to check the system accuracy (Freudenthaler et al., 2018) will be presented.

## References

Freudenthaler, V., Linné, H., Chaikovski, A., Rabus, D., Groß, S., 2018, Atmos. Meas. Tech. Discuss. preprint, https://doi.org/10.5194/amt-2017-395

Ilić, L., Kuzmanoski, M., Kolarž, P., Nina, A,, et al., 2018, Journal of Atmos. Sol.-Terr. Phys. 171, 250

Mattis, I., D'Amico, G., Baars, H., Amodeo, A., et al., 2016, Atmos. Meas. Tech. 9, 3009

Pappalardo, G., Amodeo, A., Apituley, A., Comeron, A., et al., 2014, Atmos. Meas. Tech., 7, 2389

# VLF propagation parameters modeling related to low intensity solar X-ray flares

**Aleksandra Kolarski, Vladimir A. Srećković and Zoran R. Mijić**

*Institute of Physics Belgrade, University of Belgrade, Pregrevica 118, 11000 Belgrade, Serbia*
*E-mail: aleksandra.kolarski@ipb.ac.rs*

Solar X-ray flare (SF) events of low intensity are rarely investigated and their impacts on the subionospheric Very Low Frequency (VLF) propagation are not thoroughly described and annotated, primarily due to the prerequisite of quiet solar activity conditions and low-level X-ray emissions of background radiation. VLF propagation under events of such low-intensity SFs is inspected on VLF radio signal (3-30 kHz) recordings with path-oriented analysis conducted. Numerical modeling of VLF propagation parameters was carried out by the means of Long Wave Propagation Capability (LWPC) software package, based on VLF data recorded by Belgrade VLF stations (Serbia). Solar X-ray radiation data is obtained from Geostationary Operational Environmental Satellite (GOES) database. Main results are presented in this paper.

**Key words:** Solar flare, VLF perturbation, numerical modeling.

International Conference on Recent Trends in Geoscience Research and Applications 2023

October 23–27, 2023, Belgrade, Serbia & virtual

# BOOK OF ABSTRACTS AND CONTRIBUTED PAPERS

Edited by Aleksandra Nina, Snežana Dragović, and Dejan Doljak

Belgrade
2023

**Scientific Committee**



**Local Organizing Committee**



**Scientific Rationale**

Geoscience research and applications are of crucial interest in science and many areas of modern life. For this reason, exchanging knowledge in various relevant areas is essential for development in scientific, engineering and programming activities. The conference aims to highlight the importance of joint research of experts in these fields and provide a platform for knowledge exchange.

**Venue:** Institute of Physics Belgrade, Belgrade, Serbia & virtual

**Organizers:** Faculty of Civil Engineering, University of Belgrade and Institute of Physics Belgrade, University of Belgrade

**Published by:** Faculty of Civil Engineering, University of Belgrade; Institute of Physics Belgrade, University of Belgrade; and Geographical Institute "Jovan Cvijić" SASA

The publication of this issue is financially supported by the Ministry for Education, Science and Technological Development of Serbia

Picture on the first cover: Dejan Doljak

ISBN 978-86-7518-239-9

eISBN 978-86-7518-240-5

**Printed by:** Curent Print, Tvrtka Velikog 14, Beograd

Number of copies: 50

*Abstract*

# AEROSOL VERTICAL PROFILES AND ABL HEIGHTS CORRESPONDING TO DIFFERENT $PM_{10}$ POLLUTION LEVELS IN BELGRADE, SERBIA

*Maja Kuzmanoski* [1]*, *Zorica Podraščanin* [2], *Ana Ćirišan* [3], *Zoran Mijić* [1]

[1]Institute of Physics Belgrade, University of Belgrade, Belgrade, Serbia; e-mails: maja.kuzmanoski@ipb.ac.rs, zoran.mijic@ipb.ac.rs
[2]Department of Physics, Faculty of Sciences, University of Novi Sad, Novi Sad, Serbia; e-mail: zorica.podrascanin@df.uns.ac.rs
[3]Faculty of Ecology and Environmental Protection, Union-Nikola Tesla University, Belgrade, Serbia; e-mail: acirisan@unionnikolatesla.edu.rs

Western Balkans is among the regions with the highest level of air pollution in Europe (European Environmental Agency, 2022). Particulate matter (PM) has been recognized as one of the most harmful air pollutants, posing threat to human health. To design efficient pollution control measures, better understanding of conditions that contribute to elevated PM concentrations is necessary. The information on aerosol vertical profile, along with vertical profile of meteorological parameters, is important to understand dispersion of PM, the development of air pollution and the contribution of the long-range transport to surface PM concentrations.

In this study, the lidar measurements at 355 nm, performed in Belgrade, Serbia, are used to analyze the atmospheric boundary layer height (ABLH) and vertical profiles of aerosol backscatter coefficient. The ABLH is estimated with 1-min temporal resolution using the gradient method (Ilić et al., 2018), while the aerosol backscatter coefficient is derived from lidar signals averaged over 30-min intervals using Klett-Fernald retrieval method (Fernald, 1984; Klett, 1981). $PM_{10}$ concentrations in Belgrade, used in this study, are obtained from the Serbian Environmental Protection Agency automatic monitoring stations.

Focusing on the 2018–2020 period, excluding data collected in presence of low- or mid-altitude clouds, we analyze the aerosol vertical structure and ABLH for periods of different levels of $PM_{10}$ pollution in Belgrade, as well as the periods of different temporal changes of $PM_{10}$ concentration. Additionally, the thermodynamic stability of the ABL in the analyzed cases is discussed, based on radiosounding measurements in Belgrade.

**Acknowledgements**

MK and ZM acknowledge funding provided by the Institute of Physics Belgrade, through the grant by the Ministry of Education, Science and Technological Development of the Republic of Serbia. EU COST Action CA18235 "Profiling the atmospheric boundary layer at European scale" is acknowledged.

*Corresponding author, e-mail: maja.kuzmanoski@ipb.ac.rs

## References


European Environmental Agency. (2022). *Air quality in Europe 2022 (*Report No. 05/2022). https://doi.org/10.2800/488115

Fernald, F. G. (1984). Analysis of atmospheric lidar observations: some comments. *Applied Optics, 23*(5), 652–653. https://doi.org/10.1364/AO.23.000652

Ilić, L., Kuzmanoski, M., Kolarž, P., Nina, A., Srećković, V., Mijić, Z., Bajčetić, J., & Andrić, M. (2018). Changes of atmospheric properties over Belgrade, observed using remote sensing and in situ methods during the partial solar eclipse of 20 March 2015. *Journal of Atmospheric and Solar-Terrestrial Physics*, *171*, 250–259. https://doi.org/10.1016/j.jastp.2017.10.001

Klett, J. D. (1981). Stable analytical inversion solution for processing lidar returns. *Applied Optics*, *20*(2), 211–220. https://doi.org/10.1364/AO.20.000211

# WeBIOPATR 2023

The Ninth International WEBIOPATR
Workshop & Conference
Particulate Matter: Research and Management

## Abstracts of Keynote Invited Lectures and Contributed Papers


Milena Jovašević-Stojanović,

Alena Bartoňová,

Danka Stojanović and Simon Smith, Eds



VInča Insitute of Nuclear Sciences

National Institute of the Republic of Serbia, University of Belgrade

Vinča, Belgrade 2023

# ABSTRACTS OF KEYNOTE INVITED LECTURES AND CONTRIBUTED PAPERS

The Ninth WeBIOPATR Workshop & Conference

Particulate Matter: Research and Management

**WeBIOPATR 2023**

28th November to 1st December 2023

Vinča, Belgrade, Serbia

*Editors*

Milena Jovašević-Stojanović

Alena Bartoňová

Danka Stojanović and Simon Smith

*Publisher*

Vinča Institute of Nuclear Sciences

Prof. Dr Snežana Pajović, Director

P.O.Box 522

11001 Belgrade, Serbia

*Printed by*

Vinča Institute of Nuclear Sciences

Number of copies: 100

ISBN-978-86-7306-177-1



www.vin.bg.ac.rs/

## SCIENTIFIC COMMITTEE

Aleksandar Jovović, Serbia

Alena Bartoňová, Norway

Antonije Onjia, Serbia

David Broday, Israel

Dikaia Saraga, Athens, Greece

Griša Močnik, Slovenia

Ivan Gržetić, Serbia

María Cruz, Spain

Milena Jovašević-Stojanović, Serbia

Miloš Davidović, Serbia

Saverio de Vito, Italy

Selahattin Incecik, Turkey

Slobodan Ničković, Serbia

Simone Barreira Morais, Portugal

Zoran Mijić, Serbia

Zoran Ristovski, Australia

Zorana Jovanović-Andersen, Denmark

Renata Kovačević, Serbia

## ORGANIZING COMMITTEE

Aleksandra Stanković, Serbia

Alena Bartoňová, Norway

Andrej Šoštarić, Serbia

Anka Cvetković, Serbia

Bojana Petrović, Serbia

Bojan Radović, Serbia

Branislava Matić, Serbia

Lidija Marić-Tanasković, Serbia

Ivan Lazović, Serbia

Danka Stojanović (Secretary), Serbia

Duška Kleut (Secretary), Serbia

Marija Živković, Serbia

Maja Jovanović, Serbia

Milena Jovašević-Stojanović, Serbia

Miloš Davidović, Serbia

Mira Aničić Urošević, Serbia

Mirjana Perišić, Serbia

Nenad Živković, Serbia

Tihomir Popović, Serbia

Uzahir Ramadani (Secretary), Serbia

Vesna Slepčević, Serbia

## CONFERENCE TOPICS

1. **Atmospheric Particulate Matter - Physical and Chemical Properties**
    i. Sources and formation of particulate matter
    ii. Particulate matter composition and levels outdoors and indoors
    iii. Environmental modeling
    iv. Nanoparticles in the environment
2. **Particulate Matter and Health**
    i. Exposure to particulate matter
    ii. Health aspects of atmospheric particulate matter
    iii. Full chain approach
    iv. COVID-19 and particulate matter
3. **Particulate Matter and Regulatory Issues**
    i. Issues related to monitoring of particulate matter
    ii. Legislative aspects
    iii. Abatement strategies

## 11.2 THE USE OF AEROSOL LIDAR IN STUDY OF PM10 POLLUTION IN BELGRADE, SERBIA

**M. Kuzmanoski (1), Z. Podraščanin (2), A. Ćirišan (3), Z. Mijić (1)**

*(1) Institute of Physics Belgrade, University of Belgrade, Belgrade, Serbia, (2) Department of Physics, Faculty of Sciences, University of Novi Sad, Novi Sad, Serbia, (3) Faculty of Ecology and Environmental Protection, Union-Nikola Tesla University, Belgrade,*

*maja.kuzmanoski@ipb.ac.rs*

Improved understanding of conditions that contribute to elevated PM10 concentrations is necessary in order to design effective air pollution control measures. Knowledge of the aerosol vertical profile, along with vertical profiles of meteorological parameters, is important to understand the dispersion of PM10, the development of air pollution and the contribution of long-range transported particles to surface PM10 concentrations. Aerosol lidar provides information on vertical profiles of aerosol optical properties. It is also used to observe the temporal changes of the atmospheric boundary layer (ABL) height, using aerosols as tracers.

The aim of this study is to explore the application of aerosol lidar observations in analysis of PM10 pollution in Belgrade. Aerosol lidar measurements at 355 nm, conducted in the period of 2018-2020 in Belgrade are used, excluding data collected in the presence of low- or mid-altitude clouds. Lidar data are analyzed to derive vertical profiles of aerosol backscatter coefficient (Klett, 1981; Fernald, 1984) and ABL height (Ilić et al., 2018). The thermodynamic stability of the ABL is analyzed based on radiosounding measurements in Belgrade. The ABL height values derived from daytime lidar measurements are generally in agreement with those obtained from Global Data Assimilation System (GDAS). Furthermore, the relationship between the average backscatter coefficient within the ABL and the corresponding PM10 concentrations at ground level is analyzed. PM10 concentrations in Belgrade are obtained from the Serbian Environmental Protection Agency (SEPA) automatic monitoring stations. Large variability of values of the average backscatter coefficient in the ABL is observed in cases of elevated PM10 pollution in Belgrade, and discussed based on the corresponding vertical structure of backscatter coefficient and the ABL height temporal changes. Additionally, the use of lidar measurements in investigation of the contribution of long-range transported particles to surface PM10 concentrations is demonstrated.

### REFERENCES

Fernald, F. G., 1984. Analysis of atmospheric lidar observations: some comments. Applied Optics 23, 652-653.

Ilić, L., Kuzmanoski, M., Kolarž, P., Nina, A., Srećković, V., Mijić, Z., Bajčetić, J. and Andrić, M.., 2018. Changes of atmospheric properties over Belgrade, observed using remote sensing and in situ methods during the partial solar eclipse of 20 March 2015. Journal of Atmospheric and Solar-Terrestrial Physics, 171, 250-259.

Klett, J. D., 1981. Stable analytical inversion solution for processing lidar returns. Applied Optics, 24, 1638-1643.

Serbian Environmental Protection Agency (SEPA), public data: http://data.sepa.gov.rs (accessed on 7 April 2023).

CIP - Каталогизација у публикацији
Народна библиотека Србије, Београд

**502.3:502.175(048)**
**613.15(048)**
**66.071.9(048)**

**INTERNATIONAL WeBIOPATR Workshop Particulate Matter: Research and Management (9 ; 2023 ; Vinča)**

Abstracts of Keynote Invited Lectures and Contributed Papers / The Ninth International WEBIOPATR Workshop & Conference Particulate Matter: Research and Management, WeBIOPATR 2023, [28th November to 1st December 2023] Vinča, Belgrade, Serbia ; [organizers Vinča Institute of Nuclear Sciences, Serbia [and] Environment and Climate Research Institute NILU, Norway] ;Milena Jovašević-Stojanović ... [et al.], eds. - Belgrade : Vinča Institute of Nuclear Sciences, 2023 (Belgrade : Vinča Institute of Nuclear Sciences). - 95 str. : ilustr. ; 30 cm
Tiraž 100. - Str. 5-6: Preface / Milena Jovašević-Stojanović and Alena Bartoňová. - Bibliografija uz većinu apstrakata. - Registar.

**ISBN 978-86-7306-177-1**

1. International Conference Particulate Matter: Research and Management (9 ; 2023 ; Vinča)
a) Ваздух -- Контрола квалитета -- Апстракти
b) Здравље -- Заштита -- Апстракти
v) Отпадни гасови -- Штетно дејство -- Апстракти

**COBISS.SR-ID 13121485**

ISBN-978-86-7306-177-1

# VI Conference on Active Galactic Nuclei and Gravitational Lensing

(VI AGN&GL)

2 - 6 June 2024
Zlatibor Mt., Serbia

## PROGRAM AND ABSTRACTS

eds. J. Kovačević Dojčinović and V. A. Srećković

Astronomical Observatory
Belgrade 2024

# PROGRAMME AND ABSTRACTS:

VI Conference on Active Galactic Nuclei and Gravitational Lensing

June 02-06, 2024, Zlatibor Mt., Serbia

Editors: J. Kovačević Dojčinović and V. A. Srećković

Belgrade, 2024

# Scientific Organizing Committee

Jelena Kovačević Dojčinović (Astronomical Observatory, Belgrade, Serbia) - Co-chair
Vladimir A. Srećković (Institute of Physics Belgrade, Serbia) - Co-chair
Luka Č. Popović (Astronomical Observatory, Belgrade, Serbia)
Milan S. Dimitrijević (Astronomical Observatory, Belgrade, Serbia)
Edi Bon (Astronomical Observatory, Belgrade, Serbia)
Nataša Bon (Astronomical Observatory, Belgrade, Serbia)
Dragana Ilić (Faculty of Mathematics, University of Belgrade, Serbia)
Saša Simić (Faculty of Sciences, University of Kragujevac, Serbia)
Wolfram Kollatschny (Institute for Astrophysics, University of Goettingen, Germany)
Andjelka Kovačević (Faculty of Mathematics, University of Belgrade, Serbia)
Evangelia Lyratzi (University of Athens, Greece)
Paola Marziani, (INAF - Osservatorio Astronomico di Padova, Padova, Italia)
Evencio Mediavilla (Instituto de Astrofísica de Canarias, Spain)
Elena Shablovinskaya (Special Astrophysical Observatory, Russia)
Marko Stalevski (Astronomical Observatory, Belgrade, Serbia)
Jian-Min Wang, (Key Laboratory for Particle Astrophysics, Institute of High Energy Physics, China)
Alexander Zakharov (Institute for Theoretical and Experimental Physics, Moscow, Russia)

# Local Organizing Committee

Jelena Kovačević Dojčinović (Astronomical Observatory, Belgrade, Serbia) - Chair
Aleksandra Kolarski (Institute of Physics Belgrade, University of Belgrade, Serbia) - Secretary
Filip Arnaut (Institute of Physics Belgrade, University of Belgrade, Serbia) - Member

Saša Simić (Faculty of Sciences, Department of Physics, University of Kragujevac) - Member

# Impressum

Organized by: Astronomical Observatory Belgrade
Co-organizer: Institute of Physics Belgrade
Published by: Astronomical Observatory Belgrade, Volgina 7, 11060 Belgrade 38, Serbia
The publication of this issue is financially supported by the Ministry of Science, Technological Development and Innovation of the Republic of Serbia.
Website: `http://servo.aob.rs/AGN_GL/index.html`
Cover image design: Saša Simić
Computer text design: Vladimir A. Srećković and Jelena Kovačević Dojčinović
ISBN 978-86-82296-07-2
Printed by: Skripta Internacional, Mike Alasa 54, Beograd
Number of copies: 50

VI Conference on Active Galactic Nuclei
and Gravitational Lensing
June 02-06, 2024, Zlatibor Mt., Serbia
https://doi.org/10.69646/aob24021

# PARTICIPATION OF SERBIAN RESEARCHERS IN COST ACTIVITIES AND AN OVERVIEW OF COST PROCEDURES AND NATIONAL RULES FOR JOINING RECENTLY APPROVED COST ACTIONS

**Zoran R. Mijić, Bratislav P. Marinković**

*Institute of Physics Belgrade, Pregrevica 118,
11080, Belgrade, Serbia*

*E-mail: zoran.mijic@ipb.ac.rs, bratislav.marinkovic@ipb.ac.rs*

To strengthen Europe's ability to address scientific, technical, and social issues, COST (European Cooperation in Science and Technology) connects academics and innovators by funding excellence-driven and multidisciplinary pan-European networks - COST Actions. Over the last 50 years it has become one of the best mechanisms to promote science cooperation in the world having significant impact on young researcher carriers. In this paper the project evaluation procedure in the COST research framework (Seeber et al. 2022) will be discussed focusing on the degree of interdisciplinarity of Actions proposals - whether it can be advantage or not. In addition, a comprehensive statistical analysis of Serbian representatives participating in active COST actions will be presented (Mijic et al. 2022). Furthermore, the effects of participating in a COST Action on the level of scientific production of researchers from inclusive target countries as well as young researcher is discussed. Participation in COST activities has become progressively more competitive and researcher from

Serbia are involved in almost 97% of active Actions. In order to provide efficient joining COST Actions information on new national rules and procedures required will be presented together with overview of recently approved Actions expected to start in September 2024.

### Acknowledgments

Thanks are due to The Ministry of Science, Technological Development and Innovation of the Republic of Serbia and the Institute of Physics Belgrade for national COST office support.

### References

Mijić, Z., Marinković, B., (2022), Statistics of Management Committee Members from Serbia in COST Actions,IV Meeting on Astrophysical Spectroscopy - A&M DATA - Atmosphere, Book of Abstracts and Contributed Papers, Eds: V. A. Srećković, M. S. Dimitrijević, N. Veselinović and N. Cvetanović, pp.74-80.

Seeber, M., Vlegels, J., Cattaneo, M., (2022), Conditions that do or do not disadvantage interdisciplinary research proposals in project evaluation, The Journal of the Association for Information Science and Technology, 73, 1106 73, 1106.

CIP - Каталогизација у публикацији

Народна библиотека Србије, Београд

520/524(048)(0.034.2)

CONFERENCE on Active Galactic Nuclei and Gravitational Lensing (6 ; 2024 ; Zlatibor)

Programme ; and Abstracts / VI Conference on Active Galactic Nuclei and Gravitational Lensing, June 02-06, 2024, Zlatibor Mt., Serbia ; [organized by Astronomical Observatory Belgrade] ; [co-organizer Institute of Physics Belgrade] ; editors J. [Jelena] Kovačević Dojčinović and V. [Vladimir] A. Srećković. - Belgrade : Astronomical Observatory, 2024 (Beograd : Skripta Internacional). - X, 49 str. ; 30 cm

Tiraž 50. - Bibliografija uz pojedine apstrakte. - Registar.

ISBN 978-86-82296-07-2

а) Астрономија -- Апстракти
б) Астрофизика -- Апстракти

COBISS.SR-ID 146063113

**Building bridges between climate science and society through a transdisciplinary network**

September 10-14, 2024, Kopaonik Mt, Serbia

# BOOK OF ABSTRACTS AND CONTRIBUTED PAPERS

Edited by Vladimir A. Srećković, Aleksandra Kolarski, Filip Arnaut and Milica Langović

Belgrade, 2024

## Scientific Organizing Committe

Vladimir A. Srećković, **Co-chair**, Institute of Physics Belgrade, Serbia, President of the Scientific Society Isaac Newton
Aleksandra Kolarski, **Co-chair**, Institute of Physics Belgrade, Serbia, Secretary of the Scientific Society Isaac Newton

Luka Č. Popović, Astronomical Observatory, Belgrade, Serbia
Danica Šantić, Faculty of Geography, Belgrade, Serbia
Slavoljub Dragićević, Faculty of Geography, Belgrade, Serbia
Milan S. Dimitrijević, Astronomical Observatory, Belgrade, Serbia
Nikolay Bezuglov, Saint Petersburg State University, Saint Petersburg, Russia
Nebil Ben Nessib, Department of Physics and Astronomy, Riyadh, Saudi Arabia
Predrag Jovanović, Astronomical Observatory, Belgrade, Serbia
Duško Borka, Vinca Institute of Nuclear Science, Belgrade, Serbia
Magdalena Hristova, Department of Applied Physics, Technical University of Sofia, Bulgaria
Ognyan Kounchev, Institute of Mathematics and Informatics, Bulgarian Academy of Sciences, Bulgaria
Zoran Mijić, Institute of Physics Belgrade, Belgrade, Serbia
Nicolina Pop, Politehnica University of Timisoara, Romania
Branko Predojević, University of Banja Luka, Republic of Srpska, BiH
Aleksandar R. Milosavljevic, Synchrotron SOLEIL, Paris, France
Ljubinko Ignjatović, Institute of Physics Belgrade, Belgrade, Serbia
Felix Iacob, West University of Timisoara, Romania

**Local Organizing Committe**

Filip Arnaut, Institute of Physics Belgrade,
President of the local organizing committee
Milica Langović, Institute of Physics Belgrade,
Secretary of the local organizing committee
Sreten Jevremović, Scientific Society Isaac Newton Belgrade
Veljko Vujčić, Astronomical Observatory Belgrade
Ivan Samardžić, Faculty of Geography, Belgrade, Serbia
Mihailo Savić, Institute of Physics Belgrade, Serbia

**Organizers**

Scientific Society Isaac Newton Belgrade, Institute of Physics Belgrade, Faculty of Geography, University of Belgrade, Astronomical Observatory Belgrade

ISBN 978-86-906850-0-4



Printed by: Skripta Internacional, Mike Alasa 54, 11102, Beograd
Number of copies: 50

[https://doi.org/10.69646/bbbs2414]
*[Lecture]*

# The European Cooperation in Science and Technology - opportunity for young researchers to strengthen their careers

Zoran Mijić[1*] and Bratislav Marinković[1]

[1]Institute of Physics Belgrade, University of Belgrade, Pregrevica 118, Belgrade, Serbia

[*]Correspondence: Zoran Mijić, zoran.mijic@ipb.ac.rs

**Abstract:** COST (European Cooperation in Science and Technology) is the oldest intergovernmental funding organization in Europe with the aim to establish the research networks among scientists and innovators. It has become one of the greatest mechanisms for promoting international scientific cooperation in recent decades, with a considerable influence on the careers of young researchers. Proximity is highly critical for establishing scientific collaboration, but once established, scientists may maintain collaboration even across long distances. Participating in a COST Action, in this sense, fosters closeness by allowing scientists from various nations, research fields, and industries to meet and thereby overcome conventional boundaries (Seeber *et al.* 2022a). A particular focus of COST network is to assist early-career investigators and young scientists in developing new skills by providing opportunities to get involved in Action activities such as training schools, short-term scientific missions, workshops, conferences, etc. (Mijić and Marinković, 2024). In this paper the impact of participating in a COST Action on the level of scientific production of researchers coming from less-research-intensive COST Member countries,

known as Inclusive Target Countries (ITC), will be presented. Some recent studies demonstrate a notable average increase in scientific co-publications among active action members, as well as interdisciplinary collaborations, and an increased involvement of early career researchers (Seeber *et al*. 2022b). COST Actions continue to have a favorable impact on young researchers' careers even after they are terminated. Participation in COST activities has become progressively competitive, with researchers from Serbia accounting for more than 90% of running Actions (Mijić and Marinković, 2022). To ensure effective participation in COST Actions, information on both new national and COST procedures will be provided and discussed, as well as an overview of currently available positions in running COST Actions.

**Keywords:** COST, Networking, Collaborative publications, Inclusive target countries

**Acknowledgement**

Thanks are due to The Ministry Science. Technological Development and Innovation of the Republic of Serbia and the Institute of Physics Belgrade for national COST office support.

**References**

Mijić, Z., Marinković, B., (2022), Statistics of Management Committee Members from Serbia in COST Actions, IV Meeting on Astrophysical Spectroscopy - A&M DATA - Atmosphere, Book of Abstracts and Contributed Papers, Eds: V. A. Srećković, M. S. Dimitrijević, N. Veselinović and N. Cvetanović, pp.74-80.

Mijić, Z., Marinković, B., (2024), Participation of Serbian Researchers in COST Activities and an Overview of COST

Procedures and National Rules for Joining Recently Approved COST Actions, VI Conference on Active Galactic Nuclei and Gravitational Lensing, Book of Abstracts, Eds: J. Kovačević Dojčinović, V. A. Srećković, pp. 34-35.

Seeber, M., Vlegels, J., Cattaneo, M., (2022a), Conditions that do or do not disadvantage interdisciplinary research proposals in project evaluation, The Journal of the Association for Information Science and Technology, 73, 1106.

Seeber, M., Vlegels, J., Seeber, M., (2022b), Exploring the impact of COST Actions on scientific collaboration, 26th International Conference on Science and Technology Indicators, Proceedings, Eds: N. Robinson-Garcia, D. Torres-Salinas, W. Arroyo-Machado, sti2022.

[https://doi.org/10.69646/bbbs2416]
*[Poster]*

# Novel Research in Astrophysics and Geophysics

Vladimir A. Srećković[1,2*], Aleksandra Kolarski[1], Milica Langović[1], Filip Arnaut[1], Zoran Mijić[1], Sreten Jevremović[2], Jelena Barović[3] and Ognyan Kounchev[4]

[1] Institute of Physics Belgrade, University of Belgrade, Pregrevica 118, Belgrade 11000, Serbia
[2] Scientific Society "Isaac Newton", Volgina 7, 11160 Belgrade, Serbia
[3] University of Montenegro, Podgorica, Montenegro
[4] Institute of Mathematics and Informatics, Bulgarian Academy of Sciences, Sofia, Bulgaria

[*]Correspondence: Vladimir A. Srećković, vlada@ipb.ac.rs

**Abstract:** In the past few decades innovative approach is to foster collaboration and effective synergies among disciplines such as space exploration, atmospheric and Earth observations, laboratory and field experiments, and numerical modeling, with a high potential for direct application in Earth and other planetary research. Modeling various atmospheres with supercomputer capability, as well as diagnosing astrophysical and laboratory plasma using atomic and molecular datasets, relies on the creation and improvement of theoretical techniques and data computation methods (see e.g. Srećković et al. 2024). Multi-instrument and multi-disciplinary competence are needed to solve complicated climate concerns and its repercussions. Moreover, the growing amount of data suggests a rise in the use of automated tools and retrieval techniques (see e.g. Škoda and Adam 2020 and references therein). Model evaluation, data assimilation, satellite validation, and investigations of diverse

processes in the atmosphere and on Earth can all easily make use of the new information and retrieval products.

This contribution is progress report of work on a common topic within the bilateral project "The analysis of big data related to earth and sky observation: environmental applications and influence on life sciences" between the Bulgarian Academy of Sciences and the Serbian Academy of Sciences and Art.

**Keywords:** modeling, climate, multi-disciplinary investigation

**Acknowledgement**

This work was funded by the Institute of Physics Belgrade, University of Belgrade, through a grant by the Ministry of Science, Technological Development, and Innovations of the Republic of Serbia. We acknowledge the support COST Action CA22162 A transdisciplinary network to bridge climate science and impacts on society (FutureMed), supported by COST.

**References**

Srećković, V.A.; Dimitrijević, M.S.; Mijić, Z.R. Data in Astrophysics and Geophysics: Novel Research and Applications. Data 2024, 9, 32

Škoda, P.; Adam, F. Knowledge Discovery in Big Data from Astronomy and Earth Observation; Elsevier: Amsterdam, The Netherlands, 2020

CIP – Каталогизација у публикацији
Народна библиотека Србије, Београд

551.583:6(048)

**BUILDING bridges between climate science and society through a transdisciplinary network (2024 ; Kopaonik)**
Book of abstracts and contributed papers / Building bridges between climate science and society through a transdisciplinary network, September 10-14, 2024, Kopaonik Mt, Serbia ; edited by Vladimir A. Srećković .. [et al.]. - Belgrade : Scientific Society Isaac Newton, 2024 (Belgrade : Skripta Internacional). - 114 str. : ilustr. ; 24 cm

Tiraž 50. – Bibliografija uz većinu apstrakta

ISBN 978-86-906850-0-4

а) Климатске промене -- Мултидисциплинарни приступ -- Апстракти

COBISS.SR-ID 151804169

**International Meeting on Data for Atomic and Molecular Processes in Plasmas: Advances in Standards and Modelling**

November 12-15, 2024, Palić, Serbia

# BOOK OF ABSTRACTS AND CONTRIBUTED PAPERS

Edited by Vladimir A. Srećković, Aleksandra Kolarski, Milica Langović, Filip Arnaut and Nikola Veselinović

Belgrade, 2024

## Scientific Organizing Committee

Vladimir A. Srećković, Institute of Physics Belgrade, **Co-Chair**
Aleksandra Kolarski, Institute of Physics Belgrade, **Co-Chair**

Milan S. Dimitrijević, Serbia
Nikolai N. Bezuglov, Russia
Nebil Ben Nessib, Saudi Arabia
Vesna Borka Jovanović, Serbia
Nikola Cvetanović, Serbia
Saša Dujko, Serbia
Rafik Hamdi, Tunisia
Magdalena Hristova, Bulgaria
Ognyan Kounchev, Bulgaria
Bratislav Marinković, Serbia
Zoran Mijić, Serbia
Nicolina Pop, Romania
Luka Popović, Serbia
Branko Predojević, Republic of Srpska, BiH
Sylvie Sahal Brechot, France
Sanja Tošić, Serbia
Robert Beuc, Croatia
Felix Iacob, Romania

## Local Organizing Committee

Aleksandra Kolarski (**Co-Chair**), Institute of Physics Belgrade
Vladimir A. Srećković (**Co-Chair**), Institute of Physics Belgrade
Filip Arnaut (**Secretary**), Institute of Physics Belgrade
Zoran Mijić, Institute of Physics Belgrade
Milica Langović, Institute of Physics Belgrade
Mihailo Savić, Institute of Physics Belgrade
Nikola Veselinović, Institute of Physics Belgrade
Veljko Vujčić, Astronomical Observatory, Belgrade
Nikola Cvetanović, University of Belgrade, Faculty of Transport and Traffic Eng.

**Organizer**

Institute of Physics Belgrade

ISBN 978-86-82441-69-4



Printed by: Skripta Internacional, Mike Alasa 54, 11102, Beograd
Number of copies: 50

https://doi.org/10.69646/aob241111

# New opportunities for COST participants – actions networking tools and examples of the national funding schemes

**Mijić, Z.R.[1] and Marinković, B.P.[1]**

*[1]Institute of Physics Belgrade, Pregrevica 118, 11080 Belgrade, Serbia*
*E-mail: zoran.mijic@ipb.ac.rs*

As the oldest intergovernmental funding organization in Europe COST (the European Cooperation in Science and Technology) facilitates networking among academics and innovators in order to increase Europe's ability to address scientific, technical, and societal concerns (Marinković and Mijić 2022). According to the study (Seeber et al., 2022a), participation in COST program considerably increases researchers' scientific co-publications, therefore advancing their professional careers. The findings demonstrate a 55% average increase in co-publications among active COST action participants as compared to the proposed network of the researchers of non-founded actions. This increase in collaborative co-publications is not at the expense of non-collaborative ones, resulting in a net gain in scientific production. Keeping in mind that the impact of the actions lasts beyond their lifetime, involvement in COST networking activities significantly improves researchers' productions and experience thus increasing their capacity for long-term collaborations (Seeber et al., 2022b). This is especially important for early-career researchers, as around 42% of COST action members in 2023 are young researchers. (Mijić and Marinković, 2024a).

Over the last several years running the COST action have become more and more competitive (Mijić and Marinković, 2024b). The reported success rate of the action proposals for the last open call OC-2023-1 was 11.5%. Since there is a clear benefit of scientific community involved in research network, several European countries established additional national funding to support research projects originating from successful ongoing COST Actions.

In this study, within proposed mini-project, we will discuss the new opportunities for COST participants through the actions networking tools focusing on young researchers' and ITC (Inclusiveness Target Countries) conference grants entering into force in November 2024. In addition, new technical annex, evaluation grid and introduction of the acceptability criterion for new action proposal will be demonstrated. Finally, the existing opportunities for additional funding of research projects originating from COST actions will be introduced. The recent experience and good practices of national funding schemes for COST participants in several countries will be presented together with available funding support for COST related projects in Switzerland which include project partners abroad.

**Acknowledgements:** Thanks are due to The Ministry of Science, Technological Development and Innovation of the Republic of Serbia and the Institute of Physics Belgrade for national COST office support.

**References**

Marinković, B., Mijić, Z., 2022, V Meeting on Astrophysical Spectroscopy - A&M DATA - Astronomy & Earth Observations, Book of Abstracts and Contributed Papers, Eds: Vladimir A. Srećković, Milan S. Dimitrijević, Aleksandra Kolarski, Zoran R. Mijić and Nikola B. Veselinović, p.55.

Seeber, M., Vlegels, J., Seeber, M., 2022a, 26$^{th}$ International Conference on Science and Technology Indicators, Proceedings, Eds: N. Robinson-Garcia, D. Torres-Salinas, W. Arroyo-Machado, sti2239

Seeber, M., Vlegels, J., Cattaneo, M., 2022b, J. Assoc. Inf. Sci. Technol. 73, 1106

Mijić, Z., Marinković, B., 2024a, Building bridges between climate science and society through a transdisciplinary network, Book of Abstract and Contributed Papers, Eds: Vladimir A. Srećković, Aleksandra Kolarski, Filip Arnaut, and Milica Langović, pp. 89-91.

Mijić, Z., Marinković, B., 2024b, VI Conference on Active Galactic Nuclei and Gravitational Lensing, Book of Abstract, Eds: J. Kovačević Dojčinović, and V. A. Srećković pp. 34-35.

https://doi.org/10.69646/aob241115

# New molecular dataset for planet formation chemistry and modeling

**Srećković, V.A.,[1] Pop, N.,[2] Vujčić, V.,[3] Dimitrijević, M.S.,[3] Christova, M.D.[4] and Mijić, Z.[1]**

*[1]Institute of Physics Belgrade, University of Belgrade, Pregrevica 118, Belgrade, Republic of Serbia*
*[2]Politehnica University of Timisoara, Timisoara, Romania*
*[3]Astronomical Observatory, Volgina 7, 11060 Belgrade 38, Serbia*
*[4]Department of Applied Physics, TU Sofia, Bulgaria*
*E-mail: vlada@ipb.ac.rs*

Detailed astrochemical models are essential for interpreting observations of interstellar and circumstellar molecules because they allow important physical features of the gas and its evolutionary history to be derived (Williams and Cieza 2011). Advances in astrochemical models are linked to changes in astrochemical databases, as well as experimental and theoretical estimations of rate coefficients (see e.g. Öberg et al. 2021). The science community now need access to such molecular data, including preferred ones, for further modeling, and it is critical to our knowledge of the chemistry of planet formation. As a result, atomic and molecular datasets and databases (such as VAMDC) have become critical for constructing models and simulations (see Albert et al. 2021 and references therein). The analysis of the studied rates provides valuable information on the presence of species. As a result, it is critical to investigate not only radiative processes, but also concurrent processes involving molecular ions, such as dissociative recombination (Kamp et al., 2017). Our goal is to calculate, compare, and analyze cross sections and rate coefficients for molecular ions such as hydrogen and helium for a various model parameters.

**Acknowledgments:** This work was funded by the Institute of Physics Belgrade, University of Belgrade, through a grant by the Ministry of Science, Technological Development, and Innovations of the Republic of Serbia. We acknowledge the support the Science Fund of the Republic Serbia, Grant No. 3108/2021—NOVA2LIBS4fusion and COST Action CA22133 - The birth of solar systems (PLANETS).

## References

Albert, D.; Antony, B.; Ba, Y.A.; Babikov, Y.L.; Bollard, P.; Boudon, V.; Delahaye, F.; Del Zanna, G.; Dimitrijević, M.S.; Drouin, B.J.; Dubernet, M.-L.;et al. A Decade with VAMDC: Results and Ambitions. Atoms 2020, 8, 76.

ALMA Partnership et al., 2015, ApJL, 808, L3

Kamp, I., Thi, W. F., Woitke, P., Rab, C., Bouma, S., & Menard, F. (2017). Consistent dust and gas models for protoplanetary disks-II. Chemical networks and rates. Astronomy & Astrophysics, 607, A41.

Öberg, K. I., Guzmán, V. V., Walsh, C., Aikawa, Y., Bergin, E. A., Law, C. J., ... & Zhang, K. (2021). Molecules with ALMA at Planet-forming Scales (MAPS). I. Program overview and highlights. The Astrophysical Journal Supplement Series, 257(1), 1.

Miyake, S., Gay, C. D., & Stancil, P. C. (2011). Rovibrationally resolved photodissociation of HeH+. The Astrophysical Journal, 735(1), 21.

Visser, R., Bruderer, S., Cazzoletti, P., Facchini, S., Heays, A. N., & van Dishoeck, E. F. (2018). Nitrogen isotope fractionation in protoplanetary disks. Astronomy & Astrophysics, 615, A75.

Walsh, C., Nomura, H., Millar, T. J., & Aikawa, Y. (2012). Chemical processes in protoplanetary disks. II. On the importance of photochemistry and X-ray ionization. The Astrophysical Journal, 747(2), 114.

Williams, Jonathan P., and Lucas A. Cieza. "Protoplanetary disks and their evolution." Annual Review of Astronomy and Astrophysics 49 (2011): 67-117.

**Meeting on new trends in Astronomy & Earth Observation**

November 25 – 29, 2024, Belgrade, Serbia

# BOOK OF ABSTRACTS AND CONTRIBUTED PAPERS

Edited by Vladimir A. Srećković, Aleksandra Kolarski,
Milica Langović, Filip Arnaut and Nikola Veselinović

Belgrade, 2024

## Scientific Organizing Committee

Vladimir Srećković **(Co-chair)**
(Institute of Physics Belgrade, Belgrade, Serbia),
President of the Scientific Society Isaac Newton Belgrade,
Aleksandra Kolarski **(Co-chair)**
(Institute of Physics Belgrade, Belgrade, Serbia)
Secretary of the Scientific Society Isaac Newton Belgrade,

Luka Č. Popović (Astronomical Observatory, Belgrade, Serbia)
Milan S. Dimitrijević (Astronomical Observatory, Belgrade, Serbia)
Slavoljub Dragićević (Faculty of Geography, Belgrade, Serbia)
Magdalena Hristova (Department of Applied Physics,
Technical University of Sofia, Bulgaria)
Ognyan Kounchev (Institute of Mathematics and Informatics,
Bulgarian Academy of Sciences, Bulgaria)
Nikolay Bezuglov (Saint Petersburg State University, Saint Petersburg, Russia)
Nebil Ben Nessib (Department of Physics and Astronomy; Riyadh, Saudi Arabia)
Predrag Jovanović (Astronomical Observatory, Belgrade, Serbia)
Duško Borka (Vinca Institute of Nuclear Science, Belgrade, Serbia)
Zoran Mijić (Institute of Physics Belgrade, Belgrade, Serbia)
Nicolina Pop (Politehnica University of Timisoara, Romania)
Branko Predojević (University of Banja Luka, Republic of Srpska, BiH)
Aleksandar R. Milosavljevic (Synchrotron SOLEIL, Paris, France)
Ljubinko Ignjatović (Institute of Physics Belgrade, Belgrade, Serbia)
Robert Beuc (Institute of Physics, Zagreb, Croatia)
Felix Iacob (West University of Timisoara, Romania)

**Local Organizing Committee**

Filip Arnaut (Institute of Physics Belgrade, Belgrade, Serbia)
President of the local organizing committee
Milica Langović (Institute of Physics Belgrade, Belgrade, Serbia)
Secretary of the local organizing committee
Nikola Veselinović (Institute of Physics Belgrade, Belgrade, Serbia)
Veljko Vujčić (Astronomical Observatory Belgrade)
Sreten Jevremović (Scientific Society Isaac Newton Belgrade)

**Organizer**

Scientific Society Isaac Newton Belgrade, Institute of Physics Belgrade, Astronomical Observatory Belgrade

ISBN 978-86-906850-1-1



Printed by: Skripta Internacional, Mike Alasa 54, 11102, Beograd
Number of copies: 50

[https://doi.org/10.69646/aob241212]
*[Lectures]*

# Aerosol vertical profiles and ABL heights derived from lidar measurements in Belgrade

Maja Kuzmanoski[1*] and Zoran Mijić[1]

[1]Institute of Physics Belgrade, University of Belgrade, Pregrevica 118, 11080 Belgrade, Serbia

[*]Correspondence: maja.kuzmanoski@ipb.ac.rs

**Abstract:** Information on vertical profile of atmospheric aerosols is important in studies of aerosol contribution to air pollution, their role in cloud formation and radiative effects. Aerosol lidar measurements provide information on vertical profiles of aerosol backscatter and extinction coefficients. Besides, it can be used to derive the height of atmospheric boundary layer (ABL), which determines the volume available for dispersion of air pollution. Aerosol lidar measurements at 355 nm performed in Belgrade (Mijić et al., 2023) are used to derive vertical profile of aerosol backscatter coefficient and temporal changes of ABL height (Ilić et al. 2018). These measurements are used to determine the altitude of long-range transported aerosols (such as Saharan dust) and to detect their intrusion into the ABL. Selected cases of lidar-derived aerosol backscatter coefficient profiles corresponding to episodes of elevated air pollution, as well as episodes of long-range aerosol transport and their intrusion into the ABL, will be presented. Air pollution measurements in Belgrade, obtained from the Serbian Environmental Protection Agency (SEPA) automatic monitoring stations are used to select times of high and low particulate air pollution and to analyze the contribution of long-range transported aerosol to PM10 concentrations at surface level.

**Keywords:** aerosol lidar, atmospheric boundary layer, aerosol backscatter coefficient, air pollution

## References

Ilić, L., Kuzmanoski, M., Kolarž, P., Nina, A., Srećković, V., Mijić, Z., Bajčetić, J. & Andrić, M.. (2018). Changes of atmospheric properties over Belgrade, observed using remote sensing and in situ methods during the partial solar eclipse of 20 March 2015, *Journal of Atmospheric and Solar-Terrestrial Physics*, 171, 250-259. https://doi.org/10.1016/j.jastp.2017.10.001

Mijić, Z., Ilić, L. and Kuzmanoski, M. (2023) Data quality assurance for atmospheric probing and modeling: characterization of Belgrade Raman lidar station, *Contributions of the Astronomical Observatory Skalnaté Pleso*, 53(3) 163-175, https://doi.org/10.31577/caosp.2023.53.3.163.

[https://doi.org/10.69646/aob241214]
*[Lecture]*

# Overview of Serbian involvement in COST framework – new open call and networking tools for young researchers and ITC participants

Zoran Mijić[1*] and Bratislav P. Marinković[1]

[1]Institute of Physics Belgrade, University of Belgrade, Pregrevica 118, 11080 Belgrade, Serbia

[*]Correspondence: zoran.mijic@ipb.ac.rs

**Abstract:** Serbia is COST (European Cooperation in Science and Technology) full member country and during the last decade there is an increasing interest of researchers and innovators from Serbia to actively participate in COST networking activities. In this paper the statistical overview of Serbian participants will be presented based on the available data for 2023. There is an increasing trend in country representation in active COST actions reaching 97% in 2023, and almost double leadership positions in actions comparing to 2018. Taking into the account activity, actions Management Committee (MC) members from Serbia have the leading role and mobilization of young researchers is among top five countries. Having in mind MC members are nominated by COST national coordinator following specific national procedure (Mijić and Marinković, 2024) these statistical indicators are useful to assess the quality of the current national rules and its possible improvements. New open call OC-2025-1 have been lunched and introduced young researchers and ITC (Inclusive Target Country) conference grants (Mijić and Marinković, 2024a) which will be discussed together with additional networking opportunities.

**Keywords:** COST, research network, young researchers, actions networking tools

## References

Mijić, Z., Marinković, B. 2024. Participation of Serbian Researchers in COST Activities and an Overview of COST Procedures and National Rules for Joining Recently approved COST, *VI Conference on Active Galactic Nuclei and Gravitational Lensing*, 34-35, Zlatibor, Serbia, 2-6 June, 2024.

Mijić, Z., Marinković, B. 2024a. New opportunities for COST participants – actions networking tools and examples of the national funding schemes, *International Meeting on Data for Atomic and Molecular Processes in Plasmas: Advances in Standards and Modelling*, 49-50, Palić, Serbia, November 12-15, 2024.

[https://doi.org/10.69646/aob241221]
*[Poster]*

# Novel Research in Astronomy & Earth Observation

Vladimir A. Srećković[1*], Zoran Mijić[1], Aleksandra Kolarski[1], Milica Langović[1], Filip Arnaut[1], Sreten Jevremović[2], Jelena Barović[3], Ognyan Kounchev[4] and Georgi Simeonov[4]

[1]Institute of Physics Belgrade, UB, 57, 11001, Belgrade, Serbia
[2] Scientific Society "Isaac Newton", Volgina 7, 11160 Belgrade, Serbia
[3] University of Montenegro, Podgorica, Montenegro
[4] Institute of Mathematics and Informatics, Bulgarian Academy of Sciences, Sofia, Bulgaria

[*]Correspondence: vlada@ipb.ac.rs

**Abstract:** With a high potential for direct application in Earth and other planetary research, the innovative approach of the past few decades has promoted cooperation and productive synergies among disciplines like space exploration, atmospheric and Earth observations, laboratory and field experiments, and numerical modeling. To model atmospheres with supercomputers and diagnose astrophysical and laboratory plasma using atomic and molecular datasets, theoretical methodologies and data computation methods must be developed and improved (see e.g. Srećković et al., 2024 and references therein). To address complex climate issues and their consequences, multi-instrumental and multi-disciplinary expertise is required. As data grows, automated tools and retrieval approaches are increasingly being used (e.g., Škoda and Adam 2020). We participated in this research with our contribution.

**Keywords:** AstroGeoInformatics, modeling, climate, multi-disciplinary investigation

## Acknowledgement

This work was funded by the Institute of Physics Belgrade, University of Belgrade, through a grant by the Ministry of Science, Technological Development, and Innovations of the Republic of Serbia. We acknowledge the networking opportunities from the COST Action CA22162 A transdisciplinary network to bridge climate science and impacts on society (FutureMed).

## References

Srećković, V.A.; Dimitrijević, M.S.; Mijić, Z.R. Data in Astrophysics and Geophysics: Novel Research and Applications. Data 2024, 9, 32

Škoda, P.; Adam, F. Knowledge Discovery in Big Data from Astronomy and Earth Observation; Elsevier: Amsterdam, The Netherlands, 2020

**Publ. Astron. Obs. Belgrade No. 100 (2021), 315 - 321** *Progress Report*

# ACTIVITIES OF THE SERBIAN EUROPLANET GROUP WITHIN EUROPLANET SOCIETY

I. MILIĆ ŽITNIK[1], A. NINA[2], V. A. SREĆKOVIĆ[2], B. P. MARINKOVIĆ[2], Z. MIJIĆ[2] D. ŠEVIĆ[2], M. BUDIŠA[3], D. MARČETA[4], A. KOVAČEVIĆ[4], J. RADOVIĆ[5] and A. KOLARSKI[6]

[1]*Astronomical Observatory, Volgina 7, 11000 Belgrade, Serbia*
*E–mail: ivana@aob.rs*

[2]*Institute of Physics Belgrade, University of Belgrade, Pregrevica 118, 11080 Belgrade, Serbia*

[3]*University of Belgrade School of Electrical Engineering, Bulevar kralja Aleksandra 73, 11000 Belgrade, Serbia*

[4]*Faculty of Mathematics, University of Belgrade, Studentski Trg 10, 11000 Belgrade, Serbia*

[5]*Department of Atmospheric Physics, Faculty of Mathematics and Physics, Charles University, Prague, Czech Republic*

[6]*Technical Faculty Mihajlo Pupin, University of Novi Sad, 23000 Zrenjanin, Serbia*

**Abstract.** Europlanet society connects many different scientific institutions all over the world. The Serbian Europlanet Group (SEG) was established at 2019. It currently has 20 active scientists from 6 institutions working in Serbia in different fields of planetary science as well as related fields. Here are presented activities of SEG in 2020.

## 1. INTRODUCTION

The European society promotes the European planetary science as well as related fields. Its aims are to support the development of planetary science at a national and regional level, particularly in countries and areas that are currently under–represented within the community, and early career researchers who established their network within the Europlanet: the Europlanet Early Career (EPEC) network (*https://www.europlanet-society.org/early-careers-network/*). The Europlanet consists of 10 Regional Hubs. More information about organization and activities of this society can be found at the website *https://www.europlanet-society.org/*.

Serbia is one of six countries included in the Southeast European Hub that was established in 2019. The Serbian Europlanet Group (SEG) currently consists of 20 members from 6 institutions. Details of members and activities of SEG can be found at the website *https://www.europlanet-society.org/europlanet-society/regional-hubs/southeast-europe/*. In this paper are described main activities and presented scientific research of SEG members related to the Europlanet fields in 2020.

## 2. CONFERENCES AND WORKSHOPS OF SEG 2020

### 2. 1. PARTICIPATION IN THE EUROPLANET SCIENCE CONGRESSES

The Europlanet Science Congress (EPSC) is the annual meeting of the Europlanet Society. In the Europlanet Science Congress 2020, seven scientists from Serbia participated with several lectures. It was first virtual EPSC congress attended by 1168 participants from 49 countries. Here, will be mentioned two of SEG participants.

Dušan Marčeta presented research about population of interstellar asteroids and possibility that one of the observational selection effects, known as Holetschek's effect, could be used for preliminary estimation of the size-frequency distribution of this population. Aleksandra Nina presented research on new methodology for earthquake prediction which was partially realized within the Europlanet workshop in Petnica Science Center in 2019.

### 2. 2. PARTICIPATION IN THE XII SERBIAN–BULGARIAN ASTRONOMICAL CONFERENCE

Serbian scientists organized a Europlanet session with several lectures during the XII Serbian–Bulgarian Astronomical Conference (SBAC 12). SBAC 12 was held in Sokobanja from September 25 to 29, 2020 (Popović et al. 2020). SEG presented its work (Nina et al. 2020a) and discussed with Bulgarian colleagues and with colleagues from Europlanet Southeast HUB countries about expanding of their cooperation.

### 2. 3. PARTICIPATION IN THE XIX SERBIAN ASTRONOMICAL CONFERENCE

The work of SEG was presented during the XIX Serbian Astronomical Conference (19 SAC), held at the Serbian Academy of Sciences and Arts in Belgrade from October 13 to 17, 2020 (Kovačević et al. 2020). Aleksandra Nina participated with invited lecture about investigation of the lower ionosphere disturbances as possible earthquake precursors and application of research of the lower ionosphere influences in Earth observations by satellite during influence a solar X-ray flare. Ivana Milić Žitnik gave progress report about asteroid's motion with orbital eccentricity in the range (0, 0.2) across the 2-body mean motion resonances with Jupiter with different strengths due to the Yarkovsky effect (Milić Žitnik & Novaković 2016, Milić Žitnik 2020a).

## 3. RESEARCHES OF SEG MEMBERS AT 2020

SEG members are scientists in different research fields. Here are a few researches that are in the areas of Europlanet.

### 3. 1. ASTRONOMY

#### 3.1.1. Model of interstellar asteroids and expected predominance of retrograde object among the discovered objects

Dušan Marčeta and Bojan Novaković examined the model of interstellar asteroids and comets and found analytical expressions for the distributions of their orbital elements (Marčeta & Novaković 2020). They payed special attention to objects which could be detectable by future LSST survey. Also, they found that majority of these objects should move along retrograde orbits resulting in asymmetry of the distribution of their orbital inclinations. Finally, they found that this asymmetry is a result of the Holetschek effect. Since this effect is size-dependant, its influence is stronger for populations with steeper size-frequency distributions since they are comprised of larger number of smaller objects. This fact could be used for preliminary estimation of the size-frequency distribution of the underlying true population of interstellar objects once when sufficient number of objects become discovered.

#### 3.1.2 The relationship between the 'limiting' Yarkovsky drift speed and asteroid families' Yarkovsky $V$-shape

Ivana Milić Žitnik examined the relationship between asteroid families' $V$-shapes and the 'limiting' diameters in the $(a, 1/D)$ plane. Following the recently defined 'limiting' value of the Yarkovsky drift speed at $7 \times 10^{-5}$ au/Myr (Milić Žitnik 2019), she decided to investigate the relation between the asteroid family Yarkovsky $V$-shape and the 'limiting' Yarkovsky drift speed of asteroid's semi-major axes. She has used the known scaling formula to calculate the Yarkovsky drift speed in order to determine the inner and outer 'limiting' diameters (for the inner and outer $V$-shape borders) from the 'limiting' Yarkovsky drift speed. The method was applied to 11 asteroid families of different taxonomic classes, origin type and age, located throughout the Main Belt. Her main conclusion was that the 'breakpoints' in changing $V$-shape of the very old asteroid families, crossed by relatively strong mean motion resonances on both sides very close to the parent body, are exactly the inverse of 'limiting' diameters in the $a$ versus $1/D$ plane. This result uncovers a novel interesting property of asteroid families' Yarkovsky $V$-shapes (Milić Žitnik 2020b).

#### 3.1.3 Astrobiology-habitability of exoplanets

Balbi, Hami and Kovačević (2020) present a new investigation of the habitability of the Milky Way bulge, that expands previous studies on the Galactic Habitable Zone. This work discusses existing knowledge on the abundance of planets in the bulge, metallicity and the possible frequency of rocky planets, orbital stability and encounters, and the possibility of planets around the central supermassive black hole. Another concern for habitability is the presence of the supermassive black hole in the Galactic center, but also in nearby Active galactic nuclei, that could have resulted in a substantial flux of ionizing radiation during its past active phase, causing increased planetary atmospheric erosion and potentially harmful effects to surface life as shown by Wislocka, Kovačević, Balbi (2019). This work was featured in famous Forbes Magazine in their section Innovavations. Andjelka Kovačević is a member of Working group of habitability of exoplanets of European astrobiology institute.

### 3. 2. GEOPHYSICS

#### 3.2.1 Atmospheric aerosol remote sensing and modelling

The EARLINET lidar network was established with the goal of creating a quantitative, comprehensive, and statistically significant database for the horizontal, vertical, and temporal distribution of aerosols on a continental scale. Within the network Belgrade lidar station was involved in initiative for studying the changes in the atmosphere's structure, its dynamics, and its optical properties during the COVID-19 lock-down by comparison to the aerosol climatology in Europe. Near real time delivery of the data and fast analysis of the data products proved that aerosol lidars are useful for providing information not only for climatological purposes, but also in emergency situations like detecting airborne hazards for aviation (Papagiannopoulos et al. 2020). The preliminary results indicate that the lock-down did not affected the high troposphere, but for the low troposphere a certain effect can be seen. In addition, ongoing activities are related to the participation in ESA ADM-Aeolus mission (the first high-spectral resolution lidar in space) Cal/Val activity through validation of L2A products of aerosol profiles and studying the relationship between satellite AOD measurements and ground PM concentrations (Mijić & Perišić 2019).

#### 3.2.2 Lower ionosphere

The lower ionosphere research was a continuation of research related to a possible new type of earthquake precursor in the form of signal noise amplitude reduction (Nina et al. 2020b) and examinations of the effects of the D-region which is disturbed by a solar X-ray flare on satellite signals (Nina et al. 2020c). Also, a new model for determining ionospheric parameters in the unperturbed D-region was developed.

#### 3.2.3 Investigation of a possible lithosphere-ionosphere coupling through seismo-ionospheric effect

Possible relationship between amplitude and phase delay characteristics of the NWC/19.8 kHz signal transmitted from H. E. Holt in Australia ($\varphi = 21.8°$ S, $\Lambda = 114.16°$ E) towards Belgrade AbsPAL receiver ($\varphi = 44.85°$ N, $\Lambda = 20.38°$ E) in Serbia and seismic activity reported by Helmholtz-Zentrum Potsdam - Deutsches GeoForschungsZentrum GFZ in period from December 2005 to June 2007 was investigated with the main result presented in Kolarski and Komatina (2020).

#### 3.2.4 Satellite radar technique for atmospheric water vapor measurement and modelling effects of the ionospheric disturbances

Satellite observation and measurements performed by the Synthetic Aperture Radar (SAR) and the Interferometric Synthetic Aperture Radar (InSAR) technique can be used for acquiring more information about the water vapor present within the atmosphere. The methodology of the SAR instrument and the InSAR technique is described in Radović (2020). Additionally, the focus is set on the four different satellites with SAR instruments working on different frequencies. Apart from that, in Radović (2020) is presented how neglecting the ionospheric perturbations which took place during the satellite measurements can influence modelling of the water vapor parameters derived from such measurements acquired by the SAR instruments carried by the mentioned satellites.

### 3. 3. ASTROPHYSICS

#### 3.3.1. Atomic Molecular and Optical Physics group of researchers at the Laboratory for Atomic Collision Processes

LACP[1], Institute of Physics Belgrade, University of Belgrade, has been studying several collisional processes that involve electron scattering by atomic particles (e.g. for

[1] *http://mail.ipb.ac.rs/ centar3/acp.html*

helium Jureta et al. (2014)) and laser interactions with gases (Rabasović et al. 2019), nanopowders (Šević et al. 2020a,b) and single crystal phosphors (Šević et al. 2021). Electron impact cross sections are relevant parameters in modelling of processes that occur in cometary coma (Marinković et al. 2017), collisional processes in AGNs (Dimitrijević et al. 2021) or Earth' s and other planets' atmospheres (Vukalović et al. 2021). Due to the immense importance of having full survey and accurate data of electron cross sections, there are several databases that maintain large sets of electron collisional data and even more, a unique portal for accessing such kind of data have been created through European framework programs (for a recent update of the Virtual Atomic and Molecular Data Centre[2] – VAMDC see e.g. Albert et al. (2020)).

BeamDB (Belgrade electron-atom/molecule DataBase[3]) is a collisional database that is maintained by the researchers of the LACP and it covers interactions of electrons with atoms and molecules in the form of differential (DCS) and integral cross sections for the processes such as elastic scattering, excitation and ionization (Jevremović et al. 2020). At present the output files that come from the search of BeamDB are present in the xml format of specific syntax developed by the International Atomic Energy Agency (IAEA)[4]. These so called "xsams" files contain full record of data sets including bibliographical entities, but the process of extracting values of cross sections is hard for researchers. That is why this group started to develop a converter which will convert xsams file into textual format file with simple columns that list values of impact energy, scattering angle, DSC and corresponding uncertainty. The next step would be adding a graphical presentation to the webpage of the BeamDB database. The graphics should present logarithm of DCS data points with error bars associated to the uncertainty versus impact energy and scattering angle in 3D graph.

Exploiting the fact that BeamDB contains large sets of DCS values obtained both experimentally and theoretically, they are in the process of developing machine learning algorithms for determining extrapolated DCS in the regions which are not accessed by experiments (Ivanović et al. 2020). The primary goal is to determine extrapolated values toward zero scattering angle as well as to large angles, usually from 150° to 180°.

It is envisaged that the BeamDB will contain electron spectroscopy data as well, beside the cross section data. At present, there is only a single threshold photoelectron spectrum of argon curated in the BeamDB, but the plans are to add energy loss spectra, presumably obtained in the LACP. This would allow them to develop tools for spectral classification and particular spectra identification based on data-mining methods. An overview of various data mining methods has been recently presented by Yang et al. (2020).

### 3.3.2. A&M data for stellar atmosphere modelling

Work on topics of modelling various astrophysical and laboratory plasma which are of interest for Europlanet community is continued. A&M datasets e.g. rate coefficients, Stark broadening parameters, line profiles, etc. are published during this year (see

[2] $https://portal.vamdc.eu/vamdc_portal/$
[3] $http://servo.aob.rs/emol$
[4] $https://www-amdis.iaea.org/xsams/documents/$

some of the papers: Srećković et al. 2020; Majlinger et al. 2020; Dimitrijević et al. 2020). Part of the data are hosted on SerVO at AOB[5].

## 4. CONCLUSION AND FURTHER WORK

In this paper are presented activities of Serbian scientists within Europlanet society. In the first part of the paper, are described briefly conferences that occurred in 2020 which promoted work of Serbian Europlanet Group. In the second part are presented several studies of SEG important for the Europlanet research fields. Serbian scientists plan to continue work within Europlanet society in the following years and to promote the Europlanet and SEG activities, as well as to expand SEG.

### Acknowledgments

This research is supported by the Europlanet. The authors acknowledge funding provided by the Institute of Physics Belgrade, Astronomical Observatory (the contract 451-03-68/2020-14/200002), Faculty of Mathematics University of Belgrade (the contract 451-03-68/2020-14/200104) through the grants by the Ministry of Education, Science, and Technological Development of the Republic of Serbia.

### References

Albert, D., Antony, B. K., Ba, Y. A. et al.: 2020, *Atoms*, **8(4)**, 76.
Balbi, A., Hami, M., Kovačević, A.: 2020, *Life*, **10(8)**, 132.
Dimitrijević, M. S., Srećković, V. A., Zalam, A. A., Miculis, K., Efimov, D. K., Bezuglov, N. N., Klyucharev, A. N.: 2020, *Contrib. Astron. Obs. Skaln. Pleso*, **50(1)**, 66.
Dimitrijević, M. S., Srecković, V. A., Ignjatović, Lj. M., Marinković, B. P.: 2021, *New Astronomy*, **84**, 101529.
Ivanović, S., Uskoković, N., Marinković, B. P., Mason, N. J.: 2020, *Publ. Astron. Obs. Belgrade*, **99**, 43.
Jevremović, D., Srećković, V. A., Marinković, B. P., Vujičić, V.: 2020, *Contrib. Astron. Obs. Skalnaté Pleso*, **50(1)**, 44.
Jureta, J. J., Milosavljević, A. R., Marinković, B. P.: 2014, *Int. J. Mass Spectrom.*, **365-366**, 114.
Kolarski, A., Komatina, S.: 2020, *Book of Abstracts*, International Symposium GEOSCIENCE 2020, November 20 - 22 2020, Bucharest, Romania, 81.
Kovačević, A., Kovačević Dojčinović, J., Marčeta, D., Onić, D.: 2020, *Book of Abstracts*, XIX Serbian Astronomical Conference, October 13 - 17, 2020, Belgrade, Serbia.
Majlinger, Z., Dimitrijević, M. S., Srećković, V. A.: 2020, *Mon. Not. R. Astron. Soc.*, **496(4)**, 5584.
Marinković, B. P., Bredehöft, J. H., Vujčić, V., Jevremović, D., Mason, N. J.: 2017, *Atoms*, **5(4)**, 46.
Marčeta, D., Novaković, B.: 2020, *Mon. Not. R. Astron. Soc.*, **498(4)**, 5386.
Mijić, Z., Perišić, M.: 2019, *Book of abstracts*, "Integrations of satellite and ground-based observations and multi-disciplinarity in research and prediction of different types of hazards in Solar system", Petnica Science Center, May 10-13, 2019, Geographical Institute "Jovan Cvijić" SASA, Belgrade, 51.
Milić Žitnik, I., Novaković, B.: 2016, *Aphys. Journ. lett.*, **816**, L31.
Milić Žitnik I.: 2019, *Mon. Not. R. Astron. Soc.*, **486**, 2435.
Milić Žitnik I.: 2020a, *Serb. Astron. Journ.*, **200**, 25.
Milić Žitnik I.: 2020b, *Mon. Not. R. Astron. Soc.*, **498(3)**, 4465.

[5]see e.g. *http://servo.aob.rs/mold*

Nina, A., Radovanović, M., Popović, L. Č., Černok, A., Marinković, B., Srećković, V., Kovačević, A., Radović, J., Čelebonović, V., Milić Žitnik, I., Mijić, Z., Veselinović, N., Kolarski, A., Zdravković, A.: 2020a, *Proceedings of the XII Serbian-Bulgarian Astronomical Conference (XII SBAC)*, Sokobanja, Serbia, September 25-29, 2020, Eds: L. Č. Popović, V. A. Srećković, M. S. Dimitrijević, A. Kovačević, Publ. Astron. Soc. Rudjer Bošković, **20**, 107.

Nina, A., Pulinets, S., Biagi, P. F., Nico, G., Mitrović, S. Dj., Radovanović, M., Popović, L. Č.: 2020b, *Science of the Total Environment*, 710, 136406.

Nina, A., Nico, G., Odalović, O., Čadež, V. M., Todorović, M. D., Radovanović, M., Popović, L. Č.: 2020c, *IEEE Geoscience and Remote Sensing Letters*, **17(7)**, 1198.

Papagiannopoulos, N., D'Amico, G., Gialitaki, A., Ajtai, N., Alados-Arboledas, L., Amodeo, A., Amiridis, V., Baars, H., Balis, D., Binietoglou, I., Comerón, A., Dionisi, D., Falconieri, A., Fréville, P., Kampouri, A., Mattis, I., Mijić, Z., Molero, F., Papayannis, A., Pappalardo, G., Rodríguez-Gómez, A., Solomos, S., Mona, L.: 2020, *Atmos. Chem. Phys.*, **20**, 10775.

Popović, L. Č., Srećković, V. A., Dimitrijević, M. S., Kovačević, A.: 2020, *Book of Abstracts*, XII Serbian–Bulgarian Astronomical Conference (XII SBAC) September 25 - 29, 2020, Sokobanja, Serbia, Astronomical Observatory, Belgrade, Serbia.

Rabasović, M. S., Rabasović, M. D., Marinković, B. P., Šević, D.: 2019, *Atoms*, **7(1)**, 6.

Radović, J.: 2020, Master thesis, Faculty of Physics, University of Belgrade, Serbia.

Srećković, V. A., Dimitrijević, M. S., Ignjatović, L. M.: 2020, *Contrib. Astron. Obs. Skaln. Pleso*, **50**, 171.

Šević, D., Rabasović, M. S., Križan, J., Savić-Šević, S., Rabasović, M. D., Marinković, B. P., Nikolić, M. G.: 2020a, *Opt. Quant. Electron.* **52**, 232.

Šević, D., Vlasić, A., Rabasović, M. S., Savić-Šević, S., Rabasović, M. D., Nikolić, M. G., Marinković, B. P., Križan, J.: 2020b, *Tehnika*, **75(3)**, 279.

Šević, D., Križan, J., Rabasović, M. S., Marinković, B. P.: 2021, "Temperature sensing using YAG:Dy single crystal phosphor", *Eur. Phys. J. D.*, submitted.

Vukalović, J., Maljković, J. B., Tökési, K., Predojević, B., Marinković, B. P.: 2021, *Int. J. Molec. Sci.* **22(2)**, 647.

Yang, P., Yang, G., Zhang, F., Jiang, B., Wang, M.: 2020, *Arch. Computat. Methods. Eng.*, accepted, $https://doi.org/10.1007/s11831-020-09401-9$.

Wislocka, A. M., Kovačević, A. B., Balbi, A.: 2019, *Astron. Astroph.*, 624, A71.

# II. Natural Hazards and Climate Change

Szeged, 21-23 May 2025

Conference Program

| Tuesday 20 May | |
|---|---|
| 18:00- | Ice Breaking event (Department of Physical and Environmental Geography, University of Szeged 6722 Egyetem u. 2-6 1st floor) |

| Wednesday 21 May | | | |
|---|---|---|---|
| 8:30-10:00 | Registration (Hungarian Academy of Sciences - Szeged Regional Committee, Main Building, 6720 Szeged, Somogyi utca 7.) | | |
| 10:00-10:30 | Opening Ceremony – *Main Hall (1st floor)* | | |
| 10:30-11:40 | Plenary Session – *Main Hall (1st floor)* | | |
| 11:40-12:00 | Coffee Break | | |
| 12:00-13:40 | Session 1 Advancing Hydroclimatic Hazard Assessment *Main Hall (1st floor)* | Session 2 Environmental Stressors and Agricultural Sustainability *Lecture Room 110 (1st floor)* | |
| 13:40-14:40 | Lunch | | |
| 14:40-16:40 | Session 3 Climate-Health Nexus *Main Hall (1st floor)* | Session 4 Geohazards *Lecture Room 110 (1st floor)* | Session 5 Plant Communities in Transition *Lecture Room 217 (2nd floor)* |
| 16:40-17:00 | Coffee Break | | |
| 17:00-19:00 | Poster session – short talks I *Main Hall (1st floor)* | Poster session – short talks II *Lecture Room 110 (1st floor)* | |
| 19:30- | Conference Dinner | | |

| Thursday 22 May | | | |
|---|---|---|---|
| 8:30-9:00 | Registration | | |
| 9:00-11:00 | Session 6 Health, Hazards and Awareness *Main Hall (1st floor)* | Session 7 Challenges of Water Management in a Changing Climate *Lecture Room 110 (1st floor)* | Session 8 Resilient Landscapes and Water Systems *Lecture Room 217 (2nd floor)* |
| 11:00- 11:20 | Coffee Break | | |
| 11:20-12:40 | Workshop 1 Public Health in the Context of Climate Change *Main Hall (1st floor)* | Workshop 2 Predictions and Management of Hydrological Extremes *Lecture Room 110 (1st floor)* | |
| 12:40-13:40 | Lunch | | |
| 13:40-15:00 | Workshop 3 Bridging Disciplines: Identifying Research Priorities on Nanoplastics and Climate Change *Main Hall (1st floor)* | Workshop 4 EU Funding and Green Priorities: Experiences and Expert Insights *Lecture Room 217 (2nd floor)* | Workshop 5 AI in Natural Hazards Research *Lecture Room 110 (1st floor)* |
| 15:00-15:20 | Coffee Break | | |
| 15:20- 17:20 | Session 9 Towards Resilient Agroecosystems *Main Hall (1st floor)* | Session 10 Environmental Hazards and Management *Lecture Room 110 (1st floor)* | |
| 17:20-17:40 | Closing ceremony, Young Researcher Presentation Award | | |

| Friday 23 May | |
|---|---|
| 09:00-16:00 | Field day |

# Detailed Program

| **Wednesday 21 May** | | |
|---|---|---|
| 8:30-10:00 | Registration | |
| 10:00-10:30 | Opening Ceremony<br>Main Hall (1st floor) | |
| 10:30-11:40 | Plenary Session<br>Main Hall (1st floor) | |
| 10:30-11:05 | Heatwaves and health – ways of adaptation | Anna Páldy (Specialist of Public Health and Epidemology, National Center for Public Health and Pharmacy) |
| 11:05-11:40 | Green transition or global green hype? | András Gelencsér (Atmospheric Chemist, Member of the Hungarian Academy of Sciences, University of Pannonia) |

| | | |
|---|---|---|
| 11:40-12:00 | **Coffee Break** | |

| 12:00-13:40 | Session 1: Advancing Hydroclimatic Hazard Assessment<br>*Main Hall (1st floor) Moderator: Tobias Conradt (Potsdam Institute for Climate Impact Research)* | |
|---|---|---|
| 12:00-12:20 | Evaluating unusual weather conditions in the past – a methodology and a visualisation platform | Márk Zoltán Mikes, Roland Hollós, Zsuzsanna Dezső, Rita Pongrácz |
| 12:20-12:40 | What can we learn about hail from laboratory studies? | Miklós Szakáll, Alexander Theis |
| 12:40-13:00 | Using ESA CCI Soil Moisture Data for Drought Characterization: Applications and Scientific Perspectives | Johanna Lems, Pierre Laluet, Nirajan Luintel, Wouter Dorigo |
| 13:00-13:20 | OPTRAM model based plot-level soil moisture mapping using Sentinel-2 imagery | Gábor Mátyás Gubucz, Boudewijn Van Leeuwen, Ferenc Kovács |
| 13:20-13:40 | Impact of drought on the sustainable development of the border area of Serbia with Bulgaria | Marko Sedlak , Nemanja Josifov, Vladimir Malinić |

| 12:00-13:40 | Session 2 Environmental Stressors and Agricultural Sustainability<br>*Lecture Room 110 (1st floor) Moderator: Ágnes Szepesi (University of Szeged)* | |
|---|---|---|
| 12:00-12:20 | Rhizosphere under pressure: how plastics disrupt plant growth and soil health | Gábor Feigl, Enikő Mészáros, Kamilla Kovács, Klaudia Hoffmann, Etelka Kovács, Katalin Perei, Attila Bodor |
| 12:20-12:40 | Peptaibols: bioactive natural compounds with the potential to mitigate the adverse effects of climate change in agricultural crops | Dóra Balázs, Chetna Tyagi, Tamás Marik, Gergő Terna, Fanni Kovács, Ákos Rozsnyói, András Szekeres, Mónika Varga, Csaba Vágvölgyi, Tamás Papp, László Kredics |
| 12:40-13:00 | Exploring the role of microbial infections in walnut production decline | Nóra Tünde Lange-Enyedi, Simang Champramary, Orsolya Kedves, Boris Indic, Attila Szűcs, Annamária Tüh, Árpád Brányi, Younes Rezaee Danesh, Omar Languar, Csaba Vágvölgyi, László Kredics, György Sipos |
| 13:00-13:20 | The impact of global megatrends on microfungi in the Pannonian Biogeographical Region: a climate change perspective | Donát Magyar, Zsófia Tischner, Anna Páldy, Sándor Kucsubé, Zsuzsanna Dancsházy, Ágnes Halász, László Kredics |
| 13:20-13:40 | Black Soils of Eurasia: two-decade environmental analysis (2001-2022) | Nándor Csikós, János Mészáros, Katalin Takács, Brigitta Szabó, Tamás Hermann, Éva Ivits, and Gergely Tóth |

| | | |
|---|---|---|
| 13:40-14:40 | Lunch | |

| | | |
|---|---|---|
| 14:40-16:40 | Session 3 Climate-Health Nexus<br>*Main Hall (1st floor) Moderator: Darinka Korovljev (University of Novi Sad)* | |
| 14:40-15:00 | Eco-Anxiety and Beyond: Understanding the Mental Health Dimensions of Climate Change | Zsuzsanna Máté |
| 15:00-15:20 | TÉR-EPI: a specialised spatial epidemiology system for monitoring population health at high resolution | Attila Juhász, Csilla Nagy, Beatrix Oroszi |
| 15:20-15:40 | Waterborne, water washed, water based and water-related diseases | Barbara Nieradko-Iwanicka |
| 15:40-16:00 | Climate change impacts on tourism in the 21st century: projections for Hungary and Szeged | Attila Kovács, Gergely Molnár |
| 16:00-16:20 | Consideration of climate change-related factors in vulnerability assessment frameworks for migrant health | Zoltán Katz, Kia Goolesorkhi, István Szilárd, Erika Marek |
| 16:20-16:40 | Artificial Intelligence and Machine Learning for Multi-Risk Assessment | Adanu Peter Worlasi |

| | | |
|---|---|---|
| 14:40-16:40 | Session 4 Geohazards<br>*Lecture Room 110 (1st floor) Moderator: Petru Urdea (West University of Timisoara)* | |
| 14:40-15:00 | Assessing luminescence sensitivity and ESR parameters as indicators of geomorphological processes in fluvial and aeolian settings | Gergő Magyar, Alida Timar-Gabor, Aditi K. Dave, Dávid Filyó, Tamás Bartyik, Viktor Homolya, Gábor Bozsó, György Sipos |
| 15:00-15:20 | Changes of the morphology of surface in the alluvial plane and loess plateau in the western part of Belgrade as a consequence of Pleistocene climate change and tectonic activity | David Mitrinović, Marija Perović, Branislava Matić, Srđan Kovačević |
| 15:20-15:40 | Sinkhole hazard in geoeducation: presentation of an online map | Tamás Telbisz, László Mari |
| 15:40-16:00 | Use of frequency ratio method and GIS for landslide susceptibility modeling: a case study in the South-Western part of Tajikistan | Faizulloev Shohnavaz Abduqodirovich, Alamov Bekhruz Ahmadshoevich, Rahimbekova Manizha Rahmonbekovna |
| 16:00-16:20 | The Influence of Mediterranean Hurricane Surges on Vertical Ground Motion Along the Southern Coast of Sicily, Italy | FX Anjar Tri Laksono, János Kovács |
| 16:20-16:40 | Paleotsunami records (?) and landscape reconstruction on the Western Black Sea coast (Mangalia) | Alfred Vespremeanu-Stroe, Luminița Preoteasa, Mihai Ionescu, Laurențiu Țuțuianu, Mihaela Dobre, György Sipos |

| | | |
|---|---|---|
| 14:40-16:40 | Session 5 Plant Communities in Transition<br>*Lecture Room 217 (2nd floor) Moderator: Zoltán Bátori (University of Szeged)* | |
| 14:40-15:00 | Community changes caused by an invasive alien C4 grass, and a promising biocontrol tool to suppress it | Alida Anna Hábenczyus, Csaba Tölgyesi, Róbert Pál, András Kelemen, Zoltán Bátori, Judit Sonkoly, Fanni Molnár, Kata Anna Bán, Kata Frei, Ádám Lőrincz, László Erdős, Zalán Czékus, Attila Ördög, Klára Terézia Kovács, Edina Tóth, Péter Török, Péter Poór |
| 15:00-15:20 | Climate change-related decline of Robinia Pseudoacacia forests in Hungary: a microbiome analysis | Boris Indic, Nóra Tünde Lange-Enyedi, Simang Champramary, Omar Languar, Attila Szűcs, Orsolya Kedves, Csaba Vágvölgyi, László Kredics, György Sipos |
| 15:20-15:40 | Mapping the occurrence of Asclepias syriaca using AI methods based on geotagged landscape photographs | Georgina Veronika Visztra, Péter Balázs, Ádám Makai, Ádám Katona, Márton Bence Balogh, Zalán Tobak, Péter Szilassi |
| 15:40-16:00 | Stable carbon and oxygen isotope ratios in Norway spruce (Picea abies (L.) Karst.) tree rings along an elevation gradient in the Rarău Mts (Romania) | Daniela Maria Llanos-Campana, Zoltan Kern, Ionel Popa, Aurel Perșoiu |
| 16:00-16:20 | Sown wildflower strips in urban areas–a strategy to enhance biodiversity of arthropods | Botond Magyar , Anna Viola Nagy, Helga Simon, Attila Torma |

| | | |
|---|---|---|
| 16:40-17:00 | Coffee Break | |
| 17:00-19:00 | Poster session – short talks I<br>*Main Hall (1st floor)* | Poster session – short talks II<br>*Lecture Room 110 (1st floor)* |
| 19:30- | Conference Dinner | |

## Thursday 22nd May

| | |
|---|---|
| 8:30-9:00 | Registration |

| | | |
|---|---|---|
| 09:00-11:00 | Session 6 Health, Hazards and Awareness<br>*Main Hall (1st floor) Ivan Miskulin (University of Osijek)* | |
| 09:00-09:20 | Role of public health in addressing emerging natural hazards | Tamás Pándics |
| 09:20-09:40 | Impact of Urban Green Spaces on Heatwave Mitigation in a Medium-Sized City | Nóra Skarbit, János Unger, Tamás Gál |
| 09:40-10:00 | Enhancing Climate Change Awareness in Medical Education: Assessing the Impact of CLIMATEMED Workshops in Serbia | Darinka Korovljev, Bojana Harrison, Marijana Ranisavljev, Valdemar Stajer, Nikola Todorovic, Dragan Milosevic, Borislav Tapavički, Sergej M. Ostojic |
| 10:00-10:20 | Impact of Seasonal Heating and the COVID-19 Pandemic on PM10 Levels in European Cities | Seyedehmehrmanzar Sohrab, Péter Szilassi |
| 10:20-10:40 | The Occupational Health and Safety of Climate Migrants through Accelerating Co-Innovation Capacity Building: A Conceptual Paper | Kia Goolesorkhi, István Szilárd |
| 10:40-11:00 | Non-Expert Understanding of Hazard Maps: An Eye-Tracking Study | Solmaz Mohadjer, Gökce Ergün, Max Schneider, Tom Schürmann, Michael Pelzer, and Peter Dietrich |

| | | |
|---|---|---|
| 09:00-11:00 | *Session 7 Challenges of Water Management in a Changing Climate*<br>*Lecture Room 110 (1st floor) Slobodan Kolakovic (University of Novi Sad)* | |
| 09:00-09:20 | Simplicity or complexity? Identifying the optimal approach for flood hazard mapping | Kaveh Ghahraman, Fatemeh Nooshin Nokhandan, Balazs Nagy |
| 09:20-09:40 | Advanced Mapping and Integrity Assessment of Artificial Levees Using Machine Learning–Driven Electrical Resistivity Tomography for Natural Hazard Risk Analysis | Diaa Sheishah, Enas Abdelsamei, Ahmed M. Ali, György Sipos |
| 09:40-10:00 | Cross-comparison of national drought monitoring products in Central Europe using a new drought impact database | Nirajan Luintel, Piet Emanuel Bueechi, Johanna Lems, Wouter Dorigo |
| 10:00-10:20 | Inappropriate land use and vegetation cover: water scarcity in the climate-affected lowland regions of Hungary | Benedek György Tóth, Zoltán Bátori, Alida Anna Hábenczyus, András Kelemen, Kata Frei, Orsolya Valkó, Balázs Deák, Csaba Tölgyesi |
| 10:20-10:40 | The impact of climate change on the thermal stratification of a shallow polymictic lake | Sebestyén Török, Péter Torma |
| 10:40-11:00 | Droughts and floods: monitoring, prediction and artificial intelligence in the Hungarian Water Management | Zoltan Liptay |

| | | |
|---|---|---|
| 09:00-11:00 | Session 8 Resilient Landscapes and Water Systems<br>*Lecture Room 217 (2nd floor) (Ferenc Kovács (University of Szeged)* | |
| 09:00-09:20 | Changing sodic lakes under the threat of antropogenic and climate impacts in the Southern Great Plain, Hungary | Zsuzsanna Ladányi, Zsolt Ladányi, Kitti Balog |
| 09:20-09:40 | Grazing disturbance can override habitat effects in karst doline microrefugia | Attila Torma, István E. Maák, Kata Frei, Nikolett Gallé-Szpisjak, Jelena Šeat, Ádam Lőrincz, Gábor Lőrinczi, Zoltán Bátori |
| 09:40-10:00 | Natural Water Retention Measures contribution to flood risk management | Branislava Matić, Barbara Karleuša, David Mitrinović |
| 10:00-10:20 | Geospatial analysis of beaver built ecosystem dinamics in the High-Resolution Aerial Monitoring Network System | Emese Zita Tóth, Zsolt Molnár, Gábor Bakó |
| 10:20-10:40 | Human disturbances and refugial capacity: biodiversity in doline microrefugia | Zoltán Bátori, Gábor Li, Kata Frei, Zsófia Krivács, Viktor Környei, Csaba Tölgyesi |
| 10:40-11:00 | Application of the hydrogeomorphological index (IHG) and morphological quality index (MQI) in rivers of Timiş county and Romanian Banat region to assess their fluvial quality | Daniel Ballarín, Fabian Timofte |

| | |
|---|---|
| 11:00-11:20 | Coffee Break |

| | | |
|---|---|---|
| 11:20-12:40 | Workshop 1<br>Public Health in the Context of Climate Change<br>*Main Hall (1st floor)* | Workshop2<br>Predictions and Management of Hydrological Extremes<br>*Lecture Room 110 (1st floor)* |

| | |
|---|---|
| 12:40-13:40 | Lunch |

| | | | |
|---|---|---|---|
| 13:40-15:00 | Workshop 3<br>Bridging Disciplines: Identifying Research Priorities on Nanoplastics and Climate Change<br>*Main Hall (1st floor)* | Workshop 4<br>EU Funding and Green Priorities: Experiences and Expert Insights<br>*Lecture Room 217 (2nd floor)* | Workshop 5<br>AI in Natural Hazards Research<br>*Lecture Room 110 (1st floor)* |

| | |
|---|---|
| 16:00-16:20 | Coffee Break |

| | | |
|---|---|---|
| 15:20-17:20 | Session 9 Towards Resilient Agroecosystems<br>*Main Hall (1st floor) Péter Poór (University of Szeged)* | |
| 15:20-15:40 | Microgreens and vertical farming- a sustainable tool for investigating plant salt stress responses | Ágnes Szepesi, Andrea Rónavári, Adedokun Oluwatosin Peace, Batnasan Ganbold, Rebeka Karginov, Péter Pálfi, Zoltán Kónya |
| 15:40-16:00 | Using Earth Observation and AI for Irrigation Management Amidst Meteorological Hazards: A Case Study in Limpopo, South Africa | Nxumalo Gift Siphiwe, Zsolt Feher, Ramabulana Tondani Sanah, Nagy Attila |
| 16:00-16:20 | Effect of irrigation with "greywater" on Triticum aestivum | Brigitta Roxána Horváthné Dani, Martin Horváth, Anna Skribanek |
| 16:20-16:40 | The Role of Historical and Recent Land Use and Land Cover Changes in Promoting Biological Invasions in Hungary | Márton Bence Balogh, Zalán Tobak, Dominik Kaim, Péter Szilassi |
| 16:40-17:00 | Large scale production of peptaibols for plant protection | Gergő Terna, Bence Váczi, Dóra Balázs, Fanni Kovács, Chetna Tyagi, Ákos Rozsnyói, András Szekeres, Mónika Varga, Csaba Vágvölgyi, Tamás Papp, László Kredics, Tamás Marik |
| 17:00-17:20 | Assessment of Vegetation Water Demand and Drought Index in Arid and Semi-Arid Regions Using Satellite Data and Plant Water Metabolism | Mukesh Singh Boori, Komal Choudhary |

| | | |
|---|---|---|
| 15:20-17:20 | Session 10 Environmental Hazards and Management<br>*Lecture Room 110 (1st floor) Péter Szilassi (University of Szeged)* | |
| 15:20-15:40 | Conservation potential of abandoned sand mines | Szandra Sárszegi-Pék, Márton Szabó, Balázs Deák, Orsolya Kiss, Kristóf Süveges, Orsolya Valkó, András Kelemen |
| 15:40-16:00 | The devastating impact of a landslide on a home (case study in Slovenia) | Joze Janez, Nina Gognjavec, Vlasta Benedik |
| 16:00-16:20 | Introducing the first ecovoltaic parks of Hungary: a reconciliation between solar development and nature conservation | Csaba Tölgyesi, Botond Magyar, Kata Frei, Alida Anna Hábenczyus, Róbert Gallé |
| 16:20-16:40 | From micropollutant removal to greenhouse gas monitoring: New challenges in the wastewater treatment sector | Csenge Nagy-Mezei, Anikó Bezsenyi, Imre Gyarmati, Levente Kardos |
| 16:40-17:00 | Microplastic Pollution in Hungarian Water Bodies: Urban Ponds and the Tisza River System | Viktória Blanka-Végi, Alexia Balla, Tímea Kiss, Gabriella Hertelendy, Izabella Babcsányi |
| 17:00-17:20 | The effect of water pollution caused by detergent residues on living aquatic organisms | Brigitta Roxána Horváthné Dani, Martin Horváth, Anna Skribanek |

| **Poster Session I (Wednesday, 21 May 17:00-19:00)**<br>*Main Hall (1st floor) Izabella Babcsányi (University of Szeged)* | |
|---|---|
| Agroclimatic Trends and Adaptation: Challenges and Future Perspectives in Hungary | Erik Kovács, Balázs Zay, János Puskás |
| Biodiversity of cultivable bacteria in the rhizosphere of industrial crop plants in Hungary | Orsolya Kedves, Tamás Zsolt Polyák, Katalin Perei, Csaba Vágvölgyi, László Kredics |
| Comparison of salt stress induced biochemical responses of Lepidium sativum (garden cress) and the salt tolerant Lepidium crassifolium | Batnasan Ganbold, Adedokun Oluwatosin Peace, Rebeka Karginov, Ágnes Szepesi |
| Development of a healthy casing alternative from spent mushroom compost | Henrietta Allaga, Dóra Horkics, Ádám Bordé, András Varga, Rita Büchner, Terézia Kovács, András Misz, Csaba Csutorás, Judit Bajzát, Nóra Bakos-Barczi, Csaba Vágvölgyi, László Kredics |
| Effect of plasma-activated water seed priming on the development of Arabidopsis thaliana seedlings in a drought stress model system | Tamás Bodor, Gábor Fejes, Kinga Kutasi, Zsuzsanna Kolbert |
| Future crop yield trends across Europe from past observations and ISIMIP climate scenarios | Tobias Conrad |
| Isolation, identification and characterisation of potential biocontrol agents of walnut pathogens in Turkey and Hungary | Ahmet Akköprü, Younes Rezaee Danesh, Orsolya Kedves, Semra Demir, Emre Demirer Durak, Adnan Yaviç, Solmaz Najafi, Gokhan Boyno, Ceylan Pınar Uçar, Betül Yıldız Fırat, Árpád Brányi, Nóra Tünde Lange-Enyedi, Simang Champramary, Boris Indic, György Sipos, Csaba Vágvölgyi, László Kredics |
| Osmotic stress-induced anatomical changes in pea (Pisum sativum L.) leaves | Réka Szőllősi, Gábor Fejes, Tamás Bodor, Zsuzsanna Kolbert |
| Enhancing hydrocarbon biodegradation: Repeated application of extracellular organic matter from Micrococcus luteus in used lubricant oil-contaminated soils | Klaudia Hoffmann, Enikő Mészáros, Gábor Feigl, Krisztián Laczi, Katalin Perei, Attila Bodor |
| A Research Station Plan for the Global Challenges of the 21st Century | László Horváth, Zoltán Bozóki, Edit Mikó |
| Plasma activated water-based seed pre-treatment affects the development, in planta reactive oxygen- and nitrogen species and photosynthetic activity of osmotic-stressed pea plants | Gábor Fejes, Tamás Bodor, Réka Szőllősi, Kinga Kutasi, Zsuzsanna Kolbert |
| Cellulose content in annual increments of Norway spruce (Picea abies (L.) Karst.) along an elevation gradient in the Rarău Mts (Romania) | Daniela Maria Llanos-Campana, Zoltan Kern, Ionel Popa, Aurel Perșoiu |
| Frost rings in Swiss Stone Pine (Pinus cembra) from Rodna Mts. (Romania) - Anatomical evidence of late spring frost in the past centuries | Eszter Mocsári, Balázs Nagy, Ionel Popa, Zoltán Kern, Árvai Mátyás |
| The impact of polyethylene-based plastics and heavy metals on rapeseed root growth | Kamilla Kovács, Enikő Mészáros, Dorottya Hicz, Gábor Feigl |
| The role of chitosan-encapsulated NO-donors in enhancing tomato resistance to fungal infections | Dóra Kondak, Selahattin Kondak, Tamás Bodor, András Kukri, Réka Szőllősi, Zsuzsanna Kolbert |
| In silico assessment of the ecotoxicological characteristics of terbuthylazine as a pollutant in surface waters | Mitrović T. , Obradović D., Lazović S., Perović M. |
| Zinc Oxide Nanoparticles: Dual Effects on Broccoli Growth Under Nutrient and Salinity Stress | Adedokun Oluwatosin Peace, Batnasan Ganbold, Rebeka Karginov, Andrea Rónavári, Ágnes Szepesi, Zoltán Kónya |
| The role of climate microrefugia in shaping intraspecific trait variability in Myrmica ruginodis | Bonita Ratkai , Kata Anna Bán , Kata Frei , Gergely Horváth, Gábor Li, Ádám Lőrincz , Gábor Lőrinczi , Fanni Pécsy, Zoltán Bátori, István Elek Maák |
| Temperature and geographical location induced fluctuations of population density of European ground squirrels in Hungary | Csongor Gedeon; Olivér Váczi; Felix Knauer; Mátyás Árvai; Franz Suchentrunk |
| The accelerated spruce dieback in Central Europe is a warning sign of the climate change | Zsuzsa Lisztes-Szabó , Mihály Braun, Albert Tóth, Elemér László, József Lennert , Anna F. Filep |
| Extreme Dry Events in Vojvodina: Observations and Climate Change Projections | Atila Bezdan, Jovana Bezdan |
| Observed long-term trend in various extreme precipitation-related climate indices | Csilla Simon, Mónika Lakatos, Olivér Szentes |
| Eutrophication in Freshwater Ecosystems: Impacts of Nutrients, Groundwater, and Climate Change | Marija Perović, Vesna Obradović, David Mitrinović, Tatjana Mitrović |

| **Poster Session II (Wednesday, 21 May 17:00-19:00)**<br>*Lecture Room 110 (1st floor) György Sipos (University of Szeged)* | |
|---|---|
| Biodegradable plastics: A growing concern for early plant development | Enikő Mészáros, Kamilla Kovács, Gábor Feigl |
| Lateral channel migration and riverbank degradation: A natural process or environmental threat? | Marko Langović, Slavoljub Dragićević, Nenad Živković |
| Urbanisation effect on the butterfly communities of river dikes | Szabolcs Borbáth-Székely-Varga, Attila Torma |
| 1500 Years of Flooding in Romania: Climatic and Anthropogenic Influences | Ioana Persoiu, Maria Radoane, Gabriela Florescu, Aurel Persoiu, Alexandru Hegyi |
| Statistics on the frequency of rain and snow-rain floods on rivers of the Tisza basin within of Ukraine | Stanislav Moskalenko |
| Improving wind hazard assessment using high-resolution numerical weather prediction models and interpolation techniques in Hungary | Kinga Bokros, Beatrix Izsák, Natália Szalontainé Gáspár, Dávid Lancz, Mónika Lakatos, Rita Pongrácz |
| Natural Hazards and Society in Croatia: Impacts and Public Health Interventions | Ivan Miskulin, Ivana Kotromanovic Simic, Nika Lovrincevic Pavlovic, Jelena Kovacevic, Maja Miskulin |
| Investigating Mortality Trends in a Warming Climate with a special focus on urban population in Asia | Rita Pongrácz |
| The influence of small canopy gaps and previous logging on understorey plant communities in topographic depressions | Kata Frei, Gábor Li, Bonita Ratkai, Benedek György Tóth, László Erdős, Csaba Tölgyesi, Zoltán Bátori |
| Effects of natural and anthropogenic disturbances on microrefugia: the soil microbiota of dolines | Zsófia Krivács, Kata Frei, Gábor Li, Csaba Tölgyesi, Attila Bodor, Roland Wirth, Gergely Maróti, Zoltán Bátori |
| Advancing soil erosion mapping with Machine Learning: A comparative performance assessment | Fatemeh Nooshin Nokhandan, Erzsébet Horváth |
| Geospatial and Geomorphometric Analysis on Landslides based on UAV Remote Sensing and GIS – Case from the Crnik Landslide in North Macedonia | Bojana Aleksova, Ivica Milevski Tin Lukić |
| Geospatial Modeling of Landslide and Wildfire Susceptibility Using GIS and Remote Sensing Data in Djerdap UNESCO Global Geopark, Serbia | Uroš Durlević, Nina Čegar, Aleksandar Kovjanić, Natalija Batoćanin |
| Landscape changes and remediation in illegal landfill near Sombor, Serbia (2015-2025): Environmental hazards and recovery | Aleksandar Pilipovic, Petróczy Máté Dániel, Szatmári József |
| Small canopy gaps increase the refugial capacity of karstic microrefugia in the face of anthropogenic climate change | Gábor Li, Bonita Ratkai, Benedek György Tóth, László Erdős, Csaba Tölgyesi, Kata Frei, Zoltán Bátori |
| Natural multihazards analysis in Hungary | Gábor Mezősi |
| Macroeconomic challenges of climate change and the contribution of the circular economy to community resilience to natural disasters | Milica Stanković, Gordana Mrdak |
| Natural disaster beyond media barricades? Online news coverage on the 2022 drought in Hungary | Péter Kacsó, Viktória Priszcilla Hafenscher, Ferenc Jankó |
| Prospects of social action - Possible legal framework in avoiding climate change crisis | Csaba Jaksa |
| DIRECTED Project: Enhancing Disaster Resilience in Europe | Levente Huszti |
| Investigation of the relationship between solar activity, natural hazards and human mobility: Evidence from the Balkans | Milica Langović, Vladimir A. Srećković, Zoran Mijić, Marko Langović |
| AI-Driven Geoinformatics Solutions for Precision Agriculture in a Climate-Stressed Region | Boudewijn van Leeuwen |
| Hydrologic and hydraulic analysis of the 2005 flood on the Bârzava River and its impact on hydrotechnical infrastructure | Minda-Codruța Bădăluță , Petru Urdea, Alexandru Onaca, Fabian Timofte |
| Evaluating Levee Stability: Simulating Flood Scenarios Using Time-Lapse ERT for Improved Risk Mitigation | Ahmed M. Ali, Attila Timar, James Boyd, Enas Abdelsamei, Diaa Sheishah, Alexandru Hegyi, György Sipos |

# Investigation of the relationship between solar activity, natural hazards and human mobility: Evidence from the Balkans

Milica Langović[1], Vladimir A. Srećković[1], Zoran Mijić[1], Marko Langović[2]
[1]*Institute of Physics Belgrade, University of Belgrade, Belgrade, Serbia*
[2]*Faculty of Geography, University of Belgrade, Belgrade, Serbia*

Solar activity, as the main feature of the Sun, determines the changes in the solar-terrestrial environment and affects technologies, nature, humans and their activities on earth. The aim of this paper is to investigate the complex relationship between solar activity, natural hazards and human mobility in the Balkan Peninsula in the period 2008-2023. The primarily hypothesis of this study is that all processes in the solar-terrestrial environment are interconnected and that the change of one element in this system influences the changes of another element. In this regard, special emphasis is placed on the study of the characteristics of environmental migration as a phenomenon triggered by natural hazards, and possibly related to solar activity. The methodological framework includes data on Solar cycle 24 and Solar cycle 25 (current cycle) and environmental migration, as well as the application of statistical methods based on correlation procedures. The research results indicate intertwined connections among the mentioned categories, and revealed a statistically significant correlation between the number of sunspots (as indicator of solar activity) and internal displacements caused by weather-related hazards in the Balkans during the observed period. The paper offers insights into a new transdisciplinary field in which human mobility patterns have not yet been incorporated into the understanding of the Sun-Earth system, and provides guidelines for future research on this issue.